ASME
SETTING THE STANDARD

Journal of Fluids Engineering

Published Bimonthly by ASME

VOLUME 128 • NUMBER 4 • JULY 2006

Transactions of the ASME, Journal of Fluids Engineering (ISSN 0098-2202) is published bimonthly (Jan., Mar., May, July, Sept., Nov.) by The American Society of Mechanical Engineers, Three Park Avenue, New York, NY 10016. Periodicals postage paid at New York, NY and additional mailing offices.
POSTMASTER: Send address changes to Transactions of the ASME, Journal of Fluids Engineering, c/o THE AMERICAN SOCIETY OF MECHANICAL ENGINEERS, 22 Law Drive, Box 2300, Fairfield, NJ 07007-2300.
CHANGES OF ADDRESS must be received at Society headquarters seven weeks before they are to be effective. Please send old label and new address.
STATEMENT from By-Laws. The Society shall not be responsible for statements or opinions advanced in papers or ... printed in its publications (B7.1, Par. 3).

TECHNICAL PAPERS

(Contents continued on inside back cover)

This journal is printed on acid-free paper, which exceeds the ANSI Z39.48-1992 specification for permanence of paper and library materials. ♾™
♻ 85% recycled content, including 10% post-consumer fibers.

TECHNICAL BRIEFS

The ASME Journal of Fluids Engineering is abstracted and indexed in the following:

Applied Science & Technology Index, Chemical Abstracts, Chemical Engineering and Biotechnology Abstracts (Electronic equivalent of Process and Chemical Engineering), Civil Engineering Abstracts, Computer & Information Systems Abstracts, Corrosion Abstracts, Current Contents, Ei EncompassLit, Electronics & Communications Abstracts, Engineered Materials Abstracts, Engineering Index, Environmental Engineering Abstracts, Environmental Science and Pollution Management, Excerpta Medica, Fluidex, Index to Scientific Reviews, INSPEC, International Building Services Abstracts, Mechanical & Transportation Engineering Abstracts, Mechanical Engineering Abstracts, METADEX (The electronic equivalent of Metals Abstracts and Alloys Index), Petroleum Abstracts, Process and Chemical Engineering, Referativnyi Zhurnal, Science Citation Index, SciSearch (The electronic equivalent of Science Citation Index), Shock and Vibration Digest, Solid State and Superconductivity Abstracts, Theoretical Chemical Engineering

Simulations and Measurements of Pressure Oscillations Caused by Vortex Ropes

Zhengwei Wang
Department of Thermal Engineering,
Tsinghua University,
Beijing, P.R.C. 100084
e-mail: wzw@mail.tsinghua.edu.cn

Lingjiu Zhou
College of Water Conservancy and
Civil Engineering,
China Agricultural University,
Beijing, P.R.C. 100083

Pressure oscillations caused by vortex rope were measured in the draft tube of a prototype Francis turbine. The three-dimensional, unsteady Reynolds-averaged Navier-Stokes equations with the RNG $\kappa-\epsilon$ turbulence model were solved to model the flow within the entire flow path of the prototype hydraulic unit including the guide vanes, the runner, and the draft tube. The model was able to predict the pressure fluctuations that occur when operating at 67–83% of the optimum opening. The calculated frequencies and amplitudes of the oscillation show reasonable agreement with the experiment data. However, the results at 50% opening were not satisfactory. Pressure oscillations on the runner blades were found to be related to the precession of vortex ropes which caused pressure on the blades to fluctuate with frequencies of $-f_n+f_d$ (f_n is the rotational frequency and f_d is vortex procession frequency). The peak-to-peak amplitudes of the pressure oscillations on the blades at the lower load conditions (67% opening) were higher than at higher load conditions (83% opening). Fluctuations on the suction side tended to be stronger than on the pressure side. [DOI: 10.1115/1.2201631]

Introduction

Francis turbines usually experience unsteady flow fluctuations at partial loads, due to a strong helical vortex rotating like a whirling rope in the center of the draft tube. The precession of the vortex rope causes pressure fluctuations in the draft tube which sometimes can lead to variations in the power output or vibrations of the shaft and damage to the runner blades. Extensive investigations have been done on the phenomenon through in situ measurements. The results have included frequencies and amplitudes of the fluctuations caused by the vortex rope precession as well as system resonance [1,2]. Computational fluid dynamics simulations and improved measurement techniques have provided more results. Ruprecht et al. [3], Sick et al. [4] and Arpe and Avellan [5] compared calculated results with experimental data from the model tests to show that the amplitudes and frequencies agreed quite well before the elbow. Skoták et al. [6], Zhou and Wang [7] and Wu and Dai [8] investigated the influence of the draft tube inlet condition on the vortex rope behavior; Wang and Zhou [9] related the pressure oscillations to the operating conditions. Recently Lowys et al. [10] reported measurements of the pressure fluctuations on a Francis runner blade and gave a primary analysis and a simple relationship between fluctuation amplitude and the power load. However, few comparisons have been made between simulation results and experimental data for prototypes, because the blade profile cannot be easily obtained and the pressures on the runner blades can not be easily measured. Experimental measurements are difficult since lots of flow paths are buried in concrete so transducers cannot be easily installed. For prototypes the available experimental data are limited. Numerical simulations can be used to interpret the complex flow phenomena in cooperation with limited experimental information. For example, many simulations (even for models) and measurements have focused on the draft tube itself because of the difficulty in performing measurements in rotating flow channels. For practical engineering designs, more information is needed about how the vortex rope in the draft tube affects the dynamic loads on the runner blades.

The present paper describes simulation of a prototype water turbine with comparison to experimental results. The main flow features are then analyzed based on the simulation results, with a detailed analysis of the pressure oscillations on the runner blades.

Experimental Prototype

The pressures were measured in a Francis turbine with a non-dimensional specific speed of 10.93. The runner had 13 blades with 20 guide vanes. The rotational speed of the runner was 100 rpm. A meridian view of the runner and a cross section of the draft tube are shown in Fig. 1. The draft tube cross section gradually changed from circular to rectangular in the elbow. A splitter was installed in the diffusion part of the draft tube.

The operating conditions for the simulation are listed in Table 1. In the table the number after "g" indicates the guide vane opening, for example, "g8" means guide vane angle of 8 deg. The number after "H" indicates head. For example, "H68" means an operating head of 68 m. Column a/a_o is the relative opening where a_o represents the optimum opening at the operating head. For the selected operating conditions, the Reynolds number Re was estimated to range from 6×10^6 to 1.2×10^7.

Another case with a non-dimensional specific speed of 12.075 was also analyzed with 53–78% openings with the results compared with the experimental data. The results were similar so they are not presented here.

Computational Domain and Recording Points

The runner and the draft tube were both included in the calculation to include the hydrodynamic coupling between the runner and the draft tube. The spiral case and stay vanes were not included to reduce calculation time. The inlet velocity direction was calculated using a steady flow analysis which included the spiral case, stay vanes, and guide vanes. This simplification was too coarse if the efficiency was to be evaluated, but practical experience shows that the main flow features were captured by the analysis.

The final mesh had about 250,000 nodes, with 56,000–60,000 nodes inside the guide vanes (depending on the operating conditions), 105,436 nodes insider the runner and 88,191 nodes inside the draft tube. A mesh with about 350,000 nodes was also tested and showed no evident improvement. Further increases in the number of nodes made the iteration too slow.

Contributed by the Fluids Engineering Division of ASME for publication in the JOURNAL OF FLUIDS ENGINEERING. Manuscript received June 23, 2004; final manuscript received January 20, 2006. Assoc. Editor: Akira Goto.

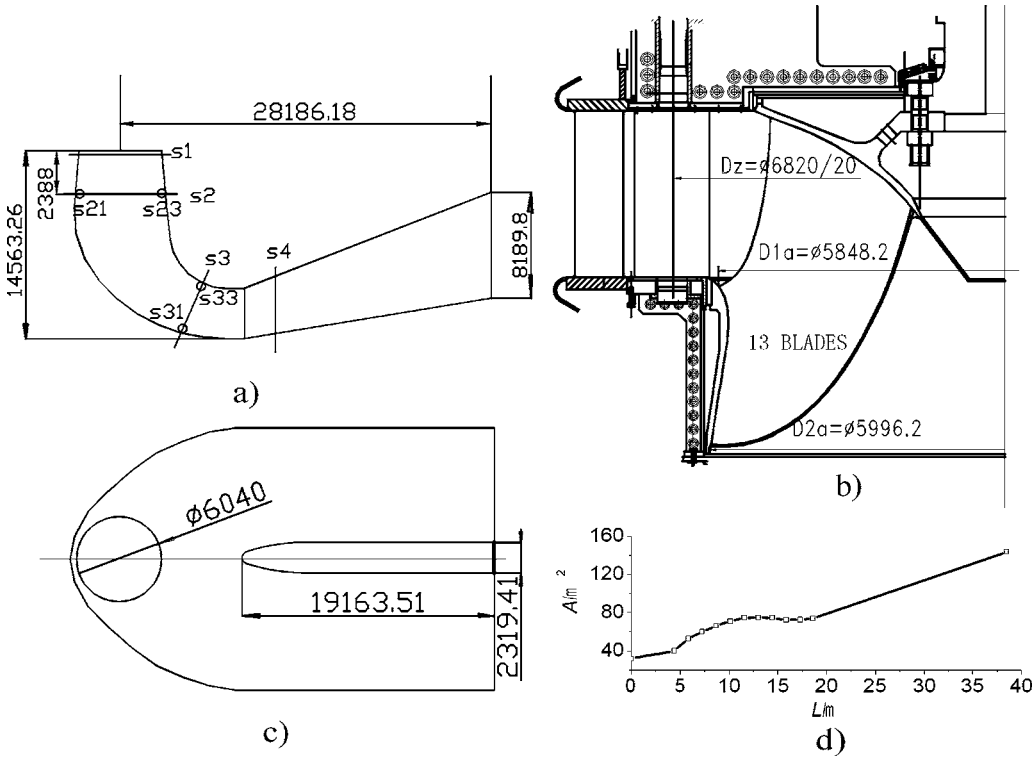

Fig. 1 Francis turbine geometry (unit in mm): (*a*) side view of the draft tube; (*b*) planform of the draft tube; (*c*) meridian view of the runner; (*d*) cross section of the draft tube

Recording Points

During the calculations, data were saved at 27 specific points inside the one channel between two blades. Among them, 9 were on the blade pressure side as shown in Fig. 2 (namely bp-1–bp-9), 9 were on the suction side arranged in the same order (namely bs-1–bs-9), and 9 were between the two blades. These points rotated with the runner. In this way, the data reflect the pressures on the blade during operation. Data points were also set in four sections (namely, s1, s2, s3 and s4, see Fig. 1) in the draft tube as shown in Fig. 2. These points were in the stationary frame of reference. Among them, s1 was near the draft tube inlet, s2 was located at the height of measuring point in the draft tube, s3 was in the middle of the elbow and s4 was after the elbow. The arrangement of points is shown in Fig. 2. Point 1 on the s2 plane was named s21 and point C on the s1 plane was named s1C with the other points named in the same way. Point s21 was the measuring point which was near the entrance hole of the draft tube (also shown in Fig. 1).

Table 1 Operating conditions for simulations

Operating conditions	a/a_o	Operating conditions	a/a_o
g12-H68	50%	g20-H68	83%
g16-H68	67%	g20-H75	83%
g16-H75	67%	g24-H68	100%

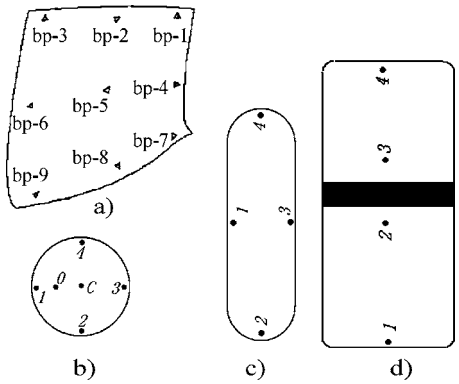

Fig. 2 Recording points: (*a*) on the blade surface; (*b*) on section s1 and s2; (*c*) on section s3; (*d*) on section s4

Numeric Method

Turbulence Model. The computer's capacity limited the mesh size and the selection of the turbulence model. For the flow field inside the prototype turbine, the large eddy simulation method requires a very fine mesh near the wall and in areas with high shear which would require extremely long calculation times. Therefore, a Reynolds averaged Navier-Stokes (RANS) simulation was performed with combination of the RNG $\kappa-\epsilon$ turbulence model with model constants $c_{1\epsilon}=1.42$, $c_{2\epsilon}=1.68$, $C_\mu=0.0845$, $\beta=0.012$, $a=1.39$, and $\eta_0=4.38$ [11,12]. Log-law wall condition was adopted.

Discretization. An unstructured mesh was used so that the cell density could be controlled manually based on the flow features. The water was considered to be incompressible. The time-dependent RANS model was discretized using the control-volume technique with the SIMPLEC scheme and a collocated grid combined with momentum interpolation. A second-order upwind scheme was used for the convection terms with a central difference scheme for the diffusion terms in the momentum equations. The time step was 0.008333 s, which was 1/72 of runner rotational period.

Boundary Condition. With the guide vanes included in the calculational domain, the inlet boundary conditions were the natural flow conditions. The total pressure and the turbulence condi-

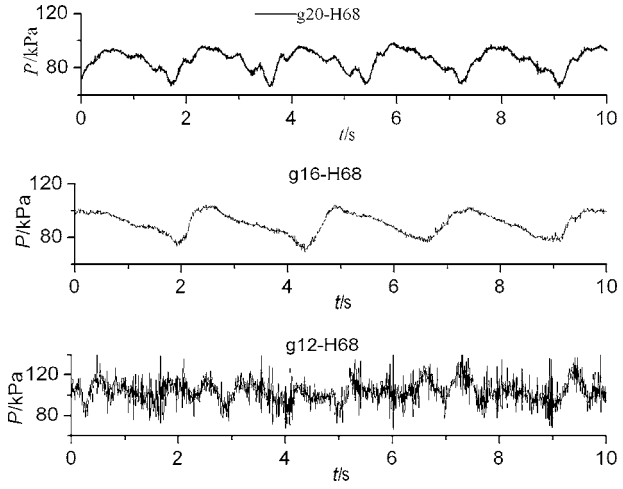

Fig. 3 Measured pressure fluctuations at point s21 (without filtering)

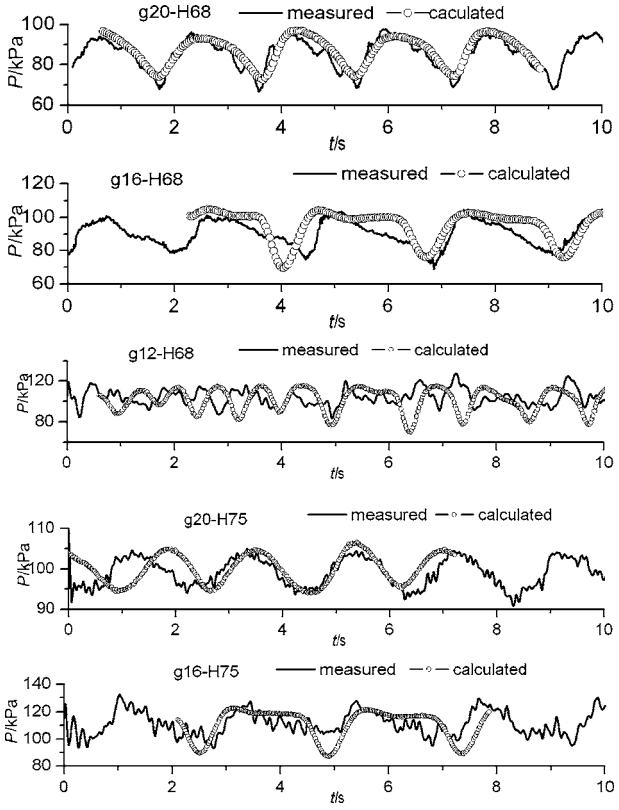

Fig. 4 Comparison of experimental data and calculated pressure fluctuations at point s21 (The measured pressure fluctuations were filtered with cutoff frequencies of 30 Hz for g20-H68 and g16-H68, 8 Hz for g12-H68 and g16-H75 and 10 Hz for g20-H75.)

tion were set at the inlet of the guide vanes with the inlet velocity direction defined from a steady flow calculation including the spiral case (with about 63,400 nodes), stay vanes (with about 39,600 nodes), and guide vanes (with 56,000–60,000 nodes). The inlet turbulence kinetic energy and dissipation rate were set to be 0.0655 and 0.0052. The model including the guide vanes was expected to capture the pressure oscillations caused by the rotor-stator interaction. The outlet static pressure condition was set based on the downstream water level when the measurements were taken. The interfaces between the guide vanes, the runner, and the draft tube were modeled with a sliding interface to model the rotating mesh in the runner domain. The upstream variables were passed to the downstream locations by interpolation at the interfaces.

Experimental Measurements

A pressure transducer was installed near the draft tube entrance (Point s21 in Fig. 1), since this was the only point that accessible. The transducer measurement range was −100–500 kPa with a precision of ±0.2%FS. The sampling frequency was 204.8 Hz with samples recorded to 20 s. The calculations were compared with the experimental results only at this point.

Results and Comparison

Of the various operating conditions simulated in this study, g24-H68 was closest to the optimum conditions. Both the calculated and measurement results showed no obvious pressure oscillations at this point. So the pressure waves were not compared for this condition. The calculated and measured results then were compared here for the other conditions.

Measurement Results. The experimental results show that as the flow rate is reduced, the pressure oscillations changed from regular waves to signals with much turbulence at a specific operating head. The low frequency rotation and precession of the vortex core was most significant at 83% and 67% openings (Fig. 3, conditions g20-H68 and g16-H68). However, much turbulence also appeared at 50% opening (Fig. 3, g12-H68) whose low frequencies were no longer obvious. The pressure fluctuations showed the same tendencies at high heads (H=75 m) with the openings of 83% and 67%.

Comparison of Calculations and Measurements. After about 2 s (3–4 rotational periods), the pressure fluctuations of the monitored points became quite regular. The pressures for all the selected points were then recorded. The calculated pressure oscillations at point s21 are plotted in Fig. 4 for comparison. The measured signals were filtered for comparison with the calculated data. For all conditions, the dominant frequency and its amplitude calculated using fast Fourier transform (FFT) analysis and measured signals is listed in Table 2. The low frequencies for measured g12-H68 signal were within a wide band so the band range was given in Table 2.

The calculated pressure oscillations agree reasonably well with the experimental data at the 67% and 83% opening. The lower frequencies were reasonably well predicted, but all the calculated waves were relatively smooth while the measured waves contained various high frequencies. This was especially obvious for the g12-H68 case where the predicted pressure fluctuations were far from acceptable. The data in Table 2 show that the amplitudes for the dominant frequencies were slightly overestimated, especially for the smaller openings (67% and 50%).

Flow Patterns in the Draft Tube. The flow patterns inside the draft tube are presented in Fig. 5 for two typical conditions. The vorticity magnitude iso-surface in the draft tube appears like the

Table 2 Comparison of predicted and measured low frequency and amplitude

Operating condition	Calculated		Measured	
	f/f_n (Hz)	A (Pa)	f/f_n (Hz)	A (Pa)
g12-H68	0.499	6748.2	0.09–0.874	1241.0
g16-H68	0.224	5220.1	0.27	3315.8
g20-H68	0.327	4914.8	0.33	4728.4
g16-H75	0.245	6172.3	0.266	4689.2
g20-H75	0.333	2635.0	0.293	2226.9

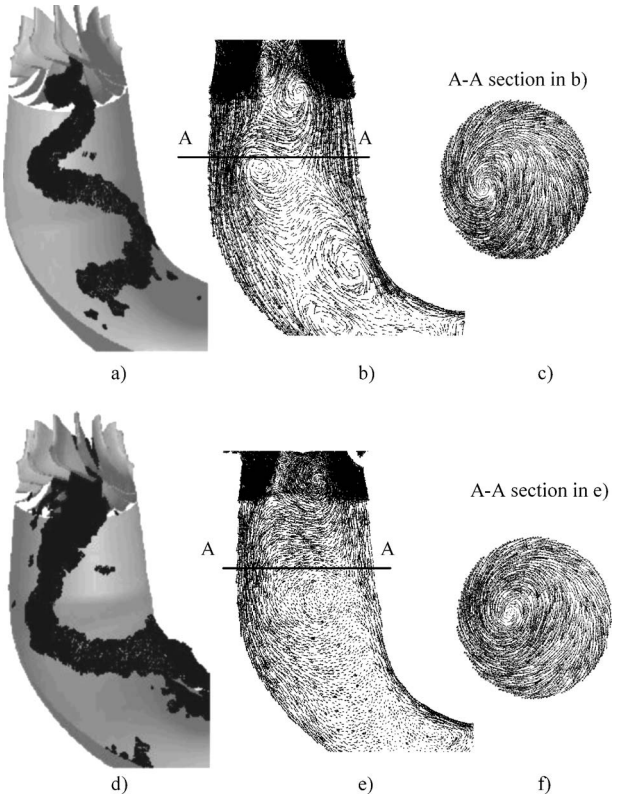

Fig. 5 Flow features in the draft tube. Parts *a-c* are for g20-H68, (*a*) vortex rope; (*b*) velocity vectors on the middle plane of the draft tube; (*c*) velocity vectors in section A-A in part *b*. Parts *d-e* are for g16-H68; (*d*) vortex rope; (*e*) velocity vectors on the middle plane of the draft tube; (*f*) velocity vectors in section A-A in part *e*.

vortex rope observed in the model test. The results show that an organized vortex rope was usually accompanied by a regular wave. In Fig. 5 the g20-H68 case (83% opening) had a very regular vortex rope in the draft tube. With decreasing flow rate, the vortex core gradually expanded (g16-H68, 67% opening) and the turbulence increased (Fig. 5(*e*)). With further decreases in the opening, the vortex breaking induced more instabilities and turbulence in the draft tube with the vortex rope was then no longer obvious.

The vorticity at any point on the helical vortex rope has two main components. One is the tangential component which is seen in the middle plane of the draft tube (Figs 5(*b*) and 5(*e*)). The other component is the axial component which is shown in Figs. 5(*c*) and 5(*f*). The angle of the helix rope depends on the ratio of the tangential and axial vorticities. For example, the ratio for the g20-H68 case was larger than for the g16-H68 case, so the vortex rope for g20-H68 has more twist than for g16-H68. Near the center of the hub the flow is reversed because of the tangential vortex (Figs. 5(*b*) and 5(*e*)). The reversed flow greatly affected the flow field inside the runner as will be discussed later. Figure 5 clearly shows the differences in the vortex rope behavior for the different operating conditions with the vortex rope for g16-H68 thicker than for g20-H68. Near the hub the reversed flow area for g16-H68 is also wider than for g20-H68.

Discussion of Results

Generally, the calculated waves were smoother than the experimental measurements. So the high frequencies were not well predicted perhaps due to the inherent limitations in the $\kappa-\epsilon$ turbulence model and the relatively coarse mesh. The $\kappa-\epsilon$ model is based on the ensemble averaged Navier-Stokes equations. For

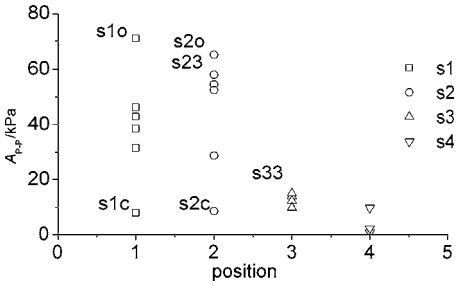

Fig. 6 Pressure amplitudes at various locations in the draft tube

67% and 83% opening the predictions gave a very regular vortex rope (Fig. 5). In such cases the pressure field was dominated by the periodic rotating and precession of the vortex rope, so the solution of the unsteady RANS with a relatively coarse mesh can reflect these averaged pressure fluctuations. For the small 50% opening, the vortex was broken and the pressure field was more affected by small scale turbulence. However, the RNG $\kappa-\epsilon$ model with a coarse mesh cannot reveal the detailed information of the turbulence at all scales, so the calculated results were not satisfactory for 50% opening.

The overestimation of the amplitudes at the smaller opening may also be due to the single phase assumption. At smaller opening, the pressure in the vortex core was very low with cavitation, thus the real vortex core contained a large amount of vapor. The vapor changes the wave speed which was not considered in the present calculations since the fluid was assumed to be incompressible water. Vapor in the liquid will increase the fluid compressibility and reduce the pressure oscillation amplitudes. Future calculation will include cavitation.

Pressure Fluctuations at Various Points Inside the Draft Tube

Generally in a power plant, pressure measurement locations in the draft tube are very limited because the draft tube is buried in concrete. The draft tube entrance was the only accessible location in this case, so only the predictions at entrance (s21) can be compared with measurements. The flow conditions for which the predicted results agree well with the measurements were chosen for further analysis of the pressure amplitudes at various locations in the draft tube. The peak-to-peak amplitudes of the pressure fluctuations at these points are plotted in Fig. 6.

On s1 and s2 point 0 always has the highest amplitude while point C has the lowest amplitude compared with the other points because point 0 is located very near the vortex core while point C is at the center of the section. Point 3 on s3 always had higher amplitude than points 1, 2, and 4. This phenomenon was also observed in some model experiments [9] which found that fluctuations near the inner surface of the elbow were higher than near the outer surface due to the influence of the curved elbow.

Figure 6 also shows that the pressure amplitudes gradually decrease along the draft tube. The pressure fluctuations on the s4 section were always much lower than on the other sections mainly due to the splitter wall which breaks up the vortex rope. Due to the combined effect of curved elbow and the splitter wall, the averaged pressure amplitudes on the s3 section were also much lower than on the s2 section.

Pressure Fluctuations Inside the Runner

Pressure Fluctuation Frequencies. At first glance the pressure waves inside the runner seem to not correlate with those inside the draft tube. As shown Fig. 7 the pressure waves on runner blades

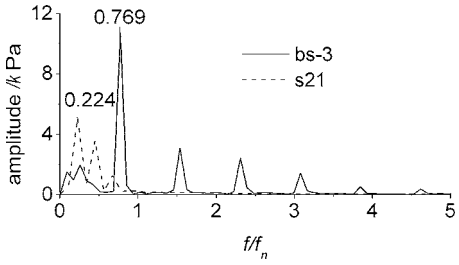

Fig. 7 Pressure fluctuations inside the runner and the draft tube for case g16-H68

do not have the same main frequency as those inside the draft tube.

For the case shown in Fig. 7, the basic fluctuation frequencies in the draft tube were 0.224 f_n and its harmonic 0.448 f_n, while inside the runner the dominant frequency was 0.769 f_n. However, since the recording points inside the runner were fixed in a rotating reference frame, in view of these points, the draft tube was rotating at a reversed frequency of $-f_n$. Therefore, the vortex rope precessing at a frequency of 0.224 f_n relative to the draft tube would be seen as a frequency of $-f_n+0.224f_n=-0.776f_n$ at recording points inside the runner, as seen in Fig. 7. The small difference between 0.776 f_n and 0.769 f_n was due to FFT analysis error since the length for the FFT analysis was not exactly an integer number of the oscillation periods.

Further proof to this relationship is given in Table 3 which lists statistics for the various operating conditions with two other cases with specific speeds of 12.07 and 10.35. The results are also listed in Table 3. For all cases, the sum of f_r/f_n and f_d/f_n is almost 1.

Table 3 Frequencies inside the runner and inside the draft tube caused by the vortex rope

	Operating condition	f_r/f_n	f_d/f_n	$(f_r+f_d)/f_n$
Present case $n_s=10.93$	g16-H68	0.769	0.224	0.993
	g16-H75	0.762	0.245	1.007
	g20-H68	0.663	0.327	0.990
	g20-H75	0.667	0.333	1.000
Case with $n_s=12.07$	g200-H68	0.764	0.243	1.007
	g200-H78	0.736	0.285	1.021
	g240-H68	0.666	0.328	0.994
Case with $n_s=10.35$	g14-H114	0.759	0.248	1.007
	g14-H137	0.743	0.254	0.997
	g16-H137	0.729	0.277	1.006

f_r: frequency in the runner caused by the vortex rope; f_d: rotating frequency of the vortex rope in the draft tube; f_n: rotational frequency of the runner.

For the 67% opening, the pressure fluctuations inside the runner had a dominant low frequency of f_n-f_d as shown in Fig. 7 and Figs. 8(*a*)–8(*d*) due to the influence of the vortex rope. For all the calculated cases, the oscillations at this frequency had higher amplitudes near the outlet than near the inlet because the outlet was closer to the draft tube. However, for higher partial load (83% opening), other frequencies besides f_n-f_d, such as rotational frequency and its second-, third-, and fourth-order harmonics were also observed at some points and even became dominant, especially near the runner band and the inlet (Fig. 8(*f*)). As noted

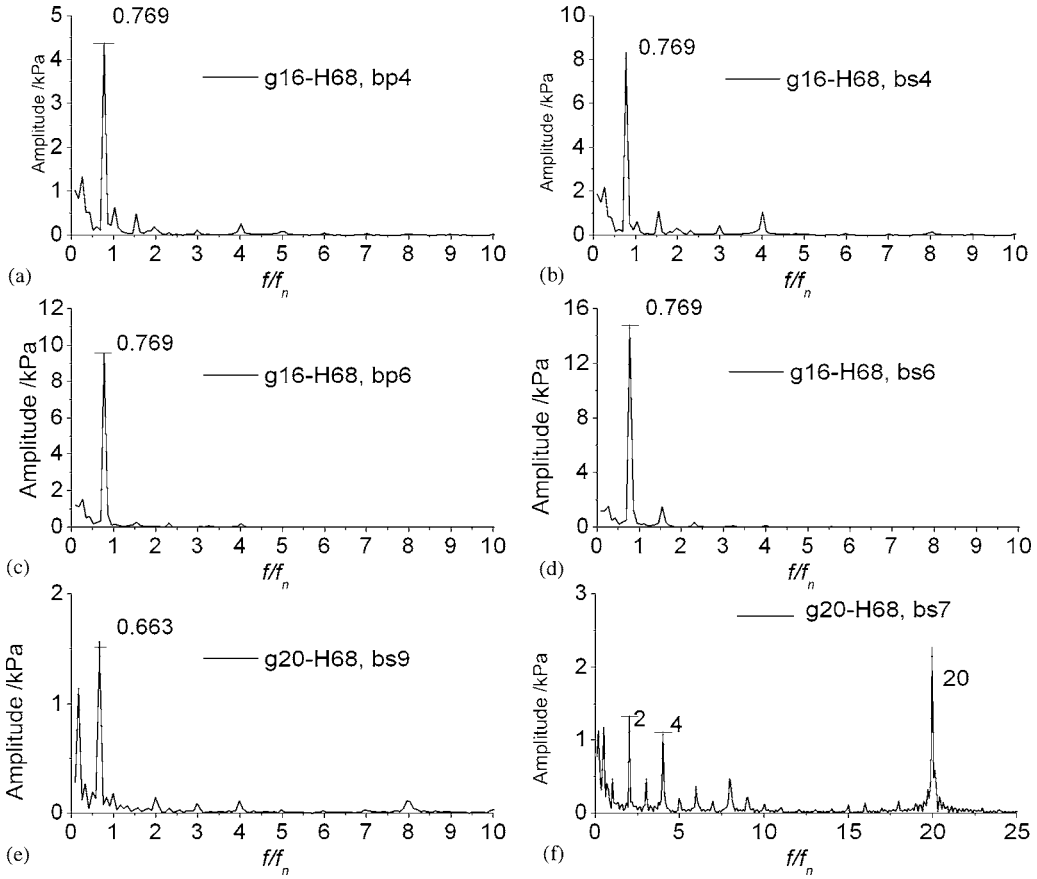

Fig. 8 Examples of pressure fluctuation spectra on the blades

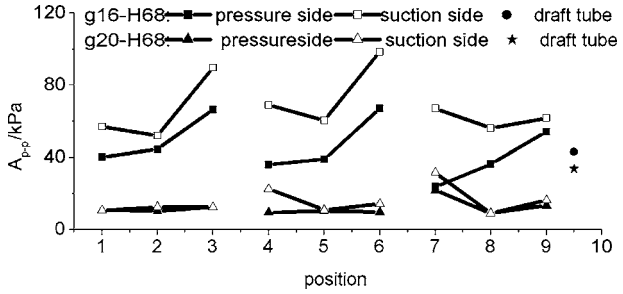

Fig. 9 Peak-to-peak amplitudes of pressure fluctuations on blades

Table 4 Measured stresses in the runner and pressure oscillations in the draft tube

	In the runner		In the draft tube	
a/a_o	$A_{P\text{-}P}$ (MPa)	f_r/f_n	$A_{P\text{-}P}$(m)/H	f_d/f_n
54%	37.38	0.71	12.47%	0.28
57%	37.38	0.73	12.15%	0.27
60%	36.31	0.71	12.02%	0.27
69%	30.98	0.63	15.13%	0.36
76%	27.78	0.99	10.55%	0.36
83%	24.57	0.99	5.17%	0.35

earlier, the vortex rope for g16-H68 was thicker than for g20-H68 and the reversed flow area near the hub for g16-H68 was larger than for g20-H68. The thicker vortex rope should have a great effect on the flow field in the runner than thinner vortex rope, so the amplitudes of the $f_n - f_d$ oscillations should be greater at 67% opening than at 83% opening.

In some cases, a high frequency of $N_g \times f_n$ was observed (where N_g is the number of the guide vanes), especially near the band inlet which is obviously related to the guide vane blade passing. The distance between the guide vanes and the runner blades thus greatly influences the amplitude of these oscillations at the blade passing frequency. These oscillations had higher amplitudes near the band than near the crown.

Peak-to-Peak Amplitudes of Pressure Oscillations in the Runner. From a practical point of view, the peak-to-peak amplitudes (A_{P-P}) of the pressure oscillations in the runner are very important since the pressure oscillations in the runner apply dynamic load to the blades which create dynamic stresses and serious fatigue damage to the blades. In all the cases studied the overall peak-peak amplitudes on the suction side were higher than on the pressure side perhaps because the suction side of the blade faces the draft tube inlet while the pressure side faces away from the draft tube. Thus, the suction side is affected more by the vortex precession.

Figure 9 shows that at smaller 67% opening, the peak-to-peak amplitude of the pressure oscillations was usually higher than at the larger 83% opening.

The phenomena similar to those shown in Fig. 9 were observed in all the other calculated cases listed in Table 3. Unfortunately, measurements could not be obtained inside the runner for comparison. However, these phenomena have been observed in many other prototypes. Figure 10 and Table 4 show the measured dynamic stresses near the outlet of a Francies runner blade close to the crown and the pressure fluctuations in the draft tube. The non-dimensional specific speed of the runner was 11.93, close to the studied cases. The dynamic stresses in the runner blade vary with a frequency of $f_n - f_d$. For the lower partial load (54–69% opening) the frequency of $f_n - f_d$ was dominant. For the higher partial loads (76% and 83% opening) besides the $f_n - f_d$ frequency, the rotational frequency was also obvious. Table 4 also shows that the peak-to-peak amplitude of dynamic stresses in the blade and the pressure fluctuations in the draft tube changed with the load, with the amplitude of the dynamic stresses increasing as the load decreased from 83% to 54%. This result was also observed in the calculated results as was shown in Figs. 5 and 9. The relatively lower peak-to-peak amplitude at the higher partial loads inside the runner corresponds to a thin vortex rope, while relatively higher peak-to-peak amplitudes at lower partial loads usually corresponds to a thicker, expanded vortex rope. The reversed flow near the center of the hub also greatly influences the pressure field in the runner.

Conclusions

Comparison of the calculated results and measured results has shown that:

The RANS equation with the RNG $\kappa - \epsilon$ turbulence model can predict the vortex rotating frequency and amplitude reasonably well at relatively larger 67–83% of optimum openings. The low frequency vortex precession was reasonably well predicted but the high frequency flow turbulence is not seen in calculated results. This may due to the inherent limitation in the $\kappa - \varepsilon$ model. With small openings (67% opening), the amplitudes of the dominant low frequency waves are not well predicted because cavitation is not included in the model.

Since the runner was rotating relative to the draft tube, the pressure oscillations inside the runner at partial loads had frequencies of $-f_n + f_d$, which indicates their relationship to the precession of the vortex rope in the draft tube. In the runner this frequency is usually more obvious at lower loads than at higher loads, and is more obvious near the exit than near leading edge. For higher

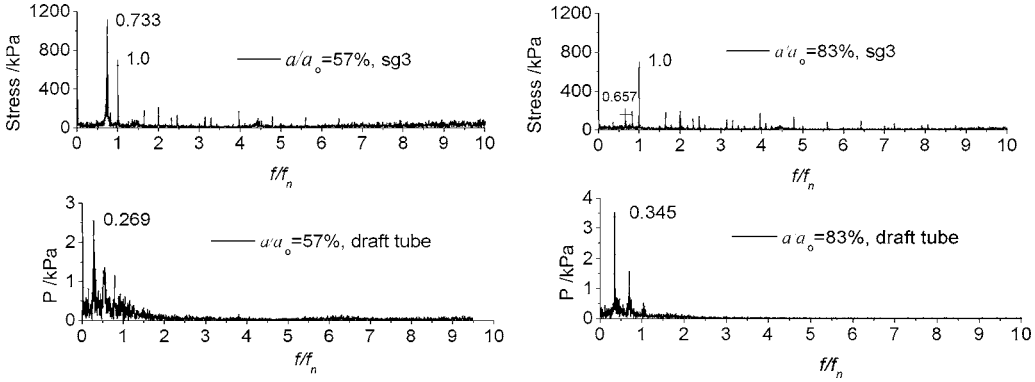

Fig. 10 The measured dynamic stress in the blade and the pressure fluctuations in the draft tube. Sg3 was measuring point near the conjunction of the blade outlet and the crown.

loads, the rotating frequency and its harmonics are observed in addition to the oscillations at the frequency of $-f_n+f_d$.

The peak-to-peak amplitudes of the pressure oscillations in the runner at small lower 67% opening were usually higher than that at higher 83% opening. Oscillations at small openings are associated with a thicker vortex rope while larger openings have a thin vortex rope. The peak-to-peak amplitudes on the suction side are always higher than on the pressure side because the suction side faces the draft tube inlet.

Nomenclature

$A_{P\text{-}P}$ = Peak-to-peak amplitude (Pa)
A = amplitude of a frequency component f (Pa)
a = guide vane opening (mm)
a_0 = optimum guide vane opening (mm)
f = frequency (Hz)
f_n = runner rotational frequency (Hz)
f_d = vortex rope precession frequency in the draft tube (Hz)
H = operating head (m)
n_s = non-dimensional specific speed defined as $n\sqrt{Q}/(gH)^{0.75}$, where n is the rotational speed, Q is the flow rate, g is the gravity acceleration
N_g = the number of the guide vanes
P = pressure (kPa)
Re = the Reynolds number defined as $V_{\text{avg}}D_1/\nu$, where V_{avg} is the averaged velocity, D_1 is the runner diameter, and ν is the water viscosity

Acknowledgment

The authors express their deep thanks to Mr Luoping Pan for providing the measured data in Fig. 10 and Table 4.

References

[1] Jacob, T., and Prenat, E., 1996, "Francis Turbine Surge: Discussion and Data Base," *XVIII IAHR Symposium*, E. Cabrera, V. Espert, and F. Martinez, eds., Kluwer, Dordrecht, pp. 855–864.
[2] Bhan, S., Codrington, J. B., and Mieke, H., 1988, "Reduction of Francis Turbine Draft Tube Surges," *Fifth International Symposium on Hydro Power Fluid Machinery*, D. R. Froehlich, S. K. Wagner, and D. R. Webb, eds., The America Society of Mechanical Engineering, New York, pp. 95–101.
[3] Ruprecht, A., Helmrich, T., Aschenbrenner, T., and Acherer, A., 2002, "Simulation of Vortex Rope in a Turbine Draft Tube," *Proceedings of the 21st IAHR Symposium on Hydraulic Machinery and Systems*, F. Avellan, G. Ciocan, and S. Kvicinsky, eds., EPFL/STI/LMH, Lausanne, Switzerland, pp. 257–264.
[4] Sick, M., Doerfler, P., Sallaberger, M., Lohmberg, A., and Casey, M., 2002, "CFD Simulation of the Draft Tube Vortex," *Proceedings of the 21st IAHR Symposium on Hydraulic Machinery and Systems*, F. Avellan, G. Ciocan, and S. Kvicinsky, eds., EPFL/STI/LMH, Lausanne, Switzerland, pp. 249–256.
[5] Arpe, J., and Avellan, F., 2002, "Pressure Wall Measurements in the Whole Draft Tube: Steady and Unsteady Analysis," *Proceedings of the 21st IAHR Symposium on Hydraulic Machinery and Systems*, F. Avellan, G. Ciocan, and S. Kvicinsky, eds., EPFL/STI/LMH, Lausanne, Switzerland, pp. 593–602.
[6] Skoták, A., Mikulášek, J., and Lhotáková, L., 2002, "Effect of the Inflow Conditions on the Unsteady Draft Tube Flow," *Proceedings of the 21st IAHR Symposium on Hydraulic Machinery and Systems*, F. Avellan, G. Ciocan, and S. Kvicinsky, eds., EPFL/STI/LMH, Lausanne, Switzerland, pp. 284–291.
[7] Zhou, L. J., and Wang, Z. W., 2002, "Investigation of Draft Tube Surge and Runner Outlet Flow Patterns," Journal of Tsinghua University, **42**(12), pp. 29–32 (in Chinese).
[8] Wu, G., and Dai, Y. F., 2000, "Relations Between Flow Field and Pressure Fluctuation in Draft Tube of Francis Turbine," Int. J. Hydroelectric Energy, **118**(1), pp. 58–61 (in Chinese).
[9] Wang, Z. W., and Zhou, L. J., 2002, "Experimental Study on Pressure Surge in Draft Tube," *Proceedings of the 21st IAHR Symposium on Hydraulic Machinery and Systems*, F. Avellan, G. Ciocan, and S. Kvicinsky, eds., EPFL/STI/LMH, Lausanne, Switzerland, pp. 612–617.
[10] Lowys, P., Paquet, F., Couston, M., Farhat, M., Natal, S., and Avellan, F., 2002, "Onboard Measurements of Pressure and Strain Fluctuations in a Model of Low Head Francis Turbine – Part 2: Measurements and Preliminary Analysis Results," *Proceedings of the 21st IAHR Symposium on Hydraulic Machinery and Systems*, F. Avellan, G. Ciocan, and S. Kvicinsky, eds., EPFL/STI/LMH, Lausanne, Switzerland, pp. 873–880.
[11] Yakhot, V., Orszag, S. A., Thangham, S., Gatski, T. B., and Speziale, C. G., 1992, "Development of Turbulence Models for Shear Flows by a Double Expansion Technique," Phys. Fluids A, **4**(7), pp. 1510–1520.
[12] Zhang, Y., and Orszag, S. A., 1998, "Two-Equation RNG Transport Modeling of High Reynolds Number Pipe Flow," J. Sci. Comput., **13**(4), pp. 471–483.

Experimental Validation of the Addition Principle for Pulsating Flow in Close-Coupled Catalyst Manifolds

Tim Persoons
Department of Mechanical Engineering,
Katholieke Universiteit Leuven,
Celestijnenlaan 300A,
B-3001 Leuven, Belgium
e-mail: tim.persoons@mech.kuleuven.be

Ad Hoefnagels
BOSAL International,
Advanced Engineering and Testing,
Lummen, Belgium

Eric Van den Bulck
Department of Mechanical Engineering,
Katholieke Universiteit Leuven,
Celestijnenlaan 300A,
B-3001 Leuven, Belgium

Designing an exhaust manifold with close-coupled catalyst (CCC) relies heavily on time-consuming transient computional fluid dynamics. The current paper provides experimental validation of the addition principle for pulsating flow in CCC manifolds. The addition principle states that the time-averaged catalyst velocity distribution in pulsating flow equals a linear combination of velocity distributions obtained for steady flow through each of the exhaust runners. A charged motored engine flow rig provides cold pulsating flow in the exhaust manifold featuring blow down and displacement phases, typical of fired engine conditions. Oscillating hot-wire anemometry is used to measure the bidirectional velocity, with a maximum measurable negative velocity of -1 m/s. *In part load and zero load conditions, instantaneous reverse flow occurs following the blow-down phase. The two-stage nature of the exhaust stroke combined with strong Helmholtz resonances results in strong fluctuations of the time-resolved mean catalyst velocity. The validity of the addition principle is quantified based on the shape and magnitude similarity between steady and pulsating flow distributions. Appropriate nondimensional groups are used to characterize the flow and quantify the similarity. Statistical significances are provided for the addition principle's validity. The addition principle is valid when the nondimensional scavenging number S exceeds a critical value* S_{crit}, *corresponding to cases of low engine speed and/or high flow rate. This study suggests that the CCC manifold efficiency with respect to catalyst flow uniformity could be quantified using a single scalar parameter, i.e.,* S_{crit}. *The results from the current study are discussed with respect to previously reported results. The combined results are in good agreement and provide a thorough statistically founded experimental validation of the addition principle, based on a broad applicability range.* [DOI: 10.1115/1.2201646]

Keywords: exhaust system, close-coupled catalyst, pulsating flow, addition principle, oscillating hot-wire anemometry, bidirectional velocity

1 Introduction

Designing a modern automotive exhaust system requires advanced knowledge on transient fluid dynamics and heat transfer. The exhaust system "hot end" consists of the exhaust manifold with an integrated close-coupled (CC) catalyst. The manifold typically features three to four exhaust runners that converge in a diffuser volume upstream of the catalyst. Downstream of the catalyst, the gas flows through the exit cone and downpipe into the "cold end" of the exhaust system. The CC catalyst is subjected to pulsating flow, alternating between each of the exhaust runners.

The distance between exhaust ports and CC catalyst is preferably as small as possible, to ensure rapid catalyst warm up, thus reducing cold start emissions. However, this requires exhaust runners with small ratios of length and curvature radius to diameter. On the other hand, obtaining high catalyst flow uniformity is crucial for guaranteeing a low pressure drop (and consequently, low engine fuel consumption), high pollutant conversion rate, and long catalyst lifetime. Designing such a manifold while ensuring flow uniformity is a formidable task, requiring state-of-the-art knowledge of fluid dynamics and heat transfer in transient internal flows.

Computational fluid dynamics (CFD) simulation of such transient three-dimensional flow is difficult using the Reynolds-averaged Navier-Stokes (RANS) approach in combination with a traditional turbulence model. The highly curved runners produce strong secondary flows. Separation and recirculation occurs in exhaust runners and diffuser. The flow is characterized by nonisotropic turbulence and three-dimensional boundary layers.

The objective of this research is to provide accurate experimental data for the catalyst velocity distribution. The data should feature a high spatial and temporal resolution to allow validation of CFD simulations.

Persoons et al. [1] discuss previous research by the present authors, using an isothermal flow rig for generating cold pulsating flow in two types of exhaust manifolds. The present paper discusses results obtained on a charged motored engine (CME) flow rig. The pulsating flow is cold, which enables the use of hot-wire anemometry (HWA). Unlike the isothermal flow rig however, the CME flow rig features pulsating exhaust flow with blow-down and displacement phases, typical of fired engine conditions.

1.1 Addition Principle. The main contribution of Persoons et al. [1] is the experimental validation of the addition principle on an isothermal flow rig. The addition principle states that the time-averaged velocity distribution in pulsating flow can be predicted by a linear combination of velocity distributions that results from stationary flow through each of the exhaust runners. The linear combination of stationary distributions may be thought of as the limit case for zero-engine speed. If the principle is valid, it implies that transient computational fluid dynamics (CFD) is not required

Contributed by the Fluids Engineering Division of ASME for publication in the JOURNAL OF FLUIDS ENGINEERING. Manuscript received August 22, 2005; final manuscript received February 1, 2006. Assoc. Editor: Timothy J. O'Hern.

for designing a manifold with close-coupled (CC) catalyst with respect to the catalyst flow distribution and that steady state CFD simulations suffice.

Two nondimensional similarity measures r_S (−) and r_M (−) are used to quantify the correlation between pulsating and stationary velocity distributions. Both scalars are correlated to the nondimensional scavenging number S (−) (see Secs. 2.3 and 3.3). S equals the ratio of flow pulsation period to diffuser residence time. The scavenging number S increases for decreasing engine speed and increasing flow rate. In that case, flow pulses from each of the runners interact only slightly, and there is a good correspondence between pulsating and stationary distributions. When S is sufficiently large, the addition principle is expected to be valid. S decreases for increasing engine speed and decreasing flow rate. In that case, flow pulses interact to a higher degree, which results in a bad correlation between pulsating and stationary distributions.

Persoons et al. [1] have validated the addition principle for two types of exhaust manifolds: One with and one without exhaust valve overlap. Pulsating flow is generated using two different pulsators: A rotating valve and a motored cylinder head, both of which are mounted on an isothermal flow rig. The isothermal flow rig consists of a large buffer vessel designed to maintain a quasi-constant pressure, which is fed by a compressor and flow rate measuring device. The flow generated by the isothermal flow rig is quite different from fired engine conditions, although time-averaged Reynolds and Mach number are roughly in accordance.

The findings in Persoons et al. [1] concerning the addition principle are confirmed to some extent by other sources in literature. Benjamin et al. [2] discuss experimental results on an axisymmetric manifold with catalyst, mounted on an isothermal flow bench with rotating disk pulsator. Although no comparison is made between pulsating and stationary flow patterns, the authors also define a nondimensional number as the ratio of pulsation period to diffuser residence time, based on the runner velocity. A good correlation exists between a nonuniformity measure and the nondimensional number.

From the same research group, Liu et al. [3] use the same experimental setup, but with more overlapping inlet velocity pulse shapes. Liu et al. [3] do not refer to any nondimensional correlation, however the authors report a lower uniformity due to overlapping inlet flow pulses when compared to the results of Benjamin et al. [2] featuring nonoverlapping pulses. According to Fig. 7 in Liu et al. [3], as the pulsation frequency increases, nonuniformity decreases, i.e., uniformity increases. This is in agreement with our findings. From the same figure, overlapping inlet flow pulses seem to result in a much lower uniformity when compared to nonoverlapping pulses. Our research confirms a slightly lower uniformity in the presence of overlap between exhaust valve openings.

Bressler et al. [4] provide qualitative confirmation of the addition principle's validity. The authors present results obtained using phase-locked laser-Doppler anemometry (LDA) in a four-runner manifold with CC catalyst, mounted on an isothermal flow rig. A nondimensional ratio is proposed of exhausted gas volume per cylinder and per cycle to the diffuser volume. This ratio is actually identical to the scavenging number S used in the current paper and the dimensional number used by Benjamin et al. [2]. Although no correlation is presented, their results indicate that the flow uniformity is unaffected by engine speed as long as dimensionless ratio remains constant.

Tsinoglou and Koltsakis [5] present a numerical study of catalyst hydrocarbon conversion efficiency in pulsating flow. The authors nondimensionalize the pulsation frequency with the catalyst residence time. This so-called "pulsation index" is used to plot the conversion efficiency for different pulse shapes. For a high pulsation index, the conversion efficiency reaches unity and becomes independent of the pulsation index. For a low pulsation index, conversion efficiency is well predicted by a quasi-steady model. The pulsation index is inversely proportional to the scavenging number used in the current paper.

The present research extends the conclusions of Persoons et al. [1] using a CME flow rig. Section 3.3 discusses the new experimental data with respect to the addition principle.

1.2 Reverse Flow. The occurrence of reverse flow in large portions of the engine operating range may be surprising, with regard to the considerable pressure drop generated by the CC catalyst. The current research uses exhaust manifolds with free discharge into the atmosphere, i.e., without exit cone and cold end exhaust pipe. Liu et al. [6], Park et al. [7], and Kim et al. [8] present experimental or numerical results showing reverse flow in the CC catalyst monolith including an outlet section, in fired conditions. Reverse flow consistently occurs after blow down. In the absence of blow down, reverse flow is not likely to occur. This is confirmed by phase-locked LDA results by Hwang et al. [9], obtained on an isothermal flow rig.

Obtaining high-quality experimental data that include reverse flow is not straightforward. Optical measurement techniques, such as LDA, are able to measure phase-locked velocity including negative velocities, however they require optical access and adequate seeding. LDA-based research in CC catalyst systems is often plagued with areas of low seeding concentration. This makes it very difficult to obtain a sufficiently high data rate for measuring full catalyst cross-section velocity distributions. Most studies using LDA only measure velocity in a single point or along a single straight line through the manifold.

On the other hand, hot-wire anemometry (HWA) requires neither optical access nor seeding, although obviously, physical access for the hot-wire probe is required. HWA features a number of advantages including high bandwidth, continuous output signal, and good spatial resolution. The main disadvantage of HWA is its inability to discern flow reversal.

A reference work on thermal anemometry by Bruun [10] contains an overview of techniques for measuring velocity in reversing flows using HWA. On the one hand, thermal wake probes relate the time of flight of a small heated amount of fluid to local velocity. This approach is characterized by low bandwidth and is better suited for near-wall measurements. On the other hand, flying HWA is used for measuring free-stream reversing flows. If the hot-wire probe moves at a sufficiently high velocity counter to the normal flow velocity, the relative velocity seen by the probe can remain positive. Traditional flying HWA devices, such as the system described by Thompson and Whitelaw [11], are quite large and cumbersome, making it impossible to use in confined geometries such as exhaust systems.

Persoons et al. [12] describe the calibration of an oscillating hot-wire anemometer (OHW) device, which is used in the current research. The OHW principle is explained in Sec. 2.2. The device is calibrated using phase-locked LDA as reference velocity measurement. It is compact enough to measure velocity distributions in the CC catalyst. The OHW features a maximum measurable negative velocity of -1.0 m/s, which is sufficient for the current research. This value is comparable to other flying and oscillating HWA devices.

2 Experimental Setup

2.1 CME. CME flow rig consists of a four-cylinder double overhead camshaft gasoline engine with four valves per cylinder, mounted on a dynamic engine test stand with an electric dc dyno. The engine is motored at a constant speed. To enable charging the engine with compressed air, the original intake system has been replaced by a reinforced intake system with identical manifold volume and runner dimensions. The engine is run without combustion and fuel injection, to obtain cold clean pulsating flow in the exhaust system. The original exhaust valve timing is unchanged (see Table 1). However, the intake camshaft is retarded by 30° crankshaft angle to avoid unphysical blow-through from the high-pressure intake to the low-pressure exhaust system dur-

Table 1 Manifold specifications

	Manifold A (Persoons et al. [1])	Manifold B (Current research and Persoons et al. [1])
Engine/cylinder head (valve timing)	3.0l V-6/DOHC 24 valves (−12|+242|−246|+10)	1.2l I-4/DOHC 16 valves (+17|+250|−220|+13)
Runners	∅31.5 mm, lengths: (1) 150 mm, (2) 90 mm, (3) 120 mm	∅28 mm, lengths: (1) 160 mm, (2) 80 mm, (3) 160 mm, (4) 80 mm
Diffuser	volume V_d=141.4 cm^3	volume V_d=390.2 cm^3
Catalyst	Ceramic 600 cpsi/3 mil, square channels, unwashcoated	Ceramic 600 cpsi/3 mil, square channels, washcoated
	Circular cross-section (∅63 mm), length 52 mm	Oval cross-section (∅151×101 mm), length 137 mm

ing intake/exhaust valve overlap.

The engine is mounted without vibration dampers onto the rigid test stand frame. An automated positioning system is fixed onto the lab floor adjacent to the test stand, taking care to avoid any relative motion between engine exhaust system and velocity probe. The OHW is mounted on the positioning system and traversed automatically through the measurement grid.

Figure 1 (left) schematically depicts the CME flow rig. The compressed air is produced using a screw compressor, which delivers a maximum flow rate of 320 kg/h at 8 atm. A pressure regulator maintains a constant pressure in the engine intake system, varying between 1.00 atm to 2.25 atm in the current study. The screw compressor's maximum flow rate has limited the engine speed in the current measurements to 3000 rpm.

The intake system flow rate is measured using a laminar flow meter. Partly because of the altered intake timing, the intake flow rate is highly pulsatile with periods of backflow. Although the laminar flow meter is designed for such flows, the intake system flow rate is further verified using a piezoelectric cylinder pressure sensor. The pressure rise during the compression stroke is used to determine the mass flow rate. The intake flow rate reading is accurate to within 5% to 10%, and serves as a reference flow rate for the flow rate obtained by integration of the catalyst velocity distribution.

Persoons et al. [1] contains details concerning the isothermal dynamic flow rig used in the previous measurement campaign. Out of manifold Types A and B investigated in Persoons et al. [1], only manifold Type B depicted in Fig. 1 (right) is used in the current research.

The cold pulsating flow generated by the CME flow rig in the exhaust system is quite different from the isothermal flow rig. By controlling the intake system pressure, the residual cylinder pressure at exhaust valve opening can be adjusted. This results in a two-stage exhaust stroke with blow down and displacement phases, typical of fired engine conditions.

For an engine speed of 1800 rpm and an exhaust flow rate of 100 m^3/h, Figure 2 shows the time-resolved nondimensional velocity inside Runner 1 of Manifold B. Simulations performed using a filling-and-emptying engine model (see, e.g., Watson and Janota [13]) result in the solid and dashed lines, for the CME and isothermal flow rig, respectively. The markers indicate the runner velocity measured in the CME flow rig. The nondimensional exhaust valve lift is plotted in grey.

The isothermal flow rig produces a single-stage exhaust pulse, resulting in four quasi-sinusoidal pulses per engine cycle. The CME flow rig produces a pulsating flow that better resembles fired engine conditions. The flow similarity between CME and fired conditions is not complete. In fired conditions, the peak blowdown flow rate is higher and the displacement flow rate is lower. In spite of the incomplete similarity, the CME flow rig features two-stage exhaust pulses, resulting in a pulsating flow with higher-frequency content. Strong Helmholtz resonances (see Sec. 3.2) are observed of the same magnitude as observed in fired engines [6–8]. Sections 3.2 and 3.3 discuss the implications of the increased frequency content of the pulsating flow on the validation of the addition principle.

2.2 OHW. To measure bidirectional phase-locked velocity in the exhaust manifold, the current research uses a OHW, which is described in detail in Persoons et al. [12]. The system uses a

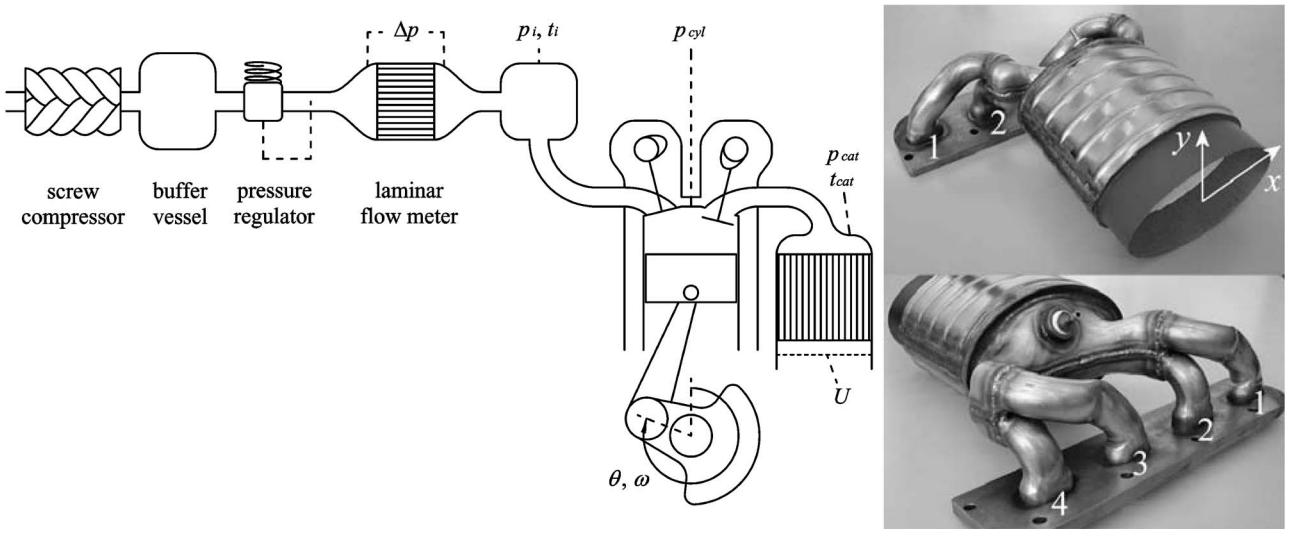

Fig. 1 CME flow rig overview (left) and Manifold B (right)

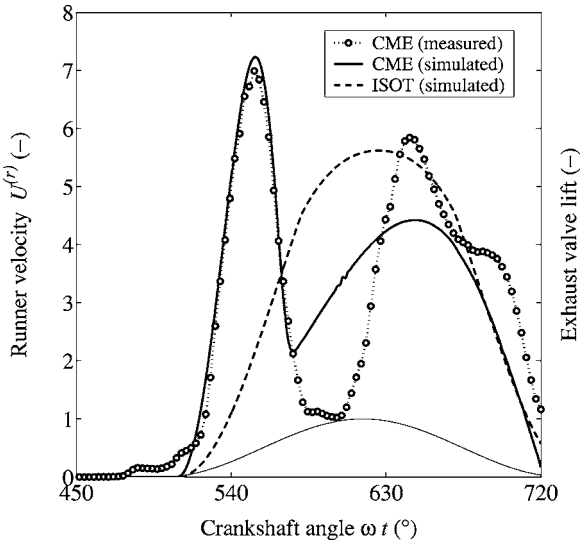

Fig. 2 Comparison of exhaust runner velocity for CME and isothermal flow rig

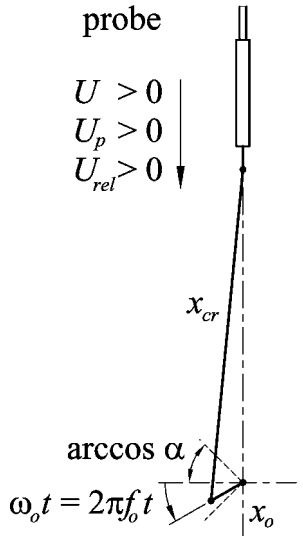

Fig. 4 OHW nomenclature

slider-crank mechanism to oscillate a hot-wire probe with an amplitude x_o=5.5 mm, at a frequency f_o from 30 to 40 Hz. A speed-controlled dc motor maintains the oscillation frequency f_o proportional to the engine speed N (rpm). The nondimensional oscillation frequency R_f is defined as $R_f = f_o/(N/120) = \omega_o/(\omega/2)$.

The positive direction of flow is indicated in Fig. 3, and Fig. 4 indicates the nomenclature. The measured OHW velocity U' is defined as $U' = U_{\text{rel}} + U_p$, where U_{rel}=relative velocity as seen by the probe (m/s) and U_p=probe velocity (m/s). The relative velocity U_{rel} is determined from the anemometer bridge output voltage, whereas the probe velocity U_p is determined from the oscillator driveshaft position.

In reverse flow when $U<0$, the OHW provides a valid measurement U' if the relative velocity $U_{\text{rel}}>0$, thus if the probe velocity $U_p<U<0$. As the probe oscillates, measurements are accepted in a window around the maximal negative probe velocity U_p, or symbolically when $U_p \leqslant -2\pi f_o x_o \alpha = -\omega_o x_o \alpha$. Approximating the probe motion as pure sinusoidal ($x_{\text{CR}} \gg x_o$), this corresponds to $-\arccos \alpha \leqslant \omega_o t + 2\pi n \leqslant \arccos \alpha (n \in \mathbb{Z})$. The tolerance factor α is chosen arbitrarily as $\alpha = \cos(\pi/4) \cong 0.71$.

When the nondimensional OHW frequency R_f is a whole number, the OHW moves in synchronization with the engine's crankshaft. In that case, the OHW measurements are taken in the same crankshaft angle intervals in consecutive engine cycles. In order to cover the entire crankshaft position range from 0° to 720°, the OHW motion slightly lags or leads the engine rotation. As such, R_f is chosen as $R_f = n \pm 1/4 (n \in \mathbb{Z})$. The value 1/4 corresponds to $\alpha = \cos(\pi/4) \cong 0.71$.

Figure 5 shows the OHW probe velocity versus crankshaft position for a particular engine speed. The whole number n is maximized, limited by the maximum oscillator frequency of 40 Hz. For the case of N=2400 rpm, this results in f_o=35 Hz for n=2 or $R_f = 2 - 1/4 = 1.75$. In this case, it takes four engine cycles to obtain measurements for the entire range of crankshaft position from 0° to 720°. Decreasing the value from 1/4 to 1/8 increases the mean probe velocity magnitude during OHW measurements, thus increasing resolution in the negative velocity range. However, instead of four, eight engine cycles are required to complete mea-

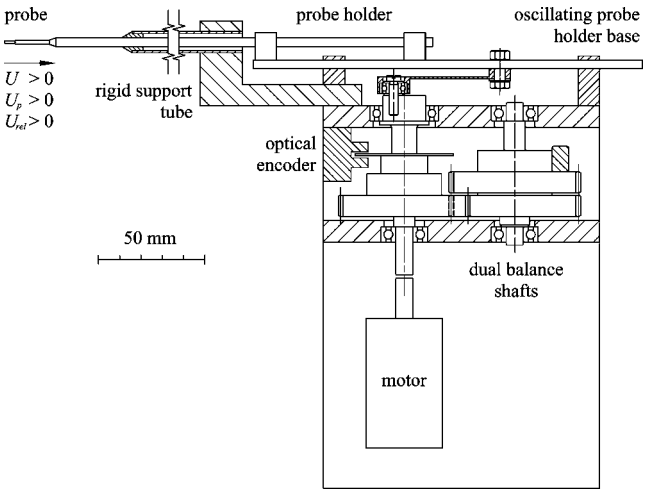

Fig. 3 OHW used to measure bidirectional velocity

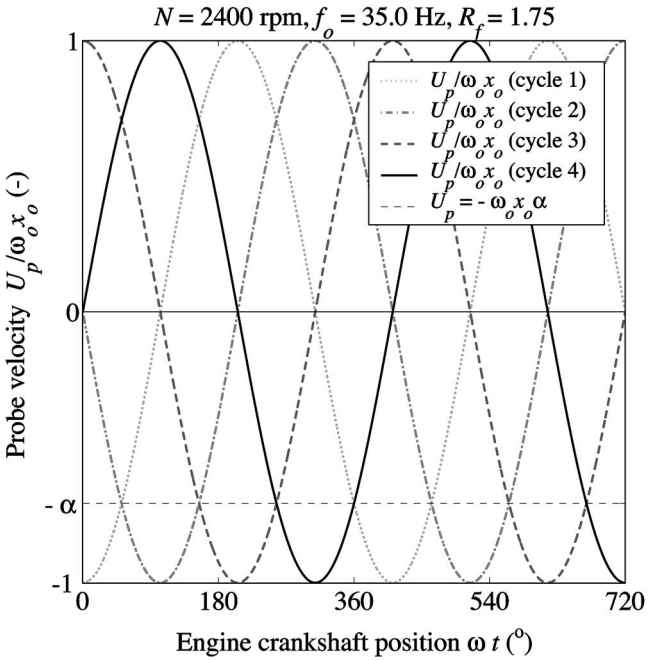

Fig. 5 OHW probe velocity, phase-locked with engine crankshaft position

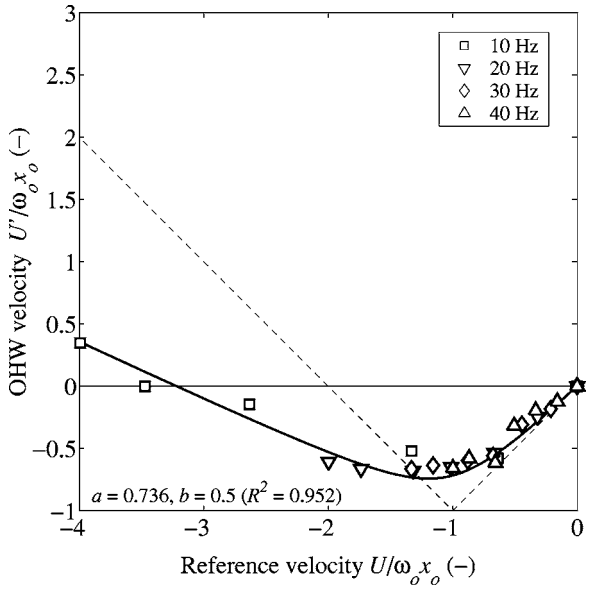

Fig. 6 Nondimensional OHW calibration chart at varying oscillation frequency

surements for one engine cycle. Obtaining valid measurements for one complete engine cycle (i.e., one ensemble) thus takes four engine cycles. Therefore, several hundred cycles are required to ensure sufficient accuracy after ensemble averaging the velocity data.

A Dantec StreamLine HWA system with Dantec type 90C10 constant temperature anemometer bridge modules has been used for the current research. A Dantec 55P11 probe with extended prongs is used, as described in Persoons et al. [12]. Calibration of the anemometer bridge output voltage to a reference velocity is performed using a Dantec-type 90H02 automated free jet calibrator.

The following nondimensional correlation is used to convert the OHW velocity reading U' to the actual reference velocity This correlation is obtained during the calibration in steady flow, with negative velocity $-1.5 \leqslant U \leqslant 0$ m/s, and positive velocity $0 \leqslant U \leqslant 10$ m/s

$$u' = \begin{cases} u + a(\sqrt{(u+1)^2 + b^2} - u - \sqrt{1+b^2}) & (u < 0) \\ u & (u \geqslant 0), \end{cases} \tag{1}$$

where $u' = U'/\omega_o x_o$, $u = U/\omega_o x_o$, a and b are nondimensional parameters. a determines the slope $(=1-2a)$ of the function as $u \rightarrow -\infty$ and $b > 0$ yields a smooth transition around $u = U/\omega_o x_o = -1$. The values are determined as $a = 0.736$ and $b = 0.5$, with a coefficient of determination $R^2 = 0.952$ [12].

Figure 6 shows the nondimensional calibration chart. The solid line represents the correlation fit of Eq. (1). The markers represent measurements at varying oscillation frequency between 10 and 40 Hz. The OHW enables the measurement of negative velocity for $-1 \leqslant U/\omega_o x_o$. For an oscillation frequency between 30 and 40 Hz, this corresponds to a maximum measurable negative velocity of -1 m/s. In the positive velocity range, the OHW velocity U' equals the reference velocity.

To obtain the catalyst velocity distribution, consecutive measurements are performed in roughly 400 locations in a measurement plane 25 mm downstream of the catalyst outlet face, within a shrouded section to avoid entrainment. Figure 1 (right) shows the coordinate system in the measurement plane. The OHW device is mounted on a Dantec type 41T50 automated positioning system, which features a positioning accuracy better than 0.25 mm.

A personal computer equipped with a dSpace DS1103 data acquisition board is used to trigger the velocity measurement and control the oscillator frequency f_o with the fixed proportionality factor R_f to the engine speed. The dSpace system reads the engine crankshaft position using a high-resolution incremental encoder (angular error below 0.1°), and the oscillator driveshaft angle using an optical encoder.

2.3 Data Reduction. Ensemble averaging is applied to obtain the phase-locked velocity distributions. As described in Sec. 2.2, one ensemble is constructed from data obtained during crankshaft angle windows of valid OHW measurements in several consecutive engine cycles. Valid OHW measurements are possible when the relative velocity U_{rel} seen by the moving hot-wire probe is positive, or during $-\arccos\alpha \leqslant \omega_o t + 2\pi n \leqslant \arccos\alpha (n \in \mathbb{Z})$. The obtained instantaneous OHW velocity in one particular point (x_i, y_i) is $U'_{ije}(x_i, y_i, \theta_j, e) = U_{\text{rel}} + U_p$, where subscripts i=grid point index, j=crankshaft angle index, and e=ensemble index. U'_{ije} is converted to U_{ije} using the calibration function defined in Eq. (1) and the appropriate parameters a and b.

The resulting complete ensembles of $U_{ije}(x_i, y_i, \theta_j, e)$ are ensemble-averaged to obtain the time-resolved velocity $U_{ij}(x_i, y_i, \theta_j)$:

$$U_{ij}(x_i, y_i, \theta_j) = \frac{1}{E}\sum_{e=1}^{E} U_{ije}(x_i, y_i, \theta_j, e), \tag{2}$$

where E=number of ensembles. Approximately 100 ensembles yield sufficient accuracy on the time-resolved velocity. More ensembles are needed when compared to the previous measurements on the isothermal flow rig. This is due to cycle-by-cycle variation, a phenomenon typical of internal combustion engine flows. Because of the absence of a combustion process, the CME flow rig is less affected by cyclic variation than a fired engine. Nevertheless, four times more ensembles are required when compared to the isothermal flow rig experiments to obtain an accuracy of 1% on the time-averaged mean velocity.

The time-averaged velocity $U_i(x_i, y_i)$ is defined as

$$U_i(x_i, y_i) = \frac{1}{J}\sum_{j=1}^{J} U_{ij}(x_i, y_i, \theta_j), \tag{3}$$

where J=number of crankshaft positions, which is determined by the sampling frequency. 256 samples are taken in each engine cycle, regardless of engine speed. For instance at 2400 rpm, this requires a sampling frequency of 5120 Hz. Roughly 2.5 times more samples per engine cycle are taken when compared to previous measurements, due to the presence of blow down and Helmholtz fluctuations (see Sec. 3.2), causing strong transients in the time-resolved velocity.

The mean (or spatial averaged) velocity $U_{mj}(\theta_j)$ is defined as

$$U_{mj}(\theta_j) = \frac{1}{A}\sum_{i=1}^{I} U_{ij}(x_i, y_i, \theta_j) A_i(x_i, y_i), \tag{4}$$

where I=number of grid points, A_i=cross-sectional area of grid cell i (m^2), A=total cross-sectional area$=\Sigma_{i=1}^{I} A_i$ (m^2). The time-averaged mean velocity U_m is defined as

$$U_m = \frac{1}{J}\sum_{j=1}^{J} U_{mj}(\theta_j) = \frac{Q}{A}, \tag{5}$$

where Q is the volumetric flow rate through the catalyst (m^3/s). In all subsequent figures of velocity distributions, the nondimensional velocity $\tilde{U}$ (−) is plotted, defined as $\tilde{U} = U/U_m$. The tilde (~) is omitted from Figs. 11–15.

The validity of the addition principle discussed in Sec. 3.3 is based on two nondimensional similarity measures r_S (−) and r_M (−). r_S quantifies the correspondence in shape of two velocity distributions, whereas r_M quantifies the correspondence in magni-

Table 2 Summary of experiments on the isothermal flow rig[a]

Geometry	N (rpm)	p_i (atm)	Q_{ref} (m^3/h)	$S^{(old)}$ (−)	S (−)	r_S (−)	P_S (−)	r_M (−)	P_M (−)
Isothermal flow	1450	—	70.8	4.186	4.221	0.965	0.000	1.126	0.096
rig, manifold A,	2130	—	69.1	2.887	2.921	0.965	0.000	1.126	0.104
rotating valve	2820	—	66.7	2.107	2.091	0.962	0.000	1.113	0.122
Isothermal flow	1330	—	68.4	4.569	4.656	0.964	0.000	1.145	0.231
rig, manifold A,	2000	—	71.2	3.021	3.094	0.956	0.000	1.191	0.172
cylinder head	2800	—	67.7	2.154	2.180	0.944	0.000	1.282	0.025
Isothermal flow	600	—	43.5	1.543	1.529	0.880	0.000	1.058	0.673
rig, manifold B,	610	—	62.2	2.660	2.666	0.884	0.000	1.154	0.548
cylinder head	600	—	97.2	3.864	3.822	0.965	0.000	1.058	0.844
	600	—	115.0	4.556	4.514	0.974	0.000	1.092	0.720
	1200	—	42.9	0.761	0.754	0.738	0.000	1.208	0.142
	1200	—	68.6	1.336	1.339	0.782	0.000	1.233	0.400
	1200	—	98.5	1.903	1.886	0.956	0.000	1.071	0.778
	1200	—	115.9	2.270	2.249	0.965	0.000	1.079	0.763
	2000	—	67.9	0.794	0.805	0.725	0.000	1.445	0.165
	2800	—	65.1	0.583	0.295	0.628	0.000	1.600	0.111
	3600	—	74.7	0.455	0.230	0.437	0.001	1.629	0.071
	4400	—	71.6	0.351	0.346	0.445	0.001	1.633	0.052

[a]See [1].

tude. r_M equals the ratio of a uniformity measure for pulsating and stationary flow. The uniformity measure used is the mean-to-maximum velocity ratio $U_m/U_{\max}$. This scalar equals unity for an ideally uniform distribution and varies between zero and unity otherwise.

$$r_M = \frac{(U_m/U_{\max})_{\text{puls}}}{(U_m/U_{\max})_{\text{stat}}} = \frac{(1/\tilde{U}_{\max})_{\text{puls}}}{(1/\tilde{U}_{\max})_{\text{stat}}} = \frac{(\tilde{U}_{\max})_{\text{stat}}}{(\tilde{U}_{\max})_{\text{puls}}}. \tag{6}$$

r_M expresses the relative increase in flow uniformity in pulsating flow, when compared to the averaged stationary distribution. $r_M > 1$ means that the pulsating flow has a better flow uniformity than the stationary averaged flow.

r_S equals the Pearson correlation coefficient:

$$r_S = \frac{\sum_{i=1}^{I} (U_{i,\text{puls}} - U_{m,\text{puls}})(U_{i,\text{stat}} - U_{m,\text{stat}})}{\sqrt{\sum_{i=1}^{I} (U_{i,\text{puls}} - U_{m,\text{puls}})^2 \cdot \sum_{i=1}^{I} (U_{i,\text{stat}} - U_{m,\text{stat}})^2}}. \tag{7}$$

The definitions in Eqs. (6) and (7) ensure that r_M is insensitive to differences in shape of the two velocity distributions, and r_S is insensitive to differences in magnitude.

The statistical significance of r_S or the Pearson correlation coefficient is based on Eqs. (19.12.4) through (19.12.7) in Hald [14]. These equations describe the transformation of the correlation coefficient to a Gaussian distributed variable. The number of degrees of freedom corresponds to the largest number of spatially independent points in the velocity distributions. Spatial dependence is quantified using Moran's index, defined by Eq. (1.44) in Cliff and Ord [15]. Based on a 95% confidence level, one can derive that two velocity distributions are significantly correlated when

$$\begin{cases} r_S > 0.317 & \text{(manifold A)} \\ r_S > 0.254 & \text{(manifold B)}. \end{cases} \tag{8}$$

The different limits are due to the different spatial dependence of the distributions of manifolds A and B.

The statistical significance is quantified by the P-value P_S (−) to a hypothesis test. When P_S is smaller than the significance level 0.05, the null hypothesis representing no correlation ($r_S=0$) is rejected. In other words, when $P_S<0.05$, the velocity distributions are significantly correlated.

The statistical significance of r_M is based on Eq. (12.4.1) in Hald [14] and the Mellin convolution, described by Eq. (4.1.7) in Springer [16]. The P-value P_M (−) quantifies the statistical significance for a hypothesis test where the null hypothesis represents similarity ($r_M=1$). Contrary to the P-value P_S, when $P_M > 0.05$, the null hypothesis is not rejected meaning the velocity distributions are significantly similar in magnitude. Values for P_S and P_M are given in the summarized results in Tables 2 and 3.

The pulsating flow in the exhaust manifold with CC catalyst enforces a periodic scavenging of the diffuser or precat chamber. The scavenging process is determined by the diffuser volume V_d (m^3), the exhausted gas volume per cylinder and per cycle, the number and layout of the exhaust runners issuing into the manifold, and the flow pulsation period T_p (s).

A nondimensional group S (−) is formed to characterize the scavenging process. The scavenging number S is used in Sec. 3.3

Table 3 Summary of experiments on the CME flow rig

Geometry	N (rpm)	p_i (atm)	Q_{ref} (m^3/h)	$S^{(old)}$ (−)	S (−)	r_S (−)	P_S (−)	r_M (−)	P_M (−)
CME flow rig,	1200	1.00	46.6	0.830	0.170	0.109	0.238	1.169	0.221
manifold B	1200	1.55	67.7	1.205	0.300	0.317	0.017	1.212	0.452
	1800	1.00	75.1	0.891	0.444	0.319	0.016	1.240	0.411
	1200	2.23	93.3	1.661	0.552	0.550	0.000	1.194	0.542
	1800	1.58	97.4	1.255	0.417	0.516	0.000	1.235	0.466
	1800	1.57	97.4	1.184	0.393	0.526	0.000	1.234	0.461
	1800	2.23	136.6	1.672	0.833	0.649	0.000	0.998	0.990
	1800	2.15	132.5	1.565	0.779	0.661	0.000	1.206	0.355
	2400	1.55	192.1	1.709	0.851	0.615	0.000	1.147	0.449
	2400	2.03	238.8	2.125	1.058	0.646	0.000	1.252	0.240
	3000	1.55	255.2	1.817	0.905	0.598	0.000	1.267	0.236

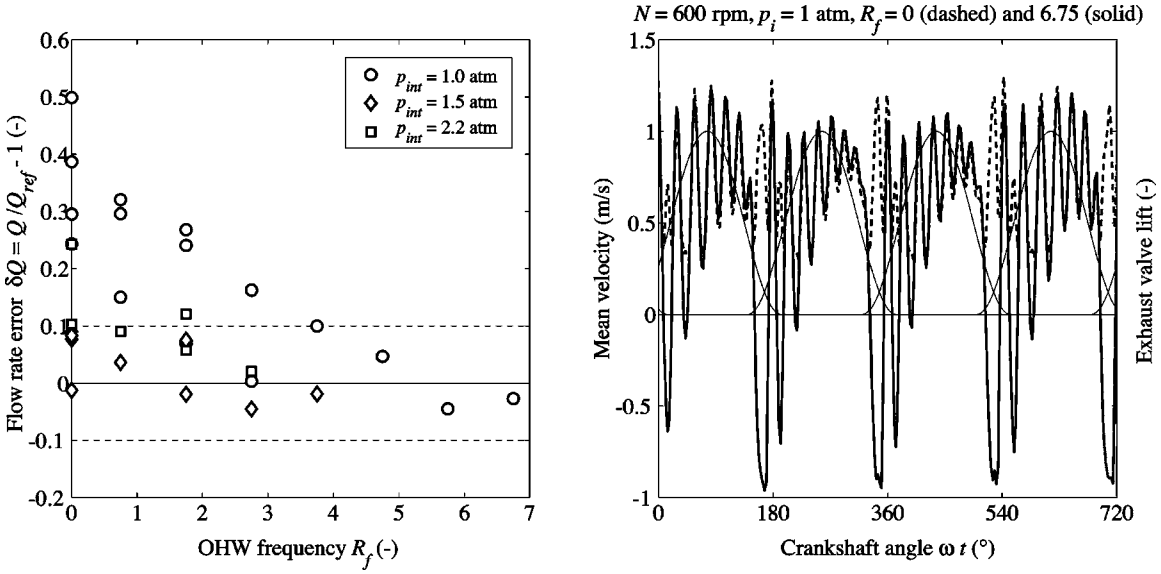

Fig. 7 Influence of OHW frequency R_f on flow rate deviation (left) and time-resolved mean velocity (right)

to correlate the similarity measures r_S and r_M. S is defined as the ratio of two time scales involved in the scavenging process:

$$S = \frac{T_p}{T_s}, \tag{9}$$

where T_s is scavenging time scale (s), defined as the ratio of diffuser volume to time-averaged volumetric flow rate Q (m^3/s) through the catalyst:

$$T_s = \frac{V_d}{Q}. \tag{10}$$

Q can be calculated from the time-averaged velocity distribution or a reference flow rate reading, which is a standardized orifice for the isothermal flow rig and a laminar flow meter for the CME flow rig. In Persoons et al. [1], the pulsation period T_p (s) was defined as

$$T_p^{(\text{old})} = \frac{120}{N}\frac{1}{n_r}, \tag{11}$$

where n_r is the number of runners issuing into the catalyst. The true flow period is one engine cycle (i.e., two crankshaft revolutions) or $120/N$. Each engine cycle features n_r exhaust pulses. Thus, T_p represents the apparent flow pulsation period experienced by the manifold.

The exhaust stroke in the CME flow rig consists of blow-down and displacement phases. This two-stage nature in combination with strong Helmholtz resonances during the displacement phase results in a smaller apparent flow pulsation period. Therefore, the following new definition of T_p is introduced:

$$T_p^{(\text{new})} = \frac{1}{f_{PSD,\max}} \tag{12}$$

where $f_{PSD,\max}$=frequency (Hz) corresponding to the maximum in the power spectral density of the time-resolved mean velocity $U_m(\theta)$. The apparent flow pulsation period experienced by the catalyst is better described by Eq. (12) than by the old definition in Eq. (11). This is further discussed in Sec. 3.2.

A high scavenging number S (e.g. low engine speed and/or high flow rate) means the diffuser scavenging occurs faster than the flow pulsation period, therefore the catalyst flow distribution should be relatively unaffected by changes in S, or indeed changes in engine speed or flow rate. A low scavenging number S (e.g. high engine speed or low flow rate) results in the opposite, meaning more interference of exhaust flow pulses from individual runners. Consequently, the flow distribution should be more sensitive to changes in S.

3 Experimental Results

The experimental results discussed in this section are obtained on the charged motored engine (CME) flow rig. These results are compared to the results discussed in Persoons et al. [1], obtained on the isothermal flow rig.

3.1 OHW. To assess the effectiveness of the OHW system, a number of engine operating points that feature reverse flow are selected. In these operating points, the oscillator frequency ratio R_f is increased from zero for a stationary probe to the maximum frequency attainable with the oscillator. As R_f increases, so does the resolution in the negative velocity range, and consequently the correspondence should improve between the exhaust flow rate calculated as the area-averaged OHW velocity distribution and the intake flow rate measured using a laminar flow meter.

Figure 7 (left) shows the nondimensional flow rate deviation $\delta Q = Q/Q_{\text{ref}} - 1$ (−). The reference exhaust flow rate Q_{ref} (m^3/s) is calculated as $Q_{\text{ref}} = \rho_s(Q_{s,\text{in}} - Q_{s,bb})/\rho$, where ρ_s and ρ are the density of air at standard conditions (0 °C, 1 atm) and exhaust conditions. The intake standard flow rate $Q_{s,\text{in}}$ (Nm^3/s) is determined by means of a laminar flow meter in the intake system. This measurement is further verified using a cylinder pressure sensor, by calculating the cylinder charge per cycle from the pressure rise during the compression stroke. The blow-by leakage standard flow rate $Q_{s,bb}$ (Nm^3/s) is estimated based on a correlation as a function of engine speed, time-averaged cylinder pressure and temperature. This correlation is based on previous measurements. At most, blow-by leakage amounts to 5% of intake flow rate, for full load at low engine speed.

The markers in Fig. 7 (left) represent experiments at engine speeds of 600, 1200, and 1800 rpm. At low engine load (p_i = 1.0 atm) strong backflow occurs. This situation is not physically possible with fired engine conditions. However, local occasional backflow occurs also at a higher engine load (p_i=1.5…2.2 atm).

Figure 7 (left) shows that for increasing OHW oscillation

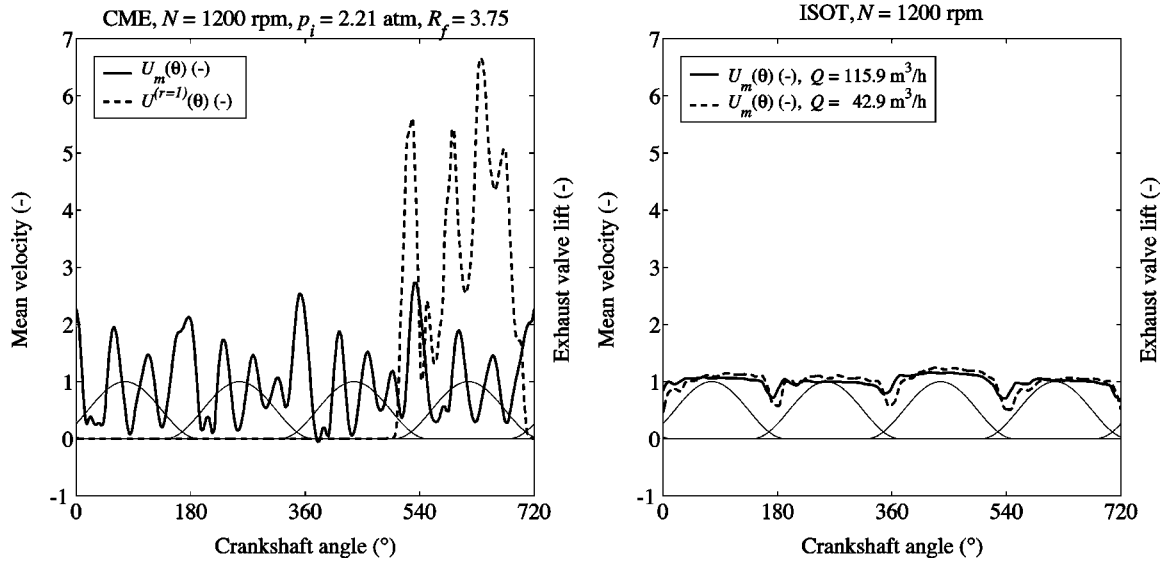

Fig. 8 Time-resolved velocity on CME (left) and isothermal (right) flow rig, for comparable engine speed and flow rate, corresponding to full load

frequency R_f, the velocity measurement becomes increasingly more accurate. Traditional HWA using a stationary probe corresponds in Fig. 7 (left) to the points at $R_f=0$. The flow rate error amounts to anywhere between 0 and 50%. The OHW approach reduces the flow rate error to within the accuracy margins on Q_{ref} (5 to 10%), represented by the dashed lines in Fig. 7 (left).

Figure 7 (right) shows the influence of using the OHW on the time-resolved mean velocity $U_m(\theta)$ (m/s). The dashed line uses a stationary probe ($R_f=0$), whereas the solid line uses an oscillating probe at $R_f=6.75$. This experiment corresponds to the rightmost circular marker in Fig. 7 (left). The mean velocity using traditional HWA ($R_f=0$) exhibits the typical rectification or folding, since HWA is only sensitive to velocity magnitude, not to direction.

3.2 Time-Resolved Velocity. The time-resolved mean velocity $U_m(\theta)$ features strong fluctuations when compared to previous measurements on the isothermal flow rig. This is due to the two-stage nature of the exhaust stroke, combined with the Helmholtz resonance effect. Figure 8 show a comparison at equal engine speed and flow rate $\cong 100$ m^3/h between the pulsating mean velocity on the CME (left) and isothermal (right) flow rig. Dashed lines in Figs. 8 (left) and 9 (left) represent the time-resolved velocity at the inlet to runner 1 $U^{(r=1)}(\theta)$. Since 0° corresponds to top dead center of Cylinder 1 and considering the engine's firing order, the time-resolved plots show the exhaust stroke of Cylinders 3, 4, 2, and 1.

The mean velocity fluctuations in Figs. 7–9 during the displacement phases are due to a Helmholtz resonance in the exhaust runners and collector volume. This phenomenon has been observed previously on an isothermal flow rig and is discussed in Persoons et al. [1]. A pipe connected to a volume V is called a Helmholtz resonator. Its zeroth-order gas dynamic resonance frequency is called the Helmholtz resonance frequency f_h (Hz). When in resonance, the gas in the pipe behaves as an incompressible oscillating mass and the gas in the volume as a compressible spring. The resonance frequency f_h equals:

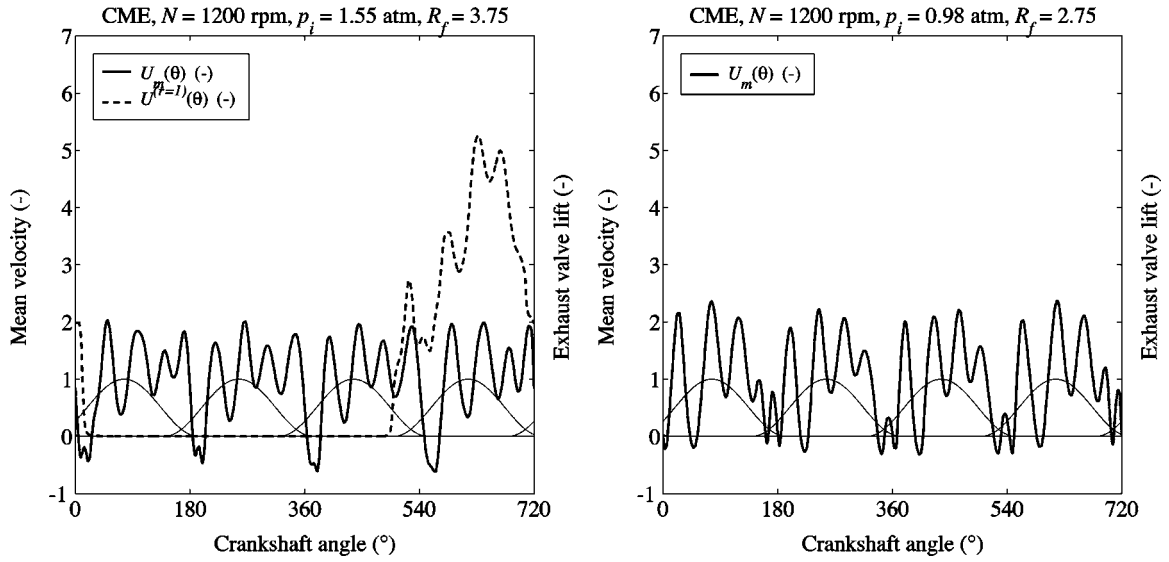

Fig. 9 Time-resolved velocity in part (left) and zero (right) load conditions on CME flow rig

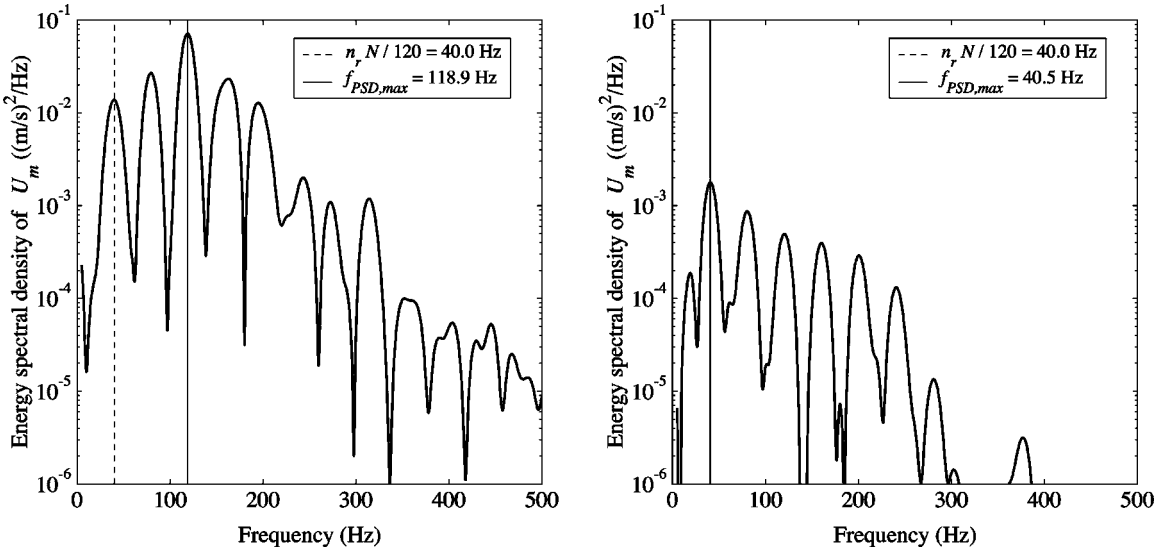

Fig. 10 Spectra of time-resolved mean velocity on CME (left) and isothermal (right) flow rig, for $N=1200$ rpm and $Q\cong 100$ m^3/h

$$f_h = \frac{1}{2\pi}\frac{c}{L}\sqrt{\frac{AL}{V}}, \tag{13}$$

where c is the speed of sound (m/s), A and L is the cross-sectional area (m^2) and length (m) of the pipe. The observed fluctuation frequencies (200 to 300 Hz) correspond to Eq. (13), where the pipe is the open runner, and the volume is the diffuser combined with the closed runners.

Figures 8 (left) and 9 represent experiments at an engine speed of 1200 rpm, with varying intake system pressure corresponding to full, part, and zero load, respectively. Even for full load conditions, the mean velocity attains near-zero values. The OHW measurement technique shows strong periodic backflow occurring throughout the catalyst cross section for part and zero load conditions.

(Near) reverse flow is most pronounced immediately following the blow-down phase. During the displacement phase, strong Helmholtz-related fluctuations may also cause negative mean velocities, as can be seen in Fig. 9 (right) for zero-load conditions.

As appears from Figs. 8 (left) and 9, the entire manifold gas volume comes to a standstill at certain instants. The flow pulsation period apparent to the manifold is therefore not determined by the engine speed alone, as is the case with the isothermal flow rig experiments. This leads to the introduction in Sec. 2.3 of a new definition of the flow pulsation period T_p in Eq. 12, for use in the addition principle's validation in Sec. 3.3. The new definition is based on the peak frequency in the power spectral density of the mean velocity.

Figure 10 shows the power spectral density plots for two cases of identical engine speed and flow rate, on the CME (left) and isothermal (right) flow rig. For the isothermal flow rig (Fig. 10 (right)), the peak frequency corresponds to $1/T_p^{(\mathrm{old})} = n_r N/120$. For the CME flow rig (Fig. 10 (left)), the pulsating flow is characterized by a higher-frequency content.

3.3 Addition Principle. The addition principle states that the time-averaged catalyst velocity distribution in pulsating flow corresponds to a linear combination of velocity distributions, obtained for stationary flow through each individual runner. For the current manifold, four stationary velocity distributions are considered, one for each runner. The stationary distributions are obtained on the isothermal flow rig, with the exhaust valves in the position of maximum lift.

The linear combination is defined as the arithmetical average of the nondimensional velocity distributions $\tilde{U}_{\mathrm{stat}}^{(r)}$ for each runner r:

$$\tilde{U}_{\mathrm{stat}}(x,y) = \frac{1}{n_r}\sum_{r=1}^{n_r} \tilde{U}_{\mathrm{stat}}^{(r)}(x,y), \tag{14}$$

where r is the exhaust runner index.

The addition principle is verified by examining the similarity between the combined stationary distribution $\tilde{U}_{\mathrm{stat}}$ defined by Eq. (14) and the time-averaged velocity distribution obtained in pulsating flow, for the same flow rate.

Figure 11 shows an example of the stationary velocity distributions $\tilde{U}_{\mathrm{stat}}^{(r)}$ (top and middle) for roughly 130 m^3/h. Figure 12 shows the corresponding stationary averaged distribution $\tilde{U}_{\mathrm{stat}}$ obtained using Eq. (14) (left), and the time-averaged velocity distribution $\tilde{U}$ (right) in pulsating flow on the CME flow rig, at a comparable volumetric flow rate. Note that the plot of the stationary averaged distribution mentions an engine speed $N=0$, since this case could be regarded as the limit for infinitely slow pulsation.

Figures 13–15 show similar combinations of stationary averaged distribution and time-averaged distribution in pulsating flow, for various experimental conditions. Figures 12 and 13 both represent experiments on the CME flow rig. Figure 12 is a result at high scavenging number ($S=0.779$) corresponding to full engine load, and Fig. 13 is a result at low scavenging number ($S=0.300$). The correspondence between steady and pulsating distributions in Fig. 13 is much worse when compared to Fig. 12.

Figures 14 and 15 both represent experiments on the isothermal flow rig, for the same manifold (Type B) and cylinder head as used on the CME flow rig. Figure 14 shows the result of an experiment at a scavenging number ($S=0.754$) comparable to Fig. 12. Both experiments are performed in completely different pulsating flows, at different flow rate and engine speed. Nevertheless, the shape similarity measures are quite comparable, $r_S=0.661$ for Fig. 12 and $r_S=0.738$ for Fig. 14.

Figure 15 is the result for a very high scavenging number $S=2.249$, obtained on the isothermal flow rig. This case is obtained for high flow rate at relatively low engine speed. Correlation between steady and pulsating distributions is very good, with r_S

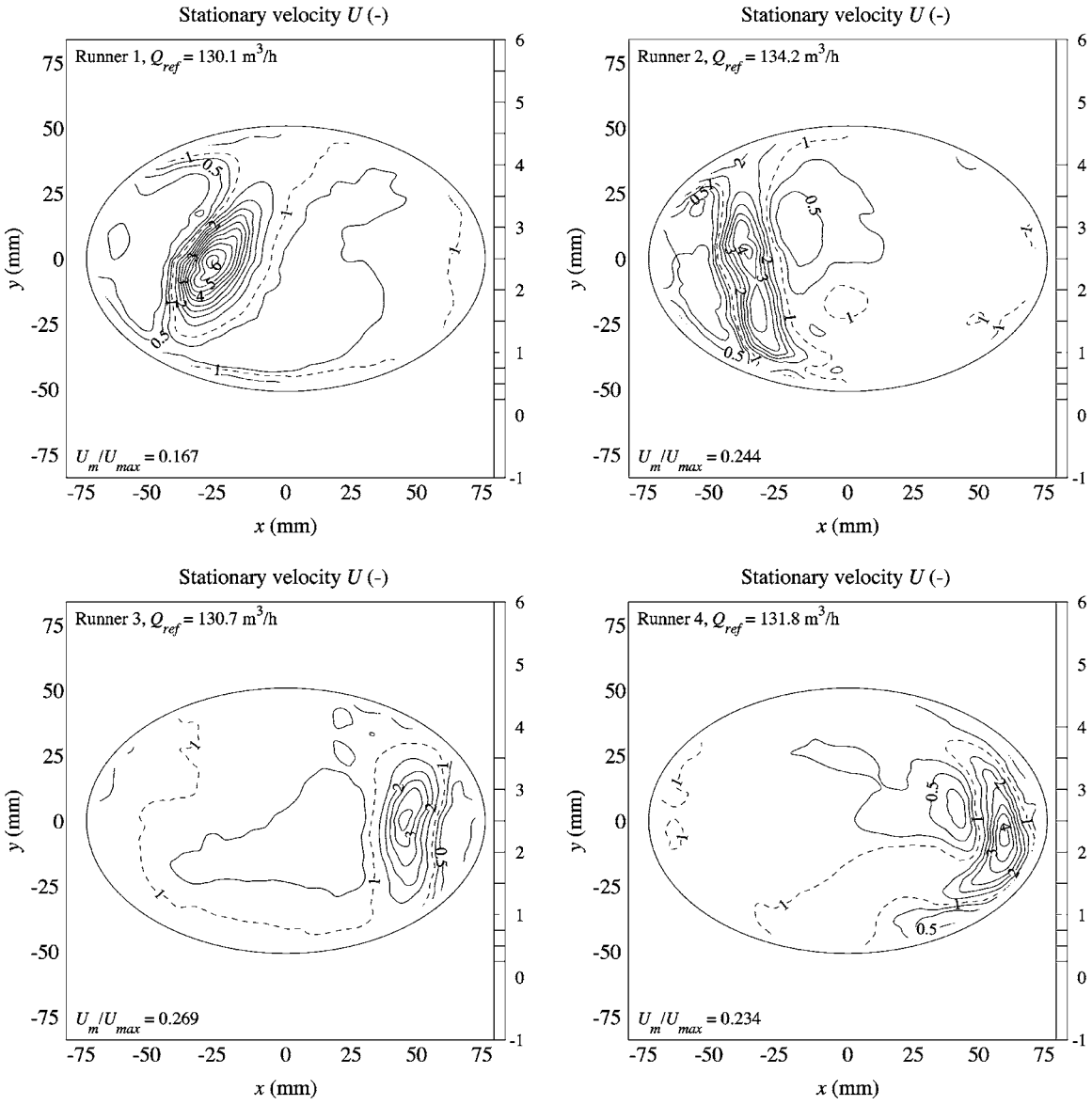

Fig. 11 Stationary velocity distributions for flow through each runner (r=1 through 4 from top left to bottom right)

=0.965.

The results presented in Figs. 12–15 indicate that the scavenging number is correlated to the degree of similarity between steady and pulsating distributions, and thus to the addition principle's validity. Upon comparing the steady and pulsating distributions in Figs. 12–15, it shows that the flow uniformity is consistently higher for pulsating than for stationary flow. The quantification and statistical significance of the similarity based on shape (r_S) and magnitude (r_M) is presented in Table 2 for the isothermal flow rig [1] and Table 3 for the CME flow rig.

Tables 2 and 3 list the scavenging number $S^{(\mathrm{old})}$ using the old definition of T_p (Eq. (11)). Since the isothermal flow rig lacks blow-down and features weaker Helmholtz resonance-induced fluctuations, the new and old definitions of T_p yield nearly identical results in Table 2. The deviation is on S is below 0.1, except in two cases featuring strong Helmholtz resonances. Since the CME flow rig features a two-stage (instead of a single pulse) exhaust stroke, the new definition of T_p (Eq. (12)) is typically one-half of the old value, which explains the approximate difference by a factor two between $S^{(\mathrm{old})}$ and S in Table 3.

The scavenging number in the CME flow rig experiments varies between 0.17 and 1.06, whereas the scavenging number in the isothermal flow rig experiments [1] varies between 0.23 and 4.66. For a fired engine and the CME flow rig, the catalyst flow rate Q increases linearly with the engine speed N, the intake manifold density and the exhaust gas temperature, at least as a first approximation. Combining $Q \sim N \cdot p_i \cdot T_{exh}$ with Eqs. (9)–(11) yields that S is nearly independent of N and varies mainly with engine load. S increases for a variation from zero to full engine load. By contrast, an isothermal flow rig allows the pulsation frequency (i.e., engine speed) and flow rate (i.e., engine load) to be controlled independently, enabling a wider range of scavenging number. The scavenging number does not differ significantly between fired engine conditions and the CME flow rig.

Figure 16 shows the nondimensional correlation of both similarity measures versus the old definition of the scavenging number using Eq. (11). The CME flow rig experiments are plotted as crosses, whereas the other markers represent experiments on the isothermal flow rig. In the figure legends, "A" and "B" denote manifold types A and B, and "RV" and "CH" denote rotating valve or cylinder head as pulsator. The exponential correlation fits $r'_S = 1 - c'_S \exp(-S/S'_{\mathrm{crit},S})$ and $r'_M = r'_{M,\infty} + c'_M \exp(-S/S'_{\mathrm{crit},M})$ are

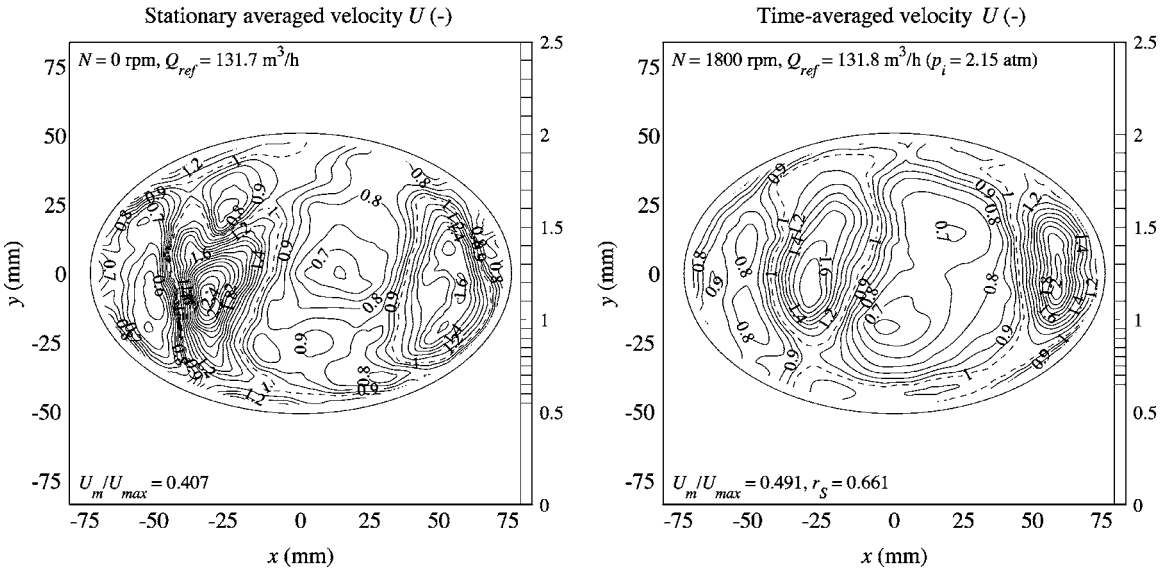

Fig. 12 Stationary averaged distribution according to Eq. (14) (left) and time-averaged distribution on CME (right), for scavenging number S=0.779

least-squares fitted to the isothermal flow rig experiments. The values in Table 2 and the fit constants shown in Fig. 16 deviate slightly from Persoons et al. [1], due to an updated data processing. The values of $S'_{\text{crit},S}$ and $S'_{\text{crit},M}$ differ, due to the greater uncertainty on r_M.

Figure 17 shows the correlation versus the new definition of the scavenging number using Eq. (12). The points corresponding to the isothermal flow rig experiments remain roughly unchanged with respect to Fig. 16. However, the crosses representing the CME flow rig experiments now correlate very well with the isothermal flow rig experiments. Correspondence is good for r_S yet only moderate for r_M. In Fig. 17 (right), the crosses representing the CME flow rig cases appear to deviate from the isothermal flow rig cases. Due to the greater uncertainty on r_M and the limited range of S obtained of the CME flow rig, the deviation is insignificant. The form of the exponential correlation fits is altered into $r''_S = 1 - \exp(-S/S_{\text{crit}})$ and $r''_M = r''_{M,\infty} + c''_M \exp(-S/S_{\text{crit}})$.

The resulting correlations for the similarity measures versus scavenging number are:

$$\begin{cases} r''_S = 1 - \exp(-S/0.709); & R^2 = 0.89 \\ r''_M = 1.124 + 0.338 \exp(-S/0.709); & R^2 = 0.34. \end{cases} \tag{15}$$

Note that these correlations combine the CME flow rig experiments with the isothermal flow rig experiments from Persoons et al. [1], obtained for two types of exhaust manifolds with and without an exhaust valve overlap, and for a rotating valve and cylinder head as a pulsator.

Regarding the statistical significance of r_S, the limits in Eq. (8) for significant similarity hold for most experiments. Indeed, the P-values P_S for the r_S hypothesis test described in Sec. 2.3 are

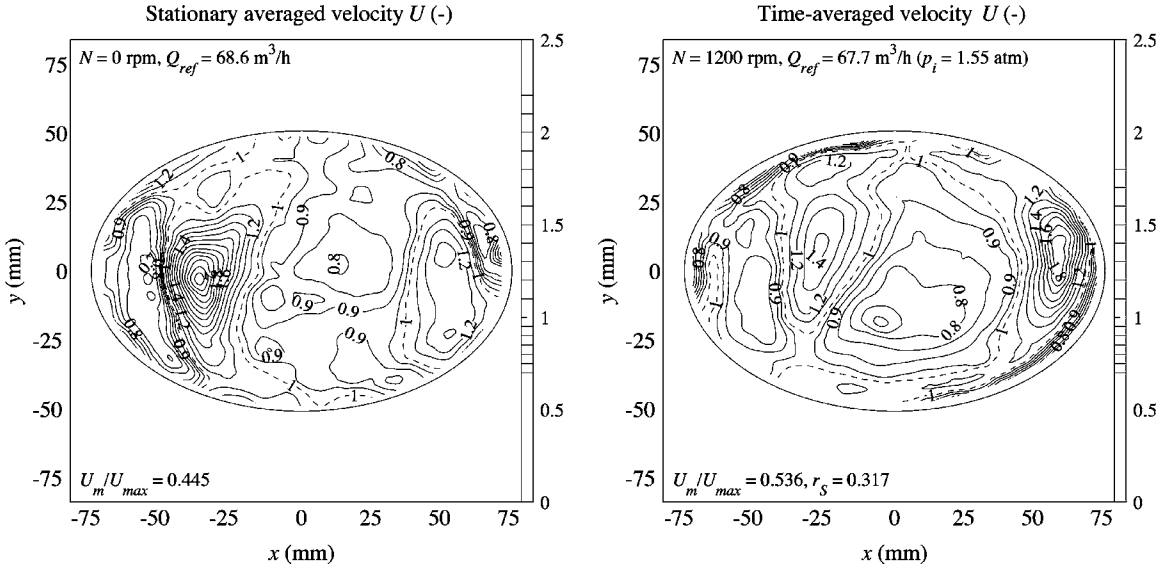

Fig. 13 Stationary averaged distribution according to Eq. (14) (left) and time-averaged distribution on CME (right), for scavenging number S=0.300

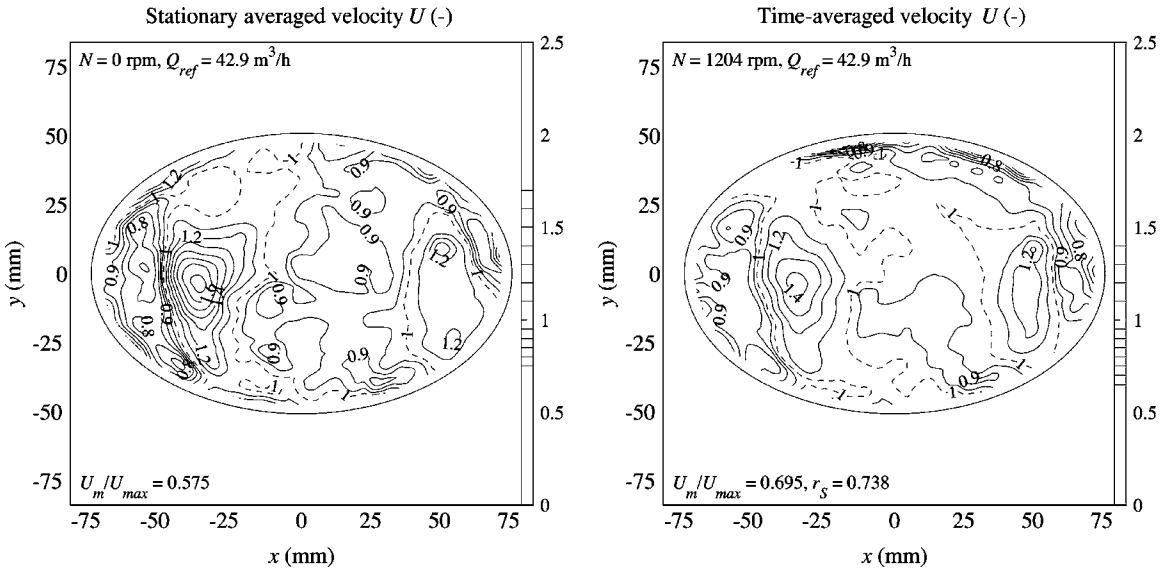

Fig. 14 Stationary averaged distribution according to Eq. (14) (left) and time-averaged distribution on isothermal flow rig (right), for scavenging number S=0.754

smaller than the significance level 0.05, with one exception.

As discussed in Sec. 2.3, the P value P_M behaves differently from P_S. A value of P_M greater than 0.05 indicates statistically significant similarity based on the r_M hypothesis test. In Tables 2 and 3, values for P_M are mostly greater than 0.05, with one exception. r_M is consistently larger than unity, indicating that the flow uniformity is higher in pulsating than in steady flow. Nevertheless, the r_M hypothesis test does not indicate a significant difference between steady and pulsating flow distributions.

The evidence based on r_M is weaker when compared to r_S. Yet strictly statistically speaking, the addition principle is valid for almost the entire range of S. Taking into account Eq. (15), it seems however more appropriate to state that the addition principle is valid when S exceeds the critical value S_{crit}=0.71, corresponding roughly to $r''_S > 0.5$ and $r''_M < 1.25$.

Figure 17 and the correlations in Eq. (15) provide substantial evidence that the addition principle remains valid under various conditions. The elegance of Eq. (15), at least for r''_S, further supports that the scavenging number is the correct choice of nondimensional group to describe this flow. An analogy holds between the current problem and the scavenging of a volume with a scalar quantity such as a concentration. For instance, assume incompressible flow through a perfectly stirred volume V (m^3) with one inlet and one outlet, containing a volumetric concentration ϕ (vol %) of some compound. The following equation and corresponding transfer function describe the concentration evolution in time:

$$\frac{\partial}{\partial t}(V\phi) = V\frac{\partial \phi}{\partial t} = Q\phi_i - Q\phi \Leftrightarrow \tau_s \frac{\partial \phi}{\partial t} + \phi = \phi_i, \qquad (16)$$

where Q is the volumetric flow rate (m^3/s), ϕ_i is the inlet concentration (vol %), and τ_s is the scavenging time constant (s), defined as $\tau_s = V/Q$. Assuming a stepwise change in the inlet con-

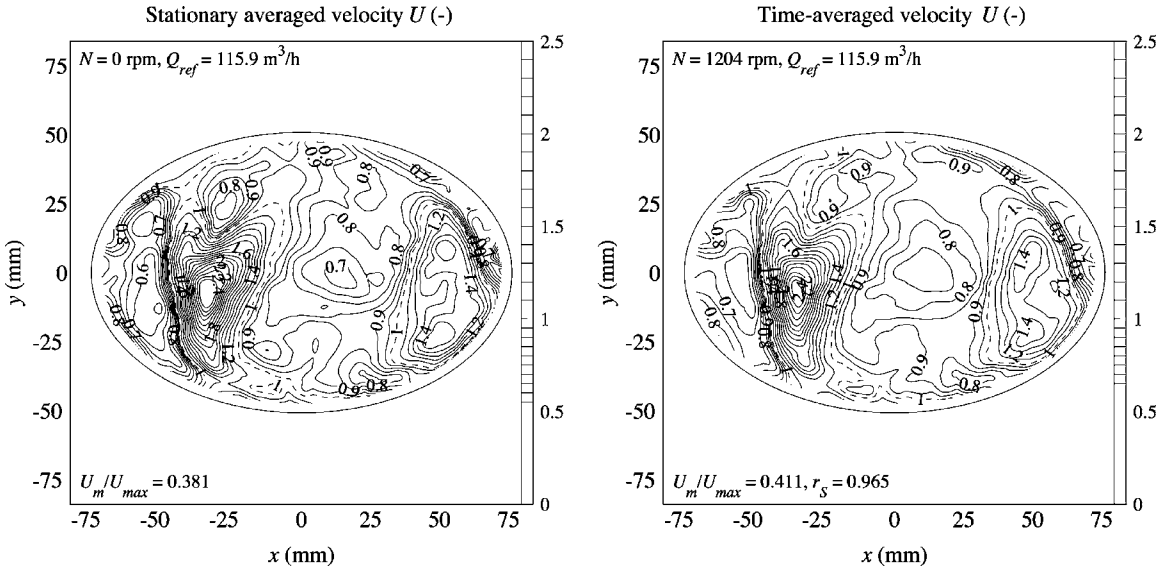

Fig. 15 Stationary averaged distribution according to Eq. (14) (left) and time-averaged distribution on isothermal flow rig (right), for scavenging number S=2.249

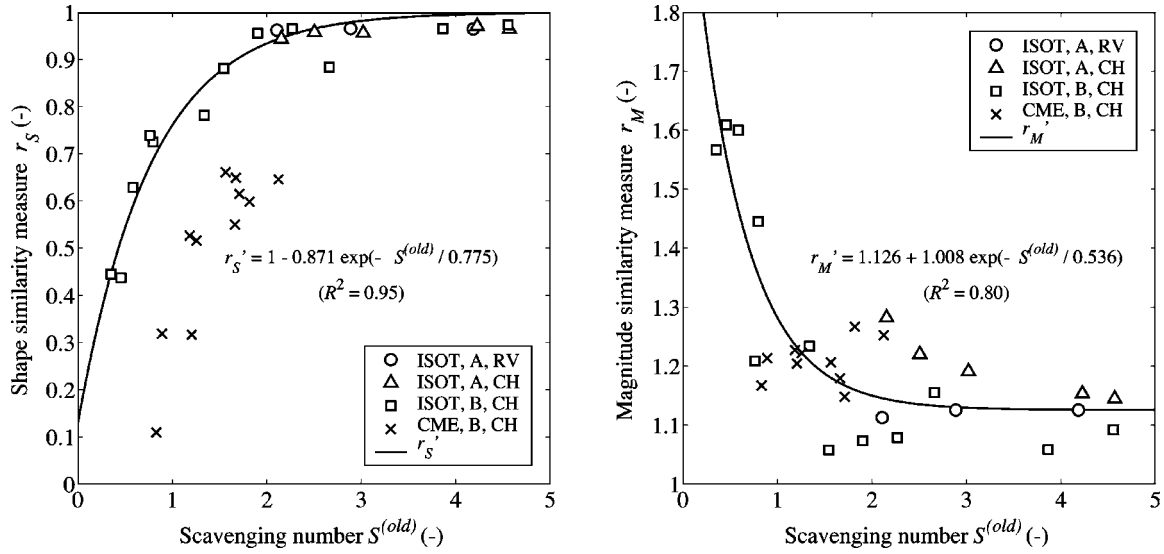

Fig. 16 Correlations of similarity measures r_S (left) and r_M (right) versus scavenging number, using old definition of T_p (Eq. (11))

centration ϕ_i at time $t=0$, and initial concentration $\phi(t=0)=0$, the solution to Eq. (16) becomes

$$\frac{\phi}{\phi_i}(t) = 1 - \exp(-t/\tau_s). \tag{17}$$

Equation (17) expresses to what extent the volume is scavenged, as a function of the nondimensional time t/τ_s. If t/τ_s is sufficiently large, the solution becomes independent of t/τ_s. The nondimensional time t/τ_s corresponds to the scavenging number $S = T_p/T_s$ used in this study. The remarkable correlation fit in Eq. (15) for r_S'' suggests that this complex multidimensional flow behaves essentially like a first order zero-dimensional scavenging process of a scalar quantity.

In light of this analogy, the critical scavenging number $S_{\text{crit}} = 0.709 < 1$ suggests that only part of the diffuser volume may be active during the scavenging process. From the introduction of an alternate scavenging number $S' = S/S_{\text{crit}} = S/0.709 = T_p Q/(S_{\text{crit}} V_d) = T_p Q/V_{d,\text{eff}}$ follows an effective diffuser volume $V_{d,\text{eff}} = S_{\text{crit}} V_d = 0.709 V_d$. The velocity distributions in Figs. 12–15 indeed indicate that some parts of the catalyst are subject to a very low flow rate, particularly the leftmost and central areas. Since r_M increases for decreasing S and S is inversely proportional to the diffuser volume V_d, the flow uniformity in pulsating flow increases for an increasing diffuser volume. As such, the ratio of the effective to actual diffuser volume $V_{d,\text{eff}}/V_d = S_{\text{crit}} = 0.709$ could be seen as the CC catalyst manifold efficiency with respect to flow uniformity. The higher the critical scavenging number, the more efficiently the diffuser distributes the exhaust gas throughout the catalyst cross section.

With regard to the generality of the above discussion, some comments can be made. For instance, one may consider the influence of the catalyst pressure drop on the addition principle, for a given collector geometry. The pressure drop can be altered by, e.g., changing the cell density and wall thickness, without altering the catalyst's outer dimensions. An increased catalyst pressure drop affects the velocity distributions, both in stationary and pul-

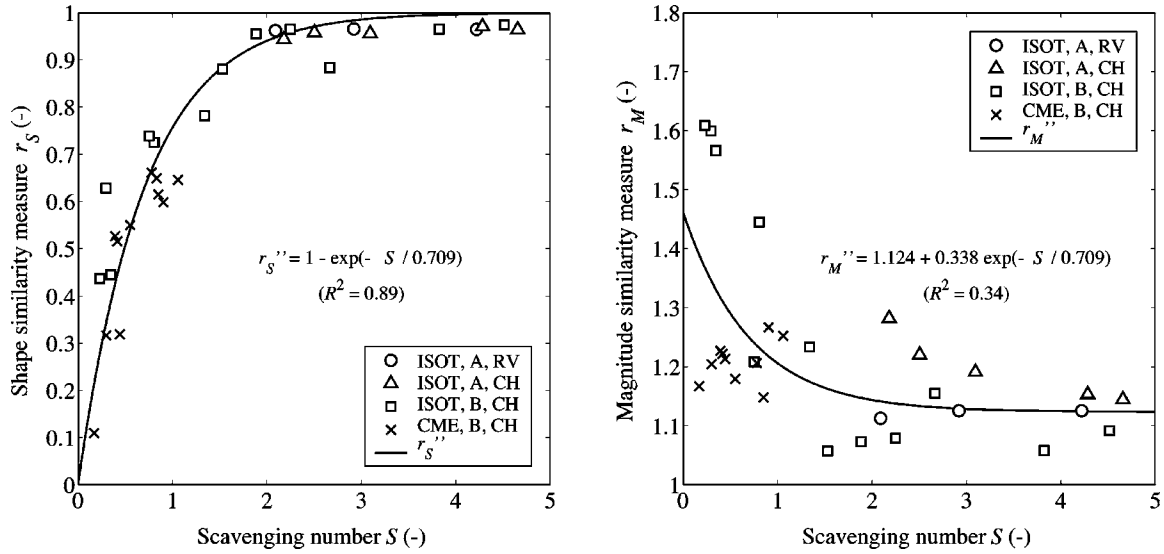

Fig. 17 Correlations of similarity measures r_S (left) and r_M (right) versus scavenging number, using new definition of T_p (Eq. (12))

sating flow conditions. It is not within the scope of this paper to determine the quantitative influence on the velocity distribution, yet it is clear that the flow uniformity will increase.

The validity of the addition principle is assessed based entirely on nondimensional numbers. The scavenging number (Eqs. (9) and (12)) is not directly affected by changing the pressure drop. Indirectly, the frequency spectrum will be affected by the attenuation of high-frequency fluctuations. The definition of r_M (Eq. (6)) ensures that equal scalar changes of the uniformity measure $U_m/U_{\max}$ in stationary and pulsating conditions do not affect the value of r_M. Equally, r_S is defined as a correlation coefficient (Eq. (7)). Thus, it is unaffected by changes in the mean value or variance of the velocity distributions in stationary and pulsating conditions.

Some influence is expected on the critical scavenging number. According to the mixing process analogy, S_{crit} corresponds to a collector efficiency, defined as the ratio of effective to actual diffuser volume. As the catalyst pressure drop increases, so does the flow uniformity. Therefore, S_{crit} is expected to increase as well. This merits further research.

In summary, the validity of the addition principle is, at least in first approximation, unaffected by particular changes in the catalyst flow resistance characteristics.

4 Conclusion

The current paper investigates the validity of the addition principle for pulsating flow in a typical close-coupled catalyst manifold. The addition principle states that the time-averaged catalyst velocity distribution in pulsating flow equals a linear combination of velocity distributions obtained for steady flow through each of the exhaust runners (Eq. (14)).

The results complement previous research on an isothermal flow rig [1]. The CME flow rig generates cold pulsating flow that better resembles fired engine conditions, featuring a two-stage exhaust stroke consisting of blow-down and displacement phases. The flow similarity between CME and fired conditions is not complete. Nevertheless, combined with Helmholtz resonances intrinsic to the manifold, the pulsating flow features a similar frequency content to fired engines [6–8]. The increased frequency content compared to the isothermal flow rig leads to a new definition of the apparent flow pulsation period T_p in Eq. (12).

An OHW is used to measure bidirectional velocity, with a maximum measurable negative velocity of −1 m/s. The effect of the OHW is demonstrated in Sec. 3.1. The time resolved velocity results presented in Sec. 3.2 indicate strong velocity fluctuations, including reverse flow typically following the blow-down phase.

The scavenging number S defined in Eq. (9) uses the new flow pulsation period definition, and provides the appropriate nondimensional number to characterize the flow. The nondimensional measures r_S and r_M quantify similarity between steady and pulsating flow distributions based on shape and magnitude, respectively. These measures are used to quantify the validity of the addition principle.

Results from the current and previous research are combined in Fig. 17 and Tables 2 and 3. Figure 17 shows the good correlation between the similarity measures r_S and r_M and the scavenging number S.

The validity of the addition principle is quantified in terms of the statistical significance of r_S and r_M in Tables 2 and 3. The correlations for r_S and r_M in Eq. (15) are:

$$\begin{cases} r_S'' = 1 - \exp(-S/0.709); & R^2 = 0.89 \\ r_M'' = 1.124 + 0.338\exp(-S/0.709); & R^2 = 0.34. \end{cases}$$

Strong statistical evidence is given in support of the addition principle, for nearly the entire range of S. However, no validity limit can be derived based on the statistical significance of r_S and r_M. Therefore, the practical limit of the addition principle's validity is when S exceeds the critical scavenging number $S_{\text{crit}}=0.71$, corresponding roughly to $r_S''>0.5$ and $r_M''<1.25$.

Some manifold design criteria may be formulated based on Fig. 17 and Eq. (15). Based on the correlation for r_S, good correspondence between stationary flow simulations or measurements and pulsating flow is obtained for a high scavenging number. Thus, for a given engine geometry and operating range, decreasing the diffuser volume increases the scavenging number, thereby improving the correspondence between stationary and pulsating flow. In the validity region of the addition principle, steady-state CFD simulations can be used instead of time-consuming transient simulations for the design of a CC catalyst manifold, resulting in a significantly shorter development time.

Based on the correlation for r_M, flow uniformity is always higher in pulsating flow compared to stationary flow. A manifold that is designed based on stationary CFD simulations, and that satisfies the preset criteria for flow uniformity, will likely feature a better flow uniformity in pulsating flow conditions.

Flow uniformity in a pulsating flow is higher for a small scavenging number. Increasing the diffuser volume decreases the scavenging number, thereby increasing flow uniformity. This expected conclusion will be subject to compromise in terms of underhood packaging constraints.

Based on the elegance of the r_S correlation in Eq. (15), this complex multidimensional flow behaves essentially like a zero-dimensional scalar mixing process. In that respect, the critical scavenging number $S_{\text{crit}}=0.71$ equals the ratio of the effective to actual diffuser volume. S_{crit} can be considered the manifold efficiency with respect to catalyst flow uniformity. Indeed, by maximizing the manifold efficiency, flow uniformity is optimized, and consequently so is the catalyst durability, conversion efficiency, and exhaust system backpressure. The correlations in Eq. (15) are valid for two different exhaust manifolds. Further investigations would be required to determine to what extent the critical scavenging number depends on the manifold geometry.

Figure 17 and the correlations above are based on the results for CME and isothermal flow rig, for two exhaust manifolds (Types B and A, respectively, with and without exhaust valve overlap) and for two pulsator devices (rotating valve and cylinder head with poppet valves). Based on the excellent agreement of current and previous results, the addition principle's validity is established through nondimensional correlations and statistical analysis in a broad range of applicability.

Acknowledgment

This work has been partly sponsored by IWT-Vlaanderen under Grant Nos. VLIET/970375/BOSAL and IWT/030582/BOSAL.

Nomenclature

A = cross-sectional area, m^2
f_0 = OHW oscillation frequency, Hz
N = engine speed, rpm
n_r = number of runners (−)
P_S, P_M = P-value for the shape and magnitude similarity hypothesis test (−)
p_i = intake system pressure, atm, absolute
Q = volumetric flow rate, m^3/s
R^2 = coefficient of determination (−)
R_f = OHW dimensionless oscillation frequency (−), $R_f=f_0/(N/120)$
r_S, r_M = shape and magnitude similarity measure (−)
S = scavenging number (−), $S=T_p/T_s$
T_p = flow pulsation period, s, $T_p^{(\text{old})}=(120/N)/n_r$ and $T_p^{(\text{new})}=1/f_{\text{PSD,max}}$
T_s = diffuser scavenging time scale, s, $T_s=V_d/Q$
U = axial velocity, m/s
V = volume, m^3

x, y = coordinates in the measurement plane, m
x, y = coordinates in the measurement plane, m
x_0 = OHW oscillation amplitude, m

Greek symbols

α = OHW tolerance factor on maximal negative probe velocity $(-)$
θ = engine crankshaft position, °
ρ = density, kg/m^3
ω = engine speed, rad/s
ω_0 = OHW oscillation speed, rad/s

Subscripts

d = diffuser
e = phase-locked ensemble index
i = measurement point index
j = crankshaft position index
M = magnitude similarity
m = mean (spatial)
max = maximum (spatial)
p = hot-wire probe
puls = pulsating conditions
ref = reference flow rate measurement in the intake system
rel = relative to hot-wire probe
S = shape similarity
stat = stationary conditions

Superscripts

(old), (new) = old and new definition of the flow pulsation period T_p, Eqs. (11) and (12)
(r) = runner index

References

[1] Persoons, T., Van den Bulck, E., and Fausto, S., 2004, "Study of Pulsating Flow in Close-Coupled Catalyst Manifolds Using Phase-Locked Hot-Wire Anemometry," Exp. Fluids, **36**(2), pp. 217–232, DOI: 10.1007/s00348-003-0683-0.

[2] Benjamin, S. F., Roberts, C. A., and Wollin, J., 2002, "A Study of Pulsating Flow in Automotive Catalyst Systems," Exp. Fluids, **33**(5), pp. 217–232, DOI: 10.1007/s00348-002-0481-0.

[3] Liu, Z., Benjamin, S. F., and Roberts, C. A., 2003, "Pulsating Flow Maldistribution Within an Axisymmetric Catalytic Converter: Flow Rig Experiment and Transient CFD Simulation," SAE Tech. Paper 2003-01-3070.

[4] Bressler, H., Rammoser, D., Neumaier, H., and Terres, F., 1996, "Experimental and Predictive Investigation of a Close-Coupled Catalyst Converter with Pulsating Flow," SAE Tech. Paper 960564.

[5] Tsinoglou, D. N., and Koltsakis, G. C., 2005, "Influence of Pulsating Flow on Close-Coupled Catalyst Performance," Trans. ASME: J. Eng. Gas Turbines Power, **127**(3), pp. 676–682.

[6] Liu, Z., Benjamin, S. F., Roberts, C. A., Zhao, H., and Arias-Garcia, A., 2003, "A Coupled 1D/3D Simulation for the Flow Behaviour Inside a Close-Coupled Catalytic Converter," SAE Tech. Paper 2003-01-1875.

[7] Park, S. B., Kim, H. S., Cho, K. M., and Kim, W. T., 1998, "An Experimental and Computational Study of Flow Characteriztics in Exhaust Manifold and CCC (Close-Coupled Catalyst)," SAE Tech. Paper 980128.

[8] Kim, H. S., Min, K., Myung, C. L., and Park, S., 2002, "A Combined Experimental and Computational Approach to Improve Catalyst Flow Uniformity and Light-Off Behaviour," Proc. Inst. Mech. Eng., Part D (J. Automob. Eng.), **216**(5), pp. 413–430.

[9] Hwang, K., Lee, K., Mueller, J., Stuecken, T., Schock, H. J., and Lee, J. C. T., 1995, "Dynamic Flow Study in a Catalytic Converter Using LDV and High-Speed Flow Visualisation," SAE Tech. Paper 950786.

[10] Bruun, H. H., 1995, *Hot-Wire Anemometry: Principles and Signal Analysis*, Oxford University Press, Oxford, UK, Chap. 8.

[11] Thompson, B. E., and Whitelaw, J. H., 1984, "Flying Hot-Wire Anemometry," Exp. Fluids, **2**(1), pp. 47–55.

[12] Persoons, T., Hoefnagels, A., and Van den Bulck, E., 2006, "Calibration of an Oscillating Hot-Wire Anemometer for Bidirectional Velocity Measurements," Exp. Fluids, **40**(4), pp. 555–567.

[13] Watson, N., and Janota, M. S., 1982, *Turbocharging the Internal Combustion Engine*, The MacMillan Press Ltd, London, UK, Chap. 15.

[14] Hald, A., 1952, *Statistical Theory with Engineering Applications*, Wiley, New York, Chap. 12 and 19.

[15] Cliff, A. D., and Ord, J. K., 1973, *Spatial Autocorrelation*, Pion, London, UK, Chap. 1.

[16] Springer, M. D., 1979, *The Algebra of Random Variables*, Wiley, New York, Chap. 4.

Bifurcation Characteristics of Flows in Rectangular Sudden Expansion Channels

Francine Battaglia[1]
Department of Mechanical Engineering,
Iowa State University,
Ames, IA 50011
e-mail: francine@iastate.edu

George Papadopoulos
ATK GASL,
Ronkonkoma, NY 11779
e-mail: George.Papadopoulos@atk.com

The effect of three dimensionality on low Reynolds number flows past a symmetric sudden expansion in a channel was investigated. The geometric expansion ratio in the current study was 2:1 and the aspect ratio was 6:1. Both experimental velocity measurements and two- and three-dimensional simulations for the flow along the centerplane of the rectangular duct are presented for Reynolds numbers in the range of 150 to 600. Comparison of the two-dimensional simulations with the experiments revealed that the simulations failed to capture completely the total expansion effect on the flow, which is influenced by both geometric and hydrodynamic effects. To properly do so requires the definition of an effective expansion ratio, which is the ratio of the downstream and upstream hydraulic diameters and is therefore a function of both the expansion and aspect ratios. When two-dimensional simulations were performed using the effective expansion ratio, the new results agreed well with the three-dimensional simulations and the experiments. Furthermore, in the range of Reynolds numbers investigated, the laminar flow through the expansion underwent a symmetry-breaking bifurcation. The critical Reynolds number evaluated from the experiments and the simulations were compared to other values reported in the literature. Overall, side-wall proximity was found to enhance flow stability, thus sustaining laminar flow symmetry to higher Reynolds numbers. Last, and most important, when the logarithm of the critical Reynolds number was plotted against the reciprocal of the effective expansion ratio, a linear trend emerged that uniquely captured the bifurcation dynamics of all symmetric double-sided planar expansions.
[DOI: 10.1115/1.2201639]

Keywords: bifurcation, channel flow, critical Reynolds number, effective expansion ratio, sudden expansion

Introduction

Considerable work has been reported in the past on two-dimensional, or nominally two-dimensional flow past planar double-sided expansions, both at low Reynolds numbers where the separating flow is laminar and for moderately high Reynolds numbers where the separating flow is turbulent. The double-sided expansion is characterized by an expansion ratio, defined as the downstream-to-upstream channel height. A significant conclusion of these studies has been that while the geometry is symmetric, asymmetric flow develops under certain Reynolds number and geometric conditions. At low Reynolds numbers the flow remains symmetric with separation regions of equal length on either side of the expanding channel. The length of the separation regions is observed to increase with increasing Reynolds number. At higher Reynolds numbers, however, separation regions of unequal length develop and the asymmetry remains in the flow even up to turbulent flow conditions. The conditions of asymmetry and the value of the transition critical Reynolds number have been reported in the literature both experimentally and numerically.

Experimental investigations of suddenly expanding flows for low Reynolds numbers include the work of Durst et al. [1], Cherdron et al. [2] and Ouwa et al. [3]. In general, the experimental results indicated that the jet produced by the sudden expansion remained symmetric, but became asymmetric with increasing Reynolds number, whereby the asymmetric jet attached to one of the walls in the downstream section. The early experiments of Durst et al. [1] were for a channel expansion of 3:1, and were revisited by Cherdron et al. [2] for expansion ratios of 3:1 and 2:1.

The two dimensionality of a water jet in a rectangular channel for low Reynolds numbers was investigated by Ouwa et al. [3]. They observed that the formation of the downstream vortex continued to grow with increasing Reynolds number. Eventually, the flow became unstable destroying the two dimensionality of the large vortex downstream of the expansion plane, where the vortex became less discernible due to random fluctuations of the flow. Ouwa et al. [4] used numerical simulations to confirm their experiments, and found both studies to be in agreement.

Experiments for turbulent flow past symmetric double-sided expansions [5–8] indicated that symmetric and asymmetric zones developed depending on the expansion ratio. For small expansion ratios, the flow on each expanding wall section develops independently, similar to a local backward-facing flow. Hence, under the same inflow conditions the regions of separation on each wall are the same and the double-sided expansion exhibits a symmetric flow field. However, above some critical value the double-sided flow pattern becomes asymmetric, and remains asymmetric thereafter. In recent investigations by Papadopoulos and Ötügen [9] and Papadopoulos et al. [10], an effective expansion ratio was introduced to capture the three-dimensional effects of side-wall proximity, in addition to expansion ratio effects. The effective expansion ratio was then used to scale expansion characteristics, such as the reattachment length, for all possible geometries [10].

The instability of low Reynolds number expanding planar flows led to several numerical studies that investigated the symmetry-breaking bifurcation using a linear stability approach to locate bifurcation points of the transition between symmetric and asymmetric flows. One of the original studies was by Sobey and Drazin

[1]Corresponding author.

Contributed by the Fluids Engineering Division of ASME for publication in the JOURNAL OF FLUIDS ENGINEERING. Manuscript received May 19, 2005; final manuscript received November 30, 2005. Assoc. Editor: Timothy J. O'Hern. Paper presented at the 2005 ASME Fluids Engineering Division Summer Meeting and Exhibition (FEDSM2005), June 19–23, 2005, Houston, Texas.

[11] for analyses of a flow in symmetric two-dimensional channels with smooth (gradual) expansions. Corresponding experiments were performed to verify the numerical simulations but the experiments did not produce the hysteresis effects on the bifurcation as predicted by the numerical simulations. A similar study by Shapira et al. [12] investigated flows in both smooth and sudden expansion. A linear stability analysis showed that the velocity disturbances were due to the instability of a vortex core along the centerline. Shapira et al. found good agreement between their results and Sobey [13] for the critical Reynolds number. A comparison between the results of Shapira et al. and the experiments by Cherdron et al. [2] showed a disparity in the value of the Reynolds number at which the flow became unstable. Shapira et al. suggested the possibility that disturbances were generated by the experiments due to imperfections with the apparatus or slight asymmetries in the geometry.

Another study of particular interest was performed by Fearn et al. [14] that included comparisons of bifurcation calculations with experiments. Results indicated that as the Reynolds number was increased above a critical value, the symmetric flow lost stability and transitioned to an asymmetric flow forming a pitchfork bifurcation. Fearn et al. concluded that the transition to nonsymmetrical flow was abrupt, which disagreed with claims by Shapira et al. [12] that the transition was smooth. Durst et al. [15] used numerical predictions to confirm previous experimental findings [1,2] and found that the pitchfork bifurcation had a smooth transition from symmetric to asymmetric flow. Albeit the findings on the transition characteristics for the symmetry-breaking bifurcation were not all in agreement, recent literature reports similar values for the critical Reynolds number [16–19] for a range of expansion ratios.

While two-dimensional asymmetric flow has been extensively investigated, little has been reported on the characteristics of the asymmetry based on three-dimensional effects. A truly two-dimensional flow past a symmetric double-sided expansion is not plausible experimentally; hence, results are based on a nominally two-dimensional analysis at the centerplane of a ducted test section with a large aspect ratio (step span to step height). Perhaps that is why recent numerical simulations show discrepancies in the value of the critical Reynolds number when compared with earlier experimental studies. The most recent comprehensive numerical studies that report bifurcation calculations are by Battaglia et al. [17] and Drikakis [19]. Other recent studies include Refs. [20–25]. Given the limitation of experimental verification of the asymmetry, some effort has been spent on looking at the effects of geometry, such as expansion ratio and aspect ratio, on the critical Reynolds number. These investigations establish no systematic dependencies but report that in general the value of the critical Reynolds number decreases with increasing expansion ratio and increasing aspect ratio.

Recently, Papadopoulos et al. [26] began investigating the effects of three dimensionality on low Reynolds number flows past a symmetric sudden expansion in a rectangular channel. Particle image velocimetry (PIV) was used to obtain whole field data at various planes in the duct. The proximity of the side walls was found to enhance flow stability, helping sustain flow symmetry to higher Reynolds numbers in comparison to nominally two-dimensional double-expansion geometries, which were investigated numerically. In the current work, the effective expansion ratio formulation will provide a means to capture the significant role of the geometry in the bifurcation process.

The current paper builds on the recent effort reported by Papadopoulos et al. [26] by presenting three-dimensional numerical simulations for the double-sided expansion in a duct with an expansion ratio of 2:1 and an aspect ratio of 6:1. The flow is numerically predicted using a time-marching finite difference procedure to investigate the three-dimensional flow field characteristics of the bifurcating phenomenon. It will be shown that discrepancies in the literature for computational fluid dynamics (CFD) simulations using a two-dimensional domain were because the models did not account for the three-dimensional geometry. Although linear stability theory can accurately and efficiently predict bifurcation behavior, CFD is used to demonstrate that two-dimensional simulations can predict the correct behavior using a proper geometric relationship. Therefore, if one is restricted to two-dimensional simulations, the effective expansion ratio will ensure more accurate predictions. The results will compare numerical simulations with particle image velocimetry measurements over a range of symmetric flows. The validation confirms the concept that the effective expansion ratio completely captures the effects of the geometry on the expanding flow, and subsequently leads the authors to propose an empirical formulation that captures the dynamics of the bifurcation process.

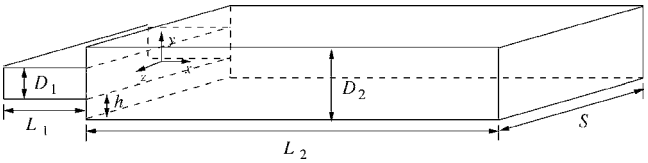

Fig. 1 Schematic of the geometric configuration and coordinate system

Formulation of the Problem

Geometry. A schematic of the expanding channel geometry under consideration is shown in Fig. 1. The geometry is symmetric about the *x-y* and *x-z* planes through an origin placed in the center of the plane of expansion. The geometry is typically characterized by the expansion ratio $\mathrm{ER}=D_2/D_1$ and the aspect ratio $\mathrm{AR}=S/h$ where $h=(D_2-D_1)/2$. To account for the rectangular, three-dimensional behavior of a fluid passing through the channel, an appropriate single measure of the expansion effect is given by the effective expansion ratio [9,10]

$$\Delta_h = \mathrm{ER}\frac{2+\mathrm{AR}(\mathrm{ER}-1)}{2\cdot\mathrm{ER}+\mathrm{AR}(\mathrm{ER}-1)} \tag{1}$$

The lengths of the entrance and outflow regions L_1 and L_2, respectively, are chosen sufficiently long so that the flow profiles far upstream and downstream can be regarded as fully developed. This means that for low Reynolds number flows, the profiles are parabolic at the vertical and horizontal centerplanes, for both inflow and outflow. The Reynolds number is defined as $\mathrm{Re}=u_0D_1/\nu$, where u_0 is the maximum velocity at the inlet and ν is the kinematic viscosity.

Experimental Setup. A Plexiglas model of the geometry (refer to Fig. 1) was constructed for easy optical access. The dimensions of the model are listed in Table 1. The working fluid was air at ambient conditions (typically at 24 °C and 1 atm). Changes in the ambient temperature and pressure over the duration of each ex-

Table 1 Values for characteristic parameters of the experimental model geometry

Parameter	Magnitude
L_1	757.2±0.5 mm
L_2	767.0±0.5 mm
h	12.3±0.3 mm
$D_1=D_2-2h$	24.5±0.9 mm
D_2	49.1±0.5 mm
S	75.8±0.5 mm
ER	2.00±0.07
AR	6.16±0.20
Δ_h	1.61±0.10

perimentation phase were small, resulting in less than 1% uncertainty in the flow Reynolds number. The test section was operated in the suction mode, open to the laboratory environment. Air entered the inlet section via a bellmouth entry, which featured a honeycomb section for flow conditioning. The length of the inlet section was long enough to ensure fully developed flow conditions prior to expansion, in the range of Reynolds numbers investigated. The flow rate, hence flow Reynolds number, was controlled using a Variac to set the speed on a fan located downstream of the test section.

Measurement Methods. Two optical measurement techniques were used during the investigation, one for acquiring a reference velocity upstream of the expansion and another for acquiring the velocity of the flow past the expansion. For the former measurement, a one component laser Doppler anemometer (LDA) system was used, while for the latter, a two-dimensional (2D) particle image velocimetry system was used. Smoke generated from a theatrical fog generator was used for seeding, with a typical particle size of about 3–5 μm. In order to disperse the smoke evenly into the test section, the generator was placed far from the entry to the duct and allowed to fill the lab room before commencing the measurement.

The LDA system (Dantec FlowLite LDA) consisted of a 10-mW He–Ne laser source ($\lambda=632.8$ nm) along with LDA electronics (including a 40-MHz Bragg cell for frequency shifting) in a turn-key style enclosure, which featured a 5-m long fiber optic connection to a 60-mm diameter probe housing the sending and receiving optics (backward-scatter mode). The focal length of the probe was 160 mm, while the beam diameter and spacing was 1.35 mm and 38 mm, respectively. This optical arrangement resulted in a measurement volume of 96 μm in diameter and 810 μm in length. The Doppler signal was processed using a fast Fourier transform (FFT)-based processor featuring 4-bit signal quantization and 14-bit frequency resolution at each selected bandwidth. A frequency bandwidth corresponding to a velocity range of −0.2 m/s to 0.7 m/s was used during the duration of the investigation. Processor control and recording of signal was done via software running on a personal computer.

The LDA probe volume was placed in the center of the duct cross section, 65-mm upstream of the plane of separation. The beams were oriented so as to measure the streamwise component of velocity at that location. The velocity obtained from this point measurement served as reference for normalizing out minor flow variations during the course of each experimental run.

The PIV system (Dantec FlowMap PIV2100) consisted of a 50-mJ, double-cavity Nd:Yag laser system operating at $\lambda=532$ nm, an 8-bit double-frame charge-coupled device (CCD) camera having a resolution of 1008×1018 pixels, a hardware-based FFT processor for performing on-line cross-correlation analysis of acquired particle images, and software for data-acquisition control, data storage, and postanalysis. The PIV system was mounted on a three-dimensional computer-controlled traverse having a resolution of 0.01 mm on all axes.

Sheet forming optics mounted on the exit portal of the double-cavity laser system were used to form a 1-mm thick light sheet, which defined the measurement plane. Following proper alignment of the light sheet with respect to the test section, the CCD camera was focused in order to clearly image smoke particles illuminated by the sheet. A 50-mm Nikon lens was used, set at $f-2.8$ to achieve a narrow depth of field. The CCD field of view was set so as to capture the entire duct cross section.

A 16×16 pixel interrogation area was used for the cross-correlation analysis between image pairs, at 25% overlap, yielding a field of 83×84 vectors. The spatial resolution was 0.93 mm^2. The timing between laser pulses, hence between image pairs, was such that seeding particles moving with velocity u_0 traveled, on the average, 30% to 35% of the interrogation area size. This resulted in an estimated velocity magnitude resolution of better than 0.5% of u_0 for each measurement.

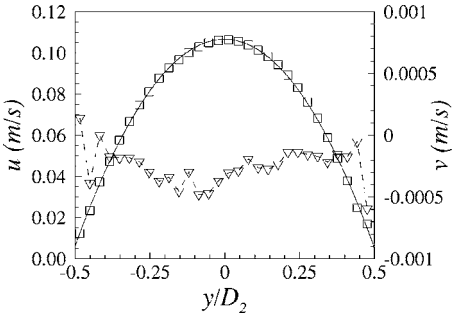

Fig. 2 Velocity profiles along the *x-y* plane at *z*=0 measured with PIV at $x/D_2=-0.163$ for Re=171: Streamwise mean velocity *u* shown as □; solid line is parabolic fit; transverse mean velocity *v* shown as ▽.

At each measurement location, 200 PIV acquisitions were performed in order to obtain a statistical average of the separated flow. Long time scales, on the order of 0.2 s to 0.4 s, required that sampling rates are kept low, hence a PIV acquisition rate of 1.5 Hz was used. Vector validation was performed using a 20% primary-to-secondary correlation peak signal-to-noise criteria test, and a local continuity check with a 3×3 moving average technique. The percentage of invalid vectors was typically low, less than 2%, and only the valid vectors after postanalysis using the aforementioned validation criteria were sampled to construct the average vector field. The statistical uncertainty of this field in the mean was estimated at less than 1%.

Measurements along the centerplane of the channel at low Reynolds numbers were conducted to quantify the flow conditions using the two experimental techniques. Velocity profiles are shown in Fig. 2 upstream of the expansion ($x/D_2=-0.163$) for Reynolds number of 171, based on PIV measurements. The u-velocity profile demonstrates a parabolic shape and the maximum velocity measured is 106 mm/s. This value compares well with an average velocity of 104 mm/s measured with LDA at the location of $x/D_2=-1.328$. The v-velocity profile is relatively flat, exhibiting a very minor negative velocity tendency that is within the estimated 2% to 3% absolute uncertainty of the measurements.

Numerical Methods

The incompressible three-dimensional Navier-Stokes equations for a Cartesian coordinate system (x,y,z) are expressed in conservative vector form as

$$\frac{\partial Q}{\partial t}+\frac{\partial E}{\partial x}+\frac{\partial F}{\partial y}+\frac{\partial G}{\partial z}=\frac{\partial E_\nu}{\partial x}+\frac{\partial F_\nu}{\partial y}+\frac{\partial G_\nu}{\partial z} \tag{2}$$

where

$$Q=\begin{pmatrix}0\\u\\v\\w\end{pmatrix};\quad E=\begin{pmatrix}u\\u^2+p\\uv\\uw\end{pmatrix};\quad F=\begin{pmatrix}v\\vu\\v^2+p\\vw\end{pmatrix};\quad G=\begin{pmatrix}w\\wu\\wv\\w^2+p\end{pmatrix}$$

$$E_\nu=\nu\begin{pmatrix}0\\\partial u/\partial x\\\partial v/\partial x\\\partial w/\partial x\end{pmatrix};\quad F_\nu=\nu\begin{pmatrix}0\\\partial u/\partial y\\\partial v/\partial y\\\partial w/\partial y\end{pmatrix};\quad G_\nu=\nu\begin{pmatrix}0\\\partial u/\partial z\\\partial v/\partial z\\\partial w/\partial z\end{pmatrix}$$

In this form, Q is a vector of conservative dependent variables. The velocity field corresponds to the streamwise velocity u, transverse velocity v, and spanwise velocity w. The pressure field appearing in Eqs. (2) is modified to account for the density and ν is the kinematic viscosity. The incompressible equations form a set

of parabolic-elliptic partial differential equations; however, the pressure does not appear explicitly in the continuity equation. In particular, the conservative variables vector Q does not constitute a complete set of variables for the incompressible problem. Thus, the vector Q creates a system of Eqs.(2) that has a singularity due to the missing time derivative term in the continuity equation. To circumvent this, the vector quantity inside the time derivative can be changed from the conservative to the primitive variable set. Then, preconditioning techniques can be used, which have been shown to improve convergence for time-marching methods [27] and therefore make the system well posed for numerical solution.

The preferred choice of dependent variables for vector Q is the viscous variable set Q_v, which includes all of the primitive variables, where $Q_v=(p,u,v,w)^T$ and is incorporated into Eqs. (2) using the chain rule

$$\frac{\partial Q}{\partial Q_v}\frac{\partial Q_v}{\partial t}+\frac{\partial E}{\partial x}+\frac{\partial F}{\partial y}+\frac{\partial G}{\partial z}=\frac{\partial E_v}{\partial x}+\frac{\partial F_v}{\partial y}+\frac{\partial G_v}{\partial z} \tag{3}$$

Overall, the new system of Eqs. (3) have the same form as Eqs. (2) but an additional term is present, the Jacobian matrix $\partial Q/\partial Q_v$. Computing the Jacobian results in the form

$$\Gamma=\begin{pmatrix}0&0&0&0\\0&1&0&0\\0&0&1&0\\0&0&0&1\end{pmatrix}$$

where $\partial Q/\partial Q_v$ has been replaced with the notation Γ. The true transient formulation is restored when the time derivative is multiplied by the matrix Γ. The form of Eqs. (3) can be conveniently solved for steady-state solutions using the artificial compressibility method, which is a special case of preconditioning for incompressible flows [28].

Equations (3) are converted to the artificial compressibility formulation by changing the physical time t to a pseudotime τ and replacing matrix Γ with matrix Γ_p

$$\Gamma_p=\begin{pmatrix}1/\beta&0&0&0\\0&1&0&0\\0&0&1&0\\0&0&0&1\end{pmatrix}$$

where β is the artificial compressibility parameter. The value of β is chosen such that the eigenvalues are approximately the same order of magnitude for efficient convergence (refer to [29] for more details). The Euler portion of Eqs. (3) becomes fully hyperbolic so that time-marching schemes can be used for either the Euler or Navier-Stokes equations. The matrix Γ_p however, implies that the equations are no longer physically correct for transients, but they regain meaning in the steady-state limit. Time accuracy can be recovered by combining the artificial compressibility formulation with a dual-time stepping scheme [30] in which the pseudotime derivative $\Gamma_p\partial Q_v/\partial\tau$ is added to the physical time derivative already appearing in Eqs. (3) such that

$$\Gamma_p\frac{\partial Q_v}{\partial\tau}+\Gamma\frac{\partial Q_v}{\partial t}+\frac{\partial}{\partial x}(E-E_v)+\frac{\partial}{\partial y}(F-F_v)+\frac{\partial}{\partial y}(G-G_v)=0 \tag{4}$$

The real time solution is then obtained by iterating in pseudotime until $\partial Q_v/\partial\tau\rightarrow 0$.

The set of equations shown in Eq. (4) are discretized using an implicit three-point, second-order finite-differencing scheme for the physical time. A fourth-order Runge-Kutta method is used for the pseudo-time and a second-order central finite-differencing scheme is used for all spatial terms. The inflow boundary conditions were specified for parallel flow with a parabolic streamwise velocity profile and the outflow pressure was set to 0 gauge. The no-slip velocity boundary was enforced at all surfaces.

Table 2 Grid convergence studies for a coarse (3), medium (2) and fine (1) grid comparing reattachment position. Superscript notation refers to a comparison between two grids

Grid size (N cells)	x_R/D_2
12,592	1.537
25,184	1.046
33,600	1.047
Approximate (a) relative error	
e_a^{32}	4.496%
e_a^{21}	0.172%
Extrapolated (ext) relative error	
e_{ext}^{32}	0.18%
e_{ext}^{21}	0.06%
Grid convergence index	
$\text{GCI}_{\text{medium}}^{32}$	0.226%
$\text{GCI}_{\text{fine}}^{21}$	0.075%

Numerical tests were performed to determine the grid size required to adequately resolve the flow field. The simulations were based on a geometry of $L_1=10D_1$ and $L_2=30D_1$. As in the study of Battaglia et al. [17], a rectangular grid with clustering close to the channel walls and expansion was continually refined until solutions were relatively grid insensitive. Solutions on three grid sizes were examined: 384×32 cells, 384×64 cells and 512×64 cells, and the grid aspect ratio ($\Delta x/\Delta y$) was maintained in the range of 1.5–3.5. The grid convergence index method [31] was used to quantify the discretization error and numerical uncertainty. Table 2 shows the grid convergence studies based on the streamwise velocity and indicates that the numerical uncertainty is approximately 0.1% for the fine grid. In order to use CFD to predict the symmetry-breaking bifurcation, a numerical procedure was used akin to experimental procedures. Symmetric and asymmetric flows were simulated, whereby the Reynolds number was gradually increased for each symmetric flow and decreased for each asymmetric flow. Eventually, the simulations provide a small range of Reynolds numbers in which the bifurcation must occur. An interesting point is that a more stringent convergence criterion was used in order to numerically predict the range of Reynolds numbers that capture the symmetry-breaking bifurcation. When the flow Reynolds number is very close to the critical Reynolds number for the symmetry-breaking bifurcation, the numerical simulations are more sensitive to round-off error. Also, the small expansion ratio produces a highly stable flow that is sensitive to numerical precision. Thus, a root mean square error tolerance smaller than 10^{-12} was necessary for successive pseudotime iterations to ensure residuals dropped 6–8 orders of magnitude.

Results

Symmetric Flow. Detailed particle image velocimetry measurements were obtained for fully developed flow past the double-sided expansion with ER=2 and AR=6. At a low Reynolds numbers, such as Re=171, the flow along the centerplane is observed to develop symmetrically downstream of the expansion. Of particular interest is the effect of geometry on the flow field when assuming two-dimensional flow for numerical simulations. Historically, a two-dimensional assumption is used when the spanwise channel length is sufficiently large so that wall effects are negligible at the centerplane. Thus, a two-dimensional flow implies that the aspect ratio is infinite.

In order to determine the effects of geometry, a two-dimensional numerical simulation was performed for ER=2. The simulations also predicted a symmetric flow for Re=171. The resulting flow patterns downstream of the expansion plane are shown in Fig. 3 for the normalized streamwise velocity profiles at various nondimensional streamwise locations to demonstrate how the flow expands. The velocity profiles show that the flow develops symmetrically downstream of the expanding section for both

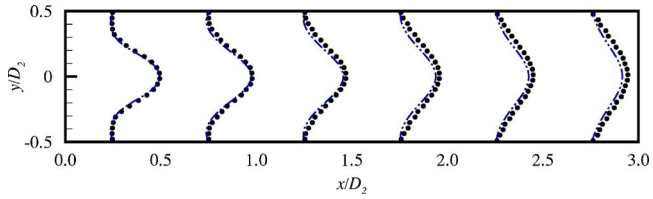

Fig. 3 Normalized streamwise velocity u/u_0 profiles shown relative to channel positions x/D_2 along the centerplane for Re=171: Symbols are PIV measurements (every other measurement shown for clarity); dashed line represents numerical simulations for ER=2

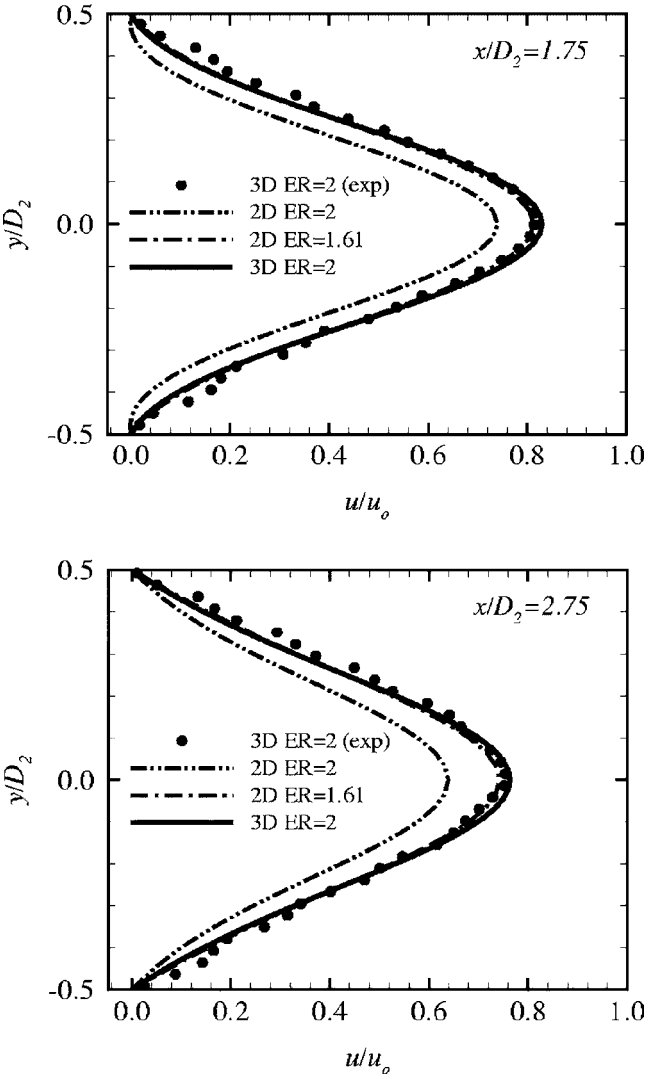

Fig. 4 Normalized streamwise velocity profiles u/u_0 at x/D_2 =1.75 and 2.75 along the centerplane of the channel for Re =171: Symbols are PIV measurements (every other measurement shown for clarity); various lines represent numerical simulations

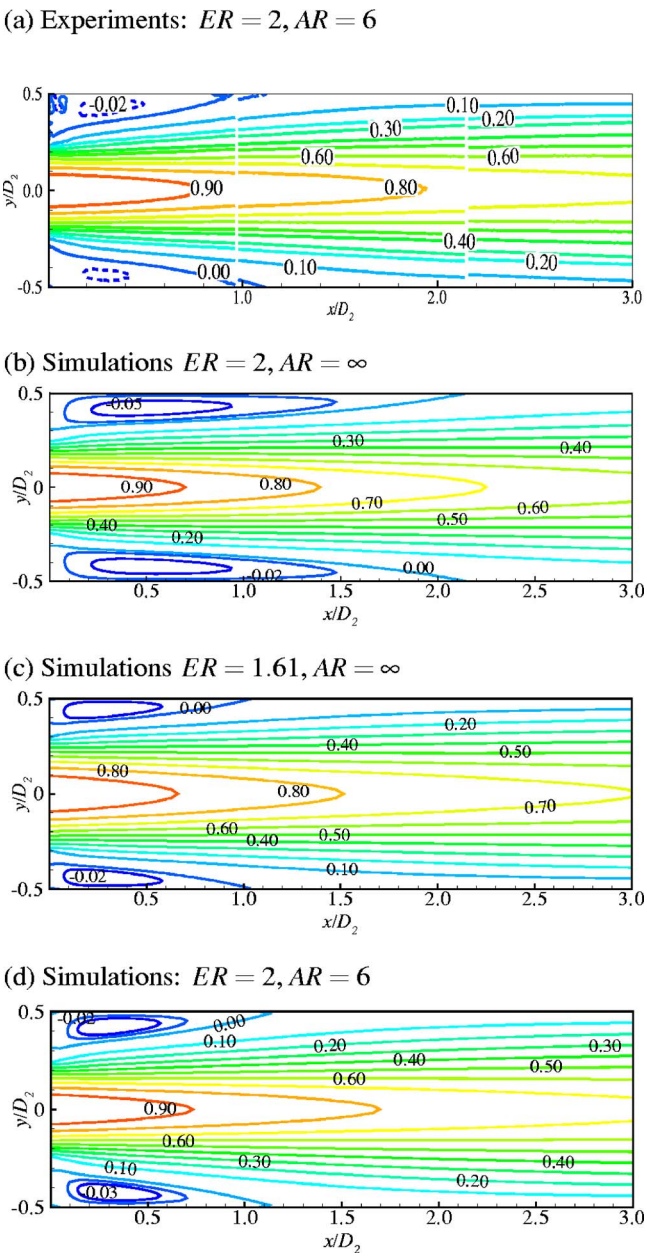

Fig. 5 Normalized streamwise velocity u/u_0 contours along the channel centerplane for Re=171: (*a*) measured using PIV for ER=2; and numerically predicted by two-dimensional simulations for (*b*) ER=2, (*c*) ER=1.61, and three-dimensional simulations for (*d*) ER=2

the experiments and simulations. However, the numerical simulation for ER=2 underpredicts the velocity field. The deviation between experiments and simulations is more pronounced with increasing streamwise distance, as shown in Fig. 4 for x/D_2=1.75 and 2.75. The average error between the simulation and experimental data is 12%.

In view of these shortcomings of the numerical simulations, new simulations were performed for a two-dimensional flow using ER=1.61 to match the effective expansion ratio Δ_h=1.61 (based on ER=2 and AR=6). Furthermore, three-dimensional numerical simulations were performed for ER=2 and AR=6. Figure 4 compares data for all the simulations with the experiments. It is evident that the two-dimensional simulations using the effective expansion ratio ER=1.61 are in excellent agreement with the three-dimensional simulations and PIV data; all three data sets virtually collapse. Thus, based on the results, we conclude it is possible to use two-dimensional numerical simulations to predict three-dimensional flow behavior along the centerplane of a rectangular channel provided an effective expansion ratio is used.

The flow fields for the streamwise velocity contours at the channel centerplane ($x-y$ plane at z=0 for three dimensions) are shown in Fig. 5 for =171. Note that only a portion of the channel

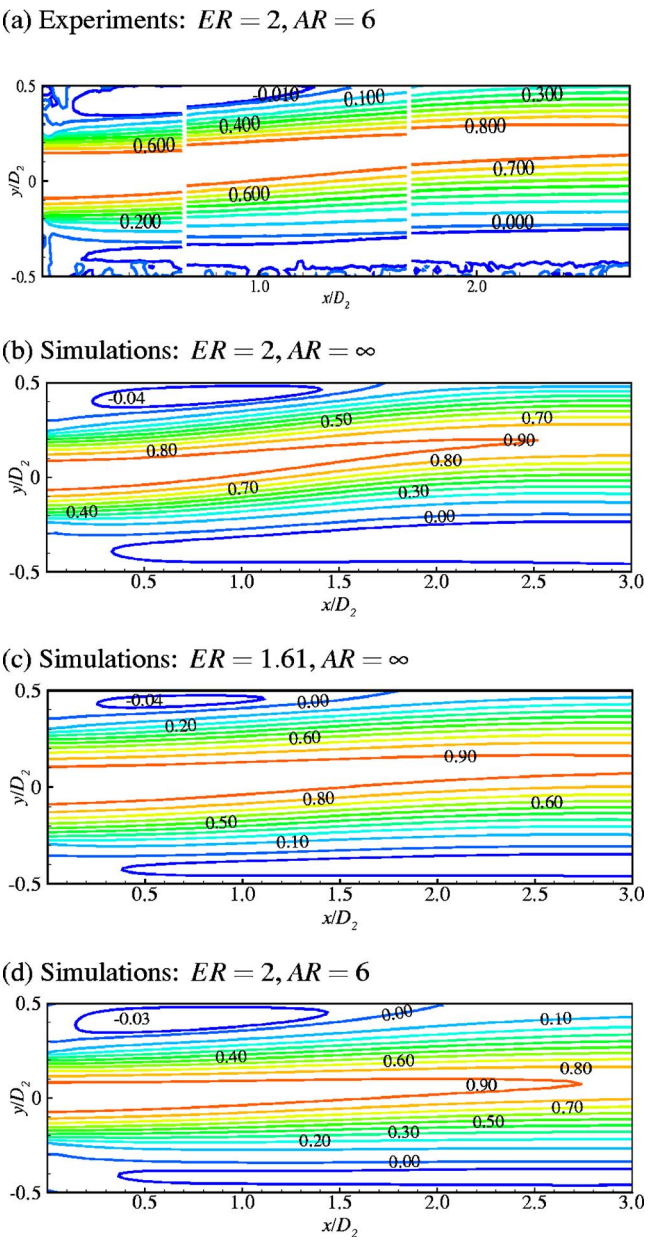

Fig. 6 Normalized streamwise velocity u/u_0 contours along the channel centerplane for Re=585: (*a*) Measured using PIV for ER=2, and numerically predicted by two-dimensional simulations for (*b*) ER=2, (*c*) ER=1.61, and three-dimensional simulations for (*d*) ER=2

is shown downstream of the expansion for $0 \leqslant x/D_2 \leqslant 3$. The PIV data is compared with the numerical simulations for two and three-dimensional flows. The streamwise velocity is primarily positive in the direction of flow except for the two small recirculation regions that form immediately downstream of the expanding channel where the jet attaches to the upper and lower walls. A noteworthy point is that the transverse velocities are zero along the centerline ($y=0$). Elsewhere, the transverse velocities are very small as expected for a symmetric jet. It is the reattachment point x_R that elucidates the discrepancy with the two-dimensional numerical solution using ER=2. The nondimensional reattachment position x_R/D_2 as measured using PIV is 1.027. The predictions from the two-dimensional numerical simulations for ER=2 and 1.61 are $x_R/D_2=2.154$ and 1.028, respectively; the three-dimensional predictions (ER=2) give a value of 1.076. Except for the two-dimensional simulations using ER=2, the numerical data are in excellent agreement with the experiments.

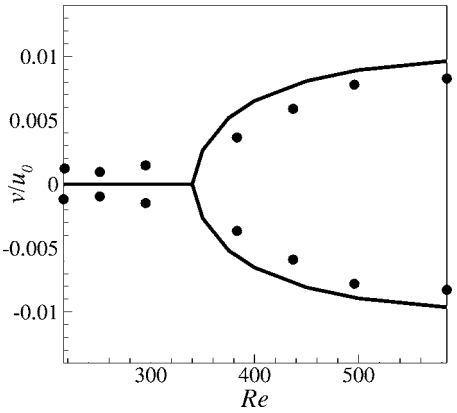

Fig. 7 Symmetry-breaking pitchfork bifurcation measured at the channel centerline at x/D_2=0.877 for ER=2 and AR=6: Symbols are PIV measurements; solid line represents numerical simulations

Asymmetric Flow. As discussed previously, low Reynolds number flows develop symmetrically downstream of the sudden expansion. However, symmetry disappears as the flow rate increases. To illustrate the asymmetric behavior of the flow, Fig. 6 shows the flow fields for the normalized streamwise velocity contours at the channel centerplane ($x-y$ plane at $z=0$) as measured using PIV and predicted by the numerical simulations for Re =585. The streamwise velocities demonstrate that the jet develops asymmetrically and attaches along the upper wall forming a small recirculation zone.

An additional effect of the larger expansion ratio for two-dimensional simulations (e.g., ER=2 versus 1.61) is that it causes the flow to become more unstable at lower Reynolds numbers. The consequence is that predictions of the bifurcation will be significantly in error, as will be presented next. As a final note, because the transverse velocity is distinctly nonzero at $y=0$ due to the lack of symmetry immediately downstream of the expansion, the transverse velocity field can be exploited to provide a means to determine the bifurcation behavior.

Critical Reynolds Number. The transition from a symmetric to an asymmetric jet is marked by a bifurcation at a critical Reynolds number. The critical Reynolds number was determined by performing PIV measurements of the transverse velocity magnitude at the centerline ($y=0$ and $z=0$) and $x/D_2=0.877$ for each flow rate. The critical Reynolds number at which asymmetry ensues was found experimentally in the range of Re_{cr}=320 to 380. The two-dimensional numerical simulations for ER=2 predict a critical value of Re_{cr}=217. This value is lower than the minimum value determined by the experiments, since significant flow three-dimensionality due to side-wall proximity has the tendency to stabilize the flow, delaying the onset of bifurcation until higher Reynolds numbers. Two-dimensional simulations for ER=1.61 and three-dimensional simulations for ER=2 and AR=6 predict the same Reynolds number range within which the flow bifurcates. Figure 7 compares the bifurcation trends between the three-dimensional numerical simulations and PIV measurements and shows that there is very good agreement. The numerical simulations predict that the bifurcation occurs between Re_{cr}=340 and 345 which is within the range measured experimentally. Error between the numerical simulations and PIV is expected to be large near the critical Reynolds number, which is historically difficult to measure. However, for well developed symmetric and asymmetric

Table 3 Critical Reynolds numbers for bifurcation determined using experimental methods

Reference	ER	AR	Δ_h	Re_{cr}
Cherdron et al. [2]	2	4	1.50	368
	2	8	1.67	267
	2	16	1.80	194
	2	32	1.89	153
	3	4	2.14	112
	3	8	2.45	65
	3	16	2.68	40.5
	3	32	2.83	35
Durst et al. [1]	3	27.6	2.80	56–114
Durst et al. [15]	2	32	1.89	120–200
Fearn et al. [14]	3	24	2.78	70
Ouwa et al. [3]	5	12.5	4.33	45
Present results	2	6	1.60	320–380

flows away from the critical Reynolds number, the error is significantly less.

The critical Reynolds number for the symmetry-breaking bifurcation is a function of the expansion geometry, as numerous investigations have shown. Although most researchers have focused only on the expansion ratio, the aspect ratio also influences the value of the critical Reynolds number, as first reported by Cherdron et al. [2]. They found that for a fixed expansion ratio the critical Reynolds number increased as the aspect ratio of the double-sided expansion decreased. A tabulation of this data along with other experimental data on the double-sided planar expansion is shown in Table 3. In all these cases the upstream velocity conditions were reported as being fully developed.

Numerical simulations and bifurcation theory analyses have for the most part dealt with the two-dimensional ($AR=\infty$) expansion geometry, and thus reported only on the effect of expansion ratio. Results for Re_{cr} from such numerical studies are summarized in Table 4, including the current two- and three-dimensional simulations. In all the cases listed in Table 4, a fully developed Poiseuille flow (parabolic profile) was reported as the initial condition upstream of the sudden expansion.

In practical applications, however, the geometry is three dimensional, and the influence of aspect ratio needs to be incorporated to fully capture the hydrodynamic effects of the planar expansion. As realized earlier in the comparisons of the centerplane velocity profiles, this is accomplished through the definition of the expansion downstream-to-upstream hydraulic diameter ratio Δ_h which captures both the geometric effect of the expansion, as well as, the hydrodynamic effect of the rectangular channel. The parameter Δ_h therefore can be considered to uniquely define the expansion problem, as indicated in Fig. 8. In the figure, the influence of the aspect ratio is shown in terms of Δ_h/ER, this latter quantity identifying the relative (or effective) reduction in the geometric expansion parameter that is produced as the aspect ratio decreases from infinity to a value of unity. The three-dimensional surface indicates that as the values of $AR \to 1$ and $ER \to \infty$, $\Delta_h/ER = 1/3$. Thus, for the same expansion ratio ER, the effective expansion ratio Δ_h decreases as aspect ratio AR decreases, pointing to an increasingly stabilizing flow scenario resulting in higher attainable Reynolds numbers before the flow becomes asymmetric. Figure 8 encompasses all symmetric two-sided planar expansions, all defined by the single parameter Δ_h, as previously reported by Papadopoulos et al. [10]. All experimental geometries (Table 3) and three-dimensional simulations found in the literature and reported in the current paper are plotted on the surface and projected on the $ER^{-1}-AR^{-1}$ plane to identify their relative departure from the two-dimensional expansion concept ($AR^{-1}=0$ line).

Table 4 Critical Reynolds numbers for bifurcation determined using numerical methods

Reference	ER	AR	Δ_h	Re_{cr}
Alleborn et al. [16]	2	∞	2	218
	3		3	80
	5		5	42.5
	1000		1000	8.5
Battaglia et al. [17]	2	∞	2	225–233
	3		3	85–87
	4		4	52–60
	5		5	40–45
Battaglia et al. [17]	1.5	∞	1.5	446
	2		2	215
	3		3	81
	4		4	54
	5		5	43
	7		7	16
Drikakis et al. [19]	2	∞	2	216
	3		3	80
	4		4	53
	5		5	41
	6		6	33
	8		8	28
	10		10	26
Durst et al. [15]	2	∞	2	125–200
Fearn et al. [14]	3	∞	3	80.9
Hawa and Rusak [18]	3	∞	3	80.7
Kadja and Touzopoulos [25]	2	∞	2	200
Kudela [21]	3	∞	3	84–187
Luo [20]	3	∞	3	92.4
Manica and de Bortoli [24]	3	∞	3	80–100
Shapira et al. [12]	2	∞	2	215
	3		3	82.6
Schreck and Schäfer [22]	3	∞	3	81
	3	2	1.8	113
	3	5	2.25	91
Present results	1.61	∞	1.61	340–345
	2	∞	2	217
	2	6	1.60	340–345

The experimental data along with the results from the three-dimensional simulations are shown graphically in Fig. 9 (top). The plot shows clearly the inappropriateness of ER in regards to capturing the total effects of the planar expansion. When the same data is plotted in Fig. 9 (bottom) against the reciprocal of Δ_h, a nice collapse of all the data is observed. Slight differences in observation methods and facility preparation between experimental investigations can have significant influence on the reported values for the critical Reynolds number, but even so, a unique trend is apparent. This gives credence to the currently proposed idea of using Δ_h to define geometric expansion ratio effects for planar symmetric expansions.

Taking all the experimental and numerical data from Tables 3 and 4 and re-plotting the critical Reynolds numbers logarithmically versus the reciprocal of the hydraulic diameter ratio reveals a linear trend

$$\log_{10}(Re_{cr}) = \alpha\Delta_h^{-1} + \beta \tag{5}$$

where $\alpha = 2.21 \pm 0.22$ and $\beta = 1.12 \pm 0.09$. Figure 10 demonstrates the logarithmic relationship, with the dashed-dot lines designating the statistical bounds of the empirical fit to 95% confidence.

The validity of Eq. (5) is confirmed by the results reported in a

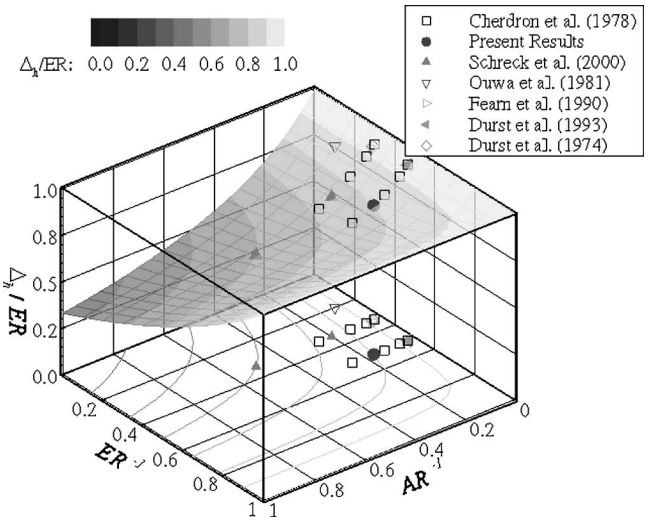

Fig. 8 Aspect ratio influence on the effective expansion ratio for the double-sided planar expansion: Symbols denote experimental and 3D numerical investigations involving finite ER and AR parameters

recent paper by Chiang et al. [33] for three-dimensional computations performed for a single Reynolds number (Re=120 based on the maximum velocity and upstream channel height) and for a single expansion ratio, ER=3. The results of the computations over a wide range of aspect ratios show that for AR<3.5 the flow is symmetric, while for AR>3.5 the flow past the sudden expansion is asymmetric. If this critical AR value is taken along with ER=3, then the current empirical relationship of Eq. (5) yields Re_{cr} in the range of 97.3 to 240 with $Re_{cr}=152.7$ being the median value. The value determined by Chiang et al. falls well within the range estimated by the current empirical relationship.

Last, reviewing the trends shown in Fig. 10 more closely yields a couple of interesting findings. First, we can conclude that when the flow Reynolds number is less than that indicated by the lower 95% dashed-dot line, the flow past the double-sided expansion will be, in most likelihood, symmetric, while flow Reynolds numbers higher than the upper 95% dashed-dot line will be, in most likelihood, asymmetric. Second, as $\Delta_h^{-1} \rightarrow 1$, the critical Reynolds number is observed to approach the range of $Re_{cr} \sim 2200-2300$. The parameter $\Delta_h^{-1}=1$ represents flow in a duct in the absence of any expansion, and it is well known that the value of 2300 is the traditionally accepted point of transition from laminar to turbulent flow that occurs in pipes and ducts when the flow is fully developed [32].

Conclusions

The flow past a symmetric double-sided sudden expansion in a rectangular duct was investigated for Reynolds numbers in the range of 150 to 600. The small aspect ratio of the expanding geometry introduced effects of side-wall proximity that tend to increase the three-dimensionality of the expanding flow. In the past, the effects of expansion and aspect ratio have been qualitatively reported in the literature, mostly as a means to compare experimental and numerical work. In the present paper, the expansion and aspect ratios were used to form an effective expansion ratio which is equal to the ratio of the hydraulic diameters between the upstream and downstream channel sections. Comparisons for both two- and three-dimensional simulations with experiments were presented to identify the importance of aspect ratio on the stability of the flow.

It was shown that two-dimensional numerical simulations fail to capture the effect of the expansion when the geometry is defined by expansion ratio only. However, when the effective expan-

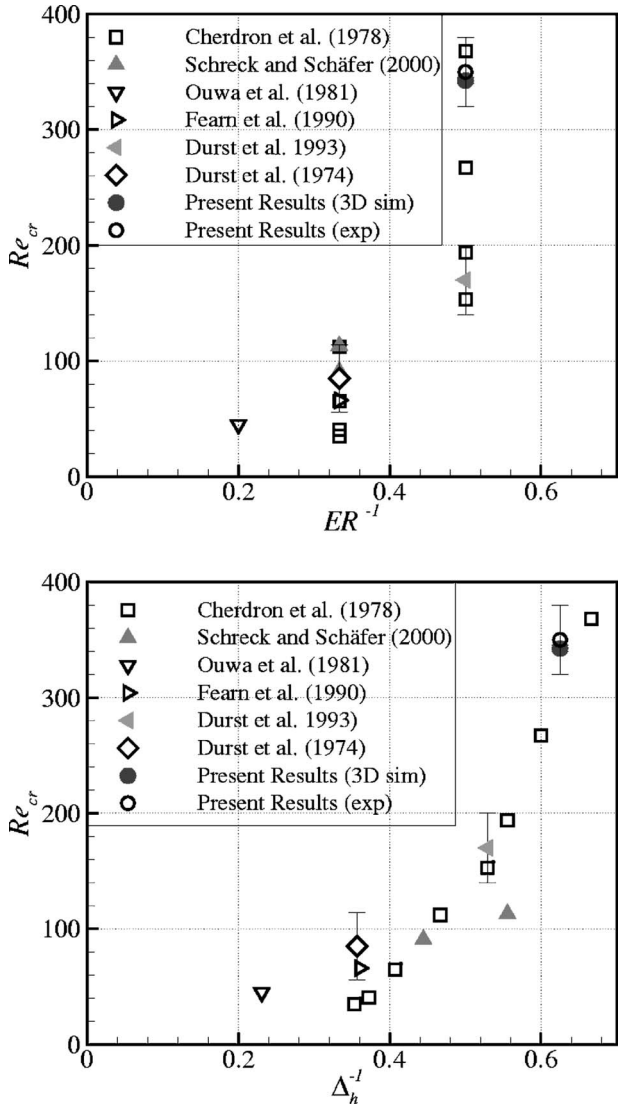

Fig. 9 Critical Reynolds number variation comparison for experimental data reporting influence of aspect ratio: Versus expansion ratio (top) and versus hydraulic diameter ratio (bottom)

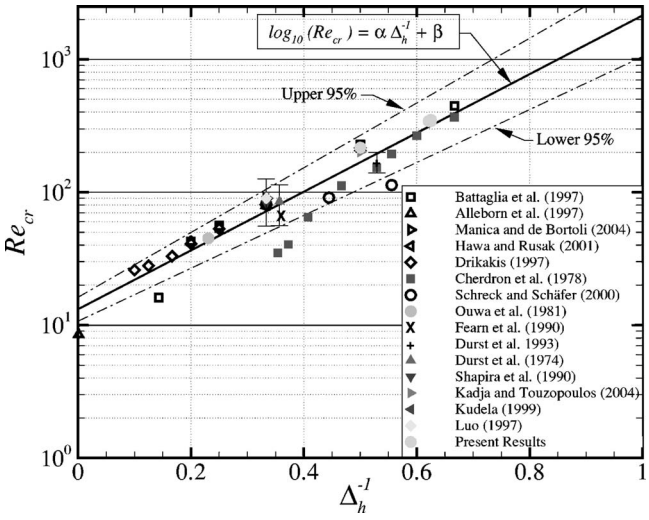

Fig. 10 Critical Reynolds number as a function of the hydraulic diameter ratio for the double-sided planar expansion

sion ratio is used to model the geometry for a two-dimensional simulation, the geometric and hydrodynamic effects are identical to three-dimensional numerical simulations and experiments. The phenomenon of a symmetry-breaking bifurcation was presented for both experiments and three-dimensional calculations, which agreed well. The critical Reynolds number which marks the bifurcation transition was compared to values reported in the literature. Of particular importance was the analysis that demonstrated a linear trend between the logarithm of the critical Reynolds number versus the reciprocal of the effective expansion ratio. Overall, this paper demonstrates that proper specification of geometric parameters will capture the bifurcation dynamics of all symmetric double-sided planar expansions.

Acknowledgment

The first author would like to thank Ian Thiele for assisting with the numerical simulations and data processing. In addition, the computer and technical support by the High Performance Computing Center at Iowa State University is appreciated. Both authors would like to thank the referees for their thoughtful critique and comments.

References

[1] Durst, F., Melling, A., and Whitelaw, J., 1974, "Low Reynolds Number Flow Over a Plane Symmetric Sudden Expansion," J. Fluid Mech., **64**, pp. 111–128.
[2] Cherdron, W., Durst, F., and Whitelaw, J., 1978, "Asymmetric Flows and Instabilities in Symmetric Ducts With Sudden Expansions," J. Fluid Mech., **84**, pp. 13–31.
[3] Ouwa, Y., Watanabe, M., and Asawo, H., 1981, "Flow Visualization of a Two-Dimensional Water Jet in a Rectangular Channel," Jpn. J. Appl. Phys., **20**(1), pp. 243–247.
[4] Ouwa, Y., Watanabe, M., and Matsuoka, Y., 1986, "Behavior of a Confined Plane Jet in a Rectangular Channel at Low Reynolds Number I. General Flow Characteristics," Jpn. J. Appl. Phys., Part 1, **25**, pp. 754–761.
[5] Abbott, D., and Kline, S., 1962, "Experimental Investigation of Subsonic Turbulent Flow Over Single and Double Backward Facing Steps," ASME J. Basic Eng., **84**, pp. 317–325.
[6] Filetti, E., and Kays, W., 1967, "Heat Transfer in Separated, Reattached, and Redevelopment Regions Behind a Double Step at Entrance to a Flat Duct," ASME J. Heat Transfer, **89**, pp. 163–167.
[7] Seki, N., Fukusako, S., and Hirata, T. 1976, "Turbulent Fluctuations and Heat Transfer for Separated Flow Associated With a Double Step at Entrance to an Enlarged Flat Duct," ASME J. Heat Transfer, **8**, pp. 588–593.
[8] Restivo, A., and Whitelaw, J., 1986, "Turbulence Chanracteristics of the Flow Downstream of a Symmetric, Plane Sudden Expansion," ASME J. Fluids Eng., **100**, pp. 308–310.
[9] Papadopoulos, G., and Ötügen, M. V., 1998, "A Modified Borda-Carnot Relation for the Prediction of Maximum Recovery Pressure in Planar Sudden Expansion Flows," ASME J. Fluids Eng., **120**(2), pp. 400–402.
[10] Papadopoulos, G., Markelov, S., and Ötügen, M., 1998, "Effects of Geometry on Turbulent Flow Past Double-Sided Symmetric Expansions in Ducts," *ASME, Proceedings of Fluids Eng. Div. Summer Meeting*, FEDSM 98-4962, Washington, D.C.
[11] Sobey, I., and Drazin, P., 1986, "Bifurcations of Two-Dimensional Channel Flows," J. Fluid Mech., **171**, pp. 263–287.
[12] Shapira, M., Degani, D., and Weihs, D., 1990, "Stability and Existence of Multiple Solutions for Viscous Flow in Suddenly Enlarged Channels," Comput. Fluids, **18**, pp. 239–258.
[13] Sobey, I., 1985, "Observation of Waves During Oscillatory Channel Flow," J. Fluid Mech., **151**, pp. 395–406.
[14] Fearn, R., Mullin, T., and Cliffe, K., 1990, "Nonlinear Flow Phenomena in a Symmetric Sudden Expansion," J. Fluid Mech., **211**, pp. 595–608.
[15] Durst, F., Pereira, J., and Tropea, C., 1993, "The Plane Symmetric Sudden-Expansion Flow at Low Reynolds Numbers," J. Fluid Mech., **248**, pp. 567–581.
[16] Alleborn, N., Nandakumar, K., Raszillier, H., and Durst, F., 1997, "Further Contributions on the Two-Dimensional Flow in a Sudden Expansion," J. Fluid Mech., **330**, pp. 169–188.
[17] Battaglia, F., Tavener, S., Kulkarni, A., and Merkle, C., 1997, "Bifurcation of Low Reynolds Number Flows in Symmetric Channels," AIAA J., **35**, pp. 99–105.
[18] Hawa, T., and Rusak, Z., 2001, "The Dynamics of a Laminar Flow in a Symmetric Channel With a Sudden Expansion," J. Fluid Mech., **436**, pp. 283–320.
[19] Drikakis, D., 1997, "Bifurcation Phenomena in Incompressible Sudden Expansion Flows," Phys. Fluids, **9**(1), pp. 76–87.
[20] Luo, L.-S., 1997, "Symmetry Breaking of Flow in 2D Symmetric Channels: Simulations by Lattice-Boltzmann Method," Int. J. Mod. Phys. C, **8**(4), pp. 859–867.
[21] Kudela, H., 1999, "Viscous Flow Simulation of a Two-Dimensional Channel Flow With Complex Geometry Using the Grid-Particle Vortex Method," *Proceedings, Third International Workshop on Vortex Flow and Related Numerical*, European Series in Applied and Industrial Mathematics (ESAIM), Methods, Société de Mathématiques Appliquées et Industrielles, Toulouse, France, Vol. 7, pp. 215–224.
[22] Schreck, E., and Schäfer, M., 2000, "Numerical Study of Bifurcation in Three-Dimensional Sudden Channel Expansions," Comput. Fluids, **29**, pp. 583–593.
[23] Neofytou, P., and Drikakis, D., 2003, "Non-Newtonian Flow Instability in a Channel With a Sudden Expansion," J. Non-Newtonian Fluid Mech., **111**, pp. 127–150.
[24] Manica, R., and De Bortoli, A., 2004, "Simulation of Sudden Expansion Flows for Power-Law Fluids," J. Non-Newtonian Fluid Mech., **121**, pp. 35–40.
[25] Kadja, M., and Touzopoulos, D., 2004, "Use of a New Convection Scheme and Multigrid Acceleration for Indepth Study of Flow Bifurcation in Channel Expansions," *Proceedings, Computational & Asymptotic Methods*, BAIL 2004, International Conference on Boundary and Interior Layers (BAIL), Toulouse, France, pp. 1–8.
[26] Papadopoulos, G., Battaglia, F., and Arik, E., 1999, "An Experimental/Numerical Study of 3-D Flow Past Double-Sided Expansions," *30th AIAA Fluid Dynamics Conference*, AIAA Paper No. 99-3696, pp. 1–10.
[27] Merkle, C., and Feng, J. Z., 1994, "Unified Time-Marching Procedure for Compressible and Incompressible Flows," J. Hydroddynamics, **7**(4), pp. 13–21.
[28] Chorin, A., 1967, "A Numerical Method for Solving Incompressible Viscous Flow Problems," J. Comput. Phys., **2**, pp. 12–26.
[29] Battaglia, F., 1997, *Numerical Simulations of Instabilities and Asymmetric Characteristics of Suddenly Expanded Channel Flows*, Ph.D. thesis, Dept. of Mechanical Engineering, Pennsylvania State University.
[30] Venkateswaran, S., and Merkle, C., 1995, "Dual Time Stepping and Preconditioning for Unsteady Computations," *33rd Aerospace Sciences Meeting & Exhibit*, AIAA Paper No. 95-0078.
[31] Celik, I., and Karatekin, O., 1997, "Numerical Experiments on Application of Richardson Extrapolation With Nonuniform Grids," ASME J. Fluids Eng., **119**, pp. 584–590.
[32] White, F., 1991, *Viscous Fluid Flow*, McGraw-Hill, New York.
[33] Chiang, T., Sheu, T. W., and Wang, S., 2000, "Side Wall Effects on the Structure of Laminar Flow Over a Plane-Symmetric Sudden Expansion," Comput. Fluids, **29**, pp. 467–492.

Identification of Transition to Turbulence in a Highly Accelerated Start-Up Pipe Flow

T. Koppel
Department of Mechanics,
Tallinn University of Technology,
Tallinn 19086, Estonia

L. Ainola
Department of Mathematics,
Tallinn University of Technology,
Tallinn 19086, Estonia

The transition from a laminar to a turbulent flow in highly accelerated start-up pipe flows is described. In these flows, turbulence springs up simultaneously over the entire length of the pipe near the wall. The unsteady boundary layer in the pipe was analyzed theoretically with the Laplace transformation method and the asymptotic method for small values of time. From the experimental results available, relationships between the flow parameters and the transition time were derived. These relationships are characterized by the analytical forms. A physical explanation for the regularities in the turbulence spring-up time is proposed. [DOI: 10.1115/1.2201640]

1 Introduction

An abrupt transition from the laminar to the turbulent flow in pipes is common for start-up flows at high acceleration. This transition process is distinguished by a regularity upon repetitive experiments. In addition, the transition to turbulence is delayed up to the supercritical Reynolds number. In some dynamic systems, the delay in the transition can be important for the dynamic control of a pipe flow. The study of start-up pipe flows will also provide information that can lead to a better understanding of the mechanism of spring-up turbulence in other types of flows.

The unsteady pipe flows fall into two groups: the periodic pulsating flows and the nonperiodic transient flows. Pulsating flows have received a marked attention because of their practical importance, whereas studies concerning transient pipe flows have been relatively rarely reported.

Accelerating flows are one of the types of frequently occurring nonperiodic transient flows. Leutheusser and Lam [1] and Koppel and Liiv [2] showed experimentally that the transition to turbulence in accelerating pipe flows is delayed. Maruyama et al. [3] studied the transition to turbulence in pipe flows, started impulsively with the supercritical Reynolds number. The authors show that a turbulent-laminar interface propagates downstream by entering the region where the laminar boundary layer is developing in time. Ainola et al. [4] analyzed the start-up flow in the pipe and reported experimental results on the transition from a laminar to a turbulent flow at a relatively high acceleration. The critical thickness of the dynamical boundary layer was used to characterize the transition moment. Kurakawa and Tanagi [5] have established that two types of flow transitions from laminar to turbulent exist in an accelerated flow. In the case of a relatively high acceleration flow, transition to turbulence takes place simultaneously over the entire length of the pipe. On the contrary, at a relatively low acceleration flow, transition occurs near the pipe inlet and forms a transition surface propagating downstream at a velocity higher than the mean flow velocity. The same problem was reported by Moss [6], based on the experiments carried out in a vertical tube. Lefebre and White [7] conducted an experimental study on the transition to turbulence in pipe flows started from rest at constant accelerations. Their experimental facility was equipped with advanced instrumentation, including six hot-film sensors, vibration and noise isolators, and flow straightening. Thirty-seven runs were made in a 50 mm dia and 30 m pipe at mean-flow accelerations varying from 1.85 m/s^2 to 11.8 m/s^2. In order to describe the transition moment to turbulence, several different parameters were used. Moss and da Silva [8] focused on the evolution of the unstable region in the impulsively started pipe entrance flows. They defined a dimensionless wall shear parameter and adopted a quasi-steady approach to establish the neutral stability curve. Das and Arakeri [9] and Greenblatt and Moss [10] have studied the stability and transition to the turbulence of wall-bounded unsteady velocity profiles with a reverse flow. In [9], the pipe flows were accelerated from rest with a simple trapezoidal piston motion maintained at a constant velocity, with a subsequent deceleration to rest. In [10], a similar technique for inducing a rapid transition to turbulence was employed, but the flow in the pipe was decelerated to a nonzero Re value. In these experiments, the deceleration generates an inflectional velocity profile with a subsequent transition to turbulence. A detailed investigation of a ram-type transient turbulent flow in the pipe, with flow rates linearly increasing or decreasing, was carried out by He and Jackson [11]. Three different delays in responses of the turbulent field to the imposed excursions of the flow rate were identified. The first response of turbulence was found to occur near the wall, at which the axial component of turbulence responds earlier than the other two components and builds up faster. Ghidaoui and Kolyshkin [12] have described the stability of unsteady axisymmetrical laminar flow in a pipe subjected to a rapid deceleration and acceleration. The base flow solutions for an unsteady one-dimensional laminar flow were derived by the method of matched asymptotic expansions. The linear stability of the base flow solutions to a three-dimensional perturbation was investigated and the results were used to reinterpret the experimental results of [9].

In this paper, the experimental results available on the transition to turbulence in start-up flows at high acceleration in a pipe are presented in the analytical form. At high acceleration, turbulence springs up simultaneously over the entire length of the pipe, near the wall, henceforth spreading to the center. Therefore, the unsteady boundary layer in an infinite pipe was studied theoretically at small values of time. The potential dimensionless transition parameters are defined, and their interrelationship explained. The experimental results of [4] are used to determine the transition curve. An analytical expression for this curve with a physical explanation for its form is proposed.

2 Unsteady Boundary Layer for Small Time

We consider the flow of the incompressible Newtonian fluid in an infinite circular pipe, which is governed by the equations

Contributed by the Fluids Engineering Division of ASME for publication in the JOURNAL OF FLUIDS ENGINEERING. Manuscript received December 10, 2004; final manuscript received December 27, 2005. Assoc. Editor: James A. Liburdy.

$$\frac{\partial u}{\partial \tau} - \left(\frac{\partial^2 u}{\partial \eta^2} + \frac{1}{\eta} \frac{\partial u}{\partial \eta} \right) - a = 0 \tag{1}$$

where

$$u = \frac{V_z R}{\nu}, \quad \tau = \frac{t\nu}{R^2}, \quad \eta = \frac{r}{R}, \quad a = -\frac{R^3}{\rho \nu^2} \frac{\partial P}{\partial z} \tag{2}$$

The initial and boundary conditions for the problem of the start-up flow of a fluid initially at rest are

$$u(\eta, 0) = 0 \tag{3}$$

and

$$u(1, \tau) = 0, \quad \frac{\partial u}{\partial \eta}(0, \tau) = 0 \tag{4}$$

Applying the Laplace transformation to the governing equation (1) with the initial condition (3), we obtain

$$\frac{\partial^2 \bar{u}}{\partial \eta^2} + \frac{1}{\eta} \frac{\partial \bar{u}}{\partial \eta} - s\bar{u} = \bar{a} \tag{5}$$

Accordingly, boundary conditions (4) take the form

$$\bar{u}(1, s) = 0, \quad \frac{\partial \bar{u}}{\partial \eta}(0, s) = 0 \tag{6}$$

The solution of Eqs. (5) and (6) becomes

$$\bar{u}(\eta, s) = \bar{a}\bar{K}(\eta, s) \tag{7}$$

where

$$\bar{K}(\eta, s) = \frac{1}{s} \left[1 - \frac{I_0(\eta\sqrt{s})}{I_0(\sqrt{s})} \right] \tag{8}$$

Here I_0 is the modified Bessel function of the first kind of order zero.

2.1 Impulsively Started Flow. First, let us consider the impulsively started flow. Although we cannot realize this motion using the pressure gradient $\partial P/\partial z$, it allows us to simplify the mathematical formulation of the boundary layer theory.

Thus, let $a = I(\tau)$, where $I(\tau)$ is the unit impulse function (Dirac δ function). Then $\bar{a} = 1$ and Eq. (7) takes the form of

$$\bar{u}_I(\eta, s) = \bar{K}(\eta, s) \tag{9}$$

Now, if we use the theorem of residues, from Eqs. (8) and (9) we obtain the velocity in the time domain as a sum

$$u_I(\eta, \tau) = 2 \sum_{k=1}^{\infty} \frac{J_0(\alpha_k \eta)}{\alpha_k J_1(\alpha_k)} e^{-\alpha_k^2 \tau} \tag{10}$$

Here J_0 and J_1 are Bessel functions of order zero and one, respectively, and α_k is zeros of function $J_0(\alpha)$.

Let us consider the flow in a pipe immediately after the start of motion at small values of time τ. For these values of time, it is difficult to analyze the velocities with Eq. (10). The asymptotic expansion for $s \to \infty$ of the Laplacean solution $\bar{u}$ gives us a small time limit $\tau \to 0$ for u. Therefore, let us proceed here from the asymptotic expansions of Bessel functions for $s \to \infty$.

The modified Bessel function for large values of s can be expressed as

$$I_n(s) = \frac{e^s}{\sqrt{2\pi s}} \left[1 - \frac{4n^2 - 1}{8s} + \frac{(4n^2 - 1)(4n^2 - 9)}{2!\,(8s)^2} - \cdots \right] \tag{11}$$

From Eqs. (8), (9), and (11) we obtain

$$\bar{u}_I(\eta, s) = \frac{1}{s} \left\{ 1 - \frac{e^{-\sqrt{s}(1-\eta)}}{\sqrt{\eta}} \left[1 + \frac{1 - \eta}{8\eta} \frac{1}{\sqrt{s}} + \frac{9(1 - \eta^2) - 2\eta(1 - \eta)}{128\eta^2} \frac{1}{s} + \cdots \right] \right\} \tag{12}$$

Here we assume that $0 \ll \eta \ll 1$.

The inverse Laplace transformation for Eq. (12) can be written as

$$u_I(\eta, \tau) = 1 - \frac{1}{\sqrt{\eta}} \left[1 - \frac{(1 - \eta)^2}{8\eta} \operatorname{erfc} \beta - \frac{1 - \eta}{4\eta^{3/2}} \sqrt{\frac{\tau}{\pi}} e^{-\beta^2} + \cdots \right] \tag{13}$$

where erfc β is the complimentary error function and

$$\beta = \frac{1 - \eta}{2\sqrt{\tau}} \tag{14}$$

For $\eta = 0$ at small values of τ, we have, respectively,

$$\bar{u}_I(0, s) = \frac{I_0(\sqrt{s}) - 1}{sI_0(\sqrt{s})} \tag{15}$$

$$\bar{u}_I(0, s) = \frac{1}{s} - \frac{\sqrt{2\pi}}{s^{3/4}} e^{-\sqrt{s}} + \cdots \tag{16}$$

and

$$u_I(0, \tau) = 1 - \frac{\sqrt{2}}{\Gamma(1/4)} \int_0^{\tau} \frac{e^{-(1/4\tau')}}{\tau'^2 (\tau - \tau')^3} d\tau' + \cdots \tag{17}$$

From Eq. (17) it follows that at the beginning of an impulsively started flow, the velocity is not constant even at the center of the pipe.

We define the distance from the wall of the pipe as

$$\delta = 1 - \eta \tag{18}$$

and assume that

$$u_I(\eta, \tau) = u_I'(\delta, \tau) \tag{19}$$

Using Eqs. (18) and (19), Eq. (13) takes the form

$$u_I'(\delta, \tau) = 1 - \frac{1}{\sqrt{1 - \delta}} \left[1 - \frac{\delta^2}{8(1 - \delta)} \operatorname{erfc} \beta' - \frac{\delta}{4(1 - \delta)^{3/2}} \sqrt{\frac{\tau}{\pi}} e^{-\beta'^2} + \cdots \right] \tag{20}$$

where

$$\beta' = \frac{\delta}{2\sqrt{\tau}} \tag{21}$$

Commonly, the thickness of the boundary layer on a flat plate is defined as the distance from the wall where the velocity differs by a predefined percent from the external velocity. To define the thickness of the boundary layer in the pipe, we proceed here from the velocity of an ideal fluid flow, which is equal to one. As a predefinition we use the 1% difference of velocities and determine the thickness of the boundary layer δ_I from the condition $u_I(\delta_I, \tau) = 0.99$.

Now, in the first approximation from Eq. (20) we obtain for the thickness of the boundary layer equation

$$\operatorname{erfc} \beta_I + \frac{1}{4} \delta_I \left(2 \operatorname{erfc} \beta_I + \sqrt{\frac{\tau}{\pi}} e^{-\beta_I^2} \right) = 0.01 \tag{22}$$

where

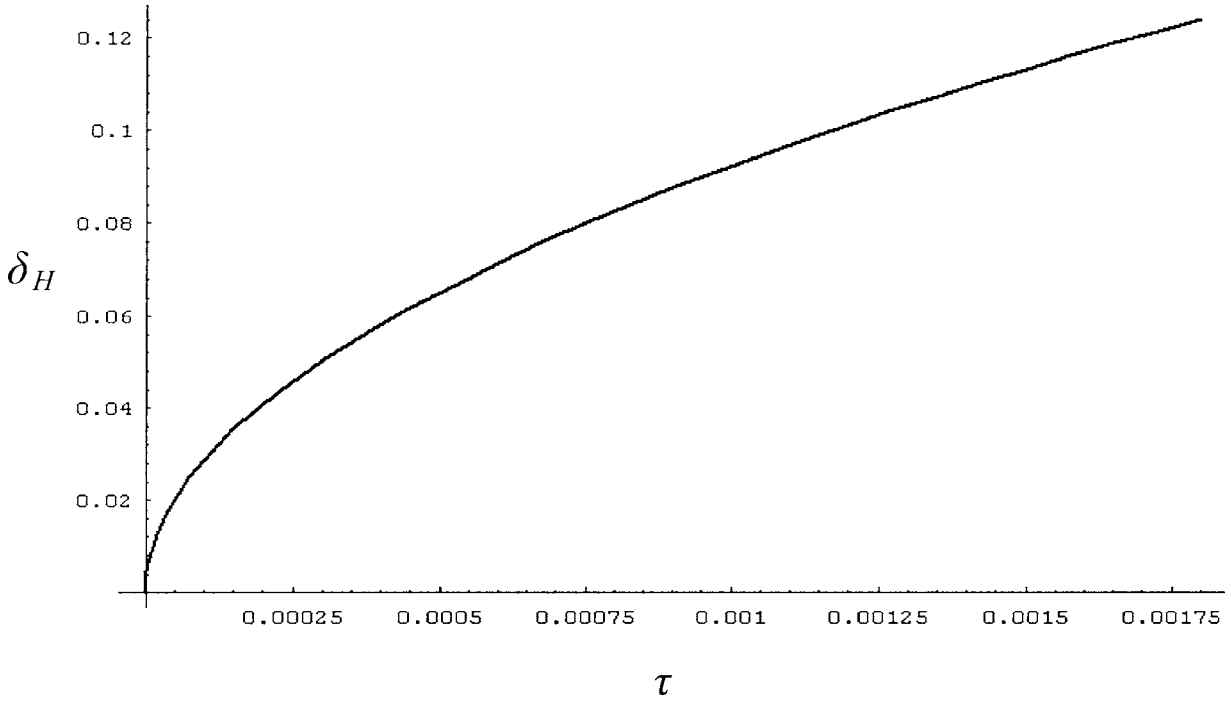

Fig. 1 Development of the thickness of the boundary layer in start-up flows at the constant pressure gradients

$$\beta_I = \frac{\delta_I}{2\sqrt{\tau}} \tag{23}$$

If we preserve only the first term in the left part of Eq. (22), then we have

$$\delta_I \approx 3.64\sqrt{\tau} \tag{24}$$

This result coincides with the thickness of the boundary of the Rayleigh's problem where the impulsive flow is considered over an infinitely flat plate [13].

2.2 Heaviside Pressure Gradient. Now let us consider the start-up flow caused by the applied constant pressure gradient in time. From Eqs. (7) and (9), it follows that the velocity of the flow for an arbitrary function $a(\tau)$ can be expressed as

$$u'(\delta,\tau) = \int_0^\tau a(\tau-\tau')u_I'(\delta,\tau')d\tau' \tag{25}$$

Let $a(\tau)=H(\tau)$, where $H(\tau)$ is the Heaviside function. Substituting Eq. (20) into Eq. (25), we obtain

$$u_H'(\delta,\tau) = \tau\left\{1 - \frac{1}{\sqrt{1-\delta}}\left[(1+2\beta'^2)\text{erfc}\,\beta' - \frac{2}{\sqrt{\pi}}\beta' e^{-\beta'^2} + \cdots\right]\right\} \tag{26}$$

Respectively, for the constant pressure gradient, the thickness of the boundary layer δ_H is determined by the equation

$$(1+2\beta_H^2)\text{erfc}\,\beta_H - \frac{2}{\sqrt{\pi}}\beta_H e^{-\beta_H^2} = 0.01\sqrt{1-\delta_H} \tag{27}$$

where

$$\beta_H = \frac{\delta_H}{2\sqrt{\tau}} \tag{28}$$

The variation of the thickness of the boundary layer δ_H versus time τ obtained from Eq. (27) is shown in Fig. 1.

From Eq. (27), it follows that in the time interval $0 \le \tau \le 0.0018$ within 1% accuracy we can take

$$\delta_H \approx 2.90\sqrt{\tau} \tag{29}$$

3 Mean and Friction Velocities for Small Time

Averaging Eq. (1) over the cross section of a circular pipe with the aid of the operator, we obtain

$$\frac{\partial U}{\partial \tau} - 2\psi_0 - a = 0 \tag{30}$$

where

$$U = 2\int_0^1 u\,\eta d\eta, \quad \psi_0 = -\left(\frac{\partial u}{\partial \eta}\right)_{\eta=1} \tag{31}$$

For an impulsively started flow, the Laplace transformation of Eq. (30) takes the form

$$s\bar{U}_I + 2\bar{\psi}_{0I} - 1 = 0 \tag{32}$$

From Eqs. (8), (9), and (32), we have

$$\bar{U}_I(s) = \frac{I_2(\sqrt{s})}{sI_0(\sqrt{s})} \tag{33}$$

Using the asymptotic expansion for $s \to \infty$ in Eq. (33) for small values of τ, i.e., Eq. (11), we obtain

$$\bar{U}_I(s) = \frac{1}{s} - \frac{2}{s^{3/2}} + \frac{1}{s^2} + \cdots \tag{34}$$

Respectively, the mean velocity at the beginning of motion can be written as

$$U_I(\tau) = 1 - \frac{4}{\pi}\sqrt{\tau} + \tau + \cdots \tag{35}$$

Now, from Eqs. (30) and (35) it follows that

$$\psi_{0I}(\tau) = \frac{1}{2}\left[I(\tau) - \frac{2}{\pi\sqrt{\tau}} - 1 + \cdots\right] \tag{36}$$

For an arbitrary $a(\tau)$, the mean velocity can be expressed as

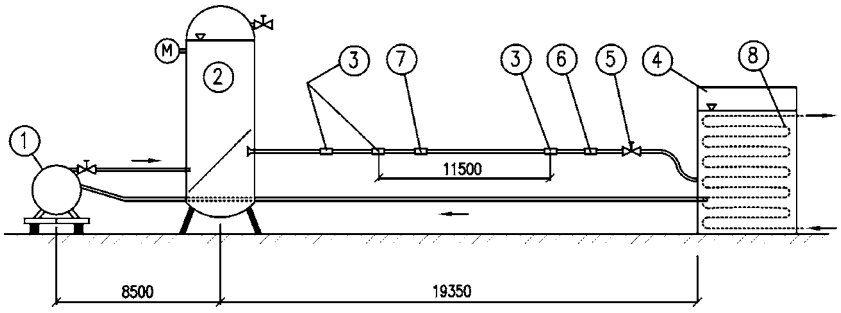

Fig. 2 Layout of the experimental hydraulic system: 1–pump, 2–upper pressure tank (0.85 m^3), 3–cross sections for pressure measurements, 4–lower open tank (0.70 m^3), 5–quick-opening valve, 6–electromagnetic flowmeter, 7–cross section for wall shear stress measurements, and 8–cooling system

$$U(\tau) = \int_0^\tau a(\tau - \tau') U_I(\tau) d\tau' \tag{37}$$

Therefore, for $a(\tau) = \alpha H(\tau)$ from Eqs. (35) and (37) it follows that

$$U_H(\tau) = \alpha \left(\tau - \frac{8}{3\pi} \tau^{3/2} + \frac{1}{2} \tau^2 + \cdots \right) \tag{38}$$

Respectively, we obtain

$$\psi_{0H}(\tau) = \alpha \left(\frac{2}{\pi} \sqrt{\tau} - \frac{1}{2} \tau + \cdots \right) \tag{39}$$

The dimensionless friction velocity at the pipe wall is defined as

$$u_f = \sqrt{\frac{\sigma_0}{\rho}} \frac{R}{\nu} \tag{40}$$

or in a dimensionless form

$$u_f = \sqrt{\psi_0} \tag{41}$$

Here σ_0 is the shear stress at the wall.

Now for $\tau \ll 1$ from Eqs. (39) and (41), we obtain

$$u_{fH}(\tau) = \sqrt{\frac{2}{\pi}} \sqrt{\alpha} \left(\tau^{1/4} - \frac{\pi}{8} \tau^{3/4} + \cdots \right) \tag{42}$$

4 Experimental Results

In [4], Ainola et al. report the results of experiments conducted to determine the transition from a laminar to a turbulent flow in the start-up flow with a constant pressure gradient in time. The layout of the experimental facility is shown in Fig. 2 [2].

An unsteady flow was produced by a quick-opening valve in the 61 mm dia test section of a 19.35 m long pipe. The transition to turbulence was monitored by the hot-film shear stress sensor (DISA 55A91). The probes were flush mounted, while the film of the probe extended up to the flow at a depth of 0.09 mm.

Table 1 shows the experimental results for the spring-up turbulence of 32 runs with different pressure gradients. Figure 3 shows the data of Table 1 in the logarithmic coordinates. Based on Fig. 3, almost linear dependence between $\log \tau_*$ and $\log \alpha$ can be concluded.

Using the least-squares fitting to the data in Table 1 for the determination of the respective function, we obtain

$$\log \tau_* = 1.80 - 0.62 \log \alpha. \tag{43}$$

For the time of the spring-up turbulence in a pipe from Eq. (43), we have

$$\tau_* = 63.1 \alpha^{-0.620} \tag{44}$$

A qualitatively similar result was obtained by Lefebre and White [7]. Their conclusion in our notations can be written as

$$\tau_* = 404 \alpha^{-0.666} \tag{45}$$

We can see that the exponents of α in Eqs. (44) and (45) are close, but the coefficients are essentially different. Evidently, this is induced by different experimental conditions, since in the experiments of Lefebre and White [7] most obvious side effects were eliminated.

To characterize the condition of the transition to turbulence in other parameters, δ_H, U_H, and u_{fH}, Eqs. (29), (38), and (42) can be used. Substituting Eq. (44) into these equations in the first approximation, we obtain

$$\log \delta_{H^*} = 1.42 - 0.310 \log \alpha$$

$$\log U_{H^*} = 1.80 + 0.380 \log \alpha$$

Table 1 Experimental results from [4]

Experiment	$\alpha \times 10^{-8}$	$\tau_* \times 10^3$	$\log \alpha$	$\log \tau_*$
1	3.43	0.356	8.535	−3.446
2	2.86	0.374	8.456	−3.427
3	2.87	0.376	8.458	−3.425
4	2.86	0.377	8.456	−3.424
5	2.64	0.392	8.422	−3.407
6	2.54	0.398	8.405	−3.400
7	2.32	0.415	8.365	−3.382
8	2.32	0.416	8.365	−3.381
9	2.32	0.420	8.365	−3.377
10	2.04	0.447	8.310	−3.350
11	1.98	0.464	8.290	−3.333
12	1.75	0.487	8.243	−3.312
13	1.72	0.491	8.236	−3.309
14	1.75	0.500	8.243	−3.301
15	1.43	0.535	8.155	−3.272
16	1.43	0.541	8.155	−3.267
17	1.20	0.610	8.079	−3.215
18	0.874	0.713	7.942	−3.147
19	0.872	0.717	7.941	−3.144
20	0.788	0.800	7.897	−3.097
21	0.643	0.922	7.808	−3.035
22	0.587	0.929	7.769	−3.032
23	0.587	0.935	7.769	−3.029
24	0.601	0.936	7.779	−3.029
25	0.585	0.936	7.767	−3.029
26	0.457	1.134	7.660	−2.945
27	0.457	1.144	7.660	−2.942
28	0.444	1.200	7.647	−2.921
29	0.414	1.249	7.617	−2.903
30	0.301	1.558	7.479	−2.807
31	0.271	1.749	7.433	−2.757
32	0.271	1.546	7.433	−2.811

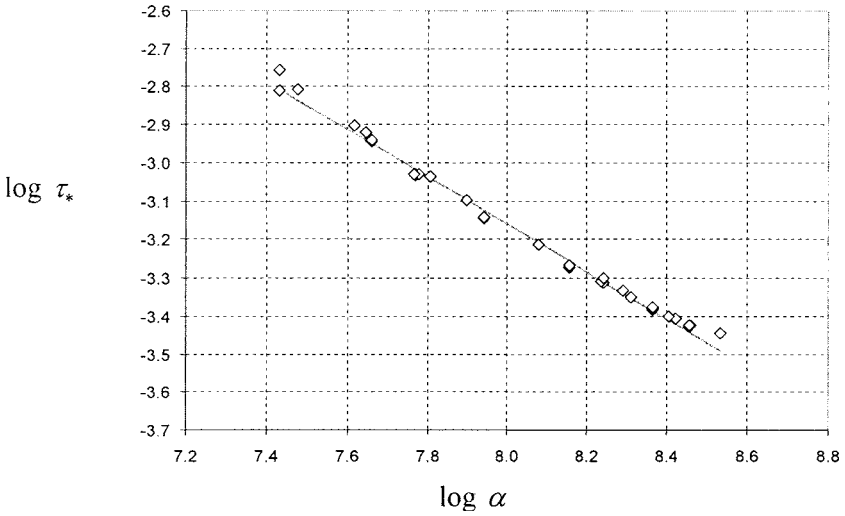

Fig. 3 Variation of the dimensionless transition time versus the dimensionless pressure gradient in a start-up flow at high acceleration

$$\log u_{fH^*} = 0.35 + 0.354 \log \alpha \tag{46}$$

The functions $\log U_{H^*}$ and $\log u_{fH^*}$ are shown in Figs. 4 and 5. In start-up pipe flows, all the dimensionless parameters τ_*, δ_{H^*}, U_{H^*}, and u_{fH^*} as the functions of acceleration α are equivalent to the description of the transition moment.

5 Discussion

In Eq. (30) at an early stage of an unsteady flow, the magnitude of the pressure gradient force a and the inertia force $\partial U/\partial \tau$ are both much larger than the shear stress force $2\psi_0$, being approximately equal. Further on, the contribution of the shear force becomes more significant. The buildup of the shear force starts in the wall region and extends toward the center. At the beginning of the imposed pressure gradient, the shear force is confined to a very thin layer of the fluid near the wall and the velocity of the fluid in the core region responds to the pressure gradient almost as in a slug flow. Therefore, steep velocity gradients are generated in the wall region. The important feature of the transient flow is that the turbulence springs up in very close proximity to the wall. Thereafter, the turbulence, originating from the wall region, propagates into the core region of the pipe.

It is suggested that at the start, the turbulence propagation toward the center of the pipe is associated with the turbulent diffusion and the turbulence propagates with the friction velocity [11]. Let us assume that the region for the turbulent diffusion is the boundary layer and the time of turbulence spring-up determined in the experiments is equal to the time of the dissipation through the unsteady boundary layer.

The friction velocity is associated with the moment τ_0 of turbulence spring-up near the wall of the pipe. As time proceeds, the turbulence at the wall is generated all the time. This turbulence has the friction velocity, which controls its spring-up time. Let the turbulence, which is generated at the time τ_0, pass through the boundary layer δ at the time τ_*. Then,

$$\delta(\tau_*) = u_f(\tau_0)(\tau_* - \tau_0) \tag{47}$$

Substituting Eqs. (29) and (42) into Eq. (47), we have

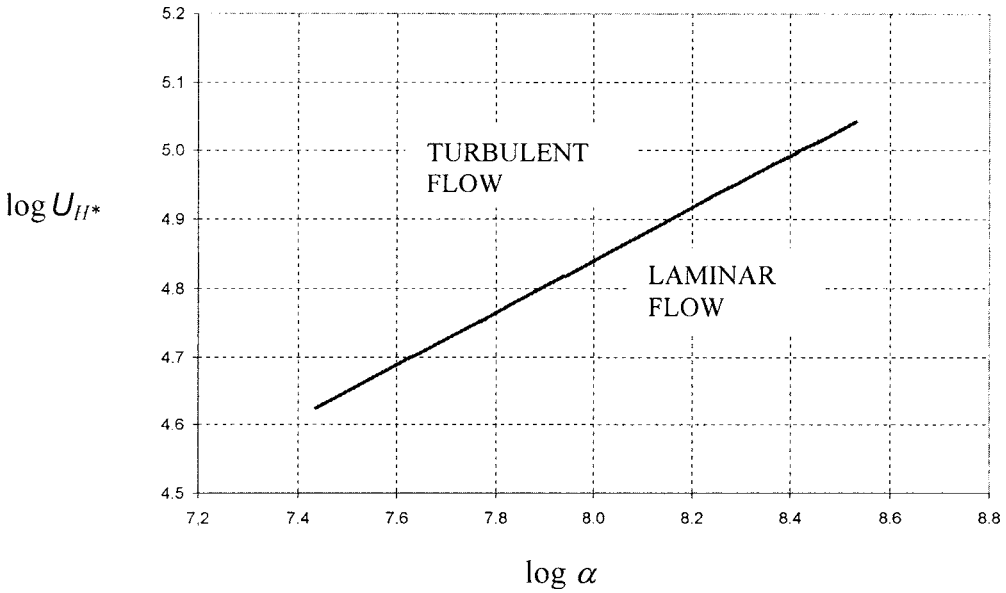

Fig. 4 Regions of laminar and turbulent flows in a highly accelerated start-up flow in the plane of the dimensionless mean velocity and the pressure gradient

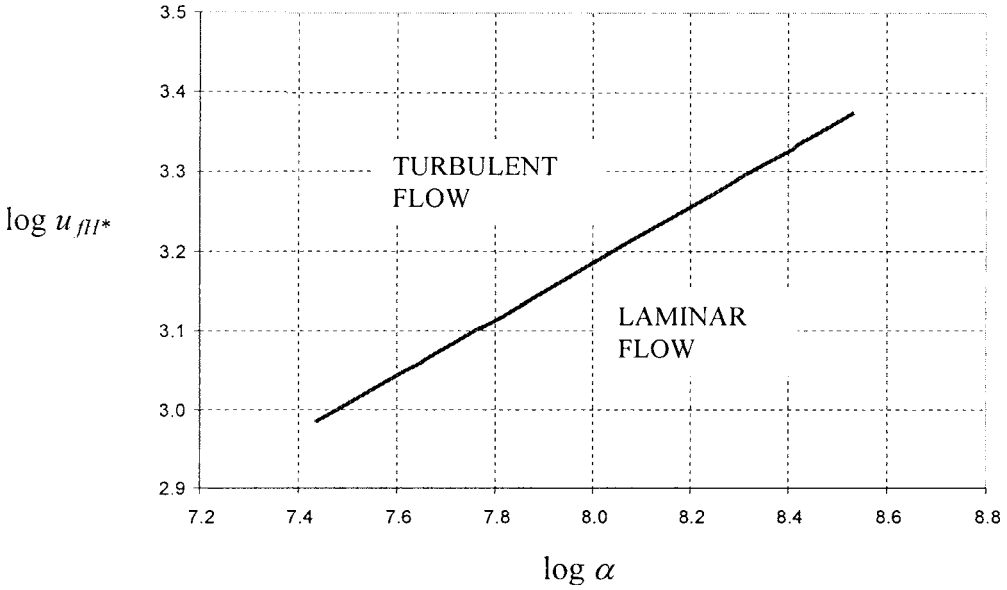

Fig. 5 Regions of laminar and turbulent flows in a highly accelerated start-up flow in the plane of the dimensionless friction velocity and the pressure gradient

$$2.90\sqrt{\tau_*} = \sqrt{\frac{2}{\pi}}\sqrt{\alpha}\sqrt[4]{\tau_0}(\tau_* - \tau_0) \tag{48}$$

Using Eq. (48), we can consider the time τ_* as the function of the time τ_0

$$\sqrt{\tau_*} = \frac{m}{\sqrt[4]{\tau_0}} + \sqrt{\frac{m^2}{\sqrt{\tau_0}} + \tau_0} \tag{49}$$

Here,

$$m = \frac{2.90\sqrt{\pi}}{2\sqrt{2}\sqrt{\alpha}} \tag{50}$$

Let us now determine the time τ_0 from a condition at which the time τ_* has the minimal value, i.e.,

$$\frac{d\sqrt{\tau_*}}{d\tau_0} = 0 \tag{51}$$

From Eqs. (49) and (51), we obtain

$$m^2\tau^{-3/2}\sqrt{1 + \frac{1}{m^2\tau_0^{-3/2}}} + m^2\tau_0^{-3/2} - 2 = 0 \tag{52}$$

or

$$\tau_0 = \left(\tfrac{4}{5}\right)^{-2/3} m^{4/3} \tag{53}$$

Substituting Eq. (53) into Eq. (49), we obtain for the minimal value of the time τ_*

$$\tau_{*\min} = \left[\left(\tfrac{4}{5}\right)^{1/6} + \sqrt{\left(\tfrac{4}{5}\right)^{1/3} + \left(\tfrac{4}{5}\right)^{-2/3}}\right]^2 m^{4/3} \tag{54}$$

From Eqs. (50) and (54), we have

$$\tau_{*\min} = 12.9\alpha^{-2/3} \tag{55}$$

Comparing Eqs. (44) and (45) with Eq. (55), we can see that their structures are quite similar and the exponents of α are very close. Consequently, the interdependence between the transition time and the flow acceleration can result from the different time interval of the turbulent dissipation through the unsteady boundary layer.

6 Conclusions

In a highly accelerated start-up pipe flow, the transition from a laminar to a turbulent flow occurs first in the unsteady boundary layer near the wall. The unsteady boundary layer was analyzed with the Laplace transformation method using the small-time asymptotic approximation. The dimensionless time, the pressure gradient, the mean, and friction velocities were defined and their interrelationship for small time determined. Available experimental results were used to derive the variations of these parameters at the transition time versus the pressure gradient. From experimental results, it follows that the logarithms of the time of transition, the mean, and friction velocities are the linear functions of the logarithm of the pressure gradient. It was shown that the similar linear functions can be obtained, theoretically, based on the turbulence spreading through the unsteady boundary layer at the friction velocity. The different time interval, which allows for the turbulence to dissipate through the unsteady boundary layer, determines the differences in the delay in the transition time

Acknowledgment

Financial support by the Estonian Science Foundation (Grant No. 5879) and targeted financing 0142514s03 is greatly appreciated.

Nomenclature

a = dimensionless pressure gradient
erfc = complementary error function
H = Heaviside function
I = unit impulse function
I_n = modified Bessel function of the first kind of order n
J_n = Bessel function of order n
p = fluid pressure
r = axial coordinate
R = pipe radius
s = Laplace parameter
t = time
T_0 = reference value of time
u = dimensionless velocity
u_f = dimensionless shear velocity

U = dimensionless mean velocity
U_0 = reference value of velocity
V = velocity vector
z = axial coordinate
α_k = zeros of $J_0(\alpha)$
δ = boundary layer thickness
η = dimensionless radial coordinate
ψ_0 = dimensionless wall shear stress
ν = kinematic viscosity
ρ = fluid density
τ = dimensionless time

Subscripts

I = values for the impulse-accelerated flow
H = values for the constant-accelerated flow
$*$ = values at the moment of transition

References

[1] Leutheusser, H. J., and Lam, K. W., 1977, "Laminar-to-Turbulent Transition in Accelerated Fluid Motion," *Proc. of 17th Cong. IAHR*, Baden-Baden, Germany, Institute for Hydrology and Water Management, Karlsruhe University, Karlsruhe, Vol. 2, pp. 343–350.

[2] Koppel, T. A., and Liiv, U. R., 1977, "Experimental Investigation of the Development of Motion of Liquid in Conduits," Fluid Dyn., **12**(6), pp. 881–887.

[3] Maruyama, T., Kato, Y., and Mizushina, T., 1978, "Transition to Turbulence in Starting Pipe Flow," J. Chem. Eng. Jpn., **11**, pp. 346–353.

[4] Ainola, L., Koppel, T., Lamp, J., and Liiv, U., 1981, "On the Criteria of the Transition From Laminar to Turbulent in Starting Pipe Flow," Trans. Tallinn Polyt. Inst., **505**, pp. 17–29 (in Russian).

[5] Kurakawa, J., and Tanagi, A., 1988, "Accelerated and Decelerated Flows in a Circular Pipe," Trans. Jpn. Soc. Mech. Eng., Ser. B, **B54**, pp. 302–307.

[6] Moss, E. A., 1989, "The Identification of Two Distinct Laminar to Turbulent Transition Modes in Pipe Flows Accelerated From Rest," Exp. Fluids, **7**, pp. 271–274.

[7] Lefebre, P. J., and White, F. M., 1989, "Experiments of Transition to Turbulence in a Constant-Acceleration Pipe Flow," ASME J. Fluids Eng., **111**, pp. 428–432.

[8] Moss, E. A., and da Silva, D. F., 1993, "The Evolution of Unstable Region in Impulsively Started Pipe Entrance Flows," Phys. Fluids A **A5**, pp. 2721–2724.

[9] Das, D., and Arakeri, J. H., 1998, "Transition of Unsteady Velocity Profiles With Reverse Flow," J. Fluid Mech. **374**, pp. 251–283.

[10] Greenblatt, D., and Moss, E. A., 2003, "Rapid Transition to Turbulence in Pipe Flows Accelerated From Rest," ASME J. Fluids Eng., **125**, pp. 1072–1075.

[11] He, S., and Jackson, J. D., 2000, "A Study of Turbulence Under Conditions of Transient Flow in a Pipe," J. Fluid Mech., **408**, pp. 1–38.

[12] Ghidaoui, M. S., and Kolyshkin, A. A., 2002, "A Quasi-Steady Approach to the Instability of Time-Dependent Flows in Pipes," J. Fluid Mech. **465**, pp. 301–330.

[13] Telionis, D. P., 1981, *Unsteady Viscous Flows*, Springer-Verlag, Berlin.

Optimal Yaw Regulation and Trajectory Control of Biorobotic AUV Using Mechanical Fins Based on CFD Parametrization[1]

Mukund Narasimhan
Department of Electrical & Computer Engineering,
University of Nevada,
Las Vegas, NV 89154-4026

Haibo Dong
e-mail: haibo@gwu.edu

Rajat Mittal
e-mail: mittal@gwu.edu

Department of Mechanical and Aerospace Engineering,
The George Washington University,
Washington DC 22052

Sahjendra N. Singh
Department of Electrical & Computer Engineering,
University of Nevada,
Las Vegas, NV 89154-4026
e-mail: sahaj@ee.unlv.edu

This paper treats the question of control of a biorobotic autonomous undersea vehicle (BAUV) in the yaw plane using a biomimetic mechanism resembling the pectoral fins of fish. These fins are assumed to undergo a combined sway-yaw motion and the bias angle is treated as a control input, which is varied in time to accomplish the maneuver in the yaw-plane. The forces and moments produced by the flapping foil are parametrized using computational fluid dynamics. A finite-difference-based, Cartesian grid immersed boundary solver is used to simulate flow past the flapping foils. The periodic forces and moments are expanded as a Fourier series and a discrete-time model of the BAUV is developed for the purpose of control. An optimal control system for the set point control of the yaw angle and an inverse control law for the tracking of time-varying yaw angle trajectories are designed. Simulation results show that in the closed-loop system, the yaw angle follows commanded sinusoidal trajectories and the segments of the intersample yaw trajectory remain close to the discrete-time reference trajectory. It is also found that the fins suitably located near the center of mass of the vehicle provide better maneuverability. [DOI: 10.1115/1.2201634]

Keywords: biorobotic AUV, yaw-plane control, CFD, pectoral fins

1 Introduction

Aquatic animals present a wide diversity of maneuvering behaviors and hydrodynamic mechanisms for their locomotion. Fish use a variety of fins (dorsal, caudal, pectoral, pelvic fins, etc.) for maneuvering and propulsion [1,2]. Biological studies is motivating researchers to design biorobotic autonomous underwater vehicles (BAUVs) actuated by oscillating fins for naval applications [3,4]. Readers may refer to a special issue of *IEEE Journal of Oceanic Engineering* on biologically inspired science and technology for autonomous underwater vehicles (AUVs) for excellent review articles and related research [5–9].

Detailed studies have been conducted on fish morphology [4,5,10–13] and locomotion based on which mechanical fins have been designed. Extensive work has been conducted on the measurement of the forces and moments produced by the oscillating fins in various laboratory experiments [10–12,14,15]. Fin movements, such as lead-lag, feathering, and flapping, are identified as the basic oscillating patterns responsible for producing large lift, side force, and thrust, which can be used for the control and propulsion of BAUVs [12,15–17]. Forces and moments associated with the fin movements have also been extracted from computational fluid dynamic (CFD) simulations [18–29], where a number of different fin movement patterns have been considered.

Considerable research has been done for controlling AUVs using traditional control surfaces [31]. A sliding mode control system has been designed for the dive plane control of BAUVs by continuous cambering of dorsal fins [11]. However for fishlike maneuvering, control system design using oscillating fins is essential. Experimental results and CFD simulations of oscillating pectoral fins indicate that these fins produce periodic forces and moments, and the oscillating parameters (the amplitude of oscillation, frequency, bias angle, phase angle, etc.) can be used as control variables for maneuvering BAUVs [12–14]. Recently, control of AUVs using pectoral fins have been attempted [15–17].

An inverse controller has been designed to maneuver BAUVs in the dive plane using pectoral fins [32]. Although, the characterization of forces and moments generated by oscillating fins, when the chosen control inputs (oscillation parameters) vary in a continuous manner, is important; it seems from literature that this kind of research remains yet to be done. For simplicity, usually numerical simulations using CFD are obtained for a set of fixed oscillation parameters. Thus, for a meaningful utilization of the data obtained using CFD for modeling the forces and moments of the oscillating fins for the purpose of control, it is apparent that the control input (the oscillation parameters) should be changed at discrete intervals only after the completion of a few cycles of the fin motion. Such an attempt to parametrize the forces and moments of a plunging and pitching foil for the dive-plane control of an AUV by switching the bias angle at discrete intervals has been done in [32]. Two-dimensional foil and low Reynolds number flow conditions were chosen for the CFD simulations. The control system designed in [32] is only applicable for the control in the dive plane. Thus, it is of interest to explore the applicability of the pectoral fin control system in the yaw-plane as well. Moreover, the development of parametrizations of the fin forces and moments using new CFD algorithms is certainly desirable for the precision in control.

The contribution of the current paper lies in the parametrization of forces and moments of oscillating pectoral-like fins using CFD; and the design of an optimal control system for the regulation of the yaw angle and an inverse control system for the time-varying yaw trajectory tracking of the AUV. The mechanical foils are assumed to undergo a combined yaw-sway mode of oscillation with the bias angle of the foil as the key control parameter, which is altered at discrete intervals for maneuvering the AUV. For the computation of the fin force and moment, a finite-difference-

[1]This work is supported under ONR Grants No. N00014-03-1-0458 and No. N00014-03-1-0897.

Contributed by the Fluids Engineering Division of ASME for publication in the JOURNAL OF FLUIDS ENGINEERING. Manuscript received April 8, 2005; final manuscript received December 27, 2005. Assoc. Editor: Ugo Piomelli.

based, Cartesian grid immersed boundary solver for simulating the flow past the flapping foils is used. Three-dimensional foils with finite aspect ratio as well as high Reynolds number flow conditions are chosen in the CFD studies. This makes the simulations more realistic. Moreover, large eddy simulations (LES) are also implemented in current simulations to resolve the turbulence structures. The periodic force and moment obtained using CFD are represented by Fourier series, and a discrete-time AUV model is constructed for the design of two control systems. First, an optimal control law is designed for the control of the yaw (heading) angle by minimizing an appropriate quadratic performance index. The choice of performance criterion gives flexibility in shaping the transient responses. This is followed by the design of an inverse control system for the trajectory control of the yaw angle. It is seen that the number of unstable zeros of the transfer function of the AUV is a function of the position of the pectoral fins on the AUV and the sampling rate. Since the AUV model considered is nonminimum phase, an approximate discrete-time system is obtained by eliminating the unstable zeros from the pulse transfer function of the BAUV. Then an inverse control law is derived for the trajectory tracking based on the approximate minimum phase representation of the transfer function. Simulation results are obtained for the optimal control of the yaw angle and for the tracking of sinusoidal reference yaw angle trajectories using the inverse controller.

The organization of the paper is as follows. Section 2 describes the mathematical model of the BAUV. The CFD-based parametrization and discrete-time representation are obtained in Sec. 3. Sections 4 and 5 present the optimal control law derivation and the inverse controller design, respectively. The simulation results and conclusion are provided in Secs. 6 and 7, respectively.

2 Yaw-Plane Dynamics

Let the vehicle be moving in the yaw plane (X_I–Y_I plane) where $O_I X_I Y_I$ is an inertial coordinate system. $O_B X_B Y_B$ is a body-fixed coordinate system, X_B is in the forward direction, and Y_B points to the right. In the moving coordinate frame $O_B X_B Y_B$ fixed at the vehicle's geometric center, the dynamics for neutrally buoyant vehicle in the yaw plane are given by [33]

$$m(\dot{v} + Ur + X_G\dot{r} - Y_G r^2) = Y_{\dot{r}}\dot{r} + (Y_{\dot{v}}\dot{v} + Y_r Ur) + Y_v Uv + F_y$$

$$I_z\dot{r} + m(X_G\dot{v} + X_G Ur + Y_G vr) = N_{\dot{r}}\dot{r} + (N_{\dot{v}}\dot{v} + N_r Ur) + N_v Uv + M_y$$

$$\dot{\psi} = r \tag{1}$$

where ψ is the heading angle, $r=\dot{\psi}$ is the yaw rate, v is the lateral velocity, $x_{GB}=x_G-x_B$, $Y_{GB}=Y_G-Y_B=0$, l=body length, ρ =density, m is the mass of the AUV, and I_z is the moment of inertia. $Y_{\dot{v}}$, $N_{\dot{r}}$, $Y_{\dot{r}}$, etc., are the hydrodynamic coefficients. F_y and M_y denote the net lateral (sway) force and yawing moment acting on the vehicle due to the pectoral fins. Here, $((X_B, Y_B)=0)$ and (X_G, Y_G) denote the coordinates of the center of buoyancy and center of gravity (cg), respectively. Although, the design approach considered in this paper can be used for speed control, here for simplicity, it is assumed that the forward velocity is held steady $(u=U)$ by a control mechanism and only lateral maneuvers are considered. In this study, only small maneuvers of the vehicle are considered. As such linearizing the equations of motion about $v=0$, $r=0$, $\psi=0$, one obtains

$$\begin{bmatrix} m-Y_{\dot{v}} & mX_G-Y_{\dot{r}} & 0 \\ mX_G-N_{\dot{v}} & I_z-N_{\dot{r}} & 0 \\ 0 & 0 & 1 \end{bmatrix}\begin{bmatrix} \dot{v} \\ \dot{r} \\ \dot{\psi} \end{bmatrix} = \begin{bmatrix} Y_v U & Y_r U-mU & 0 \\ N_v U & N_r U-mX_G U & 0 \\ 0 & 1 & 0 \end{bmatrix}\begin{bmatrix} v \\ r \\ \psi \end{bmatrix} + \begin{bmatrix} F_y \\ M_y \\ 0 \end{bmatrix} \tag{2}$$

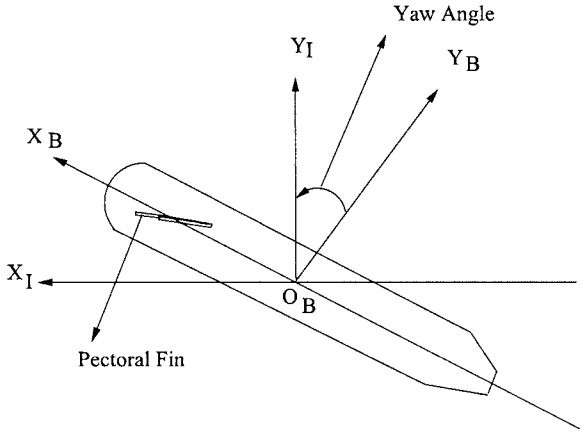

Fig. 1 Model of the underwater vehicle with the pectoral fins

Defining the state vector $x=(v, r, \psi)^T \in R^3$, solving Eq. (2), one obtains a state variable representation of the form

$$\dot{x} = Ax + B_v\begin{bmatrix} F_y \\ M_y \end{bmatrix}$$

$$y = [0,0,1]x \tag{3}$$

for appropriate matrices $A \in R^{3\times 3}$ and $B_v \in R^{3\times 2}$, where y (heading angle) is the controlled output variable.

We are interested in developing (i) an optimal control system for the heading angle regulation to given set points and (ii) an inverse controller for tracking time-varying reference trajectories, $y_r(t)$.

3 Parametrization Based on CFD and Discrete State Variable Representation

It is assumed that the BAUV model has one pair of pectoral fins that are arranged symmetrically around the body of the AUV. Figure 1 shows a schematic of a typical AUV. Each fin is assumed to undergo a combined sway-yaw motion described as follows:

$$s(t) = s_1 \sin(\omega_f t)$$

$$\theta(t) = \beta + \theta_1 \sin(\omega_f t + \nu_1) \tag{4}$$

where s and θ correspond to the sway and yaw angle of the oscillating fin, respectively. The swaying is assumed to occur about the center-chord location. Furthermore, w_f, s_1, and θ_1 are the frequency and amplitudes of oscillations, β is yaw bias angle, and ν_1 is the phase difference between the yawing and swaying motions.

As a result of this flapping motion, each fin experiences a time-varying hydrodynamic force that can be resolved into a sway force component f_y and yawing moment m_y. The pectoral fin can be suitably attached to the vehicle to produce rolling and yawing moments on the BAUV, which affect its dynamics. However, since yaw-plane dynamics and maneuvering is assumed to be affected by the sway force and yawing moment only, we limit our discussion to these components.

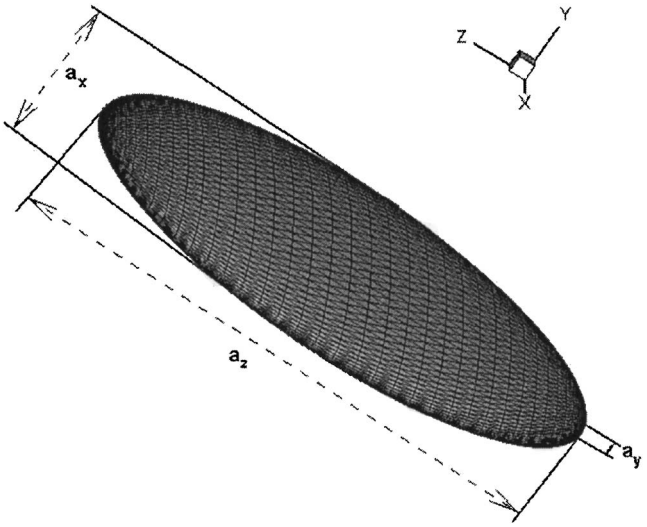

Fig. 2 A thin ellipsoidal foil defined in terms of a surface mesh with triangular elements

Since $f_y(t)$ and $m_y(t)$ produced by each fin are periodic functions, they can be represented by the Fourier series

$$f_y = \sum_{n=0}^{N} [f_n^s \sin(nw_f t) + f_n^c \cos(nw_f t)]$$
$$m_y = \sum_{n=0}^{N} [m_n^s \sin(nw_f t) + m_n^c \cos(nw_f t)] \quad (5)$$

where it is assumed that the fins produce dominant N harmonically related components and the harmonics of higher frequencies are negligible. The Fourier coefficients f_n^a and m_n^a, $a \in \{s,c\}$, capture the characteristics of the time-varying signals $f_y(t)$ and $m_y(t)$. Parametrization of these coefficients is therefore needed in order to complete the equations that govern the motion of the BAUV in the yaw plane.

3.1 CFD Based Parametrization. A finite-difference-based, Cartesian grid immersed boundary solver [22] has been used to simulate the flow past flapping foils in the current study. The key feature of this method is that simulations with complex moving bodies can be carried out on stationary nonbody conformal Cartesian grids, and this eliminates the need for complicated remeshing algorithms that are usually employed with conventional Lagrangian body-conformal methods. The Eulerian form of the incompressible Navier-Stokes equations is discretized on a Cartesian mesh and boundary conditions on the immersed boundary are imposed through a "ghost-cell" procedure [19]. The method employs a second-order center-difference scheme in space and a second-order accurate fractional-step method for time advancement. The code employs the large-eddy simulation (LES) approach in order to account for the effect of the small subgrid flow scales on the large resolved scales. A Lagrangian dynamic model [27] is used to estimate the subgrid-scale eddy viscosity. The details of the numerical method and validation of the code can be found in [28].

Thin ellipsoidal foils are employed in the current study. The geometry of the foil is defined by its three major axes denoted by a_x, a_y, and a_z, as shown in Fig. 2. The surface of the foil is represented by a fine, unstructured mesh with triangular elements. Note that the foil is oriented with the x-axis along the streamwise direction and the z-axis along the spanwise direction. Furthermore, a_x is also the chord of the foil, which in these simulations is set equal to unity, and a_y is the foil thickness. The ratio a_y/a_x and a_z/a_x in the current study is equal to 0.12 and 2.0, respectively. In addition to these foil geometric parameters, the following are the other key nondimensional parameters in the current study: Reynolds number $\mathrm{Re}=U_\infty a_x/\nu$; normalized sway amplitude s_1/a_x, yaw-bias angle β, yaw amplitude θ_1, phase advance of yawing over swaying ν_1, and Strouhal number based on the wake thickness $St=s_1\omega_f/U_\infty\pi$. In the current simulations, Reynolds number, s_1/a_x, ψ_1, ν_1, and St are fixed at value equal to 1000, 0.5, 30 deg, 90 deg, and 0.6, respectively. The yaw-bias angle, β which is the main control parameter, is varied from 0 deg to 20 deg. A nonuniform $177\times129\times105$ Cartesian mesh is employed in the simulations where the grid is clustered in the region around the flapping foil and in the foil wake. The size of computational domain as well as the number of grids have been chosen so as to ensure the simulation accuracy.

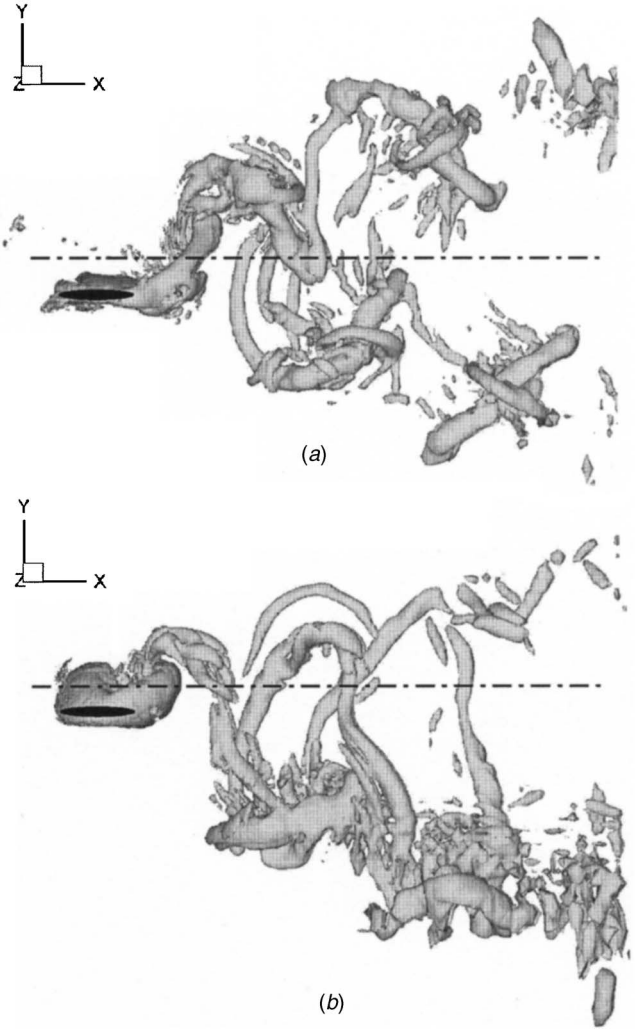

Fig. 3 Side view of wake structures for flow past the flapping foil with two yaw-bias angles: (*a*) bias angle 0 deg and (*b*) bias angle 20 deg

In the current study, the sway force coefficient and moment coefficient are defined as

$$C_Y = \frac{f_y}{\frac{1}{2}\rho U_\infty^2 A_{\mathrm{plan}}}$$
$$C_M = \frac{m_y}{\frac{1}{2}\rho U_\infty^2 A_{\mathrm{plan}} a_x} \quad (6)$$

where f_y and m_y are the sway force and yawing moment, respectively, and A_{plan} is the projected area of the foil which is equal to

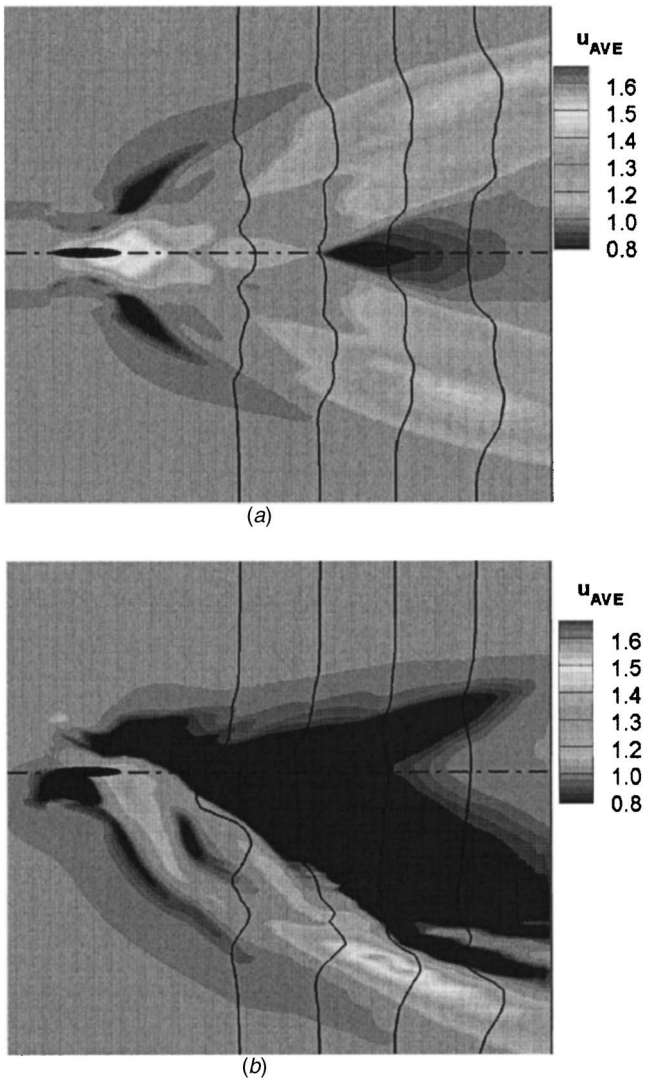

Fig. 4 Center-plane time-averaged streamwise velocity contours for flow past the flapping foil with two yaw-bias angles. Black lines are the streamwise velocity profiles: (*a*) bias angle 0 deg and (*b*) bias angle 20 deg

$(\pi/4)a_x a_z$ for the ellipsoidal foils. Forces and moments are calculated by directly integrating the computed pressure and shear stress on the foil surface.

The side views of wake topologies of a yawing-swaying flapping foil with different yaw bias angles, $\beta=0$ deg and 20 deg, are shown in Fig. 3. The isosurfaces of the eigenvalue imaginary part of the velocity gradient tensor of the flow are plotted in order to clearly show the vortex topology [30]. The key feature observed in Fig. 3(*a*) is the presence of two sets of interconnected vortex loops that slowly convert into vortex rings as they convect downstream in the case of $\beta=0$ deg. The jets formed by these two set of rings contribute equally to the thrust production of the flapping foil, and zero mean sway force is expected. As seen in Fig. 3(*b*), when yaw-bias angle increases, one of those two sets of vortex rings becomes weaker and the other one grows. This asymmetry is associated with the production of a mean sway-force on the fin. Figure 4 shows the time-averaged streamwise velocity contours for both of these cases. For the $\beta=0$ deg foil, two oblique jets with equal strength are observed. As yaw-bias angle increases, the lower jet becomes stronger while the upper jet essentially disappears. As a result of this, the sway force is modified significantly. Table 1 shows the changes in the mean sway force coefficients

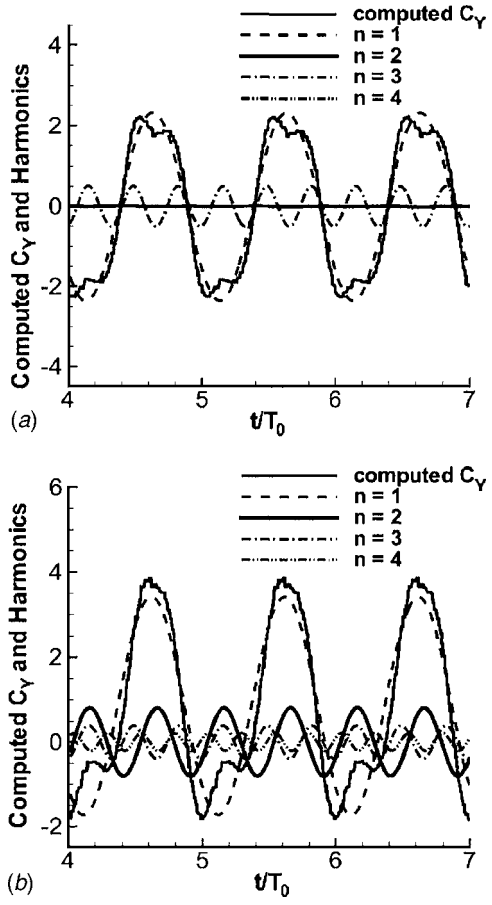

Fig. 5 Harmonic components of the force for two yaw-bias angles: (*a*) bias angle 0 deg and (*b*) bias angle 20 deg

and the mean yawing moment coefficients for different bias angles. It can be seen that small changes in the yaw-bias angle can produce large changes in the mean sway force as well as the yawing moment. This clearly suggests that the yaw-bias angle is an effective control parameter for precise maneuvering.

We assume that the bias-angle (control input) β is varied at discrete intervals and the remaining oscillation parameters are kept constant. The current simulations (Table 1) indicates that the sway force and yawing moment are nearly linear with yawing-bias angle β over a large range of this parameter. Similar variation in mean lateral force with bias angle has been noted in experiments [13,14] and simulations of two-dimensional (2D) pitching-heaving foils [29].

Expanding the fin force and moment of each fin in a Taylor series about $\beta=0$ gives

$$f_y(t,\beta) = f_y(t,0) + \frac{\partial f_y}{\partial \beta}(t,0)\beta + O(\beta^2)$$

$$m_y(t,\beta) = m_y(t,0) + \frac{\partial m_y}{\partial \beta}(t,0)\beta + O(\beta^2) \tag{7}$$

where $O(\beta^2)$ denotes higher-order terms. We assume here that for a fixed $\beta \in R$, $f_y(t+T_0,\beta)=f_y(t,\beta)$ and $m_y(t+T_0,\beta)=m_y(t,\beta)$, t

Table 1 C_Y and C_M for different yaw-bias angles

Yaw-bias angle (deg)	C_Y	C_M
0	0.00	0.00
10	1.52	−0.14
20	2.74	−0.26

Table 2 Table showing various components of force and moment coefficient for the $\beta_y=0$ deg case

n	f_n^c	f_n^s	m_n^c	m_n^s
0	0.00	0.00	0.00	0.00
1	−5.62	−5.16	0.90	1.11
2	0.08	−0.05	−0.01	0.00
3	−1.31	0.8	−0.17	0.00
4	0.09	−0.02	−0.01	0.01

>0 (T_0 denotes the fundamental period). Then, the partial derivatives of f_y and m_y with respect to β are also periodic functions of time. Using Eq. (7), one can approximately express f_y and m_y as

$$f_y = \sum_{n=0}^{N} f_n^s(0)\sin nw_f t + f_n^c(0)\cos nw_f t + \sum_{n=0}^{N}\left[\frac{\partial f_n^s}{\partial\beta}(0)\sin nw_f t + \frac{\partial f_n^c}{\partial\beta}(0)\cos nw_f t\right]\beta$$

$$m_y = \sum_{n=0}^{N} m_n^s(0)\sin nw_f t + m_n^c(0)\cos nw_f t + \sum_{n=0}^{N}\left[\frac{\partial m_n^s}{\partial\beta}(0)\sin nw_f t + \frac{\partial m_n^c}{\partial\beta}(0)\cos nw_f t\right]\beta \tag{8}$$

where $O(\beta^2)$ terms are ignored in the series expansion.

Thus, we get

$$f_y(t) = \phi^T(f_a + \beta f_b)$$

$$m_y(t) = \phi^T(m_a + \beta m_b) \tag{9}$$

$$\phi = [1 \ \sin w_f t \ \ldots \ \sin Nw_f t \ \cos Nw_f t]^T$$

where $f_a, f_b, m_a, m_b \in R^{2N+1}$ and can be obtained from Eq. (8).

Thus, in order to complete the equations that govern the motion of the BAUV in the yaw plane, the Fourier components of the force are needed. Figure 5 shows the dimensionless time variation of computed mean sway force coefficient and its harmonic components for yaw bias angles of 0 deg and 20 deg, respectively. Note the even modes ($n=2,4$) for the zero bias angle have negligible contribution to the fin force. It is also seen that fin force of larger magnitude is obtained when the bias angle is increased. Furthermore, the amplitudes of higher harmonics diminish as n increases. Tables 2 and 3 show both the force and moment Fourier coefficients for the yaw bias of 0 deg and 20 deg for different harmonics (see Eq. (8)). It is seen from the tables that the Fourier coefficients of the fourth harmonic are quite small compared to the coefficients of the first harmonic. As such, even four harmonic components are sufficient to capture most of the characteristics of the time-varying signals $f_y(t)$ and $m_y(t)$.

3.2 Discrete Time State Variable Representation. The vehicle has two attached fins; therefore, the net force and moment

Table 3 Table showing various components of force and moment coefficient for the $\beta_y=20$ deg case

n	f_n^c	f_n^s	m_n^c	m_n^s
0	2.74	0.00	−0.26	0.00
1	−6.75	−4.98	0.75	0.65
2	−0.68	2.54	0.01	−0.14
3	−1.1	0.63	−0.13	0.04
4	0.15	0.14	−0.03	0.04

are $F_y=2f_y$ and $M_y=2(d_{cgf}f_y+m_y)$, where d_{cgf} is the moment arm due to the fin location (positive forward). Using Eq. (9), the yaw-plane dynamics Eq. (3) can be written as

$$\dot{x} = Ax + B\Phi(t)f_c + B\Phi(t)f_v\beta \tag{10}$$

where $B[f_y, m_y]^T = B_v[F_y, M_y]^T$, $f_c = (f_a^T, m_a^T)^T \in R^{4N+2}$, and $f_v = (f_b^T, m_b^T)^T \in R^{4N+2}$ where

$$\Phi(t) = \begin{bmatrix} \phi^T(t) & 0 \\ 0 & \phi^T(t) \end{bmatrix} \tag{11}$$

For the purpose of control, the bias angle is changed at a discrete interval of T^*, where T^* is an integer multiple of the period T_0, i.e., $T^*=n_0T_0$, where n_0 is a positive integer. This way one switches the bias angle at an uniform rate of T^* seconds at the end of n_0 cycles. For the derivation of the control law, the transients introduced due to changes in the bias-angle are ignored. Since the bias angle switches at discrete intervals, it will be convenient to express the continuous-time system Eq. (10) as a discrete-time system. The function $\beta(t)$ now has piecewise constant values β_k for $t \in [kT^*, (k+1)T^*), k=0,1,2\ldots$.

Discretizing the state equation (10), one obtains a discrete-time representation of the form

$$x[(k+1)T^*] \doteq A_d x(kT^*) + B_d\beta_k + d \tag{12}$$

where $A_d=e^{AT^*}$, $B_0=\int_0^{T^*} e^{As}B\Phi(-s)ds$, $B_d=B_0f_v \in R^3$, and $d=B_0f_c \in R^3$.

The output variable (ψ) is

$$y(kT^*) = [0\ 0\ 1]x(kT^*) \doteq C_d x(kT^*) \tag{13}$$

4 Optimal Yaw-Plane Control

In this section, the design of an optimal feedback yaw-plane control law for the regulation of the yaw angle is considered. For the precise yaw control, it is desirable to include a feedback term in the control law that is proportional to the integral of the yaw tracking error. For this purpose, a new state variable x_s is introduced that satisfies

$$x_s[(k+1)T^*] = \psi^* - y(kT^*) + x_s(kT^*) \tag{14}$$

where ψ^*, a constant, is the desired yaw angle and $\psi^*-y(kT^*)$ is the tracking error.

Defining the state vector $x_a=(x^T, x_s)^T \in R^4$ and using Eqs. (12) and (14), the augmented system takes the form

$$x_a[(k+1)T^*] = \begin{bmatrix} A_d & 0 \\ -C_d & 1 \end{bmatrix}\begin{bmatrix} x(kT^*) \\ x_s(kT^*) \end{bmatrix} + \begin{bmatrix} B_d \\ 0 \end{bmatrix}\beta_k + \begin{bmatrix} d \\ \psi^* \end{bmatrix} \doteq A_a x_a(kT^*) + B_a\beta_k + d_a \tag{15}$$

where the constant matrices A_a, B_a, and d_a are defined in Eq. (15).

The control of the system, Eq. (15) can be accomplished by following the servomechanism design approach [34] in which d_a is treated as a constant disturbance input. The design is completed by computing a feedback control law of the form

$$\beta(kT^*) = -\mathbf{K}x_a(kT^*), k=0,1,2,\ldots \tag{16}$$

where $\mathbf{K}$ is a constant row vector such that the closed-loop matrix

$$A_c = (A_a - B_a\mathbf{K})$$

is stable. It is well known that one can assign the eigenvalues of A_c arbitrarily if (A_a, B_a) is controllable [35,36]. For the discrete-time system, this implies that one must choose $\mathbf{K}$ such that the eigenvalues of A_c are strictly within the unit disk in the complex plane.

In this study, an appropriate value of $\mathbf{K}$ is obtained by using the linear quadratic optimal control theory [35]. For this, one chooses a performance index of the form

$$J_o = \sum_{k=0}^{\infty} x_a^T(kT^*) Q x_a(kT^*) + \beta_k^2 \mu \tag{17}$$

where Q is a positive definite symmetric matrix and $\mu > 0$. The weighting matrix Q associated with x_a and the parameter μ penalizing the level of the bias angle are chosen to provide a trade-off between the convergence rate of the state variables to the equilibrium point and the bias angle magnitude.

The optimal control law is obtained by minimizing J_o for the system

$$x_a[(k+1)T^*] = A_a x(kT^*) + B_a \beta_k \tag{18}$$

which is obtained from Eq. (15) by setting $d_a = 0$. The feedback matrix K is obtained by solving the discrete Riccati equation [35]

$$P = Q + A_a^T P A_a - A_a^T P B_a (\mu + B_a^T P B_a) B_a^T P A_a \tag{19}$$

and then setting the feedback matrix as

$$K = -(\mu + B_a^T P B_a)^{-1} B_a^T P A_a \tag{20}$$

Using the feedback law Eq. (16), the yaw angle can be regulated to prescribed constant values ψ^*, but the BAUV cannot follow time-varying yaw angle trajectories. In Sec. (6), an inverse control law is derived for the tracking of time-varying trajectories.

5 Inverse Control System

The transfer function relating the output $y(kT^*)$ and the input β_k of Eq. (12) (assuming that $d=0$) is given by

$$\frac{\hat{y}(z)}{\hat{\beta}(z)} = G(z) = C_d(zI - A_d)^{-1} B_d = k_p \frac{(z+\mu_1)(z+\mu_2)}{z^3 + a_2 z^2 + a_1 z + a_0} \tag{21}$$

where z denotes the Z-transform variable, $\mu_i (i=1,2)$ are real or complex numbers, and k_p and $a_i (i=0,1,2)$ are real numbers. It is assumed that the pectoral fins are attached between the cg and the nose of the vehicle. For the AUV model under consideration, the number of unstable zeros (i.e., the zeros outside the unit disk in the complex plane) depend on the distance (d_{cgf}) of the pectoral fins from the cg, ω_f, and the sampling time T^*. It has been found that for the values of interest of the oscillation frequencies and the attachment point (d_{cgf}) of the fins, there exists a single unstable zero (i.e., the transfer function is nonminimum phase).

It is well known that the inverse control design can be accomplished only when the system is minimum phase (i.e., the zeros of the transfer function are stable). For this purpose, the original transfer function is simplified by ignoring its unstable zero. Let us assume that $\mu_1 > 1$ and $\mu_2 < 1$. For obtaining a minimum phase approximate system, one removes the unstable zero of $G(z)$ but retains the zero frequency (dc) gain. Thus the approximate transfer function $G_a(z)$ obtained from Eq. (21) takes the form

$$G_a(z) = k_p \frac{(1+\mu_1)(z+\mu_2)}{\Delta(z)} \tag{22}$$

where $\Delta(z) = det(zI - A_d)$.

We are interested in deriving a new controlled output variable y_a such that

$$y_a(kT^*) = C_a x(kT^*) \tag{23}$$

$$\frac{\hat{y}_a(z)}{\hat{\beta}(z)} = G_a(z) = C_a(zI_n - A_d)^{-1} B_d \tag{24}$$

where C_a is a new output matrix. Since the relative degree of $G_a(z)$ is 2, one has

$$C_a B_d = 0$$

$$C_a A_d B_d \neq 0 \tag{25}$$

Using the Leverrier algorithm, the approximate transfer function $G_a(z)$ can be expanded as [35]

$$G_a(z) = \Delta^{-1}(z)[(z+a_2) C_a A_d B_d + C_a A_d^2 B_d] \tag{26}$$

Comparing Eqs. (21) and (25), one can easily show that

$$C_a[B_d \; A_d B_d \; A_d^2 B_d + a_2 A_d B_d] = [0 \; K_p(1+\mu_1) \; K_p(1+\mu_1)\mu_2] \tag{27}$$

Solving Eq. (27), one obtains the modified output matrix.

For the modified system, one has

$$x[(k+1)T^*] = A_d x(kT^*) + B_d \beta_k + d$$
$$y_a(kT^*) = C_a x(kT^*) \tag{28}$$

Suppose a reference trajectory $y_r(kT^*)$ is given that is to be tracked by $y_a(kT^*)$. Using Eq. (28), one has that

$$y_a[(k+1)T^*] = C_a A_d x(kT^*) + C_a d$$
$$y_a[(k+2)T^*] = C_a A_d^2 x(kT^*) + \sum_{i=0}^{1} C_a A_d^i d + C_a A_d^{(r-1)} B_d \beta_k \tag{29}$$

In view of Eq. (29), for following the reference trajectory $y_r(kT^*)$, we choose the control input β_k as

$$\beta_k = (C_a A_d B_d)^{-1} \left[-C_a A_d^2 x(kT^*) - \sum_{i=0}^{1} C_a A_d^i d + v_k \right] \tag{30}$$

where the signal v_k is selected as

$$v_k = y_r[(k+2)T^*] - p_1\{C_a A_d x(kT^*) + C_a d - Y_r[(k+1)T^*]\} + p_0[Y_a(kT^*) - Y_r(kT^*)] \tag{31}$$

where p_0 and p_1 are real numbers.

Defining the tracking error $e(kT^*) = y_a(kT^*) - y_r(kT^*)$ and using the control law Eqs. (30) and (31) in Eq. (29) gives

$$e[(k+2)T^*] + p_1 e[(k+1)T^*] + p_0 e(kT^*) = 0 \tag{32}$$

The tracking error equation (32) satisfies a second-order difference equation. The characteristic polynomial associated with Eq. (32) is

$$(z^2 + p_1 z + p_0) = 0 \tag{33}$$

The parameters p_i are chosen such that the roots of Eq. (33) are strictly within the unit disk. Then it follows that for any initial condition $x(0), e(kT^*) \to 0$ as $k \to \infty$ and the controlled output $y_a(kT^*)$ asymptotically converges to the reference sequence $y_r(kT^*)$. In Sec. 6, it will be seen that the inverse controller designed based on the approximate transfer function accomplishes accurate yaw angle trajectory control. This completes the inverse controller design.

6 Simulation Results for Yaw Maneuvers

In this section, simulation results using the MATLAB/SIMULINK software is presented. The performance of the optimal and inverse controllers for different values of frequencies of oscillation of the pectoral fin and for different points of attachment of the fins to the BAUV (d_{cgf}) from the center of gravity of the AUV is examined.

The parameters of the model are taken from [33]. The AUV is assumed to move with a constant forward velocity of 0.7 m/s with the help of a control mechanism. The vehicle parameters are $l = 1.391$ m, mass $= 18.826$ kg, $I_z = 1.77$ kgm^2, $X_G = -0.012$, $Y_G = 0$. The hydrodynamic parameters for a forward velocity of 0.7 m/s derived from [33] are $Y_{\dot{r}} = -0.3781$, $Y_{\dot{v}} = -5.6198$, $Y_r = 1.1694$, $Y_v = -12.0868$, $N_{\dot{r}} = -0.3781$, $N_{\dot{v}} = -0.8967$, $N_r = -1.0186$, and $N_v = -4.9587$.

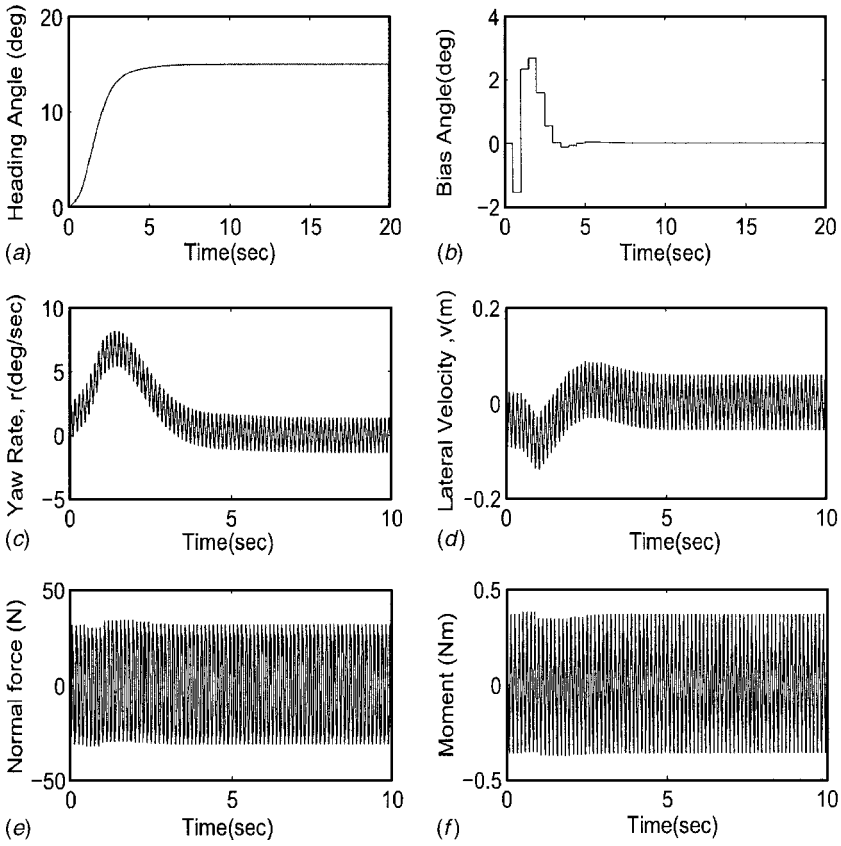

Fig. 6 Optimal control: Frequency of flapping=8 Hz, d_{cgf}=0 m for ψ^*=15 deg: (*a*) heading angle, ψ (deg); (*b*) bias angle (control input), β (deg); (*c*) yaw rate, *r* (deg/s); (*d*) lateral velocity, *v* (m/s); (*e*) lateral force, F_y (N); and (*f*) side moment, M_y (Nm)

Experimental results indicate that for zero bias angle, the mean values of f_y and m_y are nearly zero. Therefore, the vectors f_a, f_b, m_a, and m_b are found to be

$$f_a = (0, -40.0893, -43.6632, -0.3885, 0.6215, 6.2154, -10.17, -0.1554, 0.6992)$$

$$f_b = (68.9975, 0.4451, -16.4704, 64.1009, -19.5864, -0.8903, -2.2257, 2.2257, 4.8966)$$

$$m_a = (0.0054, 0.6037, 0.4895, 0, -0.0054, 0, -0.0925, 0, -0.0054)$$

$$m_b = (-0.5297, -0.3739, -0.0935, -0.2493, 0.1246, 0.0312, -0.0312, 0.0935, 0)$$

It is pointed out that these parameters are obtained from the force and moment Fourier coefficients and are computed by multiplying the Fourier coefficients by $(1/2)\rho . W_a . U_\infty^2$ and $(1/2)\rho . W_a . \text{chord} . U_\infty^2$, respectively, where W_a is the surface area of the foil. For simulation, the initial conditions of the vehicle are assumed to be $x(0)=0$ and $x_s(0)=0$.

6.1 Optimal Yaw-Plane Control. In this section, the feedback discrete control law Eq. (16) is simulated. The bias angle is changed to a new value every $T^*=n_0T_0$ seconds where $T_0=1/f_0$ is the fundamental period of f_p and m_p. Choosing a small value of n_0 increases the transients produced due to switching. Parametrization of these transients is quite difficult since they introduce a number of additional parameters into the problem. On the other hand, a large value of n_0 increases the magnitude of the intersample oscillations, which is also not desirable.

The terminal state is chosen as $x^*=(0,0,15)^T$ with $\psi^*=15$ deg. Thus, one desires to control the BAUV to a heading angle of 15 deg. For optimal control design, the weighting matrix and parameter are selected as $Q=1000I_{4\times4}$ and $\mu=1.5$. Simulation results are provided for fin frequencies of 8 Hz and 6 Hz.

Case 1. Optimal Control: Frequency of Fin Oscillation 8 *Hz*, $d_{cgf}=0$ *and* $d_{cgf}=0.15$ (m). First simulation is done for the higher frequency of 8 Hz and the fin attachment point is chosen such that $d_{cgf}=0$. Note that with this value of d_{cgf}, the sway force itself does not produce any yawing moment on the BAUV. The control law is updated every four cycles, i.e., $T^*=4T_0=0.5$ s. The value of $n_0=4$ is found to be an appropriate compromise between minimizing transients and intersample oscillations. The transfer function $G(z)$ has a stable zero at 0.0965 and an unstable zero at −1.5548. As such $G(z)$ is minimum phase. Figure 6 shows the simulated results. It can be seen that the optimal controller achieves accurate heading angle control to the target set point in ~5 s. The control input (bias angle) magnitude required is <3 deg, which is small and can easily be provided by the pectoral fins. The plots of the lateral force and moment produced by the fins are also provided in the figure. In the steady state, the lateral fin force and moment exhibit bounded periodic oscillations. The intersample yaw angle shows oscillations of tiny amplitude, however, in the terminal phase, the sample values of yaw angle is equal to the commanded value ψ^*.

Simulation results for the same frequency, but for a d_{cgf} value of 0.15 m are also presented (Fig. 7). Note that with a nonzero value of d_{cgf}, the sway force also produces additional yawing

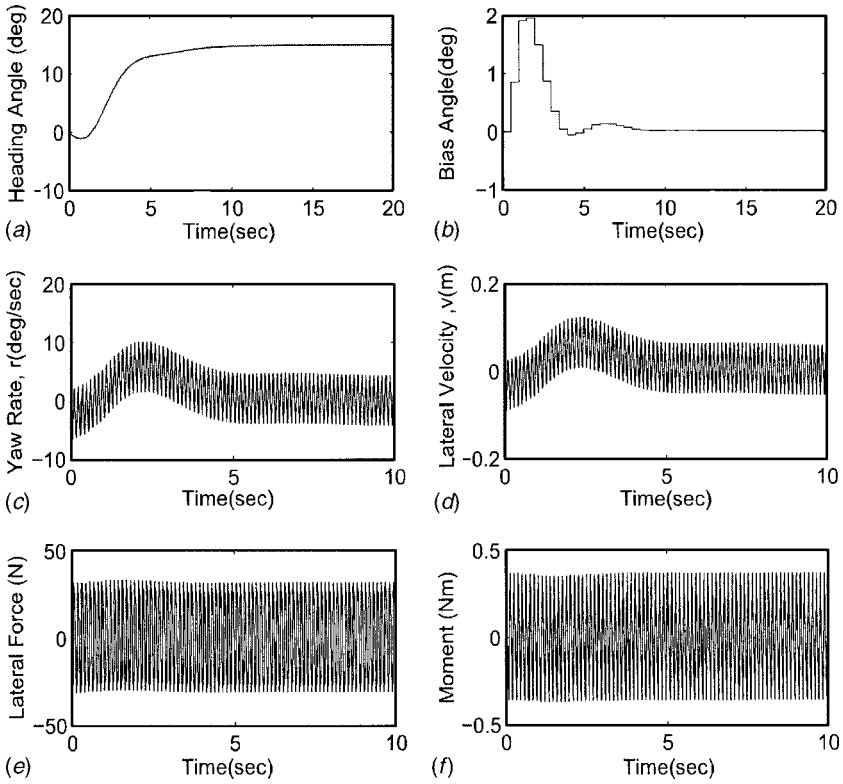

Fig. 7 Optimal control: Frequency of flapping=8 Hz, d_{cgf}=0.15 m for ψ^*=15 deg: (*a*) heading angle, ψ (deg); (*b*) bias angle (Control input), β (deg); (*c*) yaw rate, *r* (deg/s); (*d*) lateral velocity, *v* (m/s); (*e*) lateral force, F_y (N); and (*f*) side moment, M_y (Nm)

moment on the BAUV. Unlike the previous case, the zeros of $G(z)$ are now at 1.48 and −0.75. It is seen that the stable zero at 0.0965 of the model for $d_{cgf}=0$ has moved to a lesser stable position at −0.75 in the unit disk for the model with $d_{cgf}=0.15$ m. The transient response for $d_{cgf}=0.15$ m is not as good as in Fig. 6, and the settling time is larger. It is also observed that, initially, the vehicle heading angle swings in the wrong direction, but the target yaw angle is attained in the steadystate.

Case 2. Optimal control: Frequency of Oscillation 6 *Hz*, $d_{cgf}=0$ *and* $d_{cgf}=0.15$ (m). This simulation is done for a lower value of fin frequency of 6 Hz with a d_{cgf} value of 0. The sampling period T^* is still kept equal to $4T_0$, which for this case is equal to 2/3 s. Thus, compared to the case of 8 Hz, the control is updated at a slower rate. The zeros of $G(z)$ are at −1.6813 and 0.0331. The simulation results are shown in Fig. 8. One can observe that the yaw angle control is accomplished; however, intersample oscillations of larger magnitude compared to Fig. 6 are present. This is an expected phenomenon because the bias angle switches after a longer period, but the convergence time of the yaw angle is found to be almost the same. The maximum magnitude of control input required for the maneuver is also larger, and the sway force and moment were found to be less than 60 N and 1 Nm, respectively.

Simulation for a d_{cgf} value of 0.15 m was also performed at this frequency, and the results are shown in Fig. 9. In this case, it is found that the zeros (1.7138, −0.7058) of $G(z)$ have moved away from the origin compared to the model for $d_{cgf}=0$. It is observed that although the heading angle is controlled, the magnitude of the intersample oscillations has increased.

6.2 Inverse Yaw-Plane Control. For the tracking of time-varying reference trajectories, the designed inverse control system is suitable. In this subsection, simulation results for sinusoidal heading angle trajectory tracking for different fin-flapping frequencies are presented. Smooth sinusoidal reference trajectories are generated by command generators of the form

$$(E^3 + p_{c2}E^2 + p_{c1}E + p_{c0})y_r(kT^*) = (1 + p_{c0} + p_{c1} + p_{c2}) \times d^* \sin(w_r kT^*)$$

where E denotes the advance operator $(Ey_r(kT^*)=y_r[(k+1)T^*]$ and d^* is the amplitude of the sine wave and the parameters p_{ci} are chosen to be zero so that the poles of the command generator are at $z=0$. The reference trajectory generator is simulated using its state variable form with states $x_r=(x_{r1},x_{r2},x_{r3})^T$. For the simulation, $d^*=15$ deg and $w_r=0.2$ rad/s.

Simulation results for fin frequencies of 8 Hz and 6 Hz are presented in the following subsection.

Case 3. Inverse control: Frequency of Oscillation 8 *Hz*, $d_{cgf}=0$ *and* $d_{cgf}=0.15$ (m). Figure 10 shows the inverse controller performance for a $d_{cgf}=0$. The sampling period is $4T^*=1/2$. It can be observed that smooth heading angle trajectory control is achieved. One can observe that the modified output equals the reference trajectory at all sample instants. The maximum control input (bias angle) required is ~3 deg. The lateral force and moment produced by the fins are less than 40 N and 0.4 Nm, respectively. As expected, the yaw rate and the lateral velocity are sinusoidal.

Simulation are also done for $d_{cgf}=0.15$ m. The plots are shown in Fig. 11. Although the heading angle tries to follow the command trajectory, in the initial period, the yaw angle trajectory is not smooth and there is a larger tracking error compared to Fig. 10. For $d_{cgf}=0$, the tracking performance is extremely good as seen in Fig. 10. The performance of the inverse controller for time-varying trajectory tracking for nonzero d_{cgf} deteriorates because the zero dynamics (the residual dynamics) for d_{cgf}

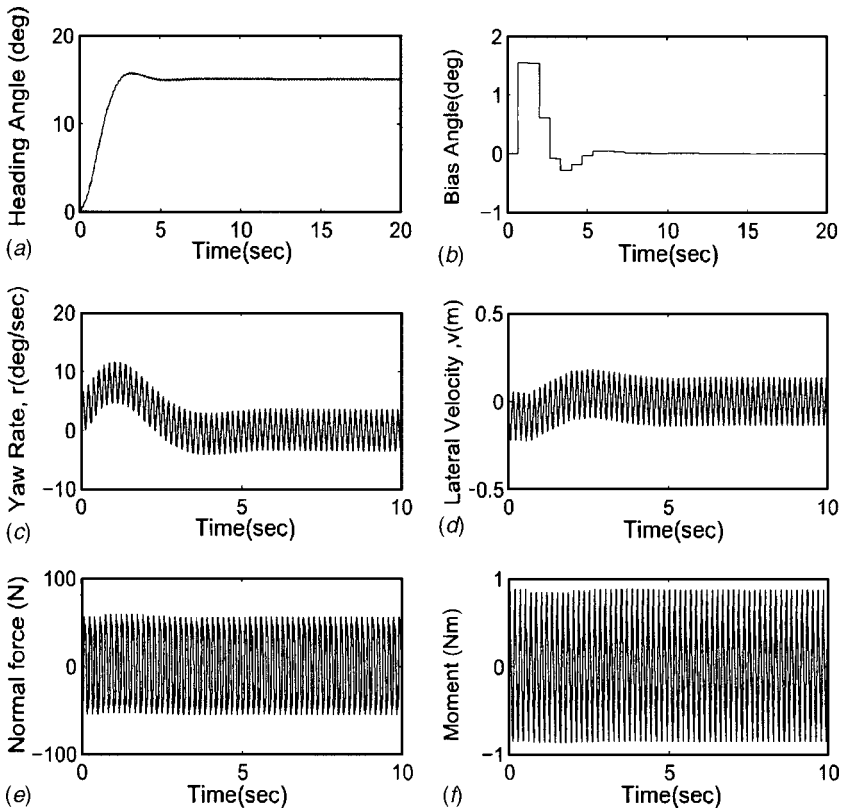

Fig. 8 Optimal control: Frequency of flapping=6 Hz, d_{cgf}=0 m for ψ^*=15 deg: (*a*) heading angle, ψ (deg); (*b*) bias angle (control input), β (deg); (*c*) yaw rate, *r* (deg/s); (*d*) lateral velocity, *v* (m/s); (*e*) lateral force, F_y (N); and (*f*) side moment, M_y (Nm)

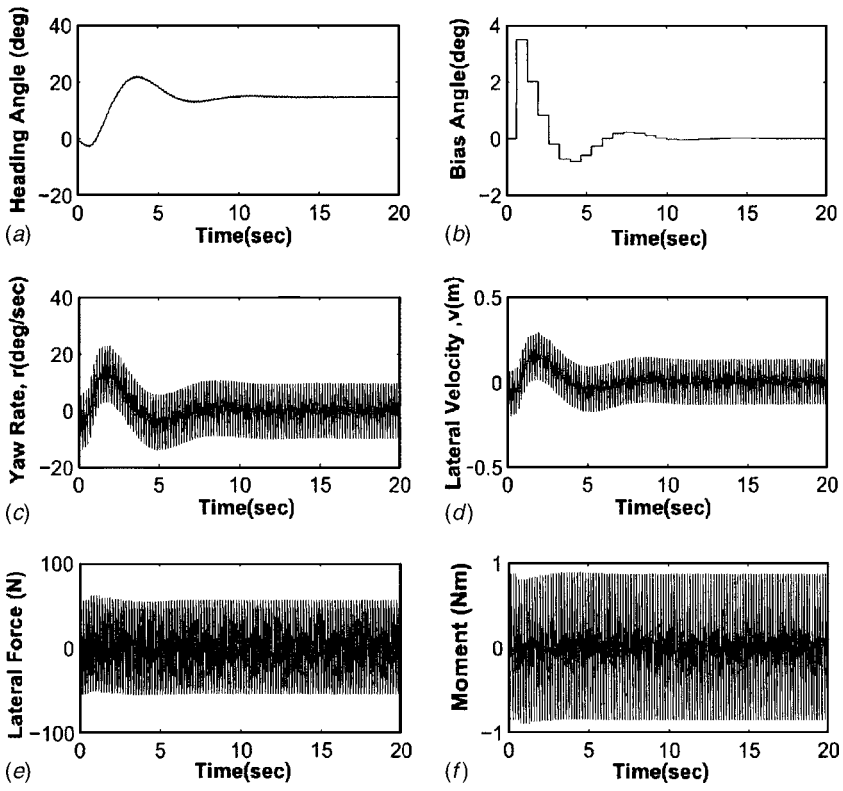

Fig. 9 Optimal control: Frequency of flapping=6 Hz, d_{cgf}=0.15 m for ψ^*=15 deg: (*a*) heading angle, ψ (deg); (*b*) bias angle (control input), β (deg); (*c*) yaw rate, *r* (deg/s); (*d*) lateral velocity, *v* (m/s); (*e*) lateral force, F_y (N); and (*f*) side moment, M_y (Nm)

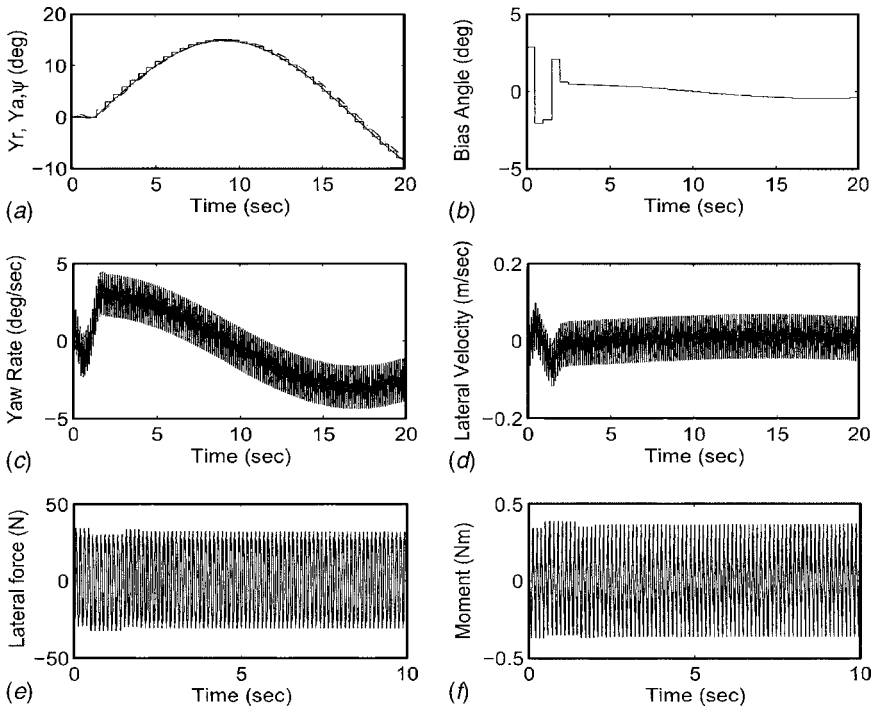

Fig. 10 Inverse control: Frequency of flapping=8 Hz, d_{cgf}=0 m for ψ^*=15 deg: (*a*) reference heading angle, Y_r (staircase); modified heading angle Y_a (broken line); and actual heading angle ψ (solid line) (deg): (*b*) Bias angle (control input), β (deg); (*c*) yaw rate, *r* (deg/s); (*d*) lateral velocity, *v* (m/s); (*e*) lateral force, F_y (N); and (*f*) side moment, M_y (Nm).

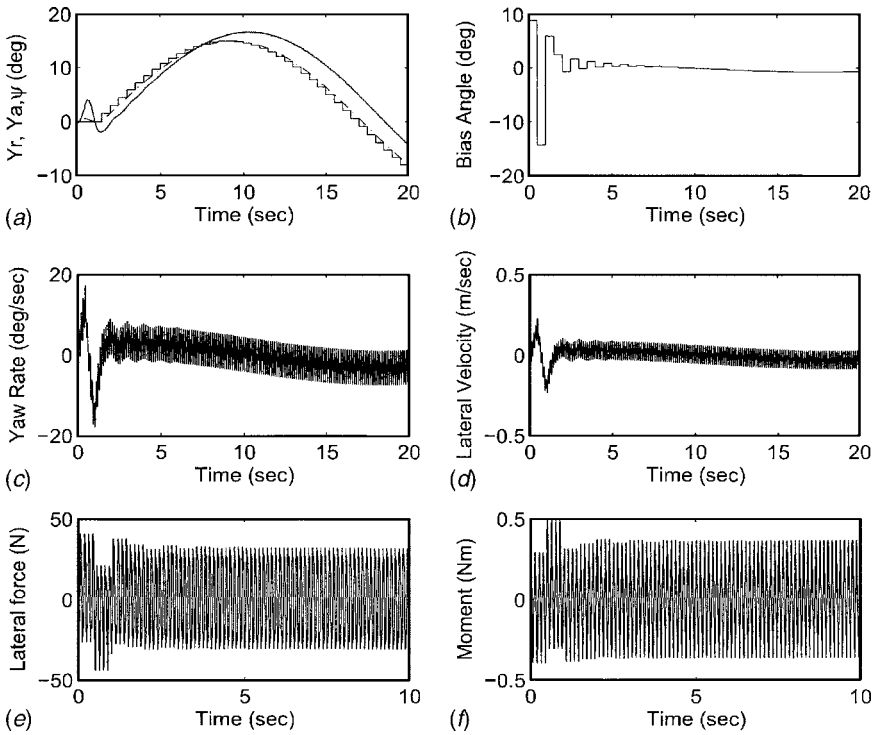

Fig. 11 Inverse control: Frequency of flapping=8 Hz, d_{cgf}=0.15 m for ψ^*=15 deg: (*a*) reference heading angle, Y_r (staircase); modified heading angle, Y_a (broken line); and actual heading angle, ψ (solid line) (deg): (*b*) Bias angle (control input), β (deg); (*c*) yaw rate, *r* (deg/s); (*d*) lateral velocity, *v* (m/s); (*e*) lateral force, F_y (N); and (*f*) side moment, M_y (Nm).

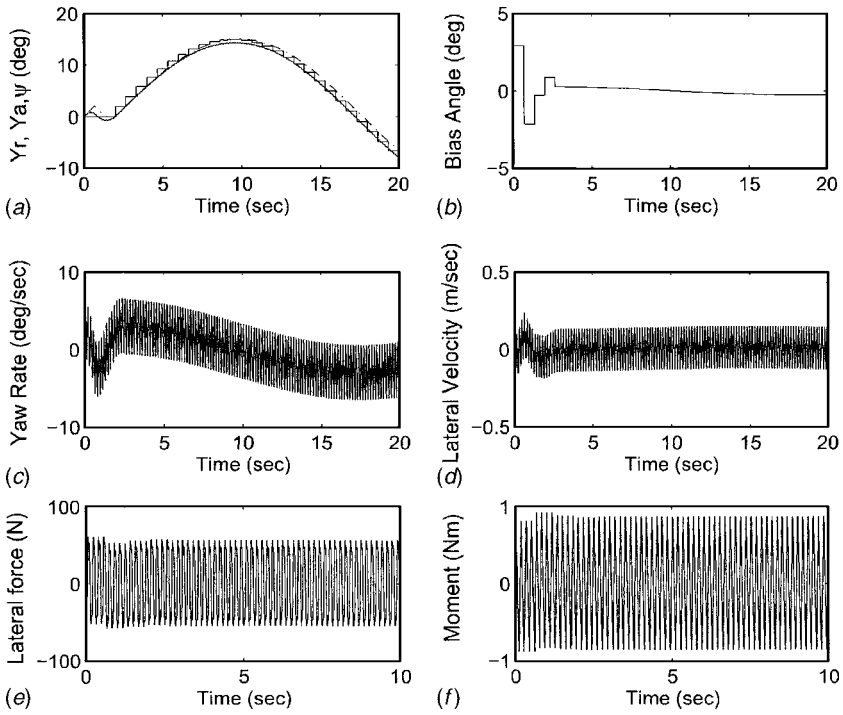

Fig. 12 Inverse control: Frequency of flapping=6 Hz, d_{cgf}=0 m for ψ^*=15 deg: (*a*) reference heading angle, Y_r (staircase); modified heading angle, Y_a (broken line); and actual heading angle, ψ (solid Line) (deg). (*b*) Bias angle (control input), β (deg); (*c*) yaw rate, *r* (deg/s); (*d*) lateral velocity, *v* (m/s); (*e*) lateral force, F_y (N); and (*f*) side moment, M_y (Nm).

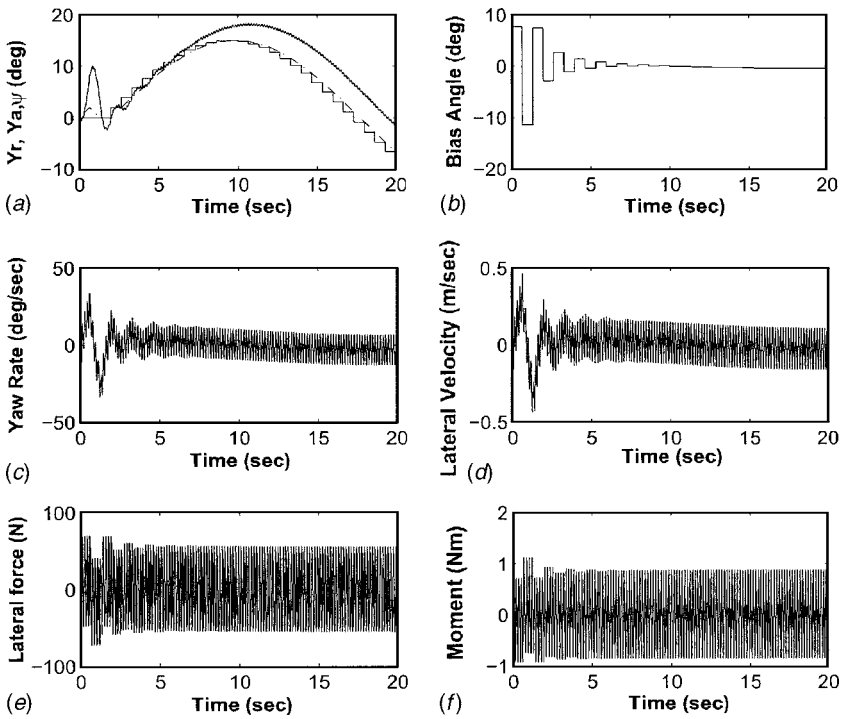

Fig. 13 Inverse control: Frequency of flapping=6 Hz, d_{cgf}=0.15 m for ψ^*=15 deg: (*a*) reference heading angle, Y_r (staircase); modified heading angle, Y_a (broken line); and actual heading angle, ψ (solid line) (deg). (*b*) Bias angle (control input), β (deg); and (*c*) yaw rate, *r* (deg/s); (*d*) lateral velocity, *v* (m/s); (*e*) lateral force, F_y (N); and (*f*) side moment, M_y (Nm).

=0.15 m are relatively less stable compared to the zero dynamics for $d_{cgf}=0$. Note that $G_a(z)$ has a zero at 0.0965 for $d_{cgf}=0$ and at a lesser stable location −0.75 for $d_{cgf}=0.15$ m.

Case 4. Inverse control: Frequency of Oscillation 6 *Hz*, $d_{cgf}=0$ *and* $d_{cgf}=0.15$ (m). The first simulation performed here is for $d_{cgf}=0$ and frequency 6 Hz. The results are shown in Fig. 12. Yaw angle tracking is achieved although intersample oscillations of comparatively large magnitude are observed. The bias angle (control input) required is <3 deg.

Simulation for $d_{cgf}=0.15$ m has also been performed, and results are shown in Fig. 13. In the closed-loop system, approximate yaw angle tracking is accomplished, but larger intersample oscillations appear. Again it is found that the inverse controller designed for $d_{cgf}=0$ performs better compared to the controller designed for $d_{cgf}=0.15$ m precisely due to the reasons indicated in case 3 for the frequency of oscillation 8 Hz.

7 Conclusion

In this paper, optimal as well as inverse yaw-plane control of a biorobotic AUV using pectoral-like fins was considered. For maneuvering the BAUV, the bias angle was treated as control input. CFD and Fourier series expansion were used to parameterize the effect of this control input on the hydrodynamical force and moment produced by the flapping foil. For the purpose of design, a discrete-time model was obtained and a minimum phase representation was derived for controller design. Then an optimum control law for the regulation of the yaw angle to set points and an inverse control law for the trajectory control of the modified output were derived. The bias angle of the flapping foils was updated at discrete intervals (multiple of the fundamental period). In the closed-loop system, the modified output and the actual yaw trajectory were found to be sufficiently close to the desirable heading angle commands. From these results, one concludes that accurate yaw angle control along time-varying paths can be accomplished using oscillating fins with relatively small (<3 deg) overall changes in the bias angle. Furthermore, improved performance of the control system can be obtained when the frequency of oscillation of the fins increases.

This paper provides an interdisciplinary approach, which combines the CFD analysis and control theory, for the design of control systems for BAUVs. But there are several questions remain to be answered in this area. Certainly, the treatment of nonlinearities; sensor and actuator dynamics; noise, wave forces, and parameter uncertainties; etc., is important. The the effect of vortices shed by the body on the fins is yet another interesting problem for future research.

References

[1] Azuma, A., 1992, *The Bio-Kinetics of Flying and Swimming*, Springer-Verlag, Berlin.

[2] Sfakiotakis, M., Lane, D. M., and Davies, J. B. C., 1999, "Review of Fish Swimming Modes for Aquatic Locomotion," IEEE J. Ocean. Eng., **24**(2), pp. 237–253.

[3] Triantafyllou, G. S., and Triantafyllou, M. S., 1995, "An Efficient Swimming Machine," Sci. Am., **272**, pp. 64–70.

[4] Bandyopadhyay, P. R., Castano, J. M., Rice, J. Q., Philips, R. B., Nedderman, W. H., and Macy, W. K., 1997, "Low-Speed Maneuvering Hydrodynamics of Fish and Small Underwater Vehicles," ASME J. Fluids Eng., **119**, pp. 136–144.

[5] Lauder, G. V., and Drucker, E. G., 2004, "Morphology and Experimental Hydrodynamics of Fish Fin Control Surfaces," IEEE J. Ocean. Eng., **29**, pp. 556–571.

[6] Walker, J. A., 2004, "Kinematics and Performance of Maneuvering Control Surfaces in Teleost Fishes," IEEE J. Ocean. Eng., **29**, pp. 572–584.

[7] Triantafyllou, M. S., Techet, A. H., and Hover, F. S., 2004, "Review of Experimental Work in Biomimetic Foils," IEEE J. Ocean. Eng., **29**, pp. 585–594.

[8] Mittal, R., 2004, "Computational Modeling in Biohydrodynamics: Trends, Challenges, and Recent Advances," IEEE J. Ocean. Eng., **29**, pp. 595–604.

[9] Westneat, M. W., Thorsen, D. H., Walker, J. A., and Hale, M. E., 2004, "Structure, Function, and Neural Control of Pectoral Fins in Fishes," IEEE J. Ocean. Eng., **29**, pp. 674–683.

[10] Bandyopadhyay, P. R., Castano, J. M., and Dick, J., 1999, "Biologically-Inspired Bodies Under Surface Waves—Part 1: Load Measurement," ASME J. Fluids Eng., **121**, pp. 469–478.

[11] Bandyopadhyay, P. R., Singh, S. N., and Chockalingam, F., 1999, "Biologically-Inspired Bodies Under Surface Waves—Part 2: Theoretical Control of Maneuvering," ASME J. Fluids Eng., **121**, pp. 479–487.

[12] Bandyopadhyay, P. R., 2002, "Maneuvering Hydrodynamics of Fish and Small Underwater Vehicles," Integr. Comp. Biol., **42**, pp. 102–117.

[13] Triantafyllou, M. S., Techet, A., and Hover, F., 2003, "Review of Experimental Work in Biomimetic Foils," 13th International Symposium on Unmanned Untethered Submersible Technology (UUST), New England Center, Durham, NH.

[14] Martin, C. B., Hover, F. S., and Triantafyllou, M. S., 2001, "Maneuvering Performance of a Rolling and Pitching Wing," 12th International Symposium on Unmanned Untethered Submersible Technology," New England Center, Durham, NH.

[15] Yamamoto, I., Terada, Y., Nagamatu, T., and Imaizumi, Y., 1995, "Propulsion System With Flexible/Rigid Oscillating Fin," IEEE J. Ocean. Eng., **20**(1), pp. 23–30.

[16] Kato, N., 2002, "Pectoral Fin Controllers," *Neurotechnology for Biometric Robots*, MIT Press, Cambridge, MA, pp. 325–350.

[17] Kato, N., 2000, "Performance in the Horizontal Plane of a Fish Robot With Mechanical Pectoral Fins," IEEE J. Ocean. Eng., **25**(1), pp. 121–129.

[18] Mittal, R., Utturkar, Y., and Udaykumar, H. S., 2002, "Computational Modeling and Analysis of Biomimetic Flight Mechanisms," AIAA Paper No. 2002–0865.

[19] Udaykumar, H. S., Mittal, R., Rampunggoon, P., and Khanna, A., 2001, "A Sharp Interface Cartesian Grid Method for Simulating Flows With Complex Moving Boundaries," J. Comput. Phys., **174**, 345–380.

[20] Ye, T., Mittal, R., Udaykumar, H. S., and Shyy, W., 1999, "An Accurate Cartesian Grid Method for Simulation of Viscous Incompressible Flows With Complex Immersed Boundaries," J. Comput. Phys., **156**, 209–240.

[21] Ramamurti, R., Lohner, R., and Sandberg, W., 1996, "Computation of the Unsteady-Flow Past a Tuna With Caudal Fin Oscillation," Adv. Fluid Mech. Series, **9**, pp. 169–178.

[22] Najjar, F. M., Mittal, R., Rampunggoon, P., and Khanna, A., 2003, "Simulations of Complex Flows and Fluid-Structure Interaction Problems on Fixed Cartesian Grids," ASME Paper No. FEDSM2003–45577.

[23] Lee, J. S., Kim, C., and Rho, O. H., 2003, "The Modification of Airfoil Shape for Optimal Aerodynamic Performance on Flapping-Airfoil in Low-Reynolds Number Flow," AIAA Paper No. 2003–421.

[24] Mittal, R., 2004, "Computational Modeling in Bio-Hydrodynamics: Trends, Challenges and Recent Advances," IEEE J. Ocean. Eng., **29**(3), pp. 595–604.

[25] Koochesfahani, M. M., 1987, "Vertical Patterns in the Wake of an Oscillating Airfoil," AIAA 25th Aerospace Sciences Meeting, Reno, AIAA Paper No. 87–0111.

[26] Mittal, R., Akhtar, I., Bozkurttas, M., and Najjar, F. M., 2003, "Towards a Conceptual Model of a Bio-Robotic AUV: Pectoral Fin Hydrodynamics," 13th International Symposium on Unmanned Untethered Submersible Technology, Durham, NH, August.

[27] Meneveau, C., Lund, T. S., and Cabot, W. H., 1996, "A Lagrangian Dynamic Subgrid-Scale Model of Turbulence," J. Fluid Mech., **319**, pp. 353–385.

[28] Bozkurttas, M., Dong, H., Mittal, R., and Najjar, F., 2005, "Towards Numerical Simulation of Flapping Foils on Fixed Cartesian Grids," Reno, NV, January, AIAA Paper No. 2005–0079.

[29] Dong, H., Mittal, R., Bozkurttas, M., and Najjar, F., 2005, "Wake Structure and Performance of Finite Aspect-Ratio Flapping Foils," Reno, NV, January, AIAA Paper No. 2005–0081.

[30] Soria, J., and Cantwell, B. J., 1993, "Identification and Classification of Topological Structures in Free Shear Flows," *Eddy Structure Identification in Free Turbulent Shear Flows*, J. P. Bonnet and M. N. Glauser, eds., pp. 379–390.

[31] Fossen, T. I., 1999, *Guidance and Control of Ocean Vehicles*, Wiley, New York.

[32] Singh, S. N., Simha, A., and Mittal, R., 2004, "Biorobotic AUV Maneuvering by Pectoral Fins: Inverse Control Design Based on CFD Parameterization," IEEE J. Ocean. Eng., **29**(3), pp. 777–785.

[33] Ridley, P., Fontan, J., and Corke, P., 2003, "Submarine Dynamic Modeling," *Australian Conference on Robotics and Automation*, Brisbane, Australia, December.

[34] Davison, E. J., 1976, "The Robust Control of a Servomechanism Problem for Linear Time-Invariant Multivariable Systems," IEEE Trans. Autom. Control, **21**, pp. 25–34.

[35] Phillips, C. L., and Nagle, H. T., 1995, "Digital Control System Analysis and Design," Prentice-Hall, Englewood Cliffs, NJ.

[36] Chen, C. T., 1998, *Linear System Theory and Design*, Oxford University Press, London.

Hot-Wire Measurements Around a Controlled Diffusion Airfoil in an Open-Jet Anechoic Wind Tunnel

Stéphane Moreau
Valeo Motors and Actuators,
78321 La Verrière,
France

Douglas Neal

John Foss

Michigan State University,
East Lansing, MI 48823

The aeroacoustic measurements in the large anechoic wind tunnel of Ecole Centrale de Lyon, which previously focused on the wall pressure distribution and the far-field acoustic pressure, are extended to velocity measurements by hot-wire probes in the nozzle jet and in the vicinity of a Controlled Diffusion airfoil. The present work focuses on the flow conditions corresponding to a Reynolds number based on the airfoil chord length $\mathrm{Re}_c = 1.6 \times 10^5$ *and a geometric angle of attack* α_g *of 8°. Midspan measurements were achieved at the exit plane of the wind tunnel nozzle upstream of the test airfoil and in a large eddy simulation domain that was embedded in the potential core around the airfoil mockup. The inlet measurements by a single hot-wire probe provided insight into the free-stream turbulence intensity upstream of the profile. The X-probe measurements on the upper and lower computational boundaries show the overall deflection of the jet potential core by the cambered airfoil. These are compared to previous Reynolds averaged Navier-Stokes predictions. The X-probe measurements in the airfoil wake provide information on the development of the airfoil boundary layer and the resulting wake after separation. The measured wake velocity defect has been compared with both numerical predictions.* [DOI: 10.1115/1.2201644]

1 Introduction

In recent years, several attempts have been made to simulate the trailing edge noise sources of several aerodynamic bodies (primarily flat plates with various trailing edge geometries and NACA 0012 airfoils at various angles of attack). They mostly relied on large eddy simulations (LES) around these aerodynamic profiles in an unbounded incoming flow [1–10]. For the noise sources, the LES prediction of the wall pressure fluctuations were compared with well-documented experiments in open-jet anechoic wind tunnels [11–14]. Reasonable agreement was found with experimental data (especially compared to existing semiempirical models). However, a detailed comparison shows that even the mean flow field on the airfoil is seldom predicted accurately. This is the case for the wall pressure coefficient in [5] (Fig. 5) and the boundary layer thickness in [6]. Furthermore, discrepancies up to 10 dB still exist between the simulated and the measured wall pressure spectra at several locations along the airfoil (Fig. 1 in [7], Figs. 8(a) and 8(e) in [5]).

Recent aeroacoustic experiments in the Ecole Centrale de Lyon (ECL) anechoic wind tunnels, on several two-dimensional profiles typical of most existing rotating machines, have extended the above trailing edge noise experimental database [15,16]. These measurements are first summarized in the next section. The following section describes the measurements which have been carried out on the controlled diffusion (CD) profile at a speed U_∞ of 16 m/s (corresponding to a Reynolds number based on the airfoil chord length $\mathrm{Re}_c = 1.6 \times 10^5$) and a geometric angle of attack α_g of 8°. This profile was developed by Valeo and it has been studied using LES carried out at Stanford University. The observed discrepancies between the measurement of the wall pressure spectra and the simulated pressure fluctuations have motivated the present hot-wire investigation of the flow field around the airfoil. The measurements have been executed at several key locations: (i) At the nozzle exit (inlet of the test section) in order to characterize the approach flow upwind of the airfoil, (ii) in the boundary layer and in the wake of the airfoil, and (iii) on the boundaries of the LES computational domain. These measurements allow detailed comparisons with the simulation results. These measurements also provide useful velocity statistics in the near wake of these CD airfoils similar to those measured by De La Riva et al. [17]. These data give insight into the correlation that exists between the wall pressure fluctuations and the velocity field in the vicinity of the trailing edge. These two pieces of information can then be used in the prediction of the far-field noise [18,19]. Finally, these velocity measurements also yield a realistic representation of turbulence for use in computing broadband noise resulting from stator-wake interactions in, for example, automotive engine cooling fan systems.

2 Experimental Setup and Background

As indicated in [20], airfoil self-noise is better measured independently of any other noise source by placing the profile in a large quiet free-jet anechoic wind tunnel, preferably without any collector downstream of the airfoil. Two such test facilities have been used at ECL to vary the airflow conditions and to study the effect of airfoil loading [16]. The airfoil is equipped with 21 flush mounted remote microphone probes (RMP) [21,22] as shown in Fig. 1 (three additional RMP are located in the spanwise direction at the same streamwise location as RMP No. 25). These RMP measure both the mean and fluctuating wall pressures within the frequency range 20 Hz–25 kHz and they characterize the corresponding noise sources. Movable B&K 1.27 cm (0.5 in.) Type-4181 microphones are placed in the far field, typically 2 m away from the airfoil, to simultaneously collect the acoustic spectra and provide the sound directivity. The mockup is held between two horizontal side plates fixed to the nozzle of the open-jet anechoic wind tunnel. Two rotating disks inside the plates allow adjusting

Contributed by the Fluids Engineering Division of ASME for publication in the JOURNAL OF FLUIDS ENGINEERING. Manuscript received January 10, 2005; final manuscript received December 6, 2005. Review conducted by Joseph Katz. Paper presented at the 2004 ASME Heat Transfer/Fluids Engineering Summer Conference (HT-FED2004), 11–15 July 2004, Charlotte, NC.

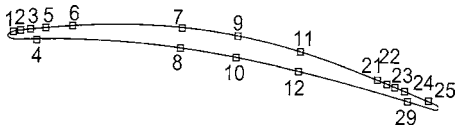

Fig. 1 Locations of measurement stations on the CD profile

the angle of attack with respect to the flow. Recent experiments at ECL have involved measurements at low speed for various incidences on a symmetric NACA 0012, a flat plate, and a cambered CD airfoil designed by Valeo. The latter has a 0.134 m chord length (C), a 0.3 m span, a 4% thickness to chord ratio and a camber angle of 12°. This instrumented CD airfoil mounted in the larger wind tunnel is shown in Fig. 2. The distance from the the nozzle exit to the mock-up leading edge is 0.2 m or about 1.5 C. The position of the closest RMP to the trailing edge is 3 mm or about 0.02 C.

The only pre-existing aerodynamic information on the flow field available in these experiments is given by the pressure trace on the airfoil surface. The initial measurements on the NACA 0012 airfoil confirmed the previous results of Brooks and Hodgson [12]. At moderate incidence, the mean pressure distribution on the airfoil could be retrieved by introducing an angle of attack correction to free air (infinite jet width) predictions [23]. However, in [5], the mean pressure coefficient on the flat plate could not be recovered with any incidence correction. Similarly significant discrepancies were found at all angles of attack for the CD profile between the measured wall pressure coefficient and the free air prediction, which could neither be accounted for by the turbulence model nor compensated by a change of angle of attack. In [20], Moreau et al. then performed detailed two-dimensional Reynolds-Averaged Navier-Stokes simulations of the complete experimental setup in the midspan plane of the mock-up with the V2F turbulence model [24]. Accounting for the experimental configuration and the nozzle jet width—mainly an airfoil embedded in the potential core of a jet instead of an unbounded approach flow—significantly improved the prediction of the pressure distribution at all angles of attack and for both jet widths tested (Figs. 13 to 15 in [20]). However, slight differences as shown by Fig. 5 in [16] remain in the leading edge and trailing edge regions of the airfoil. These differences were difficult to discern in the measurements of pressure coefficients.

These new flow conditions, extracted from the above RANS simulation within the jet potential core as shown in Fig. 3, were

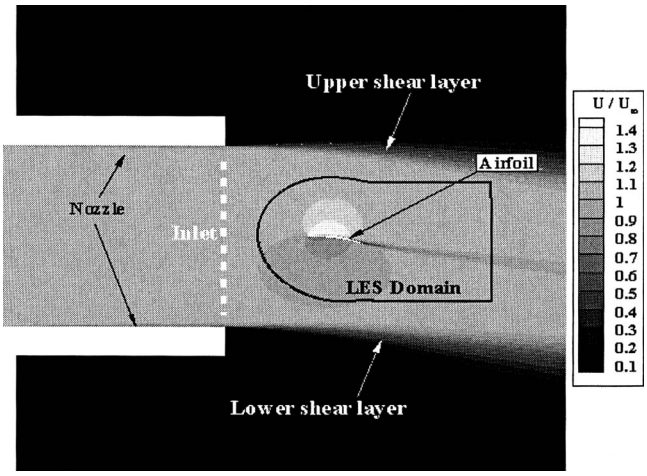

Fig. 3 RANS simulation of the CD profile mounted in the ECL large wind tunnel

then used for a LES around the CD profile [25]. The configuration in the large wind tunnel at a speed U_∞ of 16 m/s (corresponding to a Reynolds number based on the airfoil chord length $\mathrm{Re}_c = 1.6 \times 10^5$) and a geometric angle of attack α_g of 8° was selected. It corresponded to the largest possible domain within the jet potential core while, at the same time, providing the smallest Reynolds number that was more favorable for such an expensive simulation. In addition, this was a flow with an adverse pressure gradient but the suction side boundary layer was still attached at the trailing edge as is appropriate for noise predictions based on the pressure spectra at the trailing edge [18]. Figure 4 shows an instantaneous velocity field of the unsteady LES in the computational domain embedded in the jet inviscid core [25]. The boundary conditions of this simulation (velocity components at the inlet) are extracted from the above RANS simulation of the complete experimental configuration. They are imposed at each time step without any additional reconstructed turbulence fluctuations. The mean pressure distribution is again predicted quite well by the LES as shown in Fig. 5. The resulting unsteady wall pressure fluctuation power spectral distribution, Φ_{pp}, at the trailing edge is shown in Fig. 6. The LES prediction of the acoustic sources agrees quite well with the measured spectra at low frequencies (maximum difference of 2.5 dB for $f \leqslant 1000$ Hz), but the numerical spectrum

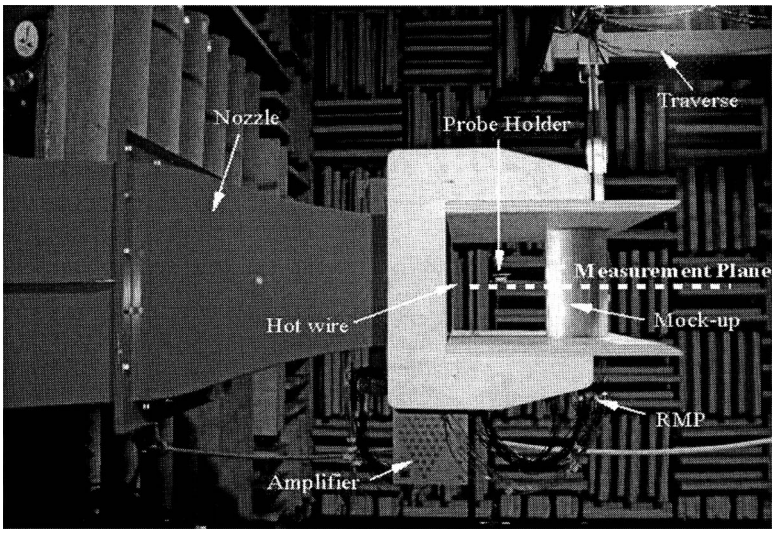

Fig. 2 CD profile mounted in the ECL large wind tunnel

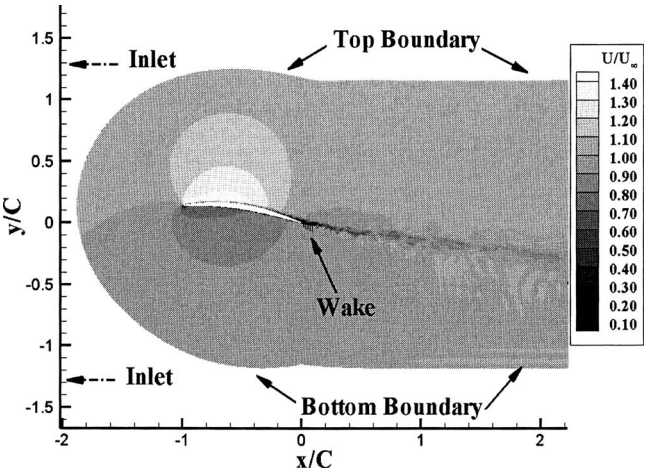

Fig. 4 Measurement locations on the LES domain (speed contours at a given time)

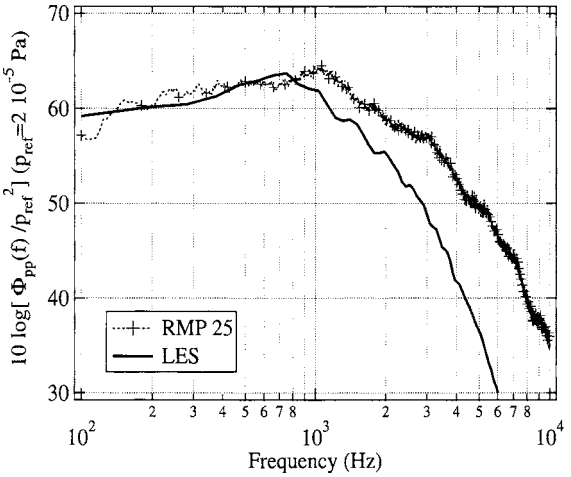

Fig. 6 Wall pressure spectra Φ_{pp} near the trailing edge

decays too early and contains fewer small structures in the sublayer that might not be captured by the LES. This is quite similar to the spectra of Figs. 8(a)–8(c) in [5], which correspond to the stations with an attached adverse pressure gradient turbulent boundary layer along Blake's slanted flat plate [11]. Less favorable agreement is found in the fore portion of the airfoil where transition freely occurs. In order to improve the agreement and understand the current discrepancies, a detailed flow mapping has been undertaken for the aeroacoustic experimental arrangement shown in Fig. 2. This also provides the first detailed *aerodynamic* characteristics of such a common aeroacoustic experimental setup.

3 Hot-Wire Data Collection

The flow mapping of the experimental configuration described in Sec. 2 has been achieved with single normal (SN) and *X* probes moved with a three-axis traverse in the midsection plane of the airfoil mockup. The SN probe is a TSI 1210. The *X* probe has been designed and fabricated at the Turbulent Shear Flows Laboratories of the Department of Mechanical Engineering of Michigan State University for this experiment. It has two 1 mm long 5 μm diameter active length tungsten sensors. These are supported, at ±45° from the probe axis, by copper-plated ends that are attached to the prongs, which are separated by 3 mm. The design of this probe follows on the recommendations of [26]. The acquisition and signal processing for both probes were achieved with a standard TSI IFA-100 anemometer. All of the experimental data in this study, including the hot-wire and pressure data, were collected at a sampling rate of 32,768 Hz for 30 s. The frequency response of the SN and the *X* probe were found to be between 30–35 kHz.

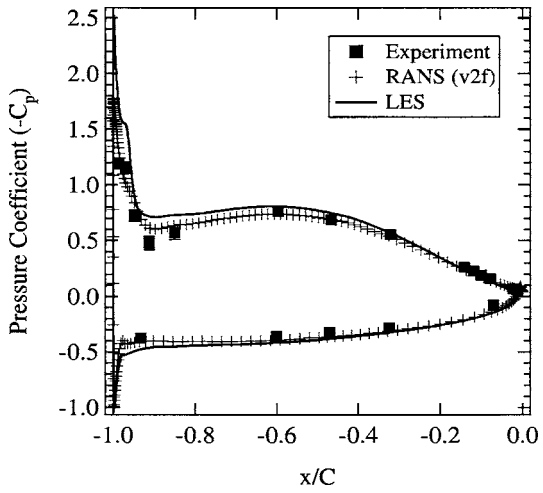

Fig. 5 Pressure coefficient on the CD profile

Figure 3 and its zoom, Fig. 4, present the locations of the various hot-wire measurements that have been acquired at the exit of the facility nozzle and in the LES numerical domain. The reference frame of the LES is also the selected coordinate system for reporting all velocity profiles of this study. Specifically, the origin of the coordinate system is set at the airfoil trailing edge. The centerline of the nozzle of the ECL large anechoic wind tunnel, which has a width of 500 mm ($\approx 3.7C$), lies at $y/C=0.151$.

The hot-wire probes have been calibrated in a separate dedicated unit that was placed close to the main ECL nozzle for speeds ranging from 4 to 35 m/s. A specially-designed probe holder allows the probe to be transferred from the calibration nozzle to the primary measurement nozzle without having to reposition the probe. This ensures that the probe is oriented identically for both the experiments and the calibrations. The *X* probe is also calibrated for 13 different angles that are equally spaced between ±36° (i.e., every 6°). For each set of measurements, a precalibration and a postcalibration have been achieved to check for any drift in the calibrations of the hot wires. Because of the ±36° calibration range, it is also imperative that the hot-wire probe be sufficiently aligned with the mean flow angle. In [27], a preliminary tuft survey had been utilized to accurately estimate the mean flow angle at each measurement location. In the present study, several numerical realizations of the reference LES (Fig. 4) were used to establish the initial alignment of the *X* probe. Figure 7 represents a close-up view of one of these instantaneous flow fields of Fig. 4 in the vicinity of the airfoil trailing edge. The velocity values were extracted from these LES results by interpolating along lines comprised of 100 points. Each intrapolation line corresponded to a downstream location where an *X*-probe survey was taken, as shown in Fig. 7 by the thick vertical solid lines. The length of each straight line is approximately 50 grid nodes in the LES domain (i.e., one point is extracted at each grid node with an additional point interpolated between). Since *X* probes have the highest accuracy for measured angles around zero, three realizations of the LES simulation were used to select the one probe orientation angle that would best align the probe at each location across the wake. An angle of −17° was selected by this process with the expectation that over 95% of the measured angles would be within the probe's acceptance range. This result was later confirmed by the *X*-probe measurements in the wake. Additional measurement stations upstream of the first measurement station in Fig.

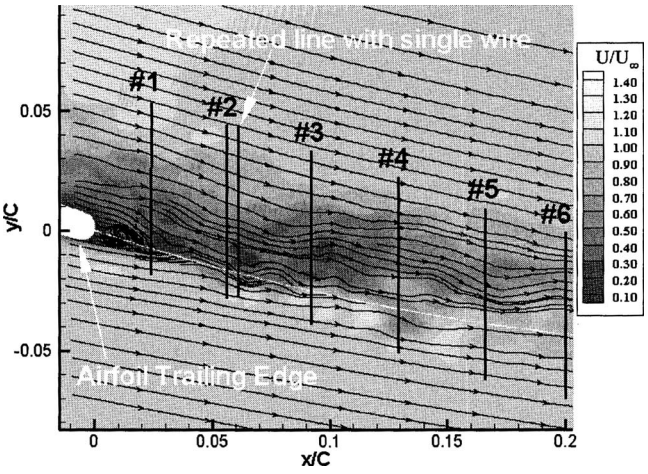

Fig. 7 LES instantaneous velocity contours in the trailing edge region

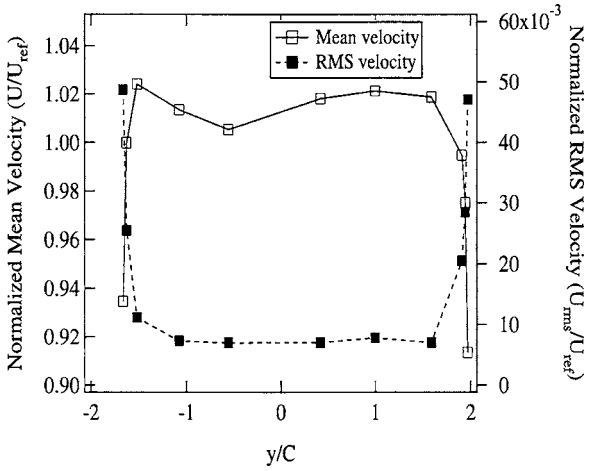

Fig. 8 Experimental inlet mean and RMS velocity profiles at $x/C=-2.48$

7 were also analyzed, but it was determined that the range of angles was too wide for accurate *X*-probe measurements. It was also shown that there is significant flow reversal (flow toward the trailing edge), which could not be reliably measured by an *X* probe. Figure 7 clearly shows that a large vortical structure has crossed the first measurement station (in this realization) just downstream of the trailing edge. The analyses of the measurement stations that lie downstream of the first measurement station showed 100% of the measured velocities falling within the acceptance cone of the *X* probe.

The hot-wire data were processed using both the precalibration and postcalibration fits and then compared to assess the level of drift that occurred during the course of the dataset. A prepostcomparison of the processed datasets for the single-wire data were within 1%. A similar prepostcomparison for the *X*-probe data yielded a maximum disagreement that was between 4–5%. Such variations have provided the error bars in all velocity measurements. The higher prepostdisagreement for the *X* probe was attributed to the repeatability in the calibration angle, which was measured using an angle indicator that was only repeatable to within a few degrees. Also, the time between the pre and postcalibrations were often longer (over 3 h) than what is typically recommended for the calibration of a constant temperature anemometer hot-wire probe to achieve minimal drift.

The power spectral density (PSD) of these processed hot-wire data were then obtained by segmenting the total time series into smaller records of 2^{13} points. This is a record length that is long enough to show the large scales and short enough to obtain sufficient records for the high-frequency analysis. These time records were Fourier transformed using standard fast fourier transform (FFT) algorithms with a Hanning window to account for the effect of the finite record. Calculating the spectra for the *X*-probe data was more complicated since there are isolated regions in which the acceptance angles, γ, exceeded the calibration range ($|\gamma| > \pm 36°$). These data were excluded from the record. A searching algorithm was used to find all the available records of the chosen length. These records were continuous strings of data of a given length that occurred between the sporadic "bad" points in the *X*-probe data. The uncertainty in the spectral levels is much less than a decibel over the whole frequency range.

4 Results

4.1 Nozzle Exit Plane. The ECL nozzle exit plane survey has been carried out at $x/C=-2.48$ for $|y/C| \leq 1.7$; that is, the mean velocities and the fluctuation intensities were measured in the upper and lower portion of the approach flow and nominally 1.5 chord lengths upstream of the airfoil leading edge, as sketched in Fig. 3. The airfoil camber and angle of attack creates an obstruction that prevents reaching the central region of the jet with the hot-wire probes mounted on the traverse.

Figure 8 shows the resulting nondimensional mean and fluctuating [root-mean-square (RMS)] velocity profiles. The normalization has been achieved with the mean inlet velocity, $U_{\text{ref}}=16.44$ m/s, measured throughout the present set of experiments with both hot-wire probes and Pitot tubes placed in the jet at the nozzle exit. The mean inlet profile (U/U_{ref}) is slightly skewed as seen in the RANS simulations. The downstream flow deflection of the CD airfoil causes this slight upstream asymmetry. The upper and lower boundary layers from the nozzle walls are also evident for $y/C=-1.6$ and $y/C=1.9$. Indeed, the velocity fluctuation level U_{RMS} increases sharply while the mean velocity U decreases as a result of the boundary layer fluid. This location is many chord thicknesses (≈ 50) above the airfoil. The turbulence intensity, $Tu=\sqrt{\overline{u'^2}}/U^2=U_{\text{RMS}}/U=0.7\%$, also agrees with previous measurements in the ECL wind tunnels (turbulence intensity always less than 1% in both facilities) [15,16,28,29].

Figure 9 presents the spectral content (PSD) of this inflow velocity field. As expected, much larger levels are obtained in the upper and lower boundary layers of the nozzle than in the jet inviscid core. Several turbulence length scales have been determined from the spectra in the jet potential core. The time autocorrelation of the streamwise velocity fluctuations, R_{11} first yields the

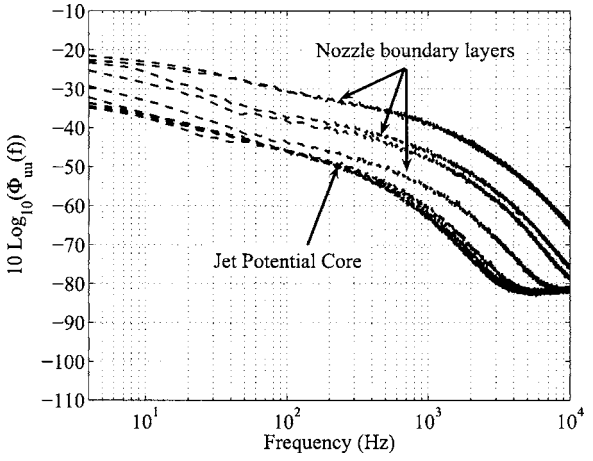

Fig. 9 Inlet velocity spectra at $x/C=-2.48$

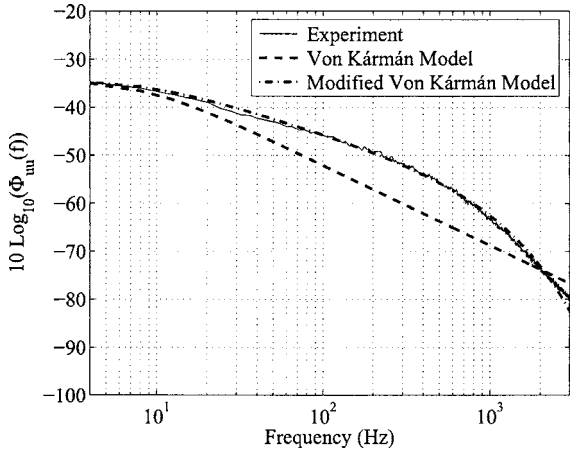

Fig. 10 Inlet velocity spectra at $x/C=-2.48$ With the von Kármán and modified von Kármán fits

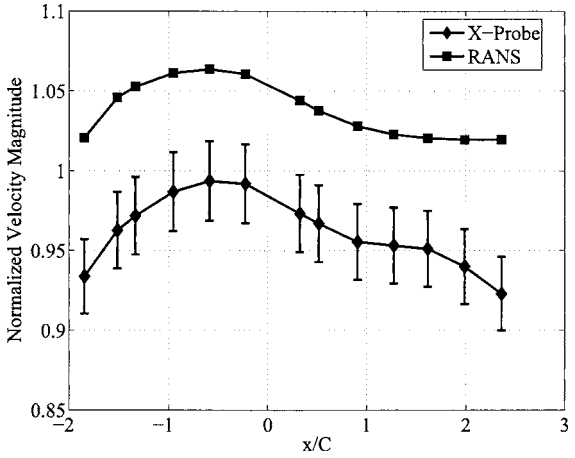

Fig. 11 Comparison of normalized numerical velocity ($|\vec{V}|/U_\infty$) and normalized experimental mean velocity ($|\vec{V}|/U_{ref}$) profiles on the suction side LES boundary

longitudinal Taylor micro scale λ_u (index 1 stands for the streamwise, jet direction) [30,31]. This autocorrelation, defined as $R_{11}(\tau)=u_1'(t)u_1'(t+\tau)/u_1'(t)^2$, can be expressed as a Taylor series at the origin:

$$R_{11}(\tau)=R_{11}(0)+\frac{\partial R_{11}}{\partial\tau}\tau+\frac{\partial^2 R_{11}}{\partial\tau^2}\frac{\tau^2}{2}+\ \ldots\ =1-\left|\frac{\partial^2 R_{11}}{\partial\tau^2}\right|\frac{\tau^2}{2}+\ldots$$

to provide a time scale $[\lambda_u]_t$ of 0.91 ms from the equation:

$$\frac{\tau^2}{[\lambda_u]_t^2}=1-R_{11}(\tau). \tag{1}$$

This time scale is related to the longitudinal Taylor microscale using the mean inlet velocity, $U_{ref}=16.44$ m/s, as the convection velocity. This yields a longitudinal Taylor microscale, λ_u, of 15 mm. The resulting Reynolds number based on this Taylor microscale is 106. The condition of locally isotropic flow can then be reasonably assumed from which the dissipation ϵ can be estimated as [30,31]:

$$\epsilon=30\nu(\overline{u'^2})/(\lambda_u^2). \tag{2}$$

A Kolmogorov length scale of 0.5 mm is then obtained from $\eta=\sqrt[4]{\nu^3/\epsilon}$. Indicated spectral content above ~5 kHz is most likely attributed to anemometer noise as it corresponds to smaller scales than the smallest values of turbulence in the flow (wavenumber at the Kolmogorov length scale η, $k\eta>1$). Finally, an integral scale Λ can be deduced from the above time autocorrelation of the streamwise velocity fluctuations, R_{11}, following for instance, the method of equivalent areas suggested by Bailly and Comte-Bellot in [31] (Fig. 6.1 p. 135). The integration of this autocorrelation over the complete range of time lags τ yields an integral scale Λ of 0.23 m. Alternatively, this integral scale can be obtained by comparing the PSD of streamwise velocity with an analytical von Kármán model for isotropic turbulence, using the measured low turbulent intensity of 0.7%:

$$\Phi_{uu}(\omega)=\frac{\overline{u'^2}}{U}\frac{\Lambda}{\pi}\frac{1}{(1+\hat{K}^2)^{5/6}}, \tag{3}$$

where $\hat{K}$ is proportional to Λ and the angular frequency ω [29]. A best fit again provides a macroscale of about 0.23 m, which is the same order of magnitude as the result obtained by Moreau and Roger in [29] ($\Lambda=0.6$ m in the small ECL wind tunnel). Similarly, as suggested in [29], the agreement can be improved at high frequency by adding an exponential decay to Φ_{uu} in the viscous range, not accounted for by Eq. (3) (similar to Pope's model spectrum of chapter 6 in [30]). The PSD of the streamwise velocity then reads $\Phi_{uu}e^{-\beta_0\hat{K}}$, where Φ_{uu} is given by Eq. (3). The same constant $\beta_0=0.015$ is obtained as in [29] (Fig. 8). However, a significant difference exists between the two sets of measurements. In the present experiment (in the large ECL wind tunnel), the inertial subrange shows some significant turbulence anisotropy in the flow and the usual $-5/3$ decay for isotropic turbulence (found in [29]) must be replaced by a shallower -1 slope to achieve the excellent agreement shown in Fig. 10. When this modified von Kármán spectrum is implemented in a model of turbulence interaction with the CD airfoil using the measured mean velocity U_{ref} and turbulence intensity, the resulting leading edge noise is found negligible compared to the trailing edge or self-noise of the airfoil, as was found in [29] in the other ECL wind tunnel. This indicates an appropriate inflow condition for the corresponding aeroacoustic investigation.

4.2 LES Boundaries. The *X* probe has provided two components of velocity along the top and bottom boundaries of the LES domain outline in Fig. 3. These boundaries are about 1.5 chord lengths away from the airfoil. Figure 11 shows the profile of the normalized mean velocity magnitude on the top LES boundary (suction side of airfoil). Figure 12 is the corresponding plot for the lower LES boundary (pressure side of airfoil). The normalization

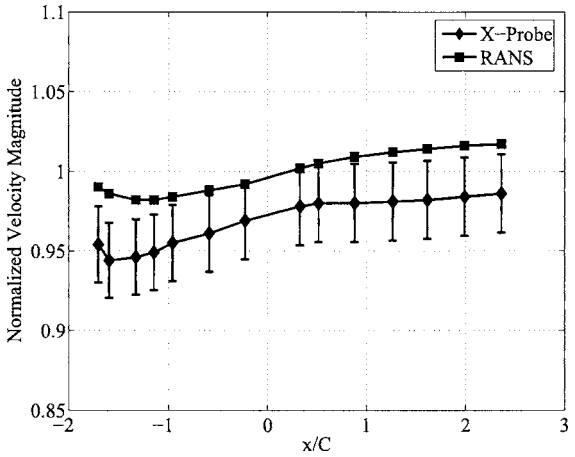

Fig. 12 Comparison of normalized numerical ($|\vec{V}|/U_\infty$) and normalized experimental mean velocity ($|\vec{V}|/U_{ref}$) profiles on the pressure side LES boundary

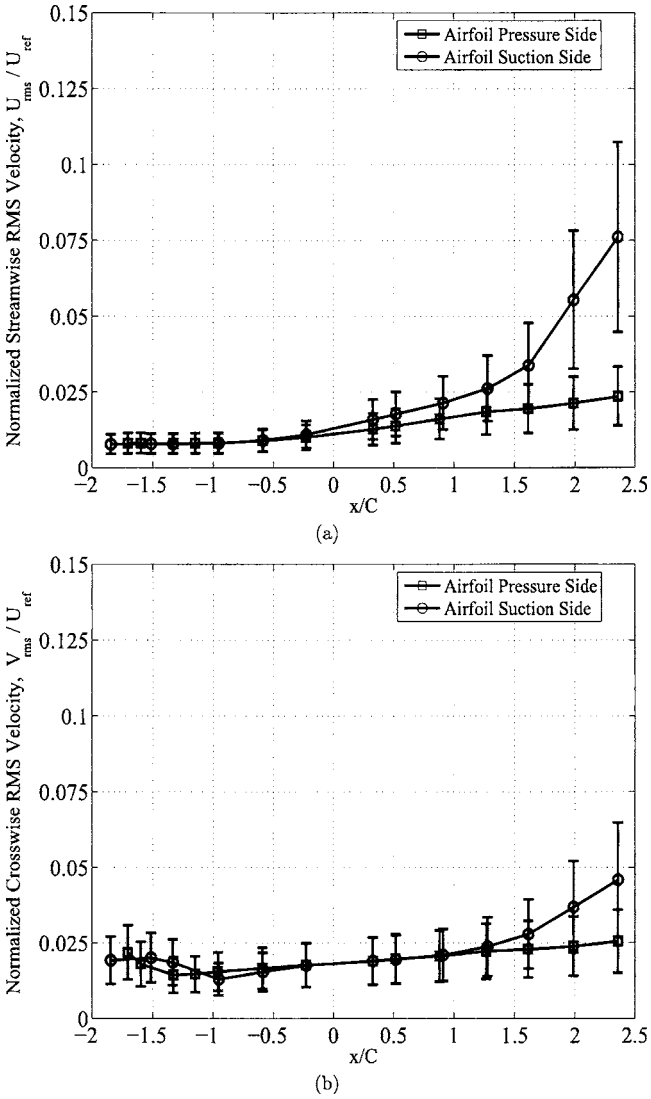

Fig. 13 Normalized experimental RMS velocity profiles on the LES boundaries: (*a*) Streamwise component (U/U_{ref}) and (*b*) Crosswise component (V/U_{ewf})

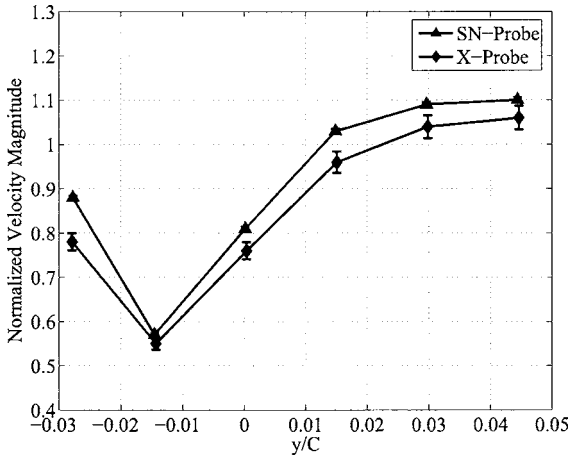

Fig. 14 Normalized experimental mean velocity ($|\vec{V}|/U_{ref}$) profiles in the wake region at $x/C=0.056$

is made with respect to the mean free stream velocity at the nozzle exit in the experiment ($U_{ref}=16.44$ m/s) and the free stream velocity in the simulations ($U_\infty=16$ m/s). Since the RANS values were used as boundary conditions for the LES simulation, both simulations have the same velocity components at this location.

The numerical results have similar profiles as the measured ones, but higher speeds for both boundaries. The suction side has a 6 to 7% difference with a noticeably larger discrepancy for the last two downstream measurement locations. Figure 13 provides the corresponding RMS velocities along these boundaries from the experimental measurements. At the downstream locations ($x/C \geq 1.25$) the velocity fluctuations U_{RMS} and V_{RMS} sharply increase up to 10% of the local mean velocity. This is taken as a clear sign of a strong local shear flow. It is inferred that the upper LES grid boundary has intersected the upper shear layer coming from the nozzle lip. The pressure side shows a smaller 2% disagreement in the mean velocities. No significant velocity fluctuations were detected, which indicates that the lower LES grid boundary does not intersect the lower shear layer. Moreover, most of the observed discrepancies in the mean velocity magnitude are due to the streamwise component, which is the dominant component in the overall velocity magnitude. The differences in the crosswise velocity component are very small for $x/C > -0.23$ and the RANS and experimental profiles are quite similar. For $x/C \leq -0.23$, the velocity profiles diverge and differences increase, with the experimental results showing a larger crosswise velocity on both LES grid boundaries. This result is consistent with the higher curvature that is seen for the shear layers in the experiment.

The larger differences in mean velocities on the suction side relate to the local larger differences in the wall pressure field shown in Fig. 5. A lack of resolution of the pressure distribution on the airfoil, especially at the leading edge, may explain this disagreement. That is, errors in the pressure represent a different circulation around the airfoil, and a different jet deflection by the CD airfoil. Another possible explanation for the observed differences is the spreading of the shear layers coming from the nozzle lips. This effect is especially pronounced on the suction side as discussed above.

4.3 Wake Planes. The *X* probe has also provided the velocity components along six traverse lines in the near wake of the airfoil (Fig. 4). The measurement locations were 5 mm (0.037 *C*) apart in the *x* direction for these six surveys. The closest traverse line is about 1.6 mm (0.012 *C*) downstream of the trailing edge. Each plane extended over 10 mm (0.074 *C*) with six different measurements. Figure 7, which sketches the six locations, also stresses that the measurements at the second station have been repeated with the SN probe.

Figure 14 shows the profile of the normalized velocity magnitude that was separately measured with a single wire. Good agreement was found between the two measurements indicating reliable techniques and good experimental repeatability. The maximum variation is about 6%. Some of the discrepancies (slightly larger wake with the single wire) can also be attributed to a slight axial shift of this traverse.

The same asymmetric velocity profile is found with the numerical results as shown in Fig. 15. However, the RANS and the LES predict a 30% larger wake deficit. On the pressure side of the airfoil, the LES goes back to the external flow region ($U > U_{ref}$) faster than the RANS and compares more favorably to the experimental data. On the suction side, both the LES and RANS predict a slower recovery suggesting a thicker suction side boundary layer than in the experiment. It should also be stressed that the LES is significantly closer to the experimental data with similar variations for both velocity components. The differences even drop to less than 10% closer to the external flow region. Similar trends are found at the other downstream stations in the wake. Therefore, the numerical wakes develop and bend in the same way as in the experiment. Their spreading by diffusion is also similar. At the

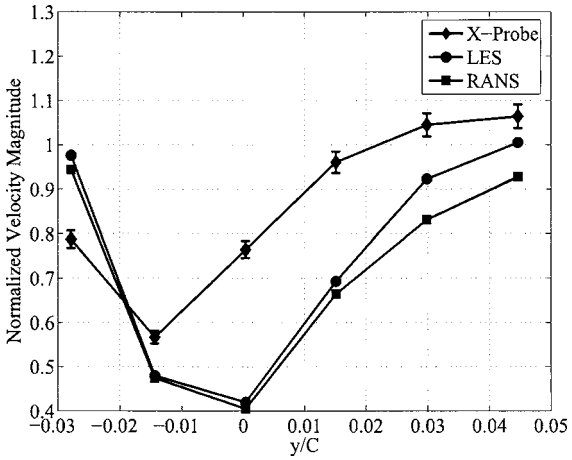

Fig. 15 Comparison of normalized numerical ($|\vec{V}|/U_\infty$) and normalized experimental mean velocity ($|\vec{V}|/U_{ref}$) profiles at $x/C=0.056$

first station, the discrepancy in the wake velocity deficit is much larger (the numerical velocities are almost four times smaller) but the large recirculating flow already pointed out in Fig. 7 makes the hot wire measurement locally unreliable (|mean flow angles| $>36°$.)

The larger suction side boundary layer at the trailing edge could again be traced to a pressure gradient not well enough resolved in the numerical predictions, as shown in Fig. 5. As most of the differences between LES and experimental values in the wall pressure occur in the leading edge region, it could be conjectured that the initial growth of the suction side boundary layer is overpredicted (the experimental favorable pressure gradient region at 10% chord length being absent in all simulations). The observed differences might also suggest that, in the RANS simulations, the shear layers coming from the nozzle lip might not be resolved properly inducing variations of velocity in the jet core and consequently in the vicinity of the airfoil (boundary layers and wake). For instance, the grid resolution in the full test facility is too coarse to properly capture the shear layers. The V2F turbulence model used in these RANS simulations also has an impact on the spreading of these shear layers. As a consequence, the shear layers might be too diffuse.

Figure 16 shows typical velocity power spectral densities across a given station in the wake. All spectra have a broadband content with a first high contribution at low and medium frequency with a weak slope up to 1 kHz. For higher frequencies, the velocity PSD has a faster decay beyond 10 kHz. Figure 16(*a*) corresponds to a location in the wake on the pressure side of the airfoil. This PSD clearly shows a tonal peak spreading between 1200 Hz and 2000 Hz on top of the broadband contribution. Using the trailing edge thickness or the size of the vortical structure shown in Fig. 4 as a characteristic length scale yields a Strouhal number of about 0.2, typical of a vortex shedding phenomenon (a von Kármán vortex street). Figures 16(*b*) and 16(*c*) show the spectral content of the velocity magnitude in the neighborhood of the maximum wake deficit. They have the highest and similar levels of fluctuations. The vortex shedding peak, at these locations, is no longer visible, and it is most likely buried in the high broadband level. The source location of Fig. 16(*d*) is at the edge of the wake. The levels of fluctuations are at least one decade lower than at any other location in the midplane. This reduction is attributed to the strongly reduced shear at this location. The composite representa-

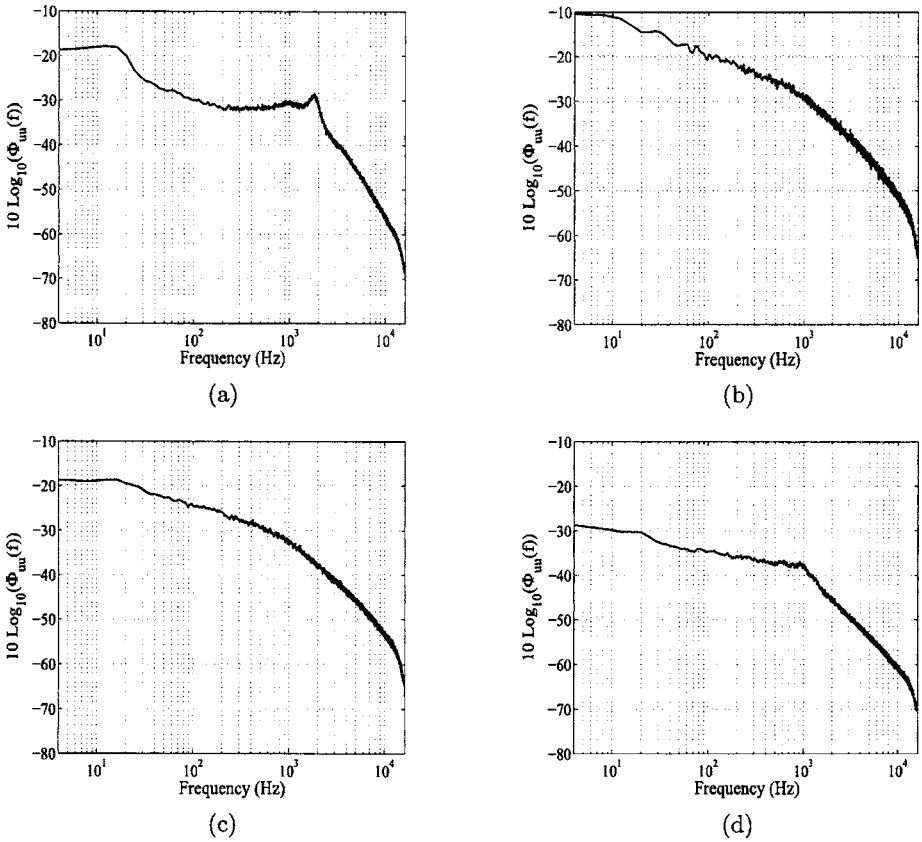

Fig. 16 Wake velocity spectra at $x/C=0.025$ and (*a*) $y/C=-0.018$, (*b*) $y/C=0.011$, (*c*) $y/C=0.026$, and (*d*) $y/C=0.057$

tion shown in Fig. 16 is also representative of the spectral distributions obtained at the additional five measurement positions.

5 Conclusions

Detailed hot-wire measurements have been successfully collected in the ECL large wind tunnel. A complete mapping across the nozzle exit plane has provided accurate inlet flow conditions upstream of the CD airfoil. A low turbulence intensity of 0.7% with a spectral content going at least up to 5000 Hz was found at this upstream station. The mean approach velocity of 16.44 m/s across the nozzle width was used to normalize the experimental measurements. The *X*-probe measurements provided velocity components at the upper and lower boundaries of the LES computational domain and in the airfoil wake at different streamwise locations. The measurements at one station in the wake were repeated with a straight wire to assess the proper experimental repeatability and uncertainty. Differences less than 6% were observed. All the mean measurements were then compared to the previous RANS and LES simulations. The computed mean velocity field in the potential core of the jet around the airfoil has good overall agreement with the measured one. However, the hot-wire measurements suggest a larger deflection of the jet by the presence of the airfoil and a thinner airfoil wake with a smaller velocity deficit. This excessive wake velocity deficit is most likely caused by an overly thick suction side boundary layer in the simulations and a slight reduction of incidence on the airfoil. These differences in velocity are consistent with the local mean pressure distribution predicted by the RANS simulations. Specifically, that simulation overpredicts the suction effect at the leading edge and it misses the favorable pressure gradient region at 10% chord that was observed in the experiment.

The spectral distributions of the pressure fluctuations at the trailing edge of the airfoil suction side were obtained experimentally and from the LES computations. Good agreement was achieved at low frequencies but the LES spectral values are distinctly smaller than the measured ones starting at a Strouhal number based on the chord length $fc/U_\infty=6.8$ or a frequency of 800 Hz. This result suggests larger structures in the simulation than in the experiment. The high-frequency content seen in the measured pressure spectra might be caused by some weak turbulence precursor existing in the inlet flow field. The velocity power spectral densities in the wake of the airfoil exhibit the same broadband frequency content as the inlet velocity PSD and the wall pressure PSD. The concentrated energy in the narrow band also suggests that a regular vortex shedding process, in addition the turbulent fluctuations, are present in the pressure-side wake.

Acknowledgment

Special thanks to Dr. Meng Wang from Stanford University for sharing his LES results with us and to the LMFA staff for their technical support at ECL.

References

[1] Wang, M., 1998, "Computation of Trailing-Edge Noise at Low Mach Number Using Large-Eddy Simulation," *Annual Research Briefs-1998*, Center for Turbulence Research, Stanford University/NASA Ames Research Center, pp. 91–106.
[2] Singer, B. A., Brentner, K. S., Lockard, D. P., and Lilley, G., 1999, "Simulation of Acoustic Scattering From a Trailing Edge," AIAA Paper 99-0231.
[3] Manoha, E., Elias, G., Troff, B., and Sagaut, P., 1999, "Towards the Use of Boundary Element Method in Computational Aeroacoustics," AIAA Paper 99-1980.
[4] Manoha, E., Troff, B., and Sagaut, P., 2000, "Trailing Edge Noise Prediction Using Large Eddy Simulation and Acoustic Analogy," AIAA J., **38**(4), pp. 575–583.
[5] Wang, M., and Moin, P., 2000, "Computation of Trailing-Edge Flow and Noise Using Large-Eddy Simulation," AIAA J., **38**(12), pp. 2201–2209.
[6] Manoha, E., Delahay, C., Sagaut, P., Mary, I., Ben Khelil, S., and Guillen, P., 2001, "Numerical Prediction of the Unsteady Flow and Radiated Noise From a 3D Lifting Airfoil," AIAA Paper 2001-2133.
[7] Manoha, E., Herrero, C., Sagaut, P., and Redonnet, S., 2002, "Numerical Prediction of Airfoil Aerodynamic Noise," AIAA Paper 2002-2573.
[8] Ewert, R., Meinke, M., and Schröder, W., 2002, "Computation of Trailing Noise via LES and Acoustic Perturbation Equations," AIAA Paper 2002-2467.
[9] Oberai, A. A., Roknaldin, F., and Hughes, T. J. R., 2002, "Computation of Trailing Edge Noise due to Turbulent Flow over an Airfoil," AIAA J., **40**(11), pp. 2206–2216.
[10] Mellen, C. P., Fröhlich, J., and Rodi, W., 2003, "Lessons From LESFOIL Project on Large-Eddy Simulation of Flow Around an Airfoil," AIAA J., **41**(4), pp. 573–581.
[11] Blake, W. K., 1975, "A Statistical Description of Pressure and Velocity Fields at the Trailing Edge of a Flat Strut," DTNSRD Report No. 4241, David Taylor Naval Ship R & D Center, Bethesda, MD.
[12] Brooks, T. F., and Hodgson, T. H., 1981, "Trailing-Edge Noise Prediction From Measured Surface Pressures," J. Sound Vib., **78**(1), pp. 69–117.
[13] Garcia, P., and Gérard, P., 1989, "Bruit d'un profil dans un écoulement," ONERA TP 1984-155, November 1984. See also *La Recherche A érospatiale. English Version*, Vol. 3, pp. 1–7.
[14] Oerlemans, S., and Migliore, P., 2004, "Aeroacoustic Wind Tunnel Tests of Wind Turbine Airfoils," AIAA Paper 2004-3042.
[15] Roger, M., and Moreau, S., 2004, "Broadband Self-Noise From Loaded Fan Blades," AIAA J., **42**(3), pp. 536–544.
[16] Moreau, S., and Roger, M., 2005, "Effect of Airfoil Aerodynamic Loading on Trailing Edge Noise Sources," AIAA J., **43**(1), pp. 41–52.
[17] De la Riva, D. H., Devenport, W. J., Muthanna, C., and Glegg, S. A. L., 2004, "Behavior of Turbulence Flowing Through a Compressor Cascade," AIAA J., **42**(7), pp. 1302–1313.
[18] Amiet, R. K., 1976, "Noise Due to Turbulent Flow Past a Trailing Edge," J. Sound Vib., **47**(3), pp. 387–393.
[19] Ffowcs Williams, J. E., and Hall, L., H., 1970, "Aerodynamic Sound Generation by Turbulent Flow in the Vicinity of a Scattering Half-Plane," AIAA J., **40**, pp. 657–670.
[20] Moreau, S., Henner, M., Wang, M., Iaccarino, G., and Roger, M., 2003, "Analysis of Flow Conditions in Free Jet Experiments for Studying Airfoil Self-Noise," AIAA J., **41**(10), pp. 1895–1905.
[21] Pérennès, S., and Roger, M., 1998, "Aerodynamic Noise of a Two-Dimensional Wing With High-Lift Devices," AIAA Paper 98-2338.
[22] Pérennès, S., 1999, "Caractérisation des Sources de Bruit Aérodynamique à Basses Fréquences de Dispositifs Hypersustentateurs," Ph.D. dissertation No. 99-32.
[23] Brooks, T. F., Marcollini, M. A., and Pope, D. S., 1986, "Airfoil Trailing-Edge Flow Measurements," AIAA J., **24**(8), pp. 1245–1251.
[24] Durbin, P. A., 1995, "Separated Flow Computations With the k-ϵ-v^2 Model," AIAA J., **33**, pp. 659–664.
[25] Wang, M., Moreau, S., Iaccarino, G., and Roger, M., 2004, "LES Prediction of Pressure Fluctuations on a Low Speed Airfoil," *Center for Turbulence Research Annual Research Briefs*.
[26] Strohl, A., and Comte-Bellot, G., 1973, "Aerodynamic Effects Due to Configuration of *X*-Wire Anemometers," Trans. ASME, J. Appl. Mech., **40**, pp. 661–666.
[27] Neal, D., Foss, J., Henner, M., and Moreau, S., 2001, "Evaluating CFD Models of Axial Fans by Comparisons With Phase-Averaged Experimental Data," VTMS5-01-89 Paper.
[28] Casalino, D., and Jacob, M., 2003, "Prediction of Aerodynamic Sound From Circular Rods via Spanwise Statistical Modeling," J. Sound Vib., **262**, pp. 815–844.
[29] Moreau, S., and Roger, M., 2004, "Competing Broadband Noise Mechanisms in Low-Speed Axial Fans," AIAA J., (to be published), AIAA Paper No. 2004-3039.
[30] Pope, S. B., 2000, *Turbulent Flows*, (Cambridge University Press, Cambridge).
[31] Bailly, C., and Comte-Bellot, G., 2003, *Turbulence*, (CNRS Editions, Paris, UK).
[32] Moreau, S., and Roger, M., 2005, "Effect of Angle of Attack and Airfoil Shape on Turbulence-Interaction Noise," AIAA Paper 2005-2973.

Multi-Element Unstructured Analyses of Complex Valve Systems

Vineet Ahuja
e-mail: vineet@craft-tech.com

Ashvin Hosangadi

Jeremy Shipman

Combustion Research and Flow Technology, Inc.,
Pipersville, PA 18947

Russell Daines

Jody Woods

Jacobs Sverdrup NASA Test Operations Group,
NASA Stennis Space Center,
MS 39529

The safe and reliable operation of high-pressure test stands for rocket engine and component testing places an increased emphasis on the performance of control valves and flow metering devices. In this paper, we will present a series of high-fidelity computational analyses of systems ranging from cryogenic control valves and pressure regulator systems to cavitating venturis that are used to support rocket engine and component testing at NASA Stennis Space Center. A generalized multi-element framework with submodels for grid adaption, grid movement, and multi-phase flow dynamics has been used to carry out the simulations. Such a framework provides the flexibility of resolving the structural and functional complexities that are typically associated with valve-based high-pressure feed systems and have been difficult to deal with using traditional computational fluid dynamics methods. Our simulations revealed a rich variety of flow phenomena such as secondary flow patterns, hydrodynamic instabilities, fluctuating vapor pockets, etc. In the paper, we will discuss performance losses related to cryogenic control valves and provide insight into the physics of the dominant multi-phase fluid transport phenomena that are responsible for the "choking-like" behavior in cryogenic control elements. Additionally, we will provide detailed analyses of the modal instability that is observed in the operation of a pressure regulator valve. Such instabilities are usually not localized and manifest themselves as a system-wide phenomena leading to an undesirable chatter at high flow conditions. [DOI: 10.1115/1.2170119]

Introduction

In this paper we discuss simulation technology used to support testing of rocket propulsion systems by carrying out high-fidelity analyses of support systems such as a cryogenic service valves, pressure regulator control valves, and cavitating control elements in a feed system. Such analyses are particularly important for the reliable operation of high-pressure valves and flow metering elements on test stands used for component testing of cryogenic pumps and propulsive devices. This is primarily because identification of transient anomalies stemming from hydrodynamic instabilities, valve timing, and/or system-based dynamic instabilities is usually difficult with empirical correlations and low-dimensional analysis methods. However, high-fidelity Navier-Stokes-based analysis of valve-based systems is typically very challenging because of the structural and functional complexity associated with such systems [1]. Structurally a valve system can consist of a complex network of embedded plugs, diaphragms, manifolds, and arterial branches with complicated junctions. For example, a control valve such as a pressure regulator valve can consist of multiple elements with complex shapes such as a variable area poppet being driven in an irregular shaped housing with very tight clearances both in the seat region and the outer housing (Fig. 1). Moreover, a network of feed channels interfaces between the inlet duct to the valve and the chamber housing the poppet. Traditional computational fluid dynamics (CFD) tools have severe limitations imposed on them, both in terms of accuracy and efficiency while carrying out high-fidelity analyses of such complicated systems. These limitations stem from the topological constraints imposed by the structural complexity of the geometry and the rich diversity of spatial and temporal scales that have to be locally resolved in the flow domain.

Functionally, characterization of such valve systems can be difficult because of the range of issues associated with them: feedback control loops, unsteady fluctuations from movement of subcomponents, system instabilities that couple with operating/testing elements, multiphase flow regimes, etc. So far, CFD analysis of such systems has been performed through the use of discrete steady-state single-phase calculations at different valve positions by isolating the main control element. Such flow characteristic curves provide important insight into mean performance related to these flow control devices. Furthermore, such analyses can serve as a first-order approximation for a variety of important transient issues that are critical to some of the primary functions performed by such systems such as pressure regulation and flow control. High-fidelity CFD analyses can also help resolve fluidic/hydrodynamic instabilities that arise from secondary flows/recirculating regions/shedding phenomena caused by the complexities in flow geometries. Unfortunately, these instabilities can couple with the valve motion and structural elements leading to undesirable "chatter" in the valve system. Pressure fluctuations can also arise from valve operation (valve opening/closing) leading to the creation of cavitation zones in feed lines. These vapor pockets in turn can collapse and manifest themselves as dynamic instabilities by coupling with pressure oscillations from the system.

In addition to the structural and functional complexities associated with valve-based high-pressure feed systems, it must be noted that rocket test facilities operate in widely varying flow regimes: from highly compressible gases feeding into preburners to cryogenic liquids used in rocket turbopumps. Simulations of cryogenic fluids can be particularly challenging as these fluids operate in proximity to their critical temperature where thermodynamic properties are very sensitive to small gradients in temperature. Furthermore, analyses of valve systems in cryogenic environments require elaborate phase change submodels embedded in the simulation framework to accurately represent valve response to flow transients [2]. For example, venturi-type flow control devices are commonly used as flow regulators in cryogenic feed lines and cavitation is the primary control mechanism used to

Contributed by the Fluids Engineering Division of ASME for publication in the JOURNAL OF FLUIDS ENGINEERING. Manuscript received January 24, 2005; final manuscript received August 24, 2005. Assoc. Editor: Surya P Vanka.

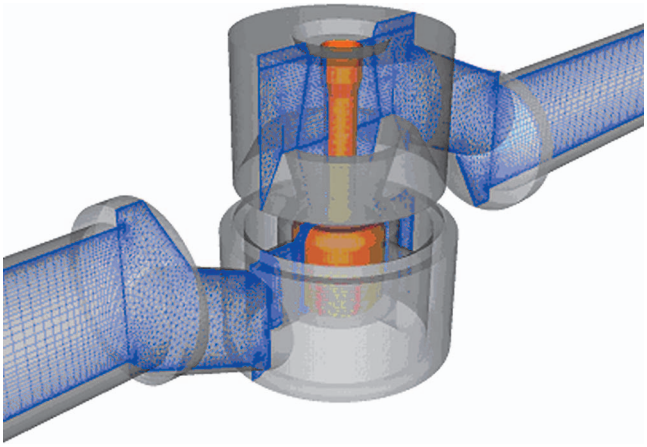

Fig. 1 Pressure regulator valve geometry with the multi-element grid (shown along the symmetry plane) used to mesh the valve flowpath

"choke" the venturi, thereby preventing any downstream pressure transients in the combustion chamber from affecting the feed line mass flow rates.

In this paper we discuss the simulation capability of the multi-element unstructured numerical framework (CRUNCH CFD®) and apply it to analyze several valve-based systems and control elements found in high-pressure liquid rocket test facilities at NASA Stennis Space Center (SSC). This multi-element unstructured based simulation capability has been proven to provide efficient and accurate solutions for complex turbomachinery and aero-propulsive applications in the past [3]. The hybrid unstructured methodology is embedded in a multi-phase framework and is used for simulations of valve systems ranging from a dome pressure regulator valve characteristic of highly compressible flow fields to incompressible liquid valve systems to venturi-type cryogenic control elements where cavitation is prevalent. In the following sections, we provide details of the multi-phase equation system and the hybrid unstructured numerical framework as applied to valve systems. We also discuss the compressible, incompressible, and multi-phase valve simulations. Our simulation results are compared against experimental data and the simulations reveal a rich variety of flow phenomena over a multitude of length and time scales.

Multi-Phase Equation System. The multiphase equation system is written in vector form as:

$$\frac{\partial Q}{\partial t}+\frac{\partial E}{\partial x}+\frac{\partial F}{\partial y}+\frac{\partial G}{\partial z}=S+D_v \tag{1}$$

Here Q is the vector of dependent variables, E, F, and G are the flux vectors, S is the source terms and D_v represents the viscous fluxes. The viscous fluxes are given by the standard full compressible form of Navier-Stokes equations [4]. The vectors Q, E, and S are given below with a detailed discussion on the details of the cavitation source terms to follow later:

$$Q=\begin{pmatrix}\rho_m\\ \rho_m u\\ \rho_m v\\ \rho_m w\\ \rho_g\phi_g\\ \rho_m h_m\\ \rho_m k\\ \rho_m\varepsilon\end{pmatrix}\quad E=\begin{pmatrix}\rho_m u\\ \rho_m u^2+P\\ \rho_m uv\\ \rho_m uw\\ \rho_g\phi_g u\\ \rho_m h_m u\\ \rho_m ku\\ \rho_m\varepsilon u\end{pmatrix}\quad S=\begin{pmatrix}0\\ 0\\ 0\\ 0\\ S_g\\ S_h\\ S_k\\ S_\varepsilon\end{pmatrix} \tag{2}$$

Here, ρ_m and h_m are the mixture density and enthalpy, respectively, and ϕ_g is the volume fraction or porosity of the vapor phase. The mixture energy equation has been formulated with the assumption that the contribution of the pressure work on the mixture energy is negligible, which is a reasonable assumption for this flow regime. The source term for the vapor phase arises from the rate of vapor mass generation due to cavitation m_t and the corresponding source term for the energy equation is given as $m_t \times h_{fg}$, where h_{fg} is the change in enthalpy resulting from the phase change and is a function of the local fluid temperature.

The mixture density and gas porosity are related locally by the following relations in a given cell volume:

$$\rho_m=\rho_g\phi_g+\rho_L\phi_L \tag{3}$$

$$1=\phi_g+\phi_L \tag{4}$$

where ρ_g, ρ_L are the physical material densities of the gas and liquid phases, respectively, and in general are functions of both the local temperature and pressure. In our formulation, we have assumed local thermodynamic equilibrium to significantly simplify Eq. (1). The thermodynamic properties of the liquid and vapor in the cavity are defined by a single variable, the saturation temperature T_{sat}. Hence, all thermodynamic properties (density, vapor pressure, viscosity, etc.) of both the liquid and the vapor phase may be generated as a tabular function of the saturation temperature. In our study here, these properties were generated from the Standard thermodynamic database 12 available from NIST for pure fluids.

The equation system as formulated in Eq. (1) is very stiff since the variations in density are much smaller than the corresponding changes in pressure. Therefore, to devise an efficient numerical procedure we wish to transform Eq. (1) to a pressure-based form where pressure rather than density is the variable solved for. An acoustically accurate two-phase form of Eq. (1) is first derived, followed by a second step of time scaling or preconditioning to obtain a well-conditioned system. We begin by defining the acoustic form of the density differential for the individual gas and liquid phases as follows:

$$d\rho_g=\frac{1}{c_g^2}dP,\quad d\rho_l=\frac{1}{c_L^2}dP \tag{5}$$

Here c_g is the isothermal speed of sound $(\partial P/\partial\rho_g)_T$ in the pure gas phase, and c_L is the corresponding isothermal speed of sound in the liquid phase, which is a finite value. We note that in Eq. (5) the variation of the density with temperature has been neglected in the differential form. This assumption was motivated by the fact that the temperature, changes are primarily due to the source term and not to the pressure work on the fluid, i.e., the energy equation is a scalar equation. This simplifies the matrix algebra for the upwind flux formulation significantly, at the potential expense of numerical stability in a time-marching procedure. However, more importantly, there is no impact on the accuracy since the fluid properties themselves are taken directly from the thermodynamic data bank for each fluid.

Following the discussion above, the differential form of the mixture density ρ_m using Eq. (5) is written as

$$d\rho_m=(\rho_g-\rho_L)d\phi_g+\frac{1}{c_\phi^2}dP\left(\frac{1}{c_\phi^2}=\frac{\phi_g}{c_g^2}+\frac{\phi_L}{c_L^2}\right) \tag{6}$$

Here, c_ϕ is a variable defined for convenience and is not the acoustic speed, c_m, in the mixture, which will be defined later. Using Eq. (6), Eq. (1) may be rewritten as

$$\Gamma\frac{\partial Q_v}{\partial t}+\frac{\partial E}{\partial x}+\frac{\partial F}{\partial y}+\frac{\partial G}{\partial z}=S+D_v \tag{7}$$

and

$$Q_v=[p,u,v,w,\phi_g,k,\varepsilon]^T \tag{8}$$

The numerical characteristics of Eq. (7) are studied by obtaining the eigenvalues of the matrix, $[\Gamma^{-1}(\partial E/\partial Q_v)]$. The eigenvalues of the system are derived to be

$$\Lambda = (u + c_m, u - c_m, u, u, u, u, u) \tag{9}$$

where c_m turns out to be the well-known, harmonic expression for the speed of sound in a two-phase mixture and is given as

$$\frac{1}{c_m^2} = \rho_m \left(\frac{\phi_g}{\rho_g c_g^2} + \frac{\phi_L}{\rho_L c_L^2} \right) \tag{10}$$

To obtain an efficient time-marching numerical scheme, preconditioning is now applied to the system in Eq. (7), in order to rescale the eigenvalues of the system so that the acoustic speeds are of the same order of magnitude as the local convective velocities.

CRUNCH CFD® Computational Framework

The CRUNCH CFD® code has a hybrid, multi-element unstructured framework that allows for a combination of tetrahedral, prismatic, and hexahedral cells [2]. The grid connectivity is stored as an edge-based, cell-vertex data structure, where a dual volume is obtained for each vertex by defining surfaces that cut across edges coming to a node. An edge-based framework is attractive in dealing with multi-elements since dual surface areas for each edge can include contributions from different element types, making the inviscid flux calculation "grid transparent."

For efficient computation of large 3D problems, a parallel framework for distributed memory systems has been implemented, along with a time-marching implicit solution procedure. The sparse implicit matrix is derived using a Euler explicit linearization of the first-order flux, and a variety of iterative sparse matrix solvers, e.g., GMRES, Gauss-Seidel procedure, are available in the code (see [4,5] for details). The parallel framework is implemented by partitioning the grid into subdomains, with each subdomain residing on an independent processor. The message passing between processors has been implemented using MPI to provide portability across platforms. The CRUNCH CFD® code has an integrated grid refinement and coarsening package operational within a multi-element framework [6].

Multi-Element Unstructured Methodology for Valve System Applications

The multi-element unstructured framework has been fine tuned to efficiently solve flows for valve system applications with structurally complicated geometries, cryogenic and real fluid effects, and flow structures that include flow separation, turbulence, and intermittency. As discussed above, the multi-element unstructured philosophy is encapsulated in the CRUNCH CFD® code, wherein an optimal combination of tetrahedral, prismatic, pyramidal, and hexahedral cells are used to efficiently solve flows in complex systems by tailoring the mesh to suit the geometrical and physical characteristics of the system. In valve systems in particular, the seat region around the plug is meshed with high aspect ratio hexahedral cells, allowing resolution of large local pressure and velocity gradients. The inlet and discharge ducts of a valve system are meshed with a combination of hexahedral and prismatic layers that help in resolving boundary layer phenomena and the transport of flow structures emanating from the seat region. The mesh in the seat region is typically stitched together with the grid in the inlet and discharge ducts with the aid of tetrahedral domains that provide topological flexibility with structurally complex-shaped systems. The strategy has proven to work very efficiently for simulations of a variety of valve systems in use at SSC such as a 10 in. LOX valve, a split-body valve, a pressure regulator valve, and a globe valve (see Refs. [7,8]). The simulations with the multi-element unstructured CRUNCH CFD® code have yielded results

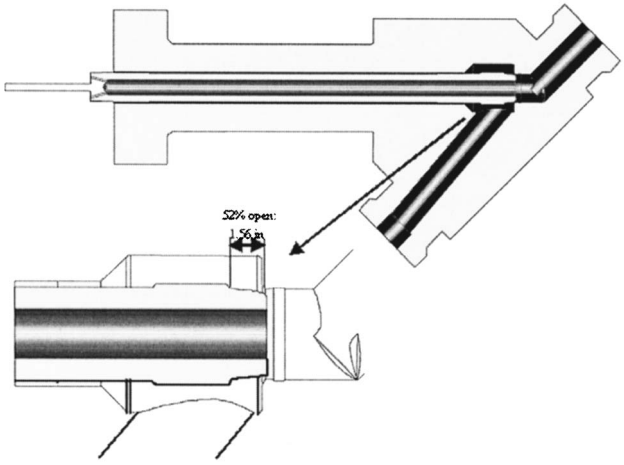

Fig. 2 Schematic of a 6 in. gaseous hydrogen valve

where the flow coefficients have been in excellent agreement with experimental/testing data. Furthermore, this strategy of simulating flows in valve systems has provided key insights into dominant flow physics during valve functioning and testing.

As an illustration of the applicability of the multi-element unstructured framework to complex valve systems, we present the grid generation methodology for a 6 in. gaseous hydrogen valve (see Fig. 2) currently in operation at SSC. This particular system is interesting both for the structural complexity in the valve geometry, particularly in the seat region, and the wide array of physical flow phenomena and flow regimes involved. Following our standard strategy for complex valve systems, structured domains are constructed around the plug and in the narrow clearances of the seat region. Figure 3 depicts the grid along the plane of symmetry clearly showing the hexahedral blocks in the seat region around the plug. Hexahedral/prismatic cells are extruded along the inlet and exhaust pipes, and a tetrahedral block is used to fill in the junctions between the pipes and the seat. The extruded hexahedral-prism blocks in the inlet and discharge ducts are also shown to interface with a region of tetrahedral cells (Fig. 3). This transition from hexahedral to tetrahedral cells permits flexibility in local resolution in different parts of the flow domain.

Simulation Results

Simulations of Pressure Regulator Control Valve. CFD simulations utilizing CRUNCH CFD® were performed to carry out detailed analysis of a pressure regulator valve. The structural complexity of the geometry and consequently the complex flow path associated with the pressure regulator valve made it particularly suitable for the multi-element framework incorporated in CRUNCH CFD®. For example, the pressure regulator valve is comprised of many enclosed regions with multiple corners, disparate shapes, and tight clearances. The flow fields associated with these regions are replete with a rich variety of length and time scales and diverse flow regimes from low Mach number flow regions to supersonic flow in the seat region. Moreover, the multiple corners and edges have secondary flow structures and transient phenomena such as shedding vortex structures. Associated with these unsteady phenomena is a dominant chattering-like behavior that has been observed when the valve is operational under certain conditions.

A multi-element grid comprised of tetrahedral, prismatic, hexahedral, and pyramidal cells was constructed for the dome pressure regulator geometry. Traditional structured hexahedral grids are very difficult to generate for such a complex geometry. The complexity in the geometry forces an awkward block topology with highly skewed and irregular cells in the case of a pure hexahedral

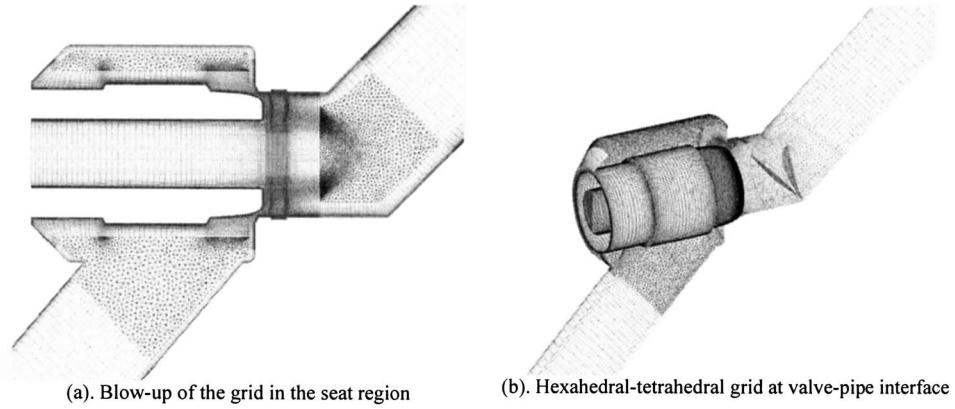

Fig. 3 (*a*) Multi-element grid for a 6 in. gaseous hydrogen valve, (*b*) blow-up of the grid in the seat region. Hexahedral-tetrahedral grid at valve-pipe interface.

grid. Furthermore, a contiguous hexahedral mesh places severe constraints on grid resolution in critical regions of the flow domain such as the seat region of the valve where the flow accelerates sharply. A grid comprised of only tetrahedral-prismatic elements is cumbersome to build because of difficulties with prismatic extrusion in concave corners and tight clearances associated with the geometry. These shortcomings are overcome in the multi-element approach wherein high-quality grids were generated very efficiently in all regions of the valve.

Figure 4 depicts a planar cross section of the multi-element grid that was generated for the dome pressure regulator valve simulations. The grid consists of 716,000 hexahedral cells with a combination of 838,989 tetrahedral, prismatic, and pyramidal cells. Most of the straight sections of the geometry such as the discharge duct and the inlet pipe were predominantly meshed with high aspect ratio hexahedral cells. Hexahedral blocks were also utilized in the seat region of the valve where very high directional gradients in the flow variables exist since high aspect ratio hexahedral cells are ideal to capture such gradients. Prismatic layers were extruded from the walls comprised of the ports and pipe connections in order to resolve the boundary layers associated with these regions. The remaining portions of the geometry such as the junctions between the inlet/discharge straight portions and the valve housing were filled with tetrahedral cells that acted as buffer zones connecting the disparate topologies in different regions of the pressure regulator valve. Both steady and unsteady simulations were performed with the multi-element grid. An ideal gas flow was assumed for both simulations. Inflow boundary conditions based on an inlet total pressure of 4400 psi and a total temperature of 540 degrees R were specified at the inlet plane to the feed duct. At the outflow plane of the discharge duct a back pressure of 800 psi was maintained. The steady simulations revealed a rich variety of flow phenomena over a multitude of length scales, as illustrated in Fig. 5.

Figure 5(*a*) shows the Mach number distribution along the plane of symmetry—it can be seen that the flow mildly accelerates as it transitions from the intake pipe to the feed ports leading into

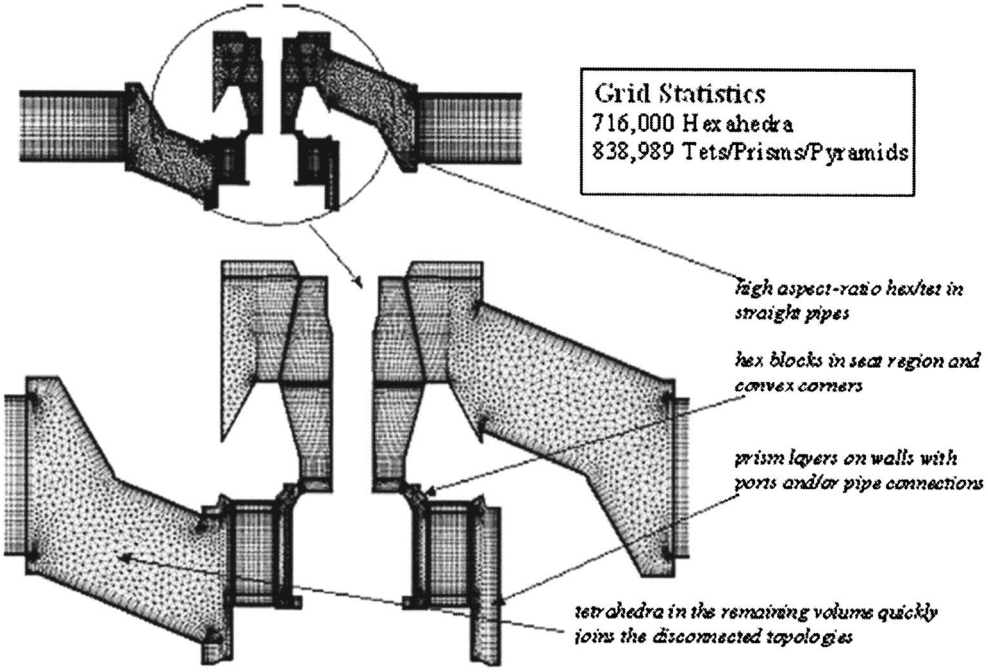

Fig. 4 Symmetry plane of the grid illustrating the multi-element mesh topology

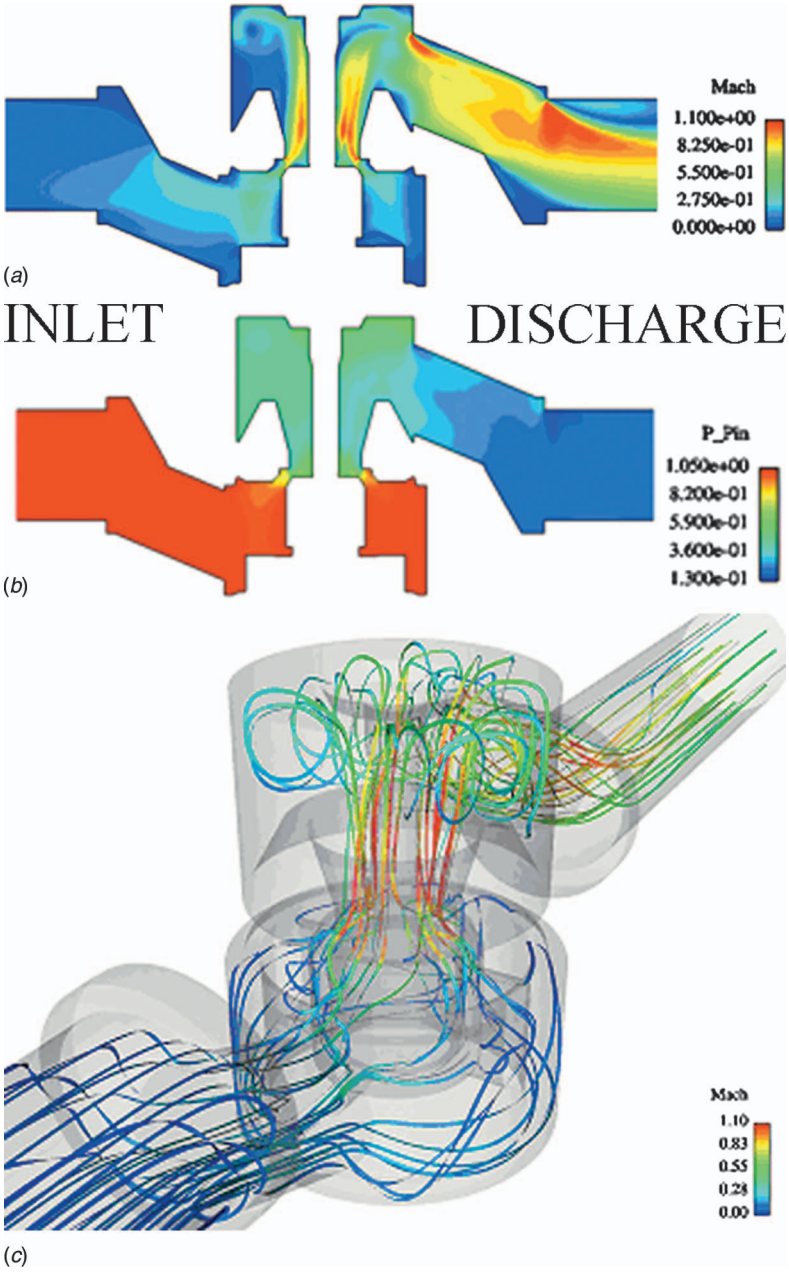

Fig. 5 Plots of (*a*) streamlines through the valve housing colored with Mach number illustrating the large recirculation region, (*b*) pressure contours, and (*c*) Mach number contours on the symmetry plane

the valve housing. The flow turns supersonic as it rapidly accelerates through the valve seat region, which has a very narrow clearance. The flow emerges from the valve seat region like a jet into the upper housing where it turns into a feed channel that exits into the discharge pipe. The Mach number distribution also reveals flow expansion in both the discharge feed channel and the discharge duct. These observations are corroborated by the pressure distribution along the plane of symmetry in Fig. 5(*b*). It is clear from the pressure distribution that most of the pressure losses accrue in the seat/throat region of the dome pressure regulator where the flow experiences a sharp acceleration. Furthermore, the pressure distribution also shows a pressure gradient in the upper housing, indicating that flow is being forced tangentially towards the discharge duct. The pressure distribution on the poppet (Fig. 5(*b*)) also shows a region of high pressure on the shaft just downstream of the throat region. This is primarily from flow mixing due to the fact that multiple feed channels located at different azimuthal locations introduce flow into the lower housing. Furthermore, the stream traces reveal a complex flow pattern with strong recirculation in the upper housing, indicating that the flow does not transition smoothly from the valve assembly into the discharge piping (Fig. 5(*c*)).

The unsteady modeling effort was geared towards understanding an observed "chatter" of the poppet-shaft assembly during operation of the valve. A transient analysis with a fixed poppet setting was performed with a time step of 3×10^{-7} s and captured a dominant oscillation of the flow with a frequency of about 4 KHz. This frequency was detected in pressure fluctuations across seven probe points located on the poppet surface. Through flow visualization of the transient simulations, an axial mode was identified as the source of the instability, which manifested itself

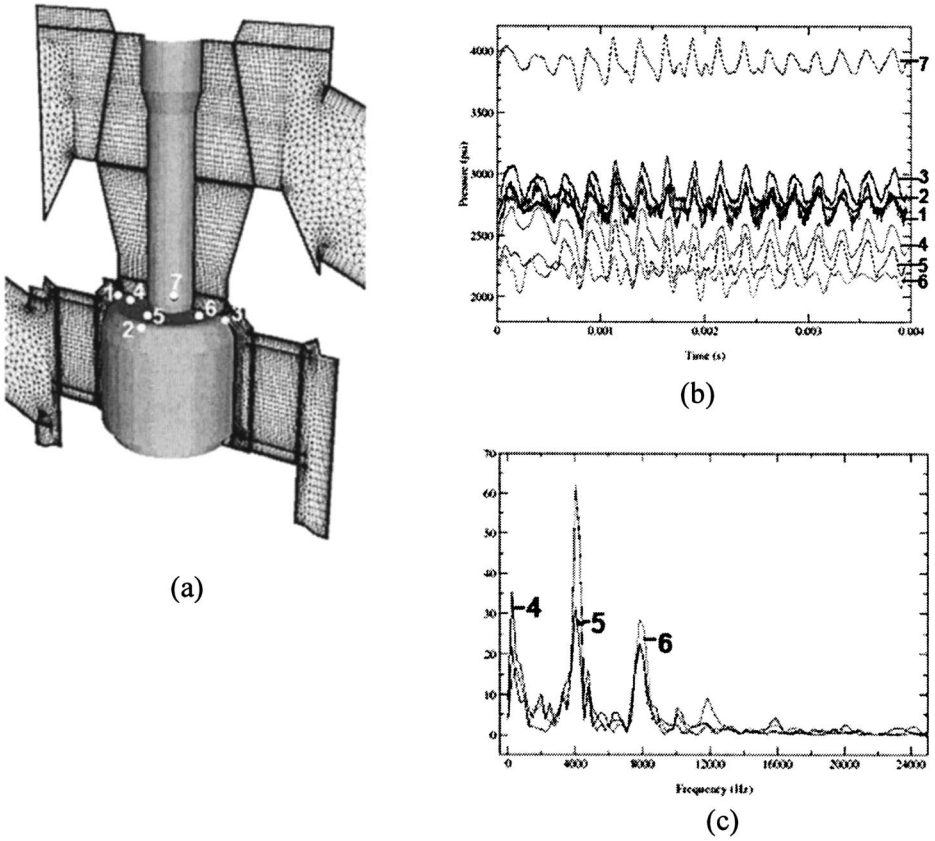

Fig. 6 Plots of the transient solution showing (*a*) location of probe points on the poppet, (*b*) pressure history for the seven points, and (*c*) frequency spectrum indicating the dominant instability modes

as a periodic pulsation of a jet-like structure through the throat coupled with tangential modes in the discharge portion of the flow. Pressure histories were recorded at seven different points on the poppet close to the throat (Fig. 6(*a*)). The recording tabs were mostly distributed along the base of the throat on the poppet. Three pairs of tabs were located on the base (on the periphery and midway on radial lines running from the shaft to the outer edges) aligned with the direction of the feeding channels leading into the inner housing. One of the taps was located on the shaft at the location where the steady-state simulations indicated a localized region of high pressure. All seven probes show an almost identical periodic variation in pressure. The variations are strongest at the three points on the periphery of the base region (1, 2, and 3) that also coincides with the throat region of the valve. Fourier decomposition of the histories indicates a fundamental mode corresponding to a frequency of 4043 Hz (see Figs. 6(*b*) and 6(*c*)). Furthermore, Fig. 6(*c*) shows significant energy associated with the first harmonic. More importantly, the Fourier decomposition also revealed an active low-frequency mode of approximately 250 Hz. This mode could be structurally significant since it could excite poppet vibration modes leading to significant noise and couple with structural modes leading to potential structural failure. Further structural analysis of this valve would be required to determine if this frequency might pose a structural coupling risk.

Simulations of the 10 in. Cryogenic Valve. A series of simulations was carried out for a 10 in. cryogenic control valve. In these simulations, the multi-element CRUNCH CFD® framework was used to estimate the valve flow coefficient as a function of the plug setting. The aim of this exercise was to compare the valve flow coefficient curve to experimental data and simulations performed at SSC [9]. The valve configuration that was used for the numerical tests is shown in Fig. 7. The plug/seat portion of the valve exactly matches the configuration used in the experimental test bed. However, in the simulations the entire valve geometry was approximated to be axisymmetric. For the purpose of simulating this cryogenic control valve, this is a valid approximation since the discharge and inlet ducts are located away from the plug/seat region where most losses occur and there few little three-dimensional flow distortions affecting the plug/seat region. A series of simulations as performed on this valve configuration pertaining to six different valve settings ranging from 8.6% open to 75% open. Liquid nitrogen was the working fluid in the control valve for all the simulations with operating conditions 162 R and 3000 psi. The density of liquid nitrogen under the operating conditions was modeled as a function of the local pressure and the valve operated with a mass flow rate that ranged from 50 to 300 lbs/s. For the sake of the simulations, the temperature was assumed to be constant in the control valve and the liquid nitrogen was modeled as a real fluid with variable density and molecular viscosity.

A series of six simulations was performed with valve settings at 8.6%, 45%, 50%, 65%, 70%, and 75% open. The mass flow rates utilized for these simulations were 50, 100, 150, 150, 300, and 300 lbm/s, respectively. The 8.6% stroke setting was primarily chosen because it represented the lowest stroke setting for which experimental/test data were available. The large pressure gradients in the seat region for this case have the potential to significantly impact the flow coefficient due to effects of real fluid property variation. A series of hexahedral grids consisting of 60,000 cells as utilized in the simulations. The simulations were run on a parallel PC-cluster (16 processors) to provide rapid turnaround times consistent with those required to support testing (5–6 h). The

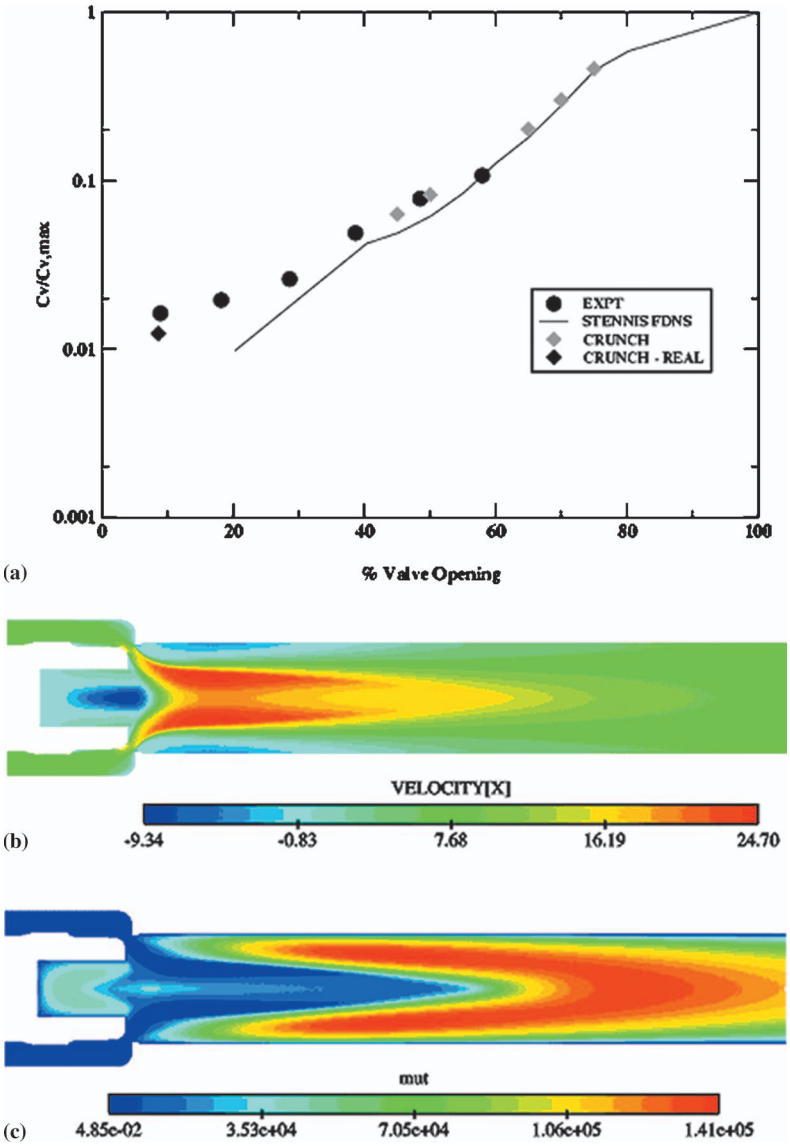

Fig. 7 10 in. cryogenic valve performance

numerical simulations were carried out using the formulation described in the previous section with a wall function procedure in the vicinity of viscous boundaries specified in conjunction with the high-Re form of the standard $k-\varepsilon$ equation. The boundary conditions were specified by fixing flow conditions at the inflow, except for pressure, which adjusts itself to sustain the prescribed mass flow and specifying the back pressure at the outflow boundary. The simulation results are summarized in Fig. 7(*a*), which depicts comparisons of the valve flow coefficient as a function of valve position with experimental observations and calculations performed at SSC. The valve flow coefficient C_v is defined as the ratio of the integrated mass flow rate (lbm/s) at the inlet to the square root of the pressure differential (psia) required to drive the flow through the control valve. The CRUNCH CFD® simulations show a monotonically increasing valve flow coefficient curve with valve opening, consistent with both experimental observations and Stennis calculations. Furthermore, the results are in excellent agreement with experimental measurements and the grid-independent values of C_v computed at Stennis Space Center [9] both in predicting the slope of the curve and the transition in slope at the lower valve settings. Close agreement can be seen between the CRUNCH simulations and the experimental data even at the 8.6% setting where real fluid effects start to dominate, in spite of the exaggerated log scale. The CFD simulations also reveal finer details of the flow physics and help in identifying regions in the valve configurations associated with pressure losses and the mechanics of flow control in the valve system. Figure 7(*b*) shows a sample axial velocity distribution for a plug setting of 75% open. The flow accelerates as it negotiates the seat region and subsequently turns along the nose of the plug towards the center of the duct aft of the seat region. The sharp turning of the flow leads to the formation of large zones of flow separation at the outer walls downstream of the seat region. In addition, stable recirculation patterns set up in the base region of the plug for all valve settings. The flow turning and recirculation patterns are further corroborated by the distribution of turbulent viscosity (Fig. 7(*c*)) that is indicative of vorticity and diffusion of the velocity core in the duct downstream of the seat/plug region.

Simulations of a Cavitating Venturi With Liquid Oxygen. The venturi is primarily used as flow control device in various applications at SSC primarily because of the insensitivity of mass flow rates to downstream pressure fluctuations. However, the cavitation-based mechanism responsible for this behavior is poorly understood. The problem is exacerbated in liquid rocket engine tests due to the use of cryogenic fluids that typically oper-

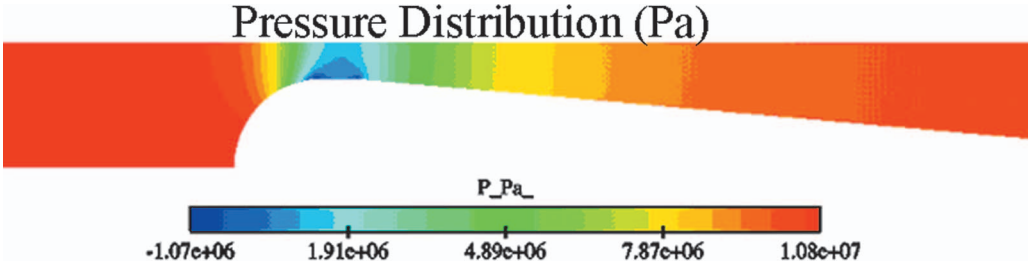

Fig. 8 Single phase pressure distribution for the venturi operating with liquid oxygen

ate at elevated temperatures relative to their critical temperatures. In such flow regimes the vapor pressure and the fluid density vary sharply with temperature, and thermodynamic effects have to be taken into consideration. The cavitating venturi under investigation has a throat diameter of 2.94 in. and an inlet diameter of 10 in. with a sharply contoured contraction region and a long divergent section. The upstream conditions for this case consisted of a freestream velocity of 11.5 m/s and freestream density of 1132.12 kg/m^3 at a temperature of 92 K. The vapor pressure at the freestream temperature was 0.1219 MPa. The simulation is initiated by first obtaining a converged single-phase solution at an elevated exit back pressure. The single-phase pressure distribution is shown in Fig. 8 where the minimum pressure is found at the throat of the venturi due to flow acceleration from area contraction. Cavitation is triggered in this case by lowering the specified pressure at the exit plane. The initial formation of the cavitation zone starts up at the throat of the venturi where the local pressure recedes below the vapor pressure at the freestream temperature. Since the time scales for phase change are extremely small, heat is drawn from a thin film of liquid surrounding the cavity, resulting in an evaporative cooling effect. This in turn lowers the temperature in the cavity and the liquid surrounding the cavity, leading to a local depression in the vapor pressure and, consequently, retardation of the cavity formation process. In general, these thermodynamic effects of cavitation, i.e., pressure and temperature depression, are a function of fluid/thermodynamic properties as well as flow geometry and head characteristic. As these complex heat and mass transfer mechanisms evolve, the cavity migrates downstream from the inception region, forming a vaporous mixture that engulfs the entire throat region of the venturi (Fig. 9).

Two important observations are noted at this point: First, the vapor cloud that covers the throat region is highly diffuse, forming a frothy-like cavity with the bulk of the void fraction in the cavity around 0.5, except close to the walls where the void fraction is closer to 1.0. Second, it should be reiterated that the diffuse cavity covers the entire cross section of the venturi just downstream of the throat. The presence of a low amount of vapor void fraction throughout the cross section of the venturi is responsible for a sharp decrease in the local speed of sound in the venturi near the throat region. Therefore, any pressure fluctuations downstream of the venturi would not directly translate into mass flow corrections at the inlet to the venturi, making the venturi an ideal device to meter propellants in liquid rocket engine test rigs. This effect can be seen in Fig. 10(*a*). A high-pressure region builds up in the closure region of the cavity that closely resembles a "shock structure" in conventional compressible flow. Pressure waves are seen shedding aft of the cavity region in the downstream divergent section due to unsteadiness associated with the cavity. There is a pressure spike visible upstream of the throat region due to the reconversion of the vapor in the throat region of the venturi to liquid. This reconversion process is primarily due to the thermodynamic effects of cavitation in cryogenic fluids that were discussed above.

The temperature distribution shown in Fig. 10(*b*) indicates the importance of accurately modeling the thermodynamics in the case of the cavitating venturi. Unlike cavitation in conventional liquids such as water, where thermodynamic effects are generally neglected, there is a substantial deviation in temperature (over 10 K) in certain regions of the cavity from the temperature in the bulk liquid. Moreover, as mentioned earlier, the cavitation dynamics are substantially altered by the reduction in temperature close to the throat region leading to the depression in vapor pressure and reconversion of vapor back to liquid.

Summary

In this paper, a wide array of valve systems were simulated utilizing a multi-element unstructured framework (CRUNCH CFD®) with embedded submodels for cryogenic fluids and cavitation. The valve systems represented varying degrees of structural and physical complexity and covered major regimes of flow physics. The multi-element framework provided flexibility in generating meshes for complicated geometries and in resolving and identifying instabilities associated with the operation of the valve systems. Furthermore, the "real fluids and cavitation" submodels permitted simulation of physical phenomena pertaining to multiphase flow dynamics dominant in the operation of venturi-type flow control elements. CRUNCH CFD® also proved to be an efficient tool for rapid turnaround of complex solutions. This ef-

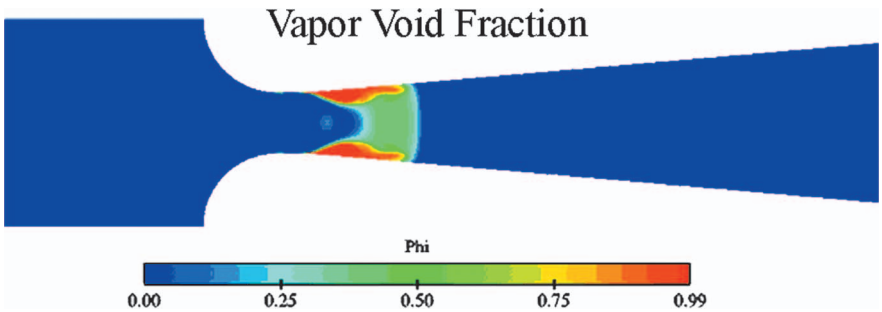

Fig. 9 Vapor void fraction in cavitating venturi indicating vapor throughout the cross section of the venturi

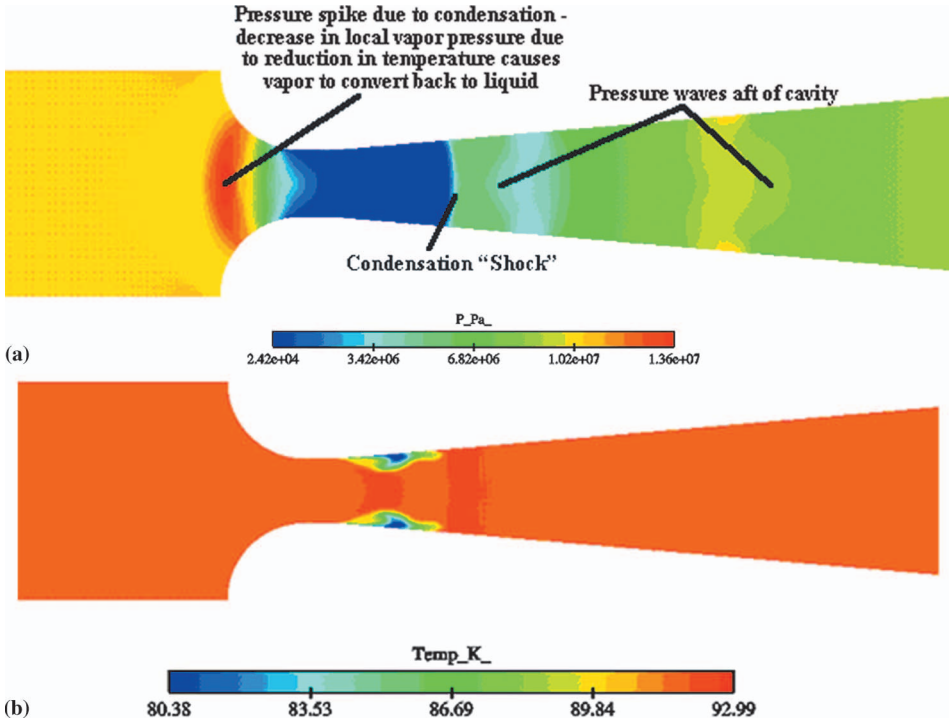

Fig. 10 Pressure and temperature distribution in the cavitating venturi

ficiency was possible primarily because the numerical scheme permits large time steps, enhanced convergence, and robust parallel execution of the flow solver.

Steady-state simulations were carried out for the operation of a 10 in. cryogenic valve at different valve settings. The flow coefficient characteristics in this case were in very good agreement with both experimental results and calculations carried out at NASA SSC. The simulations were also able to provide details of pressure losses in the seat region and give an account of the secondary flow regions that set up aft of the seat region at the wall and in the base region of the plug.

Analyses for a pressure regulator control valve were carried out with the multi-element philosophy. The pressure regulator valve is structurally very difficult to grid with conventional CFD multiblock structured (purely hexahedral) and unstructured (tetrahedral) methodologies. A multi-element grid consisting of hexahedral, tetrahedral, prismatic, and pyramidal elements was generated for the pressure regulator valve. The hexahedral cells were used to resolve the boundary layers in the feed channels, inlet and discharge ducts, and gradients in the narrow clearances around the poppet. Tetrahedral and prismatic cells were mostly used in the valve housing and the buffer regions between the inlet/discharge ducts and the valve housing. The interfacing between the tetrahedral zones and the hexahedral blocks was provided by pyramidal cells. In this manner, the cell topology was tailored to the structural complexities of the valve body, leading to a well-resolved high-quality grid.

Both steady and unsteady simulations of the pressure regulator valve were performed on the multi-element grid. The steady simulations revealed a rich variety of flow phenomena over a multitude of length scales. This included a jet-like penetration of the flow through the throat region, secondary flow patterns in the feed channels and corner regions of the valve housing, and significant flow expansion in the buffer channels feeding the discharge duct and in the discharge duct. Furthermore, flow from the throat region of the valve impinges on the upper wall of the valve assembly and forms a dominant recirculation pattern before discharging through the exhaust ducting. Our transient analyses were performed with a fixed poppet setting and captured a dominant chatter with a 4 KHz frequency. This frequency was detected across seven different probe points located at different parts of the poppet. Through flow visualization of the simulations we were able to identify an axial mode as the source of the instability. The instability was generated due to tangential discharge of flow from the far end of the upper housing that was periodically cutting off the axial flow through the throat region. A closer investigation of the frequency content of the instability modes revealed most of the energy is associated with the fundamental frequency 4043 Hz and its first harmonic. Furthermore, there was significant energy associated with a low-frequency mode (around 250 Hz). This was an important finding since this mode can potentially induce structural vibrations.

Simulations were also carried out for a LOX cavitating venturi valve utilizing the cavitation submodel with cryogenic fluids capability. The simulations demonstrated that cavitation inception initiates in the throat region where the local pressure falls below the saturation vapor pressure corresponding to the bulk temperature. As the simulation evolves, the thermodynamic effects of cavitation become more pronounced, leading to evaporative cooling near the cavity region. This results in a temperature depression, and consequently a depression in the saturation pressure at the leading edge of the cavity. These results are consistent with the findings of research carried out by Stahl and Stepanoff [10], Ruggeri and Moore [11], Hord [12], and Brennen [13]. Furthermore, our simulations reveal a vaporous mixture in the entire venturi cross section just downstream of the throat. The vapor fraction through most of the cavity is less than 0.5, indicating a highly diffused cavity. Sarosdy and Acosta [14] have made similar observations of investigating of frothy, diffusive cavities consisting of many bubbles with Freon 113. Moreover, the mass flow through the venturi gets choked due to the presence of the vapor cloud near the throat of the venturi. Any variation in back pressure is not propagated to the inlet due to a substantial reduction in speed of sound through the vaporous cavity. The computed discharge coefficient of 0.96 compares reasonably well with the experimentally observed discharge coefficient of 0.95.

Acknowledgment

We acknowledge funding for this work through an SBIR Program, Contract No. NNS04AA08C funded by NASA Stennis Flight Center. Dr. Peter Sulyma is the technical monitor and his support is much appreciated.

Nomenclature

- CFD = computational fluid dynamics
- c_L, c_g = isothermal speed of sound in the liquid phase, gas phase
- c_m = speed of sound in the two-phase mixture
- C_v = flow coefficient defined as the ratio of the integrated mass flow and the square root of pressure differential
- D_v = viscous fluxes
- E, F, G = inviscid flux vectors
- ε = turbulent dissipation rate
- h_m = mixture enthalpy
- h_{fg} = enthalpy change due to phase change
- k = turbulent kinetic energy
- m_t = rate of vapor mass generation
- $m_t \times h_{fg}$ = source term for the energy equation
- $\phi_g \phi_L$ = void fraction of gas, liquid
- p = pressure
- ρ_m = mixture density
- ρ_g, ρ_L = physical material densities of the gas and liquid phases
- Q = vector of dependent variables
- Q_v = vector of primitive variables
- S = source term
- SSC = Stennis Space Center
- T_{sat} = saturation temperature
- u, v, w = velocity components along coordinate directions
- Γ = preconditioning matrix

References

[1] Daines, R. L., Woods, J. L., and Sulyma, P. R., 2002, "Progress in Valve Modeling at Stennis Space Center," Penn State Propulsion Engineering Research Center Fourteenth Annual Symposium, State College, PA.
[2] Hosangadi, A., and Ahuja, V., 2003, "A Generalized Multi-Phase Framework For Modeling Unsteady Cavitation Dynamics And Thermal Effects," AIAA Paper No. AIAA-2003-4000, 33rd AIAA Fluid Dynamics Conference, Orlando, FL.
[3] Ahuja, V., Shipman, J. D., Arunajatesan, S., and Hosangadi, A., 2003, "Multi-Element Unstructured Methodology for Analysis of Turbomachinery Systems," J. Propul. Power, **19**(5), pp. 945–952.
[4] Hosangadi, A., Lee, R. A., York, B. J., Sinha, N., and Dash, S. M., 1996, "Upwind Unstructured Scheme for Three-Dimensional Combusting Flows," J. Propul. Power, **12**(3), pp. 494–503.
[5] Hosangadi, A., Lee, R. A., Cavallo, P. A., Sinha, N., and York, B. J., 1998, "Hybrid, Viscous, Unstructured Mesh Solver for Propulsive Applications," AIAA-98-3153, AIAA 34th JPC, Cleveland, OH.
[6] Cavallo, P. A., and Baker, T., 2000, "Efficient Delaunay-Based Solution Adaptation for Three-Dimensional Unstructured Meshes," AIAA Paper No. 2000-0809, 38th AIAA Aerospace Sciences Meeting, Reno, NV.
[7] Ahuja, V., Hosangadi, A., and Shipman, J., 2004, "Multi-Element Unstructured Analyses of Complex Valve Systems," 52nd JPM/1st LPS Meeting, Las Vegas, NV.
[8] Shipman, J., Hosangadi, A., and Ahuja, V., 2004, "Unsteady Analyses of Valve Systems in Rocket Engine Testing Environments," AIAA Paper No. AIAA-2004-3663, 40th AIAA/ASME/SAE/ASEE Joint Propulsion Conference and Exhibit, Fort Lauderdale, FL.
[9] Daines, R. L., Woods, J. L., and Sulyma, P. R., 2003, "Computation Analysis of Cryogenic Flow Through a Control Valve," FEDSM2003-45120 4th ASME/JSME Joint Fluids Engineering Conference, Honolulu, HI.
[10] Stahl, H. A., and Stepanoff, A. J., 1956, "Thermodynamic Aspects of Cavitation in Centrifugal Pumps," ASME J. Basic Eng., **78**, pp. 1691–1693.
[11] Ruggeri, S. R., and Moore, R. D., 1969, "Method For Prediction of Pump Cavitation Performance for Various Liquids, Liquid Temperature, and Rotation Speeds," NASA TND-5292.
[12] Hord, J., 1973, "Cavitation in Liquid Cryogens," NASA CR-2156.
[13] Brennen, C. E., 1973, "The Dynamic Behavior and Compliance of a Stream of Cavitating Bubbles," ASME J. Fluids Eng., **95**, pp. 533–542.
[14] Sarosdy, L. R., and Acosta, A. J., 1960, "Note on Observations of Cavitation in Different Fluids," Paper No. 60-WA-83, ASME Winter Annual Meeting, New York.

Modeling of the Onset of Gas Entrainment From a Stratified Two-Phase Region Through Branches on a Curved Surface

A. F. Andaleeb

I. Hassan[1]
e-mail: hassan@me.concordia.ca

W. Saleh

T. Ahmad

Department of Mechanical and Industrial Engineering,
Concordia University,
Montreal, Quebec, H3G 1M8, Canada

The present investigation is focused on the onset phenomena from a stratified two-phase region through a single branch located on a semi-circular wall, resembling a circular reservoir of a CANDU header-feeder configuration. Two different models have been developed, over the whole range of branch Froude number, to predict the critical height at the onset of gas-entrainment. The results showed that there is both a maximum and a minimum physical limit of prediction, which depends on the branch size and configuration. Also, at a distinct range of Froude numbers within the physical limits, the predicted values of both models collaborated to the same values. The critical height corresponding to the onset of gas entrainment was found to be a function of the branch orientation and Froude number. Three different experimental data sets at branch orientation angles of zero, 45, and 90 degrees were used to validate the present models. A good concurrence was illustrated between the experimental and theoretical values.
[DOI: 10.1115/1.2201614]

1 Introduction

The implication of modern industrial applications involving two-phase discharge from a stratified region through single or multiple branches has developed considerably in the past two decades. Examples of these applications include two-phase distribution headers where a certain incoming stream is fed into a large header divided into a number of discharging streams, such as in shell-and-tube heat exchangers, the flow through small breaks in horizontal cooling channels of nuclear reactors during loss-of-coolant accidents, and the flow distribution in the header-feeder systems of CANDU (Canada Deuterium and Uranium) reactors during accident scenarios. For the design and performance predictions of such systems, it is essential to determine the mass flow rate and the quality of the discharging streams. The development of a theoretical correlation for the critical height at the onset of gas entrainment during single and multiple discharges is therefore necessary for the prediction of such parameters, as it remains a prerequisite to determining the mass flow rate and quality of discharging flow.

It was concluded by Zuber [1] that for single discharge from a stratified flow channel, there are two types of onset phenomena, depending on the location of the horizontal gas-liquid interface relative to the branch. For the case where the interface is located above the branch, at a certain critical height, gas will begin to entrain the branch into a predominantly liquid flow (onset of gas entrainment (OGE)). However, if the horizontal gas-liquid interface is located below the branch, at a certain critical height, liquid will begin to entrain the branch into a predominantly gas flow (onset of liquid entrainment (OLE)). In regard to these phenomena, Zuber went on to develop theoretical relationships for the determination of the critical height, depending on the type of phenomena and geometrical layout of the system. Recently in literature, other researchers presented experimental data and theoretical correlations in regard to the onset phenomena (OGE, OLE), along with two-phase mass flow rates and quality between the two onsets during discharge from a stratified region (e.g. [2–9]). As an example, for the prediction of the critical height at the onset of gas entrainment, for the case of single discharge from a side branch, Smoglie and Reimann [2] experimentally developed the following correlation as a function of Froude number and branch diameter:

$$\frac{H_{\mathrm{OGE}}}{d} = 0.681\ \mathrm{Fr}^{0.4} \tag{1}$$

where

$$\mathrm{Fr} = \frac{\mathrm{v}_d}{\sqrt{gd\dfrac{\Delta\rho}{\rho_1}}}$$

Parrott et al. [6] also experimentally investigated the onset of gas entrainment during single discharge from a large, stratified two-phase region. Using the least-squares method, they developed the following correlation between the critical height at the onset of gas entrainment and the corresponding Froude number:

$$\frac{H_{\mathrm{OGE}}}{d} = 0.425\ \mathrm{Fr}^{0.529} \quad \frac{H_{\mathrm{OGE}}}{d} \le 1.15$$

$$\frac{H_{\mathrm{OGE}}}{d} = 0.508\ \mathrm{Fr}^{0.435} \quad \frac{H_{\mathrm{OGE}}}{d} \ge 1.15 \tag{2}$$

Hassan et al. [9] further investigated the single side discharge from a large, stratified two-phase region through small branches and developed a similar correlation

$$\frac{H_{\mathrm{OGE}}}{d} = 0.57\ \mathrm{Fr}^{0.4} \tag{3}$$

Recently, Ahmed et al. [10] theoretically determined the OGE during single discharge from a stratified, two-phase region through a side branch with a finite diameter. Two different models have been developed, a simplified point-sink model and a three-dimensional finite-branch model. The simplified point-sink model is given by

[1]Author to whom correspondence should be addressed.

Contributed by the Fluids Engineering Division of ASME for publication in the JOURNAL OF FLUIDS ENGINEERING. Manuscript received March 17, 2004; final manuscript received April 25, 2005.

$$\frac{H_{OGE}}{d} = \mathrm{Fr}^{0.4}\left[\frac{1}{2}\left(\frac{\Delta\rho}{\rho_1}\right)^{0.2} + \frac{1}{8}\left(\frac{\rho_1}{\Delta\rho}\right)^{0.8}\right] \tag{4}$$

and the finite-branch model is given by the following two equations:

$$I_1[h^*]I_2[h^*] = -\left(\frac{1}{\mathrm{Fr}}\right)^2\left(\frac{\rho_1}{2\Delta\rho}\right) \tag{5}$$

The critical height at the onset of gas entrainment can then be written as

$$\frac{H_{OGE}}{d} = \frac{h^*}{2} + \frac{\mathrm{Fr}^2}{2}\{I_1[h^*]\}^2 \tag{6}$$

where

$$I_1[h^*] = -2\int_0^\infty\int_0^\infty \frac{\cos(\beta h^*)}{\pi^2\lambda\sqrt{\lambda^2+\beta^2}} \times\left[\int_{-1}^{1}\sin(\lambda\sqrt{1-y^{*2}})\cos(\beta y^*)dy^*\right]d\lambda d\beta + 2\int_0^\infty\int_0^\infty \frac{\sin(\beta h^*)}{\sqrt{\lambda^2+\beta^2}}\left[\int_{-1}^{1}\sin(\lambda\sqrt{1-y^{*2}}) \times\sin(\beta y^*)dy^*\right]d\lambda d\beta \tag{7}$$

and

$$I_2[h^*] = -2\int_0^\infty\int_0^\infty \frac{\cos(\beta h^*)}{\pi^2\lambda\sqrt{\lambda^2+\beta^2}} \times\left[\int_{-1}^{1}\sin(\lambda\sqrt{1-y^{*2}})\cos(\beta y^*)dy^*\right]d\lambda d\beta - 2\int_0^\infty\int_0^\infty \frac{\sin(\beta h^*)}{\sqrt{\lambda^2+\beta^2}}\left[\int_{-1}^{1}\sin(\lambda\sqrt{1-y^{*2}}) \times\sin(\beta y^*)dy^*\right]d\lambda d\beta \tag{8}$$

For a given Froude number, h^* is first calculated from Eq. (5). Then, based on the values of h^* and Fr, the critical height is determined using Eq. (6). Ahmed et al. [10] have determined the values of $I_1[h^*]$ and $I_2[h^*]$ using numerical integration techniques as indicated by Stround [11] and Gradshteyn and Ryzhik [12].

The objective of the previous authors, regarding the onset phenomena, was to find correlations of the critical height with respect to a corresponding Froude number at different branch configurations for single or multiple discharges. However, most of these researchers' investigations were strictly related to side discharge from a flat or inclined flat wall configuration. The present investigation is related to the OGE for single discharge from a curved, semi-circular wall configuration. Dimensions of the semi-circular surface and branches were selected to be in direct proportion to those of the CANDU header-feeder system. To the authors' knowledge, there has been no previous theoretical investigation performed regarding single or multiple discharge from a branch located on a curved surface, for the branch diameter to main channel ratios proposed in the present study. Three different single discharge branch configurations from a cylindrical reservoir are considered in the present analysis. A horizontally mounted branch (0 deg), a branch mounted at 45 deg from the horizontal, and a vertical bottom branch (90 deg). A simple point-sink model is proposed for all configurations for predicting the onset of gas entrainment, and a more accurate finite-branch model is developed for each branch orientation, taking into account the branch size. It should also be noted that the term "gas entrainment" is not strictly applied to the entrainment of a gas into a predominantly liquid flow. It can also be applied to any two fluids of different densities, where the lighter fluid is entrained into the heavier fluid flow.

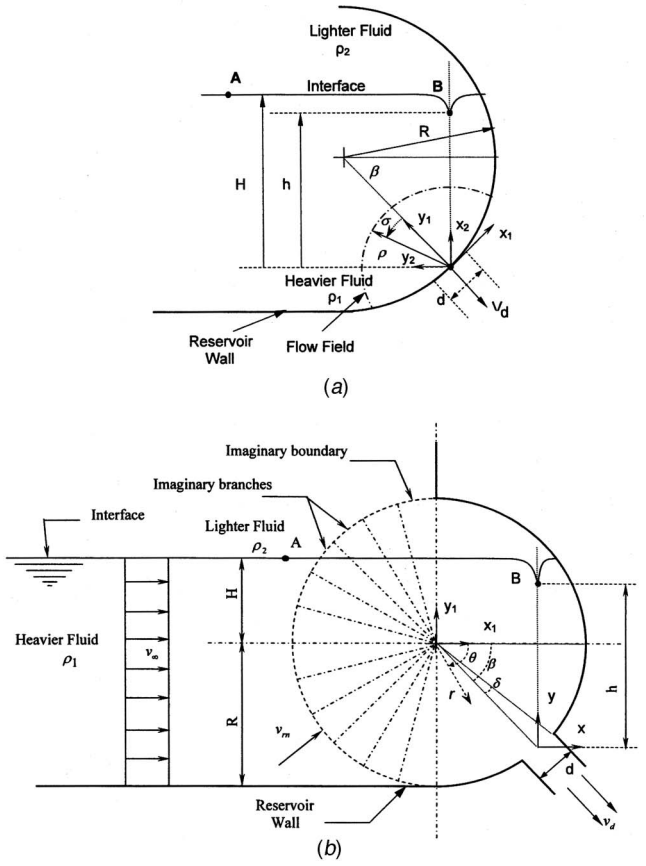

Fig. 1 (*a*) Geometry and the coordinate system in the point-sink analysis and (*b*) geometry and the coordinate system in the finite-branch analysis (β=45 deg)

2 Theoretical Analysis

The configuration considered in the present analysis is shown in Fig. 1(*a*), and consists of stratified layers of two immiscible fluids, with densities ρ_1 and ρ_2, contained in a large semi-circular pipe (reservoir) under pressure P, with equilibrium of the interface being controlled by a balance of inertia and gravity. In the present analysis, the surface tension is ignored and the liquid flow is considered inviscid, irrotational, incompressible, and quasi-steady. Therefore, the problem is governed by a single physical parameter: the Froude number. Quasi-steady-potential flow is assumed in the heavier fluid, while the lighter fluid is considered stagnant.

2.1 Criterion of the Onset of Gas Entrainment. Hassan et al. [9] showed that during single discharge from a stratified two-phase region through a side branch, if the interface level (H) is well above the branch, the branch will be flowing liquid only, and the interface will be flat. As H is lowered and approaches H_{OGE}, a "dimple" begins to form in the interface. This dimple depression becomes more pronounced and conelike until the bottom of the cone suddenly extends to the branch; this is the onset of gas entrainment. As H is reduced below H_{OGE}, the branch will be flowing two-phase mixture. The objective of the present paper is to simulate this phenomenon; the criterion used in the prediction of the onset of gas entrainment is the equality between the acceleration of the liquid above the branch and the acceleration of gravity,

at point B, and has first been proposed by Ahmed et al. [10]. Any further increase of liquid acceleration at point B above the acceleration of gravity will cause instability to the flow. This instability results in a catastrophic change in the free surface shape, which quickly extends the formed dip to the branch exit. This criterion is based on the study made by Taylor [13] to determine the onset of instability of inviscid liquid surfaces accelerated vertically.

Taylor stated that the initial stability of the upper surface of a liquid would pass over into instability if the liquid were given a downward acceleration greater than that of gravity. Moreover, when ρ_1 is much greater than ρ_2, Taylor reported in his analysis that the amplitude of a two-dimensional disturbance accelerated downwards at acceleration a is given by

$$\frac{\eta}{\eta_o} = \cosh\left\{ \sqrt{\frac{4\pi s(a-g)(\rho_1-\rho_2)}{\lambda a(\rho_1+\rho_2)}} \right\} \tag{9}$$

where η/η_o is the ratio of the amplitude of the disturbance at any time to its initial value, λ is the wavelength of the disturbance amplitude, s is the downward distance of the moving surface, a is the downward acceleration of the liquid surface, and g is the acceleration of gravity. Based on this equation, it is clear that if the acceleration a of the fluid surface is greater than the acceleration of gravity g the fluid surface would be unstable. Lewis [14] also investigated experimentally the instability of various liquids accelerating vertically downward. The instability criterion observed under a wide variety of experimental conditions has been analyzed, and good agreement between experiment and the theory of Taylor, mentioned above, was found.

2.2 Equilibrium of the Interface. In reference to Fig. 1(a), we can apply the Bernoulli equation on the interface between point A and point B:

$$p_A + \tfrac{1}{2}\rho_1 v_A^2 + \rho_1 g H = p_B + \tfrac{1}{2}\rho_1 v_B^2 + \rho_1 g h \tag{10}$$

Considering $v_A << v_B$, Eq. (10) becomes

$$p_A + \rho_1 g H = p_B + \tfrac{1}{2}\rho_1 v_B^2 + \rho_1 g h \tag{11}$$

And for the lighter fluid region, which is considered stagnant along the same streamline, the Bernoulli equation becomes

$$p_A + \rho_2 g H = p_B + \rho_2 g h \tag{12}$$

From Eqs. (11) and (12), the velocity of the liquid at point B is given as

$$v_B^2 = 2g\frac{\Delta\rho}{\rho_1}[H-h] \tag{13}$$

2.3 Point Sink Analysis. In this analysis, a single side branch installed on a semi-circular wall, shown in Fig. 1(a), is simulated as a point sink, with strength Q. The surface area S of the flow is a hemisphere intersected by a cylinder. The branch is located at the center of this flow field, with

$$v_\rho = \frac{\partial\Phi}{\partial\rho} = \frac{Q}{S} \tag{14}$$

where Φ is the potential function, ρ is the radius of the flow field given by $\rho=\sqrt{x_1^2+y_1^2+z_1^2}$, and S is the surface area of the flow field given by

$$S = 2\pi\rho^2 - 4\rho^2\int_{\cos^{-1}(\rho/D)}^{\pi/2}\sqrt{1-\left(\frac{D}{\rho}\right)^2\cos^2\sigma}\,d\sigma \tag{15}$$

The principle used for the prediction of the onset of gas entrainment is the equality between the acceleration of the liquid above the branch, and the acceleration of gravity g at point B, as given by Johnson [15]. Instability of the flow is caused by an increase of liquid acceleration in excess of g. This principle is given as

$$[a_B] = -g \tag{16}$$

where

$$[a_B] = \left.\frac{\partial\Phi}{\partial x_2}\right|_B \left.\frac{\partial^2\Phi}{\partial x_2^2}\right|_B \tag{17}$$

Although, the potential function Φ of this flow is not known, the derivatives in Eq. (17) can be determined using Eqs. (14) and (15) and the coordinate transformation properties, summarized as follows:

$$\frac{\partial\Phi}{\partial r} = \frac{Q}{S} = \frac{Q}{2\pi\rho^2 - 4\rho^4\int_{\cos^{-1}(\rho/D)}^{\pi/2}\sqrt{1-\left(\frac{D}{\rho}\right)^2\cos^2\sigma}\,d\sigma}. \tag{18}$$

With $\rho|_B=h$ at point B as shown in Fig. 1(a), Eq. (18) becomes

$$\left.\frac{\partial\Phi}{\partial x_2}\right|_B = \left.\frac{\partial\Phi}{\partial\rho}\right|_{\rho=h} = \frac{Q}{2D^2h^{*2}I_1(h^*)} \tag{19}$$

Here h^* is a dimensionless height ($h/(D)$) and $I_1(h^*)$ is given by

$$I_1(h^*) = \pi - 2\int_{\cos^{-1}h}^{\pi/2}\sqrt{1-\left(\frac{1}{h^*}\right)^2\cos^2\sigma}\,d\sigma \tag{20}$$

By rotating the coordinates an angle β from (x_1,y_1) to (x_2,y_2), as shown in Fig. 1(a), and by using the coordinate transformation properties, the second derivative of Φ in Eq. (17) is determined as

$$\left.\frac{\partial^2\Phi}{\partial x_2^2}\right|_B = \frac{-Q[h^{*2}I_1(h^*) - I_2(h^*)]}{D^3h^{*5}I_1^2(h^*)} \tag{21}$$

where $I_2(h^*)$ is defined by

$$I_2(h^*) = \int_{\cos^{-1}h^*}^{\pi/2}\frac{\cos^2\sigma}{\sqrt{1-\left(\frac{1}{h^*}\right)^2\cos^2\sigma}}d\sigma \tag{22}$$

By substituting Eqs. (19) and (21) into (17), we get

$$Q^2 = \frac{2gD^5h^{*7}I_1^3(h^*)}{h^{*2}I_1(h^*) - I_2(h^*)} \tag{23}$$

Knowing the value of Q or Fr, the corresponding value for h^* is calculated by solving Eq. (23). A computer code was developed to numerically compute the values of I_1, I_2 and h^* for each known value of Q. Based on the value of h^*, the critical height corresponding to the onset of gas entrainment, H_{OGE}, is determined by substituting Eq. (19) with $(\partial\Phi/\partial x_2)|_B = Q/[2D^2h^{*2}I_1(h^*)]=v_B$ into Eq. (13) to give

$$\frac{H_{\mathrm{OGE}}}{d} = \frac{D}{d}h^* + \frac{Fr^2gDh^{*3}I_1(h^*)}{4v_d^2[h^{*2}I_1(h^*) - I_2(h^*)]} \tag{24}$$

2.4 Two-Dimensional Finite-Branch Analysis. In this analysis, the lighter fluid is also considered stationary and the heavier fluid is considered to be incompressible, homogeneous, and irrotational. By applying the two-dimensional continuity equation in cylindrical coordinates to the heavier fluid side in Fig. 1(b), we obtain

$$\frac{1}{r}\frac{\partial}{\partial r}\left(r\frac{\partial\Phi}{\partial r}\right) + \frac{1}{r^2}\frac{\partial^2\Phi}{\partial\theta^2} = 0 \tag{25}$$

with the following boundary conditions:

$$r = R, \quad \theta \in [\beta-\delta, \beta+\delta] \quad \Rightarrow \quad \frac{\partial\Phi}{\partial r} = v_d$$

$$r = R, \quad \text{and} \quad \frac{\pi}{2} + (2n)\delta < \theta < \frac{\pi}{2} + (2n+2)\delta$$

$$\Rightarrow \quad v_{rn} = v_\infty \cos\left[\frac{\pi}{2} - (2n+1)\delta\right]$$

where $n=0,1,2\ldots$ and depends on the level of the heavier fluid inside the reservoir

$$r = R, \quad \left.\begin{array}{l} \beta + \delta < \theta < \dfrac{\pi}{2} \\ \dfrac{3\pi}{2} < \theta < \beta - \delta \end{array}\right\} \Rightarrow \frac{\partial \Phi}{\partial r} = 0 \tag{26}$$

Smith [16] obtained a solution for Equation (25) when $f(\xi) = \partial\Phi/\partial r$ is known at the boundary (Neumann problem) where the following condition must be satisfied:

$$\pi a_0 = \int_0^{2\pi} f(\xi) d\xi = 0$$

Thus, by multiplying the above equation by R, this results in balancing the inlet and outlet flow rates through the boundary. On the inlet side, opposite the slot, the area is divided into several imaginary branches with an equivalent size as the discharge branch (see Fig. 1(*b*)). The purpose is to define the radial velocity component v_{rn} in the direction of the domain center along the semi-circular inlet from the free stream velocity v_∞. From Fig. 1(*b*) the freestream velocity is defined by

$$v_\infty = v_d \frac{(2\delta R)}{R+H} \tag{27}$$

The number of branches along the imaginary boundary is determined by the height of the heavier fluid in the domain by $R+H$. After satisfying the necessary condition, the solution was as follows:

$$\pi\Phi(r,\theta) = \alpha_o R - \frac{R}{2}\int_0^{2\pi} f(\xi) \log\left\{\frac{R^2 - 2Rr\cos(\theta-\xi) + r^2}{R^2}\right\} d\xi \tag{28}$$

where

$$f(\xi) = \frac{\partial \Phi}{\partial r} = v_r \text{ at the boundaries}$$

The first and second derivatives of the potential function $\Phi(r,\theta)$ needed for the criterion of the onset of gas entrainment is given by

$$[a_B] = \frac{\partial \Phi}{\partial y}\frac{\partial^2 \Phi}{\partial y^2} = -g \tag{29}$$

where the polar coordinates (r,θ) are converted and shifted to the Cartesian coordinates (x,y) at the center of the branch, as shown in Fig. 1(*b*), with the following coordinate transformation properties:

$$r = (x_1^2 + y_1^2)^{1/2}, \quad \theta = \tan^{-1}\left(-\frac{y_1}{x_1}\right)$$

$$x = x_1 - R\cos\beta, \quad y = y_1 + R\sin\beta$$

$$\frac{\partial \Phi}{\partial y} = \frac{\partial \Phi}{\partial r}\frac{\partial r}{\partial y} + \frac{\partial \Phi}{\partial \theta}\frac{\partial \theta}{\partial y},$$

and

$$\frac{\partial^2 \Phi}{\partial y^2} = \left(\frac{\partial^2 \Phi}{\partial r^2}\frac{\partial r}{\partial y} + \frac{\partial^2 \Phi}{\partial \theta\, \partial r}\frac{\partial \theta}{\partial y}\right)\frac{\partial r}{\partial y} + \frac{\partial \Phi}{\partial r}\frac{\partial^2 r}{\partial y^2} + \left(\frac{\partial^2 \Phi}{\partial \theta^2}\frac{\partial \theta}{\partial y} + \frac{\partial^2 \Phi}{\partial r\, \partial \theta}\frac{\partial r}{\partial y}\right)\frac{\partial \theta}{\partial y} + \frac{\partial \Phi}{\partial \theta}\frac{\partial^2 \theta}{\partial y^2}$$

After making the necessary derivatives and substitutions, the final results of the first and second derivatives of the stream function are given as

$$\left.\frac{\partial \Phi}{\partial y}\right|_B = -\frac{R}{\pi}\left\{\frac{M_2}{\sqrt{M_1}}\int_0^{2\pi} f(\xi)\frac{N_2}{N_1}d\xi + \frac{-M_3}{\sqrt{M_1}}\int_0^{2\pi} f(\xi)\frac{N_3}{N_1}d\xi\right\} \tag{30}$$

$$\begin{aligned}\left.\frac{\partial^2 \Phi}{\partial y^2}\right|_B = -\frac{R}{\pi}\Bigg\{&\frac{M_2^2}{M_1}\int_0^{2\pi} f(\xi)\frac{N_1 - 2N_2^2}{N_1^2}d\xi \\ &+ \frac{-2M_2M_3}{M_1^{3/2}}\int_0^{2\pi} f(\xi)\frac{N_1N_3 - 2\sqrt{M_1}N_2N_3}{N_1^2}d\xi \\ &+ \frac{M_3^2}{\sqrt{M_1^3}}\int_0^{2\pi} f(\xi)\frac{RN_1\cos N_0 - 2\sqrt{M_1}N_3^2}{N_1}d\xi \\ &+ \left(\frac{1}{M_1^{1/2}} - \frac{M_2^2}{M_1^{3/2}}\right)\int_0^{2\pi} f(\xi)\frac{N_2}{N_1}d\xi \\ &+ \frac{2M_3M_2}{\sqrt{M_1^3}}\int_0^{2\pi} f(\xi)\frac{N_3}{N_1}d\xi\Bigg\}\end{aligned} \tag{31}$$

where

$$\begin{aligned} M_1 &= (R\cos\beta)^2 + (h - R\sin\beta)^2 & N_0 &= M_4 - \xi \\ M_2 &= h - R\sin\beta & N_1 &= R^2 - 2R\sqrt{M_1}\cos N_0 + M_1 \\ M_3 &= R\cos\beta & N_2 &= -R\cos N_0 + \sqrt{M_1} \\ M_4 &= \tan^{-1}\left(-\frac{M_2}{M_3}\right) & N_3 &= R\sin N_0 \end{aligned} \tag{32}$$

The critical height at the onset of gas entrainment can now be determined by substituting Eqs. (30) and (31) into Eq. (29), and solving numerically for the value of h, which is equivalent to the height of liquid level above the branch center. Using the calculated value of h into Eq. (30), the term $\left.\frac{\partial \Phi}{\partial y}\right|_B = v_B$ is determined. Substituting h and v_B into Eq. (13) yields

$$\frac{H_{\text{OGE}}}{d} = \frac{h}{d} + \frac{\rho_1}{2gd\Delta\rho}\left[\left.\frac{\partial \Phi}{\partial y}\right|_B\right]^2 \tag{33}$$

It should be noted here that the inputs to the model are d, R, ρ_1, $\Delta\rho$, β, and $\dot{m}$ or Fr. For each set of these values, the height H_{OGE} can be found. The values of all integrations in Eqs. (30) and (31) are calculated using numerical integration techniques.

3 Results and Discussion

In the present section, the effects of wall curvature and branch orientation on the critical height at the onset of gas entrainment were investigated. Also, comparisons between the predicted critical heights and the available experimental data, collected by Smoglie and Reimann [2], Parrott et al. [6], Hassan et al. [9], and Ahmad et al. [17] were made to validate the present analysis. Figure 2 depicts the effect of curvature on the prediction of critical height, at the onset of gas entrainment during single side-discharge (horizontal orientation), as a function of Fr number, for both point-sink and finite-branch analyses. Experimental data from Ahmad and Hassan [17] is also shown here. The results also

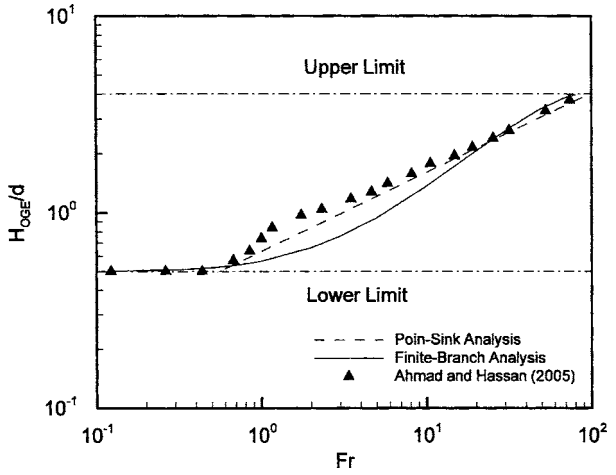

Fig. 2 Predictions of H_{OGE}/d with Fr at $\beta=0$ deg and $d/R=0.25$

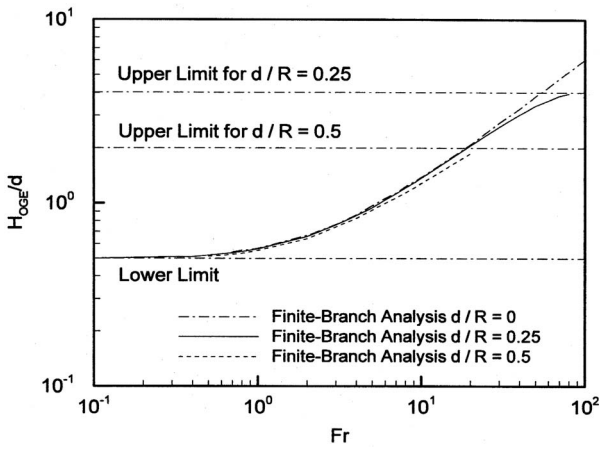

Fig. 4 Effect of d/R on the predictions of H_{OGE}/d with Fr at $\beta=0$ deg

showed that the deviation between the point-sink analysis and the finite branch analysis models and Ahmad and Hassan [17] is significant at low Froude numbers. This may be due to the effect of neglecting the viscous forces and surface tension in the present analyses. On the other hand, a good agreement is observed at high Froude numbers because the inertia forces are dominant and so the effect of viscous forces and surface tension may be neglected. Also, it is clear from the figure that the results of the two models are restricted by two physical appropriate limits, $(H/d)_{max}$ (upper limit) and $(H/d)_{min}$ (lower limit). Beyond these limits, the theoretical results are physically impossible. The upper limit of $(H/d)_{max}=R/d=4$, is characterized by the relative geometry of the cylindrical reservoir. The lower limit of $(H/d)_{min}=0.5$, is distinguished by the entrance of the branch, after which two-phase flow should exist at the branch entrance. It can be seen that the finite-branch analysis converges toward these two limits along the whole range of Fr numbers, whereas the results of the point-sink analysis are stopped at the upper limit of $(H/d=4)$ and go further down the lower limit $(H/d=0.5)$.

Figure 3 shows the percent deviation of the point-sink analysis (PSA) from the finite-branch analysis (FBA). H_{PSA} refers to the critical height at the onset of gas entrainment calculated by Eq. (24), and H_{FBA} refers to the critical height at the onset of gas entrainment calculated from Eq. (33). At very low Fr numbers there is a deviation of about +50%, where the point-sink analysis under predicts the finite-branch analysis. At moderate Fr numbers the deviation is about −32%, and the point-sink analysis overpredicts the finite-branch analysis. The overall deviation is reflected as a sinusoidal curve decaying exponentially, where at very high Fr numbers the deviation between the two analyses is negligible.

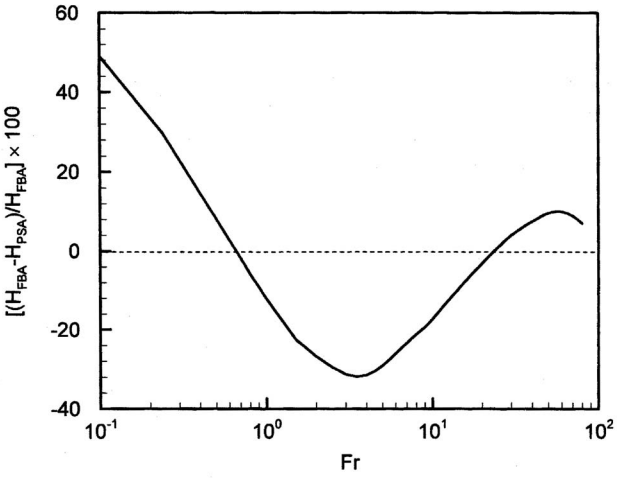

Fig. 3 Percentage deviation from the finite-branch analysis for $\beta=0$ deg and $d/R=0.25$

Figure 4 compares the behavior of the critical height as a function of Fr number for three distinct d/R ratios of finite-branch analysis and demonstrates the effect of curvature with respect to the Froude number range. The d/R ratio of 0.25 is used as input for the present analysis regarding curvature, where $R=25.4$ mm and $d=6.35$ mm. Whereas when $d/R=0, R$ can be considered as an infinite value, removing the effect of curvature and simplifying the analysis to a single side branch mounted on a flat wall, as in Ahmed et al. [10]. The third curve of $d/R=0.5, R$ is half the size of that when $d/R=0.25$. In comparing these three curves of different d/R ratios, it can be seen that for each d/R case, it is the upper physical limit that changes with respect to the d/R ratio, whereas the lower physical limit remains constant for all ratios since it is defined by the entrance of the branch. For $d/R=0$, there is no upper physical limit associated with the configuration due to the fact that it is considered as a branch mounted on a flat wall, and therefore R is assumed to be infinite. It is obvious that the d/R ratio of 0.25 has a higher upper physical limit than that of $d/R=0.5$. One can therefore conclude the prediction of the onset of gas entrainment depends on the d/R ratio, particularly at high values of Fr number >10. Also the effect of curvature does not appear when Fr number <10.

To prove the validity of the present theoretical analysis, Fig. 5 demonstrates the comparison of the present analysis to $d/R=0$, which corresponds to a single discharge through a finite-side branch mounted on a flat wall and experimental analyses in Hassan et al. [9] and Parrott et al. [6]. The experimental data here were generated during single discharge through a 6.35 mm i.d. branch located on the sidewall of a large reservoir under stratified (air-water) conditions, and different pressures ranging from 316 kPa to 517 kPa. Figure 5 shows good agreement between the present theoretical results and the experimental data of Hassan et al. [9]. The results of Parrott et al. [6] are underpredicted because they added the meniscus height (estimated to be 3.3 mm) to their values of the critical heights, while Hassan et al. [9] did not.

Figure 6 shows a comparison between the present theoretical results, found using the finite-branch analysis at two distinct d/R ratios, and corresponding experimental data given by Hassan et al. [18] and Smoglie and Reimann [2]. The experimental data of Hassan et al. [18] were generated during single discharge through a

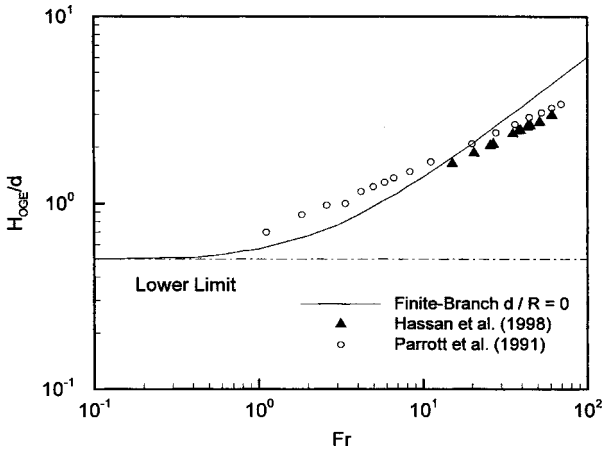

Fig. 5 Comparison between the measured and predicted values for β=0 deg and d/R=0

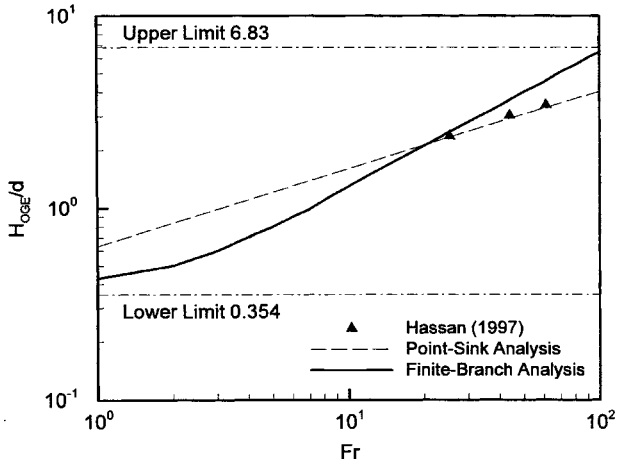

Fig. 7 Comparison between the measured and predicted values of different models at β=45 deg and d/R=0.25

635 mm i.d. side branch located on the side of a semi-circular duct (radius of 25.4 mm) under stratified (air-water) conditions, at different pressures ranging from 316 kPa to 517 kPa. At high Fr numbers, the data given by Hassan et al. [18] slightly underpredicted by the results of the same d/R ratio, = 0.25. However, the deviation is not large and the general trend of data is similar to the theoretical calculation.

The experimental results found by Smoglie and Reimann [2] in Fig. 6 are for a single discharge from a stratified region through a circular branch. Smoglie and Reimann performed their experiments using stratified air-water at 200 kPa to 500 kPa in a horizontal pipe (206 mm dia) with different branch sizes (d=6, 12, and 20 mm). The branch was simulated by pipe stubs (0.055 mm in length) with sharp-edged entrances, and the flow through the branch was controlled by a throttle valve. The onsets on entrainment were detected by the noise in the differential pressure signals across the branch. Smoglie and Reimann found their d/R ratios are between 0.03 and 0.09. In comparing the experimental data given by Smoglie and Reimann [2] to the present finite-branch analysis between d/R=0 and 0.25, it can be seen that the present theoretical results predict fairly the experimental data. The deviation of the theoretical values from experimental data is expected due to the flow conditions considered by Smoglie and Reimann [2], vortex flow entrainment with superimposed velocity, as these conditions were not incorporated in the present analyses. However, the general trend of the theoretical results is similar along the same range of Fr numbers, leading to a generally good correlation between the theoretical and experimental results given by Smoglie and Reimann [2].

For a single discharge from a 45 deg mounted branch (see Fig. 1(*b*) where β=45 deg), the available experimental data are scarce. There are only few data given by Hassan [7], and Fig. 7 shows the comparison between these data and the present predictions. It is clear that there is good agreement between the experimental data and point-sink model at Fr>20, showing the validity of the present theoretical calculations for this range. Also, the results of the two models are also restricted by two physical appropriate limits; beyond these limits the theoretical results are physically impossible. The upper limit of $(H/d)_{max}$=6.83, is characterized by the relative geometry of the cylindrical reservoir. The lower limit of $(H/d)_{min}$=0.354, is distinguished by the entrance of the branch. The two limits, as discussed before, depend on the value of d/R ratio, which is 0.25 in the case of Hassan [7].

Figure 8 shows the results of bottom branch orientation (where β=90 deg), where there is a good correlation between the experimental data and the results of the point-sink analysis. Lubin and Springer [19] performed their experiments with an initially stationary liquid in a cylindrical tank with an axisymmetrically placed circular branch at the bottom of the tank. Based on their

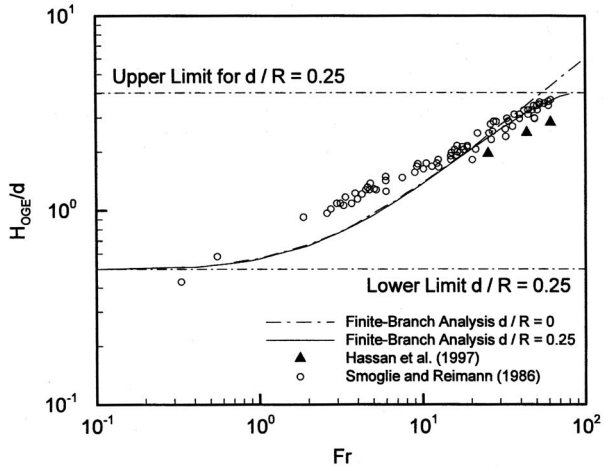

Fig. 6 Comparison between the measured and predicted values for different values of d/R and β=0 deg

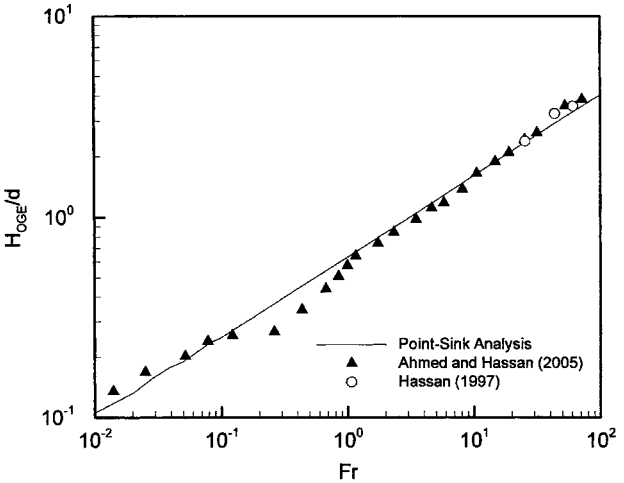

Fig. 8 Comparison between the measured and predicted values of point-sink model at β=90 deg bottom branch orientation

observations, no vortex entrainment was reported, which is similar to the present simulation. In Hassan's experiments, however, it was not possible to confirm whether the flow mode at the onset of gas entrainment was vortex or vortex free. The results also showed that the deviation between the point-sink analysis model and Ahmad and Hassan [17] is significant at low Froude numbers. This may be due to the effect of neglecting the viscous forces and surface tension in the present analyses. On the other hand, a good agreement is observed at high Froude number because the inertia forces are dominant and so the effect of viscous forces and surface tension may be neglected.

4 Conclusion

The onset of gas entrainment during single discharge from a stratified, two-phase region through a branch installed on a semi-circular wall was theoretically investigated. Dimensions of the semi-circular surface and branches were selected to be in direct proportion to those of the CANDU header-feeder system. The analysis was done using two models, a simple point-sink model and a more accurate finite-branch model, where the dimensions of the branch were considered. The critical height was found to be a function of the Froude number, the size of the circular reservoir, and the density ratio of the interface fluids. Two distinct physical limits exist in the prediction of H_{OGE}, the upper limits are due to the geometry of the circular reservoir and the lower limits are due to the entrance of the branch. The finite-branch analysis was found to converge toward these two limits along the whole range of Fr numbers, whereas the results of the point-sink analysis did not. There was relatively good agreement between the available experimental data and the theoretical analysis for the three branch configurations that were investigated (0, 45, and 90 deg). In future research, the following efforts are to be considered regarding a semi-circular wall configuration: (i) Theoretically investigate the effect of dual or triple discharge on H_{OGE} of a branch, as well the effect of superimposed velocity in the main pipe; and (ii) attain experimental data for the onset of entrainment phenomenon when the water/air interface is wavy stratified, which is closer to real applications.

Nomenclature

a_B = acceleration at point B, m/s^2
d = branch diameter, m
D = diameter of the cylindrical reservoir, m
Fr = Froude number
g = gravitational acceleration, m/s^2
H = distance above the branch hole to point A, as defined in Fig. 1, m
h = distance above the branch hole to point B, as defined in Fig. 1, m
h^* = dimensionless height, $h/2R$
$\dot{m}$ = mass flow rate, kg/s
p_A = pressure at point A from Fig. 1, Pa
p_B = pressure at point B from Fig. 1, Pa
Q = capacity, m^3/s
R = radius of the cylindrical reservoir, m
r = radius of the flow field in Fig. 1(b), m
S = surface area of the flow field, m^2
v_A = velocity at point A from Fig. 1, m/s
v_B = velocity at point B from Fig. 1, m/s
v_d = velocity at the entrance of the branch defined in Fig. 1, m/s
v_ρ = radial component of local velocity, m/s
v_m = radial velocity component at the opposite side of the branches, m/s
v_∞ = freestream velocity at the opposite side of the branches, m/s

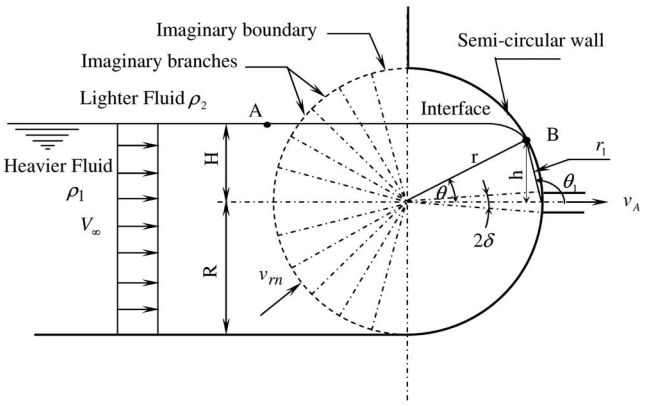

Fig. 9 Geometry and the coordinate system in the β=0 deg finite-branch analysis

Greek Letters

α_0 = constant in Eq. (27) that is eliminated in derivation
β = angle of the branch with respect to horizontal, rad
δ = angle within the branch with respect to the center of the reservoir, as defined in Fig. 1, rad
ρ_1 = density of heavier fluid, kg/m^3
ρ_2 = density of lighter fluid, kg/m^3
$\Delta\rho$ = density difference between heavier and lighter fluids ($\rho_1-\rho_2$), kg/m^3
Φ = potential function, m^3/s
ρ = radius of the flow field, m
σ = angle from Fig. 1(a)

Appendix

Three different branch configurations from a cylindrical reservoir are considered in the present analysis. Dimensions and orientation of the semicircular surface and branches were selected to be in direct proportion to those of the CANDU header-feeder system. It was difficult to present general H_{OGE} equations for all orientations, due to the difference in the onset location. For example for a 45 deg branch the onset location is assumed to be above the branch center as in Fig. 1(b), while for 0 deg branch, the onset location is assumed to be on the semi-circular surface as in Fig. 9, i.e., the onset's angle is changing with H_{OGE}. As a result, the details of the models at β=45 deg were given in Sec. 2. Similar analysis could be made at any orientation, once the onset location and direction have been specified. Following are the final equations for β=0 deg (see Fig. 9) and 90 deg (see Fig. 10) ordinations:

A.1 Finite-Branch Model for the Horizontal-Orientation Branch

The criterion of the onset of gas entrainment is given by

$$[a_B] = \left.\frac{\partial\Phi}{\partial r_1}\right|_B \left.\frac{\partial^2\Phi}{\partial r_1^2}\right|_B = -g\sin\theta_1 \tag{A1}$$

with

$$\left.\frac{\partial\Phi}{\partial r_1}\right|_B = -\frac{R}{\pi}\left\{\frac{M_3}{M_1}\int_0^{2\pi} f(\xi)\frac{N_2}{N_1}d\xi + \frac{M_5}{M_4}\int_0^{2\pi} f(\xi)\frac{N_3}{N_1}d\xi\right\} \tag{A2}$$

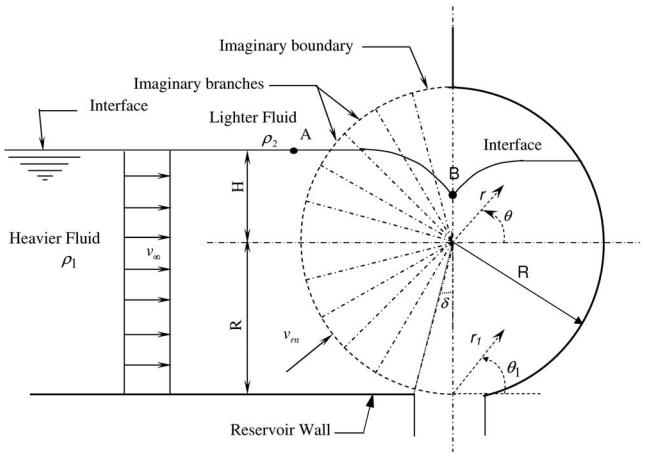

Fig. 10 Geometry and the coordinate system in the β =90 deg finite-branch analysis

$$\left.\frac{\partial^2\Phi}{\partial r_1^2}\right|_B = -\frac{R}{\pi}\left\{\frac{M_3}{M_1}\left[\frac{M_3}{M_1}\int_0^{2\pi} f(\xi)\frac{N_1-2N_2^2}{N_1^2}d\xi + \frac{M_5}{M_4}\int_0^{2\pi} f(\xi)\frac{N_1N_5-2N_2N_3}{N_1^2}d\xi\right] + M_6\int_0^{2\pi} f(\xi)\frac{N_2}{N_1}d\xi + \frac{M_5}{M_4}\left[-\frac{M_5}{M_4}\int_0^{2\pi} f(\xi)\frac{N_1N_4-2N_3^2}{N_1^2}d\xi + \frac{M_3}{M_1}\int_0^{2\pi} f(\xi)\frac{N_1N_5-2N_2N_3}{N_1^2}d\xi\right] + \frac{1}{M_4}\left(\frac{-2M_3}{M_1^2}-\frac{r_1}{M_1^2} + \frac{3r_1M_3^2}{M_1^4}+\frac{r_1M_5^2}{M_4^2}\right)\int_0^{2\pi} f(\xi)\frac{N_3}{N_1}d\xi\right\} \quad \text{(A3)}$$

where θ_1 is an angle of gas entrainment that is given by function of reservoir shape, in each $r_1|_B$

$$M_1 = (R^2 + r_1^2 + 2r_1R\cos\theta_1)^{1/2}, \qquad M_2 = \sin^{-1}\left(\frac{r_1}{M_1}\sin\theta_1\right)$$

$$M_3 = r_1 + R\cos\theta_1, \qquad M_4 = \left(\frac{M_1^2}{\sin^2\theta_1} - r_1^2\right)^{1/2}$$

$$M_5 = 1 - \frac{r_1M_3}{M_1^2}, \qquad M_6 = \frac{1}{M_1} - \frac{M_3^2}{M_1^3}$$

$$N_0 = M_2 - \xi, \qquad N_1 = R^2 - 2RM_1\cos N_0 + M_1^2$$

$$N_2 = -R\cos N_0 + M_1, \qquad N_3 = RM_1\sin N_0$$

$$N_4 = RM_1\cos N_0, \qquad N_5 = R\sin N_0$$

Numerically solving Eq. (A1), the height of liquid level above the branch center, $r_1\sin\theta_1$ is determined. Using the calculated value of r_1 into Eq. (A2), the term $(\partial\Phi/\partial r_1)|_B = v_B$ is determined. Substituting h and v_B into Eq. (5) yields

$$\frac{H_{\mathrm{OGE}}}{d} = \frac{(r_1\sin\theta_1)|_B}{d} + \frac{\rho_1}{2gd\Delta\rho}\left[\left.\frac{\partial\Phi}{\partial r_1}\right|_B\right]^2 \quad \text{(A4)}$$

A.2 Finite-Branch Model for the Bottom Orientation Branch

The criterion of the onset of gas entrainment is given by

$$[a_B] = \left.\frac{\partial\Phi}{\partial r_1}\right|_B \left.\frac{\partial^2\Phi}{\partial r_1^2}\right|_B = -g \quad \text{(A5)}$$

with

$$\left.\frac{\partial\Phi}{\partial r_1}\right|_B = -\frac{R}{\pi}\left\{\frac{M_3}{M_1}\int_0^{2\pi} f(\xi)\frac{N_2}{N_1}d\xi - \frac{M_5}{M_4}\int_0^{2\pi} f(\xi)\frac{N_3}{N_1}d\xi\right\} \quad \text{(A6)}$$

$$\left.\frac{\partial^2\Phi}{\partial r_1^2}\right|_B = -\frac{R}{\pi}\left\{\frac{M_3}{M_1}\left[\frac{M_3}{M_1}\int_0^{2\pi} f(\xi)\frac{N_1-2N_2^2}{N_1^2}d\xi - \frac{M_5}{M_4}\int_0^{2\pi} f(\xi)\frac{N_1N_5-2N_2N_3}{N_1^2}d\xi\right] + M_6\int_0^{2\pi} f(\xi)\frac{N_2}{N_1}d\xi - \frac{M_5}{M_4}\left[-\frac{M_5}{M_4}\int_0^{2\pi} f(\xi)\frac{N_1N_4-2N_3^2}{N_1^2}d\xi + \frac{M_3}{M_1}\int_0^{2\pi} f(\xi)\frac{N_1N_5-2N_2N_3}{N_1^2}d\xi\right] - \frac{1}{M_4}\left(\frac{-2M_3}{M_1^2}-\frac{r_1}{M_1^2} + \frac{3r_1M_3^2}{M_1^4}+\frac{r_1M_5^2}{M_4^2}\right)\int_0^{2\pi} f(\xi)\frac{N_3}{N_1}d\xi\right\} \quad \text{(A7)}$$

where,

$$M_1 = (R^2 + r_1^2 - 2r_1R\sin\theta_1)^{1/2}, \qquad M_2 = \cos^{-1}\left(\frac{r_1}{M_1}\cos\theta_1\right)$$

$$M_3 = r_1 - R\sin\theta_1, \qquad M_4 = \left(\frac{M_1^2}{\cos^2\theta_1} - r_1^2\right)^{1/2}$$

$$M_5 = 1 - \frac{r_1M_3}{M_1^2}, \qquad M_6 = \frac{1}{M_1} - \frac{M_3^2}{M_1^3}$$

$$N_0 = M_2 - \xi, \qquad N_1 = R^2 - 2RM_1\cos N_0 + M_1^2$$

$$N_2 = -R\cos N_0 + M_1, \qquad N_3 = RM_1\sin N_0$$

$$N_4 = RM_1\cos N_0, \qquad N_5 = R\sin N_0$$

The height of liquid level above the branch center r_1 is determined by numerically solving Eq. (A5). Using the calculated value of r_1 into Eq. (A6), the term $(\partial\Phi/\partial r_1)|_B = v_B$ is determined. Substituting h and v_B into Eq. (5) yields

$$\frac{H_{\mathrm{OGE}}}{d} = \frac{r_1|_B}{d} + \frac{\rho_1}{2gd\Delta\rho}\left[\left.\frac{\partial\Phi}{\partial r_1}\right|_B\right]^2 \quad \text{(A8)}$$

The inputs to the above model are still d, R, ρ_1, $\Delta\rho$, β, and $\dot{m}$ or Fr. For each set of these values the height, H_{OGE} can be found. The values of all integrations are calculated using standard numerical integration techniques.

References

[1] Zuber, N., 1980, "Problems in Modeling of Small Break LOCA," Nuclear Regulatory Commission Report No. NUREG-0724.

[2] Smoglie, C., and Reimann, J., 1986, "Two-Phase Flow Through Small Branches in a Horizontal Pipe With Stratified Flow," Int. J. Multiphase Flow, **12**, pp. 609–625.

[3] Schrock, V. E., Revankar, S. T., Mannheimer, R., Wang, C. H., and Jia, D., 1986, "Steam-Water Critical Flow Through Small Pipes From Stratified Upstream Regions," *Proc. of 8th Int. Heat Transfer Conf.*, San Francisco, Vol. 5, pp. 2307–2311.

[4] Yonomoto, T., and Tasaka, K., 1988, "New Theoretical Model for Two-Phase Flow Discharged From Stratified Two-Phase Region Through Small Break," J. Nucl. Sci. Technol., **25**, pp. 441–455.

[5] Yonomoto, T., and Tasaka, K., 1991, "Liquid and Gas Entrainment to a Small Break Hole From a Stratified Region," Int. J. Multiphase Flow, **17**, pp. 745–765.

[6] Parrott, S. D., Soliman, H. M., Sims, G. E., and Krishnan, V. S., 1991, "Experiments on the Onset of Gas Pull-Through During Dual Discharge From a Reservoir," Int. J. Multiphase Flow, **17**, pp. 119–129.

[7] Hassan, I. G., 1995, "Single, Dual and Triple Discharge From a Large, Strati-

fied, Two-Phase Region Through Small Branches," Ph.D. thesis, University of Manitoba, Winnipeg, Manitoba.
[8] Hassan, I. G., Soliman, H. M., Sims, G. E., and Kowalski, J. E., 1996, "Discharge From a Smooth Stratified Two-Phase Region Through Two Horizontal Side Branches Located in the Same Vertical Plane," Int. J. Multiphase Flow, **22**, pp. 1123–1142.
[9] Hassan, I. G., Soliman, H. M., Sims, G. E., and Kowalski, J. E., 1998, "Two-Phase Flow From a Stratified Region Through a Small Side Branch," ASME J. Fluids Eng., **120**, pp. 605–612.
[10] Ahmed, M., Hassan, I., and Esmail, N., 2003, "Modeling of the Onset of Gas Entrainment Through a Finite-Side Branch," ASME J. Fluids Eng., **125**, pp. 901–909.
[11] Stround, A. H., 1971, *Approximate Calculation of Multiple Integrals*, Prentice-Hall, Englewood Cliffs, NJ.
[12] Gradshteyn, I. S., and Ryzhik, I. M., 2000, *Table of Integrals, Series and Products*, 6th ed., Academic Press, New York.
[13] Taylor, G. I., 1950, "The Instability of Liquid Surfaces When Accelerated in a Direction Perpendicular to Their Planes," Proc. R. Soc. London, Ser. A, **201**, pp. 192–196.
[14] Lewis, D. J., 1950, "The Instability of Liquid Surfaces When Accelerated in a Direction Perpendicular to Their Planes," Proc. R. Soc. London, Ser. A, **202**, pp. 81–96.
[15] Johnson, R., 1998, *The Handbook of Fluid Dynamics*, CRC Press, Boca Raton, pp. 4–37.
[16] Smith, M. G., 1967, *Introduction to the Theory of Partial Differential Equations*, Van Nostrand, Princeton, pp. 74–77.
[17] Ahmad, T., and Hassan, I., 2006, "Experimental Investigation on the Onset of Gas Entrainment From a Stratified Two-Phase Region Through Multiple Branches Mounted on a Curved Surface," ASME J. Fluids Eng., 128, (in press).
[18] Hassan, I. G., Soliman, H. M., Sims, G. E., and Kowalski, J. E., 1997, "Single and Multiple Discharge From a Stratified Two-Phase Region Through Small Branches," Nucl. Eng. Des., **176**(3), pp. 233–245.
[19] Lubin, B. T., and Springer, G. S., 1967, "The Formation of a Dip on the Surface of a Liquid Draining From a Tank," J. Fluid Mech., **29**(2), pp. 385–390.

Experimental Investigation on the Onset of Gas Entrainment from a Stratified Two-Phase Region Through Multiple Branches Mounted on a Curved Surface

Tariq Ahmad

Ibrahim Hassan[1]
e-mail: ibrahimH@alcor.concordia.ca

Department of Mechanical and Industrial Engineering,
Concordia University,
Montreal, Quebec, Canada, H3G 1M8

An experimental investigation has been carried out to simulate the onset of gas entrainment phenomenon from a stratified region through branches located on a semicircular wall configuration, in close dimensional resemblance with a Canada Deuterium and Uranium (CANDU) header-feeder system. New experimental data for the onset of gas entrainment was developed during single and multiple discharge from an air/water stratified region over a wide range of Froude numbers (0 to 100), in order to thoroughly understand the onset of gas entrainment phenomenon. It was found that the critical height at the onset of gas entrainment (single or simultaneous) was a function of the corresponding Froude number of each branch, the vertical distance between the centerlines of the branches (for multiple discharge), the hydraulic resistance of the discharging lines, as well as the orientation of the branches and their diameter with respect to the main header. Concerning multiple discharge comparisons, at intermediate Fr values $(1 < \mathrm{Fr} < 10)$ *the data deviates, however at higher Fr values* (>10) *there is convergence. The present data are necessary in validating future analytical and numerical models of the onset of gas entrainment for a curved geometry, particularly at low Froude numbers.*
[DOI: 10.1115/1.2201645]

1 Introduction

The discharge of two-phase flow from a stratified region through single or multiple branches is an important process in many industrial applications and consequentially, is an ever-growing interest in the research community. Examples of industrial applications include the pumping of fluid from storage tanks, shell-and-tube heat exchangers, the fluid flow through small breaks in cooling channels of nuclear reactors during loss-of-coolant accidents (LOCA), and the flow distribution in Canada Deuterium and Uranium (CANDU) header—feeder systems during accident scenarios. Knowledge of the flow phenomena involved along with the quality and mass flow rate of the discharging stream(s) is necessary to adequately predict the critical height associated with the process.

With regards to single discharge, Zuber [1] stated that two distinct phenomena might occur under stratified flow conditions. These phenomena depend on the location of the horizontal gas-liquid interface relative to the branch. If the branch is located above the gas-liquid interface, at a certain critical height liquid begins to entrain into a predominantly gas flow, which is known as the onset of liquid entrainment phenomenon. Conversely, if the branch is located below the gas-liquid interface, at a certain critical height gas begins to entrain into a predominantly liquid flow, which is known as the onset of gas entrainment phenomenon (gas pull-through phenomenon). Following Zuber's work, other researchers began extending his findings both theoretically and experimentally with different branch orientations and geometries (e.g., Smoglie and Reimann [2], Schrock et al. [3], Yonomoto and Tasaka [4,5], Parrott et al. [6], Hassan et al. [7–9]).

In situations where multiple discharges take place, as in a CANDU header-feeder configuration where discharges take place simultaneously from several branches, the existing single-branch correlations may not apply. Kowalski and Krishnan [10] were the first to perform experiments on two-phase steam-water flow in a large manifold typical of a CANDU system. Parrott et al. [6] and Armstrong et al. [11] investigated the onset of gas entrainment during discharge through two side branches mounted on a vertical wall. Hassan et al. [8] further broadened the experimental research conducted on multiple discharges, by investigating the onsets of gas and liquid entrainment, and two-phase mass flux and quality during single, dual, and triple discharge from a large stratified two-phase region through small branches mounted on flat and curved wall configurations. Recently, Maier et al. [12,13], experimentally and theoretically analyzed the onset of liquid entrainment during dual discharge from a stratified two-phase region through horizontal branches with centerlines falling in an inclined plane.

The previous authors dealt with investigations of two-phase discharge through branches located on a flat or an inclined wall configuration. The present work complements the work of Hassan et al. [8], where branches were mounted on a curved surface resembling that of a CANDU header-feeder configuration, to thoroughly investigate the onset of gas entrainment phenomena. Hassan et al. [8] mainly studied the two-phase mass flux, with little emphasis on the onset phenomena. Experimental data for the onset of gas entrainment will be developed during single and multiple discharge from an air/water stratified region over a range of Froude numbers from 0 to 100. The effect of additional discharge(s) on the onset of entrainment at a branch will be discussed.

2 Experimental Investigation

2.1 Test Section. A typical CANDU header consists of a large horizontal pipe (approximately 6 m long and 0.356 to 0.406 m

[1]Author to whom correspondence should be addressed.

Contributed by the Fluids Engineering Division of ASME for publication in the JOURNAL OF FLUIDS ENGINEERING. Manuscript received March 7, 2005; final manuscript received January 12, 2006. Assoc. Editor: Theodore Heindel.

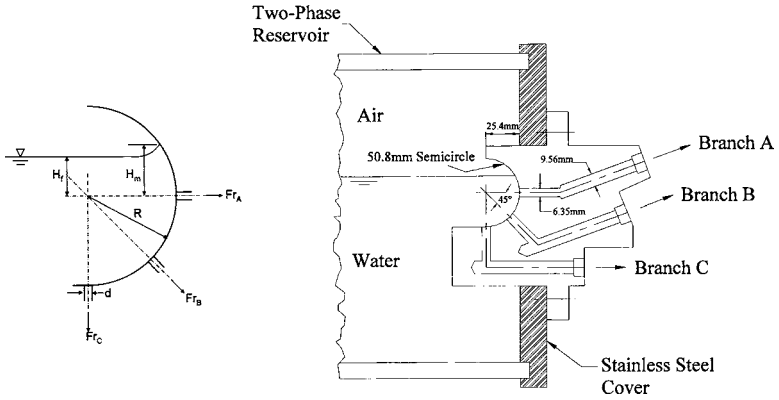

Fig. 1 Modeled test section used in the present investigation

inner diameter (i.d.)) closed on both ends with the flow entering from a number of openings ("turrets") at the top of the pipe and exiting through banks of feeders at various axial locations along the header. Each feeder bank consists of five 50.8 mm i.d. tubes attached to the header at angles of 0°, 45°, 90°, 135°, and 180° from the horizontal centerline. These feeders bring the coolant from the header to the fuel channels. Although a genuine CANDU header is a completely circular shaped tube, the test section presently used is of a semicircular shape, due to the experimental advantages. Advantages include ease of measuring the undisturbed interface relative to the location of the branches, ease of flow observation since the semicircular shape is exposed to a large open volume, and if stratified conditions are to be maintained in a circular header, the flowrates leaving the branches would have to be kept quite low.

The present test section, as shown in the Fig. 1, was fabricated from brass, and is identical to Hassan et al. [8]'s design. A brass block was machined from a semicircular shape with a diameter of 50.8 mm, and a width of 50.8 mm. Three discharge branches were drilled into the semicircular surface at angles of 0°, 45°, and 90° from the horizontal at the circle's center. These branches had an initial diameter of 6.35 mm, which was maintained for a minimum length of four diameters, then suddenly enlarged to a diameter of 9.56 mm until the exit, where copper pipe was soldered to provide a rigid support for a ball valve. A circular flange was also machined into the brass block to support the test section on the outside face of the right-hand cover of the two-phase reservoir. The dimensional scaling of the experimental test section is roughly 8:1 with an actual CANDU header-feeder system.

2.2 Test Facility. The flow loop of the experimental test facility is shown in Fig. 2. There is a close resemblance to Hassan et al. [8]'s facility at the University of Manitoba, however the present facility lacking the air-water separators, was designed to measure the mass flow rates at the onset of gas entrainment rather than measuring the mass flow rate beyond the onset point. With regards to the flow loop, the water recirculates as a closed system, however the air circulates as an open system, with a controlled supply entering the facility, then venting to atmosphere at the water tank.

A 3-hp SSV eight-stage vertical pump was used to supply filtered water from an open-air 55-gallon tank to the bottom cover of

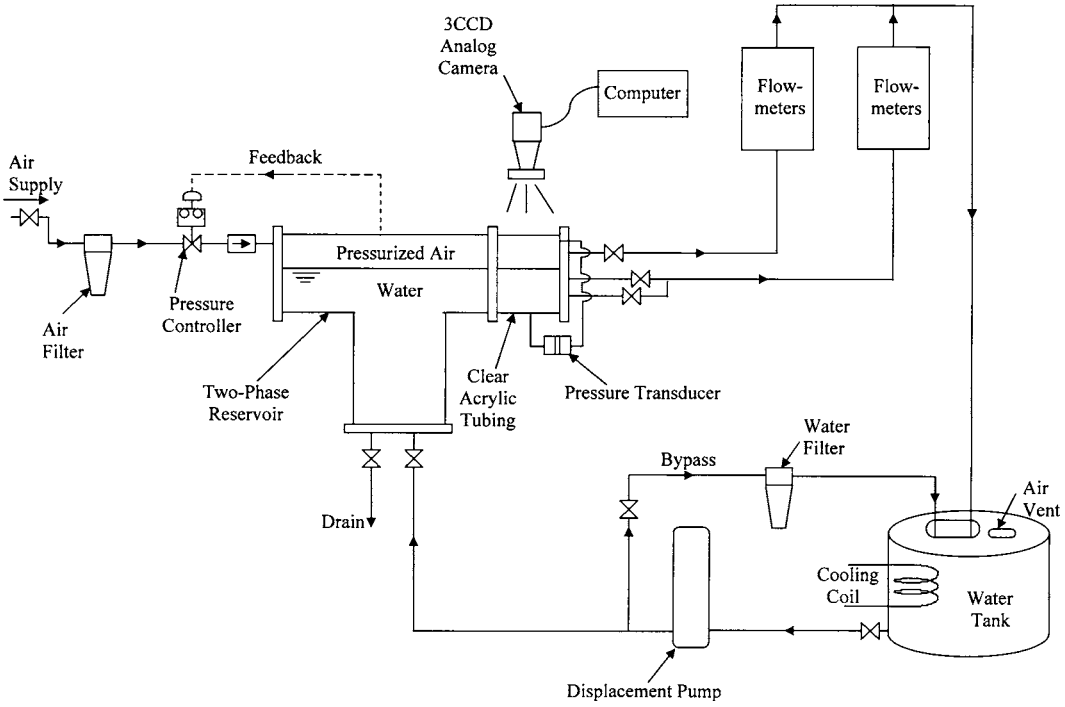

Fig. 2 Experimental test facility flow loop

Table 1 Test matrix

Data Set #	Discharge Criterion	Fr_A	Fr_B	Fr_C
1	Single	0 – 100		
2			0 – 100	
3				0 – 100
4	Dual	1 – 100	60	
5		1 – 100	50	
6		1 – 100	34.4	
7		1 – 100	30	
8		1 – 100	5	
9		1 – 100		60
10		1 – 100		40
11		1 – 100		34.4
12		1 – 100		20
13		1 – 100		5
14		0 – 1	0 – 100	
15		0 – 1		0 – 100
16			$Fr_B = Fr_C = 0 – 100$	$Fr_C = Fr_B = 0 – 100$
17	Triple	1 to 100	$Fr_B = Fr_C = 34.4$	$Fr_C = Fr_B = 34.4$
18		1 to 100	$Fr_B = Fr_C = 20$	$Fr_C = Fr_B = 20$
19		1 to 100	$Fr_B = Fr_C = 10$	$Fr_C = Fr_B = 10$
20		1 to 100	$Fr_B = Fr_C = 5$	$Fr_C = Fr_B = 5$

a two-phase reservoir (i.e., tee section) via 1 in. i.d. flexible tubing. The flowrate was controlled by a gate valve on the bypass line and a needle valve (to provide an adequate pressure drop) upstream from the two-phase reservoir. The tee section, similar to that of Parrott et al. [6] and Hassan et al. [8], was basically constructed by welding together two perpendicular hollow tubes (approx. 275 mm i.d.). Manufactured from type 304 stainless steel, the horizontal tube's length is approximately 1.1 m and the vertical tube's height is in the order of 0.320 m. A stainless-steel cover was bolted on each of the three openings of the two-phase reservoir, and along with an O-ring, provided a reliable seal.

Filtered air, used to pressurize the two-phase reservoir, enters (via 1 in. i.d. flexible tubing) through the left-hand cover of the tee section. A Fisher Pressure Controller automatically controls the air pressure entering the two-phase reservoir, with a feedback line from the reservoir to maintain a constant preselected pressure inside the tee section. Air and water dispersers are located on the inside of their respective covers. These components are meant to distribute and disperse the flows to present a smooth air-water interface, further providing a stratified region inside the two-phase reservoir. Manufacturing information regarding the dispersers is similar to that of Hassan [14].

Two Rosemount pressure transmitters were mounted on the stand supporting the tee section. A pressure tap on the top of the tee section was connected via 0.5 in. i.d. tubing to a static pressure transmitter (Rosemount model 2088G). The static pressure transducer was factory calibrated to a range of 0–830 kPa gauge. Two pressure taps were installed on the right-hand cover of the two-phase reservoir, one on the air side and one on the liquid side. These two taps were connected to a differential pressure transmitter (Rosemount model 3051CD) to measure the liquid height in the tee section from which H (interface level) was determined. The differential pressure transmitter was factory calibrated at a range of 0–255 mm H_2O. Both transmitter models are designed with their respective liquid crystal display digital display to permit the operator to directly examine the readings from the transmitters themselves.

The two-phase reservoir's discharge is located at the right-hand cover. Before the cover is a clear acrylic tube, with dimensions of 10.5 in. long and 0.5 in. wall thickness. This tube allows for observation of the onset phenomena as the fluids are discharged through the test section, whose details were previously mentioned. A camera was positioned at this point to document the visual effects of the onsets.

As shown in Fig. 2, following the reservoir's discharge are sets of water flowmeters (rotameters). The water rotameters covered an overlapping range of $1.5E{-}05$ m^3/min to 0.0415 m^3/min. The rotameters were fabricated by Omega, where they were also tested and calibrated to specifications. Also, each rotameter is equipped with a needle valve at the inlet to control the inlet flow. At the exit of the flowmeters, the flow can either be liquid flow, gas flow, or both liquid and gas (two-phase) flow. Nonetheless, the discharge is directed back to the water tank where it is separated, with the water returning to the pump and the air being vented to atmosphere.

2.3 Experimental Parameters and Procedure. Data sets were taken at all branch configurations and discharge criterion (single, dual, and triple discharge) over a wide range of Froude numbers (0–100). It was expected that the mass flow rate of the discharging streams was dependent on the reservoir pressure P_o, the pressure drop across the branches ΔP, the hydraulic resistance R, and the critical height. It was found that if the latter three parameters were maintained constant, then the onset of gas entrainment would depend only on the critical height. The majority of the data was recorded with respect to the Froude number and corresponding critical height at the onset of gas entrainment. Table 1 depicts the experimental test matrix developed in regard to attaining experimental data.

The tee-section nominal pressure was set at a constant value of 206.8 kPa for the single discharge experiments, and 413.7 kPa for dual and triple discharge experiments. The reason for this was that

Table 2 Experimental data for single discharge

a) Branches A and B

	$H_{f,OGE}/d$				
Fr_A	$Fr_B = 60$	$Fr_B = 50$	$Fr_B = 40$	$Fr_B = 34.4$	$Fr_B = 5$
62.3	3.4	3.3	3.3	3.2	3.0
52.8	3.2	3.2	3.1	3.0	2.9
42.3	2.9	2.9	2.6	2.7	2.6
31.7	2.6	2.6	2.3	2.5	2.3
21.1	2.3	2.2	2.0	2.1	1.9
14.8	2.1	2.0	1.7	1.8	1.7
10.6	1.8	1.7	1.5	1.6	1.5
8.1	1.6	1.6	1.3	1.4	1.3
5.8	1.5	1.4	1.1	1.2	1.1
4.6	1.3	1.3	0.96	1.1	1.0
3.5	1.2	1.1	0.88	0.94	0.84
2.3	1.1	1.0	0.77	0.81	0.71
1.7	1.0	0.94	0.67	0.71	0.58
1.2	0.95	0.77	0.54	0.61	0.44
1.0	0.91	0.74	0.47	0.51	0.27

b) Branches A and C

	$H_{f,OGE}/d$				
Fr_A	$Fr_C = 60$	$Fr_C = 40$	$Fr_C = 34.4$	$Fr_C = 20$	$Fr_C = 5$
62.3	3.2	3.1	3.0	3.1	3.0
52.8	3.0	2.9	2.8	2.9	2.8
42.3	2.7	2.5	2.5	2.4	2.5
31.7	2.4	2.2	2.3	2.1	2.3
21.1	2.1	1.9	1.9	1.8	1.9
14.8	1.8	1.6	1.6	1.5	1.6
10.6	1.6	1.3	1.4	1.3	1.4
8.1	1.4	1.2	1.3	1.1	1.3
5.8	1.2	1.0	1.1	0.94	1.0
4.6	1.1	0.91	0.94	0.81	0.94
3.5	0.91	0.81	0.81	0.71	0.81
2.3	0.84	0.67	0.67	0.57	0.61
1.7	0.81	0.57	0.64	0.44	0.57
1.2	0.61	0.44	0.44	0.30	0.37
1.0	0.47	0.27	0.37	0.24	0.27

c) Branches B and C

	$H_{f,OGE}/d$
Fr	$Fr_B = Fr_C$
52.9	4.2
40.1	3.9
31.7	2.9
19.0	2.3
14.8	1.9
10.6	1.7
8.1	1.4
5.8	1.2
3.5	0.91
2.3	0.77
1.2	0.51
0.85	0.3
0.45	0.1
0.26	0.03
0.08	0.03

at single discharge a high flowrate was not required as for multiple discharge experiments. The hydraulic resistances of the connecting lines discharging from the test section were all equal and remained constant, since the length and type of tubing was identical for all discharging lines. Also, since the test facility was only equipped with two sets of flowmeters, the single and dual discharge experiments were carried out with varying flowrates at each branch. However, where triple discharge was concerned, two branch flowrates always had to be the same value.

A similar experimental procedure, regardless of discharge criterion and branch configuration, was carried out for each data set: (1) Water was pumped into the two-phase reservoir until an arbitrary height well above the active branch where the onset of gas entrainment was expected to occur. All discharge valves connected to the two-phase reservoir were then closed; (2) The two-phase reservoir was then pressurized (206.8 kPa or 413.7 kPa) by means of the pressure controller; (3) The appropriate discharge valves from the CANDU test section were opened (depending on discharge criterion) and their respective water flowrates were set; (4) The pump bypass valve and the inlet valve to the two-phase reservoir were then controlled to maintain a constant, steady height depending on the chosen flowrate; (5) The height was incrementally lowered by means of the inlet valve, until onset was observed. This height was maintained and recorded. Also, photographs were taken in order to visually document the effect; and (6) Steps 4 and 5 were repeated for the whole range of Froude numbers.

All necessary instruments were calibrated by the manufacturer, as per component specifications. The maximum uncertainty in the calculation of Fr was ±0.011. The instrumental uncertainty in P_o was ±0.83 kPa. The acceptable range of P_o recorded by the authors was ±5 kPa (for 206.8 kPa and 413.7 kPa). The maximum absolute uncertainty in H was ±0.165 mm H_2O.

3 Results and Discussion

In the present section, experimental data for the onset of gas entrainment (Tables 2–4) has been developed during single, dual, and triple discharge from the two-phase stratified region. Comparisons were made for different Froude numbers, branch configurations (0° (A), 45° (B), and 90° (C) from the horizontal), and discharge criterion (single, dual, or triple). If the interface level (H) is well above the branch, the branch will be flowing liquid only, and the interface will be flat. As H is lowered and approaches H_{OGE}, a "dimple" begins to form in the interface. This dimple depression becomes more pronounced and conelike until the bottom of the cone suddenly extends to the branch; this is the onset of gas entrainment. It should be noted, as stated by Taylor [15], that the onset of gas entrainment is developed if the heavier fluid (liquid) were given a greater acceleration than that of gravity, resulting in instability in the flow, which forms a dip leading to the onset of gas entrainment. The increase in the flow acceleration is based primarily on the strength (or Froude number) of the flow through the branch, having a direct impact on the critical height at the onset of gas entrainment.

3.1 Single Discharge. Figure 3 shows the onset of gas entrainment during single discharge from branch A, B, and C, respectively. It can be seen that from Figs. 3(*a*) and 3(*b*) that a distinct lower physical limit is apparent, defined by the active branch's vertical projected area, where the critical height remains constant at low Fr values (<1). Both figures also show two sets of data; the lower data set is the critical height measured with respect to the free-surface interface ($H_{f,\mathrm{OGE}}/d$), whereas the higher data set takes into account the meniscus height ($H_{m,\mathrm{OGE}}/d$). Based on the geometry, it was correlated by the authors that for single discharge a meniscus height of H_m=2.23 mm for Branch A, and

Table 3 Experimental data for dual discharge

	$H_{f,OGE}/d$		
Fr	Branch A	Branch B	Branch C
52.9	2.9	3.3	3.6
31.7	2.3	2.7	2.6
25.4	2.0	2.5	2.4
19	1.8	2.2	2.1
14.8	1.6	1.9	1.9
10.6	1.4	1.7	1.7
8.1	1.2	1.5	1.4
5.8	1.0	1.3	1.2
4.6	0.91	1.2	1.1
3.5	0.81	1.1	0.98
2.3	0.67	0.94	0.84
1.7	0.61	0.81	0.74
1.2	0.47	0.74	0.64
1.0	0.37	0.57	0.57
0.85	0.27	0.51	0.51
0.67	0.20	0.47	0.44
0.44	0.14	0.37	0.34
0.26	0.14	0.24	0.27
0.12	0.14	0.07	0.26
0.08	0.14	0.03	0.24
0.05	0.14	0.03	0.20
0.03	0.14	0.03	0.17

Table 4 Experimental data for triple discharge

	$H_{f,OGE}/d$	
Fr	FrB = FrC = 34.4	FrB = FrC = 5
62.3	3.3	3.0
52.8	3.1	2.8
42.3	2.8	2.5
31.7	2.6	2.3
21.1	2.2	1.9
14.8	1.9	1.7
10.6	1.8	1.4
8.1	1.6	1.3
5.8	1.4	1.0
4.6	1.3	0.94
3.5	1.2	0.81
2.3	1.1	0.64
1.7	0.98	0.56
1.2	0.84	0.37
1.0	0.74	0.27

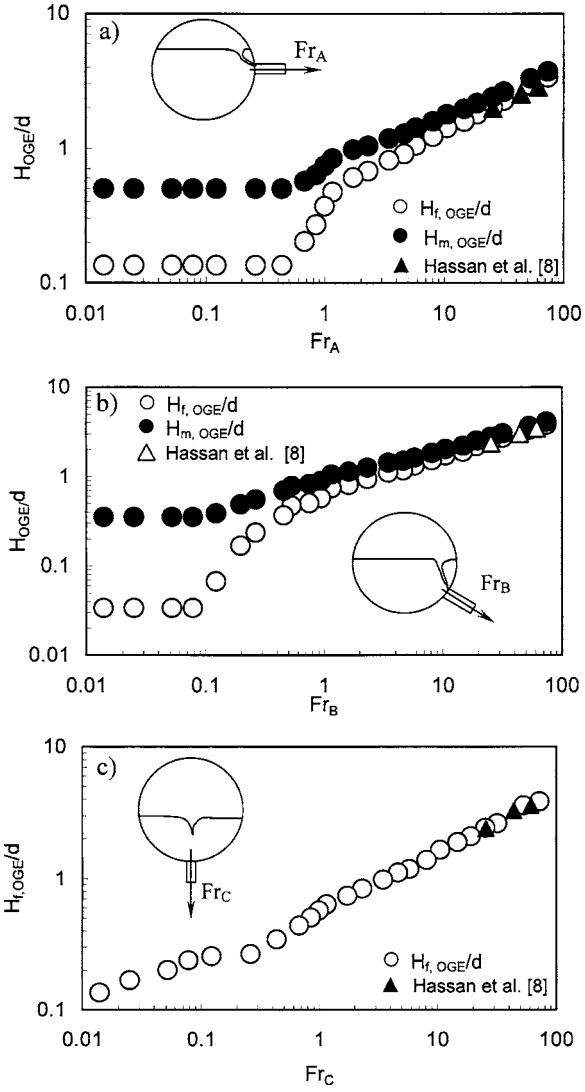

Fig. 3 The critical height at the onset of gas entrainment for single discharge experiments

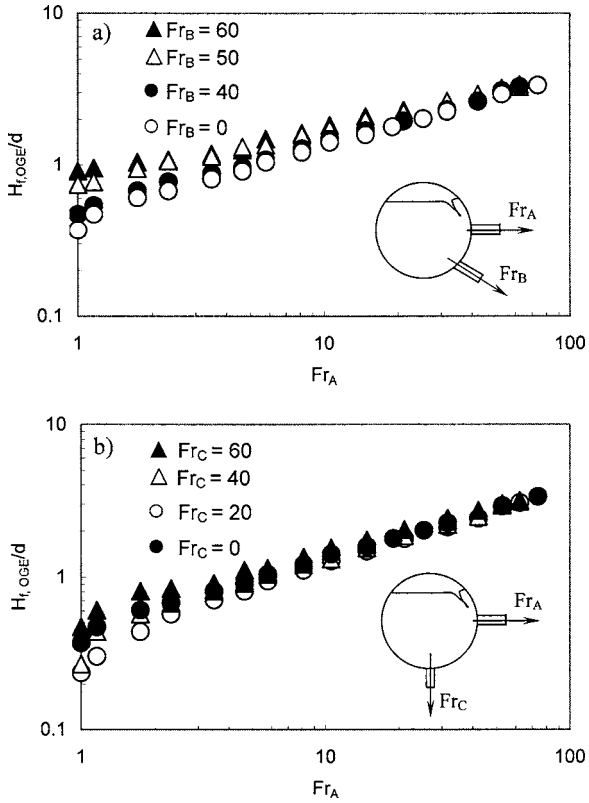

Fig. 4 Effect of an additional discharge on the onset at Branch A

$H_m = 2.03$ mm for Branch B, was used. It was observed that during discharge at low Fr values, the surface tension should be taken into account, since it has a defining impact on the onset of gas entrainment. However, the effect of surface tension cannot be quantified with the present experimental design. Figure 3(*c*) presents the results of $H_{f,OGE}/d$. Due to the normal orientation of the branch inlet relative to the air/liquid interface, the meniscus height is not considered. For all figures, it can be seen that there is good agreement with the present investigation and the available experimental data (Hassan et al. [8]).

3.2 Dual and Triple Discharge. The effect of an additional discharge on the onset of gas entrainment (OGE) at Branch A is shown in Fig. 4. Figure 4(*a*) depicts the critical height, at OGE during dual discharge with Branches A and B active, varying Fr_A from 1 to 100 for different values of Fr_B (0 to 60). It can be seen that when $Fr_B = 0$, which is single discharge through Branch A, the critical height is at its lowest. As Fr_B is increased, the critical height at OGE is gradually increased. The activation of Branch B with Branch A increases the inertia force of the fluid, overcoming gravitational and surface tension forces, and therefore increasing the critical height at the onset of gas entrainment. This occurrence is particularly evident at lower Fr_A values (<10). At higher Fr_A values the critical height is independent on the activation of Branch B, since the whole range of Fr_B values lie a common line. Also, within the whole range of Fr_A values, the onset of gas entrainment is always at Branch A, which is expected due to the geometry of the test section and the strength of the flow at Branch A (Fr_A). A similar analysis can be said for Fig. 4(*b*), with Branches A and C. However, it is noticeable from the figure that at low Fr_A values, the data set with the lowest critical height is not at single discharge through A, as in Fig. 4(*a*). Overall, Branch C has a minor effect on the OGE at Branch A.

Figure 5 shows the effect of an additional discharge on the onset at Branch B. It demonstrates a comparison between single

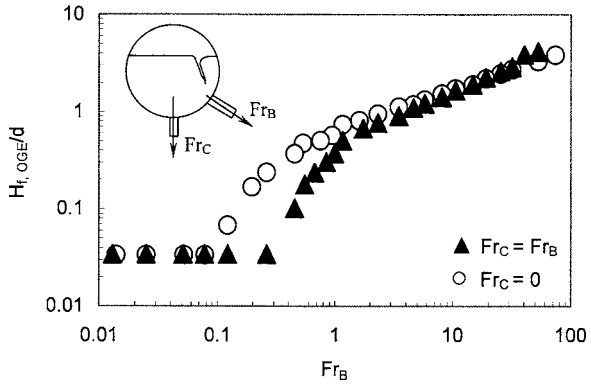

Fig. 5 Effect of an additional discharge on the onset at Branch B

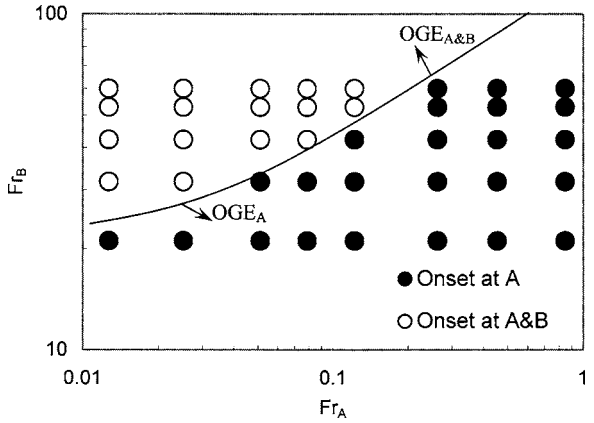

Fig. 7 Regions indicating the branch at which the onset of gas entrainment first occurs during dual discharge through Branches A and B

discharge through Branch B and dual discharge with Branches B and C active, where $Fr_B = Fr_C$. It can be seen that at low Fr_B values, the two sets of data are converged toward each other. However, within a certain range of Fr_B values ($0.1 < Fr_B < 5$), the two data sets diverge from each other, only to once again converge at higher Fr_B values above 5. Within this intermediate range of Fr_B values, OGE at single discharge through branch B occurs at a high critical height than if Branches B and C were activated with the same Fr values.

Figure 6(*a*) shows a comparison between single, dual, and triple discharge over a wide range of Fr_A values (0 to 100), while keeping the other branches maintained at Fr=5. It can be seen that for the whole range of Fr_A values, there is no significant difference in any of the data sets, showing that all points lie on a common line. This demonstrates that at low Fr numbers, such as 5, the critical height is independent of discharge criterion (single, dual, or triple). Figure 6(*b*) shows the same comparison as Fig. 6(*a*), except the branches are maintained at a relatively higher Fr number of 34.4 over the whole range of Fr_A values. Compared to Fig. 6(*a*), there is significant divergence at $Fr_A < 10$. This divergence at lower Fr values was seen in previous figures. The divergence is due to at lower Fr_A values the inertia forces developed by the activation of other branches (Fr_B and/or Fr_C) is great compared to Fr_A. Triple discharge reveals highest critical heights, followed by dual through Branches A and B, then dual through A and C and single discharge through A. Comparing Figs. 6(*a*) and 6(*b*), it is evident that there is a considerable difference in the data sets at low Fr_A values.

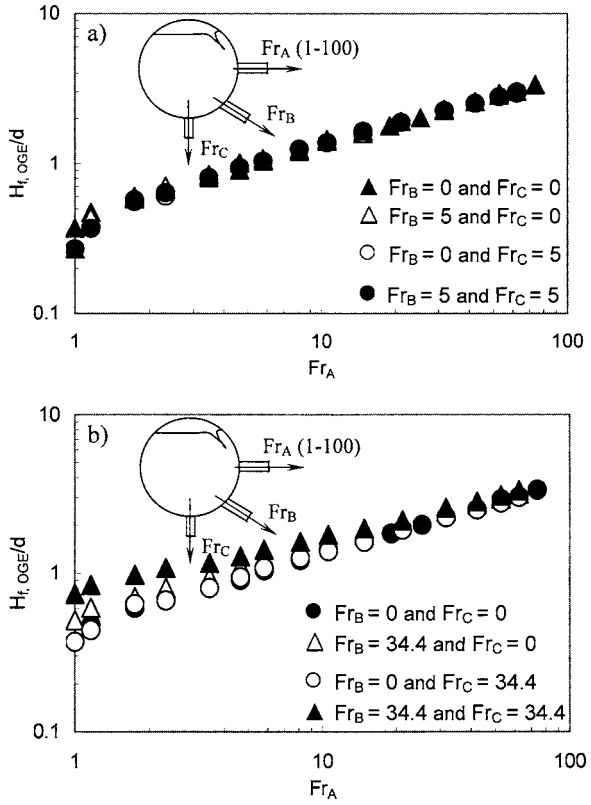

Fig. 6 Comparisons between single, dual, and triple discharge

3.3 Limits for the Onset of Gas Entrainment. Figure 7 shows the branch at which the onset of gas entrainment occurs first, during dual discharge through Branches A and B, at low values of Fr_A ($Fr_A < 1$). It can be seen from the figure that there are two regions with respect to the flowrate though Branches A and B. A region where gas begins to entrain into Branch A, and a region where gas is entrained into A and B simultaneously. The dominant region is the region where the onset is at Branch A primarily due to the geometry of the branch. However, the region where gas is entrained through A and B simultaneously is apparent at high values of Fr_B and low values of Fr_A, due to the increased strength of the flow caused by the high flowrate through Branch B. It was noticed during experiments, and apparent from Fig. 7, that the onset of gas entrainment will never occur only at Branch B during dual discharge with Branches A and B active (see photograph of Fig. 9(*b*)). The primary reason for this is the geometry of the test section, being the curved surface and the location of the branch with respect to the air/water interface. Even at very high Fr_B values and very low Fr_A values, the high strength and inertia force caused by Branch B will have a strong pull on the interface and gas will be entrained. However, since the strength is rather high, it will pull the gas and simultaneously expose the weak Branch A to the gas region, allowing gas to flow into Branch A.

Figure 8 has similar implications as Fig. 7, showing the different regions (branch) where the onset of gas entrainment will occur during dual discharge with Branches A and C active. It is obvious from the figure that there are three regions where OGE will occur depending on the respective Froude number of each branch. Like the previous figure, the dominant region is that where OGE occurs at branch A, due to its physical proximity from the liquid-air interface. This dominant region occurs over the whole range of Fr_A values, and below Fr_C values of 25. At high values of Fr_A and Fr_C, the onset will occur at both branches simultaneously. This is generally expected due to the high strengths of the flow through each branch. It is interesting to note that this region extends toward Fr_A values as low as 0.05, within a certain range of Fr_C

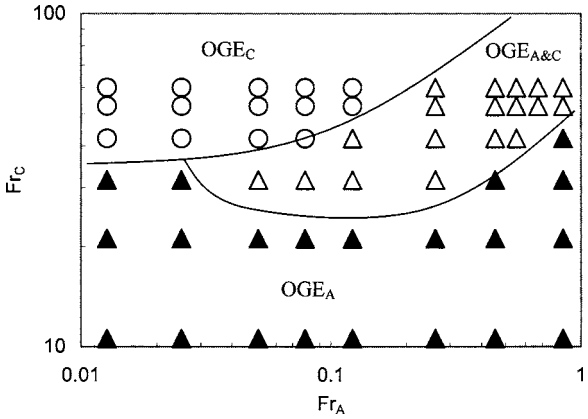

Fig. 8 Regions indicating the branch at which the onset of gas entrainment first occurs during dual discharge through Branches A and C

values above 30. In contrast to the previous figure, there is a third region where the onset occurs at Branch C. This occurrence is at low values of Fr_A and high values of Fr_C. Aside from this, the onset is able to occur only at Branch C due to the geometry of Branch C relative to Branch A. The vertical distance between the

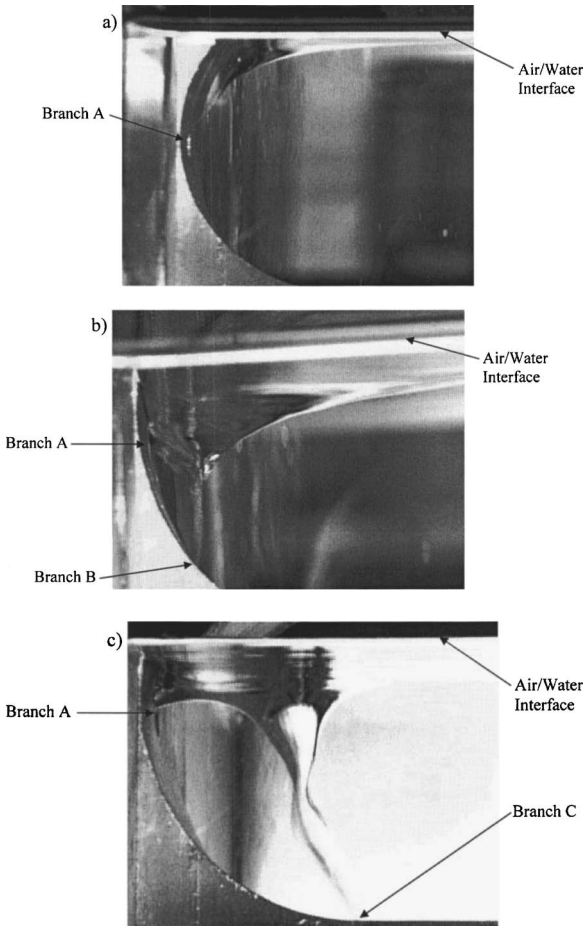

Fig. 9 (a) The onset point at single discharge through Branch A (Fr_A=52). (b) The onset point occurring simultaneously at Branches A and B, with the activation of Branch B (Fr_A=0.1 and Fr_B=52). (c) The onset point occurring simultaneously at Branches A and C, with the activation of Branch C (Fr_A=0.5 and Fr_C=52).

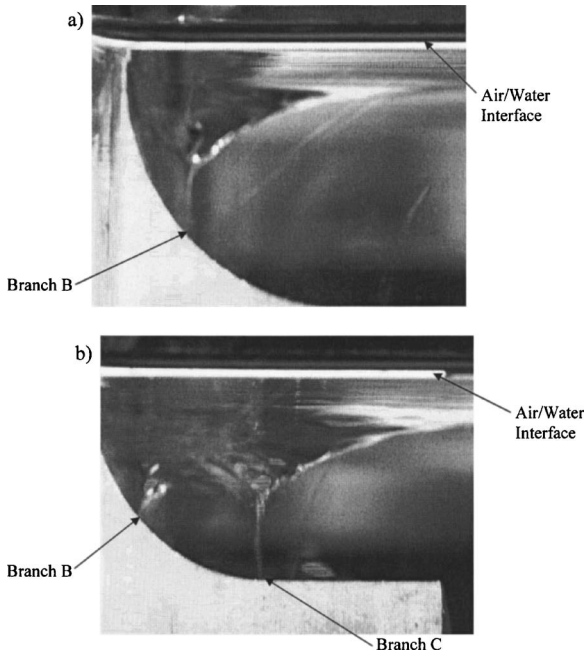

Fig. 10 (a) The onset point at single discharge through Branch B (Fr_B=52). (b) The onset point occurring simultaneously at Branches B and C, with the activation of Branch C (Fr_B=10 and Fr_C=52).

two branches is great enough that gas may entrain into Branch C without entraining into Branch A. However, this was not the case from Fig. 7 with Branches A and B active, as previously mentioned.

Figures 9 and 10 depict photographs taken at distinct Fr values to demonstrate the flow phenomenon observed during gas entrainment for single and dual discharge. It should be noted that the orientation of the branches with respect to the main header are reversed from those shown in the diagrams from Figs. 1–6. Figure 9(*a*) shows the onset at single discharge through branch A (Fr_A =52). Figure 9(*b*) shows the point at which the onset of Branches A and B occur simultaneously with the activation of Branch B. Note the influence this has on the flow field. In order to allow onset to occur at both branches simultaneously, the strength of Branch A had to be reduced significantly to Fr_A=0.1 while the strength of Branch B was high at Fr_B=52. This is necessary since this phenomenon occurs at a distinct region (see Fig. 7). Figure 9(*c*) is similar to Fig. 9(*b*), in that is shows the point at which the onset of Branches A and C occur simultaneously with the activation of Branch C. Here, Fr_A had to be reduced to 0.5, whereas Fr_C=52, which was necessary for the onset to simultaneously occur in both branches (see Fig. 8). Figures 10(*a*) and 10(*b*) are similar to the previous figures; however, they depict the onset points at Branches B and C, respectively. Figure 10(*a*) shows the onset during single discharge through Branch B (Fr_B=52). Figure 10(*b*) shows where the onset occurs simultaneously through Branches B and C. Here, Fr_B=10, and Fr_C=52, these strengths were necessary in order for the onset to occur at both branches simultaneously. It should be observed from the photographs that distinct flow fields occur inside the main header depending on the onset points, the strengths, and discharge criterion.

4 Conclusion

An experimental investigation regarding the onset of gas entrainment during single, dual, and triple discharge from a stratified, two-phase region through small branches installed on a semicircular wall was carried out. The semicircular test section was in close-dimensional resemblance with that of a CANDU header-

feeder system, with branches mounted at orientation angles of 0°, 45°, and 90° from the horizontal. New experimental data for the onset of gas entrainment was developed during single and multiple discharge from an air/water stratified region over a wide range of Froude numbers (0 to 100). It was found that the critical height at the onset of gas entrainment (single or simultaneous) was a function of the corresponding Froude number of each branch, the vertical distance between the centerlines of the branches (for multiple discharge), the hydraulic resistance of the discharging lines, as well as the orientation of the branches and their diameter with respect to the main header. Different comparisons were made from numerous configurations for single, dual, and triple discharge over the whole range of Froude numbers, in order to thoroughly understand the onset of gas entrainment phenomenon. In future research, the following efforts are to be considered regarding a semicircular wall configuration: (1) Theoretically investigate the effect of dual or triple discharge on H_{OGE} of a branch, as well the effect of superimposed velocity in the main pipe; (2) Explore the effect of surface tension on the onset of gas entrainment from a curved wall geometry at low Froude numbers; and (3) Attain experimental data for the onset of entrainment phenomenon when the water/air interface is wavy stratified, which is closer to real applications.

References

[1] Zuber, N., 1980, "Problems in Modeling of Small Break LOCA," Nuclear Regulatory Commission Report, NUREG-0724.

[2] Smoglie, C., and Reimann, J., 1986, "Two-Phase Flow Through Small Branches in a Horizontal Pipe With Stratified Flow," Int. J. Multiphase Flow, **12**, pp. 609–625.

[3] Schrock, V. E., Revankar, S. T., Mannheimer, R., Wang, C. H., and Jia, D., 1986, "Steam-Water Critical Flow Through Small Pipes From Stratified Upstream Regions," Proceedings of the 8th International Heat Transfer Conference, San Francisco, CA 5, pp. 2307–2311.

[4] Yonomoto, T., and Tasaka, K., 1988, "New Theoretical Model for Two-Phase Flow Discharged From Stratified Two-Phase Region Through Small Break," J. Nucl. Sci. Technol., **25**, pp. 441–455.

[5] Yonomoto, T., and Tasaka, K., 1991, "Liquid and Gas Entrainment to a Small Break Hole From a Stratified Region," Int. J. Multiphase Flow, **17**, pp. 745–765.

[6] Parrott, S. D., Soliman, H. M., Sims, G. E., and Krishnan, V. S., 1991, "Experiments on the Onset of Gas Pull-Through During Dual Discharge From a Reservoir," Int. J. Multiphase Flow, **17**, pp. 119–129.

[7] Hassan, I. G., Soliman, H. M., Sims, G. E., and Kowalski, J. E., 1996, "Discharge From a Smooth Stratified Two-Phase Region Through Two Horizontal Side Branches Located in the Same Vertical Plane," Int. J. Multiphase Flow, **22**, pp. 1123–1142.

[8] Hassan, I. G., Soliman, H. M., Sims, G. E., and Kowalski, J. E., 1997, "Single and Multiple Discharge From a Stratified Two-Phase Region Through Small Branches," Nucl. Eng. Des., **176**(3), pp. 233–245.

[9] Hassan, I. G., Soliman, H. M., Sims, G. E., and Kowalski, J. E., 1998, "Two-Phase Flow From a Stratified Region Through a Small Side Branch," ASME J. Fluids Eng., **120**, pp. 605–612.

[10] Kowalski, J. E., and Krishnan, V. S., 1987, "Two Phase Flow Distribution in a Large Manifold," Proceedings of the AIChE Annual Meeting, New York, NY.

[11] Armstrong, K. F., Parrott, S. D., Sims, G. E., Soliman, H. M., and Krishnan, V. S., 1992a, "Theoretical and Experimental Study of the Onset of Liquid Entrainment During Dual Discharge From Large Reservoirs," Int. J. Multiphase Flow, **18**, pp. 217–227.

[12] Maier, M. R., Soliman, H. M., Sims, G. E., and Armstrong, K. F., 2001a, "Onsets of Entrainment During Dual Discharge From a Stratified Two-Phase Region Through Horizontal Branches With Centrelines Falling in an Inclined Plane: Part 1—Analysis of Liquid Entrainment," Int. J. Multiphase Flow, **27**, pp. 1011–1028.

[13] Maier, M. R., Soliman, H. M., and Sims, G. E., 2001b, "Onsets of Entrainment During Dual Discharge From a Stratified Two-Phase Region Through Horizontal Branches With Centrelines Falling in an Inclined Plane: Part 2—Experiments on Gas and Liquid Entrainment," Int. J. Multiphase Flow, **27**, pp. 1029–1049.

[14] Hassan, I. G., 1995, "Single, Dual, and Triple Discharge From a Large, Stratified, Two-Phase Region Through Small Branches," Ph.D. thesis, University of Manitoba, Winnipeg, Manitoba.

[15] Taylor, G. I., 1950, "The Instability of Liquid Surfaces When Accelerated in a Direction Perpendicular to Their Planes," Proc. R. Soc. London, Ser. A, **201**, pp. 192–196.

R. Bavière
Ph. D. Student
Laboratory of Geophysical and Industrial Flows,
Grenoble University,
UJF-INPG-CNRS BP 53X,
38041 Grenoble Cedex 9, France
and Centre de Recherches sur les Très
Basses Températures,
CNRS B.P. 166,
38042 Grenoble Cedex 09, France

G. Gamrat
Ph. D. Student

M. Favre-Marinet[1]
Professor
e-mail: Michel.Favre-Marinet@hmg.inpg.fr

S. Le Person
Assistant Professor

Laboratory of Geophysical and Industrial Flows,
Grenoble University,
UJF-INPG-CNRS, BP 53X,
38041 Grenoble Cedex 9, France

Modeling of Laminar Flows in Rough-Wall Microchannels

Numerical modeling and analytical approach were used to compute laminar flows in rough-wall microchannels. Both models considered the same arrangements of rectangular prism rough elements in periodical arrays. The numerical results confirmed that the flow is independent of the Reynolds number in the range 1–200. The analytical model needs only one constant for most geometrical arrangements. It compares well with the numerical results. Moreover, both models are consistent with experimental data. They show that the rough elements drag is mainly responsible for the pressure drop across the channel in the upper part of the relative roughness range. [DOI: 10.1115/1.2201635]

1 Introduction

Much work in recent years has gone into the development of microchannel technology. This has been especially useful in electronics, where ever faster and smaller microchips are built, or in biology where lab on chips are currently used. Investigations of liquid flows in rough microducts present a great interest since rough surfaces are commonly found in many practical situations. The size of roughness elements is usually very small compared to macroscale in ducts of conventional size so that roughness effects may be neglected in laminar flows. However, the relative roughness becomes significant when the duct size is reduced to several hundred micrometers or less, and may play a role in the hydrodynamics, even in laminar flows. Surface roughness is due to the process used for making microchannels, and may be high when micromachining is used. In addition, rough walls are potentially interesting for enhancing heat transfer in industrial applications. It is therefore highly desirable to understand the roughness effect on flows in microducts and to quantify its influence on the pressure losses. This has motivated several studies using experimental, analytical and numerical approaches.

Mala and Li [1] experimentally found an increase in the Poiseuille number for water flows in rough microtubes ranging from 50 μm to 254 μm in diameter. For Re below 800, they measured an increase in pressure losses ranging from 7% to 15% for relative roughness (roughness element height divided by tube diameter) between 1.2% and 3.6%. For Re higher than 1000, the Poiseuille number was found to increase significantly with Re. This was interpreted by the authors as the result of an early transition to turbulence in rough microtubes, when compared to conventional size tubes. Guo and coworkers [2,3] also performed measurements in rough stainless steel microtubes. They concluded that a relative roughness of 3% to 4% increased the pressure drop from 15% to 37% when compared to the smooth case. Judy et al. [4] conducted experiments in rough stainless steel microtubes from 75 μm to 125 μm in diameter. There is no precise indication of the roughness height in their paper. They did not conclude that an increase in the pressure losses might be due to roughness elements. In their study, the Poiseuille number was found to be constant in the laminar regime. Measurements were also carried out in rough trapezoidal microchannels [5], obtained by wet-etching a silicon substrate and covering it with a Pyrex glass plate. The results revealed an increase in the Poiseuille number compared to the conventional theory in the Reynolds range investigated in the present work ($<$1500). For low Re, the increase in pressure losses varied from 8% to 30% for relative roughness ranging from 1.7% to 3%. These investigations supported the idea of an early transition to turbulence due to roughness elements. Pfund et al. [6] performed experiments in a rough rectangular microchannel 257 μm in height. They found a 26% increase in the pressure losses for a mean relative roughness (roughness element height divided by channel height) of 1.5%. Recently, Baviere et al. [7,8] investigated high aspect ratio rectangular microchannels ranging from 100 μm to 300 μm in height. In their experiments, the relative roughness ranged from 1.7% to 5%. For Re between 50 and 1000, the corresponding increase in the Poiseuille number was found to be 5% to 37%.

To summarize, most published experimental results concerning flows in rough microducts show an increase in pressure losses compared to conventional smooth wall ducts. However, some aspects of these results are conflicting. In some experiments, the Poiseuille number increases significantly with Re. On the contrary, other results show Reynolds number independency of the Poiseuille number in a wide range of Re. It is therefore important to establish the relationship between the pressure drop increase and the rough surface characteristics.

An analytical approach of roughness effects was developed by Mala and Li [1] and Qu et al. [5]. These authors proposed a roughness-viscosity model in a manner similar to the eddy-viscosity concept in turbulent flows. The model brought into play a constant which needed to be evaluated from experimental re-

[1]Corresponding author.

Contributed by the Fluids Engineering Division of ASME for publication in the JOURNAL OF FLUIDS ENGINEERING. Manuscript received April 15, 2005; final manuscript received November 22, 2005. Assoc. Editor: Ali Beskok.

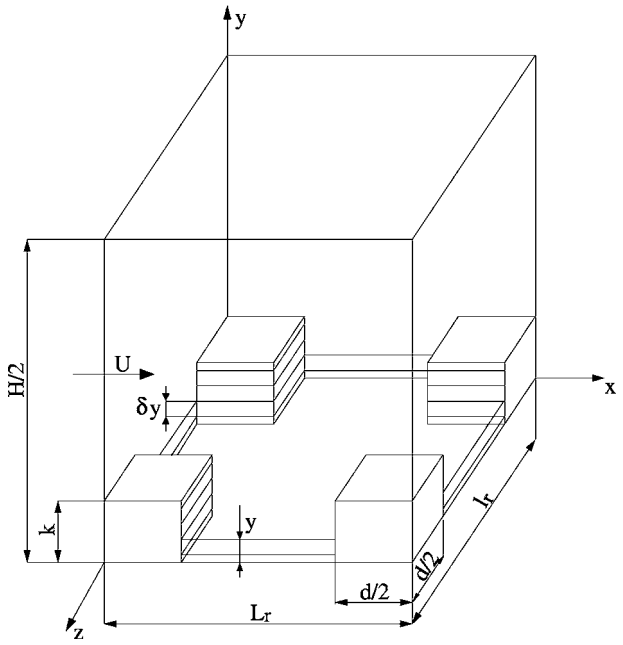

Fig. 1 Computational domain and arrangement of the rough elements

sults. More recently, Koo and Kleinstreuer [9] modeled the near-wall region by using an equivalent porous medium layer. They were able to reproduce the measurements of [1,3] by adjusting the permeability (or equivalently the Darcy factor) of this layer. They also applied the model to microjournal bearings [10].

Numerical computations were performed by Hu et al. [11] (denoted HWL hereafter), for water flows in two-dimensional microchannels with rectangular prism rough elements. Their calculations were done in channels ranging from 5 μm to 50 μm in height at Reynolds number ranging from 0.002 to 20. The authors expressed the roughness effect as a relative channel height reduction depending on the roughness elements geometry.

The aim of the present paper is to show that a very simple analytical model is able to predict the roughness effect on the flow in rough-wall microchannels. The analytical model is based on the method developed by Taylor et al. [12] for predicting the rough-wall skin friction in turbulent flows. In this paper, we combined analytical and numerical approaches of the flow and compared the results to experimental data [8] and to published numerical results [11].

2 Numerical Approach

The numerical approach pertains to the roughness model developed by Hu et al. [11]. The fluid physical properties, the basic equations, and boundary conditions follow the details of the model proposed by these authors, except that the explored range of Re number was extended to 200.

2.1 Geometrical Model of Roughness. The geometrical model of roughness consists of blocks periodically distributed on the walls of a plane channel of height H (Fig. 1). The wavelengths are L_r and l_r, in the longitudinal x and transverse z directions, respectively. The rough elements are parallelepipeds of square cross section (side length d) and of height k placed on a smooth wall, called thereafter the bottom wall. They are distributed either in symmetrical or asymmetrical arrangements. Series of calculations were performed by varying the dimensions as follows:

Roughness height ($k[\mu\text{m}]$): 0.1, 0.2, 0.3, 0.5, 0.7, 1, 2
Roughness side ($d[\mu\text{m}]$): 0.5, 1, 1.5
Roughness spacing ($L_r=l_r[\mu\text{m}]$): 2, 3, 4
Channel height ($H[\mu\text{m}]$): 5, 7.5, 10

2.2 Computation Domain and Boundary Conditions. The computational domain extends over one wavelength in the x and z directions and over the half-channel height ($H/2$) in the y direction normal to the wall (Fig. 1). The longitudinal and transverse dimensions are thus equal to the rough element spacing. The computational domain was treated as part of an extremely long channel so that the flow was considered as fully developed in the longitudinal direction. As a result, the flow properties are periodic in the x direction, except for the pressure which is composed of a linearly decreasing term and a periodic one. This assumption allows for applying periodic boundary conditions on opposite sides of the domain in the longitudinal direction. The periodic boundary condition may be written for the velocity field

$$\mathbf{U}(x,y,z) = \mathbf{U}(x + L_r, y, z) \tag{1}$$

where $\mathbf{U}$ is the velocity vector.

The lateral sides of the computational domain are chosen as the planes of symmetry of the rough elements parallel to the xy plane. As a result, the velocity gradient of U and V normal to these side planes and the transverse velocity component W are assumed to be zero.

$$\text{at } z = 0 \text{ and } z = l_r \quad dU/dz = 0, \quad dV/dz = 0, \quad W = 0 \tag{2}$$

The condition of symmetry at the top plane of the computational domain is written

$$\text{at } y = H/2 \quad dU/dy = 0, \quad V = 0, \quad dW/dy = 0 \tag{3}$$

The system of boundary conditions is completed by the no-slip condition on all the solid boundaries.

2.3 Equations. Modeling the flow as laminar, steady and incompressible, the governing equations consist of the following system:

Continuity equation

$$\nabla \mathbf{U} = 0 \tag{4}$$

Momentum equation

$$\rho \mathbf{U} \nabla \mathbf{U} = -\nabla P + \mu \nabla^2 \mathbf{U} \tag{5}$$

2.4 Numerical Scheme. Numerical computations of the flow were carried out by using the commercial code FLUENT 6.1.22. The equations were discretized by means of a second order upwind finite volume method. As these equations are nonlinear, a SIMPLEC (semi-implicit pressure linked equations consistent) algorithm was used. This algorithm is based on a prediction-correction method, which allows the equations to be linearized and solved iteratively. The pressure under-relaxation factor was set to 0.5. The calculations were performed by means of a double precision solver until the level of residuals decreased below 10^{-12}. Computations were performed on orthogonal grids generated by GAMBIT 2.1.2.

2.5 Numerical Accuracy. Grid-convergence tests were performed to verify the mesh accuracy. The tests were conducted with three grids having a number of mesh nodes equal to $32 \times 40 \times 32$, $48 \times 60 \times 48$, $64 \times 80 \times 64$ in the x, y, z directions, respectively. The pressure gradient was chosen as the control parameter during the computations. The difference in the results as given by the coarse and the intermediate grids was 1.5%, and was 0.7% between the intermediate and the fine grids. The accuracy was further estimated by means of Richardson extrapolation [13]. When two approximations of the solution T_1 and T_2 are computed with two mesh sizes h_1 (fine grid) and h_2 (coarse grid), one can estimate a third approximation T_3 whose term of leading order in the Taylor series expansion around the exact value is of higher order than that for T_1 or T_2. T_3 is given by the Richardson extrapolation

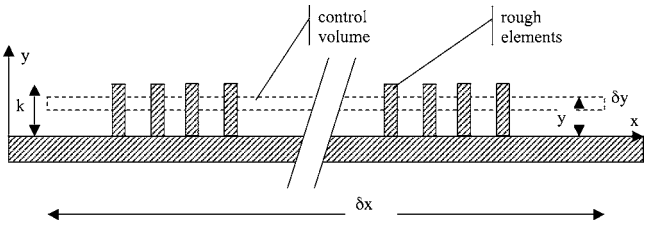

Fig. 2 Sketch of a control volume over the rough surface. Side view.

$$T_3 = T_1 + \frac{T_1 - T_2}{(h_2/h_1)^2 - 1} \tag{6}$$

The difference in the pressure gradient as obtained with the intermediate mesh and that obtained from the Richardson extrapolation applied with the intermediate and fine grids was 1.6%. This observation allowed us to assume that the numerical calculations were sufficiently accurate with the grid $48 \times 60 \times 48$, which was adopted for all the cases.

3 Analytical Approach

The analytical approach is based on the method developed by Taylor et al. [12] for predicting the rough-wall skin friction in turbulent flows. It considers the same geometrical model of roughness as the numerical analysis. The flow in a half channel consists of two adjacent layers: A roughness layer with distributed rough elements in the near-wall region and a clear layer in the central region. Like in [12], the physical effects of roughness are taken into account by using a blockage coefficient and by considering drag forces exerted by the rough elements on the fluid flow.

3.1 Equations. The present section is devoted to the derivation of the momentum equation in the roughness layer. Using the method of Taylor et al., conservation equations for mass and momentum are derived for control volumes (CV) of infinitesimal thickness δy in the direction normal to the wall, extending over a large distance compared to the rough elements spacing in the other directions (respectively, δx, $\delta z \gg L_r$, l_r, Fig. 2). Flow quantities are averaged over the lengthscales δx, δz as in homogenization methods.

3.1.1 Blockage Coefficient. The flow velocity is averaged over a surface opened to the flow at the distance y from the wall. Thus, the resulting spatially averaged velocity $U(x,y,z)$ takes into account the blockage effect due to the presence of the rough elements. For periodically distributed blocks, U is dependent on y only and it is sufficient to integrate the velocity over one wavelength in the x and z directions only. $U(y)$ is then defined by

$$U(y) = \frac{1}{L_r l_r - d^2} \int \int_{dS(x)} u(\xi,y,\zeta) d\xi d\zeta \quad \text{for } 0 \leqslant y \leqslant k \tag{7}$$

where $u(\xi,y,\zeta)$ stands for the actual flow velocity in the roughness region ($y \leqslant k$). Integration is performed over the surface $dS(x)$ open for flow in an elementary cell of sides $l_r \times L_r$ (Fig. 3). This surface is independent of y in the case of cylindrical rough elements.

The local blockage coefficient in the x direction is the fraction of the area open for flow through a slice of thickness δy in a plane $x = Cst$. This fraction is obviously a function of x in the roughness layer. Like Taylor et al. [12], we consider the averaged value of the local blockage coefficient over a large distance δx. For the particular case of periodically distributed rough elements, the averaged blockage coefficient β is given by

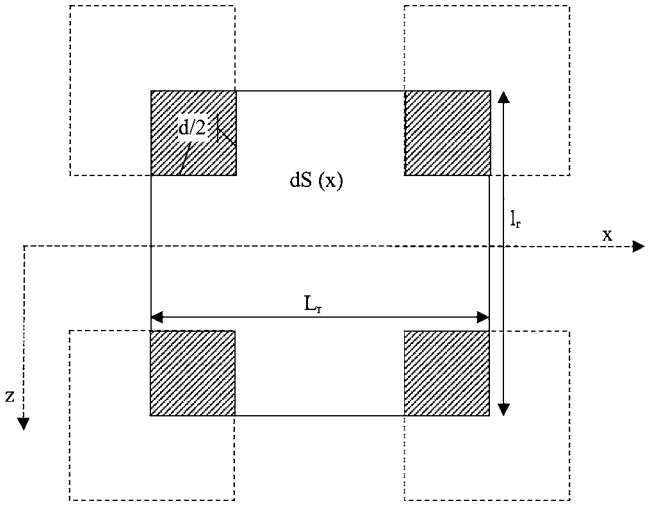

Fig. 3 Surface open for flow. Top view.

$$\beta = \frac{1}{L_r l_r} \int \int_{dS(x)} d\xi d\zeta \tag{8}$$

and is therefore

$$\beta = 1 - \frac{d^2}{L_r l_r} \quad \text{for} \quad 0 \leqslant y \leqslant k$$
$$\beta = 1 \quad \text{for} \quad k \leqslant y \tag{9}$$

This is the same expression as in [12], except that the cross section of the rough elements is square instead of being circular in [12]. In the present model of cylindrical elements, β is independent of y. The maximum blockage effect corresponds to $\beta = 0$, when the rough elements are adjacent.

We also use a filtration or Darcy velocity $u_D(y)$, in the terminology of flow in porous media. This velocity is defined with the total surface $L_r l_r$

$$u_D(y) = \frac{1}{L_r l_r} \int \int_{dS(x)} u(\xi,y,\zeta) d\xi d\zeta \tag{10}$$

so that

$$U(y) = u_D(y)/\beta \tag{11}$$

The effective velocity U is higher than the Darcy velocity because it refers to a smaller surface than u_D. In the most general case, the average velocity U would be a function of x and z. However, the flow is assumed to be two dimensional and fully developed so that U depends on y only. As a result, the transverse velocity is zero and the inertia terms are also zero in the momentum equation.

In the present approach, the pressure is spatially averaged in the roughness layer like the velocity. However, the result depends on the position x of the integration surface because of the pressure gradient in the channel.

$$\bar{p}(x,y) = \frac{1}{L_r l_r - d^2} \int \int_{dS(x)} p(\xi,y,\zeta) d\xi d\zeta \quad \text{for } 0 \leqslant y \leqslant k \tag{12}$$

We suppose that $\bar{p}(x,y)$ is independent of y in the present mean one-dimensional flow. From here, we call $P(x)$ the averaged pressure defined by Eq. (12).

3.1.2 Momentum Equation. The equilibrium of a control volume results from the competition between

Pressure forces on the upstream and downstream sides of CV

Viscous shear stresses on the upper and lower sides of CV

Drag forces due to the rough elements

The drag force due to the portion of a rough element included in CV is modeled by using a drag coefficient C_d

$$\delta F_d = \frac{1}{2}\rho U^2(y) C_d d\,\delta y \tag{13}$$

Finally, the momentum equation is

$$0 = -\frac{d}{dx}(\beta P) + \frac{d}{dy}\left(\mu\beta\frac{dU}{dy}\right) - \frac{1}{2}\rho C_d d\frac{U^2}{L_r l_r} \quad \text{for} \quad 0 \leqslant y \leqslant k$$
$$0 = -\frac{dP}{dx} + \mu\frac{d^2U}{dy^2} \quad \text{for} \quad k \leqslant y \leqslant H/2 \tag{14}$$

The expression of the pressure term results from the definition (Eq. (12)). It may be interpreted by considering that the pressure forces act on a reduced area owing to the blockage effect. In the same way, a reduced area of the CV is exposed to the viscous shear stresses. Equation (14) is identical to the momentum equation of [12], except that there are no inertia terms and no Reynolds shear stresses in the present case.

3.1.3 Boundary Conditions. A difficulty arises for the rough/clear layer interfacial conditions for the present shape of the roughness elements. In fact, the blockage factor is discontinuous at the interface, going from 1 to a constant value $\beta < 1$ across the interface. This difficulty would not exist for other shapes of the roughness elements, like conical-shaped blocks, as in the Taylor et al. paper [12]. The continuity of the local velocity across the rough/clear layer interface leads to the continuity of the Darcy velocity. As a result, the spatially averaged velocity $U(y)$ is discontinuous like the blockage coefficient at the interface.

$$\beta U(y = k^-) = U(y = k^+) \tag{15}$$

As mentioned before, this discontinuity would not exist for roughness elements of gradually decreasing cross section. In fact, it is likely that the blockage effect extends over a small distance within the clear medium away from the interface because the fluid is strongly slowed down in the vicinity of the top of the blocks. The present model does not account for this effect and this is probably a weakness of the model. It could probably be improved by introducing a smoothing of the blockage effect near the interface. This was not attempted in the present work to preserve the simplicity of the model.

In order to express the boundary condition on the shear stress at the interface, we consider a control volume of height δy and lengths δx, δz in the other directions, centered at $y=k$. The force balance on this CV requires

$$\left[\mu \left.\frac{dU}{dy}\right|_{y=k+\delta y/2} - (1-\beta)\mu \left.\frac{dU}{dy}\right|_{y=k^+} - \beta\mu \left.\frac{dU}{dy}\right|_{y=k-\delta y/2}\right]\delta x\,\delta z + \left[dP\frac{(1+\beta)}{2}\delta z - \frac{1}{2}\rho U^2(k) C_d \frac{d\,\delta x\,\delta z}{2L_r l_r}\right]\delta y = 0 \tag{16}$$

When δy tends to zero, the pressure force and the drag force become negligibly small so that Eq. (16) reduces to

$$\mu \left.\frac{dU}{dy}\right|_{y=k^-} = \mu \left.\frac{dU}{dy}\right|_{y=k^+} \tag{17}$$

or using the Darcy velocity

$$\frac{1}{\beta}\mu \left.\frac{du_D}{dy}\right|_{y=k^-} = \mu \left.\frac{du_D}{dy}\right|_{y=k^+} \tag{18}$$

Again, the discontinuity of the shear stress expressed with the Darcy velocity would not exist for an interface with continuously varying blockage factor.

The system of boundary conditions is completed by the no-slip condition at the wall bottom and the condition of symmetry on the channel axis in the case of identical rough walls on both sides of the channel.

$$U(y = 0) = 0 \tag{19}$$

$$\left.\frac{\partial U}{\partial y}\right|_{y=H/2} = 0 \tag{20}$$

For a semirough channel formed by a rough wall on one side and a smooth wall on the opposite side, the latter condition is replaced by the no-slip condition on the smooth side

$$U(y = H) = 0 \tag{21}$$

3.1.4 Drag Coefficient. The model relates the drag force $\delta F_d(y)$ exerted by the fluid on a slice of rough element of height δy to the local velocity $U(y)$. The starting point of the analysis considers a single rough element oriented across a fluid stream of uniform velocity $U_\infty = U(y)$. This flow is mainly characterized by the local Reynolds number $\mathrm{Re}_d = \rho U(y) d/\mu$, which is based on a typical dimension of a block cross section, namely, the side length d. Re_d is small in most microchannel flows: $\mathrm{Re}_d \approx 5$ at the top of the rough elements for a typically high value of $\mathrm{Re}_{D_h} = 2000$ in a channel of relative roughness 2.5% and for elements of relative width (d/H) about 2.5%. The flow is therefore dominated by viscous effects in the vicinity of the blocks.

Dimensional analysis shows that the drag force may be written

$$\delta F_d(y) = \frac{1}{2}K\left(\frac{k}{d}, \frac{y}{k}, \mathrm{Re}_d\right)\left(\mu\frac{U(y)}{d}\right)d\,\delta y \tag{22}$$

δF_d is also related to the drag coefficient C_d by Eq. (13) so that $K = C_d \mathrm{Re}_d$. Eliminating C_d by using Eqs. (13) and (22), the last term of Eq. (14) becomes $1/2 K\mu U/L_r l_r$.

It is well known [14] that inertia effects cannot be totally discarded for creeping flows near extremely long cylinders. However, the numerical simulations of the present work and those of HWL along with some experimental works [4,7] indicate that roughness effects are Re independent up to $\mathrm{Re}_{D_h} = 200$. Consequently we assume that K is a function of y/k and k/d only. The presence of these parameters in the coefficient K reflects the three-dimensional nature of the low-Reynolds number flow near the blocks. For creeping flows normal to the major axis of very slender prolate spheroids ($E \gg 1$), the drag force is given by [15]

$$D = \frac{4\pi\mu U 2a}{\frac{1}{2} + Ln\frac{2a}{b}} \tag{23}$$

where $E = a/b$, $2a$ = major axis, $2b$ = minor axis of the spheroid.

Following the form of Eq. (23), we propose for K the following expression:

$$K = \frac{K_1}{1 + K_2 Ln\frac{k}{d}} \quad \text{for} \quad \frac{k}{d} \geqslant 1$$
$$K = K_1 \quad \text{for} \quad \frac{k}{d} \leqslant 1 \tag{24}$$

The drag force is, however, also dependent of the geometrical arrangement of the rough elements like in a bank of tubes in a cross-flow exchanger. The coefficient K_1 was therefore deduced from the numerical simulations conducted in typical arrangements of the rough elements. For a given flow field, the elementary drag force δF_d was obtained by integrating the pressure forces on the front and rear sides of a block slice of height δy and the viscous forces on its lateral sides. The numerical results have shown that the coefficient K_1 is nearly independent of y in the upper part of

the blocks, as presented later. For $k/d \leqslant 1$, K_1 was found to be 116 for the following geometrical arrangement of the rough elements ($d/H=0.2$, $0.1<k/H<0.2$, $L_r/d=l_r/d=2$). For $k/d>1$, the best agreement of the model with the HWL results was obtained for $K_2=0.5$. The dependence of K on the geometrical parameters was not systematically explored in the present work. The same constants were used for all the geometrical arrangements considered in this study. The model could probably be improved with a better estimation of K as a function of the actual arrangement of the rough elements.

3.1.5 Analytical Solution. The system of equations is reduced to dimensionless form by normalizing the lengths with the channel height H and the effective velocity with the bulk velocity of the Poiseuille flow in a smooth channel

$$U^* = \frac{U}{-\frac{1}{\mu}\frac{dP}{dx}\frac{H^2}{12}} \tag{25}$$

Modeling K as independent of y, straightforward computations lead to the following equations for the velocity profile in a channel with two rough sides:

for $0 \leqslant y^* \leqslant k^*$

$$U^*(y^*) = \frac{12}{A^*}\left\{1 + \frac{\sqrt{A^*}\left(\frac{1}{2}-k^*\right)\sinh(\sqrt{A^*}y^*) - \cosh[\sqrt{A^*}(k^*-y^*)]}{C_1}\right\} \tag{26}$$

for $k^* \leqslant y^* \leqslant \frac{1}{2}$

$$U^*(y^*) = \frac{12\beta}{A^*}\left[1 + \frac{\sqrt{A^*}\left(\frac{1}{2}-k^*\right)S_1 - 1}{C_1}\right] + 6[y^* - y^{*2} + k^{*2} - k^*]$$

where $A^*=1/2K/L_r^* l_r^* \beta$, $C_1=\cosh(\sqrt{A^*}k^*)$, $S_1=\sinh(\sqrt{A^*}k^*)$ For a semirough channel, the expressions are

For $0 \leqslant y^* \leqslant k^*$

$$U^*(y^*) = \frac{12}{A^*}(1 - e^{-\sqrt{A^*}y^*}) + 2D_1 \sinh(\sqrt{A^*}y^*) \tag{27}$$

For $k^* \leqslant y^* \leqslant 1$

$$U^*(y^*) = (y^*-1)\left[2D_1\sqrt{A^*}C_1 + 12\left(k^* + \frac{E_1}{\sqrt{A^*}}\right)\right] + 6(1-y^{*2})$$

where $E_1=\exp(-\sqrt{A^*}k^*)$

$$D_1 = \frac{6}{\sqrt{A^*}(k^*-1)C_1 - \beta S_1}\left[\frac{k^{*2}}{2} - \frac{1}{2} + (1-k^*)\left(k^* + \frac{E_1}{\sqrt{A^*}}\right) + \beta\left(\frac{1-E_1}{A^*}\right)\right]$$

Integration of the velocity profile gives the flow rate Q as a function of the pressure gradient, the geometrical parameters k^*, β, and of A^*.

4 Results

The numerical computations were conducted for Re_{D_h} varying between 1 and 200. All the results were found to be Re independent. This was also observed by HWL in the range of $\mathrm{Re}_{D_h}=0.002-20$. The symmetrical and asymmetrical arrangements of rough elements gave identical results.

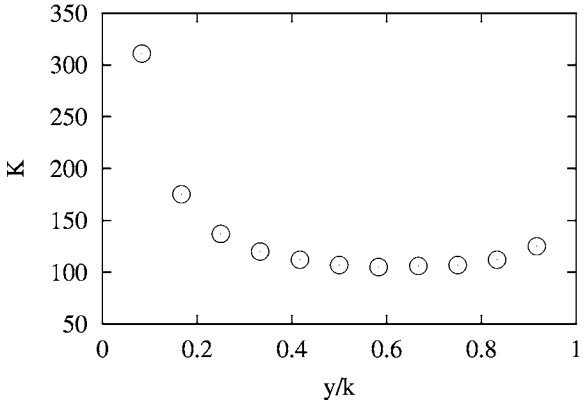

Fig. 4 Distribution of the drag law coefficient K along a rough element. $k^*=d^*=L_r^*/2=l_r^*/2=0.2$, $\beta=0.75$, Re=200.

4.1 Drag Coefficient of the Roughness Elements. As can be seen in Fig. 1, the blocks were divided into separate slices of height δy for calculating the local force density exerted by the fluid as a function of the local effective velocity $U(y)$. This approach allowed for computing the coefficient $K(y)$ defined by Eq. (22) from the numerical results. Figure 4 displays the variation of K with the position along a rough element ($y=0$ corresponds to the bottom wall) for a typical value of k^* (=0.2). It shows that K slightly varies in the upper part of the block ($y/k>0.3$). The strong increase in K observed for the lowest part of the block is obviously due to the influence of the bottom wall and associated three-dimensional effects. The same computation used with a condition of slip on the bottom wall gave a constant value of K all along the block. However, this deviation of K from a constant value is of little consequence on the solution given by the model because the contribution of the drag force to the flow dynamics is of minor importance in the near-wall region as shown in the next section. It follows that the assumption of constant K used in the analytical approach is quite reasonable.

4.2 Velocity and Shear Stress Profiles. Figure 5 compares the velocity profiles given by the analytical and numerical solutions for a rough and a semirough channel. The analytical model slightly overestimates the velocity across the channel. In fact, the deviation is only 3% to 3.5% in the central region of the channel for the two cases studied. It can be concluded that there is a very

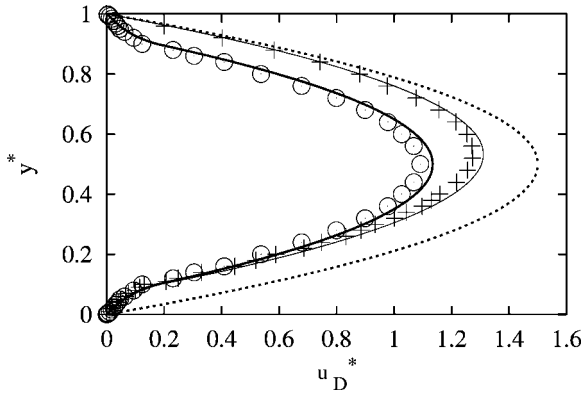

Fig. 5 Velocity profiles. $k^*=0.1$, $d^*=L_r^*/2=l_r^*/2=0.2$, $\beta=0.75$, Re =1; semirough channel, plus indicates numerical computations, thin lines indicate analytical model; fully rough channel, open circle indicate numerical computations, thick lines indicate analytical model; smooth channel, dotted lines indicate Poiseuille flow.

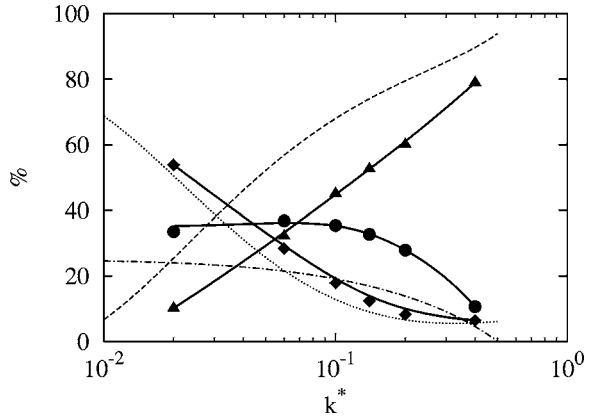

Fig. 6 Contribution of viscous and drag forces to the pressure gradient. $d^* = L_r^*/2 = l_r^*/2 = 0.2$, $\beta = 0.75$. Solid diamonds and dotted lines indicate friction on the bottom wall: $F_{\nu w}/F_T$, solid circles and dash-dotted lines indicate friction at the top of the rough elements: $F_{\nu t}/F_T$, solid triangles and dashed lines indicate drag force: F_D/F_T. Solid symbols correspond to numerical computations, continuous lines correspond to the analytical model.

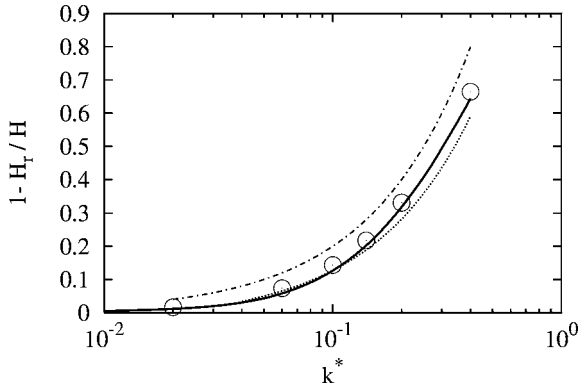

Fig. 7 Influence of the roughness element height on the channel height reduction. $d^* = l_r^*/2 = l_r^*/2 = 0.2$, $\beta = 0.75$. Open circles indicate numerical computations, thick lines indicate analytical model, dotted lines indicate HWL's results, dashed-dotted lines indicate $1 - H_r/H = 2k^*$.

good agreement between the two solutions, given the crude assumptions of the model and the numerical accuracy. The dimensionless Poiseuille profile is also drawn in Fig. 5 for comparison. The three curves correspond to the same pressure gradient. The presence of roughness significantly reduces the mass flow rate, as expected. The reduction in the maximum velocity is about 28% for the fully rough channel and approximately the half (13%) for the semirough channel. For this latter case, the velocity profile merges with the smooth channel curve when y^* tends to 1 and with the rough channel one when y^* tends to 0.

Both the analytical and numerical models enable the separation of the role of viscous and drag forces in the flow dynamics. Considering a control volume of height $H/2$ based on an elementary cell of sides $L_r \times l_r$ (Fig. 1), the force F_T due to the pressure gradient is balanced by the tangential force $F_{\nu w}$ due to friction on the bottom wall (surface $\beta L_r l_r$), the tangential force $F_{\nu t}$ due to friction at the top of the rough elements (surface $(1-\beta)L_r l_r$) and the drag force F_D on the rough elements. Figure 6 shows the contribution of the three components to the total force F_T as a function of the dimensionless roughness height for a fully rough channel. For very small rough elements, the pressure gradient is mainly due to the bottom wall viscous force. This contribution decreases rapidly when the height of the rough elements is increased. In the case of high rough elements, the fluid is strongly slowed down in the rough layer (Fig. 5) and the velocity gradient decreases at the wall. At the same time, the rough elements merge in a region of higher velocity and the drag force increases accordingly. For $k^* > 0.03-0.06$, the contribution of the drag force to F_T is dominant. The contribution of $F_{\nu t}$ tends to $1-\beta$ when k^* tends to zero. It remains approximately constant up to $k^* \approx 0.1$. This may be understood as follows: The top of the blocks is located in a region of increasing velocity and is subjected to increasing velocity gradient when k^* is increased. In these conditions, $F_{\nu t}$ still contributes to the pressure gradient unlike $F_{\nu w}$ which corresponds to a weakening velocity gradient when k^* is increased. For high rough elements ($k^* > 0.1$), the contribution of $F_{\nu t}$ decreases and the pressure gradient is mainly due to the drag force. The numerical and analytical models give the same trend for the various phenomena. However, significant differences are present from a quantitative point of view. In particular, the contribution of $F_{\nu t}$ is much weaker in the analytical model. This may be due to the discontinuity of β, as discussed before. It is likely that the blockage effect is not completely accounted for by the analytical model so that the velocity gradient is underestimated near the top of the rough elements by this model. In fact, the model ignores the development of boundary layers on the top of the rough elements so that the shear stress is underestimated for $y=k$. This may also explain why the velocities as given by the analytical model are higher than the numerical ones.

4.3 Influence of the Roughness Elements Geometry on the Poiseuille Number. For given channel height and roughness geometry, the flow is characterized by the Poiseuille number

$$\mathrm{Po} = -\frac{1}{\mu}\frac{dP}{dx}\frac{2H^3}{Q} \tag{28}$$

Roughness effects are conveniently interpreted by introducing an apparent channel height H_r which corresponds to a smooth channel giving the same flow rate as the rough channel when it is submitted to the same pressure gradient. H_r satisfies the following relation for fully developed Poiseuille flow in a plane smooth channel

$$24 = -\frac{1}{\mu}\frac{dP}{dx}\frac{2H_r^3}{Q} \tag{29}$$

As a result, H_r is deduced from the Poiseuille number as given either by the analytical model or the numerical simulations for given channel geometry.

$$\frac{H_r}{H} = \left(\frac{24}{\mathrm{Po}}\right)^{1/3} \tag{30}$$

The following figures compare the relative channel height reduction $1-H_r/H$ as given by the analytical model and the numerical results of the present work. HWL interpolated their numerical results and proposed equations for the channel height reduction as a function of the geometrical parameters. Their results are also displayed on the following graphs.

4.3.1 Influence of the Roughness Element Height. The apparent channel height reduction is moderate up to $k^* \approx 0.05$ (Fig. 7), then increases rapidly with k^*. The graph has also been drawn for very high values of k^* (0.4) which are obviously very far from usual physical situations. There is an excellent agreement between the three approaches. The slight differences of the present numerical results with those of HWL may be explained by the fact that HWL interpolated their results and that inaccuracies may result from this approximation. The expected maximum value for $1-H_r/H$ is obviously $2k^*$ and is displayed in Fig. 7. The figure reveals that the actual blockage effect is about 25% smaller for the present arrangement of rough elements when k^* is high (>0.1). The blockage effect is less pronounced for small rough elements.

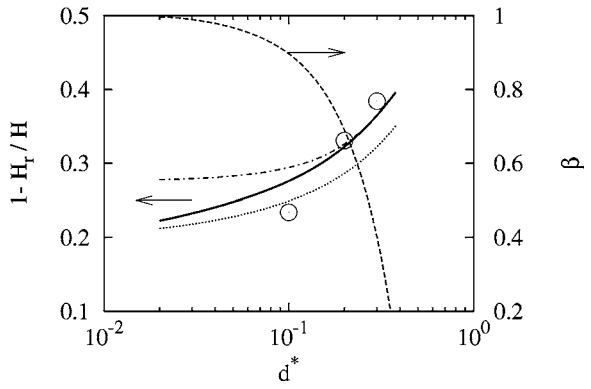

Fig. 8 Influence of the roughness element side length on the channel height reduction. $k^*=L_r^*/2=l_r^*/2=0.2$. Dashed lines indicate β. Open circles indicate Numerical computations, analytical model, dashed-dotted lines indicate $K_2=0$, thick line indicate $K_2=0.5$, dotted lines indicate HWL's results.

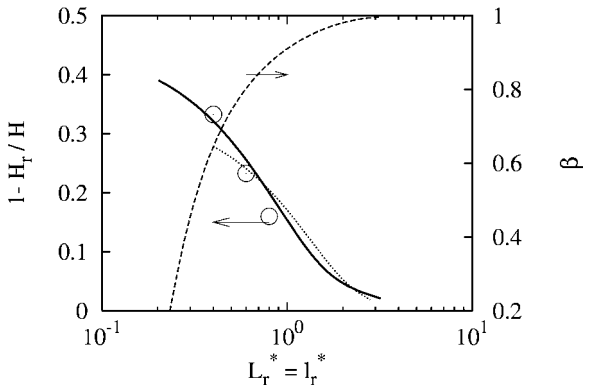

Fig. 9 Influence of the roughness element spacing on the channel height reduction. $k^*=d^*=0.2$. Same symbols as in Fig. 8.

4.3.2 Influence of the Roughness Element Side Length. The blockage coefficient directly depends on the roughness element side length d for given wavelengths in x and z directions (Eq. (9)) and is drawn in Fig. 8. The apparent channel height reduction increases with d^* for given k^*, as expected (Fig. 8). The maximum value as given by the analytical model is reached for $d^{*2}=L_r^* l_r^*$ ($d^*=0.4$ in the present case) and is close from $2k^*$. The three models show a continuous decrease of $1-H_r/H$ when β is increased. Small values of d^* correspond to slender blocks placed at relative long distances $L_r/d^*=l_r/d^*$ apart. In this case, the HWL results indicate that the roughness effect is still significant although the blockage coefficient becomes very close from 1. This suggests that in this situation the drag force F_D exerted by the rough elements still plays an important role in the flow dynamics. The analytical model is consistent with this statement since the drag force (or A^* in Eq. (26)) is independent of d when the drag coefficient K is taken as a constant. However, the model used with $K_2=0$ significantly overestimates the channel height reduction as given by HWL for $d^*<0.1$. The agreement is much better when the drag coefficient is used with $K_2=0.5$ (Eq. (24)). When d^* tends to zero, the aspect ratio of the blocks becomes very high and the correction factor K_2 Ln(k/d) in Eq. (24) plays a more important role in the drag. This suggests that three-dimensional effects must be taken into account in F_D in this case.

4.3.3 Influence of the Roughness Element Spacing. The other way to vary the blockage coefficient is to change the rough elements spacing while keeping their shape constant ($k^*=d^*=0.2$ in Fig. 9). Unlike the preceding case, the channel height reduction continuously decreases from the maximum value $2k^*$ to zero when the rough element spacing is increased. This result suggests that the role of the drag force becomes less important when the rough elements spacing is increased. This is consistent with the analytical model where the term corresponding to the drag force in Eq. (14) is inversely proportional to $L_r l_r$. The roughness effect becomes vanishingly small when the density of the roughness elements tends to zero while keeping their shape constant. Again, Fig. 9 reveals an excellent agreement of the analytical model with the numerical simulations.

4.4 Comparison With Experiments. In parallel with the analytical and numerical approaches, experiments were conducted in water flows through rough rectangular microchannels [7,8]. In these experiments, the channel walls consisted of parallel bronze blocks separated by a foil of thickness e_f ($0.1\ \text{mm}<e_f<1\ \text{mm}$) with a hollowed out central part 25 mm in width. The length of the microchannel was 82 mm. The blocks were locally treated by electrochemical deposition of a thin Ni layer (thickness e_{Ni} $\approx 2\ \mu$m), together with small SiC particles (5 to 7 μm in height). The height of the roughness elements was estimated to be the size of the deposited particles (5 μm) and their spacing was found by visualizations to be around 15 μm. The channel height was given by e_f-2e_{Ni}. The pressure drop was measured by two pressure transducers flush mounted at the wall of sumps located upstream/downstream of the channel. The experimental surface finish was obviously far from the regular arrangement of the proposed models. However, the measured pressure drop may tentatively be compared to the predictions of the analytical model. Figure 10 displays the experimental Poiseuille number Po_{exp} deduced from the measured pressure drop and flow rate and the model's results obtained for three values of the rough elements height (6.2, 7.2, and 8.2 μm). The experimental uncertainties are also shown in Fig. 10. The analytical model was used with the following relations: $k^*=d^*=L_r^*/2=l_r^*/2$ for three values of k. Numerical computations were performed with $k=d=5\ \mu$m, $L_r=l_r=15\ \mu$m and the results are also displayed in Fig. 10. The trend exhibited by Po_{exp} is well reproduced by the analytical and the numerical models. Considering the analytical model, the best agreement with the experimental results is obtained for $k=7.2\ \mu$m, which is slightly higher than the estimated height of the roughness elements. The same tendency may be deduced from the numerical model: A better agreement with the experimental data would have been obtained for higher roughness elements. Apart from the experimental and numerical

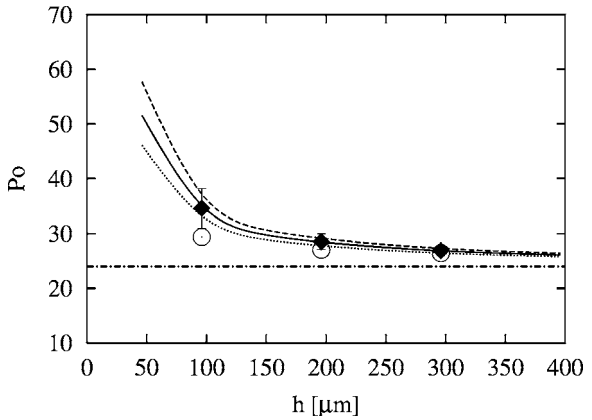

Fig. 10 Poiseuille number. Comparison of numerical computations and analytical model with experimental results. ♦ Experimental results; ○ Numerical computations, $k=5\ \mu$m; analytical model, dotted lines indicate $k=6.2\ \mu$m, thick lines indicate 7.2 μm, dashed lined indicate 8.2 μm, dash-dotted lines indicate Po=24.

errors and the uncertainties inherent in the analytical model, this discrepancy may also be due to the experimental surface finish. In fact, it is possible that the layer of nickel was not perfectly smooth but may have included small rough elements besides the largest particles of SiC. As a consequence, the assumption of a smooth bottom wall both in the analytical and numerical models would underestimate the friction on this part of the wall.

5 Conclusions

Numerical modeling and analytical approach were used to compute laminar flows in rough-wall microchannels. Both models considered the same arrangements of roughness elements in periodical arrays. The numerical results have confirmed that the flow is independent of the Reynolds number in the range 1–200.

The analytical approach was based on a previous work [12] devoted to the prediction of the rough-wall skin friction in turbulent flows. The analysis has pointed out the difficulties of setting the boundary conditions at the clear/rough layer interface in the case of rectangular prism rough elements. For given geometrical characteristics of the roughness elements, the analytical model only needs two constants K_1 and K_2 to compute the flow. They correspond to the drag coefficient of the rough elements. In most cases, a good approximation of the flow characteristics is obtained by using only one constant, namely, K_1. Despite the simplicity of the model, a very good agreement is found with the numerical results of the present work and those of Hu et al. [11]. The results show that the rough elements drag is mainly responsible for the pressure drop across the channel in the upper part of the relative roughness range ($k^* > 0.03-0.06$). For very high rough elements ($k^* > 0.1$), the wall friction has a negligible contribution to the pressure drop. For a concentrated arrangement of the rough elements ($d^* = L_r^*/2 = l_r^*/2 = 0.2$, Fig. 7), a very simple approximation of the roughness effect consists in considering a relative channel height reduction equal to $2k^*$. The accuracy is about 25% in $1 - H_r/H$ for $k^* > 0.1$. This blockage effect reduces when the rough elements are small or more dispersed (increasing blockage coefficient β). However, it remains significant for slender blocks, even if the side length becomes very small.

This study was restricted to patterns of periodic rough elements. The good agreement with experimental results obtained with randomly distributed roughness on microchannel walls is therefore striking. It seems that the models catch the main features of the physical phenomena involved in these microflows. The two main ingredients of the analytical model are the blockage coefficient β and the relative roughness height k^*. The knowledge of these parameters seems therefore to be of primary importance to predict the roughness effects in rough microchannels. This study will be soon extended to roughness effects on heat transfer in microchannels.

Acknowledgment

This research was supported by the CNRS. Roland Bavière and Gabriel Gamrat were supported by the French Ministry of Education which is gratefully acknowledged. The authors are also very grateful to Eric Chainet for the roughening of the microchannel walls.

Nomenclature

C_d = drag coefficient, dimensionless
d = width of roughness elements, m
D_h = hydraulic diameter, m
F_D = drag force on roughness elements, N
H = channel height, m
K = drag law coefficient, dimensionless
k = height of roughness elements, m
L_r = longitudinal distance between two roughness elements, m
l_r = transverse distance between two roughness elements, m
P = pressure, pa
Po = Poiseuille number, dimensionless
Q = volumetric flow rate per unit length, $m^3\ s^{-1}\ m^{-1}$
Re_d = Reynolds number based on local effective velocity and dimension of rough elements, dimensionless
Re_{D_h} = Reynolds number based on bulk velocity and hydraulic diameter, dimensionless
U = spatial average of longitudinal velocity, $m\ s^{-1}$
u_D = filtration or Darcy velocity, $m\ s^{-1}$
V = spatial average normal velocity, $m\ s^{-1}$
x = abscissa along the channel, m
y = coordinate normal to the wall, m
z = transverse coordinate, m

Greek symbols

ρ = fluid density, $kg\ m^{-3}$
τ_w = wall shear stress, $N\ m^{-2}$
μ = dynamic viscosity, $kg\ m^{-1}\ s^{-1}$
ν = kinematic viscosity, $m^2\ s^{-1}$

References

[1] Mala, G. M., and Li, D., 1999, "Flow Characteristics of Water in Microtubes," Int. J. Heat Fluid Flow, **20**, pp. 142–148.
[2] Li, Z. X., Du, D. X., and Guo, Z. Y., 2003, "Experimental Study on Flow Characteristics of Liquid in Circular Microtubes," Microscale Thermophys. Eng., **7**, pp. 253–265.
[3] Guo, Z. Y., and Li, Z., 2003, "Size Effect on Microscale Single-Phase Flow and Heat Transfer," Int. J. Heat Mass Transfer, **46**, pp. 149–159.
[4] Judy, J., Maynes, D., and Webb, B. W., 2002, "Characterization of Frictional Pressure Drop for Liquid Flows Through Microchannels," Int. J. Heat Mass Transfer, **45**, pp. 3477–3489
[5] Qu, W., Mala, G. M., and Li, D., 2000, "Pressure-Driven Water Flows in Trapezoidal Silicon Microchannels," Int. J. Heat Mass Transfer, **43**, pp. 353–364.
[6] Pfund, D., Rector, D., Shekarriz, A., Popescu, A., and Welty, J., 2000, "Pressure Drop Measurements in a Microchannel," AIChE J., **46**, pp. 1496–1507.
[7] Bavière, R., Ayela, F., Le Person, S., and Favre-Marinet, M., 2004, "An Experimental Study of Water Flow in Smooth and Rectangular Microchannels," *Second International Conference on Microchannels and Minichannels, Rochester*, June 2004, S. G. Kandlikar ed., ASME, New York, pp. 221–228.
[8] Bavière, R., "Etude de l'Hydrodynamique et des Transferts de Chaleur dans des Microcanaux," Ph.D. thesis, UJF Grenoble University, http://tel.ccsd.cnrs.fr/.
[9] Koo, J., and Kleinstreuer, C., 2003, "Liquid Flow in Microchannels: Experimental Observations and Computational Analyses of Microfluidic Effects," J. Micromech. Microeng., **13**, pp. 578–579.
[10] Kleinstreuer, C., and Koo, J., 2004, "Computational Analysis of Wall Roughness Effects for Liquid Flow in Micro-Conduits," J. Fluids Eng., **126**, pp. 1–9.
[11] Hu, H., Werner, C., and Li, D., 2003, "Influence of Three-Dimensional Roughness on Pressure-Driven Flow Through Microchannels," J. Fluids Eng., **125**, pp. 871–879.
[12] Taylor, R. P., Coleman, H. W., and Hodge, B. K., 1985, "Prediction of Turbulent Rough-Wall Skin Friction Using a Discrete Element Approach," J. Fluids Eng., **107**, pp. 251–257.
[13] Roache, P. J., 1997, "Quantification of Uncertainty in Computational Fluid Dynamics," Annu. Rev. Fluid Mech., **29**, pp. 123–160.
[14] White, F. M., 1991, *Viscous Fluid Flow*, McGraw-Hill, New York.
[15] Sherman, F. S., 1990, *Viscous Flow*, McGraw-Hill, New York.

Ejection Interaction of Two Adjacent Micropumps

H.-P. Cheng[1]
Associate Professor
Air-Conditioning and Refrigeration Engineering,
National Taipei University of Technology,
Add: 1, Sec. 3,
Chung-Hsiao E. Rd.,
Taipei 106, Taiwan, R.O.C.
e-mail: hpcheng@ntut.edu.tw

C.-P. Chien
Associate Researcher
Mechanical Industrial Research Laboratories,
Advance Vehicle & Power Technology Division,
ITRI, Add: Bldg. 58, 195-3, Sec. 4 Chung Hsing
Rd., Chutung, Hsinchu, 310, Taiwan, R.O.C.

This research intends to apply thermal bubble micropumps to motorcycle's fuel atomizer system with ink and Stoddard solvent as the work liquids, and then utilize computational fluid dynamics to discuss the fluid interaction of two adjacent micropumps under continuous ejection with time lag, which covers the particle shape and movement track of ejected droplets, fluid interaction of ejected droplets, and velocity of droplets as well as work liquid replenishment. The micropump consists of 50 independent micropumps, with orifice of 50 μm *in diameter and working frequency of* 5 kHz. *As shown in results, when the external air velocity is* 0 m/sec, *the velocity of droplets ejected later is faster than that of droplets ejected earlier. If the work liquid is ink, the replenishing rate of two adjacent micropumps is higher than that of single micropump. If the work liquid is Stoddard solvent, the replenishing rate of two adjacent micropumps is similar to that of single micropump. When the external air velocity is* 15.0 m/sec *and work liquid is ink, the velocity of droplet ejected later is slower than that of droplet ejected earlier, and the replenishing rate of two adjacent micropumps is lower than that of single micropump with the external air velocity of* 0 m/sec. *If the work liquid is Stoddard solvent, the velocities of two adjacent droplets are approximate, while the replenishing rates of two adjacent micropumps are approximate to that of single micropump with the external air velocity of* 0 m/sec. [DOI: 10.1115/1.2201638]

Keywords: CFD, micropump, fluid interaction, replenishing rate

1 Introduction

Since Taiwan is densely populated and faced with problem of traffic congestion on limited land, the motorcycle has thus become one of the most important vehicles in Taiwan due to its features of space efficiency, low cost, and convenient parking. The data from the Statistical Department, Ministry of the Interior show that, from 1991 to the end of May 2004, the number of motorcycles in Taiwan increased from 7,409,175 to 12,510,000, which was an average of one motorcycle for every 1.8 persons, indicating Taiwan as a country with the highest density of motorcycles in the world [1]. Nonetheless, an increasing number of motorcycles has resulted in waste gas pollution/emission, sounding an alarm bell for the air quality in Taiwan. To resolve this problem, the advanced motorcycle pollution control technology has applied the direct fuel atomizer system, and best-in-class computer hardware and software are utilized to control the fuel ejection quantity accurately, thereby achieving a better fuel-air ratio and minimizing the fuel consumption. However, given the fact of an expensive fuel atomizer system, the public has not shown a strong desire for purchase, whereas the nozzles of a fuel atomizer system are difficult to design and fabricate, and the quality of fuel ejection is not easy to control, so the study for improving a fuel atomizer system is of crucial importance.

With the continuous advancement in microsystem processing technology in recent years, a variety of products are intended for mass production using microsystem processing technology to reduce cost and improve product quality. The micropump technique, a branch of the microsystem technology, is more frequently applied to inkjet printhead. Micropumps are currently available in piezoelectric type and thermal bubble type, of which thermal bubble micropumps are widely applied to inkjet printhead due to a thin profile and simple operating mechanism. Since ejected droplets of micropumps are in perfect uniform, and the ejection quantity can be controlled accurately, it is rather feasible to apply micropump technique to a motorcycle's fuel atomizer system.

The operating principle of thermal bubble micropump is the voltage pulse in a microcavity generates high heat flux by flowing through a resistance layer in a thin-profile heater at the bottom of a cavity, such that the work liquid in the microcavity can absorb an enormous amount of heat rapidly, and bubbles are formed immediately to push the work liquid in the micropump outward. Then, work liquid is automatically replenished to the cavity for the next ejection. The following is some research literature concerning thermal bubble nozzles: For the lateral nozzle, Asia [2] described via theoretical mode the growing behavior of bubbles after homogeneous nucleation. Afterward, Asia [3] utilized a three-dimensional Navier-Stokes equation to calculate via the numerical method unstable flow of ink and ink droplets in the lateral nozzle, and then compared with observed results with a view to surface tension on free surface. For frontal nozzle, Chen et al. [4] divided the growing process of bubbles into two phases (earlier and later phases). The actuating pressure at an earlier phase is represented by the Clapeyron-Clausius equation, and that at a later phase represented by a decreasing exponential function. In addition, Chen et al. [5] established an observation system to observe ejected ink droplets, and also explored the impact of the electric pulse's conditions upon evolution process of shape of ink droplets and the length of ink droplets. Subsequently, Chen [6] conducted an experimental study of ejected droplets based on a HP51626A frontal thermal bubble nozzle. Likewise, Rembe et al. [7] utilized an observation system to observe the evolution process of the ink droplets' shape, the varying length of ink droplets, and the growing process of bubbles in the cavity. At the same time, they developed a mathematical model to calculate internal pressure of thermal bubbles and an one-dimensional expansion process of ink droplets under different ambient pressures. Tsai et al. [8] developed a two-passageway micropump (including an increasing and decreasing passageway), wherein the fluid is regularly replenished from one passageway depending on the sizes of aperture and fluid diffusion principle. Carmona et al. [9] simulated the motion of micropumps using the finite element method (FEM), which was

[1]Corresponding author.

Contributed by the Fluids Engineering Division of ASME for publication in the JOURNAL OF FLUIDS ENGINEERING. Manuscript received April 18, 2005; final manuscript received January 17, 2006. Assoc. Editor: Ali Beskok.

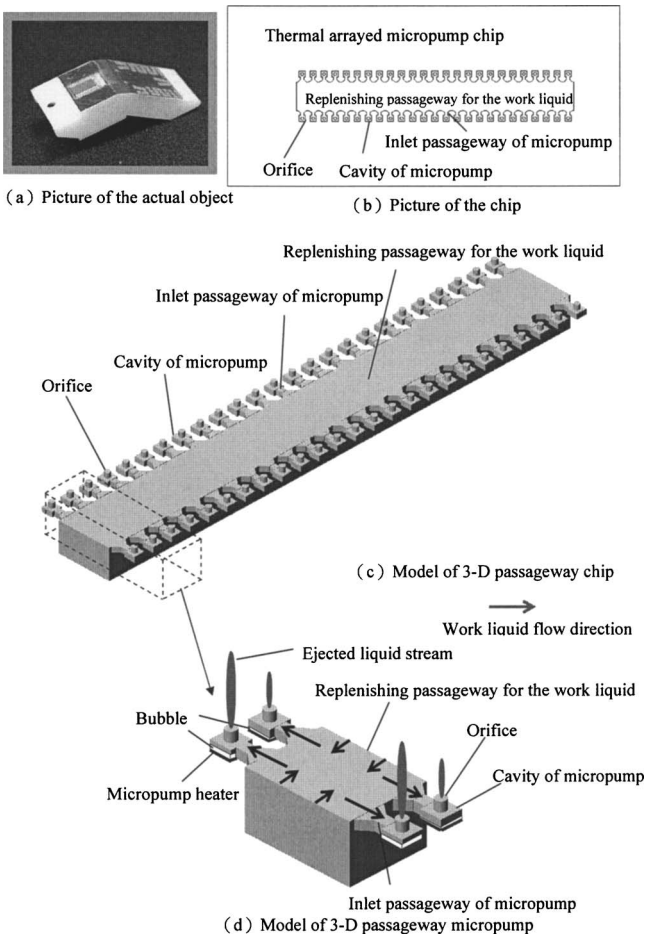

Fig. 1 Picture of micropump and passageway structure

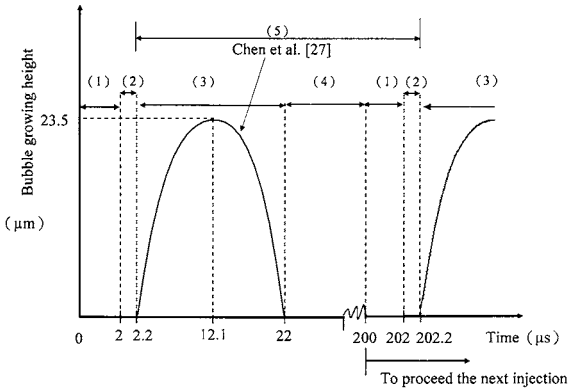

Period (1) Heating period (2μs)

Period (2) Heating end and bubble growing period (0.2μs)

Period (3) Bubble growing and diminish period (19.8μs)

Period (4) Droplet projection and work liquid replenishment period (178μs)

Period (5) Period calculated by this research study (200μs), including (3), (4), (1), (2)

Fig. 2 Bubble formation and time relation

already applied to thermal bubble micropumps. Lee et al. [10] developed a unique thermal bubble micropump and successfully processed an ink feed channel by using an electrochemical etching technique, which was coupled to a silicon-base nozzle. Lee et al. [11] also initiated a two-dimensional nozzle and ink feed configuration mode, with ink ejection of 2400 dpi, nozzle diameter of 10 μm, and cavity volume of 6 pl. Lee et al. [12] invented a new thermal bubble nozzle "DomeJe," which includes a circular ink cavity and film-type nozzle and has successfully replaced Samsung ink nozzle. Cheng et al. [13–18] utilized a numerical method to simulate the fluid property of micropumps applied to fuel system, while Peng [19–23], and Peng and Gao [24,25] also published relevant patent documents and papers with regard to micropumps applied to a motorcycle's fuel atomizer system.

Using ink and Stoddard solvent as the work liquids, this research intends to utilize computational fluid dynamics software CFD-ACE+® [26] to analyze various characteristics of fluid interaction of two adjacent thermal bubble micropumps under continuous ejection with time lag, which covers particle shape and movement track of ejected droplets, fluid interaction for ejected droplets, and velocity of droplets as well as work liquid replenishment.

2 Fuel Atomizer System and Bubble Formation by the Thermal Micropump

For information about a thermal micropump fuel atomizer system diagram and the photo of the throttle body and ejection, see Cheng et al. [17]. The photo of the micropump and the diagram of the passageway structure are as shown in Fig. 1. For details, see Cheng et al. [17]. This thermal micropump for a fuel atomizer consists of 50 independent micropumps, with an orifice of 50 μm in diameter and working frequency of 5 kHz. The individual micropump is similar to HP51626A. As mentioned in the literature review previously [4–7,13–18,27], when the bubble is formed inside the cavity of the micropump, if assumed that the interface between the air and liquid on the tip of bubble is leveled and has an area equal to the two-dimensional surface of the bottom of the cavity of micropump, the relationship of the growth of height and time is shown in Fig. 2, as based on Cheng et al. [17] and Chen et al. [27]. With an input of 18 V voltage, the heater at the bottom of the cavity of the micropump heats the work liquid once every 200 μs, each time for a period of 2 μs. Then the bubble begins to grow at 2.2 μs. After 19.8 μs of growth, the bubble disappeared at 22 μs [17,27]. The calculation cycle of this study is 200 μs beginning from 2.2 μs until 202.2 μs. The time lag of ejection starting time for two adjacent pumps is 15 μs.

3 Numerical Method

3.1 Governing Equations. According to Asia et al. [3], this paper assumed that the work liquid ejected by the micropump and the external air were at constant temperature, and both were incompressible Newtonian fluids. Moreover, if the size of the micropump is minute, the microscale effects due to the surface tension of work liquid would increase. The surface tension of work liquid has a significant effect on the droplet ejection of a micropump. Therefore, this paper used a three-dimensional Navier-Stokes equation with surface tension effects to describe the motions of the fluids. To describe the motion of the ejected droplets, the method of volume of fluid (VOF) [28] along with the piecewise linear interface construction (PLIC) technique [29] were adopted

$$\frac{\partial F}{\partial t} + \nabla \cdot \vec{V}F = 0 \tag{1}$$

where, F refers to liquid volume fraction. The calculation of Eq. (1) must be conducted with that of the mass conservation equation and the momentum conservation equation. After the discretization of the governing equations, a group of finite difference equations can be obtained. A second-order upwind scheme was used to approximate the convective terms of the governing equations. A second-order central difference scheme was used for the viscous and source terms. For time advancing, the first-order Euler scheme was employed. After solving the above equations by

Table 1 Physical properties chart of work liquid

	Density (kg/m^3)	Kinematic viscosity (m^2/s)	Surface tension (N/m)
Ink	1020	1.28E−06	0.0433
Stoddard solvent	785	2.56E−06	0.0261

means of a pressure based semi-implicit method for pressure-linked equations consistent (SIMPLEC) algorithm, the relevant physical quantities in the computing lattice can be attained. The study adopted two work liquids for the analysis-ink and Stoddard solvent, whose density, coefficient of viscosity, and surface tension were assumed constant, as shown in Table 1. The detailed method of calculation was described by Cheng et al. [17] and CFD-ACE(U)® manual [26].

3.2 Boundary Setting and Computing Lattice for the Simulation. Figure 3 is the boundary setting of numerical calculation, which includes the passageway for work liquid replenishment, the inlet passageway, cavity, and orifice of the micropump as well as the external air. The key dimension of the calculation domain is also shown in Fig. 3. The left end of the replenishing passage is the entrance, with a fixed pressure of 1.01E+05 Pa. The movable solid boundary is used for simulating the growing and reduction of vapor bubbles. The starting pressure of the external air is 1.0E+05 Pa. In addition, in order to simulate the impact of the speed of the air current on the ejection of the micropump when it flew into the engine from the intake pipe, the boundary speed of the air current at the entrance of region [external air] adopted two modes, 0 m/s and 15 m/s. The direction of external flow air is the *Y*-axis direction.

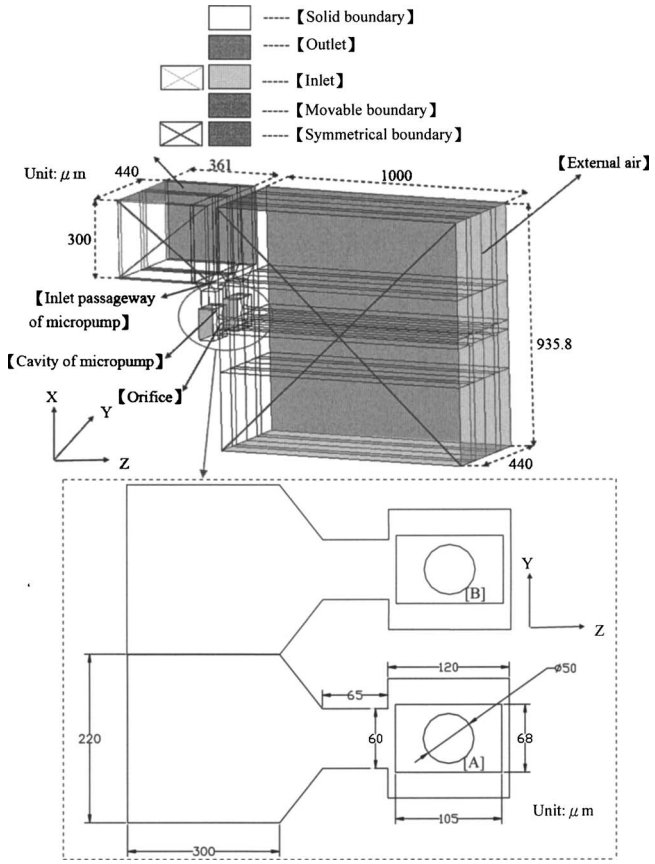

Fig. 3 Boundary setting for numerical simulation and key dimension description for calculation domain

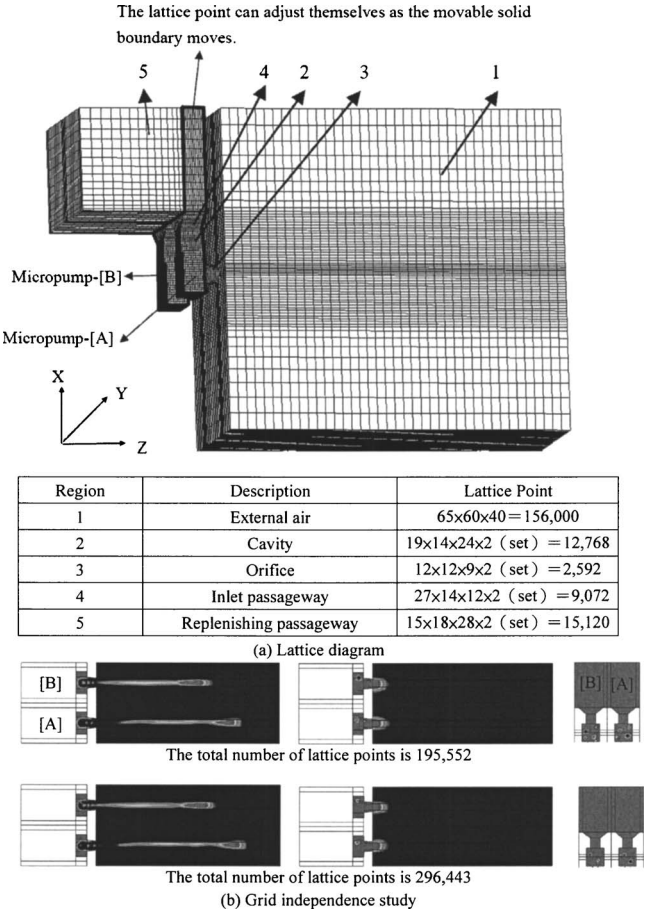

Region	Description	Lattice Point
1	External air	65x60x40=156,000
2	Cavity	19x14x24x2 (set) =12,768
3	Orifice	12x12x9x2 (set) =2,592
4	Inlet passageway	27x14x12x2 (set) =9,072
5	Replenishing passageway	15x18x28x2 (set) =15,120

(a) Lattice diagram

The total number of lattice points is 195,552

The total number of lattice points is 296,443

(b) Grid independence study

Fig. 4 Computational mesh for numerical simulation

Figure 4(*a*) is the adopted computing lattice, and the total number of lattice points is 195,552. The lattice points in regions 2, 4, and 5 (regions surrounded by black thick lines) can adjust themselves as the movable solid boundary moves, but those in the other sections remain unchanged. This study increased the computing lattice of each region evenly to the total number of lattice points as 296,443, and conducted computation for case I (see Table 2) for grid independence study. The comparison of different lattice points is shown in Fig. 4(*b*). As seen from the VOF computation results, in which the ejection time was at $t=52.2$ and 202.2 μs, the shapes of the ejected droplets based on the two set of computing lattice were approximate, while the positions of the residual air hole inside the cavity of the micropump changed slightly. The droplet velocity and work liquid replenishing rate showed errors of 2% and 1.5% in the case of micropump [A]. Based on the above results, to shorten the computation time spent

Table 2 Case description (refer to Cheng et al. [17]. for the detailed results of cases 1—4)

Case description	Number of micropump	Work liquid	External air velocity (m/sec)
Case 1	1	Ink	0
Case 2	1	Stoddard solvent	0
Case 3	1	Ink	15
Case 4	1	Stoddard solvent	15
Case I	2	Ink	0
Case II	2	Stoddard solvent	0
Case III	2	Ink	15
Case IV	2	Stoddard solvent	15

Table 3 Velocity of micropump's ejected droplet top moving towards *z* axis

Case		Time (μs) 12.1	22.2	27.1	37.2	52.2
Case 1		20 m/sec	17.5	17.5	17	15
Case 2		20	17.5	17.5	17	16
Case 3		19	17.5	17	16.5	15.5
Case 4		19	19	17	16.5	16
Case I	[A]	20	17.5	16.8	15.7	14.8
	[B]	0	24.0	22.0	19	16.3
Case II	[A]	20.2	18	17.2	16.3	15.6
	[B]	0	24.0	22.0	20.0	17.1
Case III	[A]	20.2	18	15.8	14	12
	[B]	0	23	19	15	12.5
Case IV	[A]	20.0	19	17.2	16.3	15.6
	[B]	0	24.0	22.0	19	16.5

on the cases in this study, computing lattice with the total number of lattice points of 195,552 was adopted in this paper. The calculation adopted 0.1 μs as the calculating time step.

4 Results and Discussions

The case description of this paper is listed in Table 2. Of which, cases 1–4 are computation simulations for a single micropump, and the size and ejection condition of the micropump were the same as that of this study. For detailed computation results, see Cheng et al. [17]. Cases I–IV are the computations for two adjacent micropumps. The velocity of the droplet top can be estimated from the VOF figure in conjunction with time item. Table 3 is a speed sheet of ejected droplet top moving toward the z axis in the case of micropumps at t=12.1, 22.2, 27.1, 37.2, and 52.2 μs.

4.1 Verification of Numerical Simulation Method. According to Chen et al. [27], the numerical method adopted in this study was used to simulate the two-dimensional model of single micropump [14], and the results were approximate to the observation results of Chen et al. [27]. In addition, Fig. 5 shows the observation chart of ejected droplet for case II (the work liquid is Stoddard solvent). The length indicator in units of 500 μm is shown at the bottom of the figure to view the length of ejected droplet. The main observation equipments included light emitting diode (LED) synchronized flash controller with multimode flash, and microscopic charge coupled device (CCD) camera. The controller controls the micropump driver and delayer simultaneously, and uses the delayer to control the delay time of the light emiting diode (LED) flash and the number of flash. Last the microscopic CCD camera captures the image and displays it on the computer monitor [19,20,24,25]. As seen in Fig. 5, when t=2 μs, since it was at the initial stage of droplet ejection, the ejected droplet that could be observed was not obvious, and only the arrayed micropump nozzles were visible. Also because the work liquid, Stoddard solvent, was transparent, it was difficult to focus the camera on it and the chip surface would reflect light due to residual oil, thus, the appearance of an observed droplet was slightly vague. The light reflection of the photo was due to the reflection of residual Stoddard solvent on the chip. When t=12 μs, since the bubble inside the cavity of the micropump grew to the maximum, the Stoddard solvent was massively pushed out from the nozzle, and the appearance of the droplet was in column shape. At 22.0 μs, the ejected droplet was pushed out of the nozzle continuously as time went by, and the droplet length increased. At 32.0 μs, the length of the ejected droplet continued to increase, and the length indicator at the bottom of the figure could be used to estimate the droplet velocity to be 17 m/sec. The velocity matches with the computation results for micropump [A] of case II in Table 3.

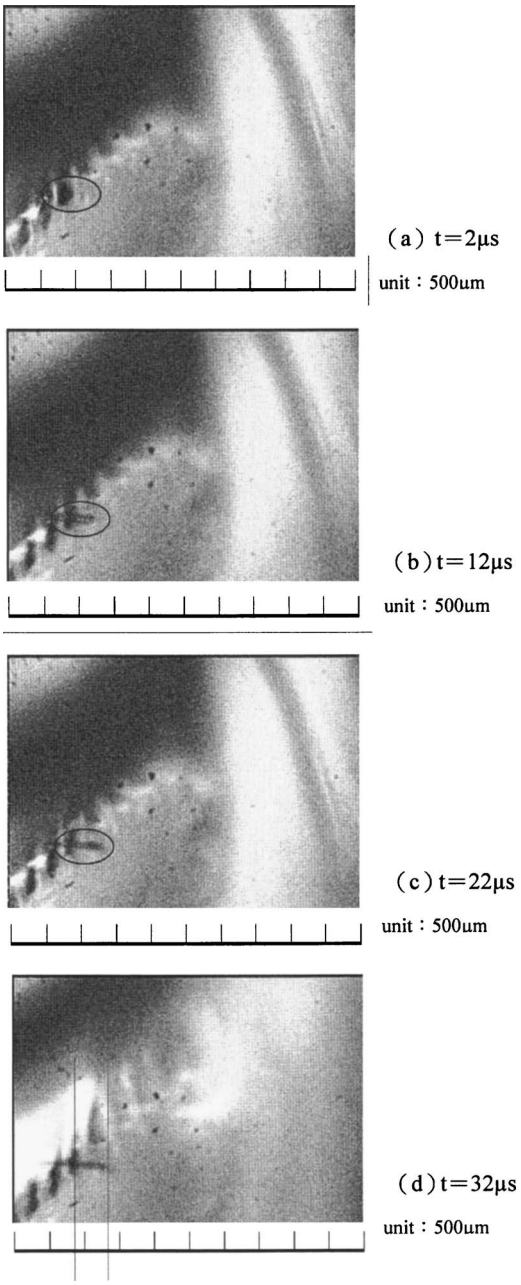

Fig. 5 Observational diagram of ejected droplets in case II

4.2 Particle Shape and Movement Track of Ejected Droplets. Figure 6 shows the particle shape and movement track of ejected droplets of two adjacent micropumps under continuous ejection with time lag, with time points of 12.1, 22.2, 27.1, 37.2, and 52.2 μs. y-z plane was obtained along central axis (z axis) of orifice, while the shape of droplets can be clearly attained from VOF value, and marked onto various profiles via different shades. Among them, the one shade refers to VOF=1, indicating that all fluids in the computing lattice are work liquids, and another shade refers to VOF=0, indicating that all fluids in the computing lattice are ambient air. In addition, there is a length indicator at the bottom of the figure for t=52.2 μs, which is used to check the length of ejected droplets (in a unit of 100 μm). Besides, [A] and [B] are two adjacent micropumps, where the starting time of micropump [A] is 15.0 μs, which is faster than that of micropump [B].

As seen in Fig. 6, the ejected work liquids of cases I and II (external air velocity=0.0 m/sec) are approximate in terms of

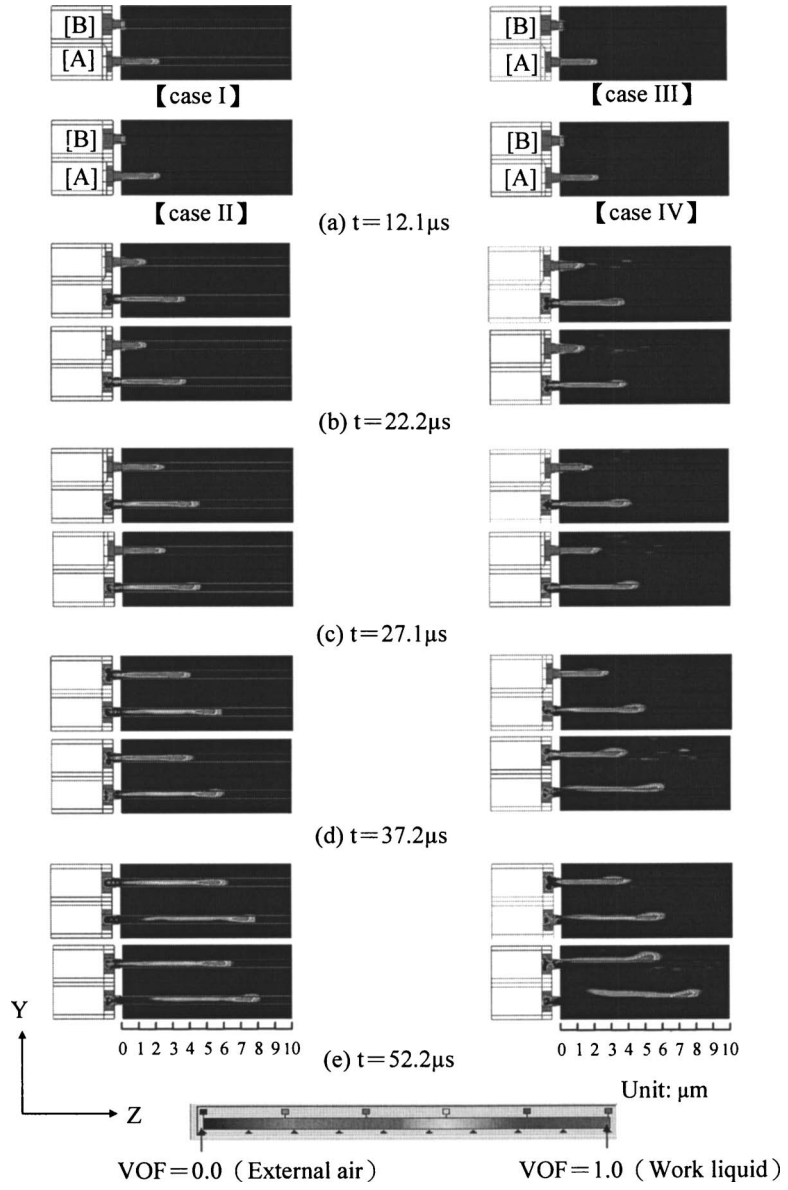

Fig. 6 Comparison diagram of ejected droplets of micropump

shape and velocity during the growing and fading cycles (as shown in Figs. 5(*a*)–5(*d*). When $t=12.1$ μs, the bubble from micropump [A] grew up to the maximum top, and ejected the droplet was in a column shape. Since no bubble from micropump [B] occurred prior to the signal trigger phase, no droplet was ejected. At 22.2 μs, the bubble from micropump [A] disappeared and the ejected work liquid droplet gradually formed a taper shape. In such a case, some of the ambient air entered into nozzle [A], thus enabling the tail of the ejected droplet to become thinner and allowing the separation of droplet almost from the nozzle. As for micropump [B], the droplet was also ejected from the nozzle due to the occurrence of bubble.

When $t=27.1$ μs, the bubble from micropump [A] disappeared, and the ejected droplet along with the liquid in the nozzle moved continuously toward the downstream. Since the bubble from micropump [B] was approaching the growing phase, the liquid was ejected as the bubble pushed outward, and the ejected droplet was almost in a column shape. When $t=37.2$ μs, the ejected droplet from micropump [A] along with the liquid in the nozzle moved continuously toward the downstream, while the droplet from micropump [B] was also smoothly ejected from the orifice. Similar to the ejection of micropump [A] at 22.2 μs, the ejected work liquid droplet gradually formed a taper shape. In such a case, some of ambient air entered into nozzle [B], thus enabling the tail of the ejected droplet to become thinner and allowing the separation of the droplet almost from the nozzle.

As seen in figures of $t=37.2$ and 52.2 μs, the shape of the droplet top became flat owing to the blocking of ambient still air. According to the decreasing trend of the velocity of the droplet top as listed in Table 3, the kinetic energy of the ejected droplet gradually reduces owing to the blocking of still air. Comparatively, the velocity of droplets in case II is faster than that in case I. When $t=52.2$ μs, the velocity of droplets from micropumps [A] and [B] in case II was 0.8 m/sec faster than that in case I. Additionally, the velocity of the droplet top from micropump [B] was also faster than that of micropump [A] within the same running time of droplet. Take the ejection time of 37.2 μs, for example, the velocity (16.3 m/sec) of the droplet from micropump [B] in case I was 0.6 m/sec faster than that from micropump [A] (15.7 m/sec), whereas the velocity (17.1 m/sec) of droplet from

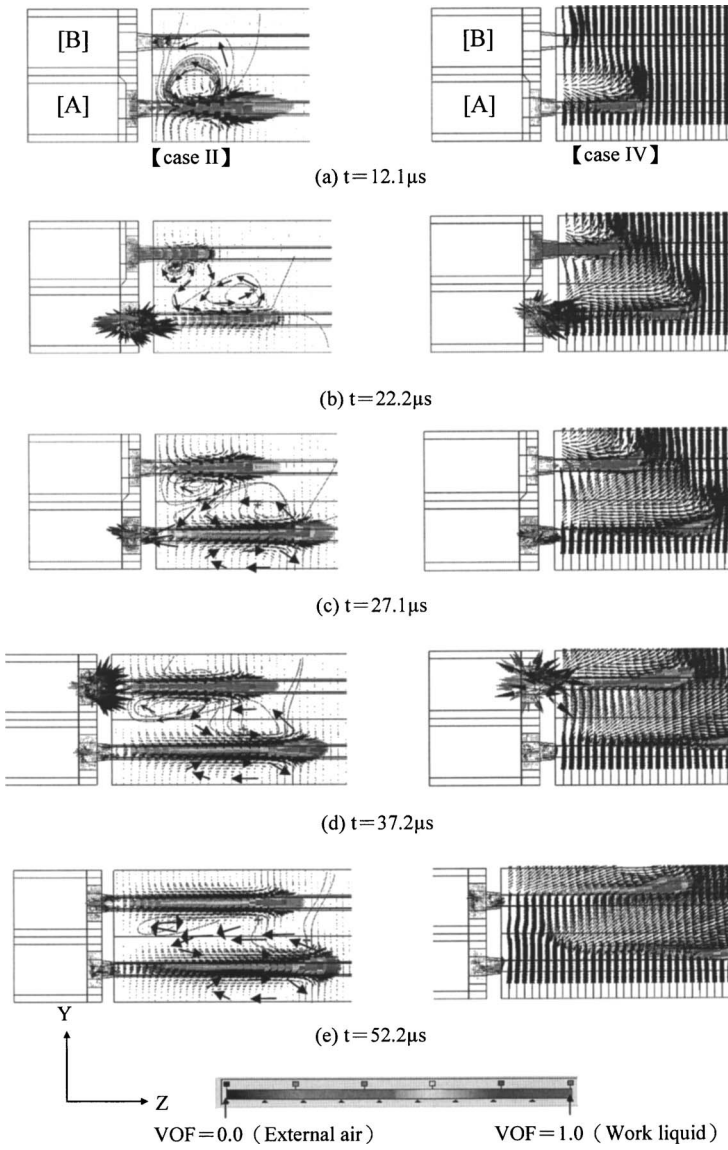

Fig. 7 Velocity field diagram of ejected droplets of micropump

micropump [B] in case II was 0.8 m/sec faster than that from micropump [A] (16.3 m/sec). The following paragraphs provide detailed description of such phenomena.

For cases III and IV (external air velocity=15.0 m/sec), the profiles of the ejected droplet differ significantly from those in cases I and II due to the disturbance of ambient mobile air. In this case, the droplet deviated from the central axis of orifice toward the *y* axis. Since the density of Stoddard solvent was smaller than that of ink, and the droplet of case IV was lightweight, the droplet deviated apparently from the central axis of orifice. When $t=52.2$ μs, the ejected droplets of cases III and IV presented irregular shapes, and the deviation range of droplet toward the *y* axis in case IV was considerably bigger than that in case III. As seen in Table 3, the velocity of the droplet in case IV was faster than that in case III. When $t=52.2$ μs, the velocity of the droplet from micropumps [A] and [B] in case IV was 3.6 and 4.0 m/sec faster than in case III. Additionally, the velocity of the droplet top from micropump [B] in case III was slower than that of micropump [A] within the same running time of droplet. Take the ejection time of 37.2 μs, for example, the velocity of droplet from micropump [B] was 1.5 m/sec slower than that from micropump [A], whereas the velocity of droplets from micropumps [A] and [B] in case IV was approximate. The velocities of these droplet tops were distinguished from those in cases I and II, indicating that ambient mobile air had an impact on the characteristics of ejected droplets. The reason is that, after ambient mobile air passes through the ejected droplet from micropump [A], the change of velocity field restrains the velocity of ejected droplet from micropump [B], and especially in case III which can be demonstrated from the velocity field pattern in the next section.

It is worthy to note that, during the fading process of bubble, external air entered into the nozzle and cavity of the micropump, where the air cavity was shaped, then left in the nozzle and cavity of the micropump, and gradually replaced by work liquid. This process is called work liquid replenishment. If there was any air left in the cavity of the micropump at the next startup of ejection, the volume, shape, and track of ejected fluid of the micropump would be affected. Therefore, it is crucial to identify if residual air in the nozzle and micropump can be efficiently discharged during replenishment of work liquids.

4.3 Interaction of Droplets Ejected Outside of the Orifice. Figure 7 shows a velocity field diagram of ejected droplets in cases II and IV at time points of 12.1, 22.2, 27.1, 37.2, and

52.2 μs. The relevant flow fields can be clearly obtained from the amount and direction of the velocity vector, while the shade of the velocity vector is the VOF value. In addition, massless particles were placed at cross lines of case II, and the corresponding streamlines were calculated and displayed by using CFD-VIEW® software (ESI-CFD Inc., Huntsville, AL), wherein black arrow represents the flow direction of particles. As seen, at $t=12.1$ μs, the bubble from micropump [A] in case II was close to the growing phase. In such a case, the liquid was pushed outward by the bubble, the droplet ejected quickly would disturb the ambient air flow field, thus resulting in an air vortex close to the neck of the droplet. This vortex would drive air nearby the nozzle of micropump [B] to flow toward the nozzle orifice, and squeeze the liquid in the cavity of micropump [B].

When $t=22.2$ μs, the bubble from micropump [A] in case II was close to the fading phase, so the ejected droplet had visibly departed from the nozzle, and then disturbed the ambient air flow field continuously. Yet, there was still air vortex nearby the neck of the droplet, while some ambient air entered into the nozzle since bubble from micropump [A] was close to the fading phase. But, the bubble from micropump [B] was in the early stage, and the air vortex occurred nearby the neck of the ejected droplet. As seen from the streamline, the airflow field disturbed by ejected droplets from micropumps [A] and [B] interacted with each other, and exerted an impact on the characteristics of ejected droplets from micropumps [A] and [B].

When $t=27.1$ μs, the bubble from micropump [A] in case II disappeared, and the ejected droplet along with the liquid in the nozzle moved continuously toward the downstream, and disturbed the ambient airflow field consistently, thus affected the ejection of micropump [B]. Meanwhile, the bubble from micropump [B] was near the growing phase. As seen from the streamline, the air vortex existed nearby the neck of the droplet from micropump [A], and squeezed an ejected droplet from micropump [B], thus leading to a flat ejected droplet from micropump [B] with longer ejection range. The velocity of the droplet top from micropump [B] was faster than that of micropump [A]. According to the streamline nearby the neck of the droplet from micropump [B], the airflow field derived from an ejected droplet interacted with that from micropump [A].

When $t=37.2$ μs, the bubble from micropump [B] in case II was close to the fading phase, so some ambient air entered into the nozzle. Meanwhile, air vortex existed nearby the neck of the droplet from micropump [A], and continuously squeezed the ejected droplet from micropump [B]. The air vortex nearby the neck of the droplet from micropump [B] continued to grow and interacted with the airflow field derived from micropump [A]. The velocity of the droplet top from micropump [B] was faster than that from micropump [A].

When $t=52.2$ μs, the air vortex of micropumps [A] and [B] in case II still interacted with each other, leading to squeeze the droplet ejected later. Thus, the ejected droplet from micropump [B] becomes flatter than that from micropump [A]. The velocity of the droplet top from micropump [B] was faster than that from micropump [A].

Since ambient air in case IV had a velocity of 15.0 m/sec, the entire velocity field was strongly conditioned upon the flow velocity of ambient air. Therefore, it was impossible to observe an air vortex similar to that in case II from the velocity vector pattern. But, the shape, velocity, and direction of ejected droplets differed much from those in case II, whereas the interaction of airflow field between micropumps [A] and [B] could be visibly observed.

4.4 Work Liquid Replenishment. Figure 8 shows the velocity vector of fluids in the cavity and nozzle, or nearby the nozzle of micropumps [A] and [B] in case I. The starting time of work liquid in micropump [A] replenished to the cavity of the micropump was about 47.2 μs–52.2 μs, and that in micropump [B]

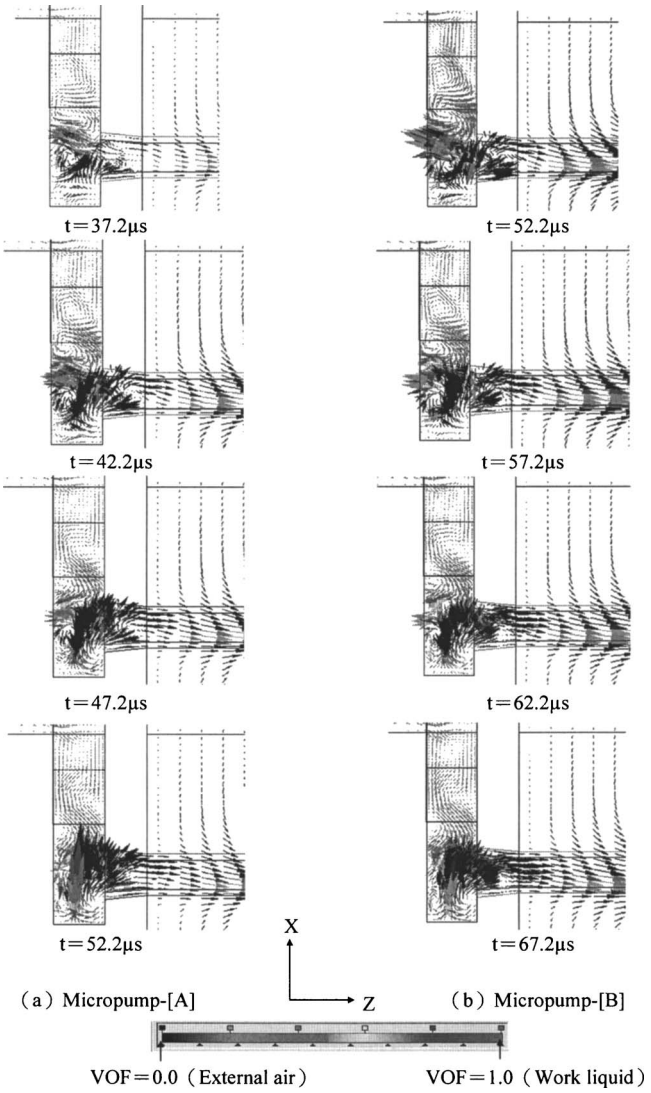

Fig. 8 Tendency chart of internal velocity field under case I

about 62.2 μs–67.2 μs. With a lag of 15 μs for ejection starting time of micropumps [A] and [B], the starting time of work liquid replenishment for two adjacent pumps was approximate. The comparison with the simulation results of a single micropump [17] shows that the starting time of work liquid replenishment for a single micropump was about 52.2 μs–57.2 μs. Thus, if the work liquid was ink, the replenishing time of work liquid could be reduced in the event of continuous ejection with a time lag of two adjacent micropumps.

Table 4 is a starting time schedule of work liquid replenishment in various cases. The data of cases I and II show that, when the flow velocity of ambient air is 0 m/sec, the starting time of work liquid replenishment (either ink or Stoddard solvent) of micropumps [A] and [B] is approximate, and the starting time of Stoddard solvent replenishment is slightly faster than that of ink. The comparison with the simulation results of a single micropump in cases 1 and 2 shows that if work liquid is Stoddard solvent, the starting time of the work liquid replenishment of micropumps [A] and [B] is the same as that of a single micropump, ranging from 37.2 μs to 42.2 μs. In addition, when the flow velocity of ambient air is 15.0 m/sec, the comparative results of cases III and IV show that, the starting time of the work liquid replenishment of micropump [B] is 5 μs faster than that of micropump [A], and the starting time of Stoddard solvent work liquid replenishment (case IV) is 5 μs faster than that of ink (case III). The comparison with

Table 4 Starting time of work liquid replenishment

Case description		Starting time of work liquid replenishment (μs)
Case 1		52.2–57.6
Case 2		37.2–42.2
Case 3		57.2–62.2
Case 4		47.2–52.2
Case I	[A]	47.2–52.6
	[B]	62.2–67.2
Case II	[A]	37.2–42.2
	[B]	52.2–57.2
Case III	[A]	57.2–62.2
	[B]	67.2–72.2
Case IV	[A]	52.2–57.2
	[B]	62.2–67.2

Table 5 Work liquid replenishing rate (%)

		Time (μs)		
Case		172.2	187.2	202.2
Case 1		82	80	61
Case 2		82	81	79
Case 3		89	87	86
Case 4		83	82	81
Case I	[A]	91	90	89
	[B]	93	91	90
Case II	[A]	81	80	79
	[B]	85	81	80
Case III	[A]	84	83	82
	[B]	85	84	84
Case IV	[A]	82	81	79
	[B]	86	84	82

a single micropump in cases 3 and 4 shows that if work liquid is Stoddard solvent, the starting time of the work liquid replenishment of two adjacent micropumps is much slower than that of a single micropump. Additionally, the comparative results of eight cases in Table 4 show that, increasing flow velocity of ambient air makes the starting time of work liquid replenishment slower.

Figure 9 shows the VOF field of cases I and III at $t=172.2$, 187.2, and 202.2 μs. Starting from $t=172.2$ μs to the next starting time of ejection ($t=202.2$ μs) in case I, the residual air cavity in the micropump cavity was scattered into small balls, which was similar to that in case III. Table 5 shows the comparative results of the work liquid replenishing rate of various cases at $t=172.2$, 187.2, and 202.2 μs. The replenishing rate is defined as the volume ratio (%) of work liquid to the total volume of inlet passageway of micropump, cavity of micropump, and orifice. As seen in the table, if work liquid is ink, the replenishing rate of two adjacent micropumps [A] and [B] in cases I and III is approximate under the same replenishing time. Take case I, for example, when the replenishing time is 187.2 μs, the replenishing rate of micropump [A] is 90%, and that of micropump [B] is also 90% ($t=202.2$ μs). Besides, the flow velocity of ambient air of 15.0 m/sec reduces the replenishing rate of work liquid. If the work liquid is Stoddard solvent (cases II and IV), the replenishing rate of micropump [B] is slightly larger than that of micropump [A] under the same replenishing time, and the flow velocity of ambient air of 15.0 m/sec has little impact on the replenishing rate. Finally, the work liquid replenishing rate of two adjacent micropumps (case I–IV) is larger than that of single micropump (case 1–4).

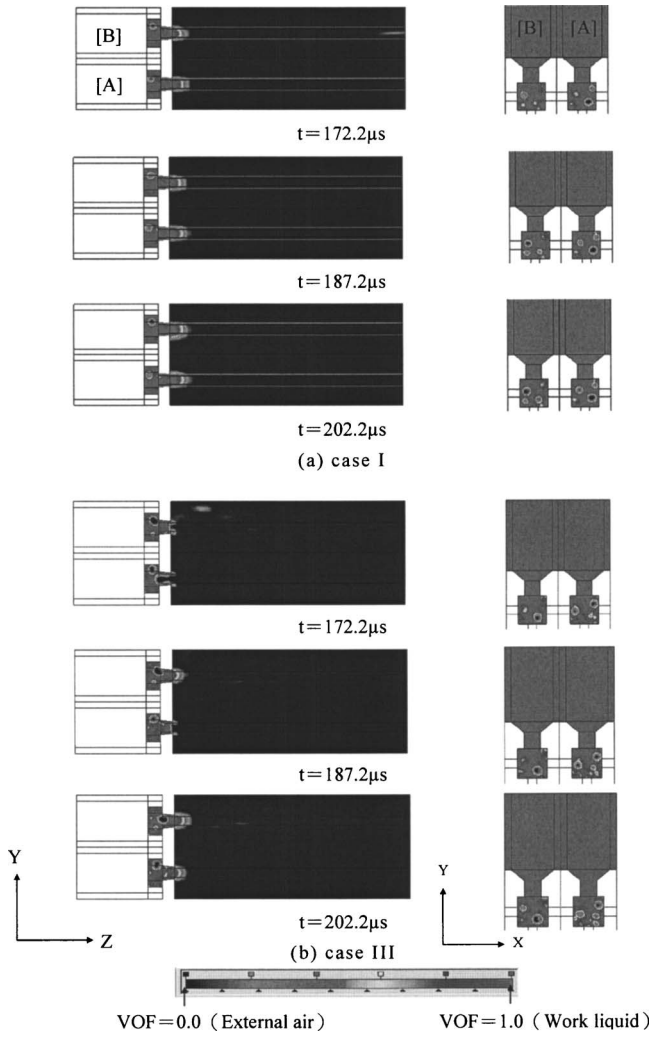

Fig. 9 Comparison diagram of work liquid replenishment under cases I and III

5 Conclusion

This paper aims to explore the fluid interaction of two adjacent micropumps under continuous ejection with time lag. The major conclusions are as follows:

1. Air vortex derived from two adjacent droplets interacts with each other. When the flow velocity of ambient air is 0 m/sec, the velocity of droplets ejected later is faster than that of droplets ejected earlier. When the flow velocity of ambient air is 15.0 m/sec, the velocity of the work liquid, Stoddard solvent, is approximate, but contrary to the case of work liquid as ink.
2. When the flow velocity of ambient air is 0 m/sec, the starting time of the work liquid replenishment for two adjacent micropumps is the same. If the work liquid is ink, the starting time of work liquid replenishment of two adjacent micropumps is faster than that of a single micropump. This leads to little residual air cavity in the micropump and a higher work liquid replenishing rate at the next starting time of ejection. If the work liquid is Stoddard solvent, the work liquid replenishment of two adjacent micropumps varies little from that of single micropump.
3. When the flow velocity of ambient air is 15.0 m/sec, the work liquid of the micropump ejected later is replenished faster. If the work liquid is ink, the work liquid replenishing rate of two adjacent micropumps is lower than that of a single micropump with a flow velocity of ambient air of 0 m/sec due to the influence of flow velocity of ambient air. If the work liquid is Stoddard solvent, the starting time of the work liquid replenishment of two adjacent micropumps

is later than that of a single micropump, but the work liquid replenishing rate is similar to that of a single micropump with a flow velocity of ambient air of 0 m/sec.

Acknowledgment

This study is sponsored by the Advanced Vehicle and Power Technology Division, MIRL, ITRI (A311XS2111-1). The author would like to extend cordial thanks to Y.-Y. Peng, T.-H. Gau, and A.-H. Lin for their assistance to this plan.

References

[1] The Statistical Information of The Ministry of the Interior, ROC, 2004.
[2] Asia, A., 1991, "Bubble Dynamics in Boiling Under High Heat Flux Pulse Heating," J. Heat Transfer, **113**, pp. 973–979.
[3] Asia, A., 1992, "Three-Dimensional Calculation of Bubble Growth and Drop Ejection in a Bubble Jet Printer," J. Fluids Eng., **114**, pp. 638–641.
[4] Chen, P.-H., Chen, W.-C., and Chang, S.-H., 1997, "Bubble Growth and Ink Ejection Process of a Thermal Ink Jet Printerhead," Int. J. Mech. Sci., **39**, pp. 683–695.
[5] Chen, P.-H., Chen, W.-C., and Chang, S.-H., 1997, "Visualization of Drop Ejection Process of a Thermal Ink Jet Printerhead," *Proc. First Pacific Symposium on Flow Visualization and Image*, Honolulu, Hawaii, February 23–26, Pacific Center of Thermal-Fluids Engineering, Tokyo, Vol. 1, pp. 132–137.
[6] Chen, W.-C., 1998, "HP51626A Inkjet Observation of Prienthead," *Fu Xing Journal*, 2nd ed., Lan Yang Institute of Technology, I Lan, Taiwan, pp. 169–173.
[7] Rembe, C., Wiesche, S., and Hofer, E. P., 2000, "Thermal Ink Jet Dynamics: Moding, Simulation, and Testing," Microelectron. Reliab., **40**, pp. 525–532.
[8] Tsai, J. H., and Lin, L., 2001, "A Thermal Bubble Actuated Micro Nozzle-Diffuser Pump," *Proc. 2001 IEEE Micro Electro Mechanical Systems Workshop*, Interlaken, Switzerland, January 21–25, IEEE, Piscataway, NJ, pp. 409–412.
[9] Carmona, M. S., Samitier, M. J., and Morante, J. R., 1996, "Dynamic Simulations of Micropumps," J. Micromech. Microeng., **6**, pp. 128–130.
[10] Lee, J.-D., Yoon, J.-B., Kim, J.-K., Chung, H.-J., Lee, C.-S., Lee, H.-D., and Kim, C.-K., 1999, "A Thermal Inkjet Printhead With a Monolithically Fabricated Nozzle Plate and Self-Aligned Ink Feed Hole," J. Microelectromech. Syst., **8**(3), pp. 229–236.
[11] Lee, J.-D., Lee, C.-S., Chun, K.-C., and Han, C.-H., 1999, "Two-Dimensional Nozzle Arrangement in a Monolithic Inkjet Printhead for High-Resolution and High-Speed Printing," *IEDM Tech. Dig*, IEEE, Piscataway, NJ, pp. 127–130.
[12] Lee, S.-W., Kim, H.-C., K., KuK., and Y.-S., Oh, 2002, "A Monolithic Inkjet Print Head: DomeJet," Sens. Actuators, A, **95**(2–3), pp. 114–119.
[13] Cheng, H.-P., Chien, C.-P., Tsai, S.-F., Peng, Y.-Y., and Gau, T.-H., 2003, "Liquid Jetting Study of the Micropump for Fuel Atomizer," *13th Conference of R.O.C. Combustion Institute*, Taipei, March 29, The Combustion Institute of R.O.C., Tainan, Taiwan.
[14] Cheng, H.-P., Chien, C.-P., Tsai, S.-F., and Peng, Y.-Y. 2002, "Numerical Liquid Refilling Investigation of the Thermal Bubble Micro Pump," *2002 IEEE/ASME International Conference on Advanced Manufacturing Technologies and Education in the 21st Century*, Chia-Yi, Taiwan, August 11–14, National Chung Cheng University, Chia-Yi, Taiwan, pp. 140.
[15] Cheng, H.-P., Lin, A.-H., Wang, H.-Y., Peng, Y.-Y., Gau, T.-H., and Chien, C.-P., 2003, "Fluid Analysis of Thermal Micropump for Fuel Atomizer," *Proc. 20th Conference of Chinese Society of Mechanical Engineers*, Taipei, Taiwan, December 5–6, Chinese Society of Mechanical Engineers, Taipei, Taiwan, pp. 121–128.
[16] Cheng, H.-P., Lin, A.-H., Wang, H.-Y., Peng, Y.-Y., Gau, T.-H., and Chien, C.-P., 2004, "Study of the Injection Flow on Arrayed Micropump," *14th Conference of R.O.C. Combustion Institute*, Tao-yuan, March 27, The Combustion Institute of R.O.C., Tainan, Taiwan.
[17] Cheng, H.-P., Chien, C.-P., Wang, James H., Peng, Y.-Y., and Kao, T.-H., 2004, "Fluids Analysis of the Thermal Micropump for Fuel Atomizer," Numer. Heat Transfer, Part B, **46**(5), pp. 473–495.
[18] Cheng, H.-P., Lin, A.-H., Wang, H.-Y., Peng, Y.-Y., Gau, T.-H., and Chien, C.-P., 2004, "Study of the Injection Flow of Single-Channel Single-Injection and Dual-Channel Dual-Injection of Thermal Bubble Micropump on Locomotive Fuel Atomization System," *Proc. Of the 9th Annual Conference on Liquid Atomization and Spray Systems-Asia*, Shanghai, P. R. China, August 22–24, ILASS-Asia, Shanghai P.R.C., pp. 202–209.
[19] Peng, Y.-Y., 2002, "Micro Pulsation Fuel Injection Technology for Fuel Supply System of IC Engine," J. the Mech. Industry, Taiwan, **236**, pp. 178–192.
[20] Peng, Y.-Y., 2003, "The Feasibility Study of Fuel Injection With Micro Pump on Engine Application," Combustion Quarterly, The Combustion Institute of R.O.C., **12**(1), pp. 20–38.
[21] Peng, Y.-Y., 2003, "Micro-Pulsation Metering Fuel Injection System," U.S. Patent No. 176530.
[22] Peng, Y.-Y., 2003, "Micropump Under Pressure Control Device," U.S. Patent No. 6,558,136.
[23] Peng, Y.-Y., 2004, "Micro-Pulsation Fuel Injection System With Under Pressure Stabilizer," U.S. Patent No. 6,672,289.
[24] Peng, Y.-Y., and Gau, T.-H., 2003, "A Study of the Micro-Pulsation Fuel Injection System," *13th Conference of R.O.C. Combustion Institute*, Taipei, March 29, The Combustion Institute of R.O.C., Tainan, Taiwan.
[25] Peng, Y.-Y., and Gau, T.-H., 2004, "A Study of the Micro-Pulsation Fuel Injection System for Applying to a Motorcycle," *14th Conference of R.O.C. Combustion Institute*, Tao-yuan, March 27, The Combustion Institute of R.O.C., Tainan, Taiwan.
[26] *CFD-ACE(U)® V2004 User's Manual*, ESI-CFD Inc., Huntsville, AL.
[27] Chen, P.-H., Chen, W.-C., and Chang, S.-H., 1997, "Ink Ejection Process of a Thermal Ink Jet Printerhead," *Proc. 14th Conference of Chinese Society of Mechanical Engineers*, Jhongli, Taiwan, December 5–6, Chinese Society of Mechanical Engineers, Taipei, Taiwan, pp. 70–77.
[28] Hirt, C. W., and Nichols, B. D., 1981, "Volume of Fluid (VOF) Method for the Dynamics of Free Boundaries," J. Comput. Phys., **39**(1), pp. 201–225.
[29] Kothe, D. B., Rider, W. J., Mosso, S. J., Brock, J. S., and Hochstein, J. I., 1996, "Volume Tracking of Interfaces Having Surface Tension in Two and Three Dimensions," AIAA Paper No. 96–0859.

Development of a Tip-Leakage Flow—Part 1: The Flow Over a Range of Reynolds Numbers

Ghanem F. Oweis[1]
Department of Mechanical Engineering,
University of Michigan,
Ann Arbor, MI 48109-2121

David Fry

Chris J. Chesnakas

Stuart D. Jessup

Naval Surface Warfare Center,
Carderock Division, Code 5400,
9500 MacArthur Blvd.,
West Bethesda, MD 20817-5700

Steven L. Ceccio
Department of Mechanical Engineering,
University of Michigan,
Ann Arbor, MI 48109-2121
e-mail: ceccio@engin.umich.edu

An extensive experimental investigation was carried out to examine the tip-leakage flow on ducted propulsors. The flow field around three-bladed, ducted rotors operating in uniform inflow was measured in detail with three-dimensional laser Doppler velocimetry and planar particle imaging velocimetry. Two geometrically similar, ducted rotors were tested over a Reynolds number range from 0.7×10^6 *to* 9.2×10^6 *in order to determine how the tip-leakage flow varied with Reynolds number. An identification procedure was used to discern and quantify regions of concentrated vorticity in instantaneous flow fields. Multiple vortices were identified in the wake of the blade tip, with the largest vortex being associated with the tip-leakage flow, and the secondary vortices being associated with the trailing edge vortex and other blade-wake vortices. The evolution of identified vortex quantities with downstream distance is examined. It was found that the strength and core size of the vortices are weakly dependent on Reynolds number, but there are indications that they are affected by variations in the inflowing wall boundary layer on the duct. The core size of the tip-leakage vortex does not vary strongly with varying boundary layer thickness on the blades. Instead, its dimension is on the order of the tip clearance. There is significant flow variability for all Reynolds numbers and rotor configurations. Scaled velocity fluctuations near the axis of the primary vortex increase significantly with downstream distance, suggesting the presence of spatially uncorrelated fine scale secondary vortices and the possible existence of three-dimensional vortex-vortex interactions.*
[DOI: 10.1115/1.2201616]

1 Introduction

Prediction of turbomachinery conduct often requires the performance and analysis of model testing. Test data are combined with similarity analysis to predict performance on the prototype scale at higher Reynolds numbers. Model testing is also needed to examine flow phenomena that result from secondary flows, such as noise production and cavitation. In the case of marine propulsors, cavitation inception [1] typically occurs first in vortices produced in the vicinity of the blade tip. As a result, inception observations made at lower Reynolds number must be scaled to provide a prediction of full-scale cavitation performance. The complexity of the flow is increased when the rotor is encased in a closely fitting shroud.

Many researchers have examined the formation and scaling of tip vortices on stationary lifting surfaces and on the blades of rotating turbomachinery, with recent reviews found in [2,3]. In the current work, we are interested in the vortical flow near the tip of a ducted rotor. The flow in the vicinity of the tip gap and in the immediate wake can be very complex. Lakshminarayana [4] details many of the important flow processes including the state of the boundary layers on the rotating blade and on the shroud, the production of flow jetting within the gap, the possible formation of "scraping vortices," and interaction with regions of flow separation. The relative size of the tip clearance is an important parameter, along with the exact geometry of the blade tip region and the blade loading distribution. A strong vortex can be created by the tip-leakage flow, and this vortex will interact with other concentrated vorticity shed by the blade, such as leading- and trailing-edge vortices. Both numerical and experimental studies of specific and canonical tip-leakage flows have been performed in order to understand and characterize the dominant flow features. Because of the practical importance of these flows, there is a large body of literature on the subject. A review can be found in a relatively recent von Karman Institute Lecture Series [5].

In the present study, we examine the tip-leakage flow of a ducted rotor. Two rotors with geometrically similar shapes but different diameters are used to extend the range of Reynolds numbers examined. Laser Doppler velocimetry (LDV) and particle imaging velocimetry (PIV) are used to capture the tip leakage vortex flow as it develops downstream of the blade trailing edge. The process of vortex roll-up is examined as the primary tip leakage vortex interacts with a trailing edge vortex and other, weaker vortices in the blade wake spiral. This flow has significant variability, and we will examine how the average and statistical characteristics of the tip-leakage flow vary with Reynolds number.

2 Experimental Setup

The experiments were performed in the David Taylor 36 in. variable pressure cavitation tunnel. The 36 in.-diam, open jet test section was used for these tests. The propeller was driven using an upstream dynamometer. Inflow to the propeller was uniform except for the wakes from three upstream shaft support struts. Two geometrically similar, ducted, three-bladed rotors were tested in this investigation (Figs. 1 and 2). The larger rotor, Propeller 5206, was sized to be the maximum possible size to fit into the 36 in. water tunnel. The rotor had a hub diameter of 0.3517 m (13.847 in.), a tip diameter $D=2\times R_P=0.8503$ m (33.475 in.), and a constant chord of 0.3812 m (15.008 in.) from hub to tip. It operated in a duct of diameter 0.8636 m (34.00 in.) placed in the open jet nozzle so that the entire tunnel flow went through the propulsor. The straight portion of the duct had a linear extent of 0.648 m (25.5 in.) and extended from a distance of $0.568\times R_P$ upstream the blade tip at the trailing edge, to a distance of $0.194\times R_P$ downstream of the blade tip.

[1]Current address: Mechanical Engineering Department, American University of Beirut, 3 Dag Hammarskjold Plz., New York, NY 10017.

Contributed by the Fluids Engineering Division of ASME for publication in the JOURNAL OF FLUIDS ENGINEERING. Manuscript received January 15, 2004; final manuscript received March 2, 2006. Review conducted by Joseph Katz.

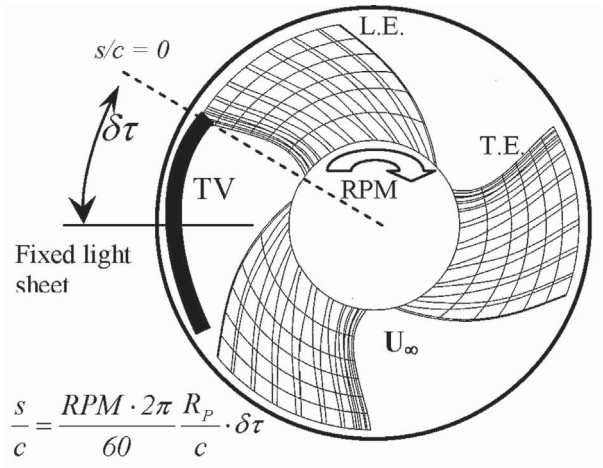

(a)

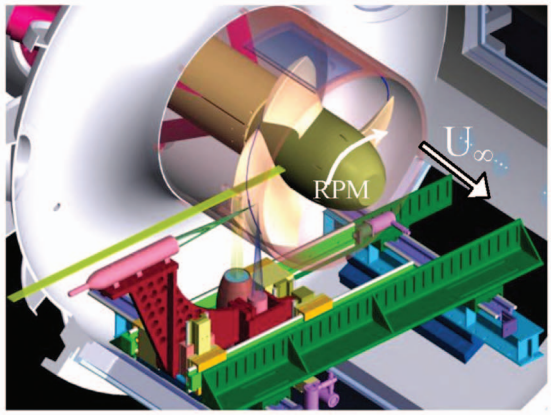

(b)

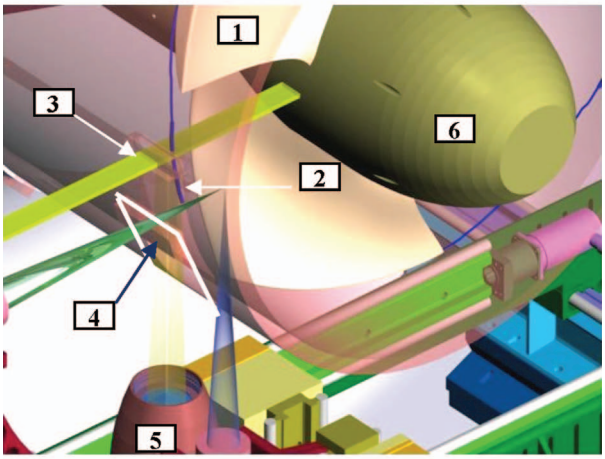

(c)

Fig. 1 (*a*) A plan view of the rotor with a depiction of the duct and the tip vortex emanating near the trailing edge of a blade. Also shown is the coordinate system used. $\delta\tau$ is the time separation from the PIV measurement location along the vortex core, to the blade trailing edge. The tunnel mean flow is out of the page. (*b*) A diagram of the open-jet test section of the David Taylor model basin 36 in. variable pressure cavitation tunnel with the three-bladed, ducted rotor P5206 installed. (*c*) A close up view of the blade tip at the trailing edge (1), the emanating tip leakage vortex on the inside of the duct—the dark curved line (2), the laser light sheet passing through a window installed in a pocket in the duct (3), another window in the duct to provide optical access for the camera (4), the underwater camera housing (5), and the hub (6) (Chesnakas and Jessup [7]).

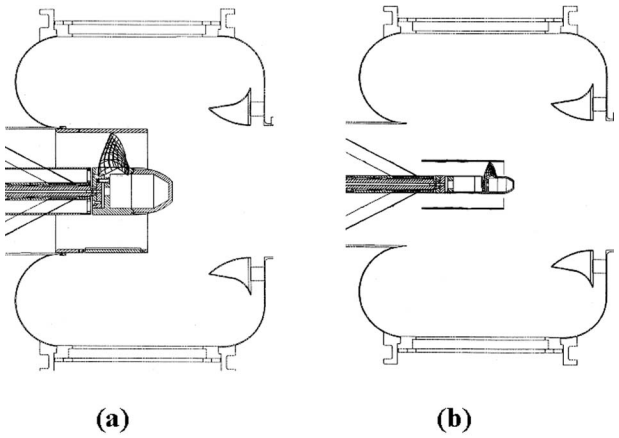

Fig. 2 (*a*) A diagram of the open-jet test section of the 36-in.-diameter water tunnel, showing the P5206 propeller duct, which is an extension of the tunnel conduit; (*b*) diagram of the open jet test section with the P5407 ducted propeller installed

The smaller rotor, Propeller 5407, had a hub diameter of 0.1261 m (4.964 in.), and a tip diameter $D=2\times R_P=0.3048$ m (12.000 in.). The duct of the small rotor had an inside diameter of 0.3096 m (12.188 in.), an outer diameter of 0.3352 m (13.215 in.), and a linear extent of 0.699 m (27.5 in.) It extended from $-4\times R_P$ upstream of the blade tip to $0.598\times R_P$ downstream of the blade tip. A bell mouth was installed on the inlet of the duct with a 3.00 in. (0.076 m) radius on the inner and outer walls. The scale ratio of the two rotors was 2.790.

The rotor geometry is detailed in Table 1. To identify where boundary layer transition would affect the results, boundary layer trips were placed on some blades. For most measurements, no influence of the boundary layer trips was noted. The ratio of the tip clearance to the maximum thickness at the tip, g/t was 0.17, which is near the optimum value of 0.2 reported by Farrell and Billet [6] to reduce the potential for tip-leakage cavitation. The propeller was made using a numerically controlled milling process and manufactured to tolerances of approximately 0.1 mm from a mono-bloc 6061T6 aluminum forging. The blade section was a NACA 66, DTMB (David Taylor Model Basin) modified thickness form, with a 0.8 mean-line camber, and with the trailing edges thickened to incorporate a typical anti-singing trailing edge bevel. The blade pitch was reduced at the hub and tip to minimize root and tip cavitation.

A window was inserted into the duct to allow for optical access to the rotor flow, as shown in Figs. 1(*b*) and 1(*c*). The installation of the window produced a pocket in the duct. While no flow passed through the window, the presence of the pocket was not entirely passive. Laser doppler velocimetry (LDV) measurements performed by Chesnakas and Jessup [7] showed that the primary vortex moved in and out of the cavity as the rotor blade passed by. However, this effect was not so pronounced to significantly alter the character of the flow in the tip region. LDV was also used to measure the inlet flow profile upstream of the rotors through a transparent window placed in the duct.

A planar particle imaging velocimetry (PIV) system was implemented for use in the water tunnel. Figures 1(*a*)–1(*c*) show a schematic drawing of the PIV setup. The double-pulsed light sheet was produced by two Nd:yttrium–aluminum–garnet lasers operating outside the test section (Quanta-Ray PRO-250 Series with maximum energy of 800 mJ per 10 ns pulse, at 532 nm). The digital camera used to record the flow images was mounted in a waterproof housing within the still-water region of the test section. The light sheet was 5 mm thick in the large rotor case (around 1 mm thick for the small rotor) and double pulsed with a time separation varying between 6 and 20 μs (large rotor) for

Table 1 Geometry of the rotors. The radial dimension is r, the rotor radius is R_P, and the diameter is D. The chord is c, the pitch is p, the total rake is i_T, the maximum thickness is t, the camber is f, and the skew angle is θ.

r/R_P	c/D	p/D	i_T/D	t/c	f/c	θ
0.416	0.446	0.92	−0.0063	0.172	−0.065	−0.4 deg
0.5	0.446	1.135	0.0063	0.148	0.000	4.2 deg
0.6	0.446	1.220	0.0145	0.119	0.037	10.0 deg
0.7	0.446	1.175	0.0227	0.102	0.047	15.9 deg
0.8	0.446	1.087	0.0309	0.100	0.047	21.5 deg
0.9	0.446	0.995	0.0391	0.100	0.038	26.3 deg
1.0	0.446	0.905	0.0473	0.100	0.020	30.0 deg

differing propeller speeds and distances from the blade trailing edge. The light sheet passed through windows in the outer wall of the test section and through the transparent duct pocket to illuminate the flow. The sheet was oriented parallel to the propeller-shaft axis, as shown in Fig. 1(c). The radial and axial positions of the camera were moved to place the mean center of the vortex in the center of the image. The whole tunnel was seeded before the start of the experiments with silicon carbide particles of 1 μm mean diameter. A LaVision FlowMaster-3S PIV system was used to control the firing of the lasers and synchronize the image capture by a (1280 by 1024 pixel) cross-correlation charge coupled device camera of 12 bit gray scale resolution. The camera axis was perpendicular to the laser sheet and recorded the in-plane motion of the tracer particles. The light sheet was sufficiently thick to reduce the adverse effect of particles that entered or exited the illuminated volume during the laser double pulse due to possible, strong cross-plane flow velocities. The lenses on the camera were chosen to have a depth-of-field larger than the thickness of the light sheet. The images were spatially calibrated by taking images of a registration target placed in the water-filled test section. A multi-pass algorithm was used to compute the in-plane velocity vectors from the particles images using 32×32 pixel interrogation windows with 15% overlap applied in the final pass. This produced a velocity field with 46×37 vectors in a field of view of 37.7 $\times29.6$ mm, at 0.83 mm vector spacing for the large rotor. For the small rotor, the field of view was 11.76×9.35 mm and the vector spacing was 0.302 mm. Timing of the PIV image capture was synchronized with the passage of the rotor blades, making it possible to capture multiple images at a given blade position. The images were taken at various downstream distances along the pitch line, s, with $s=0$ describing the case when the tip of the blade's trailing edge intersected the PIV plane. The pitch line, s, (a circular path traced by the tip of the blade's trailing edge) was computed from the product of the propeller tip velocity, and the time separation ($\delta\tau$) from the tip of the blade trailing edge location to the PIV imaging plane, $s/c=(\text{rpm-}2\pi)/60R_P/c\cdot\delta\tau$. The velocity vectors were used to compute the vorticity field by making use of Stokes theorem. The vorticity at a point was calculated from the line integral of the velocity vector around a closed loop enclosing the point under consideration divided by the total area enclosed by the closed loop. On the experimental grid, the integration loop was composed of straight, serial line segments chosen to pass through the centers of the eight neighboring cells immediately surrounding the cell of interest. Towards the edges of the PIV grid, vorticity was calculated using forward and backward differentiation schemes [8]. After the vorticity field was calculated, a 3 by 3 mean filter was used to reduce noise.

The rotor was operated at a constant advance coefficient ($J=U_\infty/nD$) where U_∞ is the average flow speed into the duct (m/s), n is the rotational speed of the rotor (rev/s), and D is the rotor diameter (m). The operating advance coefficient was selected to produce a typical leakage vortex, without unwanted flow conditions over the blade, with $J=0.971$. This is higher than the design advanced coefficient $J=0.75$ in order to avoid the formation of a leakage vortex at the leading edge of the blade and the occurrence of pressure side leading edge cavitation near the blade tip. Several rotational speeds were examined for both rotors. The blade-tip Reynolds number is based on the chord, c, and the total tip speed, ($U_\infty+\pi Dn$). The water kinematic viscosity was evaluated at the average flow temperature. The inlet absolute static pressure was maintained high enough ($P_\infty=309$ kPa at 500 rpm) during the PIV measurements to suppress cavitation. This advance coefficient resulted in a thrust coefficient $K_T=T/\rho n^2D^4=0.31$ and a torque coefficient $K_Q=Q/\rho n^2D^5=0.054$ that did not significantly vary over the range of Reynolds numbers studied. For the smaller rotor, however, there was a noticeable Reynolds number dependence of the thrust and torque coefficients at low speeds (<600 rpm). Application of roughness to the leading edge of the rotor blades did not significantly influence the measured results. Table 2 presents the conditions reported here for both rotor configurations.

3 Experimental Uncertainty

The geometrical tolerance of the machined rotors was less than 0.1 mm. Variability of the rotor gap was 0.76 mm (±0.030 in.) for the 5407 small rotor assembly, and 1.6 mm (±0.063 in.) for the 5206 large rotor. The uncertainty associated with the measurements of test parameters (i.e., rotor speed, free-stream speed, free-stream pressure and temperature, rotor thrust, and rotor torque) are ±1%. Uncertainty of the presented LDV measurements is ±0.8%. The accumulated uncertainty of the PIV velocity measurements is estimated at ±5%.

4 Inlet Flow

The inlet axial velocity, U_x/U_∞, and tangential velocity, U_T, profiles measured in the duct at a location $0.3615\times R_P$ upstream of the blade's trailing edge tip are plotted in Fig. 3 for the speeds

Table 2 Test conditions for the 5407 and 5206 rotor configurations. The advance coefficient was constant at $J=0.971$. The Reynolds number is based on the chord, c, and the total tip speed, ($U_\infty+\pi Dn$).

	U_∞ (m/s, (fps))	n (rpm)	Reynolds number
5407 Rotor "Small Rotor"	1.50 (4.9)	300	0.7×10^6
	3.0 (9.8)	600	1.4×10^6
	6.0 (19.6)	1200	2.8×10^6
	9.0 (29.4)	1800	4.3×10^6
5206 Rotor "Large Rotor"	3.11 (10.2)	250	4.6×10^6
	3.90 (12.8)	313	5.8×10^6
	4.66 (15.3)	375	6.9×10^6
	5.46 (17.9)	438	8.1×10^6
	6.22 (20.4)	500	9.2×10^6

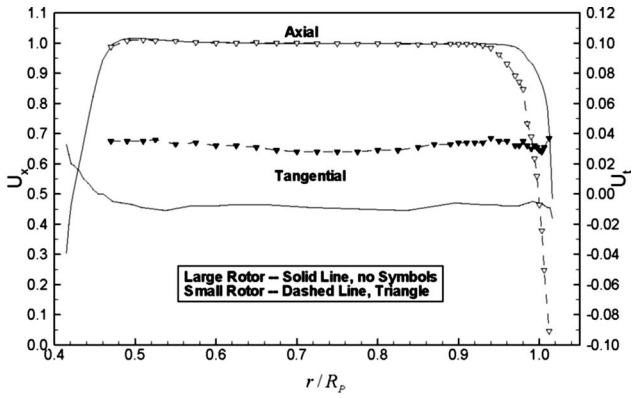

Fig. 3 Tangential (U_t/U_∞), and axial (U_x/U_∞) velocity profiles of the duct inflow for the small rotor running at 1200 rpm (triangles), and for the large rotor running at 500 rpm (solid line with no symbols)

of 1200 rpm on the small rotor and 500 rpm on the large rotor. For both rotors the axial velocity is nearly constant from $0.5 \leqslant r/R_P \leqslant 0.9$, where r is the radial distance from the propeller center of rotation. The wall boundary layer, however, is about 50% thicker for the small rotor ($\delta_1/R_P=0.090$) compared with the large rotor ($\delta_1/R_P=0.060$). Note that for both rotors the duct boundary-layer thickness is much larger than the tip gap of $g/R_P=0.015$. The small gap of the small rotor is nearly 1/6 times the inlet boundary layer, and the gap on the large rotor is 1/4 the boundary layer thickness.

Both rotors have a small amount of swirl in the in flow, with the large rotor having a small negative tangential velocity (opposite to the direction of rotor rotation) and the small rotor having a small positive tangential velocity.

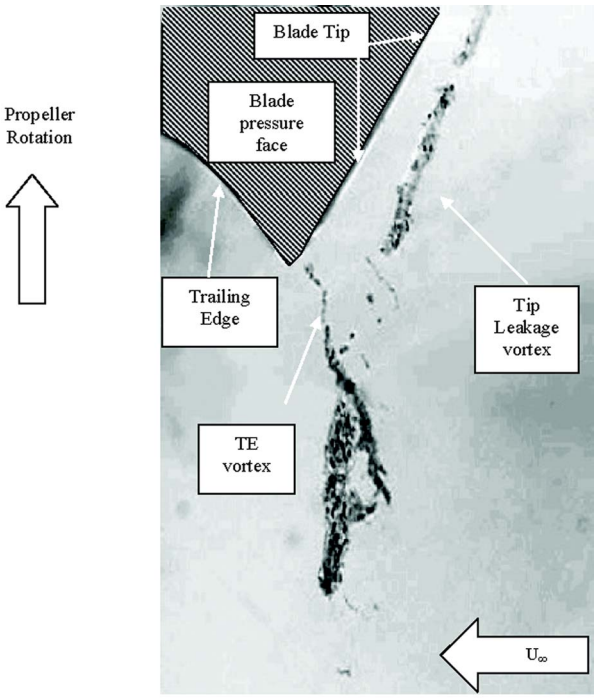

Fig. 4 A photograph of the blade trailing edge taken through a clear section of the duct. The pressure has been lowered, and developed vortex cavitation makes the tip leakage and trailing edge (TE) vortices visible. The cavitation number is $\sigma=5.6$.

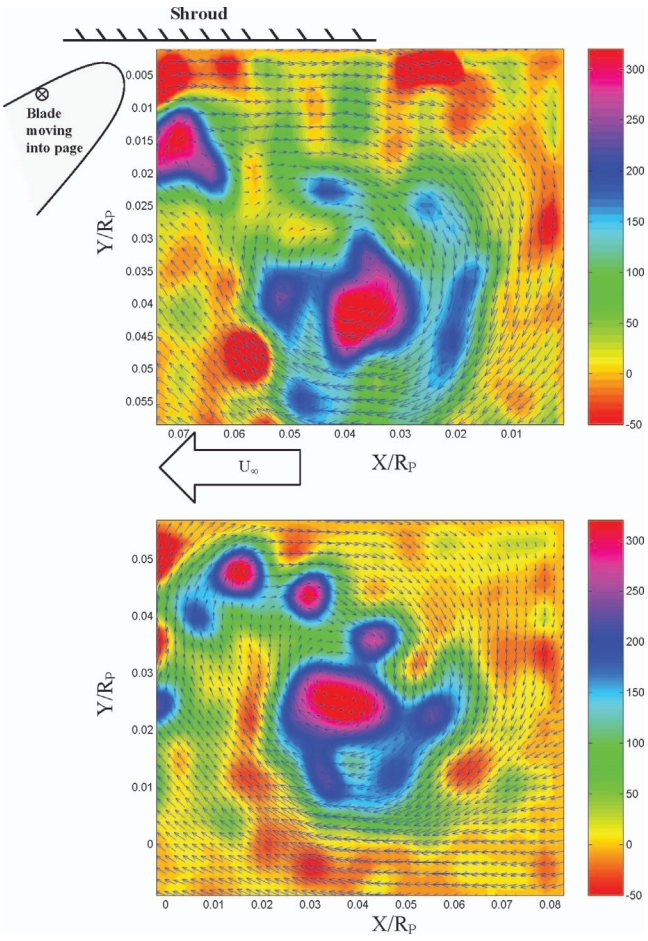

Fig. 5 Sample instantaneous PIV velocity vector fields with vorticity contours from the mini rotor at 1200 rpm (top), and the big rotor at 438 rpm (bottom) at the downstream location $s/c=0.041$. The vorticity is normalized by (U_∞/R_P).

5 Overall Development of the Tip-Leakage Flow

Both LDV measurements performed by Chesnakas and Jessup [7] and the PIV measurements discussed here reveal the general development of the flow in the tip region of the rotor operating at the given advance coefficient. The pressure difference across the blade produces a flow through the tip region and the formation of a strong tip-leakage vortex, which we will refer to as the primary vortex. A second co-rotating concentrated vortex forms at the trailing edge, and we will refer to this as the secondary vortex. Additionally, there were multiple secondary co-rotating vortices of comparable or weaker strength. Counterrotating secondary vor-

Table 3 Correlation coefficients R_V^2 and R_ω^2 averaged over all the measured locations s/c, for the two rotors

	Reynolds number	R_ω^2 %	R_V^2 %
5407 Rotor "Small Rotor"	0.7×10^6	72±10	65±12
	1.4×10^6	75±10	70±12
	2.8×10^6	75±9	68±9
	4.3×10^6	74±9	67±12
5206 Rotor "Large Rotor"	4.6×10^6	80±7	79±7
	5.8×10^6	77±9	76±9
	6.9×10^6	80±8	75±8
	8.1×10^6	77±9	75±10
	9.2×10^6	79±8	76±9

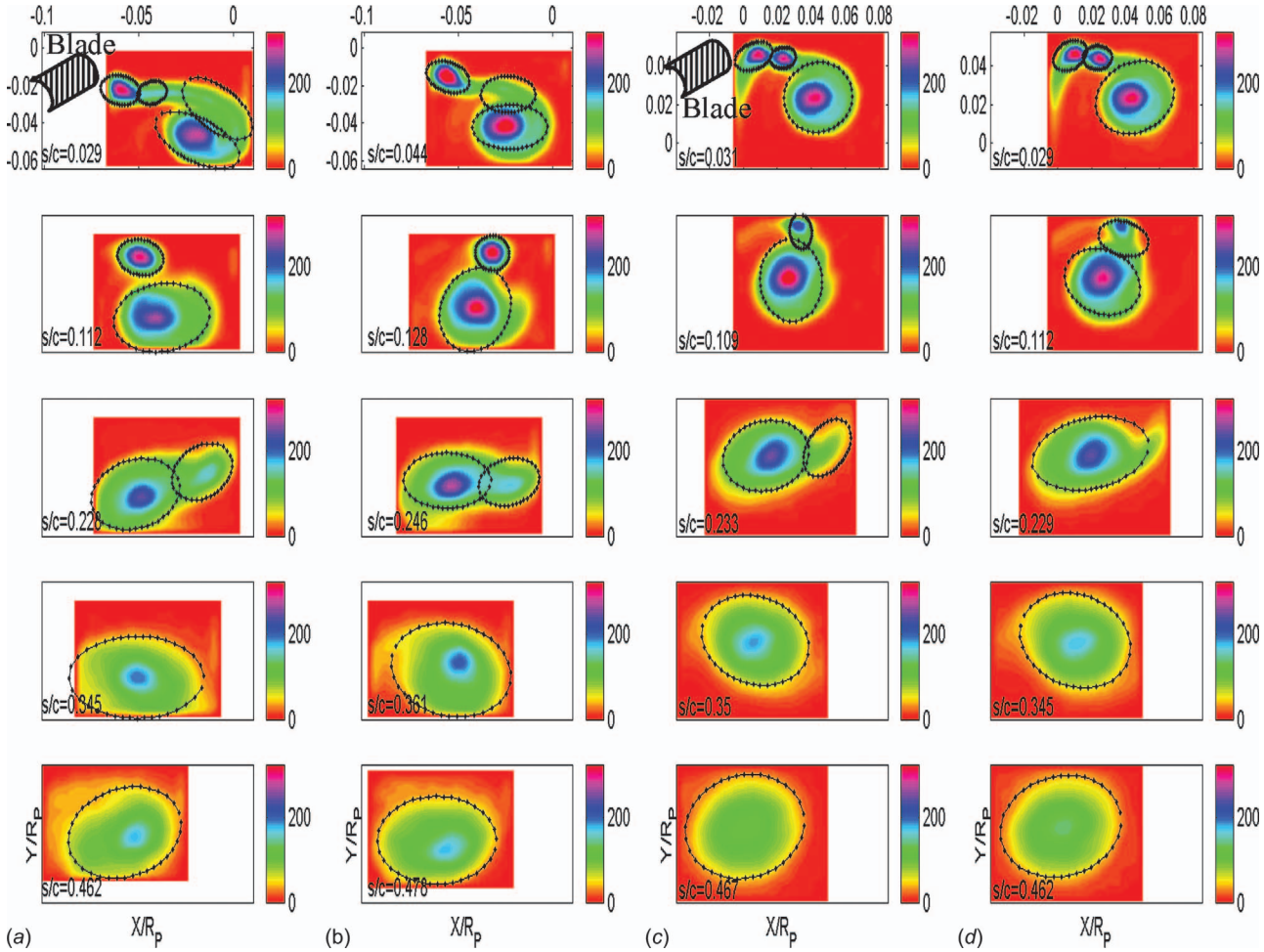

Fig. 6 Average vorticity field development as a function of the distance downstream from the blade trailing edge along the pitch line, s/c, which is noted on each frame. Shown are fields from the small rotor running at (*a*) 300 rpm, and (*b*) 1800 rpm; and from the large rotor running at (*c*) 313 rpm, and (*d*) 500 rpm. The closed contours indicate the core boundaries of the identified vortices. The axes coordinates are normalized by R_P and the vorticity by (U_∞/R_P).

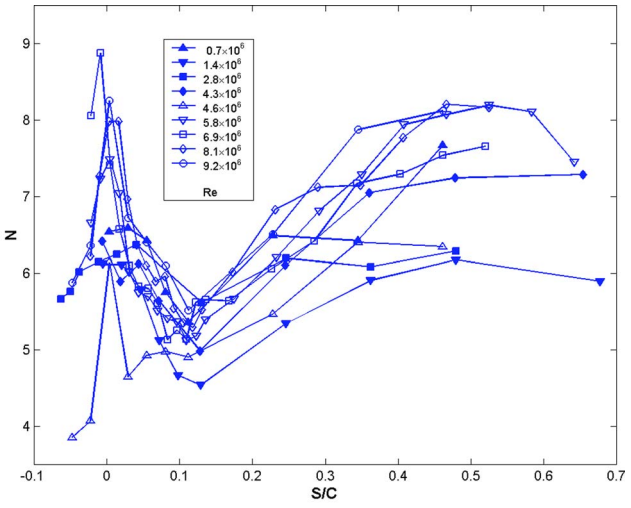

Fig. 7 The average number of identified vortices, N, in the instantaneous flow field as a function of the distance downstream from the blade trailing edge along the pitch line, s/c for various Reynolds numbers. Closed symbols correspond to the small rotor, open symbols to the large rotor.

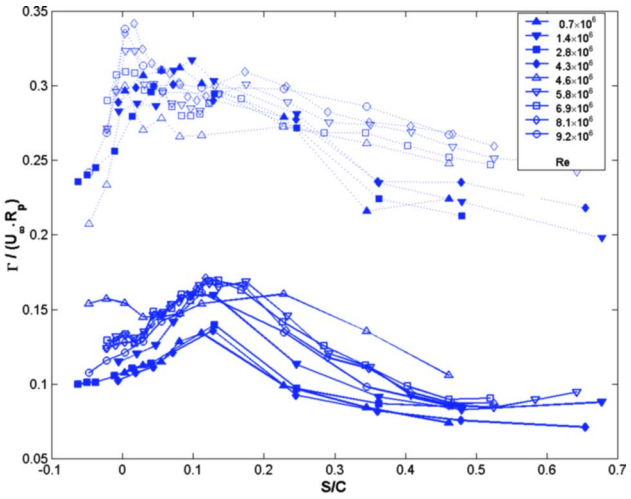

Fig. 8 Average circulation of the instantaneous primary vortex (solid line), and the average sum of the circulation of the identified instantaneous vortices in the field (dashed line). Closed symbols correspond to the small rotor, open symbols to the large rotor.

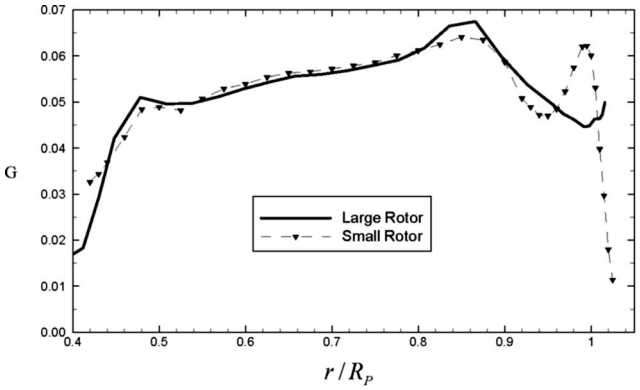

Fig. 9 Circulation, G, measured downstream of the large and small rotors at $x/R_P=0.650$

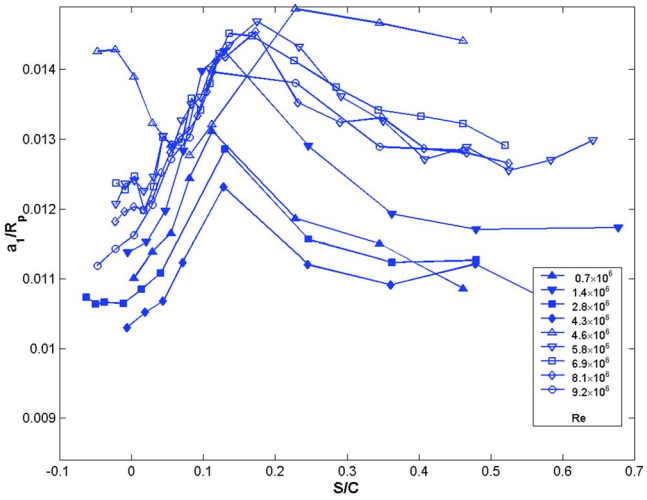

Fig. 10 Average core radius of the instantaneous primary vortex as a function of the downstream distance s/c. Closed symbols correspond to the small rotor, open symbols to the large rotor.

tices were also present. Fig. 4 shows the primary and secondary vortices visualized by cavitation in their respective cores. In addition, concentrated vorticity is also present in the blade wake. The mean axes of the primary and secondary vortices are not necessarily perpendicular to the plane made by the PIV light sheet, but the largest portion of the vorticity is in this plane, as discussed below. At increasing downstream distances from the blade trailing edge, these vortices orbit around each other in a manner often seen in merger processes.

Figure 5 shows two sample instantaneous PIV images taken on the large and small rotors. The vortices are not generally axisymmetric as measured in the PIV plane. This is due to both the orientation of the vortex with respect to the PIV plane and the asymmetric nature of the flow itself. Also, the cross-plane flow is not uniform across the PIV plane. However, the cross-plane vorticity field clearly shows that there are multiple distinct vortices with varying core sizes and strengths. It is possible to reduce the in-plane vorticity distribution into a sum of discrete, two-dimensional Gaussian vortices with axes perpendicular to the PIV plane. These vortices have velocity, $u_\theta(r)$, vorticity, $\omega(r)$, and circulation, $\Gamma(r)$, distributions as function of radial distance, r, given by

$$u_\theta(r) = \frac{\Gamma_O}{2\pi r}(1 - e^{-\eta_1(r/a)^2}) \tag{1}$$

$$\omega(r) = \frac{\Gamma_O}{\pi}\frac{\eta_1}{a^2}e^{-\eta_1(r/a)^2} \tag{2}$$

$$\Gamma(r) = \Gamma_0(1 - e^{-\eta_1(r/a)^2}) \tag{3}$$

where $\eta_1=(1.121)^2=1.257$, and the maximum tangential velocity, u_C, occurs at the core radius, a, and is given by

$$u_C = \eta_2\frac{\Gamma_O}{2\pi a} \tag{4}$$

with $\eta_2=0.715$. Integration of the radial momentum equation yields the pressure depression at the vortex centerline, $r=0$

$$\Delta P = p_C - p_\infty = -\eta_3\rho_f\left(\frac{\Gamma_O}{2\pi a}\right)^2 \tag{5}$$

where $\eta_3=0.870$ and p_∞ is the pressure far from the vortex [9].

In reality, the flow also has vorticity with components parallel to the PIV plane as well as flow nonuniformity in the cross-plane flow. However, a combination of Gaussian vortices can be used to both reconstruct the actual in-plane flow and scale the resulting vortex-induced pressure variations. Two parameters are needed to characterize each vortex: the core radius, a_i, and the total circulation $\Gamma_{O,i}$. Hereafter, the subscript, i, identifies the vortex in question, where $i=1$ is the largest or "primary" vortex, and the remaining identified vortices are "secondary."

An identification procedure was used to find and fit Gaussian vortices to the regions of concentrated vorticity in each PIV image. A detailed description of the identification process is found in Oweis and Ceccio [10]. The identification is performed with the vorticity field, where a local vorticity peak above a set field threshold is used to indicate the presence of a concentrated vortex, and gradients of the circulation are then used to determine the core size and consequently the strength of the identified vortex. Once the vortices are identified and measured, the vorticity and velocity fields are then reconstructed and compared with the original measured fields. A regression value for the velocity field correlation, R_V^2, and another for the vorticity field, R_ω^2, are computed for each PIV image as goodness-of-fit measures

$$R_V^2 = 1 - \frac{\sum_{i=1}^{j}(V_{M,i} - V_{C,i})^2}{\sum_{i=1}^{j}(V_{M,i} - \bar{V}_M)^2} \qquad R_\omega^2 = 1 - \frac{\sum_{i=1}^{j}(\omega_{M,i} - \omega_{C,i})^2}{\sum_{i=1}^{j}(\omega_{M,i} - \bar{\omega}_M)^2} \tag{6}$$

where the subscripts M and C denote, respectively, the measured and the computed (reconstructed) fields for the total number of PIV vector locations, j, in a given PIV field. Table 3 presents the average values of R_V^2 and R_ω^2 for the data presented here. The values are averaged over all realizations for the various downstream measurement locations, s/c.

6 Averaged Tip-Leakage Flow Field

Between 501 and 586 PIV images were collected at each of the multiple positions downstream of the blade trailing edge, s/c. Figure 6 shows the averaged vorticity fields for the two conditions of the small rotor ($\mathbf{Re}=0.7\times10^6$ and 4.3×10^6) and two

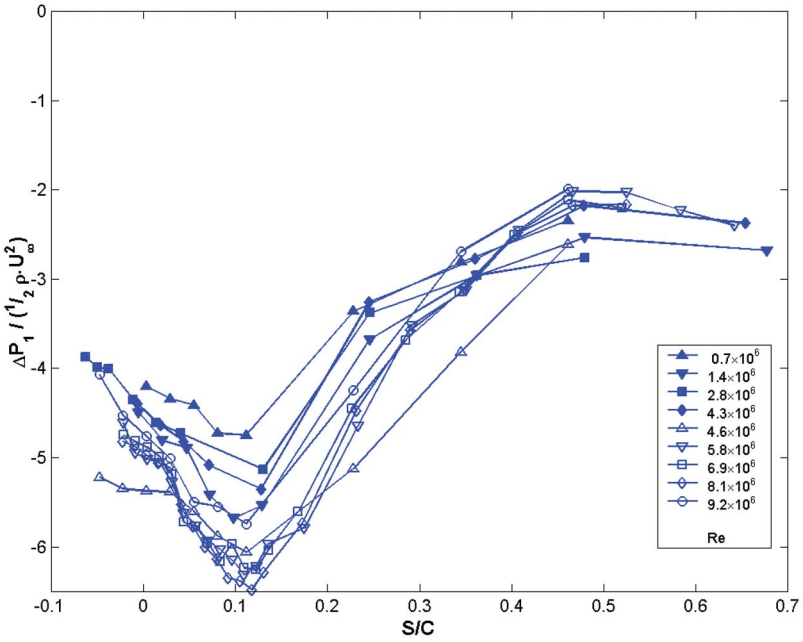

Fig. 11 Average inferred pressure coefficient of the instantaneous primary vortex $C_{P,1}=\Delta P_1/(\frac{1}{2}\rho U_\infty^2)$ as a function of s/c for varying Reynolds numbers. Closed symbols correspond to the small rotor, open symbols to the large rotor.

conditions of the large rotor ($\mathbf{Re}=5.8\times10^6$ and 9.2×10^6) for varying downstream locations s/c. Note that the values of s/c chosen are similar but not identical for the five values of s/c shown. The closed contours are the core outlines of the primary and secondary identified vortices.

Interpretation of the average flow field must be performed with care, since vortex variability and wandering are significant. Moreover, multiple secondary vortices identified in the individual flow fields are not generally stationary in space relative to the primary vortex. Figure 7 shows the average number of identified vortices

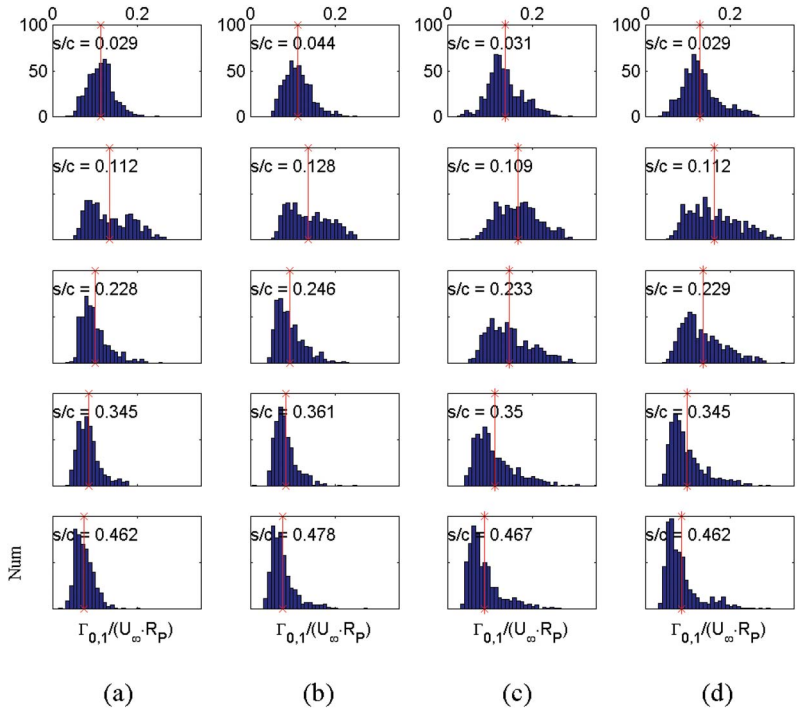

Fig. 12 Histograms of the instantaneous primary vortex circulation, $\Gamma_{O,1}/(U_\infty R_P)$, at varying downstream distance, s/c. The small rotor running at (*a*) 300 rpm, and (*b*) 1800 rpm. The large rotor running at (*c*) 313 rpm, and (*d*) 500 rpm.

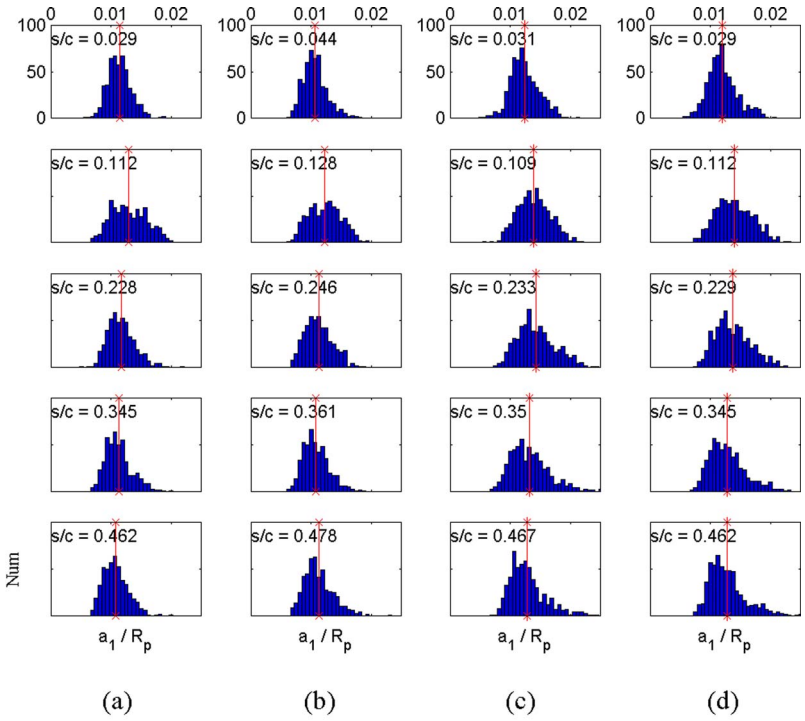

Fig. 13 Histograms of the primary vortex core radius, a_1/R_P. Conditions are the same as in Fig. 12.

with varying downstream distance. The typical number is between 5 and 8, but the averaging of multiple images will smear out those vortices that are not approximately fixed in location. As a result, fewer vortices are discernable in the averaged flow field, with only one vortex identifiable farther downstream. For these reasons, the vortex identified in the average flow field is *not* equivalent to the typical vortex identified in the instantaneous flow fields. An extended discussion of this issue is provided in [10].

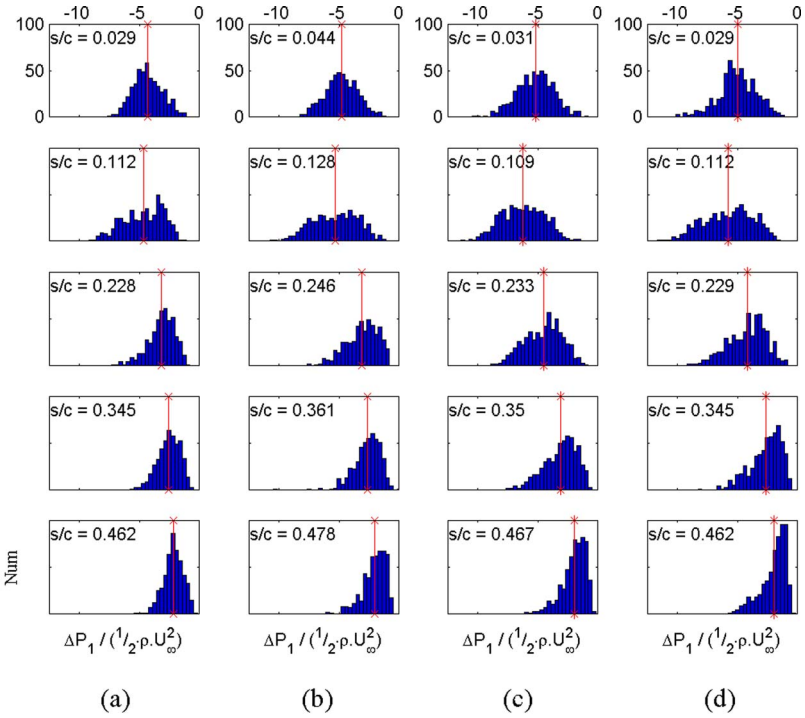

Fig. 14 Histograms of the primary vortex pressure coefficient, $C_{P,1}$. Conditions are the same as in Fig. 12.

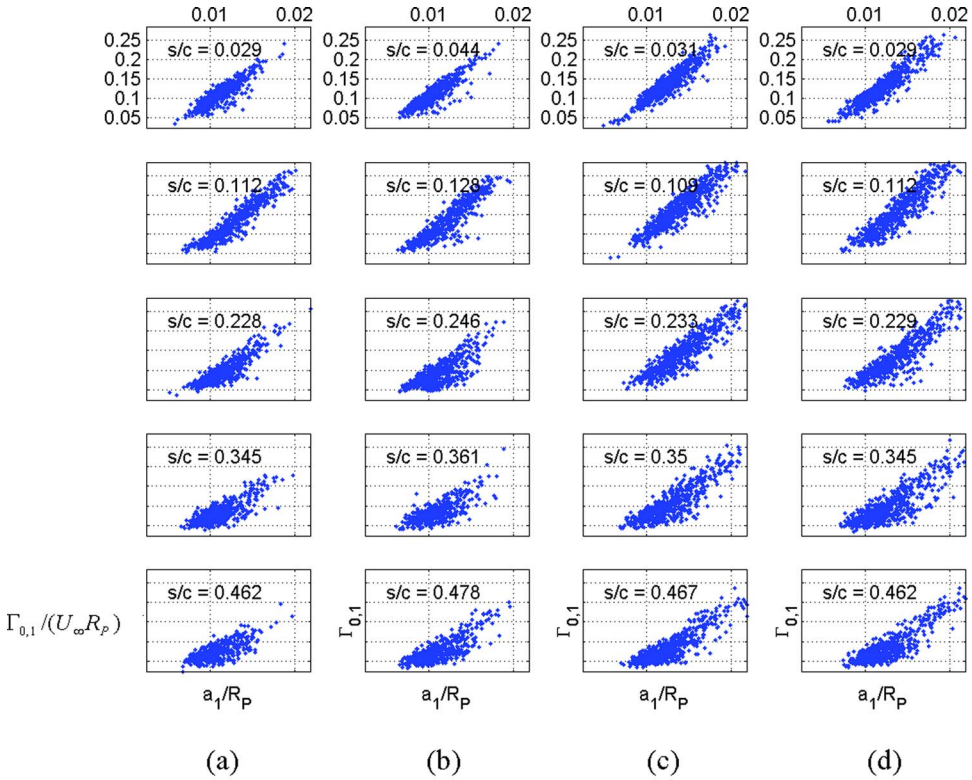

Fig. 15 A plot of $\Gamma_{0,1}/(U_\infty R_P)$ versus a_1/R_P for the conditions shown in Fig. 12

Consequently, we will present averaged quantities identified from the instantaneous images of the flow field.

7 Properties of Instantaneous Tip-Leakage Flow Field

The average value of the circulation identified in the primary vortex (dashed line) and the total identified circulation (solid line) are plotted for varying downstream distances in Fig. 8. The average values of $\Gamma_{O,1}/(U_\infty R_P)$ and $\Sigma_i \Gamma_{O,i}/(U_\infty R_P)$ lie in a band. The strength of the primary vortex is approximately one-third that of the total identified strength. The strength of the primary vortex reaches a maximum near $s/c=0.13$. For both quantities, the normalized values from the small rotor are generally less than those

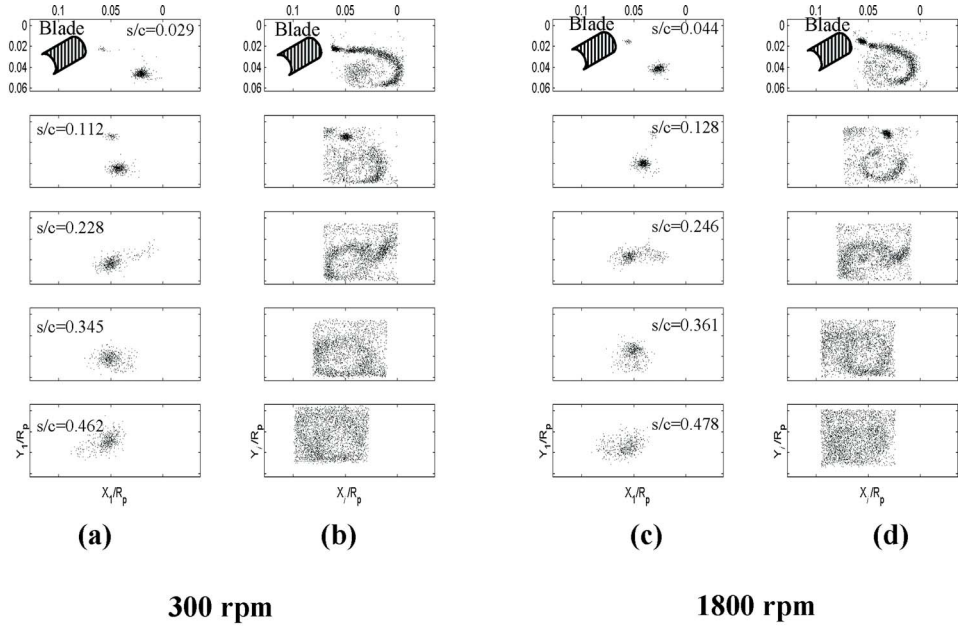

Fig. 16 Scatter plot of the center location of: (*a*), (*c*) the primary vortex; (*b*), (*d*) the secondary vortices at 300 rpm, and 1800 rpm for the small rotor, as a function of the downstream location *s*/*c*. The tip of the blade trailing edge location is noted in the first frame. The shroud is toward the top of the image. Refer to Fig. 5 for explanation of the coordinate system.

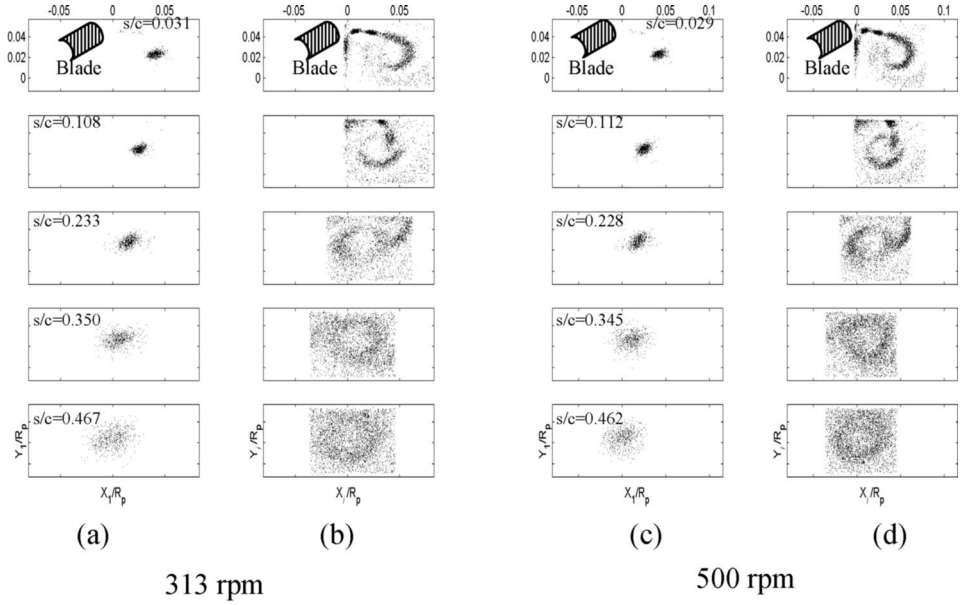

Fig. 17 Scatter-plot of the center location of: (*a*), (*c*) the primary vortex; (*b*), (*d*) the secondary vortices at 313 rpm, and 500 rpm for the large rotor, as a function of the downstream location *s*/*c*. The shroud is toward the top of the image. Refer to Fig. 5 for explanation of the coordinate system.

from the large rotor, and this is more pronounced for the strength of the primary vortex. However, there is no strong trend with Reynolds number. The case of $\mathrm{Re}=4.6\times10^6$ (250 rpm on the large rotor) is anomalous.

These values can be compared to the average circulation in the rotor wake measured with LDV, shown in Fig. 9. Here, the circulation per blade is given by

$$G=\frac{1}{Z}\frac{r}{R}\frac{U_T}{U_\infty}\cong\frac{\Gamma}{2\pi R_P U_\infty} \tag{7}$$

where $Z=3$ is the number of blades. Over most of the blade span, the circulation matches well for the two rotors. Past $r/R_P=0.95$, however, the circulation is higher on the small rotor than on the large rotor due to the thicker duct boundary layer. Since the lift produced by the blade is the product of the circulation and the velocity, the total lift produced at the tip is closer in the two rotors than the plot of circulation would indicate. It is possible that small variations in the loading distribution can cause differences in the formation of the tip leakage flow. The maximum value of $2\pi G=\Gamma/U_\infty R_P\approx0.4$ near $r/R_P=0.85$, and this is similar to the maximum total value of identified circulation.

Farrell and Billet [6] examined the effect of tip clearance on the shed circulation downstream of the blade tip. They used LDV to determine the circulation of the primary vortex identified in the average field. The shed circulation was between 40% and 80% of the average bound circulation near the tip for clearance ratios from $g/R_P=0.004$ to 0.024. The shed circulation increased with increasing g/R_P. (The inlet boundary layer profile on the duct was not reported.) In the present flow, $g/R_P=0.015$. Note that the circulation of the primary vortex is about 30% to 40% of the bound circulation near the tip. This compares to a value of approximately 40% measured in [6] for a flow of the same ratio of gap thickness to maximum blade thickness. Gopalan et al. [11] examined the strength of a leakage vortex forming at the tip of a stationary hydrofoil, for g/t 0.12, 0.28, and 0.52 (representing 22%, 52%, and 96% of the inlet boundary layer thickness). In these observations, however, the circulation of the leakage vortex was observed to decrease with increasing gap thickness. The reported lift coefficient near the tip was 0.48, implying a bound circulation of $\Gamma/U_\infty c\approx\frac{1}{2}C_L=0.24$. The average instantaneous shed circulation of the primary vortex was $\Gamma/U_\infty c=0.076$, 0.061, and 0.046, or approximately 32%, 25%, and 19% of the bound vorticity near the tip.

The average core radius of the primary vortex is plotted in Fig. 10. There are discernable differences between the radii measured downstream of the large and small rotors, with the normalized core radius downstream of the large rotor tips approximately 20% larger than those from the smaller rotor. Considering each rotor separately, increases in Reynolds number lead to a decrease in average core size, although the dependence is not strong. Again, the case of $\mathrm{Re}=4.6\times10^6$ (250 rpm on the large rotor) is anomalous, with the trend in core size with s/c opposite to the trends identified for all the other conditions. The core radius of the strongest (primary) vortex is comparable to the normalized tip clearance, $g/R_P=0.015$ ($g/t=0.17$). Reynolds number scaling of the free tip vortices often follows the analysis of McCormick [12], where the core size is related to the boundary layer thickness at the pressure side of the lifting surface. Chesnakas and Jessup [7] report the blade wake displacement thickness, δ_1/R_P, at $r/R_P=0.99$ to be 0.0121 for $\mathrm{Re}=1.4\times10^6$ and 2.8×10^6, and 0.0073 for $\mathrm{Re}=4.3\times10^6$ for the small rotor, and 0.0070 at $\mathrm{Re}=9.2\times10^6$ for the large rotor. The variation of the wake thickness with Reynolds number (a reduction of about 60%) is not paralleled by equivalent changes in the core radius of the primary vortex (a reduction of approximately 6%) for the small rotor. The general differences in the average core size between the large and small rotors may have resulted from the differences of the shroud inlet boundary layer, as discussed in Sec. 4. Farrell and Billet [6] examined the relationship between the core size identified in the average flow field as a function of tip clearance. They found that the core radius, a/t, was much larger than the gap clearance, g/t, for cases of smaller gap clearances, even after correction for vortex wandering was applied. This was surprising, since it is expected that the vortex core size should scale with the clearance. Here, the variation in the core radii identified on the individual images does not vary widely with Reynolds number and is on the order of twice the gap clearance. Several gap sizes need to be examined before any conclusion can be drawn on the dependence

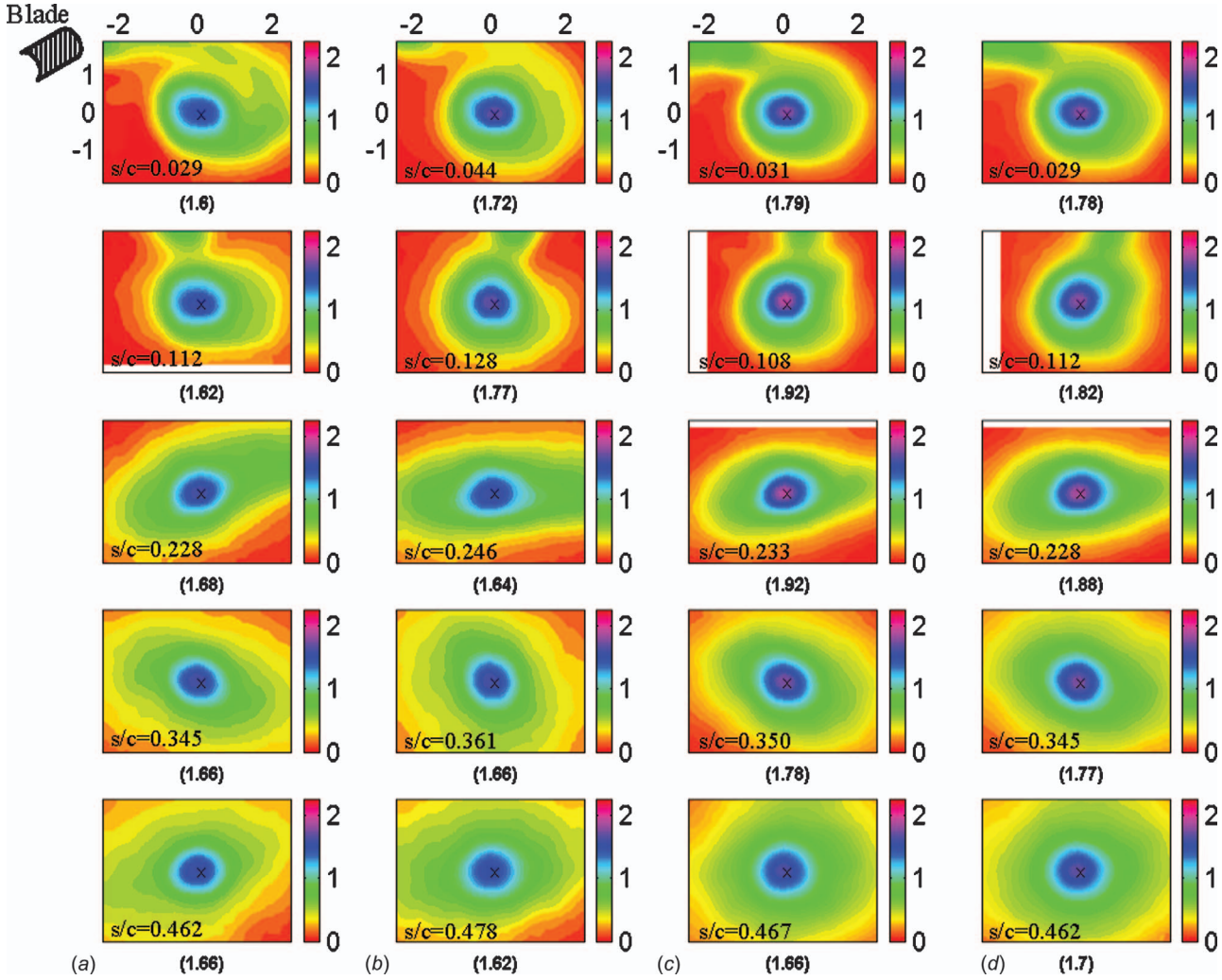

Fig. 18 Scaled and shifted average vorticity ω contours, at various downstream locations, s/c, for the small rotor running at: (*a*) 300 rpm, and (*b*) 1800 rpm; and for the large rotor running at: (*c*) 313 rpm, and (*d*) 500 rpm. The value of the vorticity contour at the center of the primary vortex marked by an (×) is noted below each frame. The tip location of the blade trailing edge is depicted in the first frame. The shroud is towards the top of the image. Refer to Fig. 5 for explanation of the coordinate system.

of the core size on the gap size. The core radii reported by Gopalan et al. [11] are on the order of $a/c=0.006\pm0.001$ ($a/t=0.06\pm0.01$) (where $c=0.050$ m was the foil chord, which was also equal to the span, and $t=0.005$ m was maximum thickness at the tip). While the resolution of these measurements is limited, the normalized core radii are smaller than those reported here, and are observed to be approximately constant with varying gap size. In the present study, the average values of a_1/t vary from 0.12 to 0.16.

Figure 11 shows the evolution of the pressure coefficient, $C_{P,1}=\Delta P_1/\frac{1}{2}\rho U_\infty^2$, of the primary vortex with downstream location. The pressure is computed using Eq. (5). The derivation does not take into account that there may be an out-of-plane axial velocity in the vortex core. Depending on whether this axial flow is of jet or wake profile, an additional pressure difference must be added to (or subtracted from) Eq. (5). This velocity component is not provided by the planar PIV measurements. While the true pressure in the location of the vortex cores is affected by the presence of the surrounding vortices and the three dimensionality of the flow, the pressure computed here scales the pressure depression due to the local concentration of vorticity. The lowest pressure reduction in the primary vortex core occurs for $0.05<s/c<0.15$. The pressure inside the core begins to increase after this downstream location. The inferred pressure coefficients are lower in general for the larger rotor, and the trend with Reynolds number is weak.

8 Variability of Instantaneous Tip-Leakage Flow Field

Significant variability exists between different instantaneous realizations of the flow. Figures 12–14, present histograms of the quantities $\Gamma_{O,1}/U_\infty R_P$, a_1/R_P, and $C_{P,1}$ all for the strongest identified vortex at various downstream locations from the blade trailing edge. Also plotted are vertical lines delineating the average of the quantity identified in each subplot. The peak values are almost twice the average values for most distributions, and the shapes of the distributions are only qualitatively similar to a normal distribution about a mean value. The typical standard deviation is between 27% and 50% of the mean value for $\Gamma_{O,1}/U_\infty R_P$, between 17% and 25% for a_1/R_P, and between 28% and 54% for $C_{P,1}$. These values are slightly higher than the standard deviations of 15% to 25% of the mean vortex strength reported in [11]. The distributions for each rotor are comparable, but there are some differences between the histograms when comparing between the two rotors, especially for the histograms of $\Gamma_{O,1}/U_\infty R_P$. There is a discernable correlation between the vortex strength and core size,

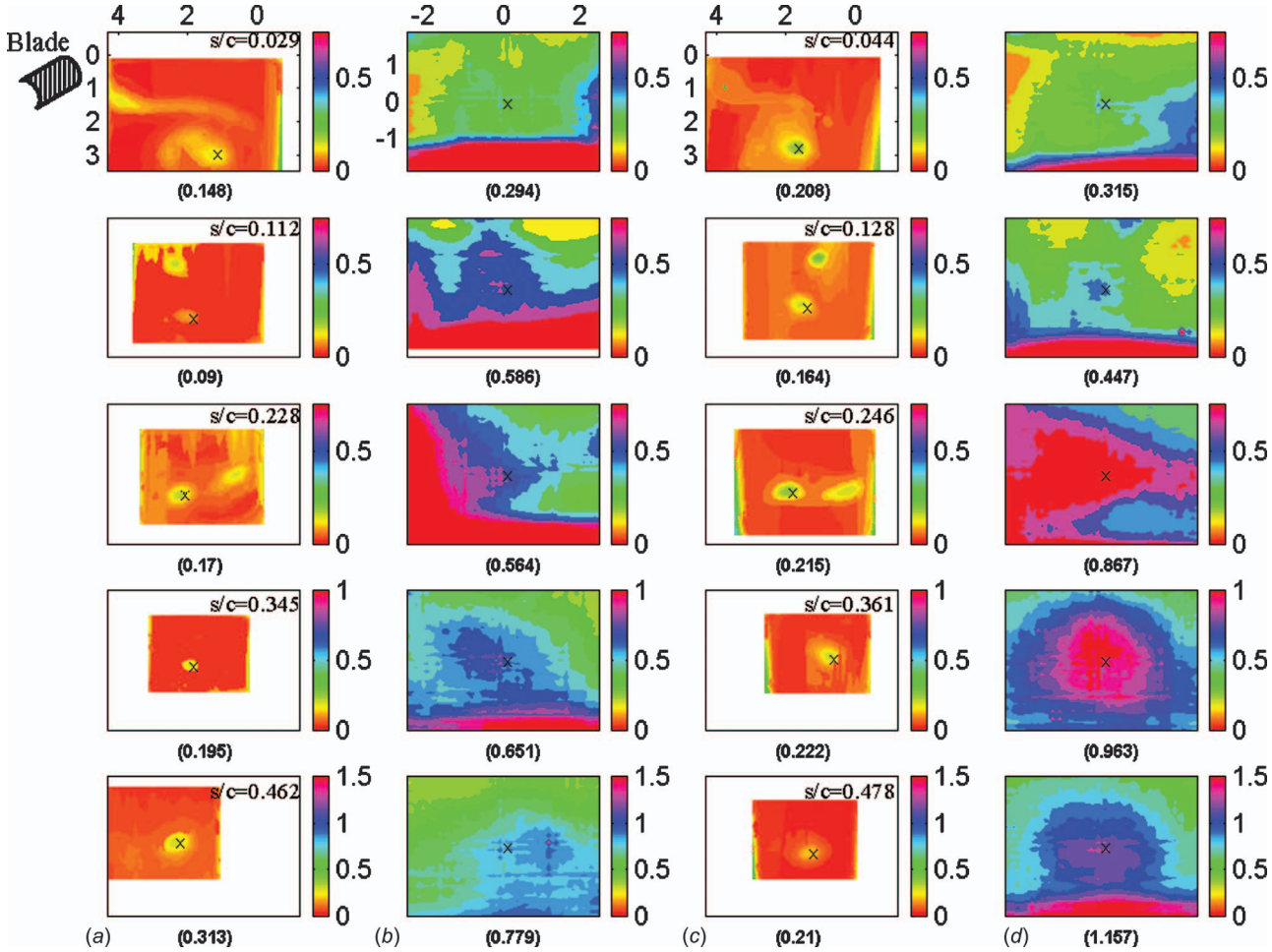

Fig. 19 Velocity fluctuations $\overline{u'^2}+\overline{v'^2}$ for the small rotor as a function of downstream location, *s*/*c*. Shown in (*a*) are the directly computed fluctuations, and in (*b*) the corresponding fluctuations after scaling and shifting of the instantaneous fields for the propeller speed of 300 rpm. Plotted in (*c*) are the directly computed fluctuations, and in (*d*) the corresponding fluctuations after scaling and shifting, for the propeller speed of 1800 rpm. The value of the contour at the center of the primary vortex marked by an (×) is noted below each frame. The tip location of the blade trailing edge is depicted in the first frame. The shroud is towards the top of the image. Refer to Fig. 5 for explanation of the coordinate system.

as indicted in Fig. 15. This suggests that the maximum tangential velocity of the vortices is relatively constant for a given rotation rate of the rotor.

Figures 16 and 17 plot the positions of the identified primary and secondary vortices. All of the primary vortices have the same direction of rotation, while a fraction of the secondary vortices are counterrotating with respect to the primary vortex. In the case of the small rotor, the primary vortex is sometimes identified in the wake spiral rather than in the position of the tip-leakage vortex. This illustrates that the strength of the strongest secondary vortex often approaches that of the primary vortex. This is much less common for the large rotor. The loci of the secondary vortices' positions near the trailing edge map out the wake spiral, and the region of highest vortex probability near the rotor trailing edge. The patterns are qualitatively similar between the small and large rotors. However, the secondary vortices in the wake spiral of the large rotor are somewhat more spatially correlated with the primary vortex, as evidenced by the stronger clustering of the secondary vortices.

The axis of the primary vortex is observed to wander in a cluster around the mean position. The amplitude of the wandering increases with increasing s/c. The standard deviation of the distance of the vortex center from the mean location, κ, varies from $\kappa/a=97\%$ near the trailing edge of the small rotor to 112% at the farthest downstream location. For the large rotor, $\kappa/a=57\%$ near the trailing edge and 106% farthest downstream location. These values are significantly lower than the approximate value of $\kappa/a > 3$ measured in [11].

9 Direct and Scaled Velocity Fluctuations

The average flow fields were calculated and properly subtracted from the mean squared instantaneous fields to compute velocity fluctuations. The PIV velocity measurements in this study resolved on the order of ten velocity measurements across the diameter of the primary vortex, and these measurements were, inherently, spatially averaged with the overlap of the PIV interrogation windows. Consequently, we do not expect to resolve the smallest scales of velocity fluctuations in the vortical flow. In order to understand the effect of vortex wandering, variable vortex strength, and the presence of multiple vortices, the individual flow fields can be shifted and scaled to reduce these effects, as discussed in Oweis and Ceccio [10]. The effect of primary vortex wandering can be reduced by the in-plane shifting of the individual flow fields such that the axes of the primary vortices are aligned before the averaging and computing of the velocity fluctuations is done. However, the spatial shifting of the individual images does not account for the variability of the strength and core size of the individual primary vortices. This effect can be

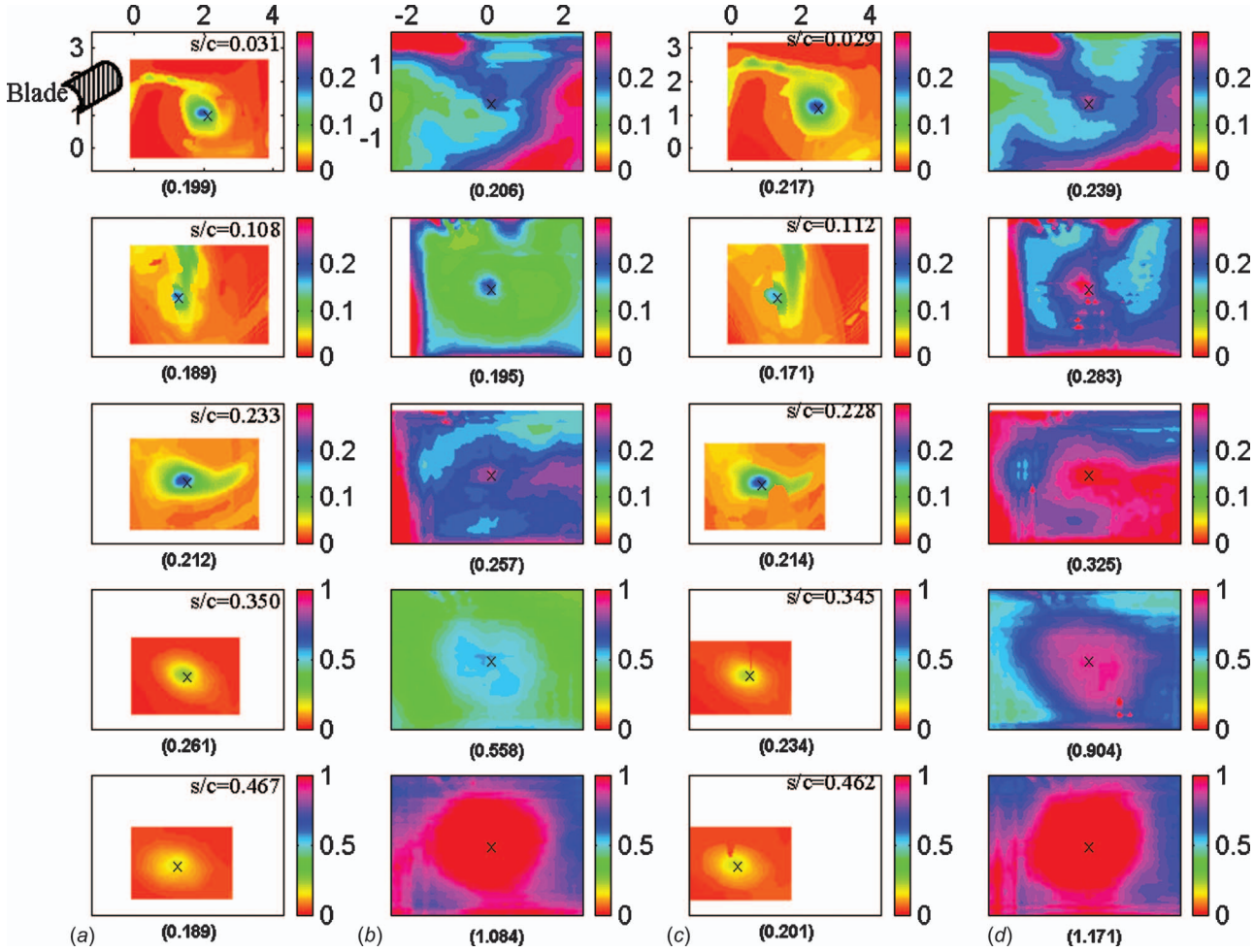

Fig. 20 Velocity fluctuations $\overline{u'^2}+\overline{v'^2}$ for the large rotor as a function of downstream location, *s*/*c*. Shown in (*a*) are the directly computed fluctuations, and in (*b*) the corresponding fluctuations after scaling and shifting of the instantaneous fields for the propeller speed of 313 rpm. Plotted in (*c*) are the directly computed fluctuations, and in (*d*) the corresponding fluctuations after scaling and shifting, for the propeller speed of 500 rpm. The value at the center of the primary vortex marked by an (×) is noted below each frame. The tip location of the blade trailing edge is depicted in the first frame. The shroud is towards the top of the image. Refer to Fig. 5 for explanation of the coordinate system.

reduced by scaling each individual flow field with the identified core size and circulation, a_1 and $\Gamma_{O,1}$, derived from each individual realization.

Figure 18 shows the averaged vorticity fields after shifting and internally scaling each image for the four conditions of Fig. 6. The vorticity is scaled by $\omega_C=\eta_2\Gamma_{O,1}/\pi a_1^2$ and is plotted in the normalized spatial coordinates $[(x/a_1),(y/a_1)]$. Comparison with Fig. 6 indicates that the positions of the strongest secondary vortices are not spatially correlated with the center of the primary vortex. The cores of the averaged field vortices shown in Fig. 6 are ellipsoidal, suggesting that the tip vortex is undergoing anisotropic wandering, as discussed in [10].

Figures 19 and 20 show the velocity fluctuations $(\overline{u'^2}+\overline{v'^2})/U_{C,1}^2$ computed directly, and also after scaling and shifting for the small and large rotors. The velocity fluctuations are normalized by $U_{C,1}=\eta_2\overline{\Gamma}_{O,1}/(2\pi\overline{a}_1)$, the maximum tangential velocity of the primary vortex based on the circulation and core size derived from the averaged flow field. Large velocity fluctuations are seen near the cores of the un-scaled vortices, with magnitudes of ~0.2. The velocity fields were shifted and normalized, and the velocity fluctuations were computed and normalized with $\eta_2\overline{\Gamma}_{O,1}/(2\pi\overline{a}_1)=0.114$. The resulting fluctuations $((ua_1/\eta_2\Gamma_{O,1})')^2+((va_1/\eta_2\Gamma_{O,1})')^2$ are plotted in the normalized spatial coordinates $[(x/a_1),(y/a_1)]$. The residual fluctuations near the primary vortex axis increase with s/c, and the largest increase occurs farthest downstream. The process of shifting and scaling has revealed how the presence of the uncorrelated secondary vortices can lead to relatively large velocity variability. This phenomenon becomes more pronounced as the Reynolds number for each rotor increases. It is interesting to note that the scaled variability increases with increasing downstream distance from the point of maximum average vortex strength.

10 Conclusions

The data presented above indicate that the strength and core size of the vortices are weakly dependent on Reynolds number, but are affected by variation in the inflowing duct boundary layer. This conclusion should be viewed in light of the differences between the two rotors' inlet boundary layers. The total circulation identified in the wake of the tip region is approximately 40% of the bound circulation near the tip, but the circulation of the largest vortex associated with the tip-leakage flow is about 1/3 of the total. Distinct vortices can be identified as far as $s/c=0.7$. The core sizes of the tip-leakage vortices do not vary strongly with varying boundary layer thickness on the blades or the duct.

There is significant variability between instantaneous flow real-

izations for all Reynolds numbers and rotor configurations. Scaled velocity fluctuations near the axis of the primary vortex show significant increase with downstream distance—suggesting the presence of spatially uncorrelated secondary vortices and the possible existence of three-dimensional vortex-vortex interactions. These changes in relative flow variability are not apparent in the un-scaled average flow fields. It is only after shifting and scaling that these flow features become apparent.

The overall picture from the instantaneous flow fields indicates that the tip-leakage vortex does not smoothly or completely merge with the co-rotating secondary vortices. Instead, a series of distinct vortices orbit and rearrange their spatial positions with increasing s/c. It is possible that complex vortex interactions are taking place between the primary and secondary vortices. Such three-dimensional vortex interactions have been observed in previous studies. For instance, Chen et al. [13] have investigated how two co-rotating vortices of dissimilar circulations merged into a single structure after a three-dimensional, unsteady merger process characterized by the production of orbiting vorticity filaments. Ortega et al. [14] have also shown how two counterrotating vortices of unequal strength can be unstable and can result in the wrapping of the weaker vortex around the stronger one. The onset of this wrapping can occur relatively far downstream of the position of the vortices' formation. The unsteadiness of the flow significantly increases. The significant increase in unsteadiness downstream near $s/c \approx 0.46$ (Figs. 19 and 20) may therefore result from such complex vortex-vortex interactions. Resolution of such a complex flow is not possible with the current planar PIV system.

Acknowledgment

This work was performed under the joint sponsorship of the NAVSEA 93R propulsor program and the Office of Naval Research 6.2 propulsor program. Support for the University of Michigan was under ONR Grant No. N00014-99-1-0307, Dr. Ki-Han Kim technical monitor.

References

[1] Oweis, G. F., van der Hout, I. E., Iyer, C., Tryggvason, G., and Ceccio, S. L., 2005, "Capture and Inception of Bubbles Near Line Vortices," Phys. Fluids, **17**(2), p. 022105.
[2] Green, S. L., 1995, *Fluid Vortices*, Kluwer, Dordrecht, Netherlands.
[3] Spalart, P. R., 1998, "Airplane Trailing Vortices," Annu. Rev. Fluid Mech., **30**, pp. 107–138.
[4] Lakshminarayana, B., 1996, *Fluid Dynamics and Heat Transfer of Turbomachinery*, Wiley, New York.
[5] Von Karman Institute for Fluid Dynamics, 1997, "Lecture Series Von Karman Institute for Fluid Dynamics," Vol. **1**, Rhode Saint Genèse, Belgium.
[6] Farrell, K. J., and Billet, M. L., 1994, "A Correlation of Leakage Vortex Cavitation in Axial-Flow Pumps," ASME J. Fluids Eng., **116**, pp. 551–557.
[7] Chesnakas, C., and Jessup, S., 2003, "Tip Vortex Induced Cavitation on a Ducted Propulsor," *Proc. 4th ASME-JSME Joint Fluids Engineering Conference*, Paper No. FEDSM2003-45320, Honolulu, Hawaii.
[8] Raffel, M., Willert, C., and Kompenhans, J., 1998, *Particle Image Velocimetry. A Practical Guide*, Springer, Berlin.
[9] Oweis, G. F., Choi, J., and Ceccio, S. L., 2004, "Dynamics and Noise Emissions of Laser Induced Bubbles in a Vortical Flow Field," J. Acoust. Soc. Am., **115**(3), pp. 1049–1058.
[10] Oweis, G. F., and Ceccio, S. L., 2005, "Instantaneous and Time Averaged Flow Fields of Multiple Vortices in the Tip Region of a Ducted Propulsor," Exp. Fluids, **38**(5), pp. 615–636.
[11] Gopalan, S., Katz, J., and Liu, H. L., 2002, "EFfect of Gap Size on Tip Leakage Cavitation Inception, Associated Noise, and Flow Structure," ASME J. Fluids Eng., **124**(4), pp. 994–1004.
[12] McCormick, B. W., 1962, "On Cavitation Produced by a Vortex Trailing From a Lifting Surface," ASME J. Basic Eng., **84**(3), pp. 369–379.
[13] Chen, A. L., Jacob, J. D., and Savaş, Ö, 1999, "Dynamics of Co-rotating Vortex Pairs in the Wakes of Flapped Airfoils," J. Fluid Mech., **382**, pp. 155–193.
[14] Ortega, J. M., Bristol, R. L., and Savaş, Ö, 2003, "Experimental Study of the Instability of Unequal-strength Counter-rotating Vortex Pairs," J. Fluid Mech., **474**, pp. 35–84.

Development of a Tip-Leakage Flow—Part 2: Comparison Between the Ducted and Un-ducted Rotor

Ghanem F. Oweis[1]
Department of Mechanical Engineering,
University of Michigan,
Ann Arbor, MI 48109-2121

David Fry

Chris J. Chesnakas

Stuart D. Jessup

Naval Surface Warfare Center,
Carderock Division, Code 5400,
9500 MacArthur Blvd.,
West Bethesda, MD 20817-5700

Steven L. Ceccio
Department of Mechanical Engineering,
University of Michigan,
Ann Arbor, MI 48109-2121
e-mail: ceccio@engin.umich.edu

The vortical flow in the tip region of a three-bladed rotor was examined using particle imaging velocimetry (PIV). The vortex forming at the tip of the un-ducted propeller was compared to the tip-leakage vortex of the ducted rotor. The planar flow fields were used to identify regions of concentrated vorticity and determine instantaneous vortex properties, revealing the presence of a primary tip-leakage vortex surrounded by a number of secondary vortices. Comparison between the ducted and un-ducted rotor indicated that the presence of the duct reduced the relative strength of the primary tip vortex, making its strength a smaller fraction of the overall shed circulation near the tip. The weaker tip-leakage vortex then became closer in strength to the other secondary vortices in the tip-flow region. However, for the rotor tip geometry considered here, the radius of the primary vortex core did not vary substantially between the ducted and un-ducted cases. The variability of the flow was larger for the ducted case, in terms of the primary vortex position, its identified circulation, core size, and inferred core pressure. This variability was also observed in the scaled velocity fluctuations near the core of the vortex.
[DOI: 10.1115/1.2201619]

1 Introduction

Researchers have extensively examined the formation of tip vortices on open propulsors, often with the aim of understanding the inception of tip-vortex cavitation. See Green [1], Spalart [2], and Arndt [3], for recent reviews. In Oweis et al. [4] hereafter referred to as Part 1, laser Doppler velocimetry (LDV) and particle imaging velocimetry (PIV) were employed to examine the formation of a tip-leakage vortex on two geometrically similar but different diameter ducted rotors. The system of vortices formed near the blade tip-gap region was examined as the flow developed downstream of the blade trailing edge. PIV was used to identify the instantaneous vortices properties in the flow field. Significant variability was observed in the identified flow quantities including the positions of the vortices, their strengths, core sizes, and inferred vortex core pressures.

Reported here are the results of a companion study. The influence of the duct on the tip-vortex formation was explored by comparing the vortical flow with and without the presence of the duct. The geometry of the rotor blades was not varied between the ducted and un-ducted experiments. While the un-ducted blade-tip geometry typically would not be found in practical implementation of an open propeller, it is instructive to examine the differences between the two flows. In both the ducted and un-ducted tip flows the pressure difference across the blade tip is believed to drive the leakage flow from the pressure side to the suction side. It is also believed that the presence of the duct modifies the blade loading distribution and, consequently, the tip-leakage flow. It is generally expected that leakage flows in ducted propellers would follow similar prediction rules used for unducted propellers after correcting for the clearance gap size [5].

2 Experimental Setup

The experiments were performed in the David Taylor 36 in. variable pressure cavitation tunnel using the test setup described in Part 1. In the present study, the rotor designated 5407 was employed. The rotor had a hub diameter of 0.1261 m (4.964 in.), and a tip diameter of 0.3048 m (12.000 in.). Detailed geometry of the rotor is provided in Part 1.

In one set of experiments, a duct was placed around the rotor. The duct had an inside diameter of 0.3096 m (12.188 in.) an outer diameter of 0.3352 m (13.215 in.), and a linear extent of 0.6985 m (27.5 in.). The rotor tip diameter was 0.3048 m (12.00 in.). A bell mouth was installed on the inlet of the duct with a 0.076 m (3.00 in.) radius on the inner and outer walls. A window was inserted into the duct to allow for optical access for LDV and PIV measurements, as described in Part 1. The ratio of the tip clearance to the maximum thickness at the tip, g/t was 0.17. Lastly the duct was removed to examine the flow of the open propeller. Figure 1 shows schematic diagrams of the two configurations. Three component LDV and planar PIV were used to characterize the flow in the wake of the rotors. Description of the test setups, data processing, and measurement uncertainties are provided in Part 1.

For both the ducted and un-ducted configurations, the rotor was operated at a constant advance coefficient $J=0.971$, where $J=U_\infty/nD$, U_∞ is the average flow speed into the rotor, n is the rotational speed of the rotor, and $D=2\times R_P$ is the rotor diameter. This was higher than the design advance coefficient $J=0.75$ in order to avoid the formation of the leakage vortex at the leading edge of the blade and the occurrence of pressure side leading edge cavitation near the blade tip in the ducted configuration. Several rotational speeds were examined for both rotors. The blade-tip Reynolds number was based on the chord, c, and the total tip speed, $(U_\infty+\pi Dn)$. The water kinematic viscosity was evaluated at the average flow temperature. The inlet absolute static pressure was maintained high enough during the PIV measurements to suppress cavitation. The advance coefficient resulted in a thrust coefficient $K_T=T/\rho n^2D^4$ and a torque coefficient $K_Q=Q/\rho n^2D^5$. Ap-

[1]Current address: Mechanical Engineering Department, American University of Beirut, 3 Dag Hammarskjold Plz., New York, NY 10017.

Contributed by the Fluids Engineering Division of ASME for publication in the JOURNAL OF FLUIDS ENGINEERING. Manuscript received January 15, 2004; final manuscript received March 2, 2006. Review conducted by Joseph Katz.

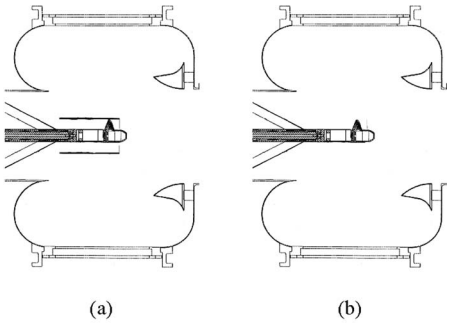

Fig. 1 Schematic diagram of the propeller setup in the open jet test section, showing the drive shaft and its supporting struts; (*a*) the ducted configuration, and (*b*) the un-ducted configuration

plication of roughness to the leading edge of the rotor blades did not significantly influence the measured results. Table 1 presents the conditions reported here for both rotor configurations.

The inlet axial velocity, U_x/U_∞, and tangential velocity, U_T, profiles were measured in the duct at a location $0.3615 \times R_P$ upstream of the blade tip for the ducted rotor. For both rotors the axial velocity was nearly constant from $0.5 \leqslant r/R_P \leqslant 0.9$. The wall boundary layer thickness on the duct upstream of the rotor was $\delta_1/R_P = 0.090$, making the gap about 1/6 times the inlet boundary layer thickness. The inlet flow profiles were presented in Part 1.

Table 1 Test conditions for the ducted and un-ducted rotor configurations

	U_∞ (m/s, (fps))	n (rpm)	K_T	$10 \times K_Q$
Ducted	1.5 (4.9)	300	0.176	0.49
	3.0 (9.8)	600	0.265	0.54
	6.0 (19.6)	1200	0.307	0.55
Open	1.5 (4.9)	300	0.143	0.34
	3.0 (9.8)	600	0.143	0.34
	6.0 (19.6)	1200	0.143	0.34

Table 2 Average correlation coefficients R_V^2 and R_ω^2 for the all measured conditions s/c

	n (rpm)	R_ω^2 %	R_V^2 %
Ducted	300	72±10	65±12
	600	75±10	70±12
	1200	75±9	68±9
Open	300	79±8	83±7
	600	78±9	80±9
	1200	85±5	76±8

3 Overall Development of the Vortical Flow in the Tip Region

The pressure difference across the blade produces a flow through the tip region and causes the formation of a strong tip-leakage vortex, which we will refer to as the primary vortex. A second co-rotating concentrated vortex forms at the trailing edge,

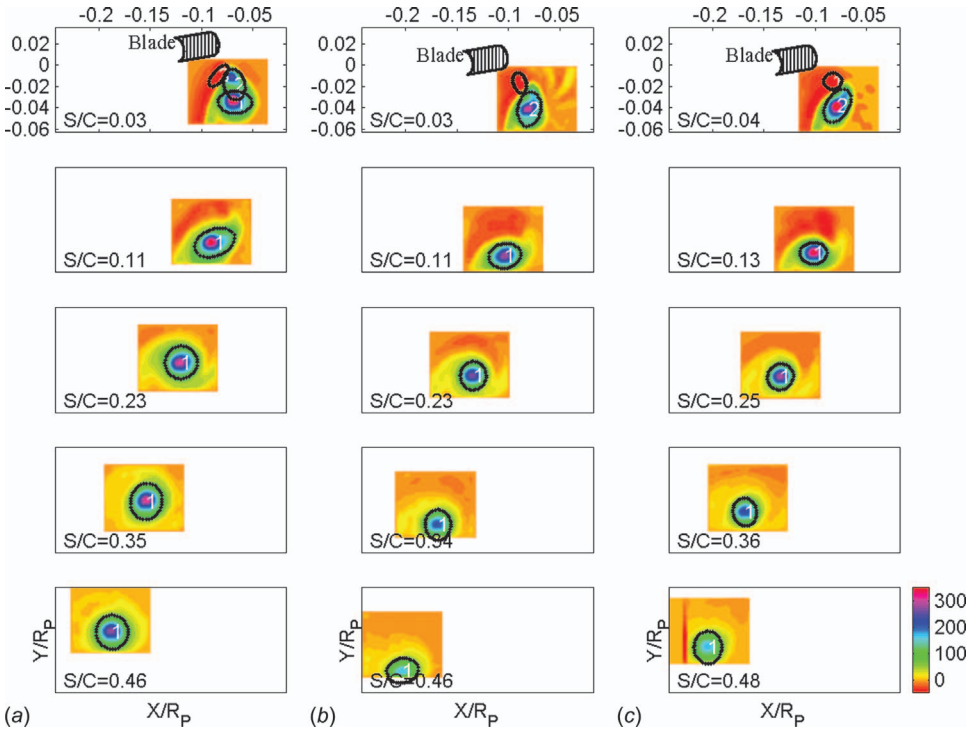

Fig. 2 Iso-vorticity contours of the mean flow field of the tip vortex on the un-ducted rotor as a function of the distance downstream from the blade trailing edge (TE), s/c. Shown are the fields for three propeller speeds (*a*) 300; (*b*) 600; and (*c*) 1200 rpm. The coordinates are normalized by the propeller radius, R_P, while vorticity is normalized by (U_∞/R_P).

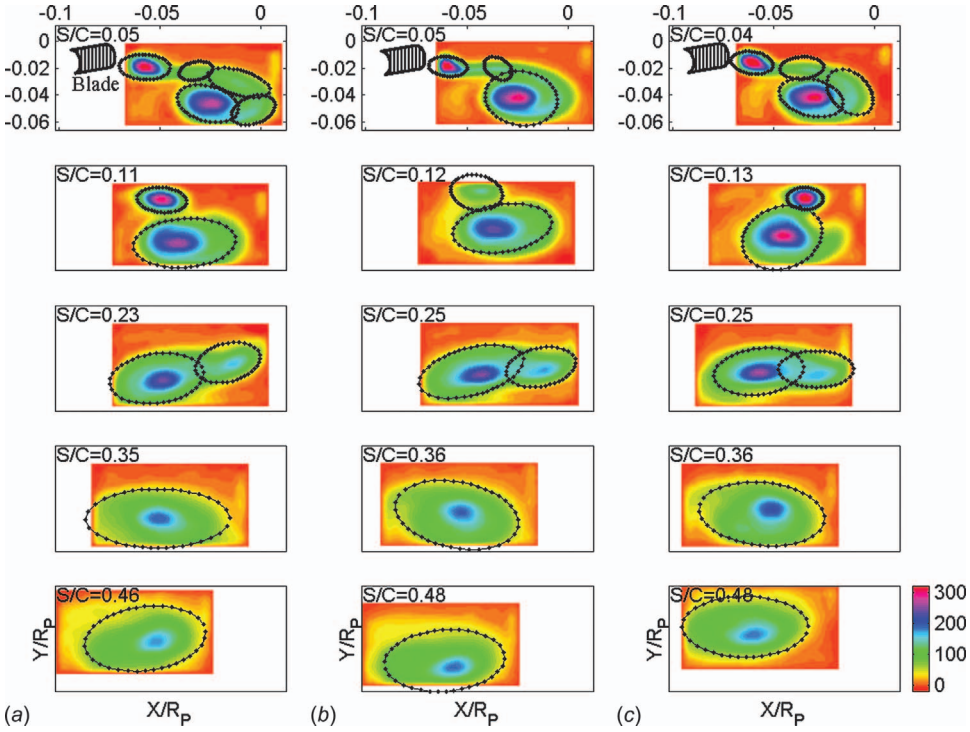

Fig. 3 Iso-vorticity contours of the mean flow field of the tip vortex on the ducted rotor as a function of the distance downstream from the blade TE, *s/c*. Shown are the fields for three propeller speeds (*a*) 300; (*b*) 600; and (*c*) 1200 rpm. The axes coordinates are normalized by R_P, while vorticity is normalized by (U_∞/R_P).

and we will refer to this as the secondary vortex. Additionally, multiple secondary co-rotating vortices of comparable or weaker strength, and counterrotating secondary vortices are also present. At increasing downstream distances from the blade trailing edge, these vortices begin an orbiting and merger process. The coordinate system used in these measurements is s/c, where s is the circular arc length traced by the tip of the blade's trailing edge. The value of s is zero when the trailing edge tip intersects the light sheet, and increases as the vortex leaves the blade (s increases with vortex "age").

The identification procedure described in Part 1 is used here to find and fit Gaussian vortices to the regions of concentrated vorticity in each instantaneous PIV flow field. Once the strengths and core sizes of the vortices are identified in a given flow field, the vorticity and velocity fields are then reconstructed and compared with the original measured fields at each downstream location. A regression value for the velocity field, R_V^2, and for the vorticity field, R_ω^2, are computed for each PIV image. A value of unity corresponds to an exact match between the reconstructed and original fields. Table 2 presents the average values of R_V^2 and R_ω^2 for the data presented here. The values are averaged over all realizations and over the various downstream locations, s/c.

4 Averaged Tip-Leakage Flow Field

Between 505 and 550 PIV images were collected at each downstream position s/c. Figures 2 and 3 show the average vorticity fields of the un-ducted and ducted configurations with increasing downstream distance from the blade trailing edge s/c. Note that the values of s/c chosen are closely similar but not identical for the five cases shown. The closed contours are the outlines of the primary and secondary identified vortices. The number and average contours of the identified vortices vary considerably between the ducted and un-ducted cases. The vortices of the open rotor appear to roll up rapidly into a single, concentrated vortex with a nearly circular core. Spiraling arms of vorticity can be noticed around the core in a nearly symmetric fashion. However, multiple vortices persist longer in the case of the ducted propeller and the average vortex has a less symmetric, elliptical core.

Interpretation of the average flow field must be performed with care, since vortex variability and wandering will be significant. Moreover, at a given s/c location multiple secondary vortices identified in the individual flow fields vary their spatial locations relative to the primary vortex with various realizations. Figure 4 shows the average number of instantaneously identified vortices with increasing downstream distance, s/c. The vertical bars $+/-$ one standard deviation computed around the mean from all the instantaneous realizations at the specific s/c location. (Hence, in this figure and the ones that follow they are a measure of the *cyclic variability* of the flow field itself). The typical number of vortices is between 5 and 8, but averaging multiple images will smear out those vortices that are not approximately fixed in location. As a result, fewer vortices are discernable in the averaged flow field, with only one vortex identifiable farther downstream. For these reasons, the vortex identified in the average flow field is *not* equivalent to the typical vortex identified in the instantaneous

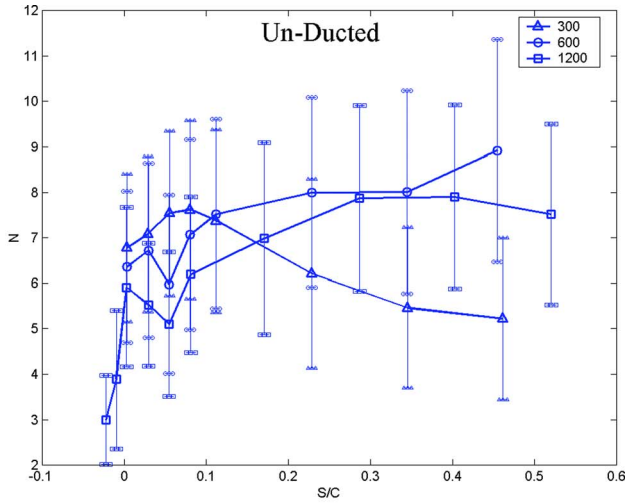

(a)

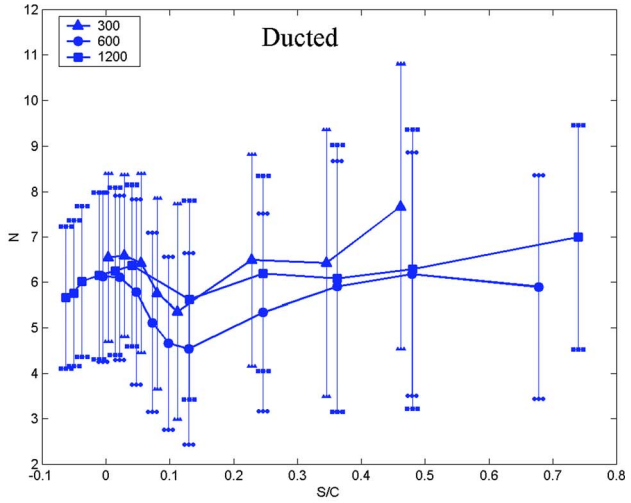

(b)

Fig. 4 Average number of identified vortices in the instantaneous flow field, *N*, for three different propeller speeds (300, 600, and 1200 rpm) for the un-ducted configuration (*a*); and for the ducted configuration (*b*). The vertical bars indicate ± one standard deviation about the mean.

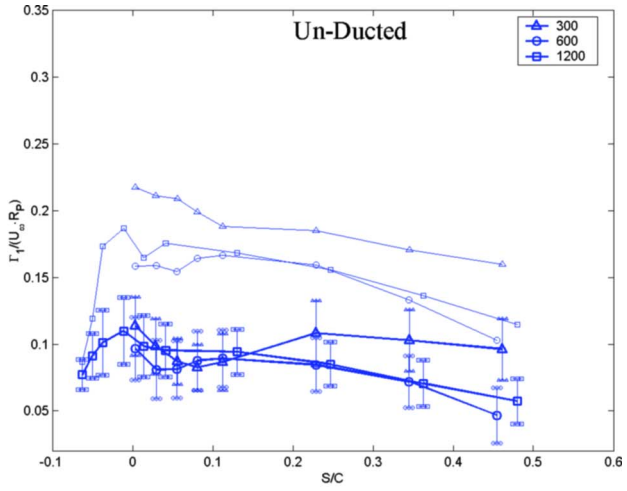

(a)

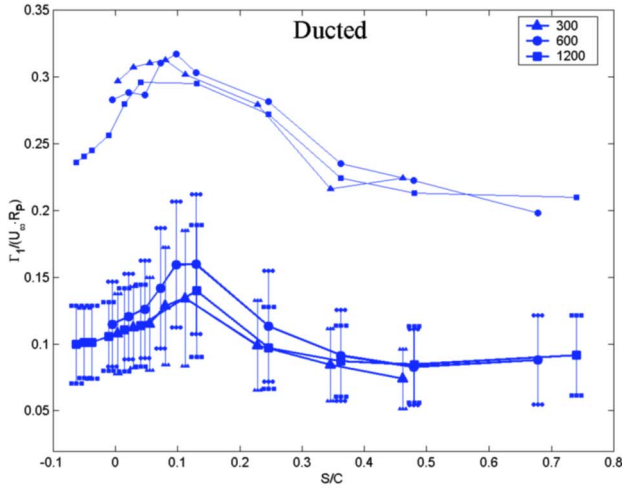

(b)

Fig. 5 Average circulation of the primary vortex, $\Gamma_{O,1}/(U_\infty R)$, (thick lines) and the summed circulation of all the vortices identified in the instantaneous flow field, $\Sigma_i\Gamma_{O,i}/(U_\infty R)$, (thin lines) for the same conditions of Fig. 4; (*a*) un-ducted configuration; (*b*) ducted configuration. The vertical bars indicate ± one standard deviation about the mean.

Table 3 Mean and standard deviations of the measured quantities for 1200 rpm for the open propeller (*a*), and the ducted propeller (*b*)

s/c	a_1/R_P	σ_{a_1/R_P}	$\Gamma_{O,1}/(U_\infty R_P)$	$\sigma_{\Gamma_{O,1}/(U_\infty R_P)}$	C_{P1}	$\sigma_{C_{P1}}$	$\Gamma_{O,2}/\Gamma_{O,1}$	$\sigma_{\Gamma_{O,2}/\Gamma_{O,1}}$	$\Sigma\Gamma_{O,I}/\Sigma\lvert\Gamma_{O,I}\rvert$
0.041	0.00984	0.00149	0.0953	0.0198	−4.13	0.82	0.24	0.28	60%
0.130	0.00995	0.00134	0.0942	0.0169	−3.97	0.76	0.17	0.26	64%
0.246	0.00991	0.00148	0.0851	0.0164	−3.27	0.68	0.20	0.23	69%
0.362	0.00978	0.00167	0.0706	0.0174	−2.31	0.63	0.32	0.25	74%
0.479	0.00957	0.00166	0.0573	0.0169	−1.61	0.57	0.41	0.28	79%

(a) Open rotor.

s/c	a_1/R_P	σ_{a_1/R_P}	$\Gamma_{O,1}/(U_\infty R_P)$	$\sigma_{\Gamma_{O,1}/(U_\infty R_P)}$	C_{P1}	$\sigma_{C_{P1}}$	$\Gamma_{O,2}/\Gamma_{O,1}$	$\sigma_{\Gamma_{O,2}/\Gamma_{O,1}}$	$\Sigma\Gamma_{O,I}/\Sigma\lvert\Gamma_{O,I}\rvert$
0.041	0.01101	0.00187	0.1138	0.0306	−4.67	1.22	0.58	0.17	99%
0.130	0.01283	0.00277	0.1397	0.0493	−5.10	1.68	0.51	0.19	99%
0.246	0.01147	0.00217	0.0970	0.0307	−3.18	1.11	0.70	0.20	99%
0.362	0.01103	0.00202	0.0870	0.0266	−2.80	1.03	0.61	0.25	99%
0.479	0.01111	0.00229	0.0845	0.0286	−2.59	1.00	0.60	0.25	99%

(b) Ducted rotor.

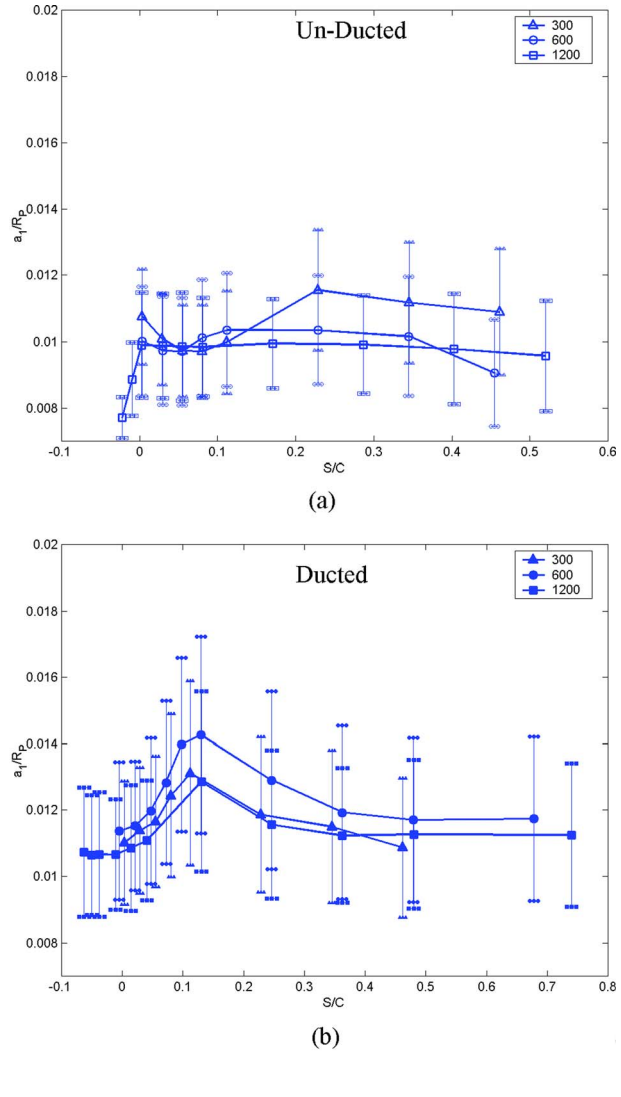

Fig. 6 Average radius of the primary vortex, a_1/R_P, for the conditions of Fig. 4

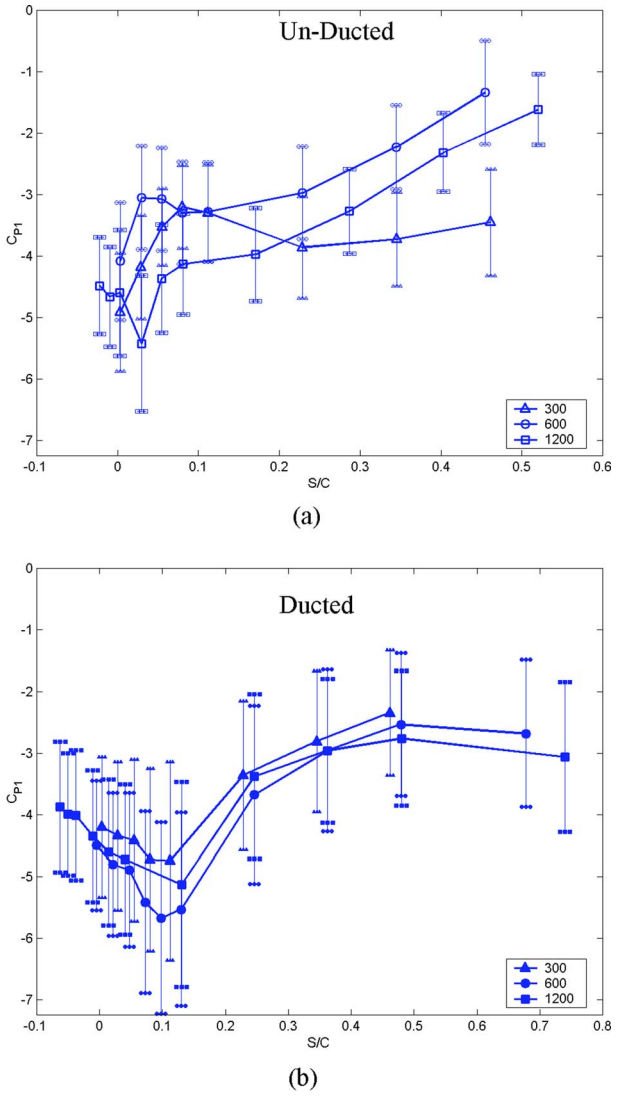

Fig. 7 Average pressure coefficient of the primary vortex, $C_{P,1}$, for the conditions of Fig. 4

flow fields. Oweis and Ceccio [6] provide an extended discussion of this issue. Consequently, we will present quantities identified from the instantaneous flow fields.

5 Properties of Instantaneous Tip-Leakage Flow Field

The average instantaneous circulation of the primary vortex (dashed line) and the total circulation of all vortices in the instantaneous field (solid line) are plotted for varying downstream distance in Fig. 5. The average values of $\Gamma_{O,1}/(U_\infty R)$ and $\Sigma_i \Gamma_{O,i}/(U_\infty R)$ lie in a band. Figure 5(*a*) shows the data for the un-ducted case. The circulation of the largest identified vortex represents approximately 2/3 of the sum of the identified circulation near the tip. This ratio is smaller for the case of the ducted rotor shown in Fig. 5(*b*). Here, the primary vortex represents less than 1/2 of the total identified circulation. Table 3 presents the mean and standard deviation of $\Gamma_{O,1}/U_\infty R_P$ for varying s/c. Note that the primary vortex of the un-ducted rotor typically has a circulation four times greater than the second largest vortex, while the ratio for the ducted rotor is less than two times. Also tabulated are the ratio of the strength of the strongest secondary vortex to that of the primary vortex, $\Gamma_{O,2}/\Gamma_{O,1}$, and the ratio $\Sigma\Gamma_{O,I}/\Sigma|\Gamma_{O,I}|$. If the identified circulation had the same rotational direction in the measurement plane, then $\Sigma\Gamma_{O,I}/\Sigma|\Gamma_{O,I}|=1$. If the circulation was evenly divided between co- and counterrotating flows, then $\Sigma\Gamma_{O,I}/\Sigma|\Gamma_{O,I}|=0$.

The identified core radius of the primary vortex, a_1/R_P, is plotted in Fig. 6 and tabulated in Table 3. The average core radius in the un-ducted propeller is about 10% smaller than in the ducted propeller. As discussed in Part 1, the core radius of the largest vortex in the ducted case is comparable to the normalized tip clearance, $g/R_P=0.015$ ($g/t=0.17$, where t is the maximum section thickness), and the core diameter is insensitive to variation in Reynolds number and the resulting variation in blade wake thickness. For the un-ducted case, the variation in the core size with Reynolds number is not strong, but the core size does decrease with increasing rotation speed (i.e., Reynolds number).

Figure 7 and Table 3 show the evolution of the pressure coefficient, $C_{P,1}=\Delta P_1/\frac{1}{2}\rho U_\infty^2$, of the primary vortex with downstream location. The pressure is computed using the relationship incorpo-

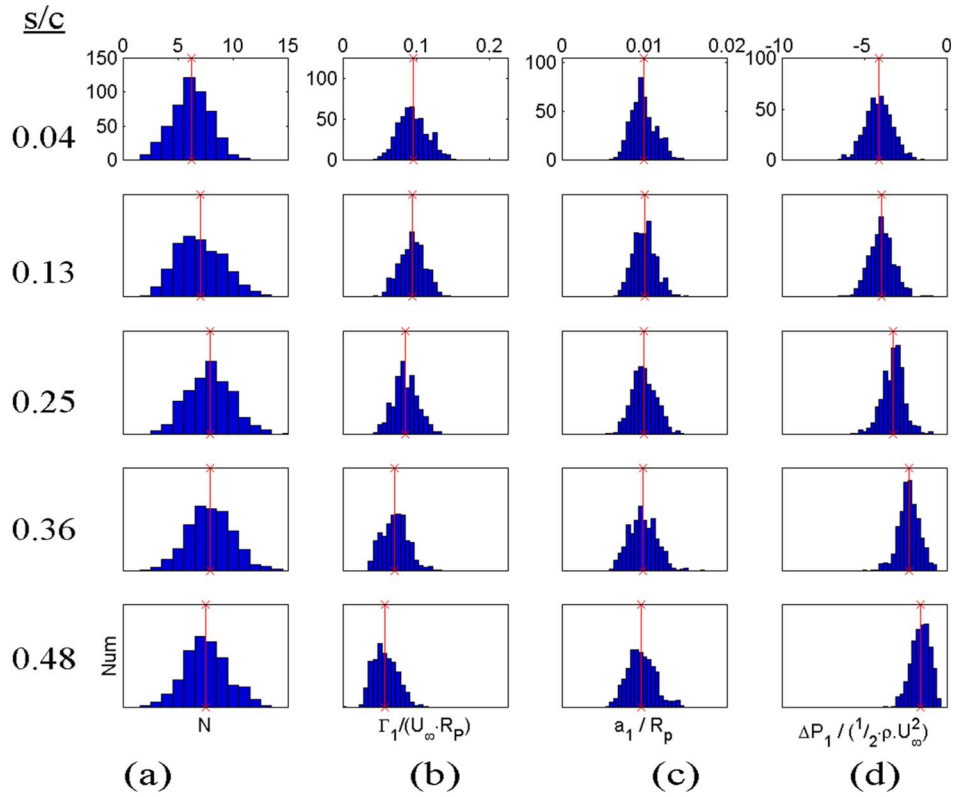

Fig. 8 Histograms of (*a*) the number of vortices identified in the instantaneous flow field, (*b*) the circulation of the primary vortex, (*c*) the core radius of primary vortex, and (*d*) the pressure coefficient of primary vortex for the open rotor operating at 1200 rpm

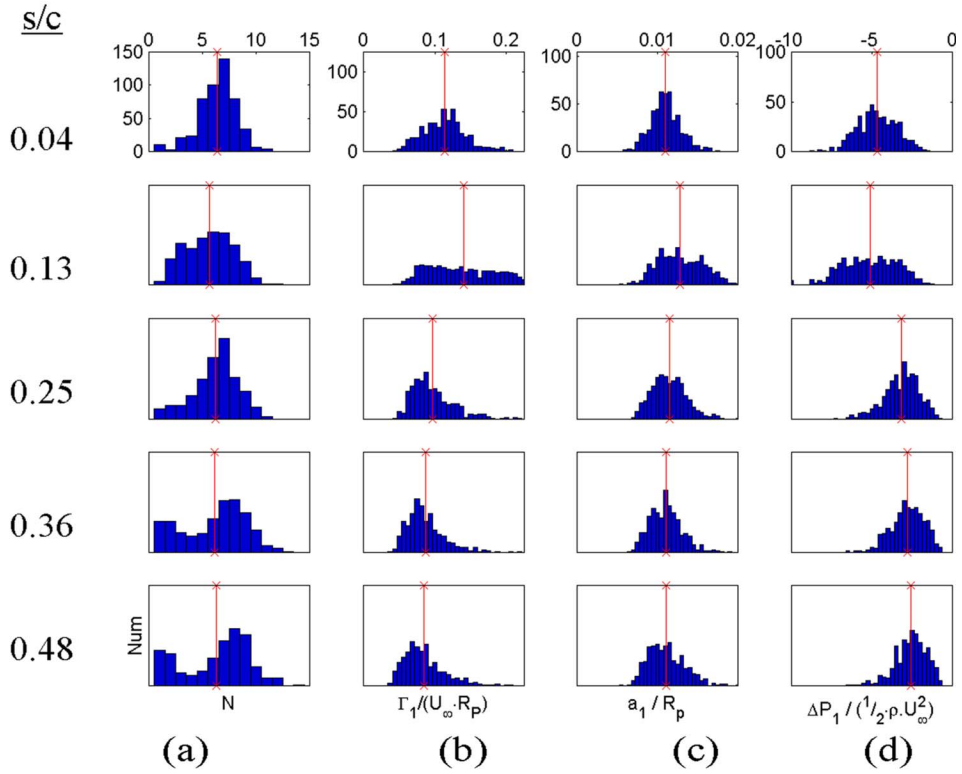

Fig. 9 Histograms of (*a*) the number of vortices identified in the instantaneous flow field, (*b*) the circulation of the primary vortex, (*c*) the core radius of primary vortex, and (*d*) the pressure coefficient of primary vortex for the ducted rotor operating at 1200 rpm

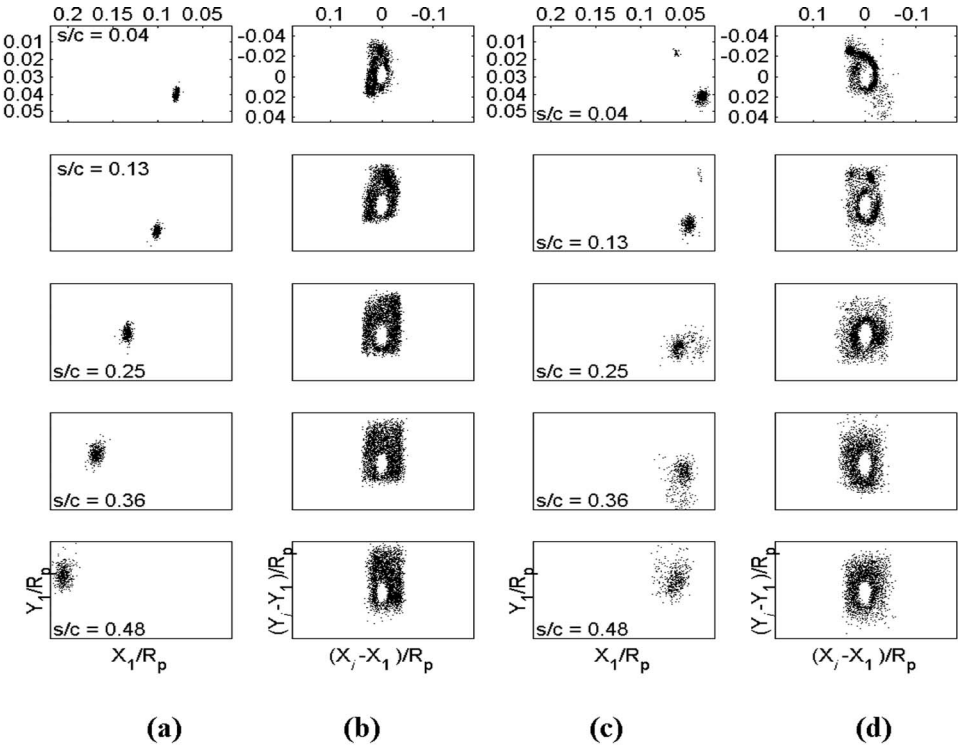

Fig. 10 Scatter plots of the instantaneous position of the primary vortex *(a), (c)* and the instantaneous positions of the secondary vortices *(b), (d)* relative to the instantaneous primary vortex with downstream location *s/c. (a), (b)* the open propeller; and *(c), (d)* the ducted propeller. The operating condition was 1200 rpm.

rating the vortex strength and core radius of a Gaussian vortex, as discussed in [7] and in Part 1. While the true pressure in the location of the vortex core is affected by the presence of the surrounding vortices and the three dimensionality of the flow, the pressure computed here scales the pressure depression due to the local concentration of vorticity. The minimum pressure coefficient achieved in the un-ducted case occurs near the trailing edge, $s/c \sim 0$, and increases thereafter. The 300 rpm case does not follow this trend, however, as the pressure coefficient remains relatively constant with increasing s/c. This is due in part to the increasing circulation for this case shown in Fig. 5(*a*).

6 Variability of Instantaneous Vortical Flow in Tip Region

Significant variability exists between different instantaneous realizations of the flow. Figures 8 and 9 present histograms of the quantities N, $\Gamma_{O,1}/U_\infty R_P$, a_1/R_P, and $C_{P,1}$ all for the strongest identified vortex for the 1200 rpm condition. The variability of the ducted case is larger than that of the open rotor. The distributions for the ducted case are wider, and this is also seen in the standard deviations tabulated in Table 3. In particular, the standard deviation of the inferred pressure coefficient of the ducted case is about twice that of the un-ducted case.

The position of the primary vortex, $[X_1, Y_1]$, and the positions of the secondary vortices relative to the primary vortex, $[X_i - Y_1, Y_i - Y_1]$, are shown in Fig. 10 for the case of 1200 rpm. There is increased variability in the primary vortex position with downstream distance, and this is stronger for the case of the ducted rotor. The secondary vortices are more spatially correlated for the open rotor at $s/c=0.04$, which results in clusters of the secondary vortices positions. The secondary vortices on the ducted rotor are somewhat less spatially correlated, resulting in a spiraling band of points at $s/c=0.04$. By s/c of 0.25, these correlated vortices appear to have rolled up close to the primary vortex. However, a significant amount of identified circulation remains distinct from the primary vortex, and this is consistent with the data in Fig. 5, where the circulation of the primary vortex does not grow significantly with downstream distance.

7 Direct and Scaled Velocity Fluctuation

The individual PIV images can be shifted and scaled to reduce the effects of vortex wandering and variability, as discussed in [6] and in Part 1. Figure 11 shows the averaged vorticity fields after shifting and internally scaling each image for the four conditions of Figs. 2(*c*) and 3(*c*). The vorticity is scaled by $\omega_C = \eta_2 \Gamma_{O,1}/\pi a_1^2$ and is plotted in the normalized spatial coordinates $[(x/a_1),(y/a_1)]$. Comparison with Fig. 2 indicates that the positions of the strongest secondary vortices are not spatially correlated with the center of the primary vortex.

Figure 12 shows the velocity fluctuations $(\overline{u'^2}+\overline{v'^2})/U_{C,1}^2$ computed directly and after scaling and shifting for the three conditions of Fig. 11. The velocity fluctuations are normalized by

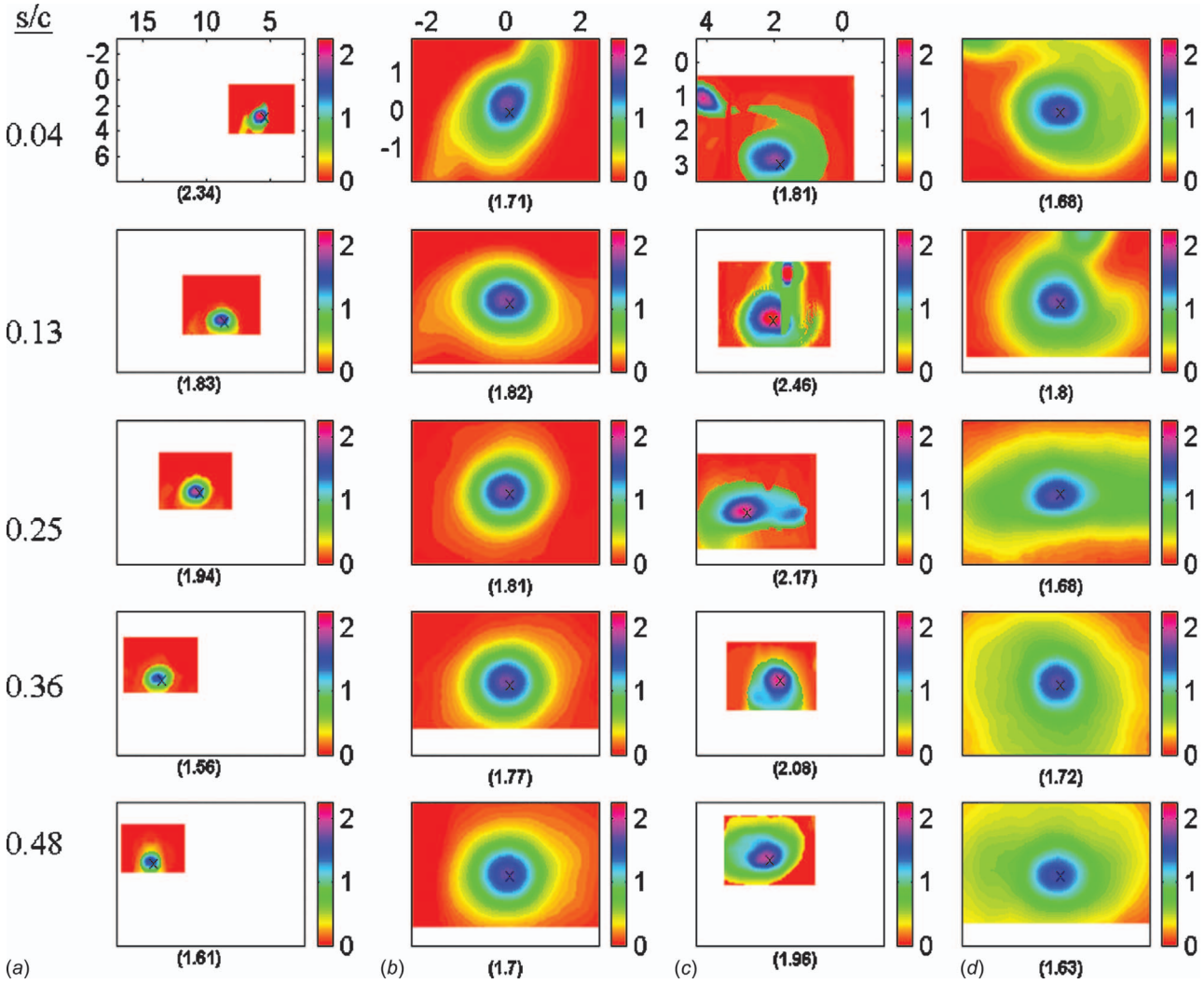

Fig. 11 Vorticity contours of the averaged tip vortex field for different downstream locations *s/c*: *(a), (c)* computed directly $\bar{\omega}/(2\overline{U_C}/\overline{a_1})$ and plotted in $[x/\bar{a}, y/\bar{a}]$ coordinates; in *(b), (d)*, the instantaneous fields were scaled and shifted prior to computing the average $\omega/(2U_C/a_1)$, and plotted in $[x/a_1, y/a_1]$. Contours in *(a), (b)* are from the open rotor, and *(c), (d)* are from the ducted rotor operating at 1200 rpm. The value of the contour at the vortex center (×) is noted below each frame.

$U_{C,1}=\eta_2\overline{\Gamma_{O,1}}/(2\pi\overline{a_1})$, where the maximum tangential velocity of the primary vortex based on the circulation and core size derived from the averaged flow field. The velocity fluctuations at the center of the average vortex for the un-ducted rotor are typically larger than in the case of the ducted rotor. The influence of vortex wandering and correlation on the velocity fluctuations can be significant, and the magnitudes of velocity fluctuations due to the wandering vortex are a strong function of the wandering amplitude compared to the instantaneous core radius. To reduce the effect of vortex wandering, the spatial measurement fields were shifted and normalized, and the velocity fluctuations were computed and normalized with $\eta_2\overline{\Gamma_{O,1}}/(2\pi\overline{a_1})=0.114$. The resulting fluctuations $((ua_1/\eta_2\Gamma_{O,1})')^2+((va_1/\eta_2\Gamma_{O,1})')^2$ are plotted in the normalized spatial coordinates $[(x/a_1),(y/a_1)]$. Interestingly, the *scaled* fluctuations of the ducted rotor are much greater, indicating that the ducted vortex has a larger wandering amplitude and less spatial correlation with the secondary vorticity.

8 Conclusions

Comparison between the ducted and un-ducted rotor cases indicates that the presence of the duct reduces the relative strength of the primary tip vortex, making its strength a smaller fraction of the overall shed circulation. The weaker tip-leakage vortex then becomes closer in strength to the other secondary vortices in the tip-flow region. However, for the rotor tip geometry considered here, the radius of the primary vortex core does not vary substantially between the ducted and un-ducted cases. The variability of the flow is larger for the ducted case, both in terms of the vortex positions and the identified circulation, core sizes, and inferred core pressures. This variability is also observed in the scaled velocity fluctuations near the core of the primary vortex.

Acknowledgment

This work was performed under the joint sponsorship of the NAVSEA 93R propulsor program and the Office of Naval Research 6.2 propulsor program. Support for the University of Michigan was under ONR Grant No. N00014-99-1-0307, Dr. Ki-Han Kim technical monitor.

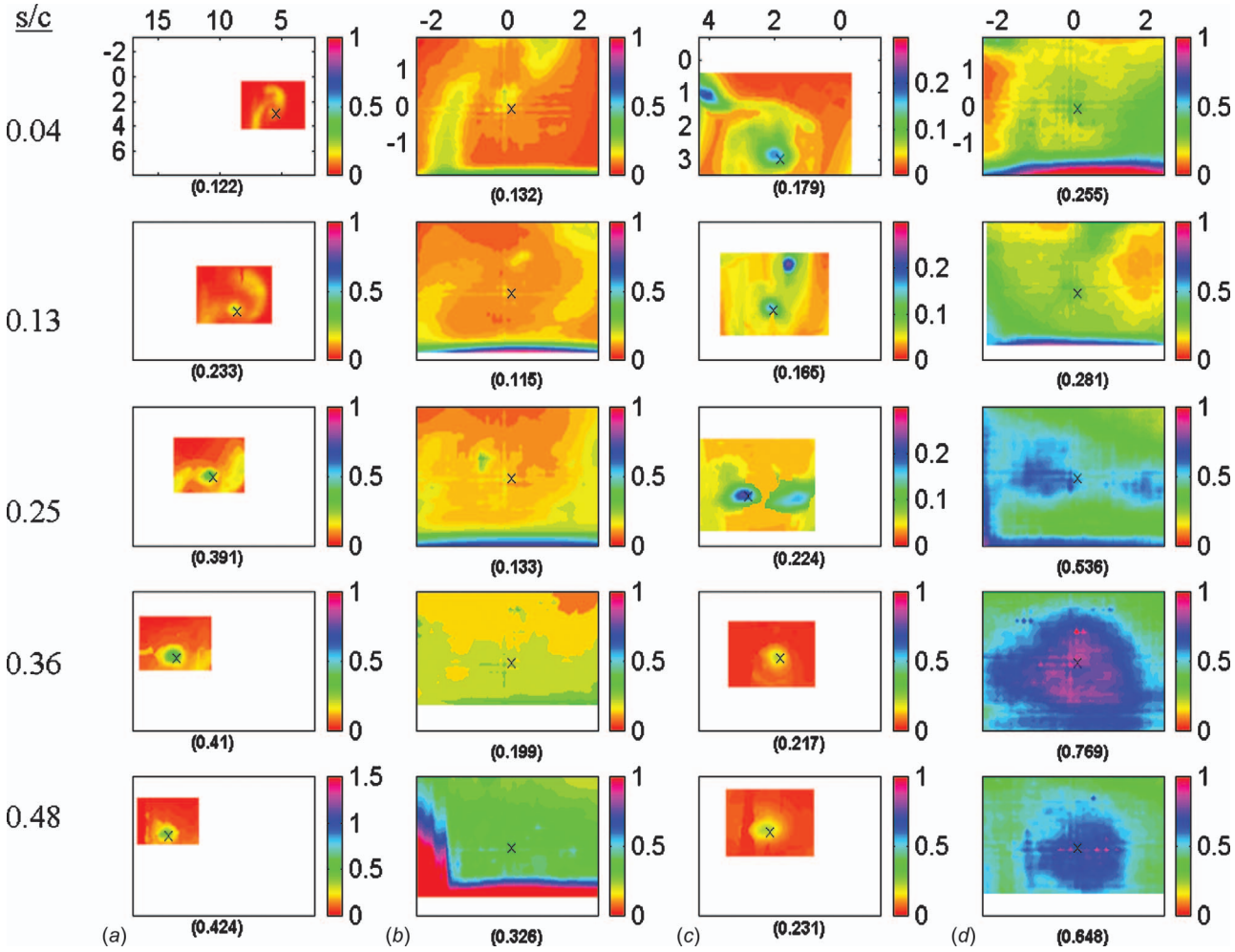

Fig. 12 Velocity fluctuations $(\overline{u'^2}+\overline{v'^2})/\overline{U_c^2}$. Otherwise the same as Fig. 11.

References

[1] Green, S. L., 1995, *Fluid Vortices*, Kluwer, Dordrecht, Netherlands.

[2] Spalart, P. R., 1998, "Airplane Trailing Vortices," Annu. Rev. Fluid Mech., **30**, pp. 107–138.

[3] Arndt, R. E. A., 2002, "Cavitation in Vortical Flows," Annu. Rev. Fluid Mech., **34**, pp. 143–175.

[4] Oweis, G. F., Fry, D., Chesnakas, C., Jessup, S., and Ceccio, S. L., 2006, "Development of a Tip-Leakage Flow. Part 1: The Flow Over a Range of Reynolds Numbers," ASME J. Fluids Eng., **128**, pp. 751–764.

[5] Farrell, K. J., and Billet, M. L., 1994, "A correlation of Leakage vortex cavitation in axial-flow pumps," ASME J. Fluids Eng., **116**, pp. 551–557.

[6] Oweis, G. F., and Ceccio, S. L., 2005, "Instantaneous and Time Averaged Flow Fields of Multiple Vortices in the Tip Region of a Ducted Propulsor," Exp. Fluids, **38**(5), pp. 615–636.

[7] Oweis, G. F., Choi, J., and Ceccio, S. L., 2004, "Dynamics and noise emissions of laser induced bubbles in a vortical flow field," J. Acoust. Soc. Am., **115**(3), pp. 1049–1058.

Blade Angle Effects on the Flow in a Tank Agitated by the Pitched-Blade Turbine

Yeng-Yung Tsui[1]
Professor
e-mail: yytsui@mail.nctu.edu.tw

Jian-Ren Chou
Graduate Student

Yu-Chang Hu
Graduate Student

Department of Mechanical Engineering,
National Chiao Tung University,
Hsinchu 300, Taiwan R. O. C.

This paper presents a study of the influence of the blade angle on the flow in a tank stirred by the pitched-blade turbine. The flow induced by the pitched-blade turbine is usually described as an axial type with a principal ring vortex dominating the flow structure. However, it is known that as the blade becomes vertical, i.e., as the pitch angle of the blade becomes 90 deg*, the flow is of the radial type, with two main ring vortices occupying the tank. Thus, a transition of flow type must take place when the blade angle is varied. This motivates the current study. A computational method was developed, which incorporates the unstructured grid technique to deal with the complex geometry in the tank. Multiframe of reference was employed to handle the rotation of the impeller. The results show that the transition from the axial type to the redial type is not progressive, but occurs all of a sudden at a particular angle, depending on the configuration. This critical angle decreases as the off-bottom clearance and the impeller size are increased. Its influences on the flow angle of the discharge stream, the power requirement, the induced flow rate through the impeller, and the pumping efficiency are discussed. The mechanism to cause the sudden change of flow type is addressed through observing the flow on the surface of the turbine blade.* [DOI: 10.1115/1.2201636]

1 Introduction

Flow agitation is an important process in the chemical and biotechnical industries. It is usually used to blend different liquids, erase concentration or temperature gradients, perform chemical reactions or biotechnical conversions, and for suspension of solid particles or dispersion of gases in liquids. To agitate the fluid a rotating impeller is introduced into the tank. For fluid mixing the contact surface between the fluids is distorted by the agitated flow, leading to elongation of the interface. As a result of the elongated interface, the mixing rate is accelerated since the gradients in the contact surface are smoothed out by the molecular diffusion. This process can be further enhanced in the turbulent field because the contact surface is largely wrinkled by turbulent fluctuations.

The most popular agitator adopted in the industry is either the disc-type flat-blade turbine, referred to as the Rushton turbine, or the pitched-blade turbine. For the former a number of flat blades are vertically installed on the periphery of a disc. The centrifugal force caused by the rotating impeller generates a radial jet stream. After impinging of the jet on the wall of the tank, two ring vortices are formed: one occupies the upper volume of the tank and the other the lower part. This kind of flow is termed radial style [1]. There is no disc installed in the pitched-blade turbine. The blades are inclined to the horizontal plane to form a blade angle. Different from the Rushton turbine, for which the discharge stream emerges from the periphery of the impeller, the flow of the pitched-blade turbine is discharged from the lower side of the blade passages. Therefore, it is a large ring vortex dominating the flow pattern in the stirred tank. This is called axial style [1]. In addition to the ring vortices, trailing vortices were observed in the low pressure regions behind the blades in both types of agitators [2–5]. The trailing vortex possesses the characteristic of high shear stress and has a beneficial effect on generation of turbulence. This is helpful to flow mixing and particle dispersion.

In this study we are concerned with the pitched-blade turbine. The geometry of the impeller has significant effects on its performance. Ranade and Joshi [6] used the laser Doppler anemometer to examine the flow characteristics in certain ranges of blade angles (30 deg–60 deg), blade widths (0.2 D–0.4 D), and impeller diameters (0.25 T–0.5 T). The pumping capacities and hydraulic efficiencies have also been reported. It was indicated that the hydraulic efficiency increases with the blade angle and the impeller diameter within the range studied. Besides the dominant vortex mentioned above, there may exist a smaller vortex, also induced by the discharge stream, located at the center region below the impeller. The influence of the impeller geometry on these vortex flows was conducted by Mao et al. [7]. The pumping numbers of the primary and secondary vortices were reported. The off-bottom clearance has great impact on the strength of the secondary vortex [7–9]. At low clearances, the secondary vortex is restricted in the center region. As the clearance becomes large, the discharge stream is directed toward the horizontal direction and the secondary vortex expands in size.

It is interesting to notice from the studies by Nouri and Whitelaw [10] and Hockey and Nouri [11] that a change of the flow pattern can take place by reducing the rotating speed, i.e., the Reynolds number. The measurements of axial velocity by Nouri and Whitelaw imply a rapid shift from an axial flow to a radial flow at a Reynolds number of around 650 while the sharp drop of power consumption measured by Hockey and Nouri indicates a transition of flow pattern at a Reynolds number of 1200. The difference in the critical Reynolds number is ascribed to different impeller sizes used.

In view of the above studies the configuration of the agitator setup has a decisive influence on the flow structure and its performance. It was seen that although, in general, the axial type of flow will be formed, it may be transformed into the radial type by choosing different off-bottom clearances or rotating speeds. Later in this study similar phenomena will be observed by varying the blade angle.

Computational fluid dynamics (CFD) provides an alternative tool for fluid flow analysis. The flow in the stirred tank is inherently periodic and unsteady. Fully time-dependent computations require excessive computer resources. The steady-state computations by Wechsler et al. [12] showed an excellent agreement with

[1]Corresponding author.

Contributed by the Fluids Engineering Division of ASME for publication in the JOURNAL OF FLUIDS ENGINEERING. Manuscript received May 1, 2005; final manuscript received January 24, 2006. Assoc. Editor: Akira Goto.

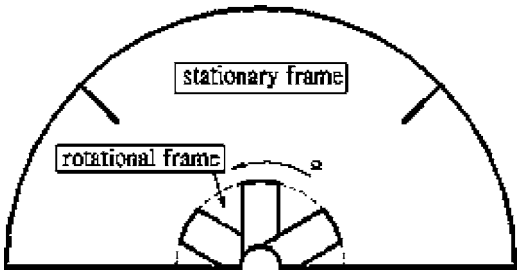

Fig. 1 Multiframe of reference

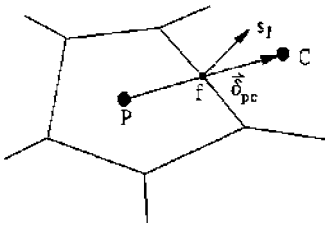

Fig. 2 Illustration of a control volume

fully unsteady computations, but at a fraction of expense. Thus, for engineering analysis it is sufficient to assume a quasisteady state. In the steady-state model the impeller is fixed at a particular position relative to the wall of the tank and the grids are stationary without moving. However, the flow in the tank needs to be induced in calculations with some methods. In the early stage measured profiles of mean velocity and turbulence were prescribed around the impeller as boundary conditions [13–17]. In this way, extensive experimental work is required. Thus, the usefulness of this approach is severely restricted. Xu and McGrath [18] treated the impeller blades as airfoils. The lift and drag forces produced on the airfoils are implemented as a momentum source to drive the flow. Ranade and Dommeti [19] described the interaction between the fluid and the blades by applying appropriate mass and momentum sources at the blade surface. Recently, a popular method adopted is to mount the blade-swept volume on a rotating frame of reference and the rest part of the tank on the stationary frame [12,20]. The body forces generated by the rotating frame will trigger the fluid flow.

In the present study the multireference frame is employed to model the three-dimensional turbulent flow in a tank stirred by the pitched blade turbine. To cope with the complex geometry prevailed in the tank, unstructured grids are used. The turbulence needs to be characterized by turbulence models. A number of turbulence models, including Reynolds stress model [15,17], algebraic stress model [16], and variant k-ε and k-ω models [21,22] have been tested. In general, all these models obtained an overall qualitative agreement with measurements, but poor predictions in some parts of the tank, especially in the discharge region. There is no particular model much superior to the others. Hence, the most popular k-ε model is adopted in the present computations. Under different settings of configuration we will examine the transition of the flow structure by varying the blade angle. The effects on the flow and the performance will be shown.

2 Mathematical Method

As shown in Fig. 1, the tank is divided into two parts. The blade-swept region rotates with the impeller while the other region is fixed without moving. Define the grid velocity as

$$\vec{U}_g = \vec{\Omega} \times \vec{r} \text{ in the blade-swept region} \tag{1a}$$

$$\vec{U}_g = 0 \text{ in the stationary region} \tag{1b}$$

where $\vec{\Omega}$ is the angular speed of the impeller and $\vec{r}$ the position vector of the considered nodal point. The continuity equation and the transport equations in the Cartesian coordinates can then be cast into the following form:

$$\frac{\partial}{\partial x_j}[\rho(U_j - U_{gj})] = 0 \tag{2}$$

$$\frac{\partial}{\partial x_j}[\rho(U_j - U_{gj})\phi] = \frac{\partial}{\partial x_j}\left(\Gamma_\phi \frac{\partial \phi}{\partial x_j}\right) + S_\phi \tag{3}$$

where ϕ represents $U_j - U_{gj}$, k, and ε, ρ is the fluid density, and Γ_ϕ the diffusion coefficient. $U_j - U_{gj}$ denotes the flow velocity with respect to the grid. In the momentum equation the rotation-induced body forces, including centrifugal force and Corriolis force, must be accounted for as sources.

$$S'_{U_j} = -\rho\varepsilon_{mnj}\Omega_m(\varepsilon_{pqn}\Omega_p x_q) + 2\rho\varepsilon_{mnj}\Omega_m(U_n - U_{gn}) \tag{4}$$

Here, ε_{ijk} is the alternating unit tensor. It is noted that in the stationary region S'_{U_j} must be set to zero. The turbulence is characterized by the standard k-ε model of Launder and Spalding [23]. The wall function is used to bridge the near wall region to avoid excessive grid nodes there.

To deal with the irregular geometry in the tank one method is to use block-structured grids, as done by Harvey et al. [20] and Wechsler et al. [12]. In this way the blocks are globally unstructured, but the grids are locally structured. Transformation of the coordinate system is necessary, rendering the governing equations much more complicated. In addition, a solution must be iterated among the blocks. Special care must be taken at each interface between neighboring blocks to ensure coupling. An alternative, which can circumvent the above inconveniences, is the use of unstructured grids. To construct difference equations the differential equations are integrated over a control volume. By applying the divergence theorem of Gauss the volume integrals for the convection and diffusion terms are then transformed into surface integrals. The convection and diffusion fluxes through the surface of the control volume can be expressed as

$$F^c = \sum_f [\rho(\vec{V} - \vec{V}_g) \cdot \vec{s}]_f \phi_f \tag{5a}$$

$$F^d = \sum_f (\Gamma \nabla \phi \cdot \vec{s})_f \tag{5b}$$

where the subscripts f denote the faces of the control volume, $\vec{s}_f$ is the surface vector of the considered face (see Fig. 2), and the summation is taken over all the faces. In the convection flux the face value is approximated by

$$\phi_f = \phi^{\mathrm{UD}} + \gamma(\nabla\phi)^{\mathrm{UD}} \cdot \vec{\delta} \tag{6}$$

Here the superscripts UD denote the value evaluated at the adjacent node in the upwind direction of the face, $\vec{\delta}$ is the distance vector directed from the upwind node to the centroid of the face. In the equation, γ is a blending factor between 0 and 1. For a value of 0 it represents an upwind difference scheme, and for a value of 1 a second-order scheme. In the following computations, 0.9 is assigned to γ.

The diffusion flux is estimated by the following approximation:

$$F^d = \frac{\Gamma_f s_f^2}{\vec{\delta}_{PC} \cdot \vec{s}_f}(\phi_C - \phi_P) + \Gamma_f \overline{\nabla\phi}_f \cdot \left(\vec{s}_f - \frac{s_f^2}{\vec{\delta}_{PC} \cdot \vec{s}_f}\vec{\delta}_{PC}\right) \tag{7}$$

where, see Fig. 2, the superscripts P and C denote the principal and the neighboring nodes sharing a common face, and $\vec{\delta}_{pc}$ is a

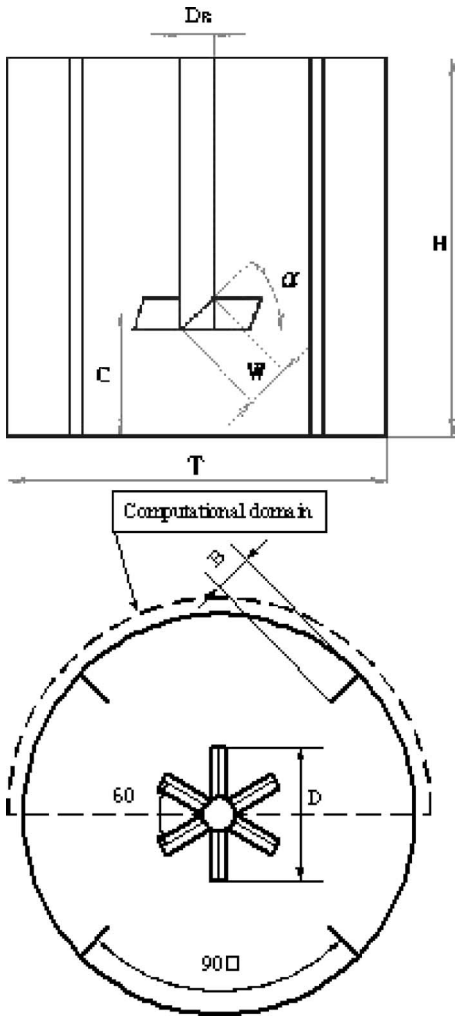

Fig. 3 A sketch of a stirred tank

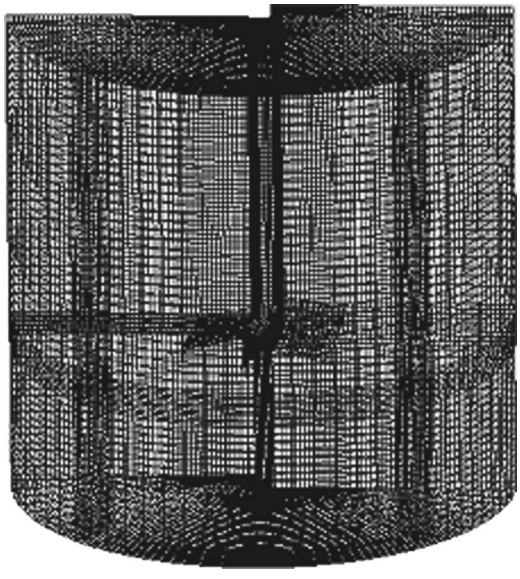

Fig. 4 A typical computational grid

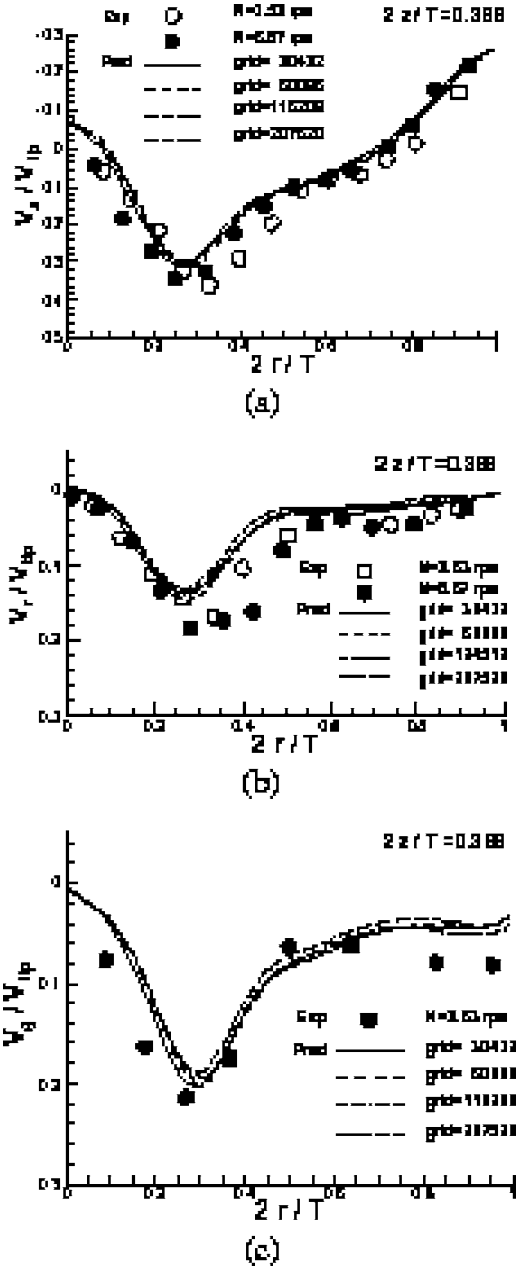

Fig. 5 Comparison of predictions with measurements

vector connecting these two nodes. The face gradient $\overline{\nabla\phi}_f$ is obtained via interpolation from the values at the two nodes P and C.

It needs to be noted that the computational molecule for the nodes next to the interface between the two reference frames comprises nodes in the other frame. The velocity at these neighboring nodal points must be transformed onto the same frame as the one for the principal node P to evaluate the momentum flux transported through the interface.

The coupling between the momentum and continuity equations are treated according to the SIMPLE (Semi-Implicit Method for Pressure-Linked Equations) algorithm. The velocity and pressure are collocated on the centroid of each control volume. To avoid decoupling between velocity and pressure fields the momentum interpolation technique is applied. More details about this method are referred to in the study by Tsui and Pan [24].

The baffles and the impeller are arranged in a symmetrical manner, as seen in Fig. 3. Due to the symmetrical arrangement the flow becomes periodic. Therefore, only half the tank is considered in calculations and periodic conditions are imposed on the symmetrical boundary planes. The fluxes out of the 0 deg radial plane must be carried into the 180 deg plane, and vice versa. To ensure a correct transfer of fluxes auxiliary control volumes along the

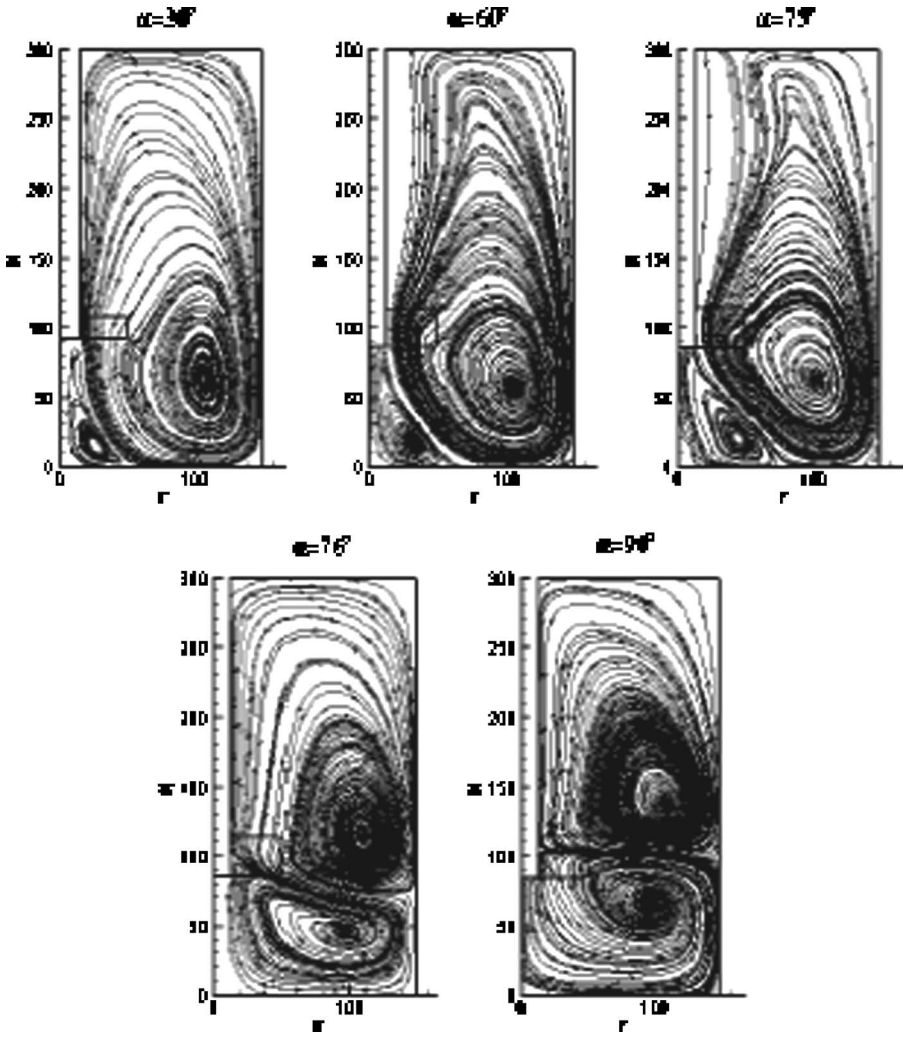

Fig. 6 Flow streamlines for $D=T/3$, $C=T/3$

symmetrical planes are added. The boundary data in the auxiliary control volumes is updated after each outer iteration of the SIMPLE algorithm.

3 Results and Discussion

A sketch of a typical stirred tank is shown in Fig. 3. The diameter of the tank is denoted as T, and the height of the tank as H. There are four equally-spaced baffles fitted on the surrounding wall with a width B. The clearance of the impeller is C, which is measured from the center line of the blade to the bottom of the tank. The impeller holds six blades and has a diameter D. The blades have a pitch angle α and a width W. To generate unstructured grids the computational domain is first divided into 40 blocks. In each block a simple method, such as an algebraic method, is used to create a suitable grid. After the grids for all the blocks are constructed, the grid nodes are readdressed. An example of the resulted grid is presented in Fig. 4.

To validate the current mathematical model, computations have been performed to compare with the measurements of Ranade and Joshi [6]. The specifications of the stirred tank configuration studied by them are: $T=H=300$ mm, $D=C=100$ mm, $W=B=30$ mm, and $\alpha=45$ deg. To examine the grid sensitivity of the solution four different levels of grids were tested, including node numbers of 30,432, 60,096, 116,208, and 207,520. Figure 5 presents the predicted velocity components V_z, V_r, V_θ in the axial, radial, and circumferential directions at an axial station $2z/T=0.366$ below the center of the impeller blade. In the figure V_{tip} represents the blade tip velocity. The rotational speed is set at $N=3.53$ rps, i.e., at a Reynolds number ($=\rho ND^2/\mu$) of 3.53×10^4. Another set of measurements for $N=6.67$ rps is also included for comparison. It can be seen that the velocities are accelerated quickly to reach a position roughly corresponding to the tip of the blade, followed by a gradual decrease. The negative axial velocity in the region near the side wall of the tank implies the existence of a circulation loop, i.e., an axial vortex there. The predictions capture these characteristics quite well, though, in comparison with measurements, some degree of discrepancy exists. More comparison in terms of pumping number and power number will be given later. Not much difference was observed for different grids used. In the following, the grid with about 120,000 nodes is adopted. It needs to be emphasized here that the disagreement between the predictions and the measurements is partly attributed to the imperfection of the eddy viscosity model which cannot cope with such a complex vortex and swirling flow. Another factor affecting the prediction accuracy is the assumption of steady state. In a real situation the impeller blades keep changing their position relative to the baffles, but not in the numerical simulation. It is noted that the experiments conducted by Ranade and Joshi were obtained over 360 deg of impeller revolution, i.e., the time averaging was undertaken. The angle-resolved measurements for a pitched-blade turbine by Hockey and Nouri [11] revealed a variation of the mean velocity and the turbulence fluctuation with the revolution

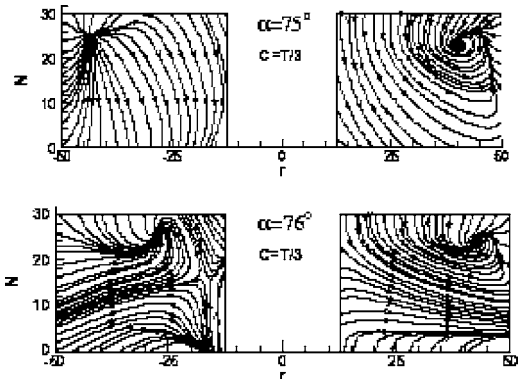

Fig. 7 Limiting streamlines on the surface of the blade for α =75 deg and 76 deg. The sketches on the left are referred to the front surface and those on the right to the back surface.

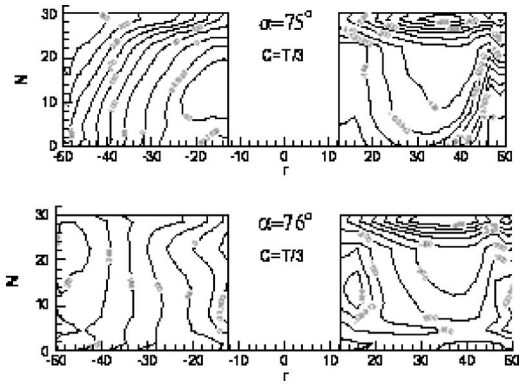

Fig. 8 Pressure contours on the surface of the blade for α =75 deg and 76 deg. The sketches on the left are referred to the front surface and those on the right to the back surface.

angle. It was shown by them that the blade-to-blade differences in the mean velocity and the root-mean square (rms) fluctuation are within 5% in the 1.08 deg angle-resolved measurements. The time averaging can lead to an overestimate of the rms fluctuation by up to twofold. The blade-to-blade variation of the mean velocity surely contributes to the rms fluctuation in the time-averaging. However, the cause of the overestimate of the turbulent fluctuation is mainly due to the periodic variation in the mean velocity.

The blade angle α is varied first while the other parameters remain the same as above. It was recognized from the experiments of Dong et al. [25] that the pitched blade turbine behaves like the Rushton turbine when the blades are in the vertical position (α =90 deg). This behavior is confirmed in Fig. 6. The flow field shown in the figure is in the midplane between two blades. It can be seen, according to this figure, that in the range α =30 deg–75 deg the flow is of the axial type, with a large circulation loop occupying most part of the tank and a much weaker one restricted in the center region below the impeller. The size of the smaller circulation loop gradually increases with the blade angle. A dramatic enlargement occurs when the blade angle is increased to 76 deg. The jet stream discharged from the impeller impinges on the side wall, instead of the bottom wall as observed in the lower blade angles. The minor circulation loop now almost overwhelms the whole volume beneath the impeller and the flow field changes from the axial type to the radial type. By further increasing the blade angle the jet stream adjusts its direction slightly until fully radial direction is reached at α=90 deg.

To gain insight into the detailed flow near the blades, the limiting streamlines, which are streamlines passing very close to the blade surface, are shown in Fig. 7 for the cases of α=75 deg and 76 deg with $C=D=T/3$. In the figure the cross sections show the two surfaces of the turbine blade. The sketches on the left are referred to the front surface of the blade and those on the right to the back side. On the front there is a repelling spiral-focal point at the upper corner near the blade tip for the subcritical angle of 75 deg. This nodal point behaves like a source, or a stagnation point, where fluid flows toward the surface and sprays over the front surface, mainly in the direction down to the lower edge. When the critical angle of 76 deg is reached, the source is shifted toward the base side. In the meanwhile, fluid is drawn from the lower edge close to the base. As a result, a saddle point is formed at the midheight position near the base. Fluid is then forced to flow radially from the saddle point toward the outer edge. At the back side, it is evident that there exists an attracting spiral-focal point which plays the role of flow sink. It draws fluid from the top side and the upper tip and transports the fluid away from the back surface. This sink simply represents the center of the trailing vortex mentioned in the Introduction. The trailing vortex is located at the upper corner near the tip, which is similar to the results reported by Schafer et al. [4] and Wechsler et al. [12]. It is interesting to note that, especially for α=75 deg, some streamlines close to the tip merge into one streamline before they end at the sink point. This behavior of merging streamlines from both sides of the streamline implies that this line segment is a line of separation, i.e., flow starts to separate here. The line of separation is not so obvious for α=76 deg.

Pressure distribution on the blade is illustrated in Fig. 8. Generally speaking, adverse pressure gradient prevails in the radial direction on the front surface due to the tendency for it to balance the centrifugal force prevailing outside the boundary layer. For α=75 deg the highest pressure is situated at the upper corner near the tip, where the stagnation point is located. For this case the pressure gradient, as well as the shear force, drives the flow from

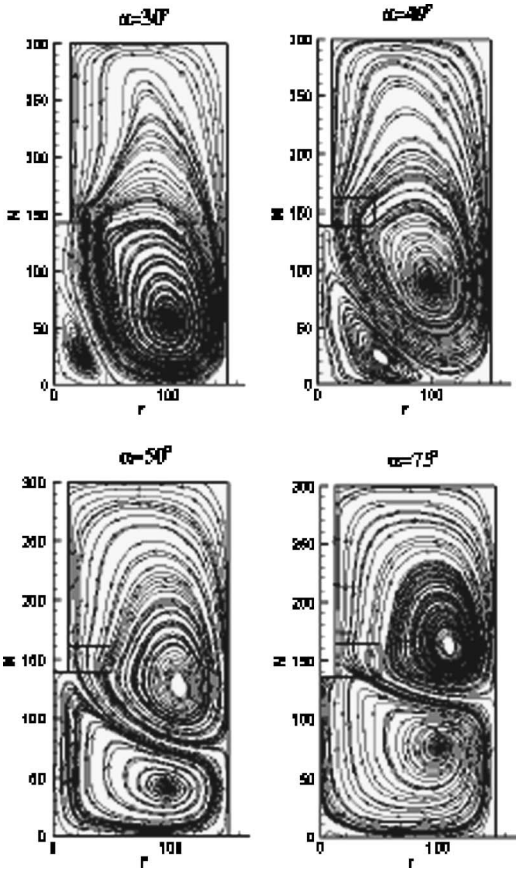

Fig. 9 Flow streamlines for $D=T/3$, $C=T/2$

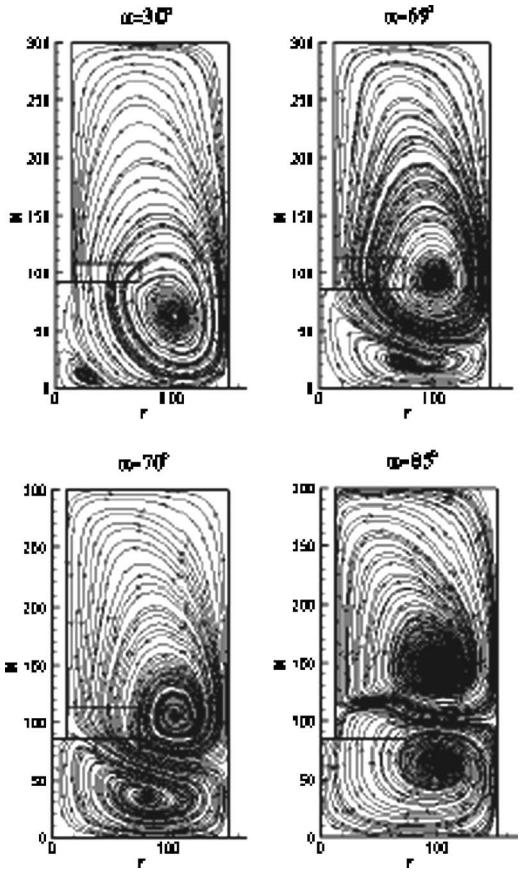

Fig. 10 Flow streamlines for $D=T/2$, $C=T/3$

the region in the upper edge to the lower edge, as seen in the previous figure. As for $\alpha=76$ deg it is mainly the shear force alone to control the fluid to flow radially outward. On the back surface the pressure is lower in comparison to the front surface, which is expected. The lowest pressure is always found at the upper edge because this is the leading edge of the blade airfoil.

In view of the above results, it can be concluded that the change of pitch angle will trigger flow instability at a specific angle. For blade angles greater than this angle, it is the centrifugal force prevailing in the blade passage to drive fluid to flow mainly in the radial direction. As the blade angle is reduced, a strong stagnation flow occurs in the upper region on the front surface, close to the blade tip. This results in a pressure gradient in the axial direction, which forces fluid to flow from the upper region to the lower region. Thus, the flow pattern is changed from the radial type to the axial type.

As mentioned in the literature review, the off-bottom clearance has a great effect on the flow. It can be seen from Fig. 9 that the transition of flow type takes place at an earlier angle of 50 deg by increasing the clearance C from $T/3$ to $T/2$. It is ready to find that for a fixed blade angle between 50 deg and 75 deg the change of the impeller clearance can result in a different flow pattern.

In order to investigate the effect of the blade length the diameter of the impeller D is increased from $T/3$ to $T/2$. As seen in Fig. 10, the critical blade angle is slightly reduced from 76 deg to 70 deg. The difference in the circulating flow structure between $\alpha=69$ deg and 70 deg is not as obvious as that for the smaller impeller case. For the smaller impeller the minor circulation loop is always limited in the center region and the flow remains to be of the axial type at all subcritical angles whereas for the larger one the discharge stream has impinged on the surrounding wall and the flow field has become a mixed type of axial/radial flow before the critical angle is reached

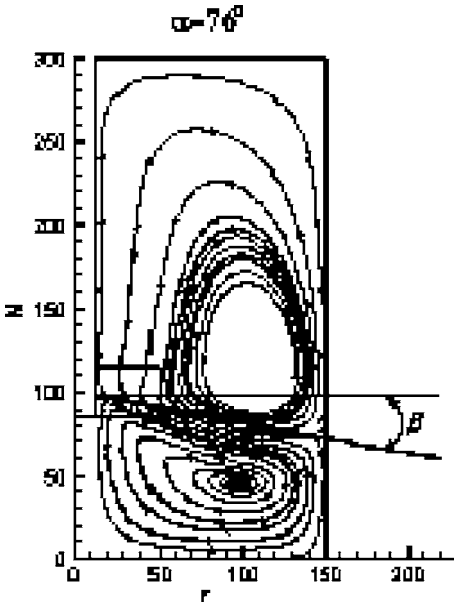

Fig. 11 Define flow angle of the discharge stream

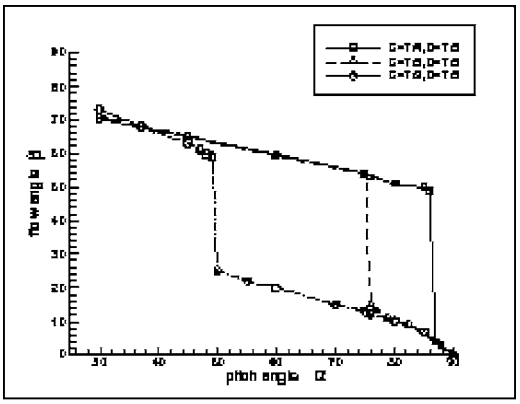

(a)

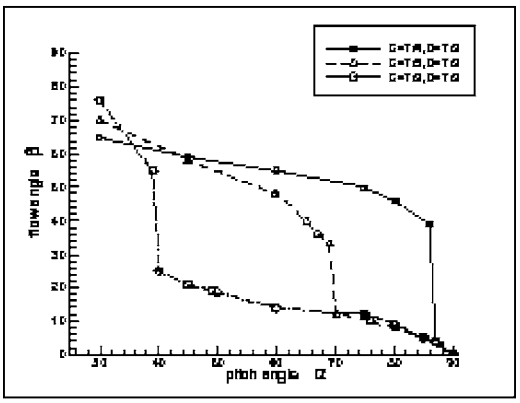

(b)

Fig. 12 Variation of the flow angle against the pitch angle of the blade for (*a*) $D=T/3$, and (*b*) $D=T/2$

An angle β, characterizing the flow orientation of the discharge stream, is defined as the inclination of the line connecting the two points separating the two circulation loops on the rotating shaft and on the wall, as illustrated in Fig. 11. The variation of this flow angle with respect to the blade angle is presented in Fig. 12. There exists a sharp drop in the flow angle at each critical blade angle. It

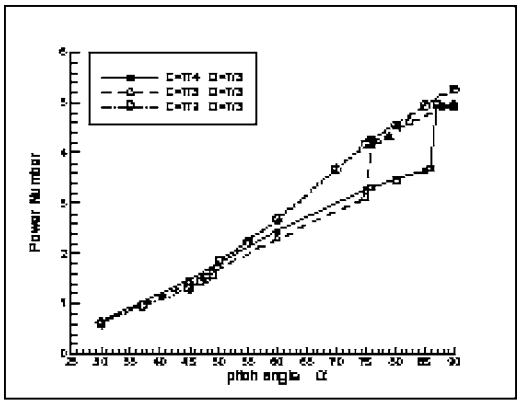

(a)

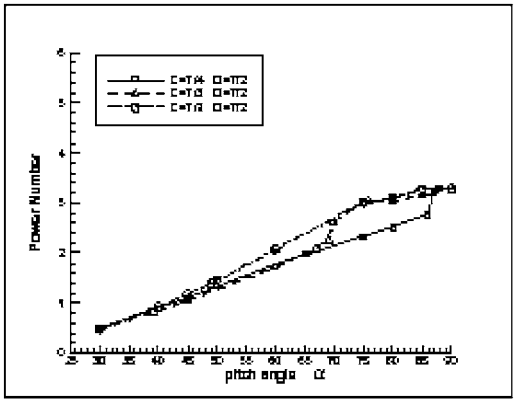

(b)

Fig. 13 Variation of the power number against the pitch angle of the blade for (*a*) *D*=*T*/3, and (*b*) *D*=*T*/2

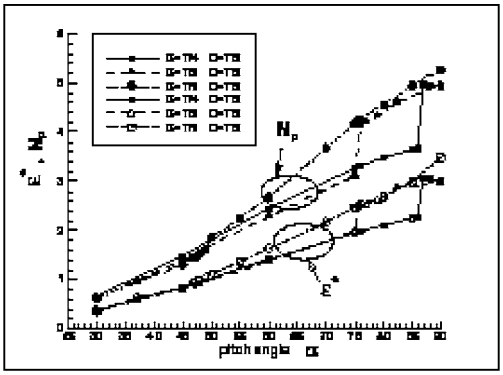

(a)

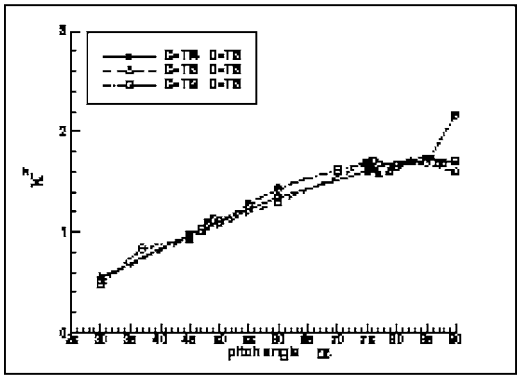

(b)

Fig. 14 Variation of (*a*) k^* and (*b*) ε^* against the pitch angle of the blade for *D*=*T*/3

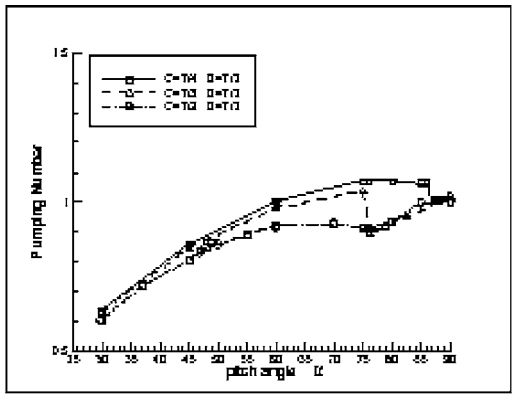

(a)

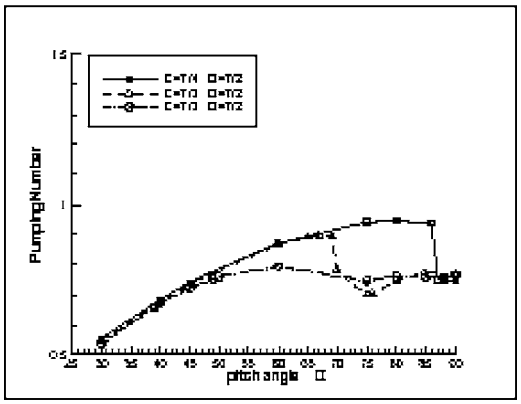

(b)

Fig. 15 Variation of the pumping number against the pitch angle of the blade for (*a*) *D*=*T*/3, and (*b*) *D*=*T*/2

is interesting to notice that for the smaller impeller case the flow angles almost fall on the same curves, being nearly linear, before and after the transition takes place. For the larger impeller case the flow angle declines first before the sharp drop occurs. The decline rate is higher as the clearance is increased. But the flow angles are on the same curve after the flow pattern changes.

The change of flow field will seriously affect the power consumption and the performance of the agitator. Power number N_p is defined by

$$N_p = \frac{2\pi N\tau}{\rho N^3 D^5} \tag{8}$$

where N represents the impeller rotational speed in rps, and τ the required torque of the impeller. The torque is calculated as the sum of the moments generated by both the pressure force exerted on the blades and the shear force exerted on the blades and the rotating shaft. The part generated by the shear force is much smaller, in general, less than 1% of the total torque. As seen in Fig. 13, the power required to drive the impeller increases with the pitch angle of the blade. There exists a jump at each critical angle. The extent of the jump decreases as the clearance and the impeller diameter are enlarged. For the case with $C=T/2$ and $D=T/2$ the jump at $\alpha=40$ deg is nearly invisible. Similar to the flow angle, the data of power number also falls on similar curves before and after the flow pattern changes.

Figure 14 shows the dependence of the total turbulent energy and its dissipation rate generated in the tank on the blade angle for $D=T/3$. Both are nondimensionalized as

$$k^* = \frac{\int_V \rho k \bullet dv}{\rho N^2 D^5} \tag{9}$$

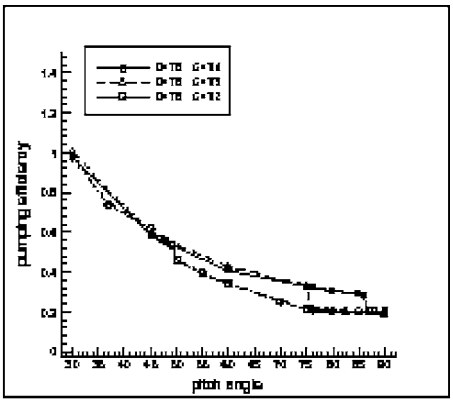

(a)

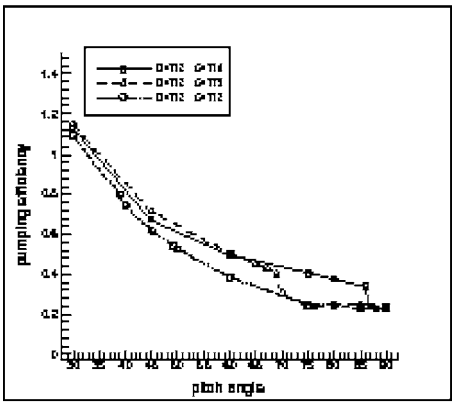

(b)

Fig. 16 Variation of the pumping efficiency against the pitch angle of the blade for (*a*) *D*=*T*/3, and (*b*) *D*=*T*/2

$$\varepsilon^* = \frac{\int_V \rho\varepsilon \bullet dv}{\rho N^3 D^5} \tag{10}$$

where the integration is taken over the entire volume of the tank. For comparison the power number shown in Fig. 13(*a*) is also included in Fig. 14(*a*). It indicates that the turbulence dissipation rate behaves in a similar manner as the power consumption, which is expected because the energy transferred from the impeller to cause the fluid flow will be cascaded into turbulence and dissipated into heat in the end. However, the total dissipation rate is much lower than the power required. Part of the reason for causing the difference is due to the inadequacy of the turbulence model. The turbulent energy produced increases with the pitch angle. However, there exists a drop at the critical angles. The drop is not as obvious as the jump in the power.

In a mixing system the circulating flow is responsible for the function of the agitation because the mixing time depends on the circulation time. This flow is originated from the stream discharged from the impeller. Therefore, the strength of the circulating flow can be characterized by the induced flow rate through the impeller. A pumping number is defined as

Table 1 A summary of critical pitch angles

	C=*T*/4 (deg)	*C*=*T*/3 (deg)	*C*=*T*/2 (deg)
D=T/3	87	76	50
D=T/2	87	70	40

$$N_Q = \frac{Q}{\rho N D^3} \tag{11}$$

where Q is the net mass flow rate through all the blade passages of the impeller. The predicted pumping numbers for the cases with $C=D=T/3$ at $\alpha=30$, 45, and 60 deg are 0.63, 0.84, and 0.98, respectively, which compares reasonably well with the experimental data of 0.6, 0.93, and 1.1 given by Ranade and Joshi [6]. Hockey and Nouri [11] reported a pumping number of 0.88 for the blade angle of 60 deg, which seems a little on the low side in comparison to the predictions and measurements by Ranade and Joshi. However, the power number of 2.2 measured by Hockey and Nouri is in very good agreement with the present value of 2.3. By increasing the impeller diameter to $D=T/2$, the predicted pumping number of 0.74 for $\alpha=45$ deg is close to the data of 0.8 obtained by Ranade and Joshi.

Figure 15 reveals that the pumping number increases with the pitch angle, but tends to level off for high angles. At the angle where the flow is transformed into the radial type the mass flux declines sharply. This phenomenon of sharp declination is more prominent in the cases with larger impellers and lower clearances.

The pumping efficiency, defined by

$$\eta = \frac{N_Q}{N_P} \tag{12}$$

is a measure of effectiveness of the impeller to generate pumping flow per unit of power input. Figure 16 shows that the pumping efficiency decreases with the blade angle and levels off when approaching 90 deg. It is especially true for the smaller impeller that all the data falls on the same curves before and after the pattern change take places. The large impeller is more efficient in circulating flow per power input because the efficiency ranges from 0.23 to 1.15 while that for the smaller impeller is in the range of 0.2–1.

The critical pitch angles are summarized in Table 1. It can be found that with the smallest clearance of $C=T/4$ the axial flow type prevails unless the blades are close to the vertical position. The critical angle is very sensitive to the clearance. The increase of clearance will cause significant decrease in this angle. The increase in the impeller size can also result in a decrease of the critical angle; with a larger impeller the transition will occur at a lower blade angle.

4 Conclusions

A computational methodology has been developed to examine the flow field in a tank agitated by a pitched-blade impeller. The flow was assumed to be in a quasisteady state. The tank was divided into two parts. The blade-swept region was situated on a rotational frame of reference and the rest on a stationary frame. Discretization was based on the unstructured mesh manner to deal with the complex geometry encountered in the tank. The effect of the pitch angle of the blade was carefully studied. A summary of the main findings is drawn in the following.

1. At low blade angles the circulating flow in the tank, generally, is of the axial type with a minor recirculation loop restricted in the center region below the impeller. The size of this small circulating flow gradually increases with the blade angle until a critical angle is reached. At this critical angle the flow is transformed into the radial type all of a sudden. With further increase of the angle to 90 deg, the pitched-blade turbine behaves like a Rushton turbine.
2. For blade angles greater than the critical angle, it is the centrifugal force which dominates in the blade passage and forces fluid to flow radially. As the pitch angle is reduced to lower than the critical angle, a strong stagnation flow is formed in the upper region on the front sur-

face of the blade, driving the fluid to flow axially downward. It is this mechanism to cause the sudden change of flow type.

3. The clearance of the impeller to the tank bottom has a significant influence on the critical angle. This critical angle decreases as the clearance increases. The enlargement of the impeller diameter may also reduce the critical angle.
4. The flow angle of the discharge stream can be regarded as a measure of the size of the smaller circulating flow. The smaller the flow angle, the larger the secondary circulation. In general, the discharge flow angle gradually decreases when the blade angle increases. However, at the critical angle a sharp drop appears, indicating a change of flow type. The extent of the sudden reduction in the flow angle is less significant for lower clearances and larger impellers.
5. The power consumption and the induced mass flow through the impeller increases with the blade angle. But the pumping efficiency decreases as the blade angle increases. The pumped flow rate and the pumping efficiency level off at large blade angles. The transition to the radial type leads to a jump in power requirement and a sharp decline in the pumped flow rate and its efficiency.

Acknowledgment

This work was supported by National Science Council of Taiwan, R.O.C., under Contract No. NSC-93-2212-E-009-012 and No. NSC-94-2212-E-009-024.

Nomenclature

B = baffle width
C = off-bottom clearance
D = impeller diameter
D_s = shaft diameter
F^c = convection flux
F^d = diffusion flux
H = tank height
k = turbulent kinetic energy
k^* = dimensionless total turbulent kinetic energy
N = rotational speed
N_P = power number
N_Q = pumping number
Q = net mass flux through all blade passages
s_f = surface vector
S_ϕ = source term of transport equation for ϕ
T = tank diameter
$\vec{U}_g, U_{gj}$ = grid velocity vector
U_j = flow velocity vector
V_r, V_θ, V_z = velocities in radial, circumferential, and axial directions
V_{tip} = blade tip velocity
W = blade width
x_j = Cartesian coordinates of the considered point
z = vertical distance

Greek Symbols

α = pitch angle
δ_{PC} = distance vector directed from P to C
ε = turbulent dissipation rate
ε^* = dimensionless total turbulent dissipation rate
ε_{ijk} = alternating unit tensor
ϕ = a flow property
γ = blending factor
Γ_ϕ = diffusion coefficient for ϕ
η = pumping efficiency
τ = torque
$\vec{\Omega}, \Omega_m$ = angular speed

Subscripts

f = face value
ϕ = for the flow property ϕ

References

[1] Tatterson, G. B., 1991, *Fluid Mixing and Gas Dispersion in Agitated Tanks*, McGraw-Hill, New York.
[2] Van't Riet, K., and Smith, J. M., 1975, "The Trailing Vortex System Produced by Rushton Turbine Agitators," Chem. Eng. Sci., **30**, pp. 1093–1105.
[3] Yianneskis, M., and Whitelaw, J. H., 1993, "On the Structure of the Trailing Vortices Around Rushton Turbine Blades," Trans. Inst. Chem. Eng., Part A, **71**, pp. 534–550.
[4] Schafer, M., Yianneskis, M., Wachter, P., and Durst, F., 1998, "Trailing Vortices Around a 45° Pitched-Blade Impeller," AIChE J., **44**(6), pp. 1233–1246.
[5] Derksen, J. J., Doelman, M. S., and Van den Akker, H. E. A., 1999, "Three-Dimensional LDA Measurements in the Impeller Region of a Turbulently Stirred Tank," Exp. Fluids, **27**, pp. 522–532.
[6] Ranade, V. V., and Joshi, J. B., 1989, "Flow Generated by Pitched Blade Turbines I: Measurements Using Laser Doppler Anemometer," Chem. Eng. Commun., **81**, pp. 197–224.
[7] Mao, D.-M., Feng, L.-F., Wang, K., and Li, Y.-L., 1997, "The Mean Flow Field Generated by a Pitched Blade Turbine: Changes in the Circulation Pattern due to Impeller Geometry," Can. J. Chem. Eng., **75**, pp. 307–316.
[8] Jaworski, Z., Nienow, A. W., Koutsakos, E., Dyster, K., and Bujalski, W., 1991, "A LDA Study of Turbulent Flow in a Baffled Vessel Agitated by a Pitched Blade Turbine," Trans. Inst. Chem. Eng., Part A, **69**, pp. 313–320.
[9] Kresta, S. M., and Wood, P. E., 1993, "The Mean Flow Field Produced by a 45° Pitched Blade Turbine: Change in the Circulation Pattern due to Off Bottom Clearance," Can. J. Chem. Eng., **71**, pp. 42–53.
[10] Nouri, J. M., and Whitelaw, J. H., 1990, "Flow Characteristics of Stirred Reactors With Newtonian and Non-Newtonian Fluids," AIChE J., **36**(4), pp. 627–629.
[11] Hockey, R. M., and Nouri, J. M., 1996, "Turbulent Flow in a Baffled Vessel Stirred by a 60° Pitched Blade Impeller," Chem. Eng. Sci., **51**(19), pp. 4405–4421.
[12] Wechsler, K., Breuer, M., and Durst, F., 1999, "Steady and Unsteady Computations of Turbulent Flows Induced by a 4/45° Pitched-Blade Impeller," J. Fluids Eng., **121**, pp. 318–329.
[13] Ranade, V. V., Joshi, J. B., and Marathe, A. G., 1989, "Flow Generated by Pitched Blade Turbines II: Simulation Using k-ϵ Model," Chem. Eng. Commun., **81**, pp. 225–248.
[14] Ranade, V. V., Bourne, J. R., and Joshi, J. B., 1991, "Fluid Mechanics and Blending in Agitated Tanks," Chem. Eng. Sci., **46**(8), pp. 1883–1893.
[15] Bakker, A., Myers, K. J., Ward, R. W., and Lee, C. K., 1996, "The Laminar and Turbulent Flow Pattern of a Pitched Blade Turbine," Trans. Inst. Chem. Eng., Part A, **74**, pp. 485–491.
[16] Armenante, P. M., Luo, C., Chou, C.-C., Fort, I., and Medek, J., 1997, "Velocity Profiles in a Closed, Unbaffled Vessel: Comparison Between Experimental LDA Data and Numerical CFD Predictions," Chem. Eng. Sci., **52**(20), pp. 3483–3492.
[17] Sheng, J., Meng, H., and Fox, R. O., 1998, "Validation of CFD Simulations of a Stirred Tank Using Particle Velocimetry Data," Can. J. Chem. Eng., **76**, pp. 611–625.
[18] Xu, Y., and McGrath, G., 1996, "CFD Predictions of Stirred Tank, Flows," Trans. Inst. Chem. Eng., Part A, **74**, pp. 471–475.
[19] Ranade, V. V., and Dommeti, S. M. S., 1996, "Computational Snapshot of Flow Generated by Axial Impellers in Baffled Stirred Vessels," Trans. Inst. Chem. Eng., Part A, **74**, pp. 476–484.
[20] Harvey, A. D., Lee, C. K., and Rogers, S. E., 1995, "Steady-State Modeling and Experimental Measurement of a Baffled Impeller Stirred Tank," AIChE J., **41**(10), pp. 2177–2186.
[21] Jenne, M., and Reuss, M., 1999, "A Critical Assessment on the Use of k-ε Turbulence Models for Simulation of the Turbulent Liquid Flow Influenced by a Rushton-Turbine in Baffled Stirred-Tank Reactors," Chem. Eng. Sci., **54**, pp. 3921–3941.
[22] Jones, R. M., Harvey, III, A. D., and Acharya, S., 2001, "Two-Equation Turbulence Modeling for Impeller Stirred Tanks," J. Fluids Eng., **123**, pp. 640–648.
[23] Launder, B. E., and Spalding, D., 1974, "The Numerical Computation of Turbulent Flows," Comput. Methods Appl. Mech. Eng., **3**, pp. 269–289.
[24] Tsui, Y.-Y., and Pan, Y.-F., 2006, "A Pressure-Correction Method for Incompressible Flow Using Unstructured Meshes," Numer. Heat Transfer, Part B, **49**, pp. 43–65.
[25] Dong, L., Johansen, S. T., and Engh, T. A., 1994, "Flow Induced by an Impeller in an Unbaffled Tank-I. Experimental," Chem. Eng. Sci., **49**(4), pp. 549–560.

Numerical and Experimental Investigation on the Flow Induced Oscillations of a Single-Blade Pump Impeller

F.-K. Benra
Professor
Mem. ASME
University of Duisburg-Essen,
Faculty of Engineering Sciences,
Institute of Energy and Environmental
Engineering, Turbomachinery,
P. O. Box 1629,
47048 Duisburg, Germany
e-mail: benra@uni-duisburg.de

This contribution is addressed to the periodically unsteady flow forces of a single-blade sewage water pump, which affect the impeller and produce radial deflections of the pump shaft. The hydrodynamic excitation forces were calculated from the time dependent flow field, which was computed by numerical simulation of the three-dimensional, viscous, time-dependent flow in the pump. A commercial computer code was used to determine the time accurate Reynolds averaged Navier-Stokes equations. The transient radial flow forces at all time steps for a complete impeller revolution affect the rotor of the single-blade pump and stimulate it to strong oscillations. To determine the influence of the vibration stimulation forces on the dynamic behavior of the pump rotor, an investigation of the rotor's structural dynamics was accomplished. A dynamic time analysis for the pump rotor provided the dynamic answer from the structural model of the rotor under the influence of the flow forces. The hydrodynamic forces, which were calculated before, were defined as external forces and applied as the load on the rotor. The resulting impeller deflections were calculated by a transient analysis of the pump rotor system using the commercial finite element method software PROMECHANICA. *To verify the results obtained by standard numerical methods, the radial deflections of the impeller of a commercial sewage water pump, which has been investigated numerical in advance, were measured for the horizontal and for the vertical coordinate direction by proximity sensors. The measured data were compared to the computed amounts for a wide range of pump operation. The results show a good agreement for a strong part of an impeller revolution for all investigated operating points. The simultaneous measurement of vibration accelerations at the outer side of the pump casing showed the effects of the time-dependent flow, which produce hydrodynamic forces acting at the impeller of the pump and stimulating it to strong oscillations.* [DOI: 10.1115/1.2201629]

Keywords: single-blade impeller, hydrodynamic forces, rotor oscillations, flow induced vibrations

1 Introduction

The transport of sewage water is almost done by single-stage pumps. In order to avoid operational disturbances, most of the pumps are equipped with single-blade impellers. With this special impeller, geometry solids and fibers up to an appropriate size can be transported without clogging. But with this minimum rotor blade number strong disadvantages for the flow behavior can be expected. The flow around the blade produces a strong asymmetric pressure field at the perimeter of the impeller and the interaction of the flow with the casing leads to a periodically unsteady force. This force acts at the impeller and excites it to strong oscillations. So this force is also indicated as hydrodynamic unbalance [1–5]. The effects of the hydrodynamic forces can be recognized as vibrations at the bearing blocks or at the pump casing.

In Fig. 1 the measured head characteristics of a single-blade sewage water pump are shown. Additionally the vibration behavior of this pump has been measured in a wide range of operation. The radial acceleration amplitudes at the pump casing for two operating points are also shown in Fig. 1. The measured accelerations are increasing with increasing flow rate and they show maximum amounts of $a_{rad}=\pm 5\ m/s^2$ for an operating point which is close to the maximum flow rate. To lessen the vibrations of sewage water pumps, the hydrodynamic forces have to be reduced and that means that the pressure fluctuations have to be decreased. In order to make appropriate changes of the pump design, the knowledge of the transient flow field within the pump is very useful.

So in earlier papers the flow in single-blade pumps has been investigated very intensively by numerical methods. More details about the results of this research can be taken from [6–8]. In the present contribution the numerical and experimental investigation of the flow induced vibrations of a commercial single-blade sewage water pump is described in detail. The goal of this research was to learn more about the interrelation of the transient flow and the resulting rotor oscillations.

2 Numerical Investigation

2.1 Transient Flow in the Single-Blade Pump. In a numerical approach the transient, three-dimensional, viscous flow in a commercial single-blade sewage water pump was calculated with the Navier-Stokes solver CFX-TASCFLOW (unsteady Reynolds averaged Navier-Stokes) [9]. To start the investigation, volume models of the rotor shaft, the impeller and the casing were generated with the three-dimensional (3D) computer aided design system PROENGINEER. As the shapes of the impeller and the casing of the pump both had no symmetric plane in circumferential direction, a complete meshing of the fluid volume for these components was

Contributed by the Fluids Engineering Division of ASME for publication in the JOURNAL OF FLUIDS ENGINEERING. Manuscript received November 1, 2004; final manuscript received December 22, 2005. Review conducted by Joseph Katz.

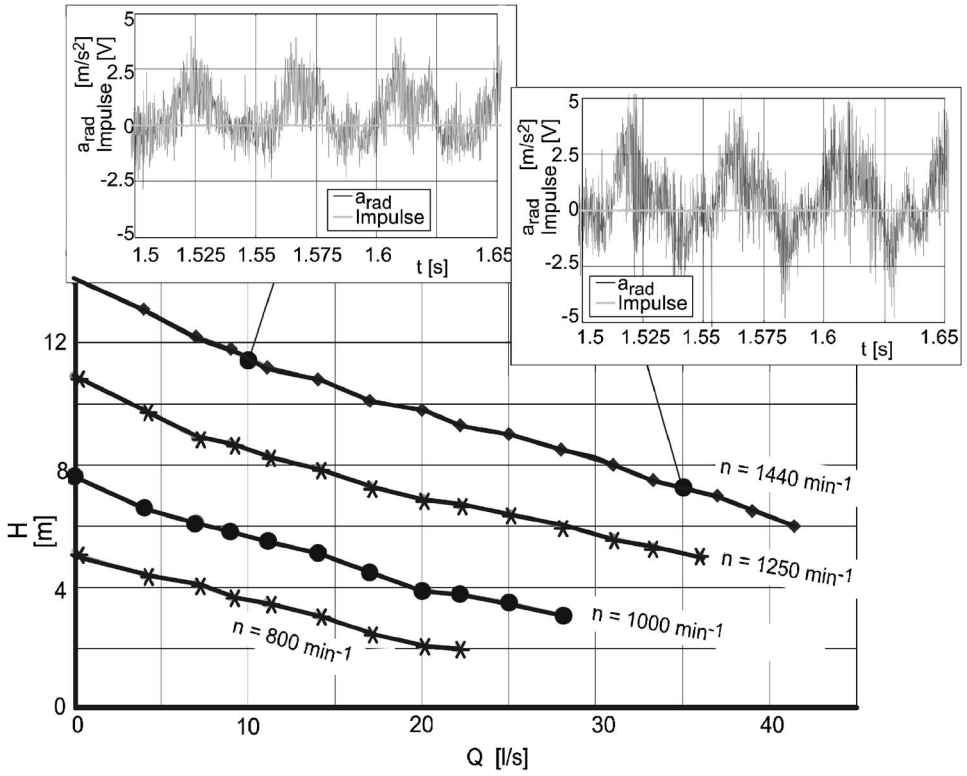

Fig. 1 Measured head characteristics and vibration amplitudes of a single-blade sewage water pump

necessary. To start the numerical investigations only the main flow path through the pump has been meshed. In a second approach the impeller side chambers, which are located between the outer side of the hub disk and the casing and between the outer side of the shroud disk and the casing, have also been taken into consideration. The calculation domain and some details of the grid at the blade leading edge and blade trailing edge are shown in Fig. 2. Separate block structured grids with 22 blocks and about 720.000 grid points for the impeller and 11 blocks and about 425.000 grid points for the casing were generated for the simulation which included the impeller side chambers. With this number of grid points the resolution of the boundary layers was sufficient. The maximum y^+ values were about 350. But these maximum amounts appeared in the vicinity of the outlet flange of the casing. Additional investigations with a larger quantity of grid points and a maximum value of $y^+ \leq 100$ have also been done. As the computed results showed only very small influence on the number of grid nodes, all calculations have been done with the coarser grid (about 1.15 million grid nodes). The time discretization has been accomplished with the implicit Euler method. This method is numerically stable and gives no limit for the time step. So the time step could be determined with the choice of an impeller angle of rotation $\Delta\varphi$ from Eq. (1). The accuracy of this time discretization is of first order, so the transient calculations exhibit likewise an accuracy of first order

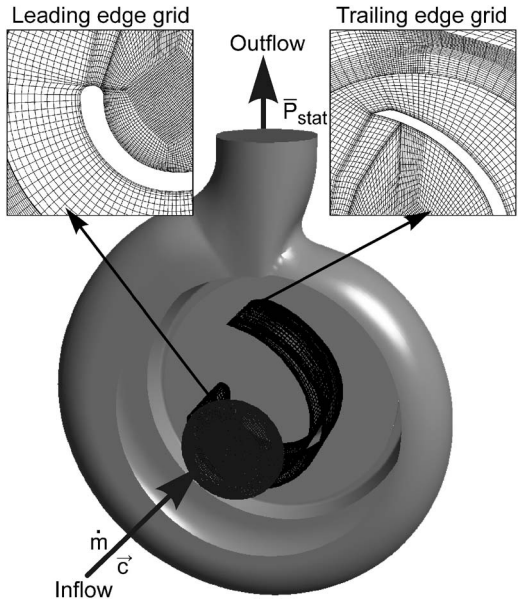

Fig. 2 Numerical model of a single-blade pump

$$\Delta t = \frac{\Delta\varphi \cdot \pi}{180|\omega|} \tag{1}$$

Calculations by Hansen [10] and Shi and Tsukamoto [11] as well as our own investigations showed that realistic transient results can be obtained with a maximum angle of rotation $\Delta\varphi = 3$ deg. Additional investigations with second order time discretization showed nearly no differences for the computed results.

The boundary conditions were stated at the inlet flange and at the outlet flange of the pump casing (see Table 1). The physical boundary conditions take into account that the walls were smooth and had a no slip condition for the fluid. The turbulence was modeled with the k-ω model using the shear stress transparent (SST) near wall formulation from Menter [12].

At starting time of the simulation an initial value distribution of the flow parameters as exact as possible has been required to allow a converging transient simulation. In the case described here, the pump impeller has been frozen in the casing in a position, which was present at the starting time of the calculation (see

Table 1 Boundary conditions and initial values for the transient numerical simulation

Boundary conditions and initial values	
Inflow	Mass flow and direction of absolute velocity vector
Outflow	Area averaged static pressure
Turbulence	k-ω turbulence model with SST function, (Tu=0.05)
Walls	Smooth walls, scaleable wall function, (u_W=0 m/s)
Fluid	Pure water, ρ=998.2 kg/m^3, ν=1.004 mm^2/s
Interface	Rotor/stator change of the frame of reference

Fig. 2). With this relative position of the computing meshes, a stationary solution for the flow has been determined to provide the initial parameter distribution (frozen rotor solution).

To evaluate the periodic flow field the results of a complete impeller revolution were needed. That means for a time step equivalent to $\Delta\varphi$=3 deg rotor turning angle 120 transient results. Since the initial value distribution of the flow parameters at the starting time emanated from a stationary solution, it did not contain the effects from the time-dependent terms of the Navier-Stokes equations. Although this was a useful starting solution, it required, however, the transient computation of several impeller revolutions to get a periodic behavior. During the numerical simulation the effects of the time-dependent terms were introduced into the calculation by continuous improvement of the solution from a previous time step. The computed delivery head of the pump had been chosen as an indicator for the periodicity of the flow. At all investigated operating points the initial value distribution was a stationary frozen rotor solution and several impeller revolutions (up to eight) were needed, until the flow became periodic.

In Fig. 3 the calculated distribution of the static pressure in a plane normal to the machine axis at half blade height of the pump is represented at four impeller positions for the last computed impeller revolution. The operating point of the pump for this result was the volume flow at best efficiency ($Q_{\text{b.e.p.}}$=33.3 L/s) at the nominal rotor speed (n=1450 min^{-1}). The first picture shows the impeller in the starting position (φ=0 deg). In this position the highest pressure level can be stated. During the rotation of the impeller the pressure level drops continuously and reaches a minimum at an angle of rotation of φ=270 deg. At the rotation angle φ=360 deg the pressure distribution at the starting position φ

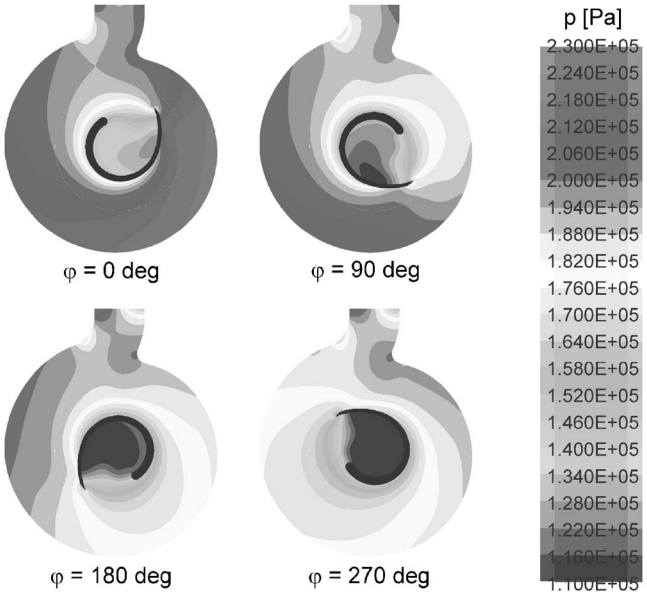

Fig. 3 Calculated static pressure distributions at several impeller positions (half blade height)

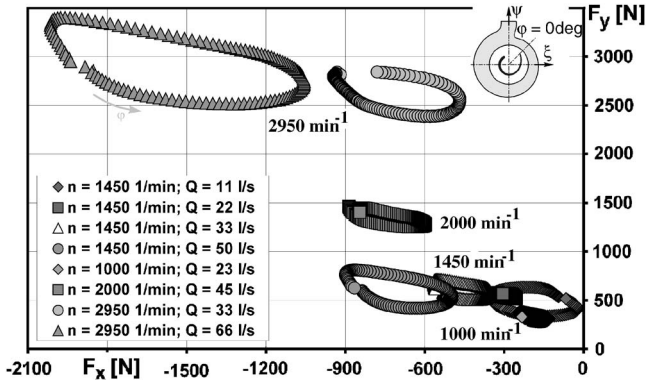

Fig. 4 Calculated radial hydrodynamic forces for several operating points without taking impeller side chamber flow into account

=0 deg is again nearly reached. This provided evidence that the buildup process of the periodic flow is finished and the flow field repeats itself per impeller revolution.

2.2 Hydrodynamic Forces. From the flow field, which was obtained by transient numerical simulation, the hydrodynamic forces acting at the impeller of the pump could be computed. The pressure forces were calculated from the normal stresses and the friction forces from the tangential stresses by integrating Eqs. (2) and (3) over the complete fluid wetted surface of the impeller. The sum of the friction and the pressure forces at all time steps for one impeller revolution has been indicated as the resulting transient hydrodynamic forces (Eq. (4))

$$\mathbf{F}_p = -\int_A p \cdot \mathbf{e}_n \cdot dA \tag{2}$$

$$\mathbf{F}_f = -\mu \int_A d\mathbf{u}/dn \cdot \mathbf{e}_n \cdot dA \tag{3}$$

$$\mathbf{F}_R(\varphi) = \mathbf{F}_p(\varphi) + \mathbf{F}_f(\varphi) \tag{4}$$

In Fig. 4 the so calculated hydrodynamic forces for several operating points at different speeds of impeller rotation are presented. These results have been obtained by numerical simulation without regarding the impeller side chambers of the pump. Using a right-angled coordinate system, which is rotating with the impeller, the y components are plotted versus the respective x components for a complete impeller revolution in 120 time steps ($\Delta\varphi$=3 deg). To investigate the oscillations of the pump impeller only the radial forces were recognized.

All radial forces appear in the second quadrant of the coordinate system and within one impeller revolution big differences of the forces were obtained. The fact that some curve paths are not completely closed is related to the buildup process of the transient flow which was not fully periodic in those cases. The forces increase strongly with increasing impeller speed of rotation and also with increasing flow rate. Also the variation of the forces within one impeller revolution become stronger with increasing impeller speed of rotation.

In Figs. 5(a) and 5(b) the results of the numerical simulations were investigated in more detail. The forces which arose during one impeller revolution were arithmetic averaged and plotted versus the flow rate (Fig. 5(a)) and versus the rotational speed of the impeller (Fig. 5(b)).

For a constant speed of impeller rotation the amounts of the averaged forces increase nearly proportional to the volume flow rate and for a constant volume flow rate the hydrodynamic forces rise strongly with increasing rotor speed. As the hydrodynamic

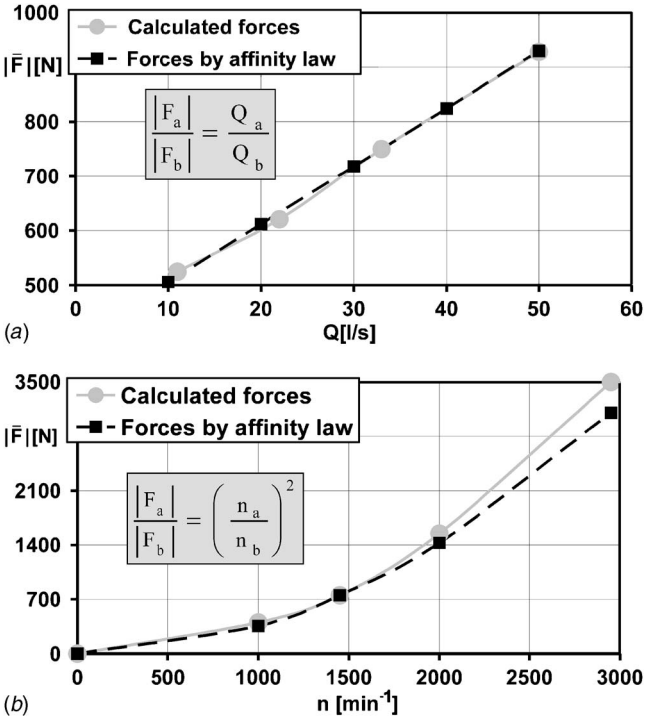

Fig. 5 (*a*) Averaged hydrodynamic forces depending on flow rate, (*b*) averaged hydrodynamic forces depending on rotational speed

forces are mainly provoked by the pressure distribution around the blade, it is obvious that the forces increase with a nearly quadratic function with increasing speed of rotation like it is already known for the pump head. So some kind of affinity laws were applied to check the dependence of the hydrodynamic forces from the flow rate and from the impeller speed of rotation. As can be seen from Figs. 5(*a*) and 5(*b*) the computed forces coming from the numerical simulation are very close to those calculated from the affinity laws, which are given by the formulas in both figures.

2.3 Structural Dynamics of the Pump Rotor. To compute the oscillations of the pump rotor induced by the calculated exciting forces, a coupled solution of the flow field in the pump and of the structural mechanics of the pump rotor is required (see Schäfer et al. [13]). In Fig. 6 the basic scheme of an arbitrary fluid-solid calculation is shown.

In the present case a simple approach has been used because of its flexibility concerning the solvers for the individual fluid and solid simulations. The choice was a fully explicit partitioned coupling involving an alternating solution of the fluid and the solid problem with simple interchange of boundary conditions by data files. So it was possible to use existing software packages and to benefit from their advanced features. For the fluid solution the choice was CFX-TASCFLOW while for the structural analysis the 3D finite element method (FEM) model PROMECHANICA has been used. Unfortunately, the nodes of the grid for the computation of

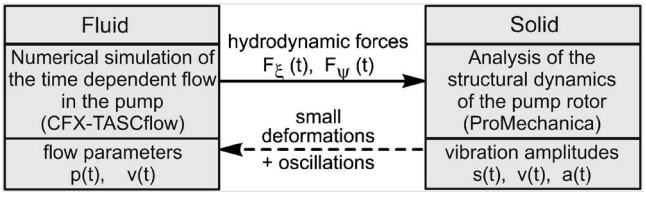

Fig. 6 Coupling model of a fluid-solid problem

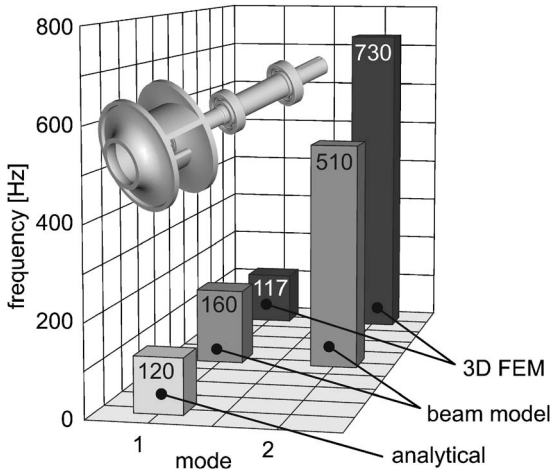

Fig. 7 Calculated natural frequencies of the single-blade pump rotor

the flow and the nodes of the grid for the solid did not match at the surface of the impeller. So it was very complicated to transfer the information about the pressure field from the flow simulation to the structural computation and vice versa by data files. To avoid these problems the information was transferred using the calculated hydrodynamic forces and with respect to expected small deflections of the pump rotor the information transfer has been directed only from the fluid problem to the solid problem in the present case (see Fig. 6). No backlash from the solid solution to the fluid solution has been taken into account.

An exact investigation of the rotor's structural mechanics requires the transfer of the real pump rotor into a computer model as realistic as possible. In relation to the reality the designed structure model of the rotor differed from the real rotor only in a few details, as, for instance, the roundings at the shaft and at the blade in the present case. The stiffness of the bearings has been modeled by data from the original bearings provided by the manufacturer, so the constraints at the bearing seats could be specified in a realistic manner.

Initially a modal analysis has been accomplished to compute the natural frequencies and the natural modes of the rotor. For this investigation the number of volume elements of the structure mesh has been varied between 3000 and 9000 to study the influence on the results. This variation resulted in negligible differences for the calculated natural frequencies. In Fig. 7 the computed natural frequencies of the first two modes are plotted as bars. To validate the numerical calculations the results from the 3D-FEM model were compared to an analytical solution and to a beam model. The analytical solution and the 3D-FEM calculation gave nearly the same natural frequencies for the first mode ($f_1 \approx 120$ Hz). The second and higher modes were not of interest for the investigation performed here because the frequencies were considerably high compared to the rotor turning frequency ($f_{\text{rotor}} \approx 24$ Hz; $f_2 \geq 700$ Hz). To save some computing time a medium number of about 6000 elements was used for the following structural analysis of the rotor.

2.4 Calculation of Rotor Oscillations Due to Hydrodynamic Forces. To calculate the deflections of the rotor provoked by the hydrodynamic exciting forces alone, a dynamic time analysis of the structural model of the rotor has been accomplished. As pump rotors usually are balanced during the manufacturing process, all forces from the mechanical unbalance were assumed to be zero in the present simulation. The before calculated hydrodynamic forces (without impeller side chambers) were applied as the load on the rotor during a time which was equivalent to eight rotor revolutions. At the beginning of the ninth revolution the load was

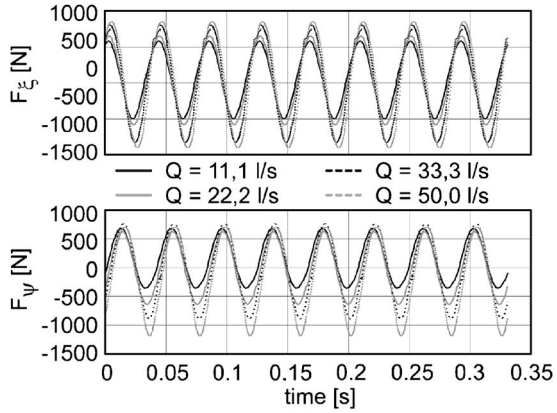

Fig. 8 Hydrodynamic forces obtained by numerical simulation for nominal speed of rotation

set to zero.

In Fig. 8 the components of the forces are transferred to the absolute frame of reference (ξ-, ψ-coordinate system) for four volume flow rates at the design speed of rotation. As also shown in Fig. 4 for the relative frame the forces increase with the volume flow rate. At this point it should be recalled that these hydrodynamic forces, which act as the loading at the impeller, were computed without regarding the impeller side chambers of the pump. As the shape of the impeller blade was strongly two dimensional, the attacking plane of the forces at the rotor has been assumed to be at a position which is characterized by half the blade height. From this attacking point, which was chosen somewhat arbitrarily and in combination with the amounts of the forces, the deflections of the rotor could be determined by a dynamic time analysis.

For these numerical simulations a global damping of 3% for the amplitudes in the modal range has been chosen. As the simulations have been done without consideration of rotor turning, no gyroscopic forces were taken into account. The goal of the dynamic time analysis was the determination of the time-dependent vibration deflections at the junctions of the structural rotor model. The computed values at the outermost point of the impeller are represented in Fig. 9 for four operating points at nominal speed of rotation ($n=1450\ \text{min}^{-1}$). The radial deflections are plotted separately for the ξ and for the ψ coordinate for about 12 impeller revolutions. The curves reflect the functions of the stimulating forces, because the amplitudes are small and the computation is in the elastic regime of the material. So the deflections are nearly proportional to the stimulating forces. They are small for small volume flow rates and they increase with the volume flow rate as the forces do (see Fig. 8). At the starting time of the simulation, the load has been applied abruptly. A strong overshooting of the calculated deflections was the result of such impulsive stimulation. After three to four rotor revolutions, the overshooting was damped out and the computed deflections were believable. When the load was set to zero after eight rotor revolutions, the rotor oscillations dyed out with nearly the frequency of the first mode within the next four impeller revolutions.

Another illustration of the impeller deflections is shown in Fig. 10. The presentation of the deflections in ψ direction versus the deflections in ξ direction for the seventh impeller revolution after applying the load gives the calculated orbit curves which are described by the impeller when it is attacked by the hydrodynamic forces shown in Fig. 8.

The arrows indicate the starting positions of the impeller. The orbits rotate in clockwise direction as the impeller does. For an impeller position where no deflection in ψ direction has been detected, the deflections in positive ξ direction are nearly the same for all operating points, while the deflections for negative ξ directions increase strongly with the flow rate. For the overload condition the maximum deflections exceed $\Delta s = \pm 0.2$ mm.

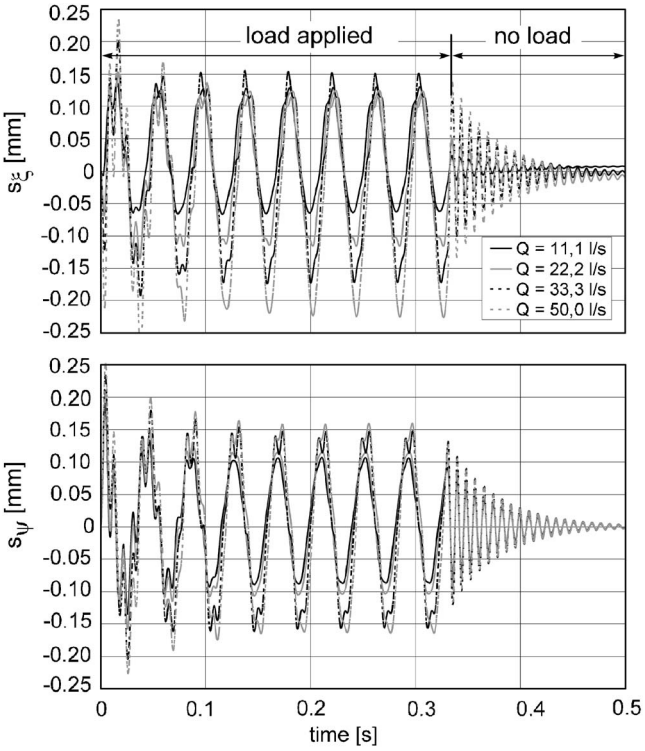

Fig. 9 Computed deflections due to hydrodynamic forces for four operating points (nominal speed of rotation)

To reflect the impact of the impeller rotating speed on the rotor deflections, the computed orbit curves are represented for several speeds of rotation in Fig. 11. Similar to Fig. 10 the shape of the curves reflects the functions of the stimulating forces and the orbits are rotating in clockwise direction. The deflections increase strongly with the rotor speed as the hydrodynamic forces do (see Fig. 4). All investigated operating points should be the operating points of best efficiency at the associated pump characteristic for a constant rotor speed. The deflections for the impeller speed of rotation $n=2950\ \text{min}^{-1}$ exceed the amount of $\Delta s = \pm 0.8$ mm which is much too high for the pump. Such strong oscillations of the impeller produce strong stresses for the shaft of the pump. So this pump is only allowed to be operated with a maximum rotor speed of $n=1450\ \text{min}^{-1}$.

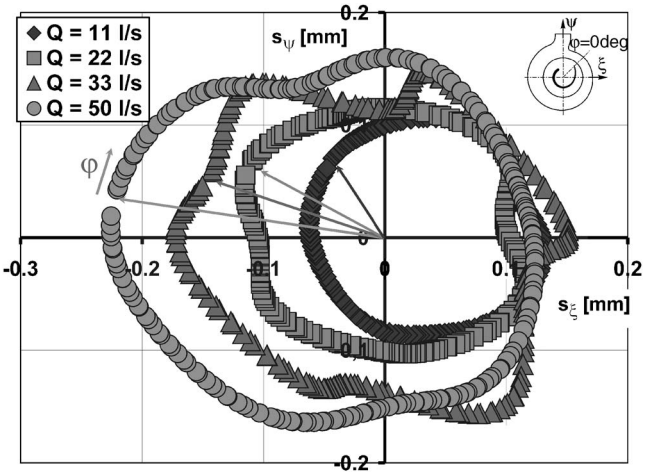

Fig. 10 Calculated impeller orbit curves

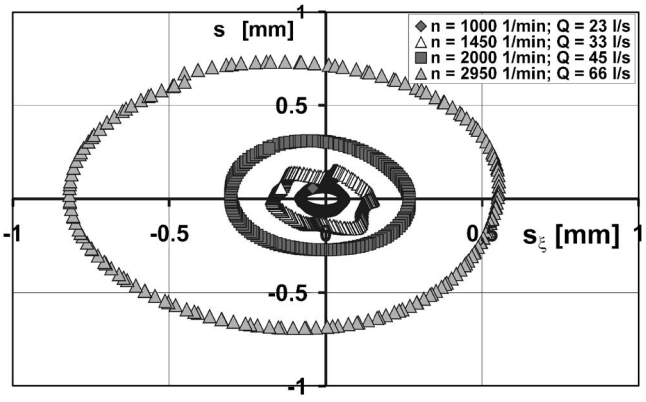

Fig. 11 Calculated rotor oscillations due to hydrodynamic forces for different speeds of rotation

3 Experimental Investigation

3.1 Test Facility. To verify the computed deflections of the impeller by experimental methods, a test stand is necessary. To accomplish the tests very practical, the before numerical investigated commercial single-blade sewage water pump has been chosen for the experimental investigations. A volume model of the complete test facility is shown in Fig. 12. The pump was horizontally arranged and the supply head was about $H_s = +1.5$ m.

The pump was appointed in an open loop. The tank contained about 8 m^3 of pure industrial water. So the heating of the water during the tests was negligible. The electric drive had been carried out with variable speed of rotation and it was attached by flexible bellow couplings to a torque meter and to the pump shaft. The inner diameter of the pipes at the suction side and at the pressure side was $d_{s,p} = 100$ mm. The volume flow rate was measured by an inductive flow meter and the point of pump operation could be adjusted by a control valve located behind the flow meter.

3.2 Instrumentation of the Pump. The pump, which had been investigated numerically in advance, has been equipped with several sensors. The pressure at the suction side (p_s), at the pump discharge (p_d) and inside the volute (p_{vol}) was measured by piezoresistive sensors which had an accuracy of 0.5% FS. The accelerations at the pump casing in radial (a_{rad}) and in axial (a_{ax}) direction were measured by small size integrated circuit piezoelectric accelerometers employing a shear sensing element with a

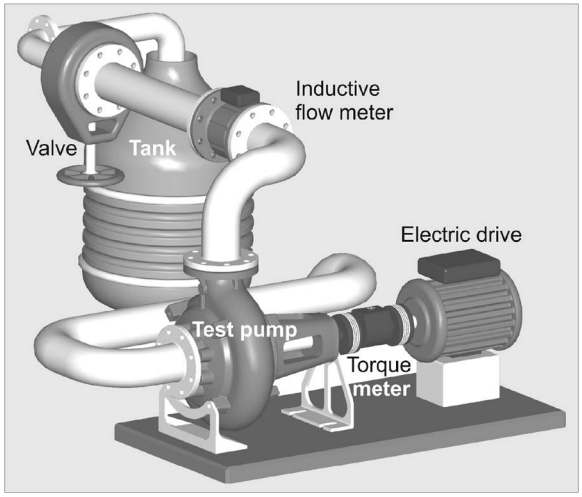

Fig. 12 CAD volume model of test facility for the single-blade centrifugal pump

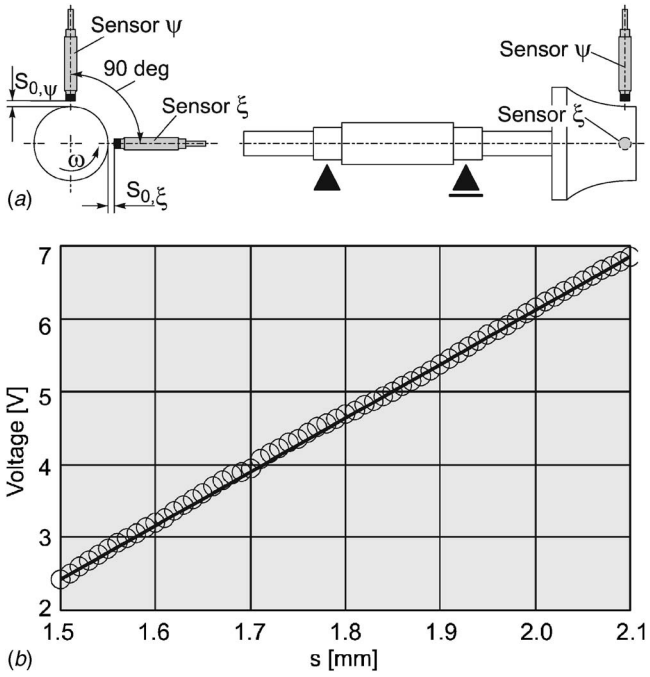

Fig. 13 (*a*) Application of proximity sensors, (*b*) sensor calibration curve

ceramic crystal [14]. The sensitivity of the sensors was about 100 mV/g. The frequency range extended from 0.27 Hz to 10 kHz (±3 dB). The sensors were attached to the outer side of the pump casing at a smooth flat contact surface by stud mounts. This fixing has been chosen because of its very rigid behavior. So a comfortable transfer of the vibrations was possible.

Non-contact displacement sensors are utilized to measure distances or positions of any electrically conductive target. The test principle is based on the electromagnetic induction and reaction. According to Faraday's induction law, the induced eddy current flows in an electrical metal conductor, if the conductor is located in a time changeable magnet field. The magnet field is generated by an alternating current flowing in a wire coil. The eddy current generates an opposite magnet field, which superimposes with the exciting magnet field. As a consequence, the impedance of the sensor coil changes. Due to the high insensitivity to water, dirt, and interference fields, etc., sensors working on the eddy current effect are eminently suitable for applications in harsh environments (see Wilde and Lai [15]). The here used proximity sensors measured the deflections of the rotor in the ξ direction and in the ψ direction at the same axial location where the calculations were done before. They were performed with a mail screw thread with small flank lead at the pump casing, so they could be mounted like studs, and the adjustment of the zero values $s_{0,\xi,\psi}$ was very easy. The sensor ψ was shifted by exactly 90 deg relative to the sensor ξ in the direction of impeller rotation. The used arrangement of the proximity sensors is shown in Fig. 13(*a*).

For precise measurements the sensors were calibrated with exactly the same material which was used for manufacturing the pump impeller (gray cast iron). The calibration of the sensors gave a nearly linear relationship between the output signal and the distance of the sensor to the rotor. The linear measurement range extended between 1 and 4 mm distance to the outer impeller suction diameter. For the measurements accomplished here only a small part of this calibration curve was used. In Fig. 13(*b*) the measured points and the developed calibration curve of the sensors are shown. The behavior of the sensors was nearly linear. When changing the distance between the sensor and the rotor by $\Delta s = 1$ mm the calibration curve gives a voltage difference of

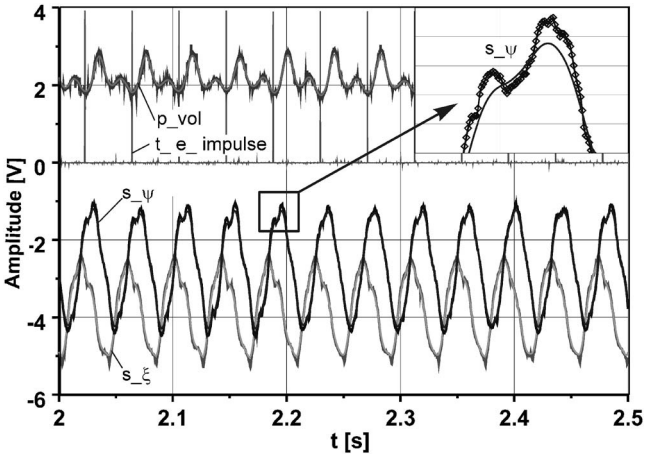

Fig. 14 Measured raw signals of sensors for the operating point: n=1440 min^{-1}, Q=11 L/s

7.838 V. For the expected maximum rotor deflections of about 0.5 mm$\leq\Delta s\leq$1 mm this sensitivity of the sensors seemed to be sufficient for the intended measurements. The sensors were attached to the casing with a distance to the impeller of about $s_{0,\xi,\psi}$=1.7–1.9 mm for no impeller rotation. The surface at the outer impeller suction diameter was properly machined in advance.

The actual angular position of the rotor was indicated by an additional inductive pulse sensor. When the trailing edge of the blade passed the position of this sensor a voltage pulse of 4 V was registered. This signal gives an additional information which is used to determine the phasing of the impeller. All measurements were accomplished by a PC driven electronic measurement data recording system [16] and a data acquisition card for 16 channels with an overall sample rate of 500 *k*Samples/s and a resolution of 12 bit. The analog signals were scanned with a frequency up to 10 *k*Samples/s per channel depending on the number of used channels [17]. Addicted to the impeller speed of rotation the data of up to 50 impeller revolutions were recorded per measurement [18].

3.3 Measured Rotor Oscillations Due to Hydrodynamic Forces Alone. In Fig. 14 the measured raw signals of the proximity sensors are represented versus the time for the best efficiency flow condition ($Q_{\text{b.e.p.}}$=33.3 L/s) at nominal impeller speed of rotation (n=1440 min^{-1}). Additionally the signal of the static pressure in the casing and the voltage pulse of the passing impeller trailing edge are plotted in this figure. It can be seen very clearly that the pressure inside the volute and also the deflections of the impeller are repeated permanently per impeller revolution. For further processing all measured pressure signals and all signals of the proximity sensors were digitally filtered with a Butterworth low-pass filter using a limiting frequency of 100 Hz. As shown, for example, for the vertical deflection of the impeller in the zoom box, with the utilized filter parameters the measured data persisted nearly unchanged except the very small oscillations of the signals, which are introduced with high frequency and can be identified as noise from the surroundings and is no mechanical deflection of the impeller.

All measurements have been done by the same procedure: First a measurement without water at a very small speed of impeller rotation ("slow rotation") has been accomplished. Thus the existing bearing clearances and the deviations from the roundness of the outer impeller suction diameter were registered. After that a measurement without water ("dry") but with the actual speed of rotation has been performed. The comparison of these two measurements showed only very small differences at all speeds of rotation. This provided evidence that the rotor was mechanically balanced sufficiently.

Subsequently, the pump was operated with the actual speed of rotation and with the actual volume flow rate ("wet"). For these cases the deflections of the rotor caused by the hydrodynamic forces, as well as by possible mechanical rest unbalances and the deviations from the roundness of the outer impeller suction diameter, were measured. The actual deflections of the rotor then were determined by substracting the measured values dry from the values wet. From this procedure positive and negative values of the real rotor deflections arise. The so calculated actual deflections for the ξ and the ψ coordinate can be plotted as functions of the impeller turning angle φ for all investigated speeds of impeller rotation and all volume flow rates. By plotting the amounts of the deflections at the same impeller turning angle for two associated curves (for the abscissa the ξ value and for the ordinate the ψ value) in a common diagram, an orbit curve of the shaft axis can be determined for every operating point under investigation. These orbit curves represent the deviations of the actual impeller axis from the machine axis due to the hydrodynamic forces alone. For the starting position of the impeller (φ=0 deg) the curves start in the second quadrant of the ξ,ψ-coordinate system. In this quadrant the ξ deflections are negative and the ψ deflections are positive. Negative values of the measured deflections mean that the distance between the sensor and the impeller is smaller than the adjusted value s_0 for no impeller rotation. This situation occurs for an impeller position where the hydrodynamic force resulting from the pressure field is acting against the positive ξ or ψ coordinate. At the starting point of the impeller the force F_R which is affecting the pressure side of the impeller leads to the negative rotor deflection in ξ direction. As the attacking angle of the hydrodynamic forces varies only little during one impeller revolution, the exciting forces seem to rotate with the impeller. Depending on the change in magnitude of the forces during an impeller revolution, the orbit curves in the absolute coordinate system become nearly circular or elliptic.

In Figs. 15(a)–15(c) the so measured orbit curves of the pump rotor are represented for three speeds of impeller rotation and several volume flow rates for each rotational speed. The results make clear that for all speeds of rotation the deflections increase with increasing volume flow rate. The largest deflections have been measured for the highest and the smallest deflections for the lowest speed of rotation. All curves show qualitatively the same tendency as the calculations do (see also Figs. 9 and 10). At the starting position of the impeller ($\varphi\approx$0 deg) the impeller deflections appear in the second quadrant of the absolute coordinate system for all speeds of rotation and all operating points. The direction of rotation of the deflection vector for all investigated operating points is in the clockwise direction.

For all operating points shown in Figs. 15(a)–15(c) the measured impeller deflections have nearly the same positive ξ value for zero ψ deflection, which is not dependent on the flow rate for a certain speed of impeller revolution. For all operating points a constant deflection magnitude has been measured for an impeller turning angle of about $\Delta\varphi$=180 deg. That means that the hydrodynamic forces have nearly the same amount at the impeller position $\varphi\approx$180 deg for the same speed of rotation. This is due to the pressure field, which is rotating with the impeller and which gives similar hydrodynamic forces for all operating points. At this impeller position the deflections in the ξ direction have a nearly equal value and the deflections in ψ direction are about zero. This result is comparable to the results of the numerical simulation in Figs. 10 and 11. At an impeller position between $\varphi\approx$300 and $\varphi\approx$330 deg the ψ deflections are again nearly zero and the ξ deflections increase strongly with increasing volume flow rate. This was also the result of the numerical investigations presented in Fig. 10. With increasing impeller turning angle all measured rotor orbit curves rotate in a clockwise direction. The impeller is also rotating in a clockwise direction. So the rotation of the shaft orbit corresponds to the rotating direction of the impeller orbit.

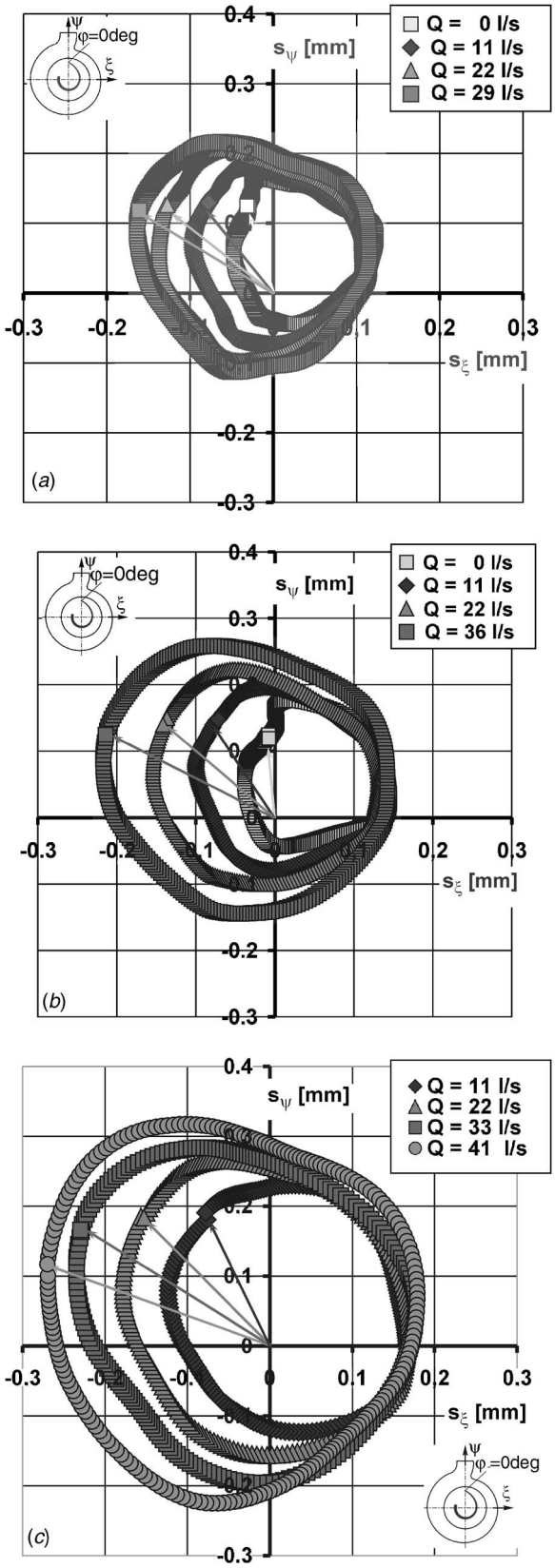

Fig. 15 (*a*) **Rotor orbits for** $n=1000\ \text{min}^{-1}$, (*b*) **rotor orbits for** $n=1250\ \text{min}^{-1}$, (*c*) **rotor orbits for** $n=1440\ \text{min}^{-1}$

3.4 Measurement of Vibration Accelerations. Beside the oscillations of the rotor, the exciting hydrodynamic forces also generate structural vibrations of the pump. The effects of the stimulating forces can be shown very clearly by measuring the vibration properties at the outside of the pump casing.

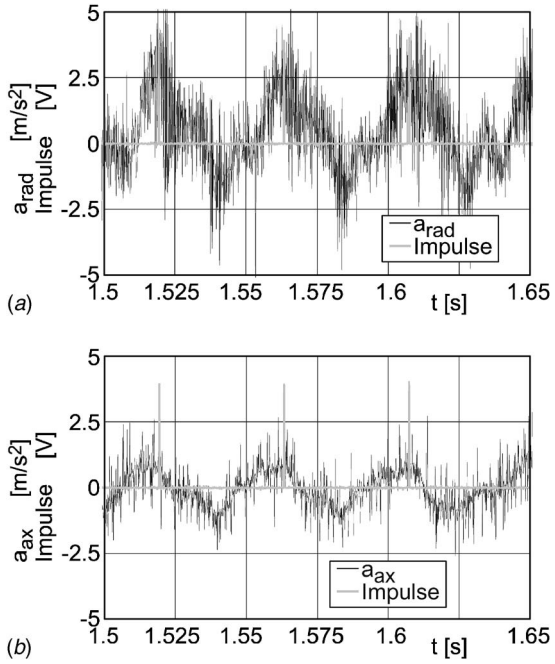

Fig. 16 (*a*) **Radial accelerations at the pump casing,** (*b*) **axial accelerations at the pump casing**

The axial accelerations for the measurements obtained in this research in general are smaller than the radial ones. The maximum amplitudes of the radial accelerations for an operating point close to the point of best efficiency at nominal rotor speed ($Q=35$ L/s, $n=1440\ \text{min}^{-1}$) are about $a_{\text{rad}}=\pm 5\ \text{m/s}^2$ and the axial accelerations $a_{\text{ax}}=\pm 2.5\ \text{m/s}^2$.

In Figs. 16(*a*) and 16(*b*) the time signals of both acceleration sensors are shown for about three impeller revolutions. The peaks at every 41 ms show the voltage pulse indicating the passing blade trailing edge. The low frequency amplitudes which appear at the rotor turning frequency ($f=24$ Hz) are superposed by amplitudes which appear at higher frequencies. From the presentation of the radial accelerations some small amplitudes at a frequency which is twice the rotors turning frequency can be found. For the axial accelerations the rotor turning frequency is dominating the time signal.

In Figs. 17(*a*) and 17(*b*) the frequency spectra obtained by fast Fourier transform are shown for several flow rates at the nominal speed of impeller rotation. The amplitude spectra of the radial accelerations show the first significant amplitude at the rotor turning frequency ($f\approx 24$ Hz). Small amplitudes appear at a frequency twice the rotor turning frequency and at a frequency of $f=50$ Hz which should be the supply frequency. The amplitudes of the third mode are much smaller than at the rotor turning frequency but they are noticeable anyway. For the fourth mode some small amplitudes were also recognized but beyond this frequency no significant amplitudes appear.

For the axial accelerations the situation is comparable to the radial accelerations for the first three modes. The amplitudes are strongest for the impeller turning frequency. At the second and third harmonic frequency the amplitudes are much smaller for all operating points. The supply frequency ($f=50$ Hz) can also be seen in the spectra. At higher frequencies (fourth and higher modes) no recognizable amplitudes can be found.

4 Comparison of Measurements to the Results of the Numerical Simulations

The numerical investigations should be validated by the measurements which were done at a commercial single-blade sewage

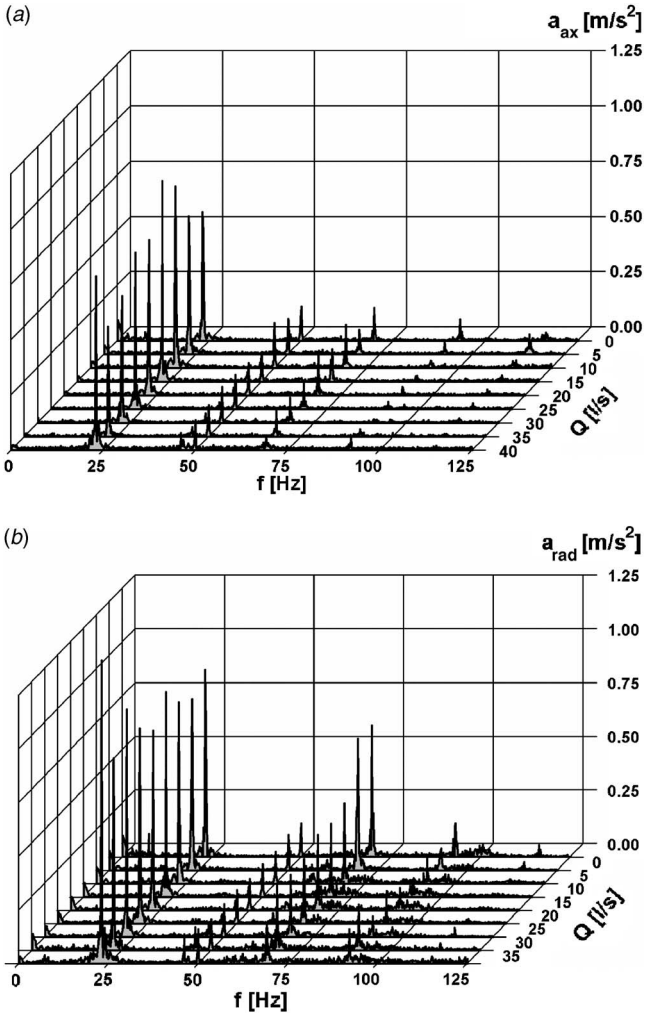

Fig. 17 (*a*) Frequency spectra of radial accelerations (n = 1440 min^{-1}), (*b*) frequency spectra of axial accelerations (n = 1440 min^{-1})

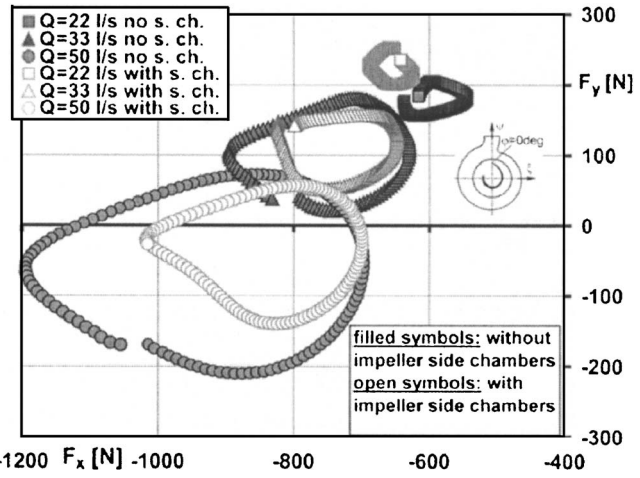

Fig. 18 Influence of impeller side chamber flow on hydrodynamic forces

water pump. For a correct comparison of numerical and experimental results it is important that the same conditions exist for the measurements and for the simulation. So the numerical simulation should cover all the flow features of the complete flow field in the pump and the results should be exactly synchronized to the measurements.

4.1 Hydrodynamic Forces Taking Impeller Side Chambers Into Account. The results of the numerical simulations presented in Fig. 4 did not take into account the fluid volume between the outer side of the hub disk and the casing and between the outer side of the shroud disk and the casing. By this method not all flow features were included in the investigation. To show the influence of the flow in these impeller side chambers on the hydrodynamic forces, for three operating points at the nominal speed of rotation, new numerical simulations including the flow in the impeller side chambers have been done. In Fig. 18 the hydrodynamic forces, which have been calculated with and without impeller side chambers, are compared to each other. As the starting position of the impeller for the calculations with and without impeller side chambers was different, for this comparison the impeller positions in the casing for both numerical examinations must be synchronized. For Fig. 18 the calculated results were converted to the impeller starting position which was present for the measurements. So the calculated hydrodynamic forces without taking the impeller side chambers into account are the same as before but the presentation differs from that in Fig. 4. Now the forces appear in the second and in the third quadrant of the relative coordinate system. As can be taken from Fig. 18 the calculated forces, including the impeller side chamber flow, also appear in the second and in the third quadrant of that coordinate system and the shapes of the curves for the forces with and without impeller side chambers for the same flow rate are very similar. The variation of the forces during one impeller revolution is somewhat smaller when taking the side chambers into account. This holds for all three operating points under investigation.

The flow between the outer sides of the disks and the pump casing seems to have a damping effect on the pressure fluctuations during the rotation of the impeller. Figure 18 shows that there is a certain influence of the impeller side chamber flow on the main flow and finally on the magnitudes of the hydrodynamic forces and in particular on the attacking angle α of the flow forces, which is changing by about $\Delta\varphi = 15$ deg for all impeller positions during one revolution.

4.2 Comparison of Measured and Calculated Rotor Orbit Curves. In this chapter the measured impeller orbit curves are compared to the curves which were obtained by numerical simulation. The impeller deflections have been recalculated by the method described in Sec. 2.4 using the hydrodynamic forces which took the impeller side chambers into account. In Figs. 19(*a*)–19(*c*) the calculated rotor orbit curves for a part load operating point ($Q = 22$ L/s), for the design point ($Q = 33$ L/s) and for an overload operating point ($Q = 50$ L/s) are compared to the measured ones for the nominal rotating speed. As the calculations have been done before establishing the test facility, at this time it was believed that the maximum flow rate at the design speed of rotation should be $Q = 50$ L/s. After construction of the test stand the maximum available discharge flow was only $Q_{\text{max,exp.}} = 41$ L/s which is compared to $Q_{\text{calc.}} = 50$ L/s in Fig. 19(*c*).

The comparison of these orbit curves shows that there is a good qualitative conformity between the measurements and the computation results for all operating points under investigation. The quantitative agreement is also very good for about half of the impeller revolution. In the other half of the impeller revolution the measurements provided stronger impeller deflections than the simulations did. The maximum difference of the calculated deflection magnitudes from the measured ones is up to nearly 30% of the measured values for all operating points during this part of impeller revolution. The rotation of both the measured and the calculated orbits are in a clockwise direction. The computed de-

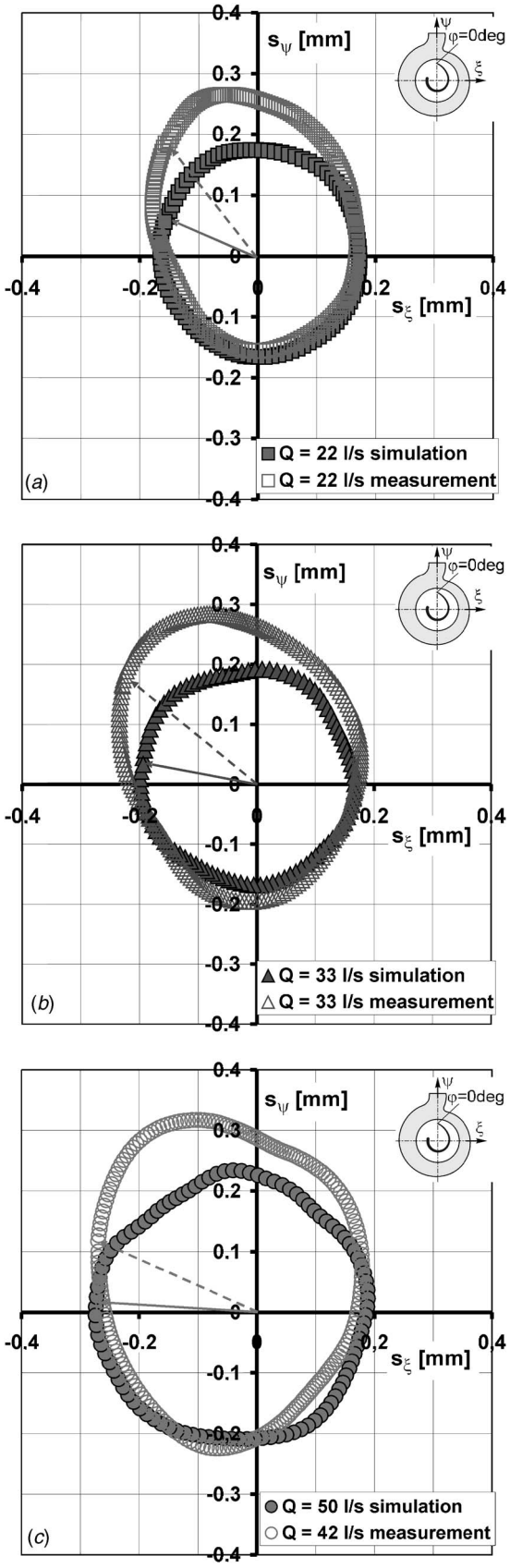

Fig. 19 (*a*)–(*c*) **Comparison of calculated and measured rotor orbit curves for three flow rates**

flections in ψ direction at the starting point of the impeller are smaller than the measured values (see the arrows) for all operating points.

The discrepancies between measurement and simulation begin to emerge when the trailing edge of the blade approaches the discharge socket of the pump. The reason may be a backlash of the pressure in the pipe to the impeller. The high pressure in the pipe comes back to the pump casing and acts at the blade suction side of the impeller which is now opposite to the discharge socket. This leads to strong deflections in the ψ direction which could not be obtained by the numerical simulation. Because of the steady boundary condition ($\bar{P}_{\text{stat}}$=const.) at the pump outlet this pressure backlash did not exist during the simulation of the transient flow. For the shown results in Figs. 19(*a*)–19(*c*) it can be stated that in general the tendency of the numerical results was confirmed by the experiments, but the measurements show strong deflections for about half of an impeller revolution. Beside the above already noted reason some more inducements for this deviation are imaginable:

(1) For the numerical calculation of rotor deflections the lever arm of the forces has been chosen somewhat arbitrarily at half the blade height. The assumption that the forces act at half the blade height makes the loading for the structural analysis in some way inaccurate.
(2) The rotation of the rotor has not been considered during the dynamic structural analysis. So the gyroscopic forces were not included in this investigation.
(3) The measured rotor deflections were in the range of about $\Delta s = \pm 0.3$ mm depending on the operating conditions. Such substantial deflections will have reactions on the flow which were not considered in this contribution, because of the utilized one way coupling between fluid and structure simulation.
(4) The bending moments produced by asymmetric axial forces have not been taken into account during the numerical simulations.
(5) The roller bearings of the pump rotor had a certain clearance. This also was not considered during the numerical investigations.

5 Conclusions

The hydrodynamic forces in a single-blade sewage water pump are decisive for strong impeller deflections. These rotor oscillations are transferred to the pump casing and to attached pipes and to other equipment. There they can be recognized as vibrations which are stressing all equipment components (pump seals and bearings, pump shaft, pipe mounts) in a considerable way. Very often the level of vibration amplitudes leads to a pump failure or to damages at the pipes and their mountings.

The numerical and the experimental investigations in this paper show that the pressure fluctuations inside the pump volute and subsequently the resulting rotor oscillations are periodic with the impeller rotation. The hydrodynamic forces during one impeller revolution increase with increasing flow rate at a constant speed of rotation. The rotor oscillations show the same behavior: The impeller deflections increase with increasing flow rate at constant rotor speed. When varying the speed of rotation for constant flow rate the strongest rotor oscillations were recognized at the highest rotor speed, where also the pressure level is highest. The amounts of the vibration amplitudes of the pump are a function of the stimulating hydrodynamic forces. The frequency spectra of the vibration accelerations measured at the outside of the pump casing show strong amplitudes at the rotor turning frequency.

The comparison of measured and calculated results shows that the determination of the rotor oscillations, which are evoked from the exciting hydrodynamic forces, is possible by using commercial numerical codes for the transient flow in the pump and for the structure dynamics of the rotor. The coupling of the computation

methods for the fluid dynamics and for the structural dynamics (FEM) must be closer the bigger the impeller deflections are. The one way coupling which was used in this paper provided a good qualitative agreement between measurements and calculation, but only for half of the impeller revolution the quantitative agreement is also good. The accuracy of the method can be improved by a stronger coupling mechanism (two way coupling) between the flow solution and the analysis of the structural dynamics. With a data interchange between the alternating solutions of flow and structural dynamics, the reaction of the rotor deflections on the flow can be taken into consideration which will lead to more sophisticated results.

The presented investigation suggests that it is possible in the near future to make a statement about the vibration behavior of a (sewage water) pump already during the design process. With the usage of this information during the design procedure of a pump the layout can be optimized regarding the pump vibration behavior.

Nomenclature

Symbols

A = area
a = vibration acceleration
d = diameter
$\mathbf{e}$ = vector normal to a wall
$\mathbf{F}$ = force
f = frequency
H = delivery head
n = speed of rotation
p = pressure
Q = volume flow rate
s = rotor deflection
t = time
$t.e.$ = trailing edge
u = velocity
x, y = coordinates in the rotating frame
y^+ = non-dimensional wall distance

Greek Letters

α = attacking angle
Δ = difference
φ = angle of rotation
μ = dynamic viscosity
ω = angular velocity
ξ, ψ = coordinates in the stationary frame

Subscripts

ax = axial
b.e.p. = best efficiency point (Q=33.3 L/s)
d = discharge
f = friction
n = normal to surface
p = pressure
R = rotor
rad = radial
s = suction
vol = volute
0 = adjusted value
1, 2 = mode

Abbreviations

CAD = computer aided design
deg = degrees
FEM = Finite element method
SST-model = Shear stress transport model
3D = three dimensional

References

[1] Agostinelli, A., Nobles, D., and Mockridge, C. R., 1960, "An Experimental Investigation of Radial Thrust in Centrifugal Pumps," ASME J. Eng. Power, 82(2).
[2] Okamura, T., 1980, "Radial Thrust in Centrifugal Pumps with a Single-Vane-Impeller," Bull. JSME, 23(180).
[3] Aoki, M., 1984, "Instantaneous Interblade Pressure Distributions and Fluctuating Radial Thrust in a Single-Blade Centrifugal Pump," Bull. JSME, 27(233).
[4] Gülich, J., Jud, W., and Hughes, S. F., "Review of Parameters Influencing Hydraulic Forces on Centrifugal Impellers," Proc. Inst. Mech. Eng., 201(A3).
[5] Siekmann, H., and Stark, M., 1990, "Analytical and Experimental Study of the Hydrodynamic Unbalance of Single-Vane Impellers," *Third International Symposium on Transport Phenomena and Dynamics of Rotating Machinery (ISROMAC-3)*, Honolulu, Hawaii, Paper No. D-28A.
[6] Benra, F.-K., Dohmen, H. J., and Schneider, O., 2003, "Unsteady Flow in Single-Blade Sewage Water Pumps," *Second International Conference on Heat Transfer, Fluid Mechanics and Thermodynamics*, Victoria Falls, Zambia, Paper No. BF1.
[7] Benra, F.-K., Dohmen, H. J., and Schneider, O., 2003, "Investigation on the Unsteady Flow in Radial Waste Water Pumps to Determine the Hydrodynamic Forces," *Proceedings of the Fifth European Conference on Turbomachinery*, Prague, pp. 551–560.
[8] Benra, F.-K., Sommer, M., Müller, M., and Töws, A., 2004, "Investigation of the Three-Dimensional Time Accurate Flow in Single-Blade Sewage Water Pumps," *Proceedings of Fourth South African Conference of Applied Mechanics, SACAM'04*, Johannesburg, South Africa.
[9] AEA Technology, CFX-TASCFLOW, Version 2.11, 2001, Computational Fluid Dynamics Software, User Documentation, AEA Technology Engineering Software Ltd.
[10] Hansen, T., 2001, "Comparison of Steady-State and Transient Rotor-Stator Interaction of an Industrial Centrifugal Pump," *CFX Users Conference*, Berchtesgaden, Germany.
[11] Shi, F., and Tsukamoto, H., 2001, "Numerical Study of Pressure Fluctuations Caused by Impeller-Diffusor Pump Stage," J. Fluids Eng., 123.
[12] Menter, F. R., 1994, "Two-Equation Eddy-Viscosity Turbulence Models for Engineering Applications," AIAA J., 32(8).
[13] Schäfer, M., Sieber, G., Sieber, R., and Teschauer, I., 2001, "Coupled Fluid-Solid Problems: Examples and Reliable Numerical Simulation," W. A. Wall, K.-U. Bletzinger, and K. Schweizerhof (eds.), *Trends in Computational Structural Mechanics, CIMNE*, Barcelona.
[14] PCB Piezotronics, Industrial Monitoring Instrumentation Division, 2003, Industrial ICP Accelerometer, Model 601A02, *Installation and Operating Manual*, New York.
[15] Wilde, J., and Lai, Y., 2002, "Design Optimization of an Eddy Current Sensor Using the Finite-Elements Method," *European Microelectronics Packaging and Interconnection Symposium*, Cracow, Poland.
[16] National Instruments Corporation, 2001, NI-DIADEM, Version 7.02, Austin, TX.
[17] Benra, F.- K., Dohmen, H. J., and Schneider, O., 2003, "Calculation of Flow Induced Vibration Amplitudes of Radial Sewage Water Pumps," *Seventh International Symposium on Emerging Technologies for Fluids, Structures and Fluid-Structure Interactions*, PVP 460, PVP2003–1947, Cleveland, OH.
[18] Benra, F.- K., Dohmen, H. J., and Schneider, O., 2003, "Calculation of Hydrodynamic Forces and Flow Induced Vibrations of Centrifugal Sewage Water Pumps," *Fourth ASME/JSME Joint Fluids Engineering Conference*, Paper No. FEDSM2003–45102, Honolulu, Hawaii, HJ.

Satoshi Ogata
e-mail: ogata-satoshi@c.metro-u.ac.jp

Asano Kimura

Graduate School of Engineering,
Tokyo Metropolitan University,
Department of Mechanical Engineering,
1-1 Minami Ohsawa, Hachiooji-shi, Tokyo
192-0397, Japan

Keizo Watanabe
Graduate School of Technology Management,
Tokyo University of Agriculture and Technology,
2–24–16 Nakacho, Koganei–shi,
Tokyo, 184–8588, Japan

Effect of Surfactant Additives on Centrifugal Pump Performance

Performance of a centrifugal pump when handling surfactant solutions was measured experimentally. It was clarified that the pump efficiency with surfactant solutions was higher than that with tap water and increased with an increase in surfactant concentration. The value of maximum flow rate also increased. The total pump head increased with an increase in concentration, and the shaft power decreased with a decrease in the impeller rotating speed. There was an optimal temperature, which maximizes the efficiency. By combining the data for the piping section and for the pump efficiency, it is possible to accurately predict the energy savings of the pumping power in the pipeline system. [DOI: 10.1115/1.2201643]

Keywords: centrifugal pump, surfactant solution, drag reduction, pump efficiency

1 Introduction

The drag reduction of surfactant solutions has attracted considerable attention from the point of view of energy conservation because mechanical degradation does not occur and the drag reduction ratio is higher than in polymer solutions in certain concentration ranges [1,2]. Therefore, the surfactant was recently added to the heating medium used in a city thermal energy supply pipeline system, and field test research on the reduction of the pumping power of the system was conducted [3,4]. In their investigations, a reduction in pumping power of about 30% was achieved at normal flow rate.

For the long straight pipes, the effect of the drag reduction is relatively predictable. However, the actual thermal energy supply pipeline system can be very complex and may include many fittings, valves, heat exchangers, pumps, etc. The flow conditions of the system may also change depending on the thermal load to be met. Therefore, the surfactant solutions should perform adequately over the full range of changing system condition, and should provide drag reduction while not impairing system performance.

Many studies of the drag reducing surfactant solutions have been conducted with respect to pressure loss in the pipeline [5,6]. The maximum values of drag reduction can be estimated by Virk's asymptote [7]. His result predicts that a pump driving the flow could be operated with only one-fifth of the original power in an ideal case.

In addition to the positive effect of drag reduction, the negative effect of significant heat transfer reduction is observed, due to the change in flow behavior [8]. This heat transfer reduction is unacceptable because a significant reduction of heat transfer may lower the energy efficiency of district heating and cooling systems even if there is conservation of energy from drag reduction. Therefore, some studies aiming to improve the performance of the heat exchanger have been carried out. Li et al. [9] reported that it is possible to improve the performance of the heat exchanger by disturbing the flow inside the heat exchanger using the mesh screen. Their experimental results indicate that the problem of the heat exchanger can be solved practically.

Few studies have been carried out on the pump performance with surfactant solution, even though the pump is a very important component of district heating and cooling systems, because of the forming bubbles and complicated temperature dependence. Gasljevic and Matthys [3] studied the effect of surfactant additives on the pump performance. Test pumps concerned a single suction centrifugal pump with 153 mm and 45 mm impellers both driven at 3450 rpm. Test fluid was a solution of a cationic surfactant (Ethoquad T13-50 by Akzo Chemical) with NaSal as counterion. The concentrations varied from 2000 ppm to 4500 ppm. It was found that the head-flow characteristics were unaffected for both test pumps and that the power required by the pump was reduced by up to 10% in some cases. They also clarified that cavitation onset was delayed in some cases. However, they could not measure the shaft power of the pump and not clarify the effect of the surfactant solutions on the pump efficiency.

On the other hand, the frictional resistance of an enclosed rotating disk is closely related to the estimation of the performance of a pump in general. Ogata and Watanabe [10] reported the drag reduction due to surfactant solutions (Ethoquad O/12 by Lion) with NaSal for an enclosed rotating disk by measuring the torque acting on the disk. The maximum drag reduction ratio was ~30% in the Reynolds number range of $Re_w > 3 \times 10^5$. This drag reduction effect indicates that the power loss of the pump can be decreased by using surfactant solution, so that the improvement of the pump performance can also be expected. In addition, they clarified that the amplitude of the circular vortex on a rotating disk in surfactant solution was reduced and the flow direction on the disk was turned outward to the circumferential direction compared to that of tap water. Therefore, the surfactant solution can significantly change the flow condition around the impeller in a pump. As mentioned above, little research has been done about the effect of surfactant solution on the pump performance systematically (including pump efficiency, shaft power and total pump head). The effects of the diameter and rotational speed of an impeller and the effects of concentration and temperature on the pump performance are not known at present.

The purpose of this study is to clarify the centrifugal pump performance when handling surfactant solution, experimentally, in a closed-loop system. The effects of the concentration and temperature of surfactant solution and the rotational speed of an impeller on pump performance were investigated from the viewpoint of the practical application for district heating and cooling systems.

Contributed by the Fluids Engineering Division of ASME for publication in the JOURNAL OF FLUIDS EINGINEERING. Manuscript received December 10, 2004; final manuscript received December 7, 2005. Assoc. Editor: Akira Goto. Paper presented at the 2003 ASME International Mechanical Engineering Congress (IMECE2003), November 15–21, 2003, Washington, DC.

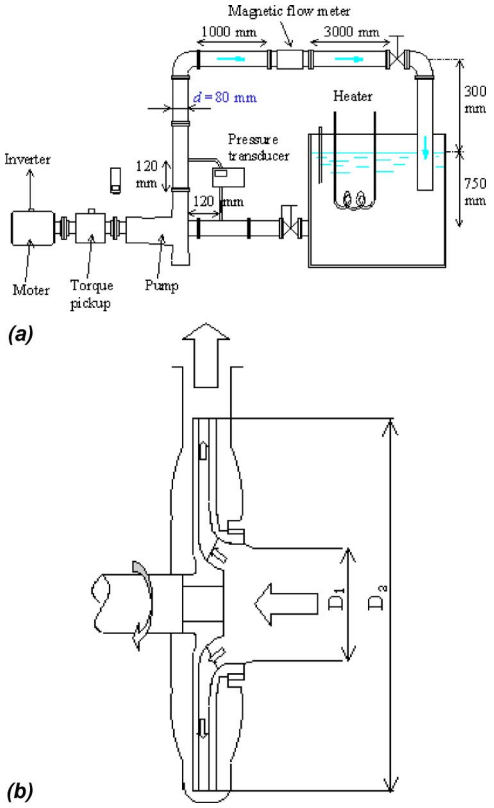

Fig. 1 (*a*) **Experimental apparatus and** (*b*) **cross section of test pump**

2 Experimental Apparatus and Procedure

Figure 1 shows the experimental apparatus. The test pump is a centrifugal pump having the specifications $D_1=80$ mm and $D_2=265$ mm, and the specific speed $n_s=2\pi NQ^{1/2}/(gH)^{3/4}=0.29$ (in SI units).

The suction and discharge pressures were measured by using a diaphragm-style pressure transducer, with a ±0.25% f.s. accuracy. Flow rate was measured using an electromagnetic flow meter with a ±0.075% (<0.3 m/s) and a ±0.25% (>0.3 m/s) accuracy, which was calibrated with test fluids by means of the gravimetric method at the low flow rate. The torque was measured using a strain-gage-style torque pickup with a ±0.2% f.s. accuracy installed between the pump and the motor. The bearing and grand torque loss is usually difficult to estimate. In this study, in order to decrease the effect of the bearing and grand torque loss on the measured value, this loss was estimated by measuring the torque in the condition that the water was removed from the pump at each rotational speed. The shaft power was calculated from the torque data by deducting this bearing and gland torque. It can be considered that the bearing and grand torque loss occupied for the shaft power is very little. A frequency inverter was used to control the impeller rotating speed, and the rotational speed was measured directly using a digital tachometer.

A tank with volume of 1 m^3 served as the reservoir for the surfactant solution. To clarify the effect of the temperature of the surfactant solution on the pump performance, a thermostat was installed to control the temperature of the solution in the tank, which was varied through heating by an electric heater. The temperature fluctuation of test fluids in the tank was thus controlled within ±1 °C around the set value.

If a bubble is generated in the surfactant solutions under experiment, it is difficult to accurately measure the pump performance. Therefore, acrylic resin pipes were fitted on the suction and the discharge pipe, so that the flow in the pipe could be observed. In addition, the termination of the pipe was submerged in the tank in order to prevent the inflow of bubbles to the pump.

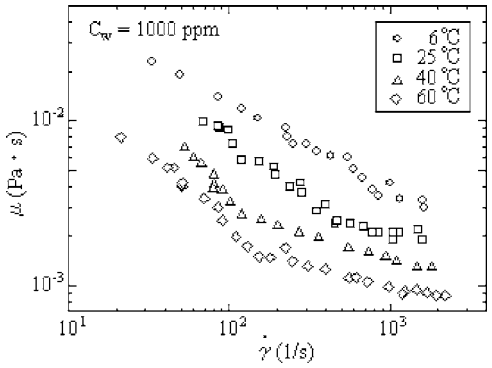

Fig. 2 Apparent viscosity of surfactant solutions

The pump and loop were cleaned between two tests with different surfactant solutions by using the water, and the validity of the data with water was confirmed before the several tests.

Test fluid was aqueous solutions of Oreyl-bishydroxyethyl-methyl-ammonium $(C_{18}H_{35}N(C_2H_4OH)_2CH_3Cl$, trade name: Ethoquad O/12) at concentrations of 200, 500, and 1000 ppm. Sodium salicylate (NaSal.) was added as a counterion. The concentration ratio of sodium salicylate to Ethoquad O/12 was set at 1:1 in molar ratio. The Ethoquad O/12 and sodium salicylate were dissolved separately, and the solutions were left to stand for 24 h before the experiment. The temperatures of test fluids were $T=6$, 25, 40, and 60 °C.

Measurement of the viscosity of the surfactant solutions was carried out by capillary viscometers, and the data of 1000 ppm solution are presented versus shear rate in Fig. 2. It can be seen that the viscosity increased with decreasing solution temperature and decreased with shear rate although tended to a constant value in the high-shear-rate region. The viscosity differed with the type of viscometer [11], and the hysteresis of the viscosity occurred [12]. Because the viscosity of surfactant solution was complicatedly dependent on many parameters, the Reynolds number was calculated using the viscosity of tap water in this study (Re_w).

3 Experimental Results and Discussions

Figure 3 shows the experimental results for pump performance in the case of $N=1300$ rpm and $T=25$ °C. In Fig. 3(*a*), it is shown that the pump total head with the surfactant solution increases compared to that of tap water over the entire flow rate range and increases with an increase in the surfactant concentration. Figure 3(*b*) shows there is only a slight difference between the shaft power with surfactant solution and that of tap water in the 200 and 500 ppm solutions. However, in the case of the 1000 ppm solution, the shaft power significantly decreases. In Fig. 3(*c*), it is shown that the pump efficiency with surfactant solution increases in comparison to that with tap water, and increases with the increase of the surfactant concentration. The maximum flow rate with the surfactant solution increases and the value of the flow rate that shows maximum pump efficiency with surfactant solution also increases in comparison to that of tap water.

Figure 4 shows the effect of the surfactant concentration on the pump total head. In this figure, an increased ratio of the pump total head I_H is defined as follows:

$$I_H=\frac{H_S-H_N}{H_N}\times 100(\%) \tag{1}$$

where H_N and H_S are the pump total head of tap water and surfactant, respectively. Figure 4 shows that the pump total head with the surfactant solution increases with an increase in the surfactant concentration clearly.

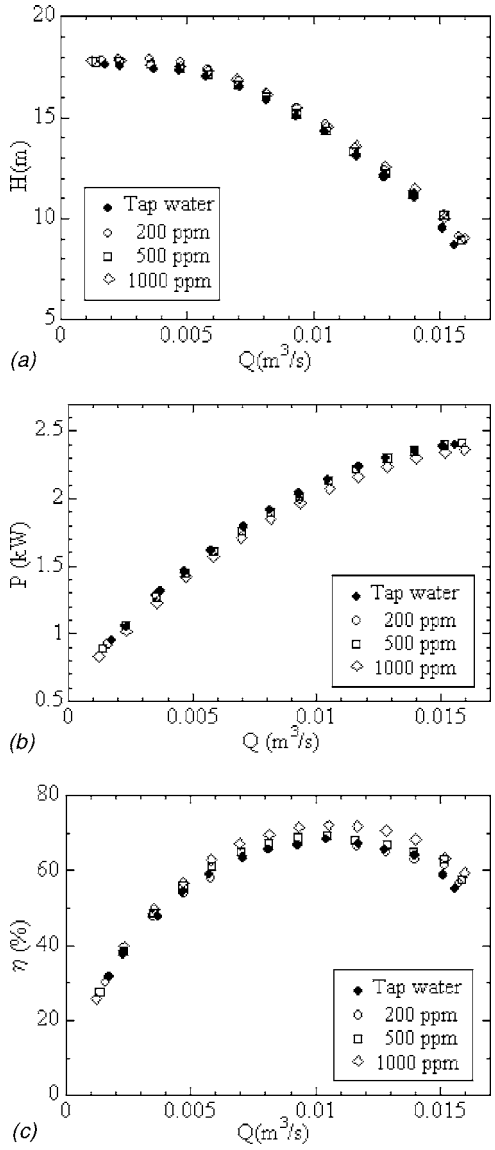

Fig. 3 Pump performance curve at 1300 rpm: (*a*) Pump head, (*b*) shaft power, and (*c*) pump efficiency

As is well known, the pressure loss of the turbulent flow in a circular pipe is decreased with surfactant solution. Zakin and Chang [1] reported that the drag reduction for pressure loss due to surfactant solution occurred in the Reynolds number range of $\mathrm{Re} > 2300$ and that the drag reduction ratio increased with the increase in the surfactant concentration and temperature. The surfactant solution used in this study exhibits the drag reduction effect up to $T = 60\,^{\circ}\mathrm{C}$. With respect to the frictional resistance of the rotating disk, the drag reduction with surfactant solution occurred $\mathrm{Re}_w > 3 \times 10^5$ and the drag reduction ratio increased with the increase in the surfactant concentration and temperature. After the maximum value of the drag reduction is reached, the drag reduction gradually decreases [10].

Figure 5 shows the relationship between the total head and the system head curve of the pump, in the cases of both tap water and surfactant solution. Because of the drag reduction of pressure loss mentioned above, the system head curve of the pump with surfactant solution is decreased compared to that with tap water (from H to H''). In addition, the pump head increases with surfactant solution as seen in Fig. 3(*a*). Therefore, the operating point A for tap water is moved to a new operating point A'' for surfactant solution in the high flow side.

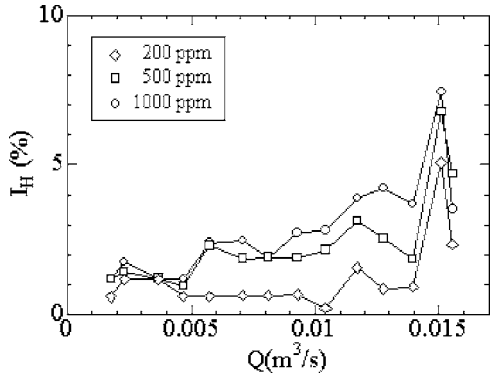

Fig. 4 Effect of surfactant concentration on total pump head at 1300 rpm

Assuming that the drag reduction occurs only in the straight piping section and follows the Virk's MDRA [7], we can estimate the reduction of pressure loss (ΔH) and the increase of flow rate (ΔQ). As a result of this estimation, at the flow rate of maximum efficiency point in the case of the pipeline system in this experiment (at the conditions of 1300 rpm, 1000 ppm, and $T = 40\,^{\circ}\mathrm{C}$), ΔH and ΔQ were calculated to be about 8% and 4%, respectively. Of course, ΔH and ΔQ will increase in the large-scale system with a longer piping section because the system head curve becomes lower due to drag reduction with surfactant solution.

Figure 6 shows the effect of the rotational speed of an impeller on the pump performance. In Fig. 6, ϕ, ψ, and τ are the flow coefficient, head coefficient, and power coefficient, respectively. These dimensionless coefficients are defined as follows:

$$\phi = \frac{Q}{(D_2^3 N)} \tag{2}$$

$$\psi = \frac{H}{(D_2^2 N^2)} \tag{3}$$

$$\tau = \frac{P}{(\rho D_2^5 N^3)} \tag{4}$$

where Q, H, P, and N are the flow rate, pump total head, shaft power, and rotational speed of an impeller, respectively.

In Fig. 6(*a*), it is seen that the head coefficient of surfactant solutions increases and this has no evident correlationship with rotational speed may be because the speed variation (1000–1300 rpm) is too small to be detachable. However, as shown in Fig. 6(*b*), the power coefficient of surfactant solution is dependent on the rotational speed, unlike the case of tap water, and the power coefficient decreases with the decrease in rotational

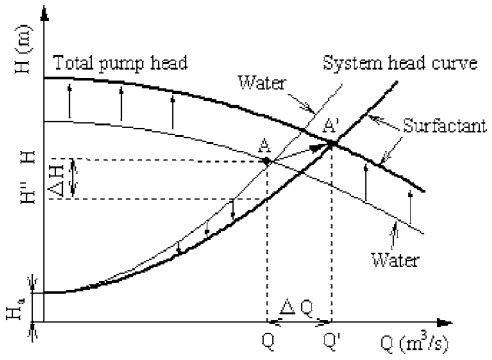

Fig. 5 Pumping operation point with surfactant solution

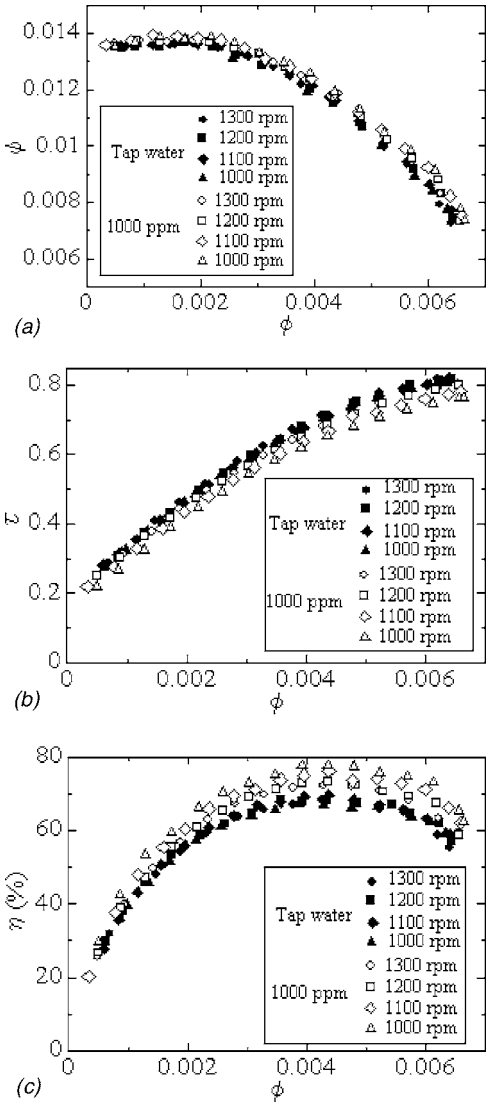

Fig. 6 Effect of rotational speed on pump performance: (*a*) Head coefficient (*b*) power coefficient, and (*c*) pump efficiency

speed. It is shown that the pump efficiency of surfactant solution increases with decreasing rotational speed in Fig. 6(*c*).

Considering that the surfactant solution causes the drag reduction in pipe flow, it can be considered that the head coefficient increases because of the reduction in the friction loss of the impeller and pump casing with surfactant solution. In addition, the surfactant solution reduces the frictional resistance of a rotating disk [14], so that the power coefficient decreases by using the surfactant solution. Therefore, it can be considered that the hydraulic loss of the pump was reduced by the use of surfactant solution.

The frictional resistance of a rotating disk is a factor of the shaft power loss, so that the experimental value of the shaft power depends on the Reynolds number Re_w, based on the impeller radius. Figure 7 shows the effect of the Reynolds number Re_w on the reduction ratio of shaft power K defined as follows:

$$K = \frac{|(P_S - P_N)|}{P_N} \times 100(\%) \tag{5}$$

where P_N and P_S are the shaft powers of tap water and surfactant solution at maximum efficiency point of 200 ppm, respectively. In Fig. 7, the Reynolds number was calculated based on the radius and angular velocity of an impeller.

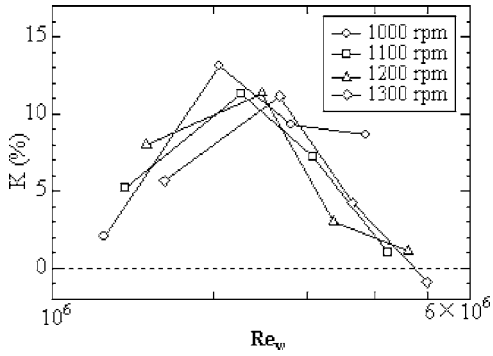

Fig. 7 Effect of Reynolds number on power coefficient (200 ppm)

Figure 7 shows that the reduction ratio of shaft power increases as the Reynolds number increases up to $\mathrm{Re}_w = 2 \times 10^6$, above which it decreases gradually. This tendency is similar to the behavior for the frictional resistance of a disk in surfactant solution [10]. Therefore, it can be considered that the reduction of a disk friction is a large factor for the reduction effect of the shaft power.

In order to clarify the effect of drag reduction for the frictional resistance of the disk on the pump efficiency, it seems necessary to estimate the percentage of the frictional resistance of the disk occupied for the shaft power. We calculated the ratio of disk friction loss to shaft power at a maximum efficiency point in $\mathrm{Re}_w = 2.2 \times 10^6$ (N=1300 rpm) by using the equation of Daily and Nece [13] for the disk friction. The conditions of calculation are region IV [13], smooth disk, and the value of the moment coefficient C_m=0.0018. As a result, ~17% was obtained as the percentage of the frictional resistance of the disk occupied for the shaft power. On the other hand, the effect of drag reduction for the friction resistance of the disk on the pump efficiency was calculated by using the drag reduction obtained experimentally for the disk in 200 ppm surfactant solution [10]. Because there was no result for the frictional resistance of the rotating disk at higher concentration, the result of 200 ppm solution was chosen for this calculation. As a result of calculation, the pump efficiency increased ~1% for the drag reduction of the disk in 200 ppm solution. In a similar manner, the percentage of improvement was found to be ~2% by using the equation of Pfleiderer [15] for the disk friction calculation.

Finally, to estimate the degree of increase of the pump efficiency due to the use of the surfactant solution, the experimental result was rearranged in terms of the increase ratio of the pump efficiency E, defined as follows:

$$E = \frac{\eta_S - \eta_N}{\eta_N} \times 100(\%) \tag{6}$$

where η_N and η_S are the pump efficiencies of tap water and surfactant solution at the maximum efficiency point, respectively.

Figure 8 shows the effect of the surfactant concentration on the increase ratio of the pump efficiency E for the 1300 rpm. It is clarified that the pump efficiency with the surfactant solution increases with the increase in the surfactant concentration. Figure 9 shows the relationship between temperature and the increase ratio of the pump efficiency E for the 1300 rpm. This figure shows the pump efficiency increase with the gradual increase in the surfactant temperature, and has a maximum value at T=40 °C. The maximum percentages of the increase of pump efficiency are about 4, 7, and 13% in 200, 500, and 1000 ppm solutions, respectively.

The efficiency of the pump is a product of external mechanical efficiency, disk friction efficiency, hydraulic efficiency, and volumetric efficiency. With respect to the disk friction efficiency, it was clarified that this loss was decreased by the use of the surfac-

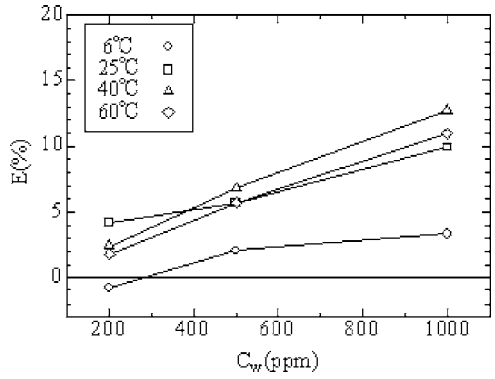

Fig. 8 Effect of surfactant concentration on pump efficiency at 1300 rpm

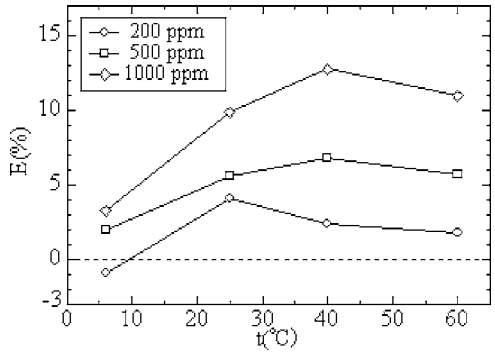

Fig. 9 Relationship between surfactant temperature and pump efficiency at 1300 rpm

tant solution because of the drag reduction for the rotating disk friction. Concerning the hydraulic efficiency, the experimental results in this study show that the hydraulic loss was reduced and head increased by the use of the surfactant solution. However, there are many unclear points concerning the hydraulic loss. Additionally, there are no data for volumetric efficiency. In order to clarify the pump performance in greater detail, it is necessary to examine the flow inside a pump by using both a flow visualization technique and also advanced future research including turbulence and shear flow stress.

4 Conclusions

The effect of surfactant additives on centrifugal pump performance was investigated experimentally. It was clarified that the total pump head of surfactant solution increased and the shaft power of surfactant solution decreased, comparing to those of tap water. The pump efficiency with surfactant solutions is increased in comparison to that with tap water. Additionally, the maximum flow rate of the pump also increased with the use of surfactant solutions. The pump efficiency of surfactant solutions increased with an increase in surfactant concentration. The surfactant temperature affected the pump performance, and it was clarified that there was an optimum temperature, which maximized the pump efficiency. The variation of pump performance with rotational speed in the presence of surfactant solutions shows apparently unexpected tendency, which requires more investigation before making a sound clear conclusion.

Acknowledgment

This research was supported by a Grant-in-Aid for the Encouragement of Young Scientists (B), No. 14750122 from the Scientific Research Fund of the Japanese Government.

Nomenclature

d = diameter of test pipe (m)
D_2 = diameter of impeller (m)
H = total pump head (m)
H_a = actual pump head (m)
N = rotational speed of an impeller (rpm)
P = shaft power (W)
Q = volumetric flow rate (m^3/s)
Re = Reynolds number based on pipe diameter $=(4\rho Q)/(\pi\mu d)$
Re_w = Reynolds number based on impeller radius $=(D_2^2\rho\omega)/(4\mu)$
T = temperature of test fluid (°C)
ϕ = flow coefficient
$\dot{\gamma}$ = shear rate (1/s)
η = pump efficiency (%)
μ = viscosity of test solution (Pa s)
ρ = density of test solution (kg/m^3)
τ = power coefficient
ω = angular velocity of impeller (rad/s)
ψ = head coefficient

References

[1] Zakin, J. L., and Chang, J. L., 1974, "Polyoxyethylene Alcohol Non-Ionic Surfactants as Drag Reducing Additives," *Proc. Int. Conf. on Drag Reduction*, BHRA Fluid Engineering, St. Johns College, Cambridge, Vol. D1, pp. 1–14.
[2] Ohlendorf, D., Interthal, W., and Hoffmann, H., 1986, "Surfactant Systems for Drag Reduction: Physico-Chemical Properties and Rheological Behavior," Rheol. Acta, **25**, pp. 468–486.
[3] Gasljevic, K., and Matthys, E. F., 1992, "Effect of Drag-Reducing Surfactant Solutions on Centrifugal Pumps Performance," *Proc. ASME in Recent Advances in Non-Newtonian Flows*, ASME, New York, Vol. AMD-153/PED-141, pp. 49–56.
[4] Gasljevic, K., and Matthys, E. F., 1996, "Field Test of Drag-Reducing Surfactant Additives in a Hydraulic Cooling System," *Proc. ASME Fluid Eng. Div. Summer Meeting*, ASME, New York, Vol. FED-237, pp. 249–260.
[5] Bewersdorff, H. W., and Ohlendroff, D., 1988, "The Behavior of Drag-Reducing Cationic Surfactant Solution," Colloid Polym. Sci., **266**, pp. 941–953.
[6] Warholic, M. D., Schmidt, G. M., and Hanratty, T. J., 1999, "The Influence of a Drag-Reducing Surfactant on a Turbulent Velocity Field," J. Fluid Mech., **388**, pp. 1–20.
[7] Virk, P. S., Mickley, H. S., and Smith, K. A., 1970, "The Ultimate Asymptote and Mean Flow Structure in Toms' Phenomenon," ASME J. Appl. Mech., **37**, pp. 488–493.
[8] Steiff, A., and Klopper, K., 1996, "Application of Drag-Reducing Additives in District Heating Systems," *Proc. ASME Fluid Eng. Div. Summer Meeting*, ASME, New York, FED-237, pp. 235–242.
[9] Li, P., Kawaguchi, Y., Daisaka, H., Yabe, A., Hishida, K., and Maeda, M., 2001, "Heat Transfer Enhancement to the Drag-Reducing Flow of Surfactant Solution in Two-Dimensional Channel With Mesh-Screen Inserts at the Inlet," ASME J. Heat Transfer, **123**, pp. 779–789.
[10] Ogata, S., and Watanabe, K., 2000, "Flow Characteristics of a Rotating Disk in Surfactant Solutions," *Proc. Int. ASME Rheology and Fluid Mechanics of Nonlinear Materials*, ASME, New York, FED-252, pp. 41–48.
[11] Bewersdorff, H. W., 1996, "Rheology of Drag Reducing Surfactant Solutions," *Proc. ASME Fluid Eng. Div. Summer Meeting*, ASME, New York, FED-237, 2, pp. 25–29.
[12] Wunderlich, A. M., and Brunn, P. O., 1989, "The Complex Rheological Behavior of an Aqueous Cationic Surfactant Solution Investigated in a Couette-Type Viscometer," Colloid Polym. Sci., **267**, pp. 627–636.
[13] Daily, J. W., and Nece, R. E., 1960, "Chamber Dimension Effects on Induced Flow and Frictional Resistance of Enclosed Rotating Disks," Trans. ASME, **82**(1), pp. 217–232.
[14] Ogata, S., and Watanabe, K., 2002, "Limiting Maximum Drag Reduction Asymptote for a Moment Coefficient of a Rotating Disk in Drag-Reducing Surfactant Solution," J. Fluid Mech., **457**, pp. 325–337.
[15] Pfleiderer, C., 1961, *Die Kreiselpumpen für Flüssigkeit ünd Gase*, Springer-Verlag, Berlin, p. 103.

RANS Simulation of Ducted Marine Propulsor Flow Including Subvisual Cavitation and Acoustic Modeling

Jin Kim[1]
e-mail: jkim@moeri.kr

Eric G. Paterson[2]

Frederick Stern

Iowa Institute of Hydraulic Research,
The University of Iowa,
Iowa City, IA 52246

High-fidelity Reynolds-averaged Navier Stokes (RANS) simulations are presented for the ducted marine propulsor P5206, including verification and validation (V&V) using available experimental fluid dynamics data, and subvisual cavitation, and acoustics analysis using the modified Rayleigh-Plesset equation along the bubble trajectories with a far-field form of the acoustic pressure for a collapsing spherical bubble. CFDSHIP-IOWA is used with the blended $k-\omega/k-\varepsilon$ turbulence model and extensions for a relative rotating coordinate system and overset grids. The intervals of V&V analysis for thrust, torque, and profile averaged radial velocity just downstream of rotor tip are reasonable in comparison with previous results. The flow pattern displays the interaction and merging of the tip-leakage and trailing edge vortices. In the interaction region, multiple peaks and vorticity are smaller, whereas in the merging region, there is better agreement with the experiment. The tip-leakage vortex core position, size, circulation, and cavitation patterns for $\sigma_i=5$ also show good agreement with the experiment, although the vortex core size is larger and the circulation in the interaction region is smaller. The simulations indicate globally minimum $C_p=-\sigma_i=-8.8$ on the suction side of the rotor tip at 84% chord from the leading edge and locally minimum $C_p=-6.4$ in the tip-leakage vortex at 8% chord downstream of the trailing edge, whereas EFD indicates $\sigma_i=11$ and the location in the tip-leakage vortex core 50% chord downstream of the trailing edge. Subvisual cavitation and acoustics analysis show that bubble dynamics may partly explain these discrepancies. [DOI: 10.1115/1.2201697]

1 Introduction

The performance of a ducted marine propulsor is influenced by a number of parameters, including tip geometry and gap, blade loading, and boundary layer inflow. Cavitation inception occurs in the tip-leakage vortex core downstream of the rotor trailing edge. Since small bubbles, or nuclei, respond to the local pressure field as they convect through the propulsor, prediction of cavitation inception requires high fidelity resolution of the pressure and associated flow features such as tip-leakage and trailing edge vortices, blade and duct boundary layers, and turbulence. Analysis of bubble dynamics is also important for prediction of cavitation inception since small micro bubbles grow and collapse as they translate and interact. Recent experiments by Judge et al. [1] related to tip-leakage vortex cavitation for the ducted rotor P5206 have quantified some of the flow physics responsible for cavitation inception.

The design of marine propulsor is largely based on potential flow theory in combination with experimental testing. While potential flow theory offers a quick way to obtain insight into the global performance characteristics of a propeller such as thrust and torque, it has substantial shortcomings resulting from the assumption of inviscid flow. Important effects like boundary layer separation due to pressure gradients at off design conditions cannot be included in this method. Empirical assumptions about the drag have to be introduced in order to include some of the effects of viscosity. However, the influence of other viscous effect and turbulence on the performance cannot be modeled in the inviscid methods.

As a result, RANS simulation of marine propulsors is receiving increased attention. RANS computations for marine propellers with practical geometry have been reported [2,3]. The detailed flow at the tip vortex and prediction of trends for various tip geometries is shown [4–6] and the capability of RANS to predict four-quadrant performance (i.e., ahead, backing, crash-ahead, and crash-back) has been studied including detailed analysis of the resulting flow field [7]. All these RANS simulations are performed on open water propellers and used structured grid systems. Each group showed reasonably good agreement with the experimental measurements. The reason for discrepancies between experiment and computation are typically cited to be low grid resolution and overpredicting the eddy viscosity in the vortex core. Recently, Brewer [8] shows a RANS solution of the ducted rotor P5206. He used an unstructured, unsteady RANS code named U^{2}NCLE with the one-equation turbulence model and approximately 3.5 million nodes for whole three blades (360 deg) computational domain.

Some researchers started predicting the traveling bubble cavitation for relatively simple flows and tip vortex flow [9–12]. They use the Rayleigh-Plesset (R-P) equation describing the evolution of a spherical bubble in a given pressure field assuming that the bubble follows a streamline or a motion equation for the trajectory. More complex bubble flow interactions are also examined for relatively simple flows. Hsiao and Chahine [13,14] simulate bubble/vortex interactions using combined Navier-Stokes simulations of the flow with a Chimera moving grid scheme to capture nonspherical bubble dynamics.

The objective of the current study is high fidelity RANS simulations for the ducted rotor P5206, including verification studies based on assessment iterative and grid convergence, validation

[1]Present Senior Research Scientist, Maritime & Ocean Engineering Research Institute, Yuseong P.O. Box 23, Daejeon, Korea.

[2]Presently Senior Research Associate, Applied Research Laboratory, Pennsylvania State University.

Contributed by Fluids Engineering Division of ASME for publication in the JOURNAL OF FLUIDS ENGINEERING. Manuscript received June 12, 2003; final manuscript received December 11, 2005. Assoc. editor: Kyle Squires.

studies using available benchmark experimental fluid dynamics data and uncertainties, and subvisual cavitation (SVC) and acoustics studies using the modified Rayleigh-Plesset equation along the bubble trajectories along with far-field form of the acoustic pressure for a collapsing spherical bubble.

2 Computational Method for RANS

The three-dimensional incompressible RANS code, CFDSHIP-IOWA [15] is used in the current study. This code has been verified and validated for a range of applications for ship hydrodynamics [16,17]. The main change compared with the previous version is the ability to handle the general overset grid and the Cartesian relative rotating frame formulation for marine propulsor application.

The unsteady three-dimensional RANS and continuity equations for the incompressible fluid are written in nondimensional form

$$\frac{\partial U_i}{\partial x_i} = 0 \tag{1}$$

$$\frac{\partial U_i}{\partial t} + U_j \frac{\partial U_i}{\partial x_j} = -\frac{\partial \hat{p}}{\partial x_i} + \frac{1}{\mathrm{Re}} \frac{\partial^2 U_i}{\partial x_j \partial x_j} - \frac{\partial}{\partial x_j} \overline{u_i u_j} \tag{2}$$

where $U_i=(U,V,W)$ are the Reynolds-averaged velocity components, $x_i=(x,y,z)$ are the Cartesian coordinate systems, $\hat{p}=(p-p_0)/\rho U_0^2$ is the piezometric pressure, $\overline{u_i u_j}$ are the Reynolds stresses, and $\mathrm{Re}=U_0 D/\nu$ is the Reynolds number. All equations are nondimensionalized by the reference velocity U_0, characteristic length D (usually the propeller diameter), reference pressure p_0, and density ρ.

For the marine propulsor flow, the current study adopts a relative frame formulation. Currently, relative-frame motion in Cartesian coordinates is restricted to steady rotation about the x-axis, which is the axis of propeller rotation. For these simple cases, the acceleration term on the left hand side of the momentum equation is replaced with the following expression

$$\frac{D\mathbf{U}}{Dt} = \frac{D\mathbf{U}'}{Dt} + \begin{pmatrix} 0 \\ -\omega_x^2 y' - 2\omega_x W' \\ -\omega_x^2 z' - 2\omega_x V' \end{pmatrix} \tag{3}$$

where (x',y',z') and (U',V',W') are the coordinates and velocity components in the relative frame. In addition to modifying the acceleration terms, the initial and boundary conditions must be transformed into the relative frame. This results in a large solid-body rotation of the free-stream velocity. Although this is the usual approach to formulating relative-frame codes, an alternative approach is used here which has the benefits of removing the solid-body rotation, moving most of the noninertial terms from the source term to the convective terms, and simplifying calculation of vorticity and wall-shear stress, such that the same algorithms may be used for either reference frame. The continuity and momentum equations in the relative rotating frame are as follows

$$\frac{\partial U}{\partial x'} + \frac{\partial V}{\partial y'} + \frac{\partial W}{\partial z'} = 0 \tag{4}$$

$$\frac{\partial U}{\partial t} + U\frac{\partial U}{\partial x'} + (V-\omega_x z')\frac{\partial U}{\partial y'} + (W-\omega_x y')\frac{\partial U}{\partial z'} = \frac{\partial \hat{p}}{\partial x'} + \frac{1}{\mathrm{Re}}\frac{\partial^2 U}{\partial x_j \partial x_j} - \frac{\partial}{\partial x_j'}\overline{uu_j} \tag{5}$$

$$\frac{\partial V}{\partial t} + U\frac{\partial V}{\partial x'} + (V-\omega_x z')\frac{\partial V}{\partial y'} + (W-\omega_x y')\frac{\partial V}{\partial z'} = -\frac{\partial \hat{p}}{dy'} + \frac{1}{\mathrm{Re}}\frac{\partial^2 V}{\partial x_j' \partial x_j'} - \frac{\partial}{\partial x_j'}\overline{\nu u_j} - \omega_x W \tag{6}$$

$$\frac{\partial W}{\partial t} + U\frac{\partial W}{\partial x'} + (V-\omega_x z')\frac{\partial W}{\partial y'} + (W-\omega_x y')\frac{\partial W}{\partial z'} = -\frac{\partial \hat{p}}{\partial z'} + \frac{1}{\mathrm{Re}}\frac{\partial^2 W}{\partial x_j' \partial x_j'} - \frac{\partial}{\partial x_j'}\overline{wu_j} + \omega_x V \tag{7}$$

The governing equations are discretized based on finite differences with a blended $k-w/k-\varepsilon$ (BKW) turbulence model [18] for turbulence closure. The idea behind the BKW model is to retain the robust and accurate formulation of the $k-\omega$ model [19] in the near wall region, and to take the advantage of the freestream turbulence independency of $k-\varepsilon$ models [20] in the outer part of the boundary layer. The physical domain is discretized in generalized curvilinear coordinate and transformed into an orthogonal computational domain. Overset grids are implemented using PEGASUS 5.1 [21]. All the equations use second-order differencing: upwind for the convection terms and central differences for the diffusion terms. The temporal terms are discretized with first-order backward differences. Continuity is enforced by solving a pressure Poisson equation resulting from a PISO algorithm [22]. ADI linear solvers are used in all algebraic equations. The details of the computational methods are shown in Paterson et al. [15].

3 Subvisual Cavitation and Acoustic Modeling

In the current study, a modified R-P equation is coupled with a bubble motion equation to understand the dynamics of traveling SVC and acoustic noise induced from collapsing small bubbles. The governing equation can be normalized by the characteristic length (D) and the free-stream velocity (U_0). The governing equation of the bubble dynamics is slightly modified from the original R-P equation [23] by adding surface tension and viscous damping as follows

$$R\frac{d^2R}{dt^2} + \frac{3}{2}\left(\frac{dR}{dt}\right)^2 = -\frac{\sigma}{2} - P - \frac{4}{\mathrm{Re}\,R}\left(\frac{dR}{dt}\right) - \frac{2}{\mathrm{We}R} + p_{G0}\left(\frac{R_0}{R}\right)^{3k} \tag{8}$$

where R is the bubble radius, R_0 is the initial bubble size, p_{G0} is the initial pressure of the gas in a bubble, and k is the gas polytropic constant. The dimensionless pressure P (same as RANS solution), the Weber number We, the Reynolds number Re, and the cavitation number σ are defined as follows

$$P = \frac{p-p_0}{\rho U_0^2}, \quad \sigma = \frac{p_0 - p_v}{1/2\rho U_0^2}, \quad \mathrm{We} = \frac{\rho U_0^2 D}{S}, \quad \mathrm{Re} = \frac{U_0 D}{\nu} \tag{9}$$

The initial bubble size R_0 can be given as the assumed nuclei size. When the initial bubble size is fixed, the initial steady state condition ($dR/dt=0$ and $P=0$) gives the initial pressure of the gas in a bubble

$$p_{G0} = \frac{\sigma}{2} + \frac{2}{\mathrm{We}R_0} \tag{10}$$

The bubble motion equation described by Johnson and Hsieh [24] is used to describe the bubble trajectory

$$\frac{d\mathbf{u}_\mathrm{b}}{dt} = -3\nabla P + \frac{3}{4}\frac{C_D}{R}(\mathbf{u}-\mathbf{u}_\mathrm{b})|\mathbf{u}-\mathbf{u}_\mathrm{b}| + \frac{3}{R}(\mathbf{u}-\mathbf{u}_\mathrm{b})\dot{R} \tag{11}$$

where $\mathbf{u}_\mathrm{b}$ is the bubble velocity vector, $\mathbf{u}$ is the fluid velocity vector, and the drag coefficient C_D is given by an empirical equation [25]

$$C_D = \frac{24}{\mathrm{Re}_b}(1 + 0.197\,\mathrm{Re}_b^{0.63} + 2.6\times 10^{-4}\,\mathrm{Re}_b^{1.38}) \tag{12}$$

where the bubble Reynolds number is defined as

$$\mathrm{Re}_b = \frac{2R|\mathbf{u}-\mathbf{u}_\mathrm{b}|}{\nu} \tag{13}$$

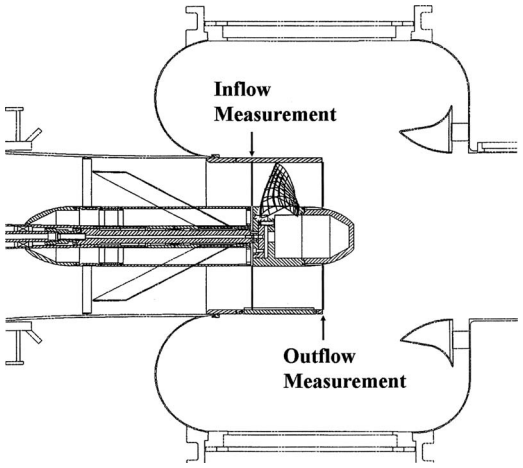

Fig. 1 Schematic view of the experiments

The first term on the right-hand side of Eq. (11) is due to the pressure gradient in the fluid surrounding the bubble. The second term is the drag force. The last term is the force due to the bubble volume variation. In this equation, the Basset term, buoyancy effects, and the Magnus effect due to the bubble spin are neglected. The Basset term is a history term, which takes into account the effect of the deviation in flow pattern. Maxey and Riley [26] have presented order of magnitude estimates for various forces acting in the bubble. They conclude that once the motion is established, the Basset history term is only of the second order when compared to the other forces. In this study, since the bubble is released with the same initial velocity as its surrounding liquid, the Basset term can be neglected.

The radiated acoustic pressure p_a, from the single spherical bubble is given as its far field form [27]. The equation also can be written in normalized form with the same nondimensional parameters used in the other governing equations

$$p_a = \frac{\rho}{4\pi\Re}\frac{d^2V}{dt^2} \tag{14}$$

where $\Re$ is the distance from the bubble center to the point of measurement.

A fourth-order Runge-Kutta scheme is applied to integrate the nondimensionalized R-P Eq. (8) and the bubble motion Eq. (11) in time. The flow field from the solution for the RANS equations provides the ambient pressure and velocities local to the bubble. The numerical solution of the RANS equations, however, can only offer the result at grid points. To obtain the values of pressure and velocities at any specified point in the computation domain, it is necessary to interpolate the values from the solution at the grid points. A three-dimensional linear interpolation scheme is applied in the present study.

In a practical computation, it is not easy to determine the initial bubble position that leads the bubble along its trajectory to the minimum pressure location. Initial positions are tested by releasing bubbles at many prescribed points on the $y-z$ plane in front of the propulsor $(x/D=-0.2)$. These prescribed points are established based on trial and error. Inverse tracking of the streamlines from the minimum pressure location can offer an appropriate matrix of points. More than 100 points tried to find the release points to lead the bubble to the minimum pressure location.

A numerical stability problem occurs with relatively large time steps. This numerical instability mostly comes from the process of the bubble collapsing and rebounding. In order to capture the bubble rebounding correctly and get numerical stability, the time step Δt is chosen in the range of $10^{-2}-10^{-4}$ μs, which is dependent on the initial bubble size and cavitation number. Another assumption is added to retain numerical stability along the total bubble trajectory. Even though a bubble collapses, the nuclei remain in same size in the physical sense. The bubble radius is reset to the initial bubble size when the bubble collapses numerically $(R<0)$.

Table 1 Measured flow conditions

N	J	U_0 (m/s)	K_T	K_Q	Re
500	0.983	6.965	0.31	0.056	6×10^6

4 Ducted Marine Propulsor P5206 and EFD Validation Data

The model propeller P5206 is a three bladed rotor in a cylindrical duct. All experimental measurements were made in the 36-in. water tunnel at the Naval Surface Warfare Center, Carderock Division (NSWCCD). The tunnel is a recirculating design with interchangeable test sections. The 36-in. diameter, open jet test section was used for these tests. Figure 1 shows a schematic of the experimental setup of the ducted rotor at the 36-in. water tunnel. This configuration produces an inner duct diameter of 0.8636 m (34 in.), which is the largest propeller operated in the 36-in. water tunnel.

The measured flow conditions are given in Table 1. The operating advance coefficient J was selected to produce a typical tip-leakage vortex. Laser Doppler velocimetry (LDV) was taken upstream and downstream of the rotor and circumferentially averaged flow data was provided at upstream $x/D=-0.179$, and downstream $x/D=-0.37$ of the rotor, shown in Fig. 1, where $x=0$ corresponds to the center of the 12-in. long propeller hub. LDV measurements were made intensively along the tip-leakage vortex at 103 different $x-r$ planes, which cover up to $S=1.6$. The planes for comparison are selected at $S=1.02$, 1.1, 1.2, 1.3, 1.4, and 1.5, defined as

$$S = \frac{R\theta}{C} + 1 \tag{15}$$

where R is the radius of rotor and C is the chord length of the blade tip. $S=1$ indicates the trailing edge of the blade tip. Figure 2 shows the schematic view of these planes.

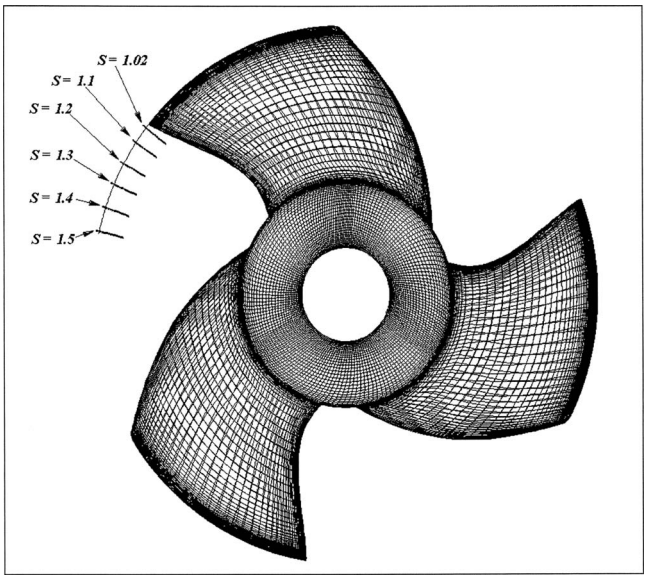

Fig. 2 Comparison planes in the *S* coordinate system

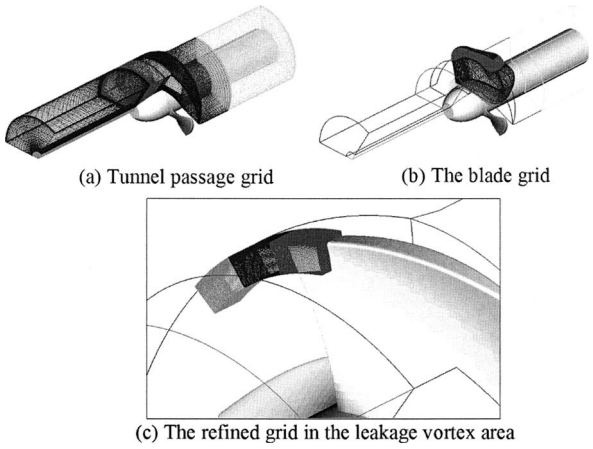

Fig. 3 The grid system: (*a*) the tunnel passage grid, (*b*) the blade grid, and (*c*) the refined grid in the leakage vortex area

5 Computational Grids and Boundary Conditions

The difficulty to construct the structured grid system of a ducted marine propulsor is due to high pitch angle of the blade and tip gap between the blade tip and the duct. The conventional H-type grid, which passes through the passage of pressure side and suction side of the propeller and is mostly used in RANS simulation of open water propellers, has a limitation to make a high-resolution grid in the region of the tip gap and expected leakage vortex area. In order to avoid the above problems, the overset grid method is adopted to achieve high resolution for the tip-gap and the leakage-vortex area. GRIDGEN software is used to generate the grid system. The whole grid system is composed of three structured grid blocks: the tunnel passage and blade and refined grids on the leakage vortex area. The H-type tunnel passage grid in Fig. 3(*a*) is generated through a passage including single blade geometry. The grid points on the side plane of the passage are kept periodic to apply the periodic boundary conditions, which means that when the periodic plane rotates to another periodic plane all the grid points should exactly match each other. The O-type blade grid in Fig. 3(*b*) is generated from the blade surface by the hyperbolic grid expansion option in GRIDGEN. The H-type refined grid in Fig. 3(*c*) covers the experimental measurement plane from $S=0.8$ to 1.6, where S is defined in Eq. (15). The numbers of grid points for coarse, medium, and fine grids are 261,936, 933,495, and 2,053,982 points, respectively.

The following boundary conditions are used as shown in Fig. 4: the inlet plane S_I; the exit plane S_E; the polar periodic plane S_{PP}; the axis pole boundary S_P; the no-slip plane S_{NS}; the rotating no-slip plane S_{RNS}; and the multiblock interface plane S_{MB}.

On the inlet plane S_I, the actual tunnel flow is not fully developed so that the boundary layer of the tunnel wall is increasing after the contraction part of the water tunnel. In order to match the measured thickness of the boundary layer at $x/D=-0.179$, the position of the inlet plane is adjusted at $x/D=-1.49$, which is achieved through several simulations of the tunnel block grids. The center point of this plane is used for the reference pressure by setting its value to zero. On the exit plane S_E at $x/D=1.5$, the first derivatives of all physical variables are set to zero. The internal flow usually needs special treatment of the boundary conditions to ensure mass conservation. The flux difference between the inlet and exit plane is corrected at the exit plane. This treatment improves the convergence of the global solution. On the polar periodic plane S_{PP}, since the Cartesian coordinate system is used, V and W velocity components are converted to the cylindrical coordinate velocity component, V_r and V_θ, in order to apply the polar periodic boundary condition. On the axis pole boundary S_P, this boundary covers the singular line along the x-axis after the fairwater up to the exit plane. On the no-slip plane S_{NS}, NSWCCD 36-in. water tunnel is open jet type, but it is simplified as closed circular tunnel. So, the duct is extended downstream with constant radius. The no-slip boundary covers the extended tunnel wall, fairwater, and propeller shaft except for the rotating hub. On the rotating no-slip plane S_{RNS} ($-0.179<x/D<0.179$), the rotating no-slip boundary condition is applied to the blade surface and the rotating part of propeller hub. On the multiblock interface plane S_{MB}, linear interpolation is used for the values of the physical variables. The boundaries related with the grid overlapping are interpolated or blanked out after the successful run of PEGASUS.

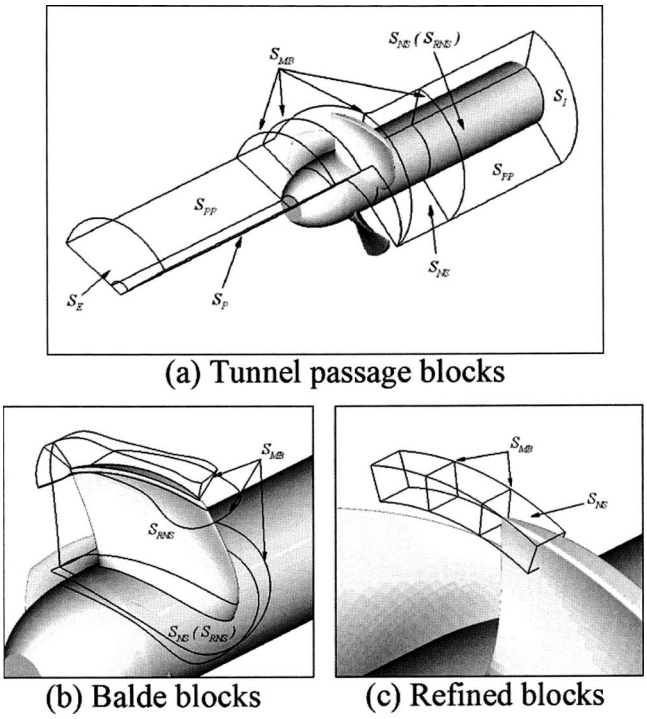

Fig. 4 Schematic view of the boundary conditions for the ducted marine propulsor P5206: (*a*) tunnel passage blocks, (*b*) blade blocks, and (*c*) refined blocks

6 Verification and Validation Analysis

Verification and validation (V&V) procedures for estimation of simulation errors and uncertainties are described in detail in Stern et al. [28]. The present study exactly followed this procedure for V&V analysis.

6.1 Verification and Validation of Integral Variables. The thrust and torque are used for the integral variables in the V&V procedure. Table 2 shows the grid convergence for the thrust coefficient (K_T) and the torque coefficients (K_Q). It also shows the change in solution. With the two solution changes (ε) known, it is

Table 2 The grid convergence of integral variables

	Coarse (S_3)	Medium (S_2)	Fine (S_1)	Data (D)
K_T	0.2830	0.2870	0.2895	0.31
	8.7%	7.4%	6.6%	
ε		−0.0040	−0.0025	
K_Q	0.05385	0.05460	0.05498	0.056
	3.8%	2.5%	1.8%	
ε		−0.00075	−0.00038	

Table 3 Validation of integral variables

	E (%D)	U_V (%D)	U_D (%D)	U_{SN} (%D)
K_T	6.6	3.3	2.2	2.4
K_Q	1.8	2.3	2.2	0.74

possible to calculate the grid convergence ratio and give information about the convergence condition. The current study displayed monotonic convergence.

The simulation numerical uncertainty U_{SN}, validation uncertainty $U_V=\sqrt{U_D^2+U_{SN}^2}$, comparison error $E=D-S$, and estimated U_D are shown in Table 3. For K_T, $|E|>U_V$ such that K_T is not validated at the $|E|=6.6\%D$ interval. For K_Q, $|E|<U_V$, such that K_Q is validated at the $|U_V|=2.3\%D$ interval.

6.2 Verification and Validation of a Point Variable. The radial velocity V_r along the horizontal-cut line from $0.07<x/D<0.12$ at $r/D=0.494$ in the plane $S=1.02$ shown in Fig. 5 is selected as a point variable. This horizontal-cut line passes through the center of the tip-leakage vortex core in the axial direction. The plane $S=1.02$ corresponds to the plane just after the trailing edge of the blade shown in Fig. 2. The grid convergence for the radial velocity along the horizontal-cut is shown in Fig. 6, including comparison with experimental data. The simulation results do not capture the gradient or magnitude of the tip-leakage vortex. A second peak is also observed in the data, which, as will be discussed later, corresponds to the trailing edge vortex.

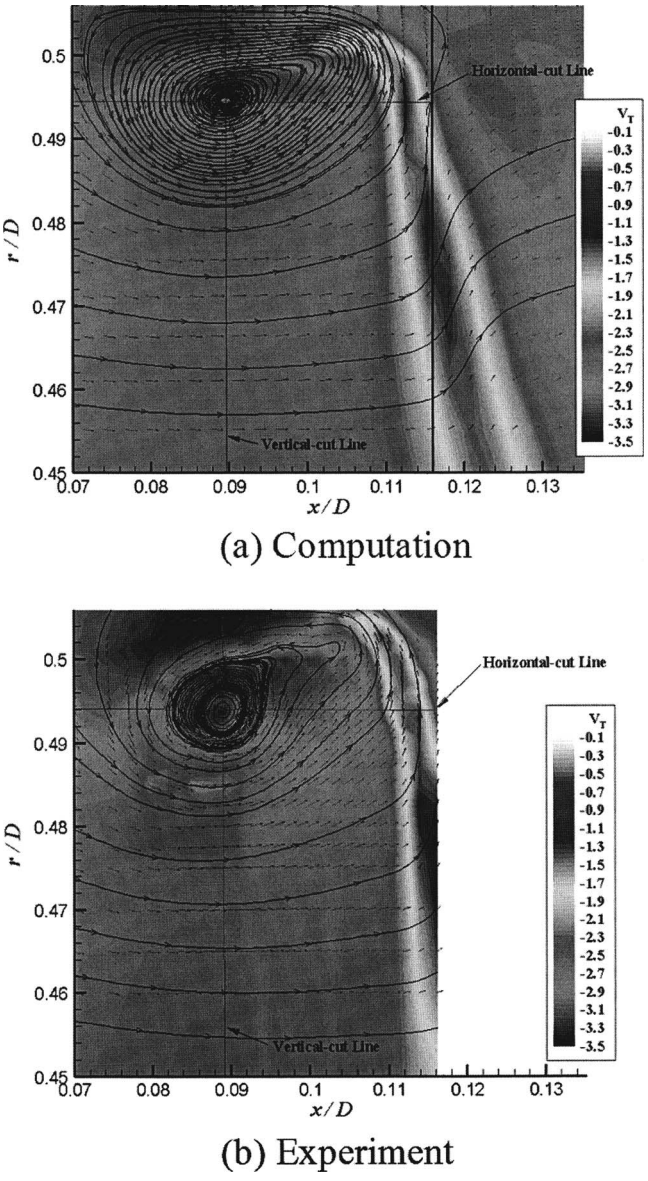

Fig. 5 Cross plane velocity vectors and tangential velocity contours at $S=1.02$: (*a*) computation and (*b*) experiment

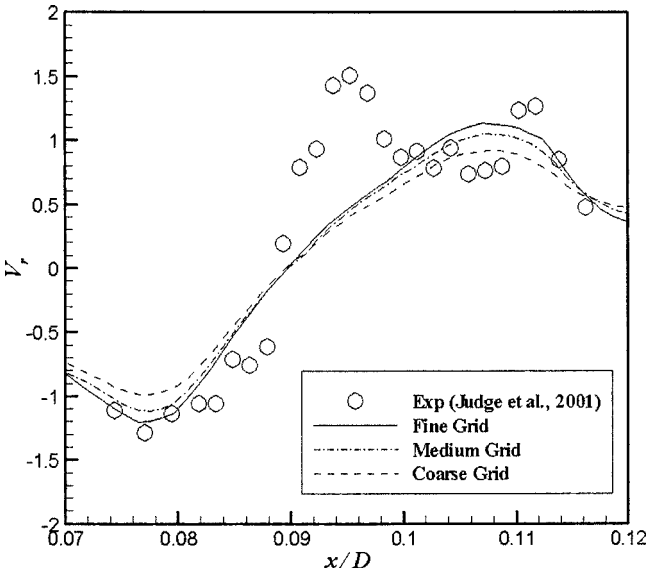

Fig. 6 The grid convergence of radial velocity profile along the horizontal-cut line

The profile-averaged validation results for the radial velocity profile are given in Table 4. Values are normalized with the maximum value for the radial velocity profile in the data ($V_{r\,\max}=1.5$). The data uncertainty for LDV measurement of the mean velocity is 2–5% of the maximum velocity [29] and so it is assumed $U_D=3.7\%V_{r\,\max}$. In Table 4, $|E|<U_V$ such that the solution is validated globally at the $|U_V|=4.5\%V_{r\,\max}$ interval.

Distributions of $(E,\pm U_V)$ along the horizontal-cut line are also computed and showed in Fig. 7. The lack of validation is mainly due to under prediction of the radial velocity gradient and magnitude near the vortex core in the simulation.

7 Analysis of Propulsor Flow and Tip-Leakage Vortex

The propulsor flow is very sensitive to the inflow coming into the propulsor blade rows. Especially, the boundary layer thickness affects significantly the performance of the propulsor such as thrust and torque. Additional effort is needed to calibrate the inflow such that the numerical simulation represents the experimental flow conditions. Calibration is performed by systematically adjusting the inlet position in order to get the same boundary layer thickness at the measured inflow condition, $x/D=-0.179$ shown in Fig. 1. As mentioned in Sec. 5, the axial inflow position x/D

Table 4 The profile-averaged validation of a point variable ($V_{r\,\max}=1.5$)

E $\%V_{r\max}$	U_V $\%V_{r\max}$	U_D $\Delta V_{r\max}$	U_{SN} $\%V_{r\max}$
3.9	4.5	3.7	2.6

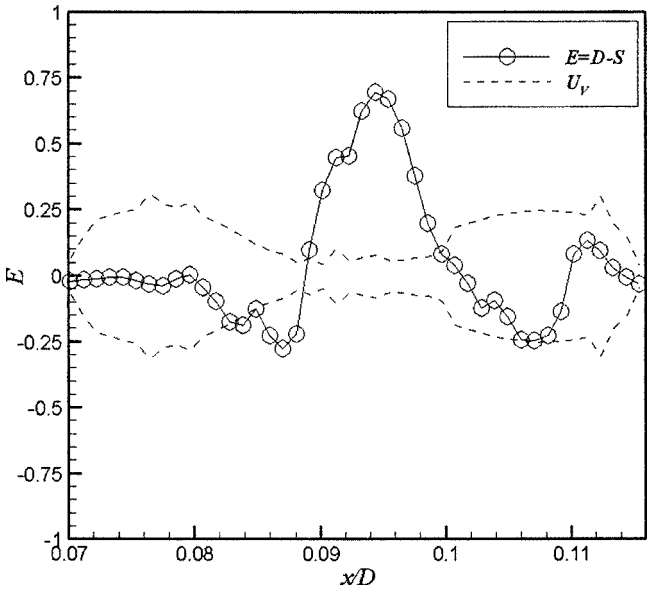

Fig. 7 The comparison error and validation uncertainty

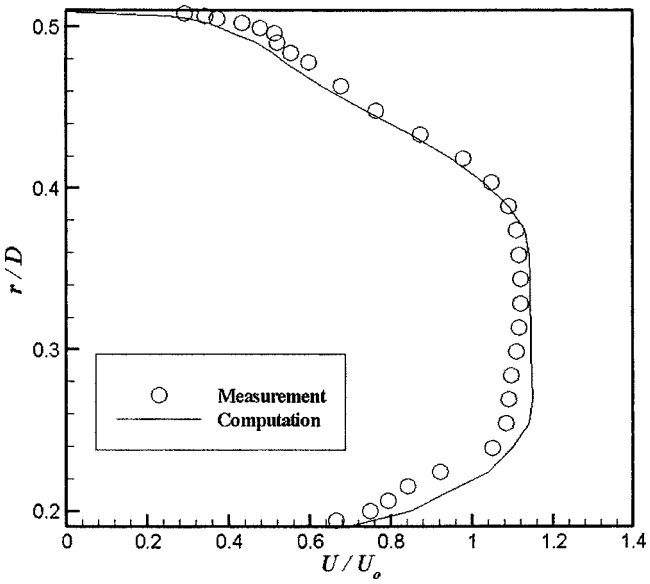

Fig. 9 Comparison of the axial velocity profile at $x/D=0.37$

$=-1.49$ gives the same boundary layer thickness with the experimental data. Figure 8 shows the matched axial velocity profile with the experimental measurements.

Comparisons of circumferentially averaged velocities for the outflow are made with the experimental measurements. Figure 9 shows the circumferentially averaged axial velocity profile including the experimental data measured at $x/D=0.37$. This position corresponds to the axial location just after the duct trailing edge. The computed profiles are in overall good agreement with the experimental data. The simulated axial velocity shows a little bigger acceleration near the hub region. The discrepancy near the duct region is due to the existence of the duct wall in the simulation modeling. On the contrary, the experimental flow is an open jet after the duct trailing edge.

Figure 10 shows the pressure distribution on the surface of the blade and hub. The denoted P in this figure is nondimensionalized by ρU_0^2 such that it can be converted to C_P by multiplying by 2. The minimum pressure on the blade surface is obtained on the suction side of blade tip at 84% of the tip chord length ($S=0.84$) with a value $P=-4.4$. Typically cavitation inception number $\sigma_i=-C_{P\,\min}$ is used as a rough estimate of the cavitation inception. The current results give the cavitation inception number $\sigma_i=8.8$. However, the cavitation inception bubble is experimentally observed to occur downstream of half the tip chord length ($S=1.5$) along the tip-leakage vortex with the value of cavitation inception number $\sigma_i=11$. Figure 11 shows the pressure distribution of the duct surface. The effects of the pressure variation of the blade tip and the tip-leakage vortex are significant on the duct surface. Low pressure along the tip-leakage vortex is clearly shown. In order to capture the flow structure of the tip-leakage vortex, ribbon tracing is performed along the tip-leakage vortex and the trailing edge vortex. Figure 12 shows how the corotating tip-leakage and trailing edge vortices interact ($S=1.02$) and merge $S>1.02$ with low pressure, especially along the tip-leakage vortex core.

Cross flow velocity vectors (U, V_r) in the $x-r$ plane and contours of the tangential velocity in the rotor rotation direction V_T

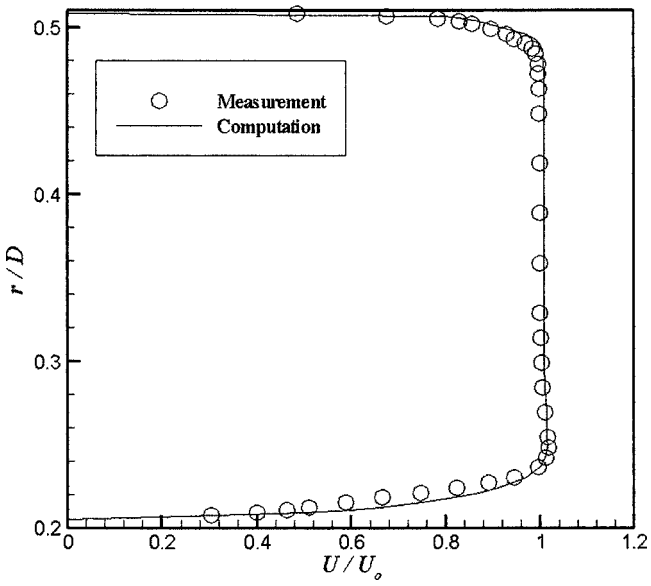

Fig. 8 Comparison of the axial velocity profile at $x/D=-0.179$

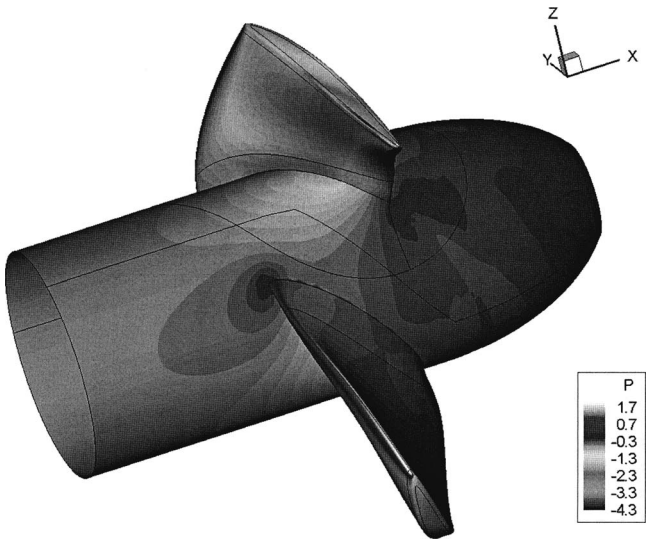

Fig. 10 Pressure on the surface of blade and hub

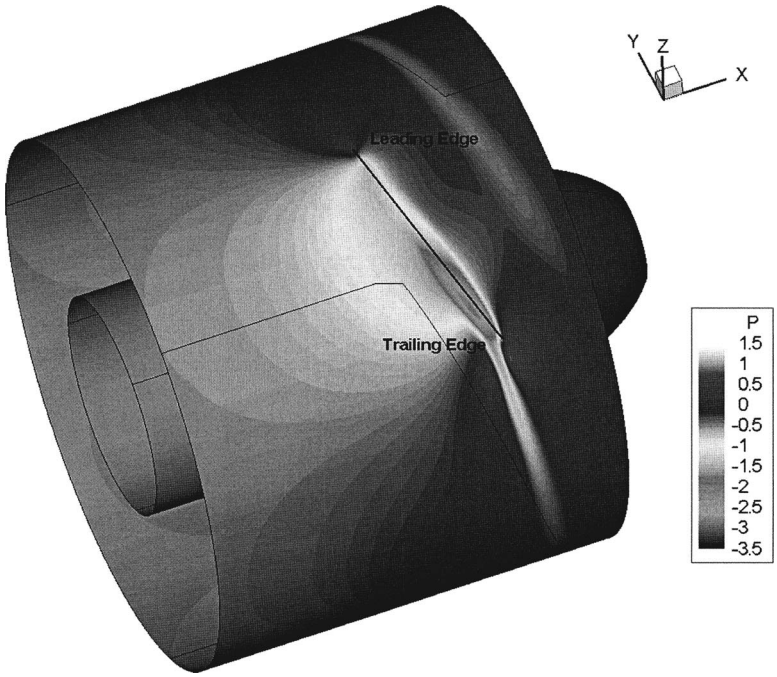

Fig. 11 Pressure on the duct surface

are compared. The streamlines are traced to capture the shape of the vortex and the vortex core center. At the plane $S=1.02$, which corresponds to just downstream of the rotor tip, both results show the blade wake and the interaction between the tip-leakage and the trailing edge vortices (Fig. 5). The computational result does not show clearly the vortical vector near the tip trailing edge (the trailing edge vortex will be shown clearly by vorticity contours in the following). The overall shape of the vortex is distorted by the effect of the interaction of the two vortices. Streamlines in the computation are more diffusive than the experiment. Both results show faster vortex core velocity in the contours of V_T than the surroundings. The position of the vortex core is well matched with the experiment.

The axial vorticity is computed with both computational and experimental results in Fig. 13. At the plane $S=1.02$, the existence of the trailing edge vortex is clearly shown in the computational result, which was not shown with the cross plane vectors in Fig. 5. The experiment shows two peak values at the center of each vortex core and another peak value between the tip-leakage vortex and the trailing edge vortex. The RANS computation only shows a peak value of vorticity at the center of the trailing edge vortex. The peak value between the tip-leakage vortex and the tailing edge vortex in the experiment seems to be related to the vortex interaction. RANS solution does not catch the vortex interaction accurately in this plane.

After the plane of the vortex interaction ($S>1.02$), the two

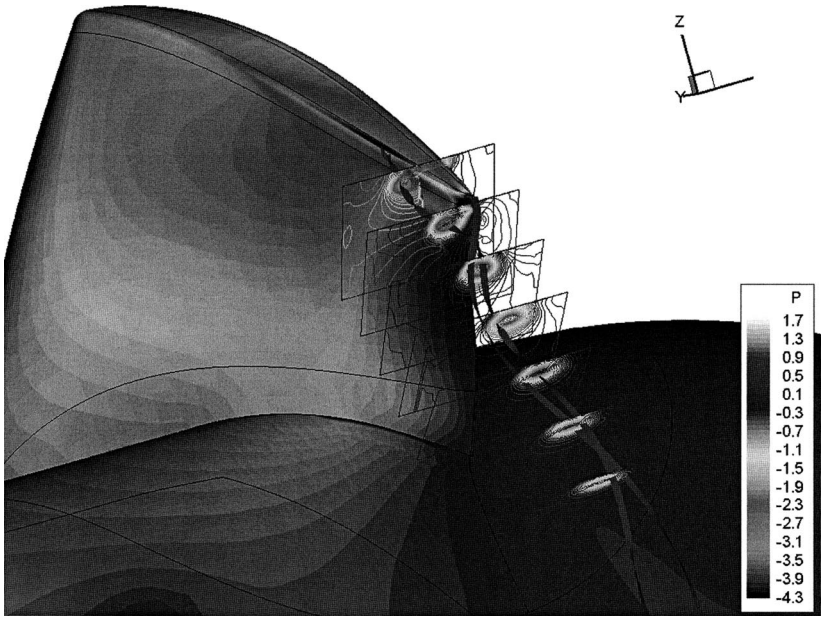

Fig. 12 The flow structure of tip-leakage and trailing-edge vortices

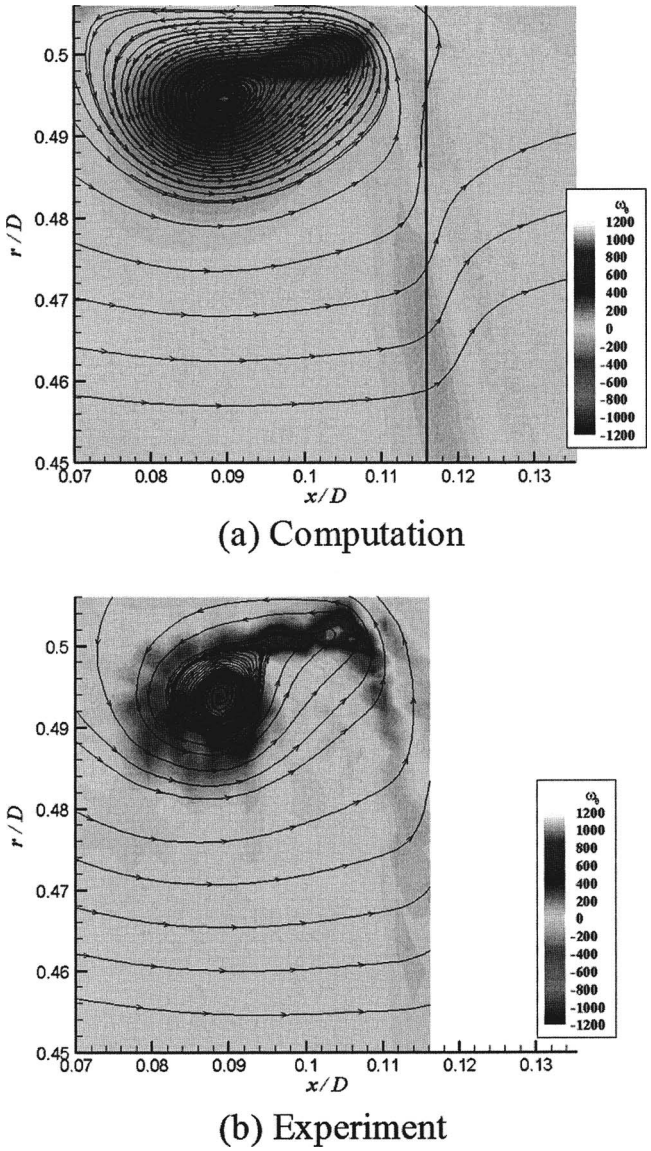

Fig. 13 Vorticity contours at $S=1.02$: (*a*) computation and (*b*) experiment

vortices merge along the tip-leakage vortex near $S=1.1$. The vortex strength temporally increases just after merging after which it decreases. The detailed comparisons at other S planes are not shown in the current paper, but it can be found in Ref. [30] including comparisons of the vortical velocity profiles at the vertical and horizontal cut lines shown in Fig. 5.

The position of the vortex core is compared with experimental data and other computational results [8] in Fig. 14. The symbols for the experiment and the current computation indicate each S plane (1.02–1.5) in sequential order. The symbols for Brewer's computation represent the S values of 1.03, 1.07, 1.17, and 1.23, respectively. The computed results show the good agreement except for $S>1.3$. From $S>1.3$, the position of the vortex core in the current computation is shifted to the axial flow direction compared to the experiment. Brewer's [8] result is overall shifted toward upstream compared to the experiment.

In order to compare the global characteristic of the tip-leakage vortex, the vortex core size and the circulation is computed. The vortex shape is not symmetric and so the core size is obtained in an averaged sense as follows

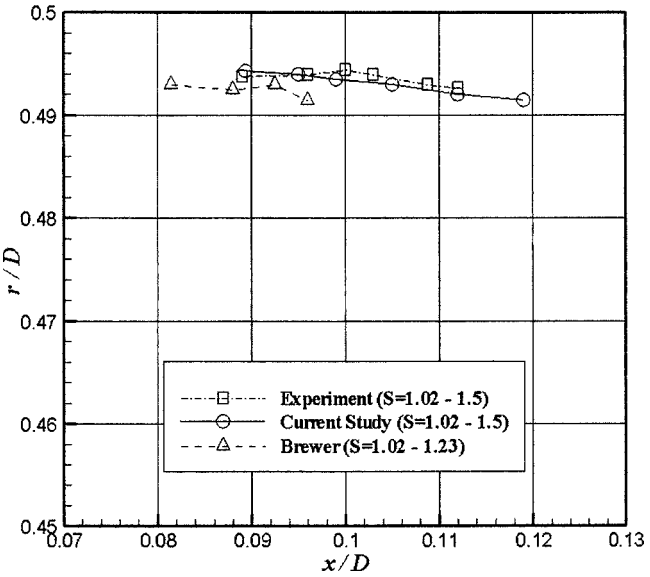

Fig. 14 The position of tip-leakage vortex core

$$a_c(S) = \frac{\sum_{j=1}^{N} a_j(\nu_{t\,\max}, \theta_j)}{N} \tag{16}$$

where a_j is the distance from the vortex core to the location of maximum tangential velocity $\nu_{t\max}$ in the given radial direction $\theta_j = 2\pi j/N$. N is taken as 36.

The computed values are shown in Figs. 15 and 16. The vortex core size in the computation is bigger than in the experiment and the circulation shows good agreement with the experiment except at the plane $S=1.02$, where the vortex interaction occurs.

Figure 17 shows the pressure coefficient C_P along the vortex core computed from the current RANS solution and the computational solution by Brewer [8]. The current study gives much lower level of the pressure coefficient than Brewer's result. The minimum pressure coefficient is obtained at $S=1.08$ with value $C_P=-6.4$. This value is higher than the coefficient of blade minimum pressure ($C_P=-8.8$) and even much higher than experimental cavitation inception number ($\sigma_i=11$). Therefore, based on the cur-

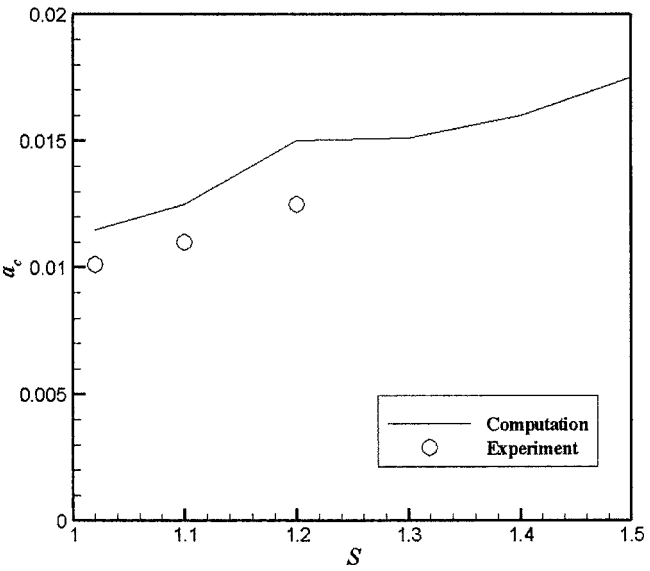

Fig. 15 Vortex core size

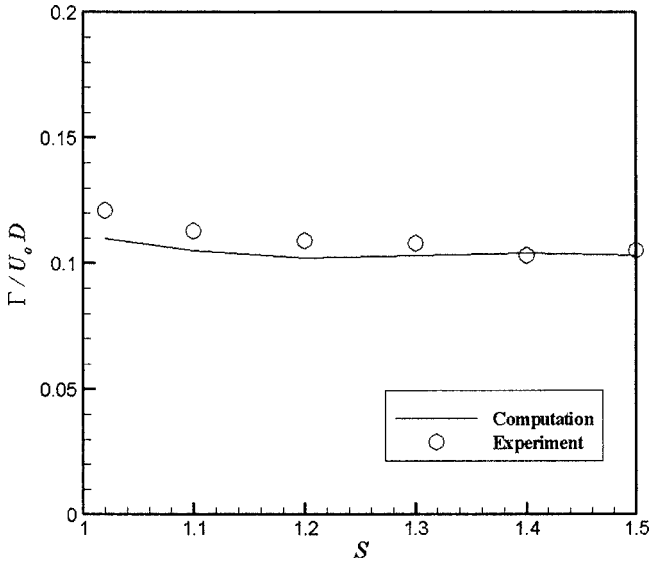

Fig. 16 Circulation

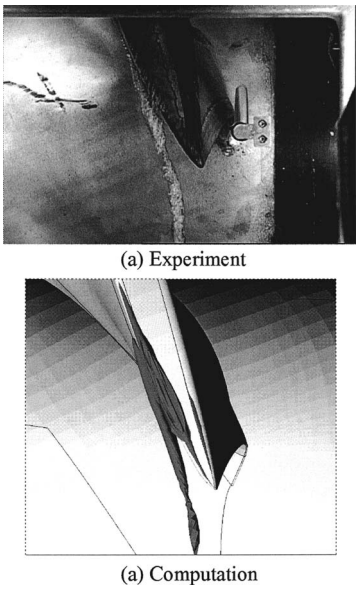

Fig. 18 Numerical cavitation inception

rent RANS solution, low pressure in the vortex core region does not affect the cavitation inception based on $\sigma_i = -C_{p\,\min} = 6.4$.

Even though the experimental data for the pressure along the tip-leakage vortex is not provided, a rough comparison is possible from the photo of the tip-leakage vortex cavitation taken in the experiment. Figure 18(*a*) shows the photo taken at 18 psi tunnel pressure. The tunnel pressure given the cavitation number through a simple calculation using the definition of cavitation number. The computed cavitation number is $\sigma = 5.0$ from the definition of cavitation number in Eq. (9). Under the assumption that a region with $C_P < -\sigma$ is cavitating, Figure 17 shows the isosurface of $C_P = -5.0$. Comparison shows very similar cavitating region. The results of the comparison being so positive lead to the conclusion that the pressure distribution in Fig. 17 is a good prediction of the distribution within the cavitation zone.

8 SVC and Acoustics

In the experiment [1], the cavitation inception occurs at $\sigma_i = 11$ and the location of cavitation inception bubble is observed at $S = 1.5$, whereas in the RANS results $\sigma_i = 8.8$ at $S = 0.84$. The RANS results also show a local minimum $C_P = -6.4$ in the tip-leakage vortex core at $S = 1.08$. Two possible explanations are suggested to explain these discrepancies.

For the first explanation, we can presume that the resolution of RANS solution is still not good enough to predict the real minimum pressure. If this is an actual problem, it is obvious that finer grids, better turbulence models, and modeling improvements like LES/DNS for improved vortex interaction simulations are required. For another explanation, the bubble dynamics model is applied to cavitation inception problem of the ducted rotor P5206.

Three different cavitation numbers, $\sigma = 8.7$, 8.6, and 8.5 near cavitation inception based on the RANS solution, are selected for the numerical simulation of SVC with three different initial bubble sizes, $R_0 = 10$, 50, and 100 μm. These values are chosen from the nuclei distribution in the actual medium size water tunnel [31] shown in Fig. 19. The smaller nuclei (<20 μm) have high

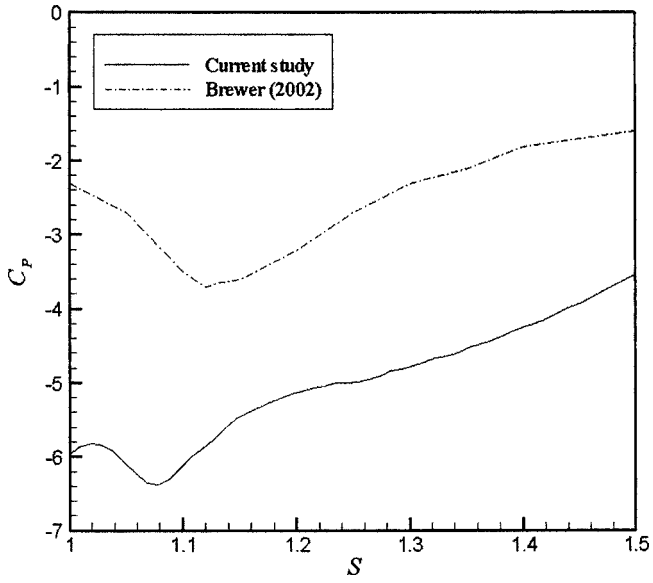

Fig. 17 Pressure along the tip-leakage vortex

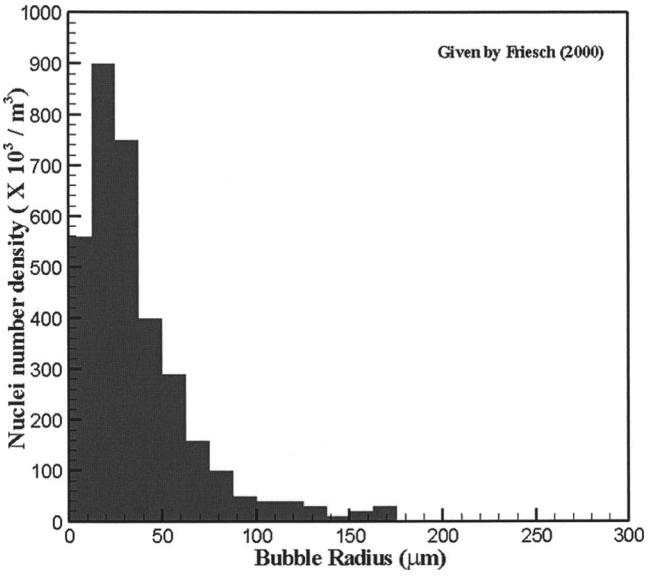

Fig. 19 Cavitation comparison with experiment: (*a*) experiment and (*b*) computation

values of number density, but 100 μm size nuclei also have about 50,000 nuclei/m^3. A bubble diameter of 1 mm is assumed as a visible size. Since the hydroacoutic pressure is normalized by the same parameters (ρU_0^2) as the hydrodynamic pressure, a value of 0.1 is assumed as detectable noise level. (very dependent on sensor used for the measurement). Neppiras [32] and Young [33] categorized two types of SVC: stable and transient. For stable cavitation, a bubble oscillates, often nonlinearly, around some equilibrium size. On the other hand, transient cavitation generally exists in finite cycles. During this cycle, the bubble expands to at least double and then collapses violently.

All computed results are summarized in Table 5–8 which include by the maximum bubble size, the position of the maximum bubble, the type of subvisual cavitation, and the hydroacoustic noise level, respectively. Based on the results of the bubble dynamics simulation, the cavitation inception is first captured at the cavitation number $\sigma=8.7$ with initial bubble size $R_0=100$ μm and the inception bubble is found near the blade tip. However, simulated visual time, i.e., $R>0.5$ mm, is very short (less than 0.05 ms) because only the first bubble crest is regarded as visible such that this event is likely captured in visual observation. Other cases with initial bubble size $R_0=10$ μm and $R_0=50$ μm do not show the visible size of bubble response in this cavitation number $\sigma=8.7$. The next possible inception case is the cavitation number $\sigma=8.6$ with the initial bubble size $R_0=100$ μm (Fig. 20). The visible size bubble is oscillating with high frequency ($f=12.5$ kHz, time period between events is 0.08 ms) downstream of the tip-leakage vortex until it reaches 65% of tip chord length ($S=1.65$). This case can explain the experimental observation of the cavitation inception bubble. However, the inception bubble is not exactly located at $S=1.5$. The inception bubble can be captured in the range of $0.85<S<1.65$. Other initial bubble sizes ($R_0=10$ μm and $R_0=50$ μm) also do not show visible events for this cavitation number $\sigma=8.6$.

The microbubbles in the real water tunnel exist in the fluctuating pressure field. Since the RANS solution only gives the mean value of the unsteady pressure fluctuation, the effect of this kind of fluctuation should be considered in the bubble dynamics model. In the current study, the following model is added to see the difference of bubble response with and without turbulence fluctuations as discussed earlier. The following fluctuation model is superimposed on the pressure field of the RANS solution

$$p'(\mathbf{x},t) = p'_{\text{amp}} \sin \omega t \tag{17}$$

where the amplitude of the pressure fluctuation is obtained from the turbulent kinetic energy in the RANS solution as follows [34]

$$p'_{\text{amp}} = 0.47k \tag{18}$$

In order to investigate the turbulent fluctuation effect on cavitation inception, i.e., the possibility of an earlier cavitation inception due to the turbulent fluctuations, the case at the cavitation number $\sigma=8.7$ with initial bubble size $R_0=100$ μm, which is barely regarded as cavitation inception, is selected. The simulation with the

Table 5 Maximum bubble size

	$R_0=10$ μm (mm)	$R_0=50$ μm (mm)	$R_0=100$ μm (mm)
$\sigma=8.7$	0.05	0.33	0.51 (visible)
$\sigma=86$	0.23	0.44	0.72 (visible)
$\sigma=8.5$	0.40	0.58 (visible)	0.96 (visible)

Table 6 The position of maximum bubble in *S* coordinate

	$R_0=10$ μm	$R_0=50$ μm	$R_0=100$ μm
$\sigma=8.7$	$S<0.9$	$S<0.9$	$S<0.9$
$\sigma=8.6$	$S<0.9$	$S<0.9$	$S=1.65$
$\sigma=8.5$	$S<0.9$	$S<0.9$	$S=1.01$

Table 7 Type of subvisual cavitation

	$R_0=10$ μm	$R_0=50$ μm	$R_0=100$ μm
$\sigma=8.7$	Stable	Stable	Stable
$\sigma=8.6$	Transient	Transient	Stable
$\sigma=8.5$	Transient	Transient	Both

Table 8 Hydroacoustic noise level

	$R_0=10$ μm	$R_0=50$ μm	$R_0=100$ μm
$\sigma=8.7$	Nondetectable	Detectable	Detectable
$\sigma=8.6$	Nondetectable	Detectable	Detectable
$\sigma=8.5$	Non detectable	Detectable	Detectable

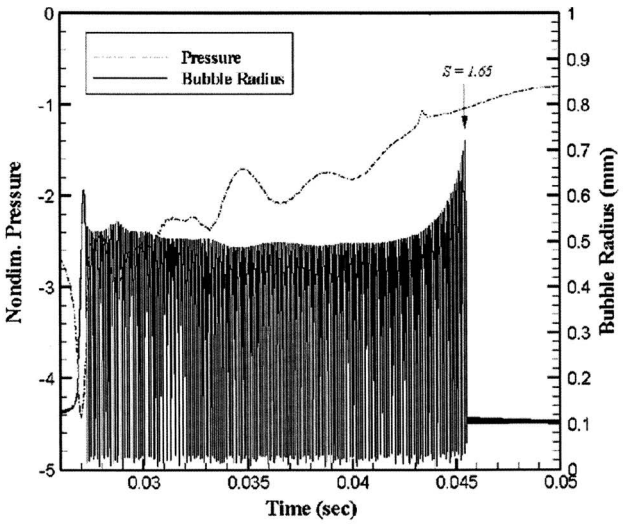

(a) Response of the bubble radius

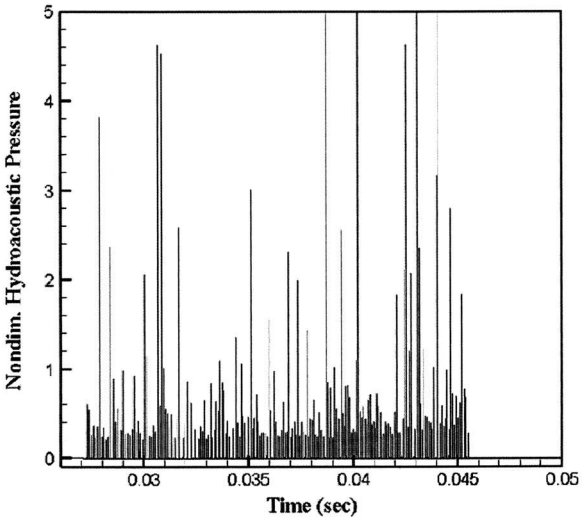

(b) Response of the hydroacoustic pressure

Fig. 20 Number of nuclei in a unit volume for the medium size water tunnel

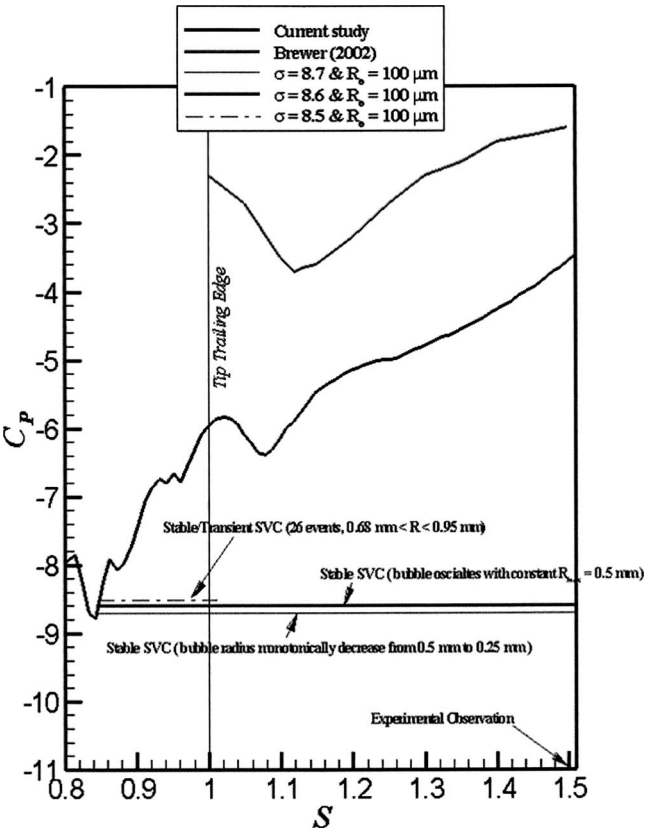

Fig. 21 SVC at $\sigma=8.6$ with $R_0=100$ μm: (*a*) response of the bubble radius and (*b*) response of the hydroacoustic pressure

fluctuation model at the frequency 10, 30, and 50 kHz are performed. These frequencies are selected from the equation of bubble natural frequency based on the range of bubble size in the result of simulation without fluctuation model. Unfortunately, even though the bubble response is not identical with the case of nonfluctuation model, the overall shape of the response was almost same. Detail results are shown in Ref. [30]. The pressure fluctuation outside of the resident time (time in $-C_P>\sigma$) does not have much affect on the cavity dynamics.

We can conclude that cavitation inception is caused from the largest nuclei, which also have enough number of nuclei for cavitation events to occur. (For the current simulation, $R_0=100$ μm is regarded as the largest nuclei size.) The resident time in $-C_P>\sigma$ decides the dynamics of bubble response. As the resident time becomes longer, maximum bubble size increases and then bubble reaches maximum bubble size and collapses (typical transient cavitation). Short resident time makes subvisual cavitation stable. Figure 21 shows a summary of the numerical investigation of cavitation inception. As we concluded, the response of the largest nuclei is the most possible reason for the downstream observation of the cavitation inception bubble. However, the smaller nuclei ($R_0\approx 10$ μm) have 20 times the number density as compared to the large nuclei ($R_0=100$ μm). Since the response of the smaller bubble continues downstream with 2–5 times of the initial bubble size, the coalescence of these bubbles can be a possible reason for the downstream observation of the cavitation inception bubble.

9 Summary and Conclusions

High-fidelity RANS CFD simulations are presented for the ducted marine propulsor P5206, including verification studies based on assessment of iterative and grid convergence, validation studies using available benchmark EFD data, and SVC and acoustics analysis using the modified Rayleigh-Plesset equation along the bubble trajectories along with far-field form of acoustic pressure for a collapsing spherical bubble. The general-purpose, parallel, unsteady RANS code CFDSHIP-IOWA is used with the BKW turbulence model and extensions for a relative rotating coordinate system and the Chimera overset grid method. Intervals of verification for thrust, torque, and profile averaged radial velocity are 2.4, 0.74, and 2.6%D, respectively, which are reasonable in comparison with previous results for open water propellers and a surface combatant. Thrust is not validated since comparison error $E=7\%D$ and validation uncertainty $U_V=3\%D$, but torque is validated at $2\%D$ interval. Just downstream of the rotor tip, the average radial velocity is validated at $5\%V_{r\max}$ interval, but magnitude and gradients in the vortex cores are underpredicted. The flow pattern displays interaction (just downstream of the rotor tip) and merging (after 10% chord length downstream of the rotor tip) of the tip-leakage and the trailing edge vortices. In the interaction region, multiple peaks and magnitude of vorticity are underpredicted. The tip-leakage vortex core position, size, and circulation show good agreement with the experimental data, although size of the vortex is overpredicted and circulation in the interaction region is underpredicted. For cavitation number $\sigma=5$ and assuming $C_p<-5$ as the cavitation condition for the simulations, experimental and RANS simulated cavitation patterns show good agreement. The simulations indicate globally minimum $C_p=-\sigma_i=-8.8$ on the suction side of the blade tip at 84% chord from the leading edge and locally minimum $C_p=-6.4$ in the tip-leakage vortex at 8% chord downstream of the trailing edge, which implies cavitation inception number $\sigma_i=8.8$ and the location on the blade near the tip trailing edge. The experiment indicated $\sigma_i=11$ and location in tip-leakage vortex core 50% chord downstream of the trailing edge. SVC and acoustics studies indicate that bubble dynamics may partly explain discrepancy, especially if coalescence considered; however, no question that finer grid, anisotropic turbulence models, and modeling improvements for improved vortex interaction simulations are required.

Acknowledgment

This research was sponsored by Office of Naval Research Grant No. N00014-00-1-0473 under the administration of Dr. Patrick Purtell and partially supported to prepare this paper by the basic research project in MOERI/KORDI.

References

[1] Judge, C. Q., Oweis, G. F., Ceccio, S. L., Jessup, S. D., Chesnakas, C.J., and Fry, D. J., 2001, "Tip-Leakage Vortex Interaction on a Ducted Rotor," CAV 2001: The 4th International Symposium on Cavitation, Pasadena, CA.
[2] Sanchez-Caja, A., 1996, "Numerical Calculation of Viscous Flow Around DTRC Propeller 4119 for Advance Number Range 0.3–1.1 Using the FINFLO Navier-Stokes Solver," Technical Report VALB141A, VTT Manufacturing Technology, Tekniihantie 12, Espoo, Finland.
[3] Abdel-Maksoud, M., Menter, F., and Wuttke, H., 1998, "Viscous Flow Simulations for Conventional and High-Skew Marine Propellers," Ship Technology Research, **45**, pp. 64–71.
[4] Hsiao, C.-T., and Pauley, L. L., 1998, "Numerical Computation of Tip Vortex Flow Generated by Marine Propeller," ASME FED Summer Meeting, Washington, DC.
[5] Feng, J., Wang, V. A., Lee, Y.-T., and Merkle, C. L., 1998, "CFD Modeling of Tip Vortex for Open Marine Propeller," ASME FED Summer Meeting, Washington, DC.
[6] Chen, B., 2000, "RANS Simulation of Tip Vortex Flow for a Finite-Span Hydrofoil and a Marine Propulsor," Ph.D. thesis, The University of Iowa, Iowa City, IA.
[7] Chen, B., and Stern, F., 1999, "Computational Fluid Dynamics of Four-Quadrant Marine-Propulsor Flow," J. Ship Res., **43**(4), pp. 218–228.
[8] Brewer, W. H., 2002, "On Simulating Tip-Leakage Vortex Flow to Study the Nature of Cavitation Inception," Ph.D. thesis, Mississippi State University, MS.
[9] Meyer, R. S., Billet, M. L., and Holl, J. W., 1992, "Freestream Nuclei and Traveling Bubble Cavitation," ASME J. Fluids Eng., **114**, pp. 672–679.
[10] Chizelle, Y. K., Ceccio, S. L., and Brennen, C. E., 1995, "Observations and Scaling of Traveling Bubble Cavitation," J. Fluid Mech., **293**, pp. 99–126.
[11] Hsiao, C.-T., and Pauley, L. L., 1997, "Numerical Study of Tip Vortex Cavitation Inception Using a Bubble Dynamics Model," ASME FED Summer Meeting (FEDSM 97-325), Vancouver, BC, Canada.

[12] Farrell, K. J., 2001, "Eulerian/Lagrangian Analysis for the Prediction of Cavitation Inception," CAV2001: The 4th International Symposium on Cavitation, Pasadena, CA.
[13] Hsiao, C.-T., and Chahine, G. L., 2001, "Numerical Simulation of Bubble Dynamics in a Vortex Flow Using Navier-Stokes Computations and Moving Chimera Grid Scheme," CAV2001: The 4th International Symposium on Cavitation, Pasadena, CA.
[14] Hsiao, C.-T., and Chahine, G. L., 2002, "Prediction of Vortex Cavitation Inception Using Coupled Spherical and Non-Spherical Models and UnRANS Computations," *Proceedings of the 24th Symposium on Naval Hydrodynamics*, Fukuoka, Japan, 2002.
[15] Paterson, E. G., Wilson, R. V., and Stern, F., 2003, "General Purpose Parallel Unsteady RANS Ship Hydrodynamics Code: CFDSHIP-IOWA," IIHR Report No. 432, The University of Iowa, Iowa City, IA.
[16] Wilson, R. V., Paterson, E. G., and Stern, F., 2000, "Verification and Validation for RANS Simulation of a Naval Combatant," Gothenburg 2000: A Workshop on Numerical Ship Hydrodynamics, Gothenburg, Sweden.
[17] Wilson, R. V., Stern, F., Coleman, H., and Paterson, E. G., 2001, "Comprehensive Approach to Verification and Validation of CFD Simulations—Part 2: Application for RANS Simulation of Cargo/Container Ship," ASME J. Fluids Eng., **123**(4), pp. 803–810.
[18] Menter, F., 1993, "Zonal Two-Equation $k-\omega$ Turbulence Models for Aerodynamic Flows," AIAA Paper No. 93-2906.
[19] Wilcox, D. C., 1988, "Reassessment of the Scale-Determining Equation for Advanced Turbulence Models," AIAA J., **26**, pp. 1299–1310.
[20] Jones, W. P., and Launder, B. E., 1973, "The Calculation of Low-Reynolds-Number Phenomena with a Two-Equation Model of Turbulence," Int. J. Heat Mass Transfer, **16**, pp. 1119–1130.
[21] Suhs, N. E., Rogers, S. E., and Dietz, W. E., 2002, "PEGASUS 5: An Automated Preprocessors for Overset-Grid CFD," AIAA Paper No. 2002-3186.
[22] Issa, R. I., 1986, "Solution of Implicitly Discretized Fluid Flow Equations by Operator Splitting," J. Comput. Phys., **62**, pp. 40–65.
[23] Plesset, M. S., 1949, "The Dynamics of Cavitation Bubbles," ASME J. Appl. Mech., **16**, pp. 228–231.
[24] Johnson, V. E., and Hsieh, T., 1966, "The Influence of the Trajectories of Gas Nuclei on Cavitation Inception," *Proceedings of the 6th Symposium on Naval Hydrodynamics*.
[25] Haberman, W. L., and Morton, R. K., 1953, "An Experimental Investigation of the Drag and Shape of Air Bubbles Rising in Various Liquids," DTMB Report No. 802.
[26] Maxey, B. H., and Riley, J. J., 1983, "Equation of Motion for a Small Rigid Sphere in a Uonuniform Flow," Phys. Fluids, **26**(4), pp. 883–889.
[27] Blake, W. K., 1986, *Mechanics of Flow-Induced Sound and Vibration*, Academic Press, New York.
[28] Stern, F., Wilson, R. V., Coleman, H., and Paterson, E. G., 2001, "Comprehensive Approach to Verification and Validation of CFD Simulations—Part 1: Methodology and Procedure," ASME J. Fluids Eng., **123**(4), pp. 793–802.
[29] Longo, J., 2002, personal communication.
[30] Kim, J., 2002, "Sub-Visual Cavitation and Acoustic Modeling for Ducted Marine Propulsor," Ph.D. thesis, The University of Iowa, IA.
[31] Friesch, J., 2000, "Ten Years of Research in Hydrodynamics and Cavitation Tunnel—HYKAT of HSVA," NCT '50 International Conference of Propeller Cavitation, New Castle, UK.
[32] Neppiras, E. A., 1980, "Acoustic Cavitation," Phys. Rep., **61**(3), pp. 159–251.
[33] Young, F. R., 1989, *Cavitation*, McGraw-Hill, New York.
[34] Hinze, J. O., 1975, *Turbulence*, McGraw-Hill, New York.

Martin Lopez de Bertodano
Department of Nuclear Engineering,
Purdue University,
West Lafayette, IN 47907
e-mail: bertodan@purdue.edu

Xiaodong Sun
Department of Mechanical Engineering,
Ohio State University,
Columbus, OH 43202

Mamoru Ishii
Department of Nuclear Engineering,
Purdue University,
West Lafayette, IN 47907

Asim Ulke
Bechtel-Bettis, Inc.,
West Mifflin, PA 15122

Phase Distribution in the Cap Bubble Regime in a Duct

*The lateral phase distribution in the cap-bubbly regime was analyzed with a three-dimensional three-field two-fluid computational fluid dynamics (CFD) model based on the turbulence model for bubbly flows developed by Lopez de Bertodano et al. [1994, "Phase Distribution in Bubbly Two-Phase Flow in Vertical Ducts," Int. J. Multiphase Flow, **20**(5), pp. 805–818]. The turbulent diffusion of the bubbles is the dominant phase distribution mechanism. A new analytic result is presented to support the development of the model for the bubble induced turbulent diffusion force. New experimental data obtained by Sun et al. [2005, "Interfacial Structure in an Air-Water Planar Bubble Jet," Exp. Fluids, **38**(4), pp. 426–439] with the state-of-the-art four-sensor miniature conductivity probe in a vertical duct is used to validate the three-field two-fluid model CFD simulations.* [DOI: 10.1115/1.2201626]

Introduction

The formulation of the turbulent constitutive relations is a necessary condition for the development of a computational fluid dynamics (CFD) two-fluid model. The constitutive relations may be divided into two categories. The first is the formulation of the models for the two-phase Reynolds stresses. An early attempt at this for bubbly flows was the work of Sato et al. [1] that proposed the superposition of bubble induced and shear induced turbulence based on an eddy viscocity model. This was followed by the formulation of a two phase turbulent kinetic energy transport equation that was consistent with the two-fluid model averaging technique, obtained by Kataoka and Serizawa [2]. Lopez de Bertodano et al. [3] used this equation to extend the idea of superposition to the k-ε model.

The second category, and the object of this work, is modeling the transport of the dispersed phase. Previous work (e.g., Lopez de Bertodano et al. [4]) was focused on the interfacial forces of drag, lift and virtual mass. However, there is another effect which is important over a wide class of industrial applications: the dispersion of the bubbles by the turbulent eddies of the continuous phase. In the past this was modeled either using a "convection-diffusion" continuity equation for the dispersed phase (e.g., Batchelor and Townsend [5]) or by a Lagrangian treatment (e.g., Sun and Faeth [6]) which tracks each bubble and where each bubble is subjected to a random interfacial force representing the effect of the eddies. However, neither of these methods is consistent with the two-fluid model because, in the first case, the two-fluid model continuity equation does not contain a diffusion term and, in the second case, the two-fluid model is Eulerian. This problem was solved for particle flows by Reeks [7,8] who used the probability distribution function of the dispersed phase (i.e., a Boltzmann-equation) to average the momentum equation. The result of this analysis is a rigorously derived averaged turbulent diffusion force. This force was recently applied to a turbulent bubbly jet with small bubbles (i.e., 1 mm diameter) by Lopez de Bertodano et al. [9]. However, the application of this force to industrial flows (i.e., larger bubbles) requires specific two-phase flow experimental data to calibrate the model due to the uncertainties of the flow around large bubbles. In particular, it is necessary to measure the void distribution and the interfacial area concentration in flows with a mixture of big and small bubbles.

A recent advance in two-phase flow instrumentation offers this capability: the state-of-the-art miniaturized four-sensor conductivity probe developed by Kim et al. [10] is designed to obtain the interfacial area concentration in complex two-phase flow situations. In particular, this probe can differentiate between small and large bubbles and it therefore offers a unique opportunity to perform further developments of the multidimensional two-fluid model.

The two-fluid CFD model presented in this paper is not fully predictive because the bubble sizes for the two bubble fields must be assigned values obtained from the experiment. However, the two-group interfacial area transport model for confined upward flow developed by Sun et al. [11] offers the capabilty to predict the bubble sizes in the cap-bubbly regime. Therefore, the long term objective of the present work is to develop a three-field two-fluid CFD model that is compatible with the model of Sun (i.e., two bubble fields) so that these two models may be coupled in the future.

Experiment

Measurements. Figure 1 shows a schematic diagram of the experimental facility including a two-phase mixing section, test section, upper plenum, water reservoir, water and air delivery systems, and instrumentation. The facility was operated at the atmospheric pressure. The de-mineralized water was supplied by a centrifugal pump while the air was delivered by an air compressor with a large storage tank.

The 200 mm $\times$ 10 mm acrylic test section provided an effective apparatus for flow visualization. Six local measurement ports for the conductivity probes were installed in the side at different elevations along the test section. The z/D_h values from Port 1 to Port 6 were 8.0, 34.8, 61.5, 88.2, 115.0, and 141.7, respectively. At each port, a conductivity probe can be installed and traversed in both directions in the cross section of the test section to obtain local data. In the current study, only Ports 2, 3 and 6 were used and the local measurements at a total of 60 points were made in a quarter of the cross sectional area of the test section.

The air-water two-phase mixture was generated by a specially designed two-phase mixing apparatus. Six porous sparger units were installed, three on each side of the duct-width, to generate bubbles of near-uniform size through pores with a mean size of

Contributed by the Fluids Engineering Division of ASME for publication in the JOURNAL OF FLUIDS ENGINEERING. Manuscript received August 31, 2004; final manuscript received January 31, 2006. Review conducted by Joseph Katz.

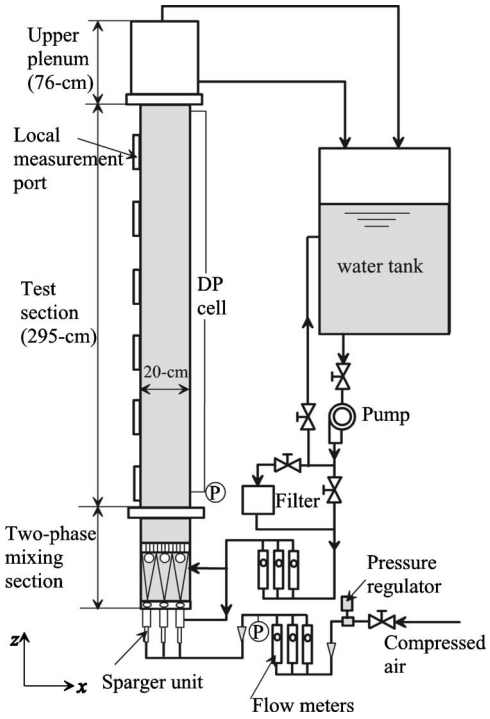

Fig. 1 Schematic of the experimental loop

10 μm. In the current experiments, only the center two sparger units were used to generate a center-peaked void profile at the inlet, similar to a planar bubble jet (Sun et al. [12]).

In the experiments, the state-of-the-art miniaturized four-sensor conductivity probe developed by Kim et al. [10] was used to acquire the local data. The configuration of the newly designed four-sensor conductivity probe is shown in Fig. 2. The significant reduction in the cross-sectional area of the probe and the sharply tapered tips of its sensors can effectively minimize both the number of missing bubbles and the deformation of passing bubble interfaces. Another significant feature of the probe is that it accommodates a built-in double-sensor probe in the four-sensor configuration, rendering it applicable to a wide range of two-phase flow regimes spanning over bubbly, cap, slug, and churn-turbulent flows.

The improved design of the four-sensor probe allows one to identify and separate the acquired signals into those of two groups of bubbles and to observe how they develop along the flow field

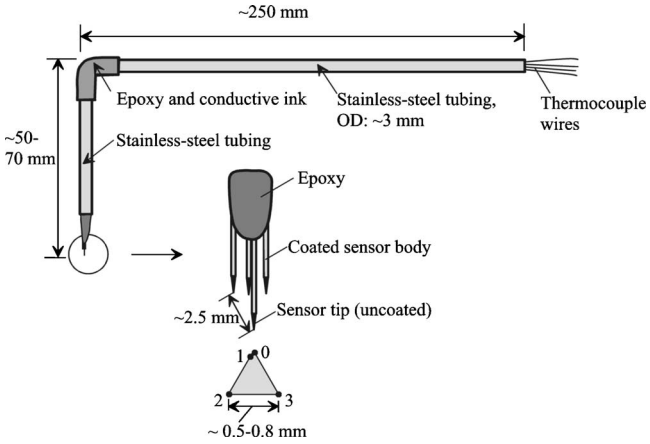

Fig. 2 Schematic of the miniaturized four-sensor conductivity probe

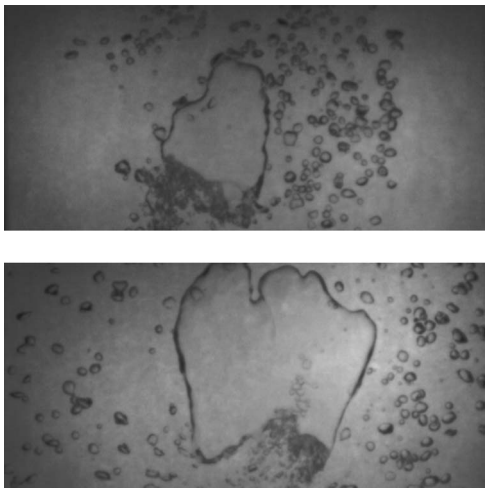

Fig. 3 (*a*) Flow structure visualization ($z/D=35$), (*b*) flow structure visualization ($z/D=142$)

even when flow regime transition occurs (Kim et al. [10]). This categorization process is important in view of interfacial transport, because it allows one to study the transport phenomena of different types of bubbles independently. In the present experiments, spherical and distorted bubbles are categorized as small bubbles while the cap and churn-turbulent bubbles were categorized as cap bubbles (Fig. 3).

In identifying bubble types, the maximum distorted bubble limit, $D_{b,\max}$, was used as the criterion for group boundary. The bubbles with a chord length smaller than $D_{b,\max}$ were categorized as small bubbles. Here $D_{b,\max}$ was given by (Ishii and Zuber [13])

$$D_{b,\max} = 4\sqrt{\sigma/g\Delta\rho} \tag{1}$$

which is approximately 10 mm for air-water flow at atmospheric pressure.

The conductivity probe data were obtained with a sampling frequency of 12 kHz over a period of 120 s, yielding at least 3000 small bubble samples and ensuring measurement accuracy within ±10%. Where the bubble population was small near the boundary between the bubble jet and continuous liquid, the sampling time was increased to maximize the number of bubble samples to obtain reasonable statistics.

The data were obtained at $j_L=0.946$ m/s and $j_G=0.095$, 0.19 and 0.38 m/s. In all these cases large cap or churn-turbulent bubbles, which may be considered as deformed cap bubbles, were encountered. The void distribution of the cap bubbles has a Gaussian shape with the peak at the center of the test section. Figures 4–6 present the data obtained at the centerline in the gap direction at different elevations for a flow condition of $j_L=0.946$ m/s and $j_G=0.19$ m/s, including the void fraction, interfacial area concentration, and bubble velocity for both groups of bubbles. In the plots, $x=0$ is the centerline of the test section in the width direction. The data clearly demonstrate the development of the flow structures as the flow evolves. Further details of the experiment have been published by Sun et al. [12].

Bubble Sizes. The actual histogram of the bubble diameter in the experiment varies with different flow conditions. For the small bubble group, the histogram of bubble size is narrowly distributed, around 2–6 mm for all the gas flows, while for cap bubbles, it can vary considerably for different gas flows, from 10 mm up (Sun et al. [12]). The clear separation of the bubble sizes shown in Fig. 3 is a remarkable characteristic of the present data.

For the current experiment, the cap bubbles were essentially two dimensional in terms of shape and motion. Theoretically, two length scales might be required to characterize the cap and churn-

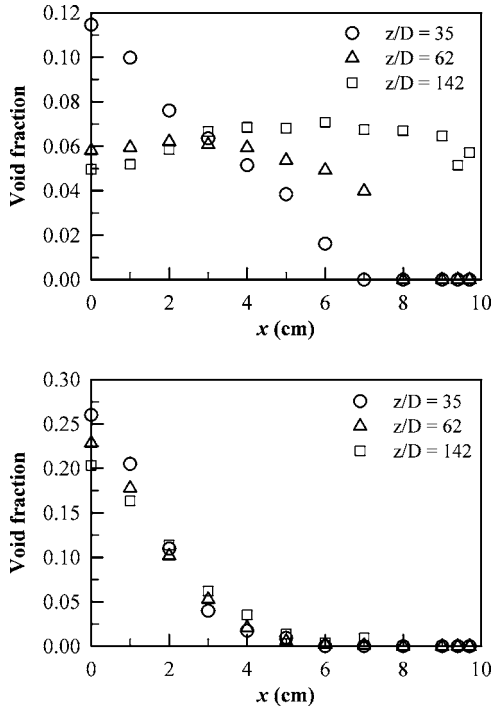

Fig. 4 (*a*) Small bubble void fraction along the centerline in the width direction (j_L=0.946 and j_G=0.19 m/s), (*b*) cap bubble void fraction along the centerline in the width direction (j_L=0.946 and j_G=0.19 m/s)

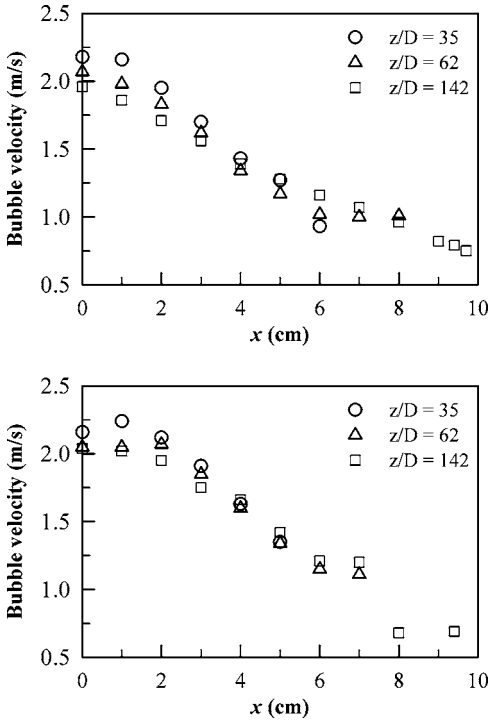

Fig. 6 (*a*) Small bubble velocity along the centerline in the width direction (j_L=0.946 and j_G=0.19 m/s), (*b*) cap bubble velocity along the centerline in the width direction (j_L=0.946 and j_G=0.19 m/s)

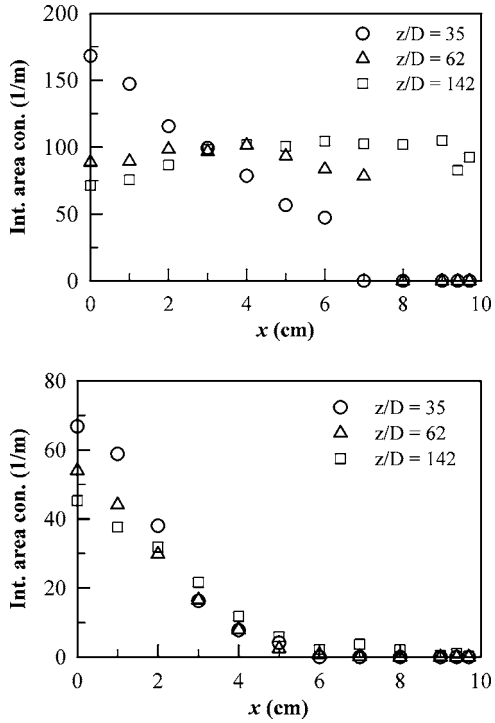

Fig. 5 (*a*) Small bubble interfacial area concentration along the centerline in the width direction (j_L=0.946 and j_G=0.19 m/s), (*b*) cap bubble interfacial area concentration along the centerline in the width direction (j_L=0.946 and j_G=0.19 m/s)

turbulent bubbles, such as the chord length and the length in the transverse direction (width direction). However, for the current local conductivity probe, due to the localization of the information, it would be difficult to instantaneously retrieve global information for the bubbles beyond where the sensors are located. On the other hand, in the cap bubbly and churn-turbulent regimes, large bubbles, i.e., cap and churn-turbulent bubbles, had relatively large size, both in the main flow direction and the transverse direction; while the small bubbles, i.e., the spherical and distorted bubbles, were usually less than 6 mm in the current air-water atmospheric pressure condition. Therefore, in the bubble categorization process, a single-length scale criterion was considered to be acceptable. Consequently, in identifying the bubble types, the maximum size of distorted bubbles, $D_{d,\max}$ in Eq. (1), was used as the criterion of group boundary. This is approximately 10 mm for air-water flow at atmospheric pressure and 20°C temperature condition. Experiments have shown that bubbles with a size larger than $D_{d,\max}$ will become cap bubble in shape.

Model

Two-Fluid Model (Three Fields). For *adiabatic* flows, the ensemble averaged two-fluid model equations (Ishii and Hibiki [14]) governing the motion of each phase have the following form:

Mass conservation:

$$\frac{\partial}{\partial t}\alpha_k\rho_k + \nabla\cdot\alpha_k\rho_k\bar{\underline{v}}_k = 0 \tag{2}$$

where α_k stands for the local void fraction of phase k, ρ_k is the density and $\bar{\underline{v}}_k$ is the averaged velocity.

Momentum conservation:

$$\frac{\partial}{\partial t}\alpha_k\rho_k\underline{\bar{v}}_k + \nabla\cdot\alpha_k\rho_k\underline{\bar{v}}_k\underline{\bar{v}}_k = -\alpha_k\nabla p_k + \nabla\cdot\alpha_k(\underline{\underline{\tau}}_k + \underline{\underline{\tau}}_k^{\mathrm{Re}}) + \alpha_k\rho_k\underline{g} + \underline{M}_{ki} \tag{3}$$

where $\underline{\underline{\tau}}_k^{\mathrm{Re}}$ represents turbulent Reynolds stresses. $\underline{M}_{ki}$ is the interfacial momentum transfer (i.e., interfacial forces per unit volume). The two-fluid model has been extended to three fields: liquid continuous ($k=1$), cap bubbles ($k=2$) and small bubbles ($k=3$).

The interfacial momentum transfer force comprises force terms due to drag, turbulent diffusion, virtual mass, lift and a wall force

$$\underline{M}_{ki} = \underline{M}_{ki}^{D} + \underline{M}_{ki}^{TD} + \underline{M}_{ki}^{VM} + \underline{M}_{ki}^{L} + \underline{M}_{ki}^{W} \tag{4}$$

Other forces like the Basset force are also present but are assumed to be negligible. The drag force of phase k is given by

$$M_k^D = -\frac{3}{4}\alpha_k\rho_1\frac{C_{Dk}}{D_{bk}}|\bar{\underline{v}}_{Rk}|\bar{\underline{v}}_{Rk} \tag{5}$$

where the drag coefficient, C_{Dk}, is given by Gaudin's correlation [15] for bubbles in tap water. D_{bk} is the Sauter mean diameter and the relative velocity is given by $\bar{\underline{v}}_{Rk}=\bar{\underline{v}}_k-\bar{\underline{v}}_1$. Gaudin's correlation is chosen because it covers the full range including small and cap bubbles.

The model for the turbulent diffusion force considers the drag of the bubble induced turbulent eddies on the transport of the bubbles and it is discussed in detail in the following section. Although the virtual mass force is very small for this problem, the model is included because it stabilizes the numerical scheme. The lift force is negligible for cap bubbles, which are the main focus of this study. The lift force was not used for the small bubbles either for reasons that are discussed in the results section. The wall force model accounts for the effect of the surface tension which keeps the centers of the bubbles that touch the wall at a bubble radius distance. This force is important when the lift force is present, but since the lift force was not used in this case, neither was the wall force.

Turbulent Diffusion Force. Physically, turbulent diffusion is the result of the fluctuating component of the forces acting on the bubbles. In the simplest case the turbulent diffusion force at a point is the ensemble average of the fluctuating component of the drag force on all the bubbles whose trajectories intersect this point. As mentioned in the introduction, the kinetic equation, similar to Boltzmann's equation, obtained by Reeks [7,8] describes the evolution of the probability density function of the bubbles in phase space, $(\underline{x},\underline{v},t)$, and so it has the information of the bubble trajectories in it. The Eulerian two-fluid momentum equation for the bubbles is obtained from the ensemble averaged first moment of the kinetic equation. For the case of bubbles in homogeneous turbulence, the diffusion force model of Reeks is

$$\underline{M}_d^{TD} = -(\rho_d + C_{VM}\rho_c)\underline{\underline{\lambda}}^T\cdot\nabla\alpha \tag{6}$$

where the subscripts "d" and "c" correspond to the dispersed and continuous phases. $\underline{\underline{\lambda}}^T$ is a phase space diffusion tensor whose components are memory integrals along particle trajectories [7].

Bubble Induced Turbulent Diffusion Force. The following analysis provides a rigorous derivation to relate $\underline{M}_d^{TD}$ to the diffusivity of the bubbles. Once this relationship is established it is possible to obtain a correlation for $\underline{M}_d^{TD}$ using the diffusivity correlation for bubbly flows of Sato et al. [1]. In particular, the relationship between the two-fluid model Eqs. (2) and (3) and a gradient diffusion model for the dispersed phase, i.e.

$$\frac{\partial}{\partial t}\bar{\alpha} + \nabla\cdot\bar{\alpha}\underline{\bar{v}}_d = \nabla\cdot v_d\nabla\bar{\alpha} \tag{7}$$

will be derived. In the process a useful relationship between the two-fluid model and the turbulent diffusivity, ν_d, will be obtained.

One may start with the two-fluid model momentum equation for the dispersed phase (3)

$$\frac{\partial}{\partial t}\alpha\rho_d\underline{\bar{v}}_d + \nabla\cdot\alpha\rho_d\underline{\bar{v}}_d\underline{\bar{v}}_d = -\alpha\nabla p + \nabla\cdot\alpha[(\underline{\underline{\tau}}_d + \underline{\underline{\tau}}_d^{\mathrm{Re}})] + \alpha\rho_d\underline{g} + \underline{M}_d^D + \underline{M}_d^{TD} + \underline{M}_d^{VM} \tag{8}$$

where the last two terms of Eq. (5) have been neglected. Furthermore, for steady quasi-developed flow in a duct the left-hand side of Eq. (8) and the virtual mass force may be neglected. If $\rho_d \ll \rho_c$ the viscous and Reynolds stresses of the dispersed phase are negligible too. Then

$$0 = -\alpha\nabla p + \alpha\rho_d\underline{g} + \underline{M}_d^D + \underline{M}_d^{TD} \tag{9}$$

or

$$0 = -\alpha\nabla p + \alpha\rho_d\underline{g} - \frac{\alpha\rho_d'}{\tau_d}(\underline{\bar{v}}_d - \underline{\bar{v}}_c) - \rho\prime_d\underline{\underline{\lambda}}^T\cdot\nabla\alpha \tag{10}$$

where the second to last term on the right-hand side represents the drag and $\rho' d=\rho_d+C_{VM}\rho_c$ includes the effect of the added mass. The time constant of the bubbles is derived from the equation of motion of a single bubble as

$$\tau_d = \frac{4}{3}\frac{(\rho_d+\rho_c C_{VM})}{\rho_c C_D}\frac{D_b}{v_R} \tag{11}$$

where $v_R=|\bar{\underline{v}}_R|$ is the rms relative velocity between dispersed and continuous phases. Assuming a hydrostatic pressure gradient (i.e., $\nabla p=(1-\alpha)\rho_c\underline{g}$) the momentum Eq. (10) may be rewritten after some rearrangement as

$$\bar{\underline{v}}_d = \bar{\underline{v}}_c - \frac{\rho_c}{\rho_d'}\tau_d(1-\alpha)\underline{g} - \tau_d\underline{\underline{\lambda}}^T\cdot\frac{1}{\alpha}\nabla\alpha \tag{12}$$

where the second term on the right-hand side is the rise velocity of a bubble and the third term is the drift velocity due to turbulent diffusion. Finally, inserting Eq. (12) into Eq. (2) results in

$$\frac{\partial}{\partial t}\bar{\alpha} + \nabla\cdot\alpha(\bar{\underline{v}}_c + \bar{\underline{v}}_R) = -\nabla\cdot\tau_d\underline{\underline{\lambda}}^T\cdot\nabla\alpha \tag{13}$$

which is equivalent to Eq. (7) with the average gas velocity given by $\bar{\underline{v}}_c+\bar{\underline{v}}_R$ and a diffusivity expressed as

$$\nu_{dij} = \tau_d\lambda_{ij}^T \tag{14}$$

so that the bubble induced component of the turbulent diffusion force is

$$\underline{M}_d^{TD} = -(\rho_d + C_{VM}\rho_c)\underline{\underline{\lambda}}^T\cdot\nabla\alpha = -\frac{1}{\tau_d}(\rho_d + C_{VM}\rho_c)\nu_d\nabla\alpha \tag{15}$$

The correlation for bubbly flow of Sato et al. [1] may now be used

$$v_d = C_{DB}\alpha D_b v_R \tag{16}$$

Finally, inserting Eqs. (16) and (11) into Eq. (15) results in the model for the bubble induced turbulent diffusion force

$$M_{BI}^{TD} = \frac{3}{4}C_{DB}C_D\rho_c\alpha v_R^2\nabla\alpha \tag{17}$$

Equation (15) shows that the model depends on the turbulent diffusivity and time constant of the bubbles, and Eq. (17) shows that these two quantities are related to the well known coefficients of other models. When Eq. (17) was inserted into the momentum equation for the cap bubbles (Eqs. (3) and (4)) the CFD calculations showed that the model did not reproduce the Gaussian shape of the cap bubble distribution data. This problem was overcome by the following modification to Eq. (17) for the cap bubbles

$$M_{BI2}^{TD} = \frac{3}{4} C_{DB2} C_{D2} \rho_c \langle \alpha_2 \rangle v_{R2}^2 \nabla \alpha_2 \tag{18}$$

where $\langle \alpha_2 \rangle$ is the cross section average of the volume fraction of the cap bubbles. Because the cap bubbles are constrained by the walls and cannot move in the direction parallel to the short axis of the test section, the diffusive force was not implemented in this direction.

The turbulent diffusion of the small bubbles induced by the turbulence of the cap bubbles may be obtained by a similar procedure if the time constant of the small bubbles (Eq. (11)) is used to characterize the response of the bubbles, but the diffusivity of the cap bubbles (Eq. (16)) is used to characterize the turbulent eddies that induce the motion. This results in

$$M_{BI3}^{TD} = \frac{3}{4} C_{DB3} C_{D3} \rho_1 \frac{D_{b2}}{D_{b3}} \langle \alpha_2 \rangle v_{R2} v_{R3} \nabla \alpha_3 \tag{19}$$

The diffusivity of the cap bubbles induced by the turbulence of the small bubbles is negligible because the corresponding eddies are too small.

Furthermore, cap bubble induced turbulence turns out to be the predominant mechanism for the bubble dispersion because the liquid superficial velocity is relatively low (i.e., Re$\cong$23,000) so the effect of shear induced turbulence is negligible. This is in effect a "separate effect" test of Eqs. (18) and (19) in a duct.

Reynolds Stresses. The closure for the Reynolds stresses in the momentum Eq. (3) is based on the two-phase k-ε model developed by Lopez de Bertodano et al. [3] and Lance and Lopez de Bertodano [16]. This model assumes that the shear induced and bubble induced turbulent stresses are added together

$$\underline{\underline{\tau}}_k^{\mathrm{Re}} = (\underline{\underline{\tau}}_k^{\mathrm{Re}})_{SI} + (\underline{\underline{\tau}}_k^{\mathrm{Re}})_{BI} \tag{20}$$

which implies that the kinetic energy of the liquid phase turbulence is

$$k_{2\phi} = k_{SI} + k_{BI} \tag{21}$$

The bubble induced turbulent kinetic energy is given by

$$k_{BI} = 1/2 \alpha_2 C_{VM2} v_{R2}^2 \tag{22}$$

where α_2 is the void fraction of the cap bubbles and it is assumed that the bubble induced turbulence of the small bubbles is negligible. The resulting expression for the diffusivity of momentum of the liquid phase is

$$\nu_{t1} = C_\mu \frac{k_{SI}^2}{\varepsilon_{SI}} + C_{DB1} \alpha_2 D_b v_{R2} \tag{23}$$

where the first term on the right-hand side corresponds to the k-ε model for the shear induced diffusivity and the second term corresponds to Sato's model [1] for the bubble induced diffusivity due to the cap bubbles. The bubble induced diffusivity due to the small bubbles is considerably smaller and has been neglected. The coefficient C_μ=0.09 is the standard value according to the k-ε model. However, the coefficient C_{DB1} will be adjusted to fit the velocity data. It is important to note that the k-ε model transport equations for the liquid phase are solved together with the continuity and momentum Eqs. (2) and (3). The standard coefficients of the k-ε model are left untouched.

Because the test section is so narrow and the cap bubbles are so big, the axes of the large bubble induced vortices are preferentially oriented in the direction of the short axis of the cross section. Therefore, the bubble induced component of the diffusivity, which is dominant in the central part of the duct, is not isotropic. To account for this anisotropy in the flow, it is assumed that the axes of the large eddies are oriented in the direction of the small axis, so the bubble induced turbulent diffusivity of momentum (i.e., Sato's model) is not implemented in the direction parallel to the short axis of the test section.

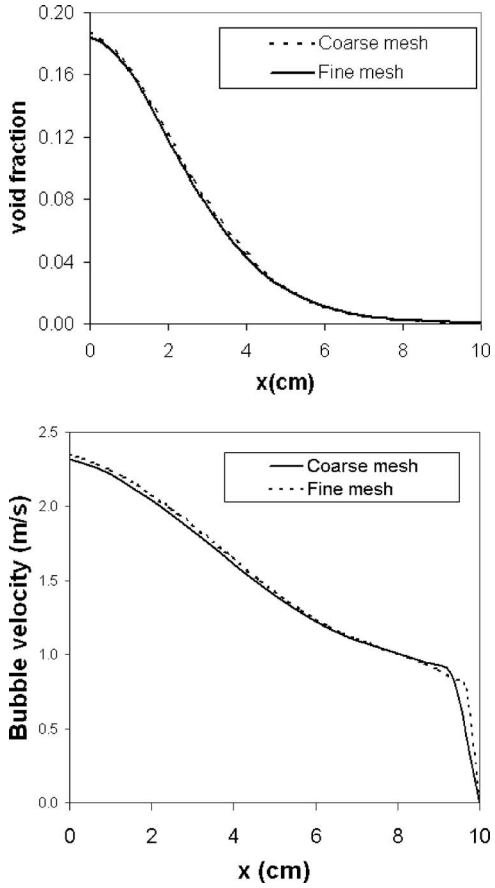

Fig. 7 (*a*) Numerical convergence test: volume fraction, (*b*) numerical convergence test: velocity

CFD Results

The two-fluid CFD model was validated with the experimental data of Sun et al. [12]. A quadrant of the rectangular cross section was considered. This 5 mm$\times$100 mm domain is divided into 30 nodes along the long axis (x direction) and ten nodes along the short axis (y direction). There are 162 nodes along the axial direction (z direction) which is 2700 mm long. The corresponding node size is 3.3 mm$\times$0.5 mm$\times$16.7 mm. The computations were performed with the FLUENT 6.1.22 code employing an elliptic solution technique. A second order upwind scheme was used. A convergence test shown in Figs. 7(a) and 7(b) indicates that the void fraction distribution varies by a negligible amount when a $15\times5\times81$ mesh is compared with the $30\times10\times162$ mesh, and the velocity distributions are very close except at the edge of the test section.

Of the three gas flow rates measured by Sun et al. [12] the one used for the comparisons was the intermediate case, j_G =0.19 m/s. The case with j_G=0.095 m/s was discarded because the volume fraction of the cap bubbles varies substantially along the length of the test section, from $\langle \alpha_2 \rangle$=0.012 at the inlet to $\langle \alpha_2 \rangle$=0.003 at the exit, but the CFD model does not account for bubble breakup and coalescence. However, the volume fraction of the cap bubbles for the case with j_G=0.19 m/s remains fairly uniform, from $\langle \alpha_2 \rangle$=0.040 at the inlet to $\langle \alpha_2 \rangle$=0.045 at the exit. The case with j_G=0.38 m/s is also uniform, but it was impossible to obtain a steady solution. A Rayleigh instability appears as shown in Fig. 8. This instability is not a numerical phenomenon but a physical one, due to the inflection in the axial velocity profile along the x direction (Schlichting [17]) which is caused by the cap bubble buoyancy because the cap bubbles remain near the

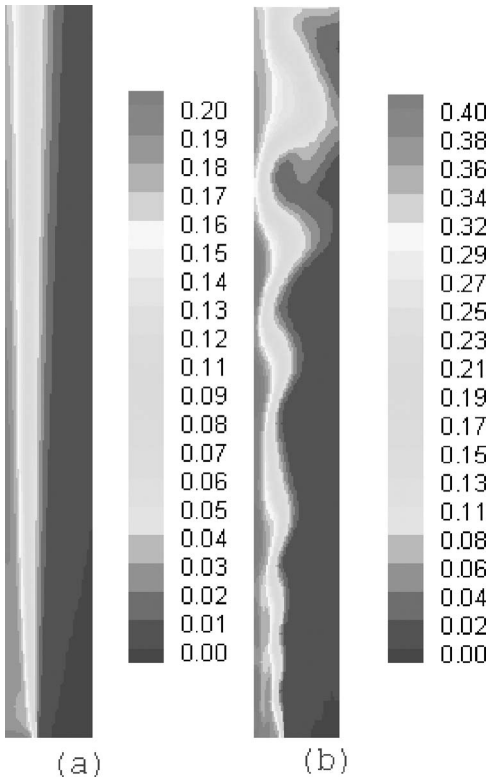

Fig. 8 Contour plots of volume fraction of the cap bubbles (*a*) j_G=0.19 m/s, (*b*) j_G=0.19 m/s, aspect ratio not to scale

center of the duct. This shows that the steady state scheme used in the present calculations cannot be applied to all cases and that for the high gas flow instance the CFD scheme must reflect the unsteady nature of the two-phase flow.

The basic strategy of the present calculations is to adjust the three coefficients, C_{DB1}, C_{DB2} and C_{DB3} in Eqs. (23), (18), and (19), respectively, to match the measured profiles of velocity and volume fractions of the cap bubbles and the small bubbles. All other coefficients in the CFD model are obtained from published correlations or models, and are left untouched.

Figure 9 is a comparison of the data with the CFD model profile of the field 2 bubbles (i.e., cap bubbles) along the long axis of the cross section (x direction) at z/D=35 and 142. The average field 2 bubble size measurement was $\langle D_{b2}\rangle$=15 mm. Gaudin's correlation [15] yields C_{D2}=3.0 for this bubble size. This results in a

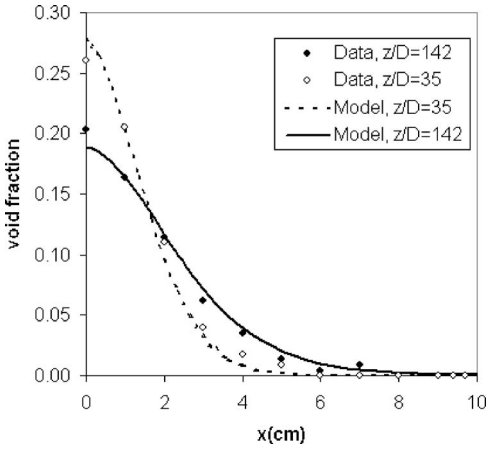

Fig. 9 Comparison of cap bubble phase distribution

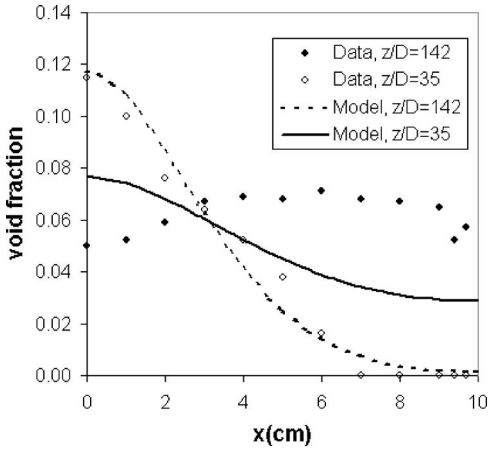

Fig. 10 Comparison of small bubble phase distribution

relative velocity of 0.33 m/s. Inserting these values and C_{DB3} =0.63 into Eq. (18) produces a reasonable match. This value for C_{DB} is practically the same obtained by Sato et al. [1] for bubbly flow.

Figure 10 shows the comparison of the void fraction distribution for the small bubbles. The average field 3 bubble size measurement was $\langle D_{b3}\rangle$=3.5 mm. Gaudin's correlation [15] yields C_{D3}=2.0 for this bubble size. This results in a relative velocity of 0.18 m/s. Inserting these values and C_{DB3}=2.1 into Eq. (19) produces reasonable agreement at z/D=35. However, the distribution of the data at z/D=142 does not exhibit a Gaussian shape, in contrast to the CFD distribution. One possible reason for this discrepancy is that the small bubbles also experience a lift force

$$M_{3i}^{L} = C_L \alpha \rho_l (v_3 - v_1) \times (\nabla \times v_1) \tag{24}$$

According to Tomiyama et al. [18] C_L=0.288 for bubbles smaller than 4.5 mm. Figures 11 and 12 show the results of the distribution of small bubbles for calculations including the lift force model, Eq. (24), with various values of *CL*. None of the profiles match the experimental data very well. At the exit the inflection in the data around x=3 cm is not reproduced and at z/D=35 the lift force moves the maximum concentration away from the center, in contrast with the data. Furthermore, the measured void fraction distributions in the y direction (i.e., the short axis direction) are practically uniform instead of showing the characteristic peak near the wall produced by lift. Based on these considerations it was decided to neglect the lift force. Although the reason for this as-

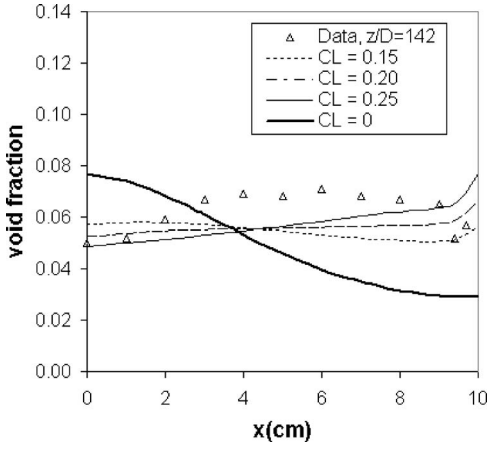

Fig. 11 Comparison of small bubble phase distribution, including lift (*z*/*D*=142)

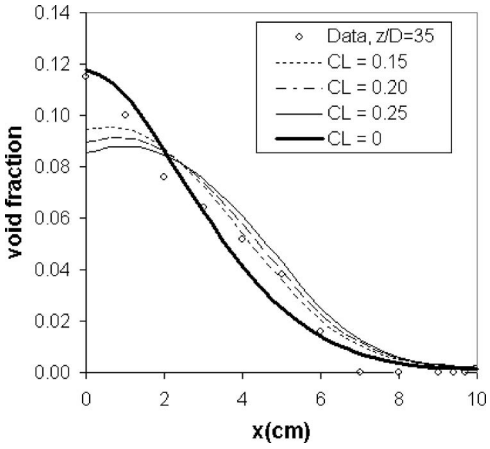

Fig. 12 Comparison of small bubble phase distribution, including lift ($z/D=35$)

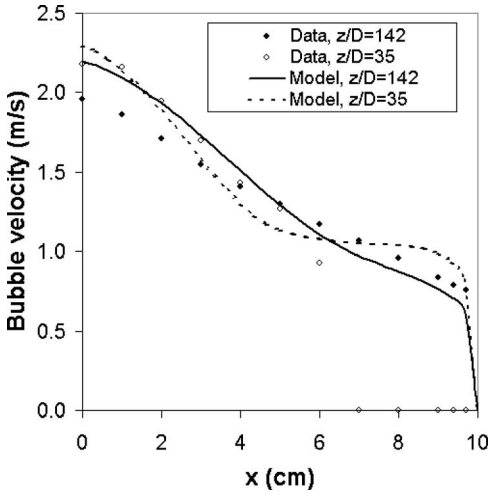

Fig. 14 Comparison of small bubble velocity distribution

sumption cannot be stated with assurance at the present time, it may be related to the high levels of turbulence produced in the wakes of the cap bubbles. Other data where the level of turbulence is very high also shows a diminished effect of lift (e.g., the data for $j_L=5$ m/s of Serizawa et al. [19]). Furthermore, there is another force on the small bubbles as they are pushed aside along the x direction by the faster moving cap bubbles that tend to concentrate in the center of the duct (see Fig. 4). This force, which has not been modeled in this paper, could explain the discrepancy in Fig. 10.

It is important to reiterate that the void fraction distributions in the direction of the short axis of the cross section (y direction) are generally uniform, except very near the wall where the void fraction goes to zero. Therefore, it is impossible to test the validity of the bubble diffusion coefficients, C_{DB2} and C_{DB3}, in this direction. However, it is expected that the bubble induced turbulent diffusion forces are smaller in the direction of the short axis because of the high aspect ratio of the test section which "squeezes" the cap bubbles and constrains the motion of the large eddies around them. In fact, it was necessary to arbitrarily reduce the turbulent diffusion force in this direction because otherwise the solution diverged. This reduction was performed for the sole purpose of obtaining a converged solution while preserving a uniform distribution in the direction of the short axis.

Figures 13 and 14 show the velocity distribution of the cap bubbles and the small bubbles, and though there is some agreement between calculations and data, there are also some significant differences. These results were obtained with $C_{DB1}=2.1$ in Eq. (23) which is the same as the value used for the transport of the small bubbles (i.e., $C_{DB1}=C_{DB3}$). This implies that the turbulent transports of the small bubbles and the momentum induced by the cap bubbles are similar, which is reasonable.

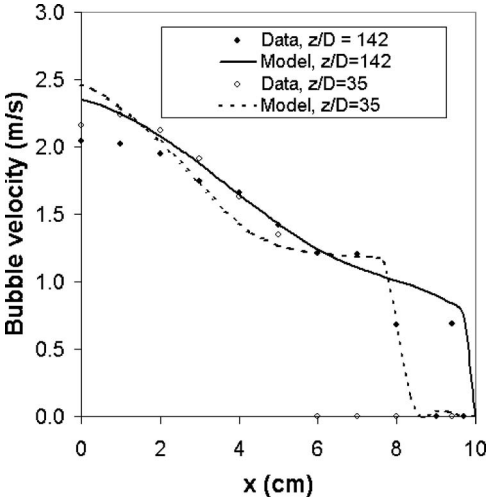

Fig. 13 Comparison of cap bubble velocity distribution

Figure 13 shows a jump in the data of the cap bubble velocity beyond $x=7$ cm at $z/D=142$. Furthermore, the measured cap velocity at that position is lower than the measured velocity of the small bubbles, which is the opposite of the rest of the measurements. To explain this difference between the data and the model it is noted that there are practically no cap bubbles in that region as can be observed from the void fraction profile for cap bubbles shown in Fig. 4(b). The signal processing program for the conductivity probe was designed in a way such that as long as a cap bubble is detected, a velocity value for that cap bubble will be calculated based on the probe spacing and time delay for the cap bubble interface between two probe sensors. And the cap bubble velocity output by the program is an averaged value over all the cap bubbles detected by the probe at that location. In the experiments, there were not enough cap bubble samples to obtain a statistically sound data at locations beyond $x=7$ cm even though the sampling time was increased considerably. Furthermore, most of the measurements beyond $x=7$ cm correspond to the edge of the cap bubbles and this introduces additional errors. For example, the interfacial velocity is measured in a direction close to but not exactly equal to the flow direction because the two sensors are offset by a sensor diameter in the x direction since the two sensors are placed next to each other. Therefore, at the edge of the cap bubbles, there will be an error involved because there will be an artificial time delay when the curved interface encounters the second sensor that is not exactly aligned with the front sensor along the flow direction. This error is amplified by the fact that the orientation of the interface at the edge of the cap bubble is almost tangential to the flow direction.

Figures 13 and 14 also show that the slopes of the calculated velocity profiles are higher than the data (i.e., the calculated velocities in the center of the channel are higher). This is because of the model assumption that there is no bubble induced diffusivity of momentum in the direction of the minor axis of the cross section. Including this effect would slow down the flow near the center of the duct where the cap bubbles are concentrated, so this disagreement could be easily fixed by adjusting the bubble induced diffusivity of momentum in the y direction. However, this adjustment would add one more constant to the model and would only be applicable to the geometry of this specific test section.

Conclusions

Detailed local data for an air-water planar bubbly jet in a rectangular test section were obtained to benchmark the two-fluid CFD model in a flow condition containing deformed large cap bubbles and small bubbles together. The experiment was performed in a narrow duct with a cross-sectional area of aspect ratio of 20. Advanced four-sensor conductivity probes were placed along the test section to measure the development of the local two-phase parameters, such as the void fraction, bubble velocity, and interfacial area concentration. To accommodate the differences between the small spherical/distorted bubbles and the large cap bubbles due to the shape, size, and motion, the detected bubbles were categorized into two groups.

The comparisons between the experimental data and the three-field two-fluid CFD model demonstrate that the behavior of the large cap bubbles can be captured by a new turbulent diffusion force model. However, the small bubble distribution cannot be correctly predicted because the present turbulent diffusion force model is developed for homogeneous turbulence, and it does not include the effect of the flow around a cap bubble which pushes the small bubbles to the side. Furthermore, the present steady CFD model could not be applied to the highest gas flow data (i.e., j_G=0.38 m/s) because of a Rayleigh instability in the solution.

In spite of these shortcomings, it is believed the present model is an evolutionary step toward the prediction of complex multidimensional two-phase flows of industrial interest.

References

[1] Sato, Y., Sadatomi, M., and Sekoguchi, K., 1981, "Momentum and Heat Transfer in Two-Phase Bubble Flow," Int. J. Multiphase Flow, **7**, pp. 179–190.

[2] Kataoka, I., and Serizawa, A., 1989, "Basic Equations of Turbulence in Gas-Liquid Two-Phase Flow," Int. J. Multiphase Flow, **15**(5), pp. 843–855.

[3] Lopez de Bertodano, M. A., Lahey, R. T., Jr., and Jones, O. C., 1994, "Development of a k-ε model for Bubbly Two-Phase Flow," ASME J. Fluids Eng., **116**, pp. 128–134.

[4] Lopez de Bertodano, M. A., Lahey, R. T. Jr., and Jones, O. C., 1994, "Phase Distribution in Bubbly Two-Phase Flow in Vertical Ducts," Int. J. Multiphase Flow, **20**(5), pp. 805–818.

[5] Batchelor, G. K., and Townsend, A. A., 1956, "Turbulent Diffusion," *Surveys in Mechanics, G. I. Taylor Anniversary Volume*, Cambridge University Press, Cambridge.

[6] Sun, T. Y., and Faeth, G. M., 1986, "Structure of Turbulent Bubbly Jets—II, Phase Property Profiles," Int. J. Multiphase Flow, **12**, pp. 115–126.

[7] Reeks, M. W., 1992, "On the Continuum Equations for Dispersed Particles in Non-Uniform Flows," Phys. Fluids A, **4**(6), pp. 1290–1302.

[8] Reeks, M. W., 1991, "On a Kinetic Equation for the Transport of Particles in Turbulent Flows," Phys. Fluids A, **3**(3), pp. 446–456.

[9] Lopez de Bertodano, M. A., Moraga, F. J., Lahey, R. T., and Drew, D., 2004, "The Modeling of Lift and Dispersion Forces in Two-Fluid Model Simulations. Part I: Jet flows," ASME J. Fluids Eng., **126**, pp. 573–577.

[10] Kim, S., Fu, X. Y., Wang, X., and Ishii, M., 2000, "Development of the Miniaturized Four-Sensor Conductivity Probe and the Signal Processing Scheme," Int. J. Heat Mass Transfer, **43**, pp. 4101–4118.

[11] Sun, X., Kim, S., Ishii, M., and Beus, S. G., 2004, "Model Evaluation of Two-Group Interfacial Area Transport Equation for Confined Upward Flow," Nucl. Eng. Des., **230**(1–3), pp. 27–47.

[12] Sun, X., Vasavada, S., Choi, S. W., Kim, S., Ishii, M., and Beus, S. G., 2005, "Interfacial Structure in an Air-Water Planar Bubble Jet," Exp. Fluids, **38**(4), pp. 426–439.

[13] Ishii, M., and Zuber, N., 1979, "Drag Coefficient and Relative Velocity in Bubbly, Droplet or Particulate Flows," AIChE J., **25**, pp. 843–855.

[14] Ishii, M., and Hibiki, T., 2005, *Thermo-Fluid Dynamics of Two-Phase Flow*, Springer Verlag.

[15] Gaudin, A. M., 1957, *Flotation*, 2nd ed., Mc–Graw Hill, New York.

[16] Lance, M., and Lopez de Bertodano, M. A., 1996, "Phase Distribution Phenomena and Wall Effects in Bubbly Two-Phase Flows," *Multiphase Science and Technology*, 8, Begell House, pp. 69–123.

[17] Schlichting, H., 1955, *Boundary Layer Theory*, 1st ed., pp. 323–324.

[18] Tomiyama, A., Tamai, H., Zun, I., and Hosokawa, S., 2002, "Transverse Migration of Single bubbles in Simple Shear Flows," Chem. Eng. Sci., **57**, pp. 1849–1858.

[19] Serizawa, A., Kataoka, I., and Michiyoshi, I., 1986, "Phase Distribution in Bubbly Flow," Data Set No. 24, *Proceedings of the Second International Workshop on Two-Phase Flow Fundamentals*, Troy, NY, 1987.

Bubble Effect on the Structures of Weakly Turbulent Couette Taylor Flow

Amine Mehel
Celine Gabillet
Henda Djeridi

Research Institute of French Naval Academy (IRENav),
Ecole Navale BP 600,
29240 Brest Armee, France

In industrial applications, rotating flows have been recognized to enhance mixing and transfer properties. Moreover, bubbly flows are also used to improve transfers. Therefore, it is interesting to study the effects of the dispersed phase on the structure of a Couette Taylor flow. Experiments are conducted for the quasi-periodic (Ta=780) *and the weakly turbulent* (Ta=1000) *flow regimes. Bubbles (0.035 times as small as the gap) are generated by agitation of the upper free surface (ventilated flow). Larger bubbles (0.15 times as small as the gap) are generated by injection at the bottom of the apparatus and by applying a pressure drop (gaseous-cavitating flow). Void fraction, bubble size, and velocity, as well as axial and azimuthal velocity components of the liquid are investigated. The bubble location in the gap clearly depends on the bubble size. For* $\alpha > 0.1\%$*, there is evidence of bubble-induced modifications of axial transfers and wall shear stress, the observed trends being different according to the bubble location in the gap.*
[DOI: 10.1115/1.2201641]

Introduction

Flows induced by rotation of the inner of two concentric cylinders are the basis of numerous chemical, biomedical, and nuclear applications. Because of the presence of Taylor vortices, the mixing is enhanced and depends on the quality of the exchange between these vortices. This particular flow is also relevant for phase separation technology. Indeed, because of the centrifugal effect, any foreign material, solid or gas, will be ejected toward the outer or inner part of the vortices respectively.

It is then necessary to investigate how a gas-liquid bubbly flow behaves in a concentric annulus whose shearing force is induced by the rotation of the inner cylinder, for various flow regimes from laminar to turbulent flow, according to the Taylor number Ta.

Shiomi et al. [1] analyzed the bubbles arrangement in a turbulent Couette Taylor flow for $3000 < Ta < 25000$. The bubbly flow was obtained by injection of a gas liquid mixture (bubbles size equal to 1/5 of the gap) at the bottom of the apparatus. According to respective gas-liquid axial volumetric fluxes, they observe different flow patterns: dispersed bubbly flow, ring form and spiral flow. Atkhen et al. [2] also conducted experiment in a two phase air-water turbulent Couette Taylor with a superimposed axial flux. In this experiment, for $2000 < Ta < 13000$, bubbles were generated by the agitation of the upper free surface (ventilation). The authors observed that air bubbles remained in the outflow regions near the inner cylinder and behave as tracers of the flow. For very high Taylor numbers the axial wave length is reduced by 20% due to the axial flux.

For lower Taylor numbers in the wavy vortex flow regime ($86 < Ta < 200$), Djeridi et al. [3] conducted experiments in a bubbly Couette Taylor flow without superimposed axial flux. Bubbles were generated by ventilation and size was 1/5 of the gap. For this flow regime, air bubbles generated by the overturning breaking waves at the free surface are driven from the upper to the deepest vortices and captured by the Taylor vortices. There is no significant effect of the bubbles on the liquid flow patterns. For this particular state of the flow, Djeridi et al. [4] obtained similar results with vapor bubbles generated in the core of the Taylor vortices by decreasing the pressure (cavitation). But for larger Taylor numbers ($320 < Ta < 600$) in the wavy vortex flow and in the modulated wavy vortex flow, for bubbles of the same size, the authors observed a change in bubble arrangement. Bubbles were located in the outflow regions, near the inner cylinder wall. These particular bubble locations are expected to be responsible for observed modifications in the primary instabilities. Indeed, ventilation, and cavitation lead to a significant growth in the axial wave length (45% and 25%, respectively) and a premature change in the second instability's wave number.

This nonexhaustive overview shows the discrepancy with the previous results according to the regime of the Couette Taylor flow. This gives rise to the following questions: Do the bubble induced effects depend on the bubble size and their localization in the gap rather than on the flow regime? To furnish some elements of response and complete a general background, experiments were conducted in a bubbly Couette Taylor flow for different bubble size and for unstudied flow regimes. Bubbles of different size are generated either by ventilation or by injection and pressure drop (gaseous-cavitation). Experiments were conducted at Ta=780 and Ta=1000, corresponding to quasi-periodic and weakly turbulent flows. In these conditions, what does the bubble arrangement look like and are there any effects of the bubble on the flow patterns? Particular attention is paid to the transition between the two regimes studied. To have a good insight into the bubbly flow patterns, it is necessary to locally quantify the void fraction, bubble size, and velocity. Consequently, a large experimental apparatus was especially built, in order to introduce optical probes. Detailed information about the liquid flow properties is given by laser doppler velocimetry measurements (LDV) and visualizations. To our knowledge, these are the first measurements of the dispersed phase characteristics achieved in a bubbly Couette Taylor flow.

Bubble-induced effects are evident from comparison between the single phase flow and bubbly flow patterns. The present paper is organized as follows: The experimental setup and measuring technics are described first. Results concerning the dispersed phase are then presented for the ventilated and gaseous-cavitating flows, respectively, and discussed afterward. An overview of the liquid flow properties is then given for ventilated and gaseous-

Contributed by the Fluids Engineering Division of ASME for publication in the JOURNAL OF FLUIDS ENGINEERING. Manuscript received January 17, 2006; final manuscript received May 25, 2005. Assoc. Editor: James A. Liburdy. Paper presented at the 2005 ASME Fluids Engineering Division Summer Meeting and Exhibition (FEDSM2005), June 19–23, 2005, Houston, TX.

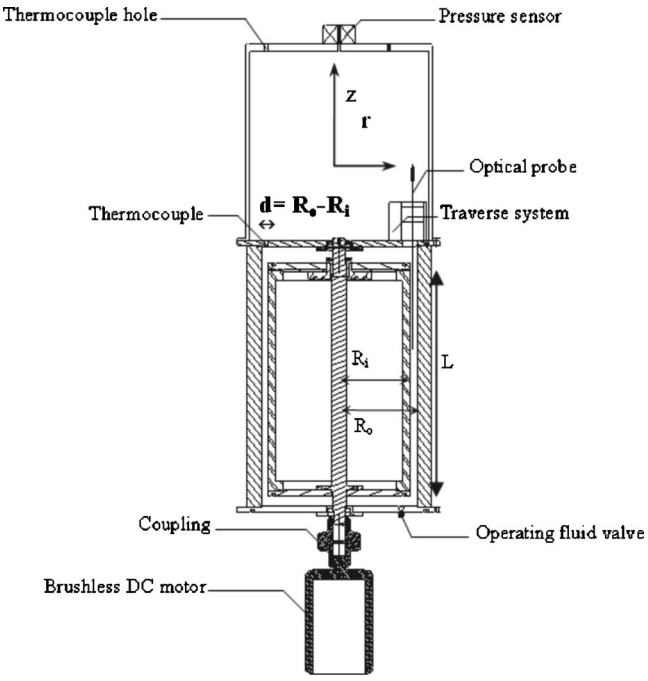

Fig. 1 General schematic of the apparatus

cavitation conditions, respectively. Bubble-induced effects are then discussed according to the bubble size, by comparing the ventilated and gaseous-cavitating flow patterns.

Experimental Details

Apparatus. The experiments were conducted in a vertical circular Couette apparatus having an inner rotating cylinder of 200 mm radius R_i, an outer fixed cylinder of 220 mm radius R_o. The characteristics of the apparatus are defined by the radius ratio $\eta=R_i/R_o=0.91$, the clearance ratio $d/R_i=0.1$ and the aspect ratio $\Gamma=L/d=44.3$, the height of the gap L being 886 mm. The general schematic of the apparatus is given in Fig. 1. The gap is filled with a mixture of glycerol and water and the rotating angular velocity is denominated Ω_i. The Taylor number $\mathrm{Ta}=\sqrt{\Omega_i^2 R_i d^3/\nu^2}$ can be varied by changing the velocity of the inner cylinder or the viscosity of the fluid ν. The relative uncertainty in the Taylor number is due to the geometric dimensions, the viscosity and the rotational velocity uncertainties. The Taylor number can be estimated with an accuracy of 0.8%. Particular attention was paid to observing the same start up procedures and limiting the acceleration of the inner cylinder, in order to ensure the same flow state.

In the Couette Taylor flow, the transition from laminar to turbulent flow occurs throughout a sequence of well-defined instabilities. For all configurations, the critical Taylor numbers corresponding to the three first instabilities and to the weakly turbulent flow are given in Table 1.

In order to obtain a two phase Couette Taylor flow for different bubble sizes, the dispersed phase was either generated by the agitation of the free surface (submillimetric bubbles), or generated both by upward injection and pressure drop (millimetric bubbles). Because of its design, the bottom of the flow domain is a fixed wall and the top is a free surface.

For the ventilated flow, the natural ventilation is obtained with sufficiently high rotation speed $\Omega_i=2.45$ rps corresponding to $\mathrm{Ta}=750$ for a mixture water glycerol of 80%. Bubbles are generated at the crest of the overturning breaking wave and driven into the liquid.

For the cavitating flow, a mixture of water-glycerol 65% is used in order to avoid ventilation. The averaged pressure, Pe, is decreased by using a vacuum pump and measured with a sensor of an absolute accuracy of 200 Pa. A special airtight box on the top of the apparatus was built in order to integrate the pressure sensor, optical probes and associated traverse system, necessary for the bubbly flow measurements. In the gap, a local pressure decrease is encountered both in the Taylor vortices due to vorticity and, near the inner cylinder, due to the rotation of the cylinder. Because of the height of the water column in the gap, and because the local pressure decrease for the present experimental device is not sufficient, it was not possible to obtain millimetric bubbles with cavitation of the mixture nuclei content. Therefore millimetric bubbles are injected in the middle of the gap, through a tube of diameter 200 μm and length 5 cm. This tube discharges in a cavity at the bottom of the apparatus. In this framework, it is more judicious to speak about gaseous cavitation—the sensitivity of the bubble size to the local pressure being quite insignificant (around one-tenth of a millimeter). Pressure drop is used here preferentially to inject bubbles through the tube and accelerate their migration from the bottom to the top of the gap. Special care was taken in order to have the same leak rate for a same Ta.

The phase arrangement and flow pattern are described in details for Ta=780 and 1000 both for the ventilated and cavitating flows. For this apparatus setup, Ta=780 corresponds to a quasi-periodic flow, whereas Ta=1000 corresponds to a weakly turbulent flow. It is therefore interesting to analyze how bubbles of different size

Table 1 Critical Taylor numbers (λ is the axial wavelength n_{cells} is the number of Taylor vortices in the gap, m, and $f0$ are the wave number and the celerity of the azimuthal wave, f' is an incommensurable frequency)

Critical Reynolds number	Flow regimes	Flow characteristics	Typical frequencies
$43.3\leq \mathrm{Ta}<49.6$	Taylor vortex flow (TVF)	$\lambda=2d$ $n_{\mathrm{cells}}=44$	
$49.6\leq \mathrm{Ta}<260$	Wavy vortex flow (WVF)	$\lambda=2.5d$	mf0, f0
		$m=3-9$	for $\mathrm{Ta}>69$
		$n_{\mathrm{cells}}=35$	$mf0=3.5\Omega i$, $f0=0.39\Omega i$
$260\leq \mathrm{Ta}\leq 700$	Modulated wavy vortex flow (MWVF)	$m=4$	$mf0=1.55\Omega i$
		$\lambda=3.1d$	$f'=0.45\Omega i$
		$n_{\mathrm{Cells}}=29$	$f'_1=mf0-f'$
			$f'_2=mf0+f'$
$700\leq \mathrm{Ta}\leq 850$	Quasi-periodic flow	$m=4$	$mf0=1.55\Omega i$
		$\lambda=3.1d$	broadband spectrum of
		$n_{\mathrm{cells}}=29$	frequencies $f'=0.44\Omega i$
			$f'_i=mf0-f'$ and
			$f'_2=mf0+f'$
$\mathrm{Ta}>860$ to 1200	Weakly turbulent flow	$\lambda=3.1d$	Disappearance of $mf0$
		$n_{\mathrm{cells}}=29$	broadband spectrum of
			frequency $f'=0.44\Omega i$

(obtained by ventilation or gaseous-cavitation) and different localization in the flow can influence the state of the flow, in the transition to turbulence.

Measurements. The main focus of this study is placed on the modification of the flow structures due to the presence of the bubbles. To compare the single phase flow patterns to those observed in the ventilated or cavitating flow, an investigation of the liquid velocity fields and characteristic frequencies is made. A two-component, three-beam, LDV Dantec system was used to measure azimuthal and axial velocities. The system was operated in backscattering mode and coupled with two Dantec enhanced burst spectrum analyzers. The liquid was seeded with micron-size Iriodine® particles. The largest dimension of the measuring volume in the radial direction corresponded to 1/25 of the gap. Because of the refractive index variation and the geometry of the interface of the outer cylinder, the deviation of the laser beams is systematically recalculated to determine the focal position of the measuring volume. A remote mechanical positioning system, with a minimum translation step of 10 μm allowed measuring the velocity field in the (x,z) plane for a nondimensional radial position x, defined as $x=r/d-(R_i+R_o)/2d$. The positioning accuracy of the measuring volume in the gap is defined as 1.6%.

Measurements in radial and axial directions of the azimuthal and axial liquid velocity components were performed for the Taylor number range Ta=750–1200. Very good visibility of the signal was achieved with a very high signal-to-noise ratio. The time histories were registered with a data rate of 2500 points per 5–35 s. This corresponds to a sample frequency of 70–500 Hz and is sufficient to obtain the mean and RMS values of the axial and azimuthal velocity components. The uncertainty in the measurements of the mean and root-mean-square (rms) values is estimated to be 1%.

A spectral analysis was performed on a time series of signals using a sample and hold interpolation method before applying a fast Fourier transform algorithm. This classical post-treatment is used for randomly sampled signals, to remove the difficulty caused by the nonequidistant successive time stepping obtained by the LDV measurements. Spectra were performed with a maximum data rate of 300 Hz, for a measurement time of 470 s. The spectral resolution Δf was 0.01 Hz.

A special dual fiber-optic probe was designed for this experiment by RBI Industry. The immerged part of the probe is made of a bent tube of 2 mm dia. The bent part of the tube is 0.6 mm large and 12 mm long. Each fiber has a cone-shaped tip of 10 μm. The distance between the two tips is 1.5 mm in the azimuthal direction of the flow. The probe is connected to an electronic system providing an output voltage signal between 0 and 10 V. The spatial resolution of the probe is estimated following the results of Cartelier [5]. The latency length is expected to be 420 μm. This is the critical size of the bubbles to ensure a good detection.

The sampling frequency is 20 kHz for the cavitating flow and 40 kHz for the ventilated flow. With these frequencies, the relative void fraction uncertainty is ±6% and ±12% for cavitating and ventilated conditions, respectively. The mean bubble velocity in the azimuthal direction is determined with a relative accuracy of ±7% for both flows. For the cavitating flow, bubble chord length can be determined with a relative uncertainty of ±13%, whereas, for the ventilated flows, the bubbles are too small to have a good estimation of their chord length and size.

Bubbles were detected by using a double threshold of the output voltage. The low threshold enables to detect the beginning of the dewetting process. It is calculated by making the same additional charge on the averaged voltage, so that the passage due to bubbles could be distinguished from noise. The high threshold enables the detection of the beginning of the rewetting process. It is calculated for each bubble and corresponds to a percentage of the maximum tension observed in each bubble.

Whenever the output voltage was greater than the threshold levels, the gas characteristic function was set to 1, otherwise to 0. The characteristic transit time, t_{trans}, of the bubbles between the two tips was deduced from the maximum cross-correlation function of the two gas characteristic functions. Two interfaces were deemed to correspond to the same bubble if their time delay is found in the range $[(1-c_1)t_{\text{trans}}:(1+c_2)t_{\text{trans}}]$, according to Gabillet et al. [6]. The bubble velocity was determined for each bubble detected on both tips of the probe. The chord length of a bubble is the length of the bubble viewed by the tip and is deduced from the bubble velocity and its residence time on the upstream tip. The mean bubble velocity was deduced from the average velocity weighted by the chord length of each bubble. The chord length distribution is used to determine the bubble size distribution, following the inverse method developed by Clark and Turton [7]. Bubbles located near the walls of the apparatus can be elongated in the azimuthal direction by the shear flow, leading to ellipsoidal bubbles. In this case, the inverse method makes it possible to obtain the large axis distribution of ellipsoidal bubbles; otherwise, the diameter distribution of spherical bubbles is found. As an example, the bubble distribution obtained for Ta=1000 in cavitating flow can be seen in Fig. 2.

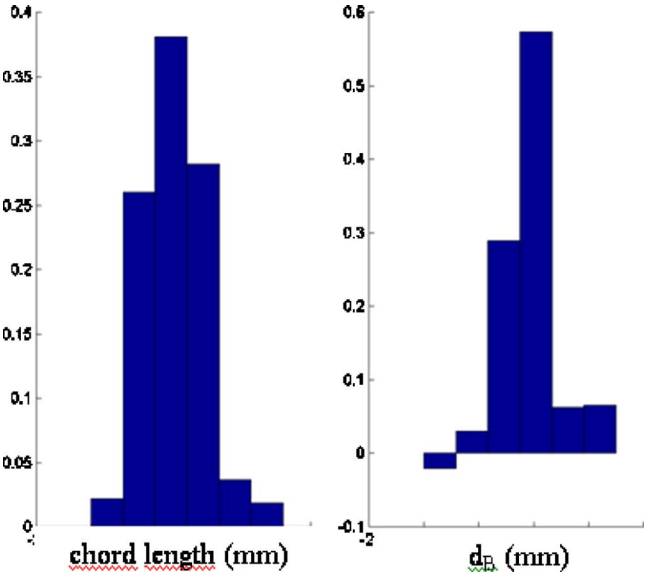

Fig. 2 Bubble size distribution for Ta=1000 in the vortices core (calculation is performed for 273 bubbles)

The measurement time (50 s and 25 s for the cavitating and ventilated conditions, respectively) was limited by the number of samples that can be recorded by the data-acquisition device (1×10^6). For each value of void fraction and mean bubble velocity that is displayed in the figures, errors corresponding to the reproducibility of the measurement, due to the measurement time, are also indicated.

The dual fiber-optic probe is moved in the radial and axial directions by a mechanical traverse system of absolute accuracy ±0.3 μm. The probe can be immersed down 6–8 Taylor vortices under the upper free surface. For the Taylor range investigated, the effect of the intrusion of the probe on the instabilities was investigated. There is a slight increase of the axial wavelength of 4% in the upper part of the flow, above the probe. For the lower part of the flow, there is no significant effect of intrusion of the probe on the axial and radial mean velocities. For both parts of the flow (above and under the probe), spectra are similar with and without the intrusion of the probe. Nevertheless, the liquid flow patterns were investigated without the intrusion of the probe.

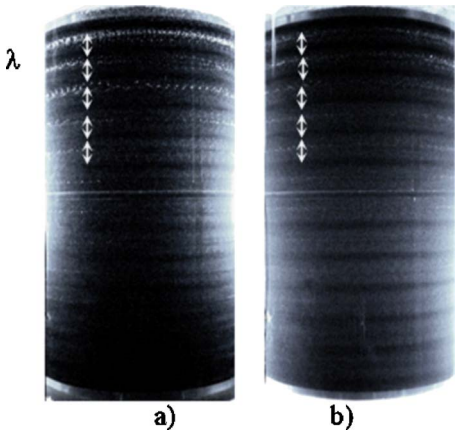

Fig. 3 Visualization of the bubble arrangement for ventilated flow: (a) Ω_i=2.45 rps (Ta=780), (b) Ω_i=3.07 rps (Ta=1000)

Characteristics of the Dispersed Phase

The arrangement of the bubbly phase in the gap obtained by vizualization, as well as void fraction profiles are presented for ventilated and cavitating flows. The localization of the dispersed phase is obviously different according to the size of the bubble, either in ventilated flow or in cavitating flow. Physical interpretation is further given.

Characteristics of Bubbly Phase in Ventilated Flow. For the ventilated flow, bubbles produced by the agitation of the free surface are driven into the gap, by "jumping" from vortex to vortex. As anticipated by Atkhen et al. [2] with a superimposed axial flow, bubbles are arranged as strings of individual spherical bubbles localized in the outflow regions near the inner cylinder. After waiting for at least 30 min, the flow reaches a steady state in which the string spacing and the void fraction do not seem to change with time. This arrangement is shown in Fig. 3 for Ta =780 and 1000.

The string spacing is identified as the axial wave length. As in single phase flow, the wavelength is homogeneous in the gap. However, it is increased in the entire gap by 5% and 7% in ventilated flow for Ta=780 and 1000, respectively, by comparison to the single phase flow. Although the bubble size was of the same order as the resolution of the optical probe, chord length inversion enables a rough approximation. By this way, bubble mean diameter d_B is estimated to be, approximately, 700 μm ($0.035d$).

Figure 4 shows the radial distribution of the void fraction measured in the outflow region for Ta=780 and Ta=1000, two wavelengths below the free surface (z/d=6.51 for Ta=780 and z/d =6.63 for Ta=1000). Measurements started at 2.5 mm (x= −0.375) from the inner cylinder's wall, exhibit an increase in the void fraction near the inner cylinder. The void fraction obviously increases with Ω_i and Ta. Indeed, ventilation is more pronounced when increasing Ω_i leading to more bubbles captured in the gap. Ten bubbles per second and 30 bubbles per second are detected in the outflow region for Ω_i=2.45 and 3.07 rps, respectively, two wavelengths below the free surface. For the Ta range studied, the bubble size is quite independent of the inner cylinder's velocity. Although there is no stratification of the axial wavelength in the gap, there is obviously an axial stratification of the void fraction. This stratification was qualified in the four first strings below the free surface. It seems that the void fraction in the outflow region expands almost exponentially with the axial wave length. $\alpha(i\lambda) = Ae^{-ik\lambda}$, approximately, for both Ta with k=7 m^{-1}. i denotes the number of the bubble string (i=1 is the string right below the free surface).

Characteristics of Bubbly Phase in Gaseous-Cavitating Flow. For the gaseous-cavitating flow, bubble arrangement is characterized by strings of individual bubbles partly localized in the outflow regions near the inner cylinder and partly localized in one in two Taylor vortex cores. This arrangement is shown in Fig. 5 for Ta=1000. The flow pattern is then characterized by a number of strings n_s and their localization in the gap. Note that n_s is representative of the averaged axial wave length $\bar{\lambda}$ in the gap

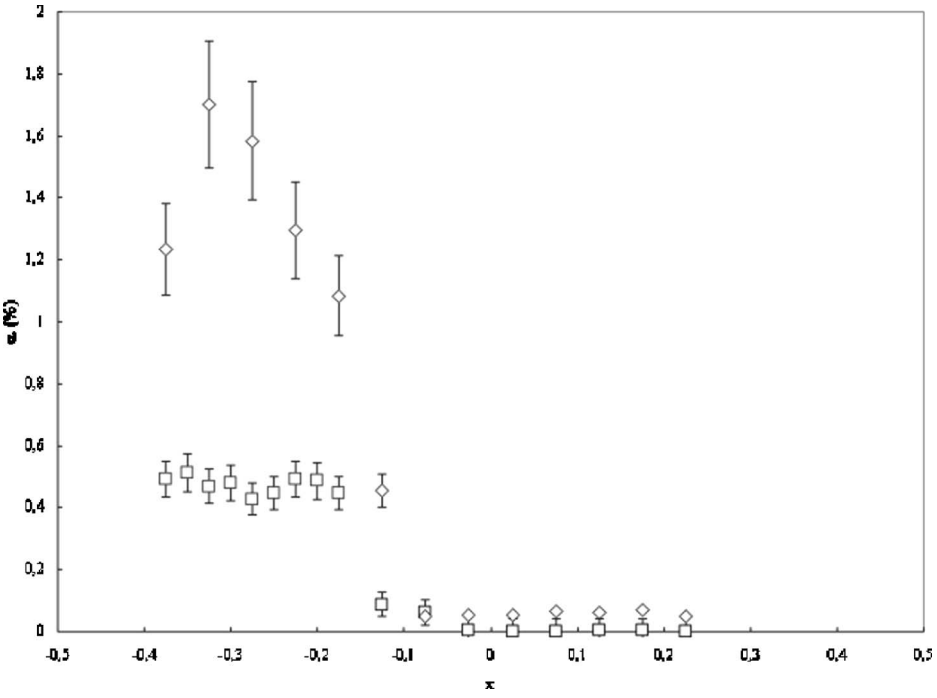

Fig. 4 Radial profiles of void fraction for ventilated flow: □: Ω_i=2.45 rps (Ta=780), ◇: Ω_i =3.07 rps (Ta=1000), $x=r/d-(R_i+R_0)/2d$

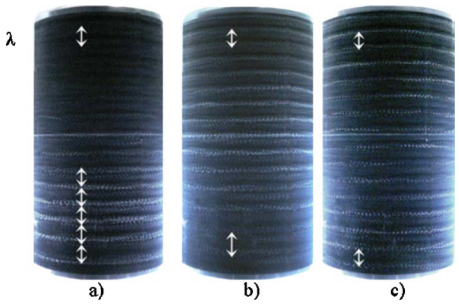

Fig. 5 Visualization of the bubble arrangement for cavitating flow at Ta=1000: (a) n_S=14, homogeneous, (b) n_S=16, stratified, and (c) n_S=16, homogeneous

deduced from $L/(n_S+0.5)$. This number of strings is observed in the outflow region. It can be seen that n_s evolves with the pressure decrease as it is summarized in the regime diagram in the coordinates (Pe, Ta) presented in Fig. 6. When decreasing the pressure, there are more bubbles spread out into more strings. A similar trend is encountered when increasing Ta for a constant pressure. n_s=14 corresponds to the gap entirely filled by bubble strings. Decreasing the pressure, new strings appear at the bottom of the gap and a linear stratification of the axial wave length is observed. Each new string leads to a new stratification. This organization of the flow corresponds to a particular regime called the transitional stage. At this stage, stabilizing the pressure leads to a reorganization of the flow with an homogeneous axial wave length. The duration of this reorganization is called transitional time and depends on Ta and n_s. Table 2 summarizes the value of the axial wave length for different states of the bubbly flow (homogeneous and stratified). λ_{max} and λ_{min} represent the axial wavelength observed at the bottom and top of the gap, respectively. λ_{max} can reach 4.25d at the bottom of the apparatus. This value corresponds to the maximum stretching of the Taylor vortices that can be observed in turbulent flow.

Table 2 Cavitating flow patterns

Ta	Flow pattern	λ_{max}	λ_{min}	α_{core} (%)
780	Single phase	3.1d	3.1d	0
780	n_S=14 (homogeneous)	3.1d	3.1d	0.08
780	n_S=14 (stratified)	4.25d	2.75d	0.1
780	n_S=15 (stratified)	4.25d	2.4d	0.35
780	n_S=15 (homogeneous)	2.85d	2.85d	0.12
1000	Single phase	3.1d	3.1d	0
1000	n_S=14 (homogeneous)	3.1d	3.1d	0.05
1000	n_S=14 (stratified)	4.25d	2.75d	0.26
1000	n_S=15 (stratified)	4.25d	2.4d	0.36
1000	n_S=16 (stratified)	4.25d	2.15d	0.75
1000	n_S=16 (homogeneous)	2.68d	2.68d	0.3

The void fraction measured in the core of a Taylor vortex in the third string below the free surface is also given in Table 2. For a given Taylor number, the void fraction increases with the increase of n_s. For $\alpha_{core}>0.1\%$, there is a change in the length of the Taylor vortices and, hence, in the flow pattern. Stabilization of the flow (i.e., the disappearance of stratification) is accompanied with a decrease in void fraction.

The spatial void fraction distribution has been characterized only for n_s=15 at Ta=780 and n_s=16 at Ta=1000, where the transitional time is sufficient to investigate the stratified flow. Radial measurements started at 2.5 mm (x=−0.375) from the inner cylinder's wall were performed in the core of the Taylor vortex

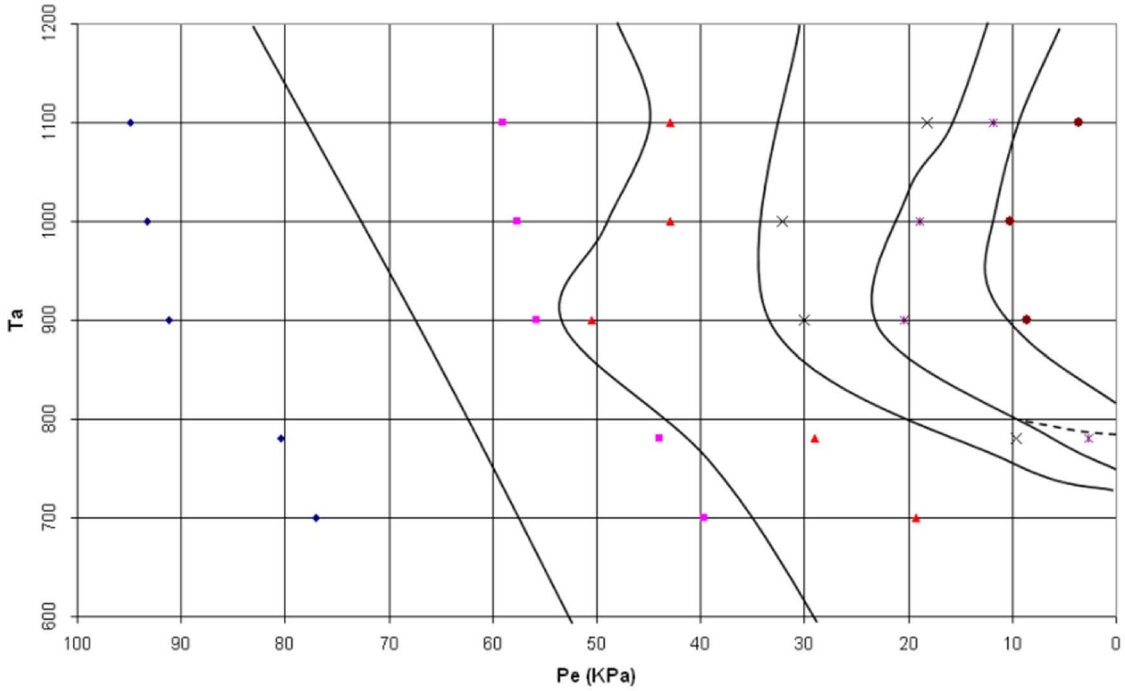

Fig. 6 Evolution of the bubble strings number in cavitating flow: ♦: 3 strings, ■: 8 strings, ▲: 14 strings, ×: 15 strings, *: 16 strings, ●: 17 strings

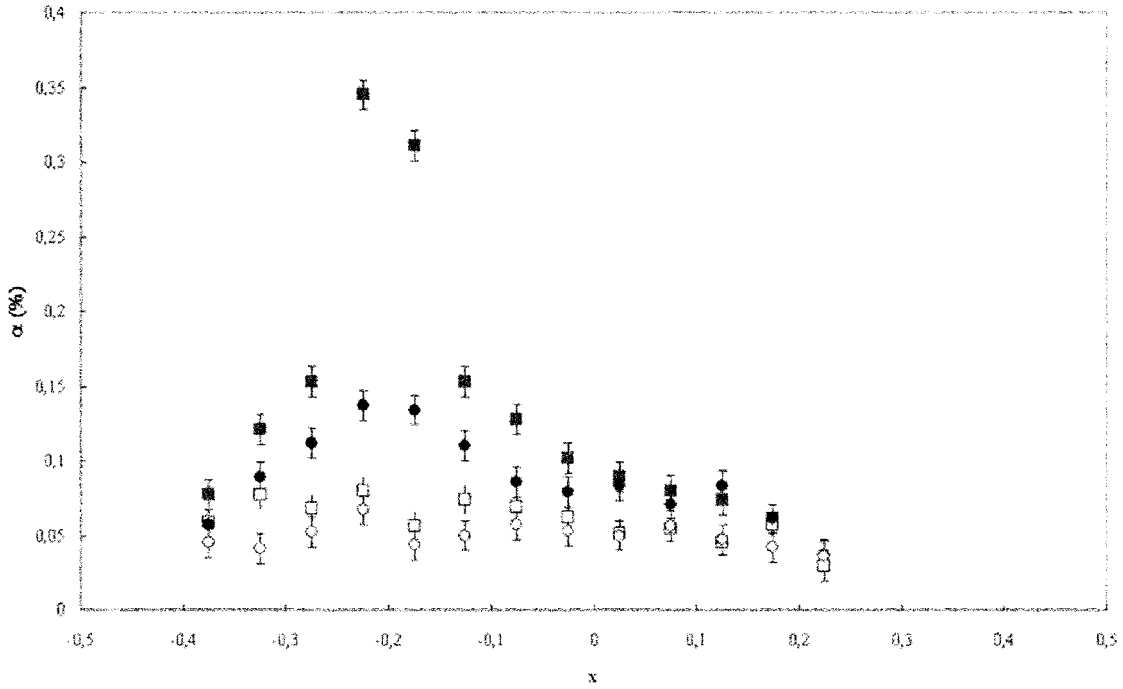

Fig. 7 Radial profiles of void fraction for cavitating flow in the 3rd bubble strings (Ta=780), $x=r/d-(R_i+R_0)/2d$: ■: core n_s=15 stratified, □: outflow n_s=15 stratified, ●: core n_s=15 homogeneous, ○: outflow n_s=15 homogeneous

and in the outflow regions. Figures 7 and 8 display the radial distribution in the third string below the free surface, for Ta =780 and Ta=1000, respectively. In the core of the Taylor vortices, bubbles are rather located at about 5.6 mm ($x=-0.22$) from the inner cylinder. In the outflow, the void fraction slightly increases near the inner cylinder. This increase is expected to be more pronounced in the region closer to the wall, where the probe is unable to take the measurements. What is surprising, is the void fraction peak observed in the outflow region for the homogeneous flow at Ta=1000 as observed in the core of the vortices. This denotes an important axial oscillation of the Taylor vortices, and bubbles captured in the core contribute to the void fraction measured in a static region, corresponding to a time-averaged outflow region. As stratification is known to inhibit movement in the same

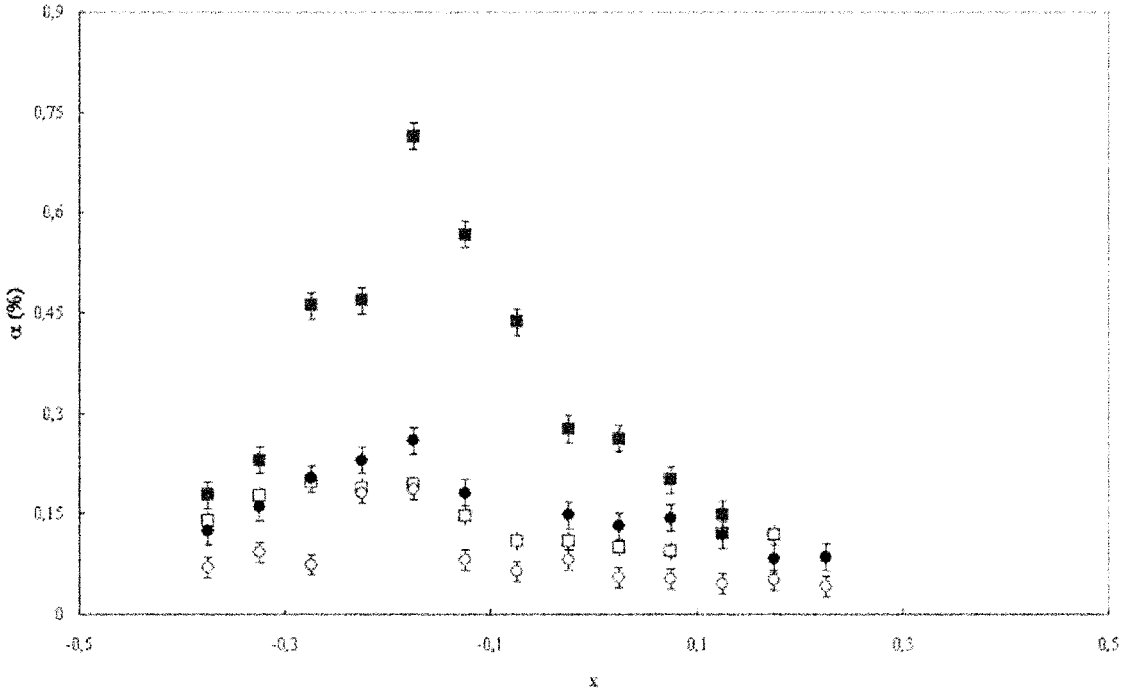

Fig. 8 Radial profiles of void fraction for cavitating flow in the third bubble stings (Ta=1000), $x=r/d-(R_i+R_0)/2d$: ■: core n_s=16 stratified, □: outflow n_s=16 stratified, ●: core n_s=16 homogeneous, ○: outflow n_s=16 homogeneous

direction, the vortex axial oscillation is more pronounced in the case of homogeneous flow than in the case of axial stratified flow. To investigate a possible axial stratification of the void fraction in the core of the Taylor vortices, axial measurements of the void fraction were performed in the core for the first three bubble strings below the free surface. Measurements exhibit an inverse axial stratification of the void fraction, which evolves linearly with the axial distance, the void fraction being more important at the top of the gap. The stratification is all the more important as the Taylor number increases ($d\alpha/dz=-0.1\%/\lambda$ for Ta=780 and $d\alpha/dz=-0.5\%/\lambda$ for Ta=1000). Axial stratification was also investigated in the outflow regions near the inner cylinder. In this region of the flow, the void fraction is maximum at the top of the gap and decreases linearly with the axial distance, the rate of expansion being four times as small as in the core of the Taylor vortices. This lets suppose that the void fraction is more important in the outflow region than in the core of the Taylor vortices at the bottom of the gap and, conversely, at the top of the gap. When the flow is stabilized (i.e., the axial wavelength is homogeneous), no axial void fraction stratification is encountered either in the vortices cores or in the outflow regions.

The bubble size can be confidently obtained in the core of the Taylor vortices. In the third string, bubble mean diameter d_B is estimated to be 3.1 mm ($\approx 0.15d$). In the outflow region, bubbles are ellipsoidal bubbles. The determination of the bubble size is very biased because bubbles are localized very close to the inner cylinder wall where the probe is unable to measure. Nevertheless, the bubble size distribution can be deduced from image processing. The average large axis $1\theta_B$, in the azimutal direction, is around 6 mm ($1\theta_B \approx 0.3d$), larger than the bubble diameter in the core of the Taylor vortices, and the average small axis $1x_B$ is around 2.6 mm ($1x_B \approx 0.13d$). No noticeable stratification of the bubble size is found for the first three bubble strings below the free surface, the expected global stratification between the bottom and the top of the gap due to hydrostatic pressure being less than one-tenth of a millimeter. As a summary, the bubble size is homogeneous, independent of both the Ta number and the state of the flow (stratified and homogeneous).

Discussion About Bubble Arrangement in the Flow. To understand the localization of the bubbles, it is necessary to underline the role of the predominant forces acting on the bubbles. For the ventilated flow, small bubbles (size $0.035d$) are located in the outflow regions near the inner cylinder. A good explanation was given by Atkhen et al. [2] for the ventilated flow with superimposed axial flux. Indeed, if the terminal velocity of the bubbles, obtained by the equilibrium between the buoyancy and the drag force, is lower than the downward velocity fluctuation, they can be captured in the separatrix regions. If the drag due to both the radial mean and fluctuating velocities compensates the centrifugal acceleration of the flow at the separatrix, an equilibrium position can be found. This condition is realized in the outflow separatrix and not in the inflow separatrix. As far as larger bubbles are considered, no real equilibrium position is found in the outflow separatrix, bubbles are either agglomerated near the inner cylinder in the outflow regions or captured in the core of the Taylor vortices. Indeed, for the cavitating wavy vortex flow studied by Djeridi et al. [4], for Ta$<$307, bubbles are found in the Taylor vortices, with alternative distance between two bubble rings of $1.2d$ and $0.8d$. For this particular flow, for Ta$>$307 or above a critical bubble size of $0.3d$, equilibrium positions no longer exist in the core of the vortices. This corresponds to a migration of the bubbles towards the inner cylinder in the outflow region.

For the cavitating Couette Taylor flow presently studied, for quasi-periodic and weakly turbulent flows conditions, bubbles of mean size $0.15d$ are localized in one in two Taylor vortex cores. Bubbles are captured in these particular vortices, for which rotation induces lift and drag forces opposed to the buoyancy force. As expected from [2] or [4], smaller bubbles or larger bubbles are not captured by the Taylor vortices and migrate into the outflow region, near the inner cylinder.

In single phase flow, at Ta=700, the modulation of frequency f' becomes chaotic and as energetic as the azimutal wave of frequency $mf0$. Beyond Ta=700, for the quasi-periodic flow, the azimutal wave is expected to yield some of its energy to the chaotic modulation, until the azimutal wave switches off (Table 1) at Ta=850. It is then interesting to determine which one of the two waves play a determinant role in the bubbles capture by the vortices. To have a better understanding, spectra of the gas characteristic function are determined in the core of the vortices. Spectra, up to 20 Hz, are deduced from *subsampling* the auto-correlation of the gas characteristic function, measured with the upstream probe of the dual fiber-optic probe. The spectrum presented in Fig. 9 for Ta=780 show a periodicity of the bubble arrangement at frequency f'. This gives the evidence that bubbles follow the more energetic wave of minor frequency to be captured by the vortices.

Characteristics of Liquid Phase

To answer the above question relative to the bubbles effects on the flow pattern, LDV measurements of the liquid phase in both ventilated and cavitating flows have been performed and compared to the single phase flow.

Characteristics of Liquid Phase in Ventilated Flow. For the ventilated flow, the particular localization of the bubbles near the inner cylinder in the outflow regions enables LDV measurements elsewhere in the gap. Thus, to provide an accurate velocity measurement of the liquid phase, spectra and axial profiles were investigated near the outer cylinder ($x=0.25$). However, to compare azimuthal velocity of bubbles and azimuthal velocity of the liquid, radial profiles must be performed in the outflow regions. Then, the contribution of the bubbles induces an error in the measurement of the liquid azimuthal velocity. This error is $\sim 2\%$. Axial profiles of the dimensionless axial velocity ($W_L d/\nu$) are plotted in Fig. 10 for Ta=1000. Profiles confirm a slight increase of the axial wavelength for the ventilated flow, by comparison to the single phase flow, depending on the inner cylinder's velocity and thus on the void fraction. The same value of the Taylor vortices expansion is obtained with LDV as with visualization of the gaseous phase in the gap, leading to $\lambda=3.26d$ and $\lambda=3.32d$ for Ta=780 and Ta=1000, respectively, instead of $3.1d$ in single phase flow. Nevertheless, no significant change is found in the value of the axial velocity at $x=0.25$, assuming that the vorticity is slightly decreased in ventilated flow. Figure 11 shows both the radial profiles of the liquid mean azimuthal velocity in single phase and ventilated flow for Ta=1000. The velocity is normalized by $V_i=2\Pi R_i\Omega_i$.To compare to the azimuthal velocity of the bubbles v_B, radial profiles obtained with optical probe are superimposed. It can be noted that near the inner cylinder, bubbles move a little slower than the liquid. For Ta=1000, the drift velocity v_L-v_B can reach 10% of the liquid velocity. For Ta=780, it is 7% of the liquid velocity. Concerning the comparison between the single phase and ventilated flow, there is a small deceleration of the liquid azimuthal velocity (4% and 6% for Ta=780 and 1000, respectively). This is due to momentum exchange, which is expected to increase with α, d_B, and (v_L-v_B). Note that the complementary spectral analysis of the axial velocity performed in single phase flow and in ventilated flow shows that the spectra are similar for both quasi-periodic flow (Ta=780) and weakly turbulent flow (Ta=1000). Thus, there is no influence of the bubbles on the transition to weakly turbulent flow.

Characteristics of Liquid Phase in Gaseous-Cavitating Flow. To quantify the bubble effect on the flow patterns in cavitating flow, mean velocity components of the liquid and spectra obtained in cavitating flow are compared to those obtained in

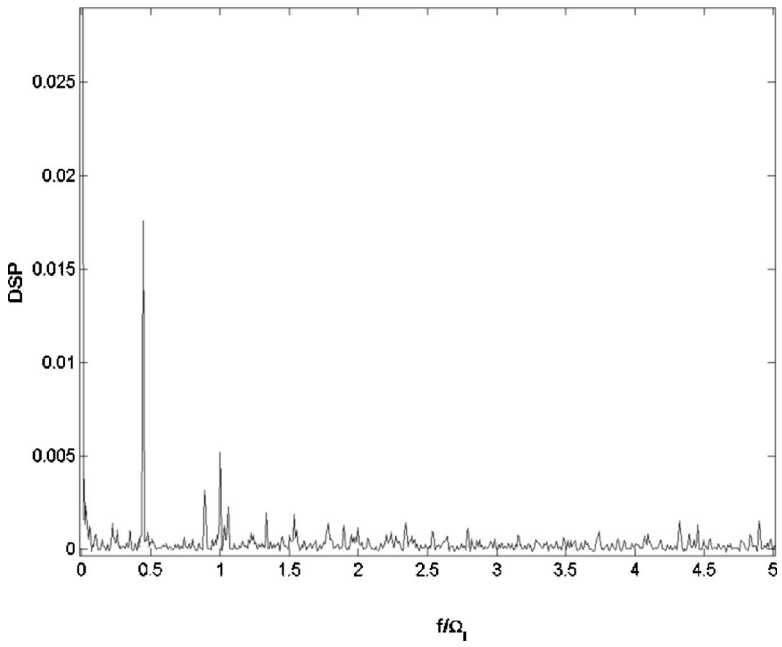

Fig. 9 Spectrum of the gas characteristic function obtained at Ta=780 for cavitating homogeneous flow (n_S=15)

single phase flow. As for the ventilated flow, axial profiles and spectra of axial velocity were measured near the outer cylinder (x=0.25) where no bubbles can contribute to the LDV signal. For the measurement of radial profiles of azimuthal velocity performed in the core of the Taylor vortices, the bubble-induced error is not as disadvantageous as in the outflow region. However, for the measurement of radial profiles of azimuthal velocity performed in the outflow regions, the bubble induced error remains small ($<1\%$).

In the case of cavitating stratified flow, the Taylor vortices tend to shift axially with time. Therefore, axial profiles and radial profiles of velocity components are only investigated in the case when the flow is homogeneous. The axial profile of mean axial velocity plotted in Fig. 12 for Ta=1000 (n_S=16), shows clearly that the axial wave length is reduced with the vapor phase, by comparison to the single phase flow. The axial wave length values investigated by LDV are in agreement with the values obtained by the visualizations and reported in Table 2. In homogeneous cavitating flow, there is both a flattening of the Taylor vortices ($\Delta\lambda/\lambda_{\text{single phase}}=-8.5\%$ at Ta=780, n_S=15 and -15.5% at Ta

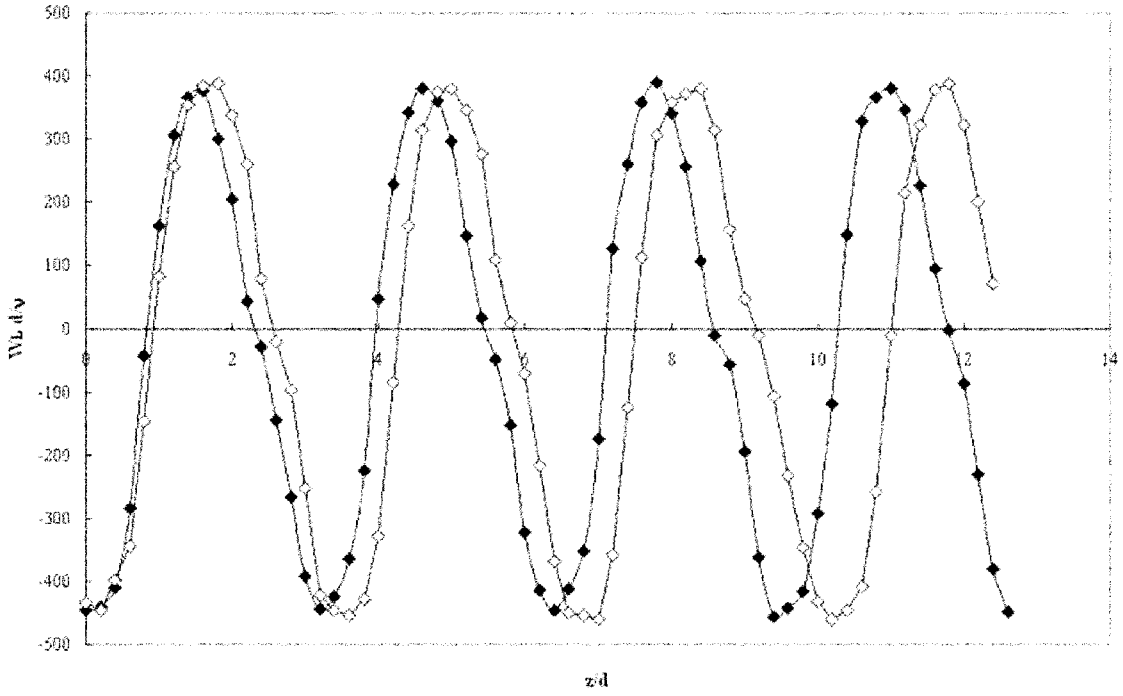

Fig. 10 Comparison between single phase flow and ventilated flow axial profiles of axial velocity for Ω_i =3.07 rps (Ta=1000): –– ♦ ––:single phase, –– ◇ ––: ventilated

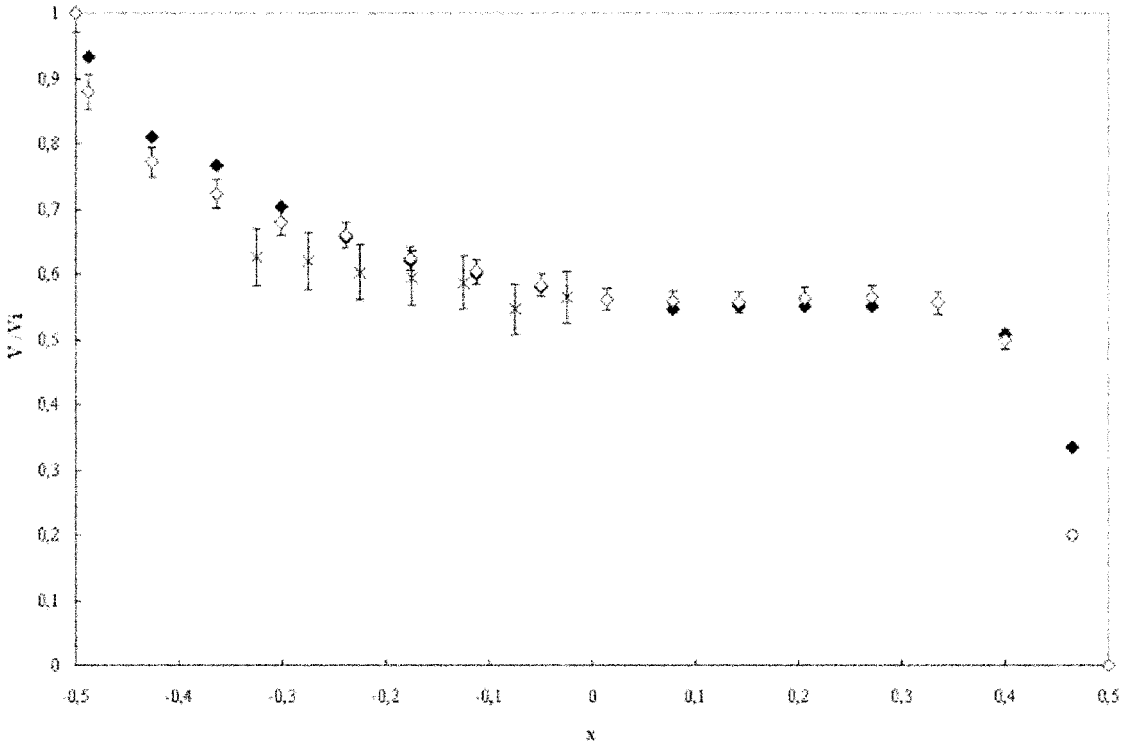

Fig. 11 Radial profiles of azimuthal velocity in the outflow region of both the liquid phase and the bubbles for Ta=1000, $x=r/d-(R_i+R_0)/2d$: ♦: single phase, ◇: ventilated, ×: bubbles

=1000, n_S=16) and a decrease of the tangential velocity ($\Delta w_L/w_{\text{single phase}}=-2\%$ at Ta=780, n_S=15 and −11.5% at Ta =1000, n_S=16). This trend is more pronounced in the Taylor vortices where bubbles are captured and reinforced when both Ta and the void fraction increase. Globally, when combining reduction of both size and tangential velocity of the vortices, it seems that the vorticity slightly increases with the vapour phase for both Ta.

A squeezing of the Taylor vortices was also observed by Atkhen et al. [2] in weakly and high turbulent Couette Taylor flow with a superimposed axial flow. Indeed, according to their measurements, at Ta=1000, the axial wavelength is reduced by 20% for a volumetric flux of the liquid corresponding to J_L=0.034 m/s (i.e.,

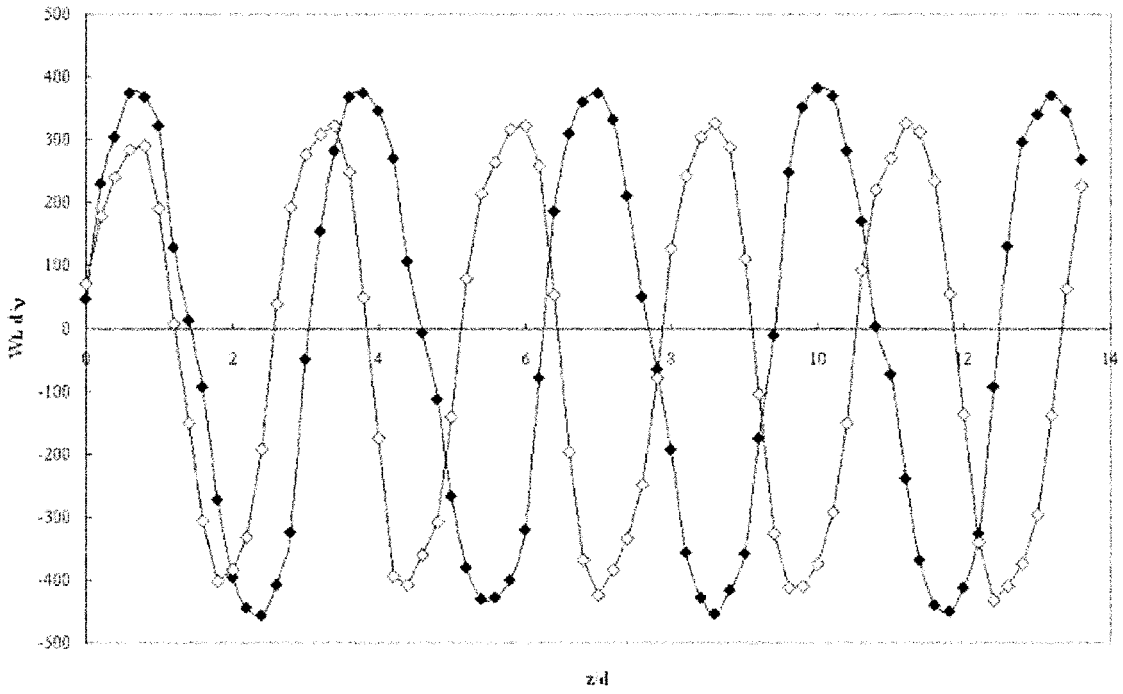

Fig. 12 Axial profiles of axial velocity for Ta=1000. Comparison between single phase flow and homogeneous cavitating flow (n_S=16): –– ♦ ––:single phase, –– ◇ ––: n_s=16 homogeneous

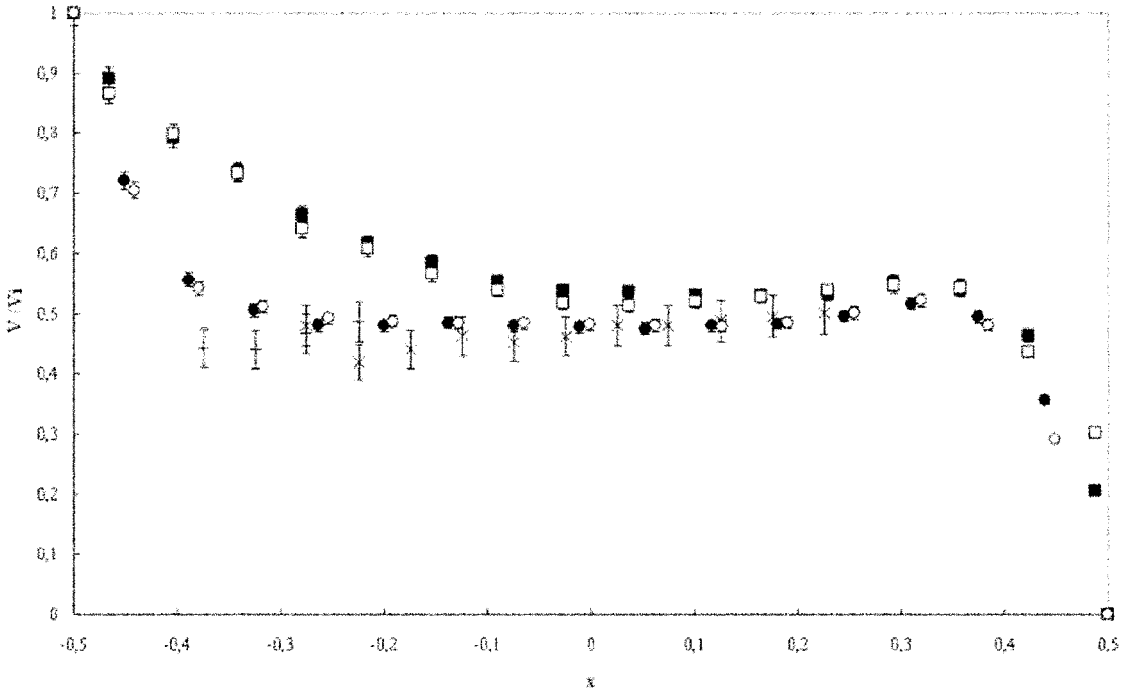

Fig. 13 Radial profiles of azimuthal velocity of both the liquid phase and the bubbles for cavitating homogeneous flow at Ta=780 (n_S=15), $x=r/d-(R_i+R_o)/2d$: ■: single phase outflow, □: n_s=15 homogeneous, outflow, -: bubbles outflow, ●: single phase core, ○: n_s=15 homogeneous, core, +: bubbles core

$J_L/V_i=0.044V_i$). Because of the difference between the inertia of vapor and liquid, the same volumetric flux of vapor would lead to less important modification of the flow patterns. This gives rise to the question: Is there any influence of the transitional axial flow superimposed during the stratification stage on the axial reduction in wavelength observed in cavitating homogeneous flow? The superficial velocity J_G due to the axial volumetric flux was roughly estimated as $1/[\pi(R_o^2-R_t^2)]\int_{R_i}^{R_o}\alpha(r)(L/t_d)2\pi r dr$, with t_d the time necessary for the bubbles to migrate from the bottom to the top of the apparatus. From the radial profile of void fraction measured in the third string below the free surface of the stratified flow at Ta=1000, we obtain J_G equal to 0.006 mm/s (i.e., $3\times10^{-6}V_i$). Compared to [2], this value is too small to ensure a modification of the flow patterns. Same conclusion is drawn, by comparison with Shiomi et al.[1]. Indeed, they underline, that there is no significant influence of a two-phase axial flux on the axial wavelength for a superficial velocity (i.e., liquid+gas) $<0.35Vi$, from Ta=3000 up to 25000. Thus, the squeezing of the Taylor vortices is likely to be due to the bubbles effect, in terms of momentum exchange and not to the superimposed gas flux during pressure drop. In Figs. 13 and 14, radial profiles of mean azimuthal velocity measured both in the core of the vortices and in the outflow region are presented together with profiles of mean bubble velocity for Ta=780 (n_S=15) and Ta=1000(n_S=16), respectively. For the homogeneous flow, the vapor moves at the velocity of the liquid in the middle of the gap. The drift velocity is particularly important in the outflow region near the inner cylinder. It is responsible for the elongation of the bubbles, observed in this region of the flow. At $x=-0.375$, the drift velocity can reach 40% and 27% of the liquid velocity for Ta=780 and 1000, respectively. This drift velocity is expected to increase in the region closer to the wall, where the probe is unable to take measurements. In the core of the vortices, the drift velocity is small, in agreement with the spherical shape of the bubbles. Figures 13 and 14 also display the radial profiles of mean azimuthal velocity measured in single phase flow. It can be seen that homogeneous cavitation has no significant influence on the azimuthal mean velocity in the core of the vortices. In the outflow region, however, there is a decrease in liquid velocity near the inner cylinder (4% and 7% for Ta=780 and 1000, respectively) that results from the momentum exchanges between the phases. This deceleration of the liquid depends on the Ta number and thus increases with the void fraction. It leads to a flattening of the radial velocity profiles, characteristic of bubbly flows in general. The flattening of the azimuthal velocity profiles and the deceleration of the liquid in the outflow regions are expected to be more pronounced in the case of stratified cavitating flow for which the void fraction is augmented by comparison to the homogeneous flow. Spectra of the liquid axial velocity performed in the outflow region are presented in Figs. 15 and 16, respectively, for Ta=780 and Ta=1000. In these figures, the spectrum obtained in single phase flow is superimposed with the spectrum obtained in stratified cavitating flow. Spectra obtained in homogeneous flow are unchanged by comparison to single phase flow (and thus are not displayed in the figures). Note that it was carefully checked that spectra were the same for the different axial positions of the outflow regions. For Ta=780, in single phase flow, incommensurable rays of frequency (f' and $mf0$) are observed, corresponding to the quasi-periodic flow with an azimuthal wave number $m=4$. For the cavitating stratified flow (n_S=15), as evidence, there is a premature disappearance of the azimuthal wave, corresponding to a premature appearance of the weakly turbulent flow. For the cavitating homogeneous flow, the spectrum recovers the same shape as in single phase flow, assuming that the premature change in turbulence development is transitional, in agreement either with a stratification state of the flow or with a void fraction in the outflow region larger than 0.1%.

For Ta=1000, as expected in Table 1 for the single phase weakly turbulent flow, the azimuthal wave of frequency $mf0$ has disappeared. The same result is encountered in both the cavitating stratified flow and in the cavitating homogeneous flow (n_S=16). Spectra analysis shows that the distribution of fluctuating energy is modified by the presence of the bubbles in quasi-periodic flow for cavitating stratified flow conditions. To explain this, it can be worth comparing the bubble size and the length scale of energy

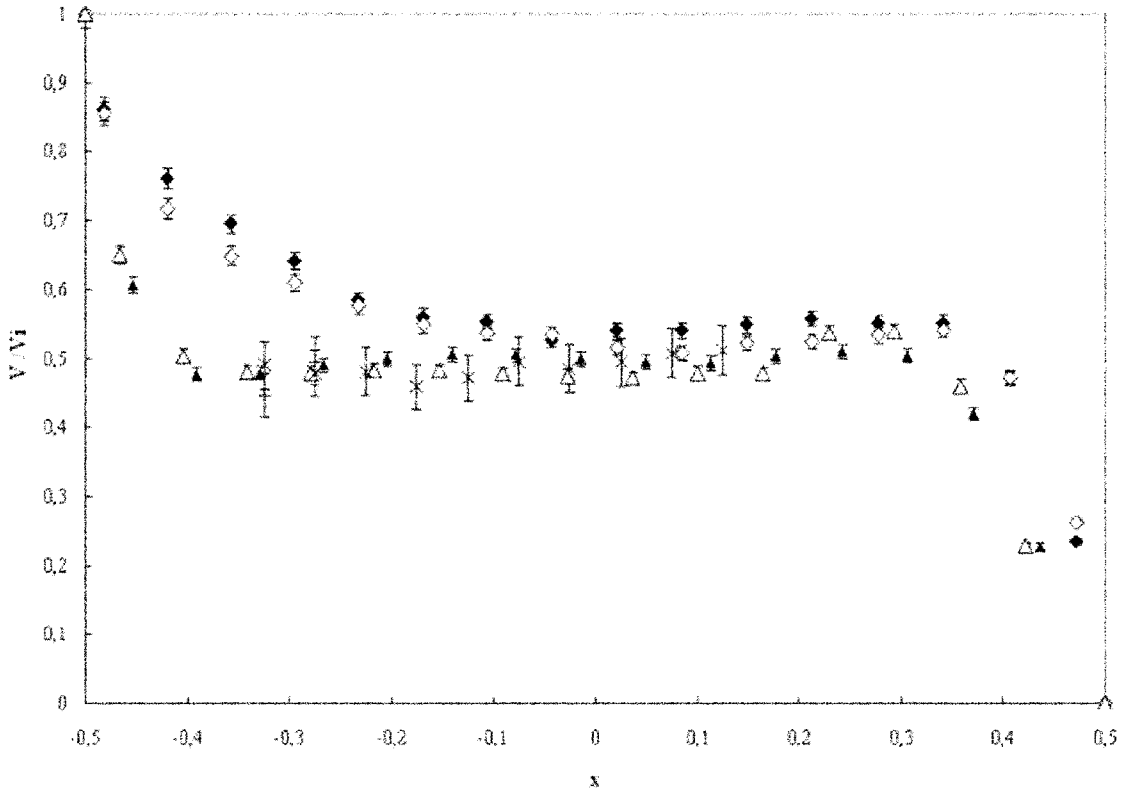

Fig. 14 Radial profiles of azimuthal velocity of both the liquid phase and the bubbles for cavitating homogeneous flow at Ta=1000(n_S=16), $x=r/d-(R_i+R_o)/2d$: ♦: single phase outflow, ◇: n_s=16 homogeneous outflow, ■: bubbles outflow, ▲: single phase core, △: n_s=16 homogeneous core, ×: bubbles core

containing eddies. The length scale of azimuthal wave can be deduced from the ratio: $l_0=W_{\mathrm{rms}}/mf_0$ and the one of the modulation from the ratio $l'=W_{\mathrm{rms}}/f'$, where W_{rms} is the rms value of axial velocity component in the outflow region. This yields to length scales of 5 mm and 16 mm, respectively. This rough estimation shows that the bubble size in the outflow region is of the same order as the azimuthal wavelength scale, as it is suggested by the premature disappearance of this wave at Ta=780. Accord-

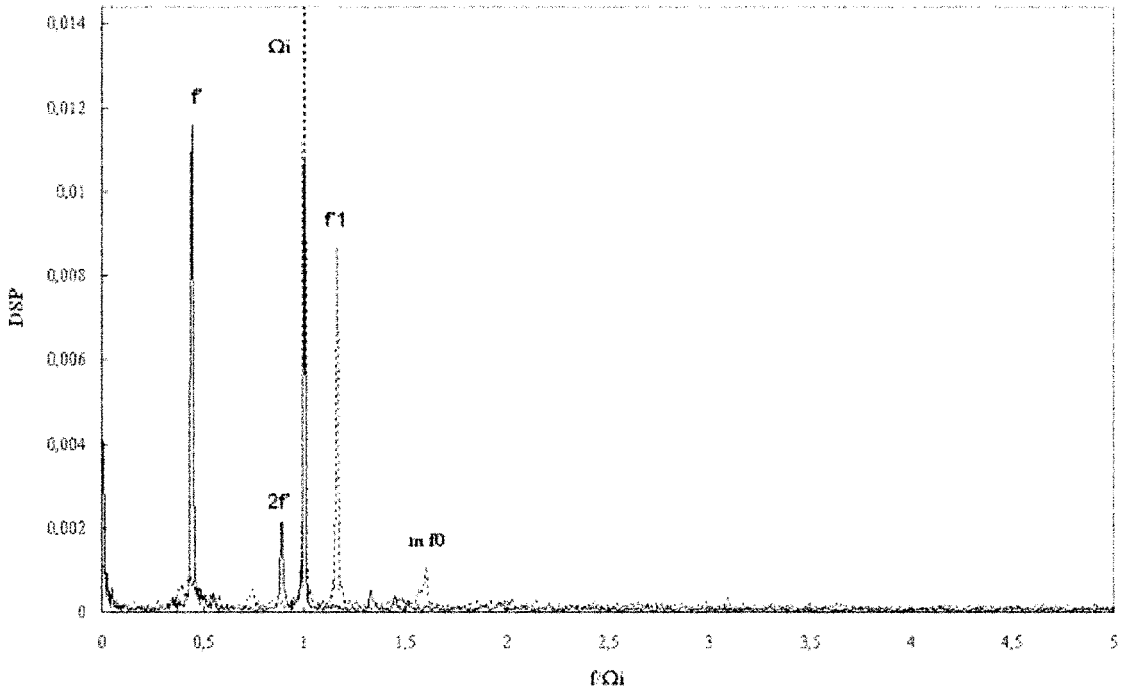

Fig. 15 Comparison of the spectra obtained at Ta=780: dotted line, single phase flow; solid line, cavitating stratified flow (n_S=15)

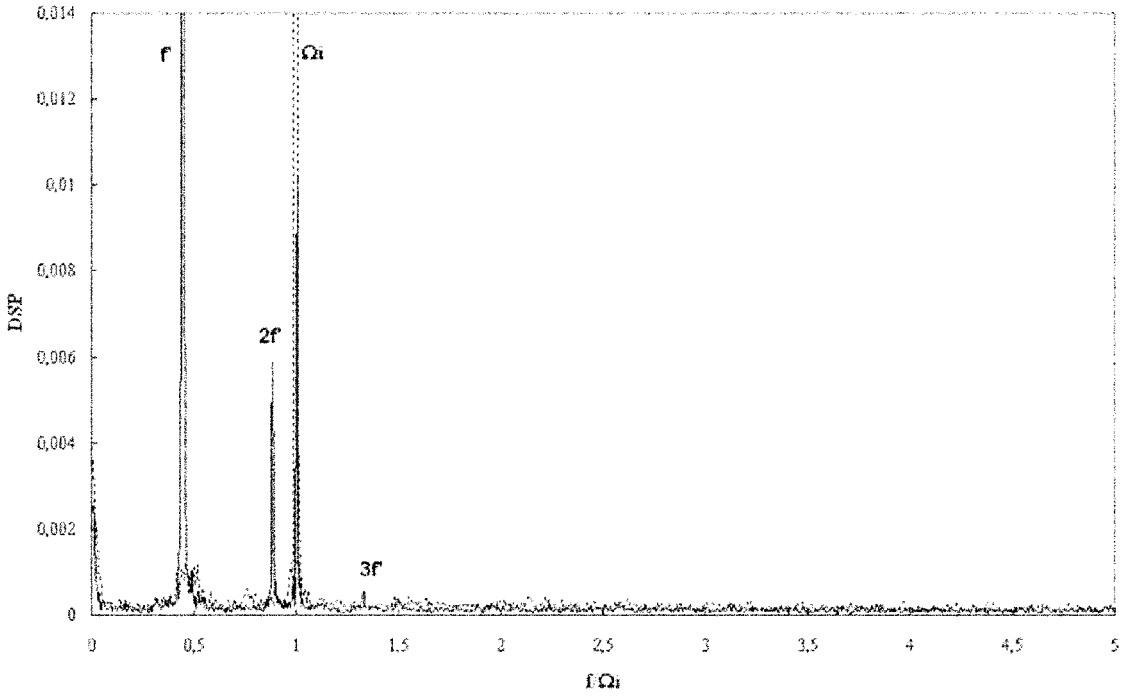

Fig. 16 Comparison of the spectra obtained at Ta=1000: dotted line, single phase flow; solid line, cavitating stratified flow (n_S=16)

ing to Cognet [8], azimuthal waves, in single phase Couette Taylor flow, are due to the significant radial jet localized in the outflow region. Therefore, it can be supposed that when bubbles of same size as the azimuthal wave characteristic length interfere with this jet, azimuthal waves are affected. Fluctuating kinetic energy of the azimuthal wave is thus transferred to the chaotic structures characterized by f'. Indeed, kinetic energy of frequency f' is promoted by the capture of the bubbles and the bubble arrangement in the core of the vortices following the waves associated with this frequency, as mentioned before. Let us now evaluate the turbulent fluctuations produced by the wake of the bubbles, i.e., pseudo-turbulence. In the outflow jet, taking into account the bubble small axis distribution, the characteristic frequency of fluctuations in the wake of ellipsoïdal bubbles can be estimated based on a Strouhal number $(f_B l x_B / U_{L,\text{outflow}}) \approx (f_B l x_B / W_L)$ around 0.13. It leads to bubble frequencies approximately equal to 12 Hz ($\approx 7\Omega i$), out of order by comparison to characteristic frequencies of the flow (f' and mf_0). Moreover, according to Lance and Bataille [9] in grid turbulence flow, the void fraction must be superior than 1% to have spectra affected by pseudo-turbulence. This condition is obviously not satisfied. The bubble induced fluctuating motion is thus clearly due to bubble capture in the vortices.

Discussion About Bubble-Induced Effects on the Flow Pattern: Comparison Between Ventilated and Gaseous-Cavitating Flows

This study provides the evidence that the ventilated and cavitating Couette Taylor flows, characterized by different bubble size, do not have the same features in the range $780 \leq \text{Ta} \leq 1000$. For the ventilated flow, there is no influence of the bubbles on the spectra of axial velocity. Bubbles, localized in the outflow region, are considered too small ($d_B/d=0.035$) to interfere with turbulent structures and bring about a premature transition to turbulence. Nevertheless, there is a slight increase in axial wave length. In Djeridi et al. [4], it is conjectured that migration of bubbles ($d_B > 0.3d$) from the cores of the vortices into the outflow regions leads to an augmentation in the axial wavelength. It is now clear that this bubble location in the outflow, whatever their size, is responsible for the vortices' size modification. This stretching of the Taylor vortices is consistent with an increase of the axial momentum transfer between the Taylor vortices [10]. The boundary region is known to act as a barrier to exchanges; thus, bubbles can act as an intermediary to transfer momentum between the vortices. For the homogeneous cavitating flow, Taylor vortices are squeezed. In the present study, it seems that bubbles, mostly trapped in the core of the vortices, are responsible for a decrease of the vortex size and an increase of the vorticity. This is in agreement with Gopalan and Katz [11]. They give the evidence that, for certain combinations of vortex strengths and bubble diameters, a few entrained bubbles at very low void fraction can reduce the core size of laminar, transitional, and turbulent vortices. According to the bubble location in the vortex core and the ratio between momentum exchange due to the bubble buoyancy effect and to the bubble pressure gradient effect given by $g d_B^3 / G^2$, the distortion can be null, marginal, or severe. G represents the vortex strength. In our case, the increase in vorticity is about 6%, assuming that the distortion is called "marginal" distortion. In [11], marginal distortion is observed for bubble distance from the center of the vortex between $0.4R$ and $0.45R$,with R the vortex radius. This is typically the case for the radial bubble location ($0.44R$). For the axial bubble location, we obtain a little more ($0.54R$). We also obtain $g d_B^3 / G^2$ larger than prescribed by [11]. Estimations give 4.10^{-3} and 3.10^{-3} for Ta=780 and Ta=1000, respectively. Nevertheless, comparisons to [11] are difficult because the distortion of the vortices seems also to be linked to the bubble number and their residence time, for bubbles agglomerated in the vortex.

Taking into account that bubble location directly influences the size of the vortices, thus, a predominant flattening of the Taylor cells is observed when the void fraction in the core of the cells is more significant than the void fraction near the inner cylinder in the outflow region (top of the gap in stratified flow and homogeneous flow). In return, a predominant growth of the Taylor cells is observed when the void fraction near the inner cylinder in the outflow region is more significant than the void fraction in the core of the cells (bottom of the gap in stratified flow). In single

phase flow, the axial wavelength growth is related to the increase in the wall shear stress [8]. Therefore, same arguments relative to the "bubble-induced wall shear stress" can be advanced to explain the growth of the Taylor cells length observed in ventilated flow and stratified cavitating flow.

For both ventilated and cavitating flows, bubbles move slower than the liquid in the azimuthal direction. The azimuthal drift velocity is reinforced in the region where the liquid is accelerated and, thus, particularly in the outflow region, near the inner cylinder. This results in a deceleration of the fluid in the azimuthal direction near the inner cylinder in the outflow region and a flattening of the azimuthal velocity radial profiles. This corresponds to an increase of the velocity gradient at the inner cylinder, leading to an increase of the wall shear stress at the inner cylinder. This increase of the local wall shear stress, which is expected to expand with the void fraction is called bubble-induced wall shear stress. It is not directly due to buoyancy effect, but rather due to modification of liquid velocity profiles near the wall, as a result of momentum transfer between gas and liquid phases. When considering the volume occupied by the bubbles α multiplied by the drift velocity, there is a ratio of 0.4 and 0.14 between cavitating homogeneous flow and ventilated flow, for Ta=780 and 1000, respectively. Thus, the momentum exchange between bubbles and liquid is greater in ventilated flow than in cavitating flow, letting suppose that bubble-induced wall shear stress is greater in ventilated flow than in cavitating flow. Therefore, radial transport of fluid azimuthal momentum from near the inner wall outward [12] and axial momentum transfer are prominent in ventilated flow. The reason why transfers are promoted in ventilated flow is that the bubble quantity and, thus, the void fraction in the outflow region near the inner cylinder are more important, regardless of the bubble size. In Djeridi et al. [4], the bubble-induced wall shear stress was expected to be responsible for the premature transition between the second and third instability. In the present experiment, it cannot explain the premature transition to weakly turbulent flow, observed for the stratified cavitating flow. This premature transition must not be considered here as an advance in the transition to turbulence. Two reasons can be invoked: First of all, millimetric bubbles present in the outflow region in cavitating flow interfere with the azimuthal wave. Secondly, millimetric bubbles to be captured by the Taylor vortices in cavitating flow reinforces the modulation f' at the cost of the azimutal wave.

Conclusion

The bubbly Couette Taylor flow was investigated for the quasi-periodic and weakly turbulent regimes. Bubbles of different size were generated either by natural ventilation ($d_B=0.03d$) or by injection and pressure drop (gaseous cavitation $d_B=0.15d$). For $\alpha>0.1\%$, bubble-induced modifications of the flow patterns are evident, depending on the bubble location in the gap and their size. For the ventilated flow, submillimetric bubbles are localized in the outflow regions near the inner cylinder. For the cavitating flow, millimetric bubbles are localized both in the outflow regions near the inner cylinder and in one in two Taylor vortex cores. While injecting and decreasing the pressure, the flow is axially stratified, the wavelength being increased at the bottom of the gap and decreased at the top. When the pressure is stabilized, the flow reorganizes to have an homogeneous axial wavelength. For a preferential bubble arrangement in the outflow region near the inner cylinder, there is a stretching of the Taylor vortices. As a consequence of their drift velocity, bubbles localized in the outflow region are responsible for an increase of the wall shear stress at the inner cylinder. Stretching is thus due to bubble-induced wall shear stress. For a preferential arrangement of bubbles in the Taylor vortices obtained either at the top of the gap for stratified cavitating flow or in the entire gap for the homogeneous flow, there is a squeezing of the vortices that increases with the void fraction. Squeezing is due to an increase of vorticity of the liquid in order to capture the bubbles. In the case of stratified cavitating flow, a premature transition from quasi-periodic flow to weakly turbulent flow is observed. This is not attributed to advanced transition to turbulence but to interference in the outflow region between millimetric bubbles and the azimuthal wave, the length scale of which is of the same order.

As a conclusion, bubbles localized near a wall in a Couette Taylor flow, and in two-phase flows, in general, are expected to improve transfers, whereas bubbles captured by Taylor vortices, are expected to reduce transfers.

Acknowledgment

This project was subsidized by the French Navy. The authors would also like to thank the crew of the Mechanical Department workshop for their technical assistance.

References

[1] Shiomi, Y., Kutsuna, H., Akagawa, K., and Ozawa, M., 1993, "Two-Phase Flow in an Annulus With a Rotating Inner Cylinder: Flow Pattern in Bubbly Flow Region," Nucl. Eng. Des., **141**, pp. 27–34.
[2] Atkhen, K., Fontaine, J., and Wesfreid, J. E., 2000, "Highly Turbulent Couette-Taylor Bubbly Flow Patterns," J. Fluid Mech., **422**, pp. 55–68.
[3] Djeridi, H., Favé, J. F., Billard, J. Y., and Fruman, D. H., 1999, "Bubble Capture and Migration in Couette-Taylor Flow," Exp. Tech., **26**, pp. 233–239.
[4] Djeridi, H., Gabillet, C., and Billard, J. Y., 2004, "Two-Phase Couette Taylor Flow: Arrangement of the Dispersed Phase and Effects on the Flow Structures," Phys. Fluids, **16**(1), pp. 128–139.
[5] Cartelier, A., 1990, "Optical Probes for Local Void Fraction Measurements: Characterization of Performance," Rev. Sci. Instrum., **61**(2), pp. 874–886.
[6] Gabillet, C., Colin, C., and Fabre, J., 2002, "Experimental Study of Bubble Injection in a Turbulent Boundary Layer," Int. J. Multiphase Flow, **28**, pp. 553–578.
[7] Clark, N. N., and Turton, R., 1988, "Chord Length Distributions Related to Bubble Size Distributions in Multiphase Flows," Int. J. Multiphase Flow, **14**(4), pp. 413–424.
[8] Cognet, G., 1984, "Les Étapes vers la Turbulence dans l'Écoulement de Taylor Couette Entre Cylindres Coaxiaux," J. Mec. Theor. Appl., Special issue, pp. 7–44.
[9] Lance, M., and Bataille, J., 1991, "Turbulence in the Liquid Phase of a Uniform Bubbly Air-Water Flow," J. Fluid Mech., **222**, pp. 95–118.
[10] Tam, W. Y., and Swinney, H. L., 1987, "Mass Transport in Turbulent Couette-Taylor Flow," Phys. Rev. A, **36**, pp. 1374–1381.
[11] Gopalan, S., and Katz, J., 1999, "Effect of Entrained Bubbles on the Structure of Vortex Rings," J. Fluid Mech., **397**, pp. 171–202.
[12] Wereley, S. T., and Lueptow, R. M., 1994, "Azimuthal Velocity in Supercritical Circular Couette Flow," Exp. Fluids, **18**, pp. 1–9.

Miguel A. Reyes-Gutiérrez
Departamento de Termodinámica,
Universidad Simón Bolívar,
Valle de Sartenejas, Baruta,
Caracas, Mirands 1080, Venezuela

Luis R. Rojas-Solórzano
Departamento de Conversión de Energía,
Universidad Simón Bolívar,
Valle de Sartenejas, Baruta,
Caracas, Mirands 1080, Venezuela

Juan C. Marín-Moreno
CEMFA,
Universidad Simón Bolívar,
Valle de Sartenejas, Baruta,
Caracas, Mirands 1080, Venezuela

Antonio J. Meléndez-Ramírez
Departamento de Termodinámica,
Universidad Simón Bolívar,
Lab. de Mecanica de los Fluidos,
Edif Fluidos y Operaciones Unitarias Of. FOP-103,
Valle de Sartenejas, Baruta,
Caracas, Mirands 1080, Venezuela
e-mail: 01-81496@usb.ve

José Colmenares
Gerencia de Exploración y Producción,
PDVSA-INTEVEP

Eulerian-Eulerian Modeling of Disperse Two-Phase Flow in a Gas-Liquid Cylindrical Cyclone

This work presents a three-dimensional computational fluid dynamics (CFD) study of a two-phase flow field in a gas-liquid cylindrical cyclone (GLCC) using CFX4.3™, a commercial code based on the finite volume method. The numerical analysis was made for air-water mixtures at near atmospheric conditions, while both liquid and gas flow rates were changed. The two-phase flow behavior is modeled using an Eulerian-Eulerian approach, considering both phases as an interpenetrating continuum. This method computed the inter-phase phenomena by including a source term in the momentum equation to consider the drag between the liquid and gas phases. The gas phase is modeled as a bimodal bubble size distribution to allow for the presence of free- and entrapment gas, simultaneously. The results (free surface shape and liquid angular velocity) show a reasonable match with experimental data. The CFD technique here proposed demonstrates to satisfactorily reproduce angular velocities of the phases and their spatial distribution inside the GLCC. Computed results also proved to be useful in forecasting bubble and droplet trajectories, from which gas carry under (GCU) and liquid carry over might be estimated. Nevertheless, moderate differences found between the computed GCU and experimental measurements suggest that new adjustments may be done to the numerical model to improve its accuracy. [DOI: 10.1115/1.2201623]

Introduction

During the last two decades, large efforts have been dedicated to research aiming to the development of multiphase flow compact separators. Today, compact separators are widely used in the industry and particularly in the oil production process, where expensive, heavy and bulky static separators have been traditionally used. The gas-liquid cylindrical cyclone (GLCC), patented by the University of Tulsa in 1994, is one of these compact devices, developed to separate gas-liquid streams. The GLCC consists on a tangential pipeline connected to the vertical cylindrical body. The incoming multiphase stream runs into the cylindrical body through the tangential pipeline, which is also inclined 30 deg downward. The gas-liquid mixture enters the separator and a first separation stage occurs. If the incoming flow velocity is too low, the gravity dominates the inertia and the mixture falls down promoting the stratification or static-like separation of phases. If the flow enters the GLCC body with a mid-high velocity, then a swirling motion begins promoting an inertia-dominated separation process. The centripetal/centrifugal and buoyancy forces drive the gas toward the body centerline and upward to the top, while impelling the liquid toward the wall and bottom of the cylindrical body (see Fig. 1). The swirling motion of the mixture at the entrance is enhanced by a nozzle. However, the excessive inflow velocity may decrease the separator performance since it also promotes the turbulent mixing of the phases.

The GLCC efficiency is determined by the quality of the outlet streams, i.e., if only gas flows through the top exit and only liquid flows through the bottom exit, then the separator efficiency is 100%. The gas carry under (GCU) and liquid carry over are also practical indexes to compute the GLCC efficiency of separation for each exit stream.

During regular operation, inside the GLCC a bubble, slug, churn or annular flow pattern is established above the injection section, while a vortex sets in underneath. The gas phase accommodates in the vortex core, whereas the liquid phase occupies its periphery [1]. At the present time, it is estimated that there are around 600 GLCC units installed worldwide. Nevertheless, it is still not widely used because of the lack of models that accurately predict its performance. Current models are hardly close yet in predicting the complex transport phenomena occurring inside the separator.

Recent research aiming to predict the GLCC performance has been based on computationae fluid dynamics (CFDE) modeling, since this approach allows a deeper understanding of the detailed hydrodynamics inside the separator. Numerical results have led to the development of mechanistic models. The accurate prediction of the vortex inside the separator, which affects the GCU, is the main focus of most of the precedent research. In 1997, Erdal et al. [2] performed CFD simulations, using CFX™, to reproduce the tangential velocity measured in a reduced-scale GLCC by Farchi [3].

In their work, Erdal et al. [2], performed single- and two-phase flow simulations using the k-ε turbulence model. Single-phase simulations were carried out to compare the flow fields computed from the almost inexpensive axis-symmetrical simulation and the memory/time consuming three-dimensional (3D) simulation. From these simulations, they found insignificant differences and

Contributed by the Fluids Engineering Division of ASME for publication in the JOURNAL OF FLUIDS ENGINEERING. Manuscript received August 12, 2004; final manuscript received November 9, 2005. Assoc. Editor: Malcolm J. Andrews.

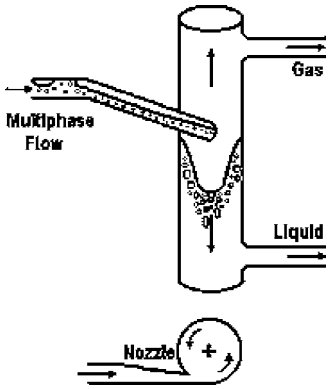

Fig. 1 Gas-liquid cylindrical cyclone

therefore performed the two-phase simulations using an axis-symmetrical geometry. However, when comparing to experiments, Erdal et al. [2] found similar tendencies, but over-prediction of the decay of the swirling strength. More recently, Motta et al. [4] compared the prediction capabilities of two CFD codes: CFX™ and TU-CFD™. Both codes are based on the finite volume method, but CFX™ uses the semi-implicit method for pressure linked equation corrected (SIMPLEC), while TU-CFD uses SIMPLER, as their pressure-computation algorithm. Furthermore, CFX™ results were obtained using the standard k-ε and the multi-fluid models, while TU-CFD computations employed the zero equation/mixing length and drift-flux models, for turbulence and inter-phase interaction, respectively. For the comparison, Motta et al. [4] used an axis-symmetric model to reproduce experimental data from Farchi [3]. Both numerical codes performed quite similarly, but CFX™ results were closer to experimental data. Erdal et al. [5] compared multiphase models available in CFX™ (homogeneous and multi-fluid) using an axis-symmetrical model of a laboratory-scale GLCC. The k-ε model was employed in this study. Numerical results were compared with visualization experiments. The authors concluded that both models might predict the free surface shape with accuracy, noticing, in general, a good agreement between experimental and numerical results.

Erdal et al. [6] studied the trajectories of small bubbles underneath the GLCC injection section and the influence of them on GCU. Single-phase, two-phase and bubble trajectory simulations were carried out by them using an axis-symmetrical computational model of a laboratory-scale GLCC. In their work, the numerical results were validated with visualization experiments. Results showed that the bubble trajectories and GCU are significantly affected by turbulence dispersion.

Finally, Erdal and Shirazi [7] carried out local velocity measurements in a laboratory model of the GLCC using laser Doppler velocimetry. The tests were conducted with single-phase liquid flow only. Experimental data were compared with flow fields obtained from three-dimensional simulations. Additionally, the performance of two turbulence models was studied. Numerical results qualitatively agreed with experimental data, but failed to accurately predict the vortex wavelength and velocities profile.

As it is shown, most of the previous numerical works on the GLCC have been limited to simplified models to tackle the high computational cost of a full (3D) simulation. Nevertheless, the complexity of the transport phenomena inside the GLCC limits the obtained results from properly predicting the efficiency of this device. The main objective of the present study is to further the CFD analyses of the GLCC by performing a more accurate multiphase and three-dimensional simulation of the flow field using the finite volume method including the multi-fluid model and the Eulerian-Eulerian approach for continuous-disperse two-phase flow. Two-phase experiments on a laboratory-scale GLCC are also performed and the data are compared with computational results.

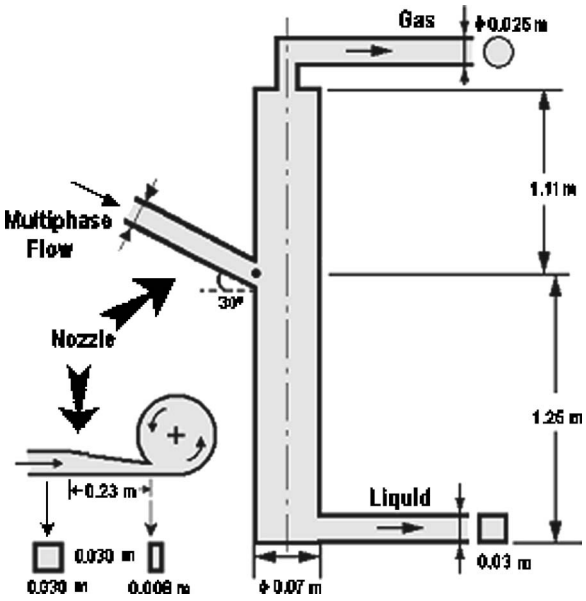

Fig. 2 Dimensions of the GLCC model

FLow Field Simulation

Single-Phase Flow Simulation. The flow field simulations were performed using CFX4.3™. This code is based on the finite volume method and uses SIMPLEC as pressure-coupling algorithm. The k-ε model has been used to compute the turbulent transport. Figure 2 depicts the main dimensions of the separator under study.

The mesh refinement analysis was performed by comparison of the angular velocity along a vertical line located at 3/8D from the central axis. Meshes of 37,000, 63,000 and 122,000 elements were compared. A mean difference of 1.2% and a maximum difference of 1.9% was encountered between the 63,000 and 122,000 element mesh results, normalized by the inlet angular velocity. According to those results, the intermediate mesh with 63,000 elements was adopted for the rest of the study. Details of the selected mesh are displayed in Fig. 3. After the mesh sensitibity analysis was carried out, the computed results, in terms of angular velocities, were compared with experimental data.

Simulations were performed with turbulence k-ε and low Reynolds k-ε models. No significant differences in the angular velocities were found between results from both models. Higher order upwind differencing scheme was used for the convective term in

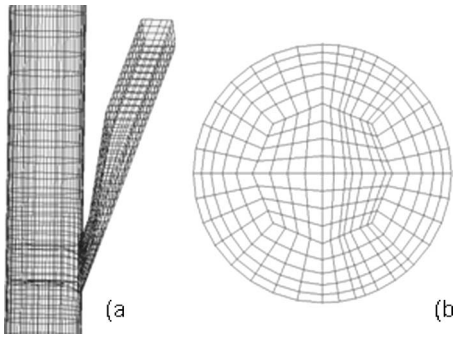

Fig. 3 (*a*) Surface mesh at separator midsection highlighting element agglomeration around the injection point; (*b*) typical transversal section of the volumetric mesh in the separator body

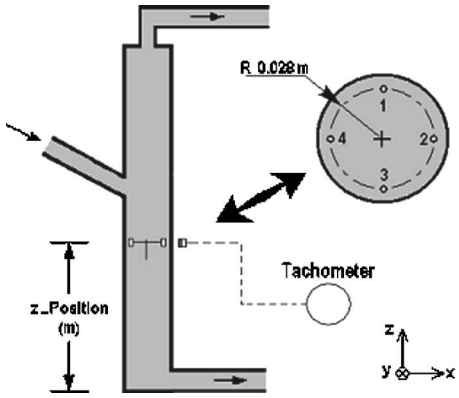

Fig. 4 Coplanar sampling points for determining the computational mean angular velocity

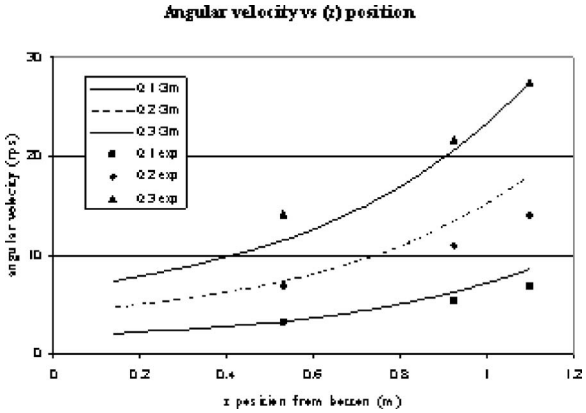

Fig. 5 Comparison of computational and experimental mean angular velocity for single-phase flow. $Q_1=7.8\times10^{-4}$ m^3/s, $Q_2=15.7\times10^{-4}$ m^3/s and $Q_3=23.0\times10^{-4}$ m^3/s.

the momentum equation. Details about this scheme can be found in Ref. [8,9]. Lower order difference schemes, such as upwind and hybrid, over-predicted the vortex dissipation along the separator body.

The experimental angular velocity of the gas-liquid mixture was measured by means of a paddlewheel meter at several locations below the nozzle section. The values reported correspond to the temporal average over a long enough interval. The computed numerical angular velocity was determined by averaging the local angular velocities at the four coplanar points shown in Fig. 4, with respect to the separator axis. Because the paddlewheel axis coincides with separator one, the proposed calculation of the angular velocity is a reasonable approximation, even though the vortex core does not coincide with the separator axis. The comparison between computational and experimental mean angular velocities is shown in Fig. 5, demonstrating a reasonable agreement. However, the computed swirling decay appears slightly deeper than in the experiments. Indeed, the average relative error in Fig. 5 is 13%, while the maximum relative error is 27%.

Figure 6 shows a three-dimensional view of the computed zero axial-velocity surface, also named the capturing surface, for the liquid single-phase simulation. Inside the volume bounded by this surface, the axial velocity is upward, while outside, it is downward. Mechanistic models assume that any bubble capable of reaching this zone can be separated. This result suggests that the flow inside of separator is three dimensional instead of axial symmetric.

Two-Phase Flow Model. Two-phase flow simulations were carried out using the CFX4.3™ multi-fluid model. This model considers each phase as an interpenetrating continuum. This means that, each phase is present in each control volume. The volume fraction of a phase represents the fraction of the control volume that is occupied by this phase. Two types of phase may be defined: continuous and disperse phase. There is one solution field for each phase separately. Transported quantities interact by means of inter-phase transfer terms. The multi-fluid model is implemented using the inter-phase slip algorithm of Spalding. For each phase the continuity (1), momentum (2), k (3) and ε (4) transport equations are solved [8]

$$\nabla \cdot (r_\alpha \rho_\alpha U_\alpha) = 0 \tag{1}$$

$$\frac{\partial \rho U_\alpha}{\partial t} + \nabla \cdot (r_\alpha(\rho_\alpha U_\alpha \otimes U_\alpha - \mu_\alpha(\nabla U_\alpha + (\nabla U_\alpha)^T) = r_\alpha(B - \nabla p_\alpha) + \sum_{\beta=1}^{N_P} c_{\alpha\beta}^{(d)}(U_\beta - U_\alpha) \tag{2}$$

$$\nabla \cdot \left(r_\alpha \left(\rho_\alpha U_\alpha k_\alpha - \left(\mu + \frac{\mu_{T\alpha}}{\sigma_k} \right) \nabla k_\alpha \right) \right) + \frac{\partial}{\partial t}(r_\alpha \rho_\alpha k_\alpha) = r_\alpha S_{k\alpha} \tag{3}$$

$$\nabla \cdot \left(r_\alpha \left(\rho_\alpha U_\alpha \varepsilon_\alpha - \left(\mu + \frac{\mu_{T\alpha}}{\sigma_\varepsilon} \right) \nabla \varepsilon_\alpha \right) \right) + \frac{\partial}{\partial t}(r_\alpha \rho_\alpha \varepsilon_\alpha) = r_\alpha S_{\varepsilon\alpha} \tag{4}$$

The subindexes α and β denote the different phases present in the domain. The inter-phase momentum transfer is only possible between the disperse phases and the continuous phase; only one continuous phase may be defined. The disperse phases might be present in the form of bubbles, drops or spherical solids. In general, the coefficient of inter-phase momentum transport is defined as follows [8]

$$c_{\alpha\beta}^{(d)} = \frac{3}{4}\frac{C_D}{d} r_\beta \rho_\alpha |U_\beta - U_\alpha| \tag{5}$$

Ihme correlation is used for the calculation of the bubble drag coefficient (Eq. (6)) along with Gidaspow volume fraction correction (power coefficient of 1.6). This correction prevents viscous drag misestimating at control volumes where disperse fraction is closer to 1 [8].

$$C_D = \frac{24}{\mathrm{Re}} + 5.48\,\mathrm{Re}^{-0.573} + 0.36 \tag{6}$$

Fig. 6 Computed capturing surface for single phase flow. $Q_3=7.8\times10^{-3}$ m^3/s.

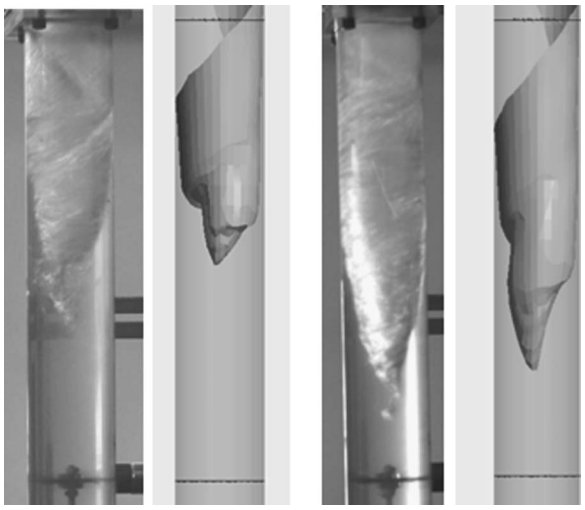

Fig. 7 Comparison of simulated and experimental free surface for q_g=0.047 sm^3/s. Left: q_l=0.0073 m^3/s; right: q_l =0.011 m^3/s.

To calculate the turbulent viscosity and the source terms of the turbulence parameters equations, the following customary expressions are used [8]

$$\mu_T = C_\mu \rho \frac{k^2}{\varepsilon} \tag{7}$$

$$S_{k\alpha} = P_\alpha + G_\alpha - \rho_\alpha \varepsilon_\alpha \tag{8}$$

$$S_{\varepsilon\alpha} = \frac{\varepsilon_\alpha}{k_\alpha}\{C_{1\varepsilon}[P_\alpha + C_{3\varepsilon} \max(G_\alpha, 0)] - C_{2\varepsilon}\rho_\alpha \varepsilon_\alpha\} \tag{9}$$

The equations of continuity, momentum and turbulent properties are solved in iterative way through the semi-implicit method for pressure linked equation corrected (SIMPLEC) of Patankar and Spalding [8].

Two-Phase Flow Simulation. The experiments were carried out with air-water mixtures. The mean pressure inside the separator was held at 17.7 psia during the tests. Water was assumed to be the continuum phase and two bubble diameters were considered for air, as the disperse phase. The bubble diameter of the disperse phase corresponding to free air was 500 μm, while the bubble diameter of the disperse phase corresponding to entrapment air was 150 μm. The bubble diameter chosen for free gas ensures that there is no free gas drag on the separator bottom for any of the operation condition studied. The selection of the bubble diameter for entrapment air was based on forces balance. In fact, this is smallest value possible which ensures equilibrium between drag and buoyancy forces for the minimum flow rate studied.

Boundary Conditions. A homogeneous gas-liquid mixture inflow was considered with the specific volume fraction for liquid (r_l) and gas (r_g) in the stream. The entrapment gas volume fraction (r_{eg}) was taken equal to the liquid volume fraction (r_l), under the assumption that it might be approximated as the highest GCU volume fraction. The free-gas volume fraction "r_{fg}" was obtained as "r_g-r_{eg}." The free-gas bubble diameter was chosen relatively larger than the entrapment gas bubble diameter in order to facilitate its buoyant release from the liquid continuous phase. In fact, free-gas migration starts occurring even along the inlet pipe, causing the stratification between free-gas and the mixture of liquid and entrapment gas approaching the nozzle.

During the experiments the liquid level inside separator was maintained at 1.15 m above the separator bottom (0.1 m under the nozzle) regulating control valves. An equivalent pressure difference between gas and liquid exits was set in the simulations. These pressure boundary conditions ensure the proper location of the vortex free surface avoiding the necessity to fix flow rate and phase volume fractions at these outlets.

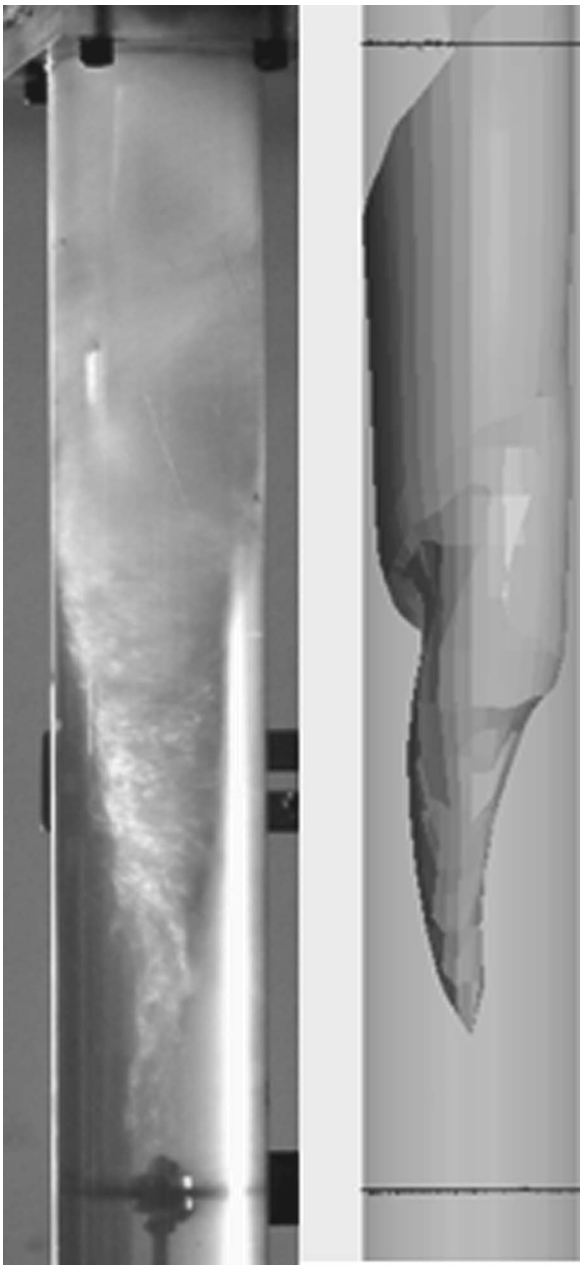

Fig. 8 Comparison of simulated and experimental free surface for q_g=0.047 sm^3/s and q_l=0.0143 m^3/s

Liquid flow rates (q_l) of: 0.0073, 0.011 *y* 0.0147 m^3/s; and gas flow rates (q_g) of: 0.023, 0.047 *y* 0.07 sm^3/s were prescribed in the simulations. Figures 7 and 8 illustrate the vortex free surface for several liquid flow rates. The lengths of the shown vortices correspond to the average of the maximum and minimum values registered in movies. The recording time of theses movies was 15 s. During this period of time between 15 and 35 fluctuations in the vortex length typically were observed. The magnitude of the fluctuations in the vortex length was 1.5 separator diameters (0.105 m).

Tables 1 and 2 show the results obtained for the flow angular velocity at 0.35 m above the injection point at different gas and

Table 1 Mean angular velocity for different gas flow rates and q_l=0.011 m^3/s

q_g (sm^3/s)	Angular velocity (rps) Exp	Sim	Error (%)
0.0024	9.64	9.76	1.2
0.0047	10.87	12.46	14.6
0.0071	11.63	13.68	17.6

Table 2 Mean angular velocity for different liquid flow rates and q_g=0.047 sm^3/s

q_l (sm^3/s)	Angular velocity (rps) Exp	Sim	Error (%)
0.00074	8.15	9.48	16.3
0.00110	10.87	12.46	14.6
0.00147	14.24	14.86	4.3

liquid flow rates.

The results show a maximum deviation around 17.6% between simulations and experiments with an average of 11% over the total sample.

The simulated free surface, presented in Figs. 7 and 8, is obtained by choosing the surface at which volume fraction $r_g=r_l=0.5$. A satisfactory match between experimental and numerical results is shown; in fact, vortex shape and length are quite similar.

Figure 9 shows the capturing surface for q_g=0.047 sm^3/s and q_l=0.011 m^3/s. This image scale was reduced 50% vertically for visual proposes. Such as in the single-phase flow, this surface presents a notorious 3D shape. It disagrees with the axis-symmetric and mechanistic models assumption as was previously mentioned.

Figure 10 depicts the volume fraction plot at the mid-longitudinal plane of the separator. This result coincides with the visualization done during the corresponding experiment and indicates that the proposed numerical model reproduces the performance of the experimental model appreciably well. It may be also

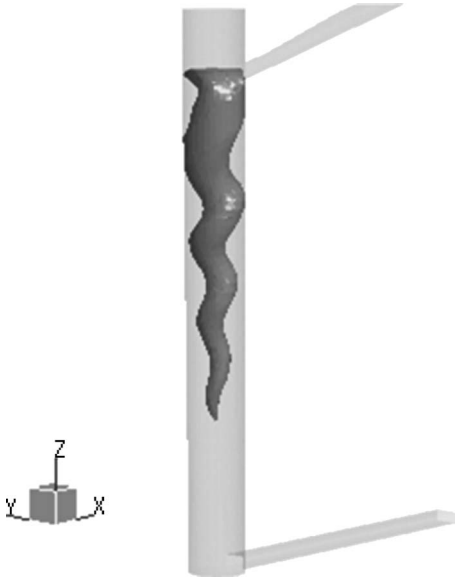

Fig. 9 Three-dimensional view of the capturing surface for q_g=0.047 sm^3/s, q_l=0.011 m^3/s

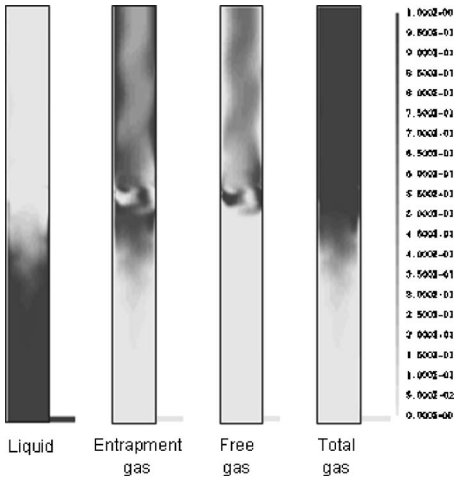

Fig. 10 Volume fractions at mid-longitudinal plane of GLCC for q_g=0.047 sm^3/s and q_l=0.011 m^3/s

observed that the entrapment gas is removed from the liquid within the vortex, while free gas, originally separated from the stream right before the entrance as mentioned, remains out of the liquid within the separator body.

Table 3 presents simulation and experimental results for different phase volume fractions at separator outlets for liquid and gas flow rates of q_l=0.011 m^3/s and q_g=0.047 sm^3/s, respectively.

As can be noticed in Table 3, the magnitude of measurements of the gas void fraction at the bottom stream (GCU) are comparable to the error associated with entire modeling process, which considers the contribution of all possible error sources. The differences between the computational and the experimental results might be considered within uncertainties.

Concluding Remarks

Three-dimensional simulations of the flow field inside a gas-liquid cylindrical cyclone GLCC separator have been carried out. Both single-phase (water) and two-phase (air-water) flows have been simulated using the finite volume method.

The obtained numerical results, in terms of vortex free surface, agree satisfactorily with images of validation experiments. Also, the mean angular velocities calculated from simulations show a reasonable match with experimental data.

The simulations showed a helical cone as a capturing surface instead of an axial symmetric paraboloid. This kind of symmetry, which is commonly assumed, might lead to important modeling errors. Hence almost any existing model is based on the capturing surface shape; the results show the necessity of further studies in order to establish the influence of the flow symmetry over the separation capability.

Because the experiments were carried out with air and water, the gas void fraction at liquid exit measured experimentally is smaller than the simulation results. The differences in these results are within the numerical and experimental uncertainties.

Table 3 Liquid and gas volume fraction for two-phase flow with q_l=0.011 m^3/s and q_g=0.047 sm^3/s

Leg	Volume fraction	Exp	Sim
Liquid	r_g	0.00005	0.007
	r_l	0.9995	0.993
Gas	r_g	1	0.9923
	r_l	0	0.0077

Acknowledgment

The authors would like to thank FONACIT-Venezuela for the financial support to this project. Antonio Melendez-Ramirez wishes to thank "Decanato de Investigación y Desarrollo" (DID) at the Universidad Simón Bolívar for supporting his M. Sc. Studies.

Nomenclature

GLCC = gas liquid cylindrical cyclonic
ε = dissipation of turbulent kinetic energy
k = turbulent kinetic energy
U = velocity vector
S_k = term of generation of turbulent kinetic energy
r = volume fraction
G = Production of turbulent kinetic energy due to the external forces
N_P = number phases
q = volumetric flow rate, m^3/s
ρ = fluid density, kg/m^3
μ = fluid viscosity, Pa s
C = constant empiric
t = time, s
m^3/s = cubic meters per second
sm^3/s = cubic meters per second at standard conditions
Scm/s = cubic meters per second at standard conditions.
rps = revolutions per second

Subscripts

α,β = phases
p = phase
D = drag
1,2,3 = index to constant different
eg = entrapment gas
fg = free gas
g = gas
l = liquid

Superscripts

T = transpose tensor
d = Drag

References

[1] Shoham, O., and Kouba, G., 1998, "The State of the Art of Gas-Liquid Cylindrical Cyclone Separator," JPT, J. Pet. Technol., **50**(7), pp. 58–65.
[2] Erdal, F., Shirazi, S., Shoham, O., and Kouba, G., 1997, "CFD Simulation of Single-Phase and Two-Phase Flow in Gas-Liquid Cylindrical Cyclone Separators," No. SPE 36645, *SPE 71st Annual Meeting*, SPEJ, 2, December, pp. 436–446.
[3] Farchi, D., 1990, "A Study of Mixer and Separator for Two-Phase Flow in M. H. D. Energy Conversion Systems," M. S. thesis (in Hebrew), Ben-Gurion University, Israel.
[4] Motta, B., Erdal, F., Shirazi, S., Shoham, O., and Rhyne, L., 1997, "Simulation of Single-Phase and Two-Phase Flow in Gas-Liquid Cylindrical Cyclone Separators," No. FEDSM97-3554, *1997 ASME Fluid Engineering Division Summer Meeting*, June.
[5] Erdal, F., Mantilla, I., Shirazi, S., and Shoham, O., 1998, "Simulation of Free Interface Shape and Complex Two Phase Flow Behavior in a Gas-Liquid Cylindrical Cyclone Separator," No. FEDSM98-5206, *1998 ASME Fluid Engineering Division Summer Meeting*, June.
[6] Erdal, F., Shirazi, S., Mantilla, I., and Shoham, O., 1998, "CFD Study of Bubble Carry-Under in Gas-Liquid Cylindrical Cyclone Separators" No. SPE 49309, *1998 SPE Annual Technical Conference and Exhibition*, September.
[7] Erdal, F., and Shirazi, S., 2001, "Local Velocities Measurement and Computational Fluid Dynamics (CFD) Simulations of Swirling Flow in a Cylindrical Cyclone Separator," No. ETCE 2001-17101, *Engineering Technology Conference on Energy*, February.
[8] AEA Technology, 1997, *CFX 4.3 Solver Manual*.
[9] Thompson, C., and Wilkes, N., 1982, "Experiments With Higher-Order Finite Difference Formulae," No. AERE-R 10493.

Natural and Forced Conjugate Heat Transfer in Complex Geometries on Cartesian Adapted Grids

Gianluca Iaccarino
Center for Turbulence Research,
Stanford University,
CA 94305-3030

Stéphane Moreau
Valeo Motors and Actuators,
1, rue Tiron,
Paris, 75004, France
e-mail: 101615.1771@compuserve.com

The Cartesian incompressible RANS solver with immersed boundaries, IBRANS, recently developed at Stanford, has been extended to include conjugate heat transfer modeling and used for the simulation of the electrical motor of an automotive engine cooling fan system. Such applications are particularly challenging, as they involve very complex geometries with tight tolerances and rotating parts. The new conjugate heat transfer capability of IBRANS has been verified on natural and forced convection flows. The former involves flows in enclosures around a sphere and electronic chips. The latter focuses on heated cylinders for Reynolds numbers covering flow regimes ranging for a steady laminar flow to unsteady turbulent flows. Excellent agreement is achieved with similar simulations with a conventional body-fitted solver (FLUENT 6.1) using equivalent turbulent models. First three-dimensional simulations of the flow and heat transfer within the complete electrical motor are presented. The numerical predictions of the pressure drop through the motor as a function of flow rate agree very well with the measured data over the complete operating range. [DOI: 10.1115/1.2201625]

1 Introduction

In the design process of new automotive engine cooling fan systems, one increasingly important problem is the interaction of the fan system with a tighter and hotter underhood environment. This creates aerodynamic and acoustic constraints on the fan system but also large thermal loads on the electrical motor driving the fan system. The aerothermal management within the fan system requires detailed conjugate heat transfer (CHT) analysis within the electrical motor.

The conventional computational fluid dynamic (CFD) approach based on body-fitted grids provides such capabilities but several outstanding issues emerge. First, the computer aided design (CAD) to CFD transfer of such large geometrical models requires user intervention even when direct interfaces between the CAD and the grid generation software are available. Surfaces representation has very different meanings in CAD and CFD environments. In the former, they are the end product and they serve as basis for manufacturing. The surfaces are typically converted to a set of points to drive a Computer Aided Manufacturing (CAM) machine or to a set of triangles for rapid-prototyping manufacturing. The distribution of the output points (or the size of the triangles) is typically based on surface curvature and it is directly controlled by the user in the CAD system. In a CFD environment, the surface representation is only a starting point and it is used as a support for the surface mesh generation procedure. Once this surface mesh is obtained, the volume mesh is built to allow for a CFD solution. There are several constraints on the surface mesh that make the direct use of CAD surfaces nearly impossible; the most important is the quality of the mesh elements. Usually, the CAD model is broken into several smaller components and surface meshes are generated in patches enforcing quality constaints. The volume meshes are also typically built in subdomains. Therefore, the grid generation for a complex geometry, such as an electric motor, is extremely time consuming and requires very skilled users. As quoted by Péniguel in [1]: "This step is representing sometimes more than 80% of the time devoted to a study." Moreover, in a typical design cycle several parametric studies must be carried out to evaluate the effect of various design solutions. This can hardly be done within typical time constraints due to the grid reconstruction step required for each new simulation. Current industrial practice is to use simplified model problems and to extrapolate the results to build several initial prototypes that are consequently tested. However, such procedures can hardly yield an optimized system and can be still very costly.

In the present study, an innovative approach based on the immersed boundary technique is proposed to overcome most of the above simulation obstacles. The method is based on the use of Cartesian grids nonconforming with the physical boundaries. Body forces are then added at the interface to enforce the boundary constraints. This recently developed approach will be described after stating the present industrial context and simulation background in the next section. Particular emphasis will be put on the grid generation and the extension of the flow solver to conjugate heat transfer problems. Verification examples focused on natural and forced convection at various flow regimes are then shown. The extension to the complete electrical motor is then tackled and the first milestone results are shown.

2 Design Background

The increasing need of flat fan systems in automotive engine cooling modules often leads to the use of compact electric engine cooling (EEC) motors as shown in Fig. 1. These compact motors should have the same efficiency as earlier designs with reduced volume and then increased heat dissipation density. Using high magnetic characteristic materials and high thermal insulation class materials would achieve this goal. Unfortunately, EEC motors are very cost sensitive products, and compromise need to be found between cost and performance. Improving heat transfer inside an EEC motor is an important way to meet these challenges, which should lead to reduced temperatures of critical parts of the motor. Reliability is then increased and high power density in the electrical motor is no longer compromised by motor life consideration. In [2], Hong et al. focused on the interaction between motor

Contributed by the Fluids Engineering Division of ASME for publication in the JOURNAL OF FLUIDS ENGINEERING. Manuscript received August 31, 2004; final manuscript received December 6, 2005. Assoc. Editor: Subrata Roy.

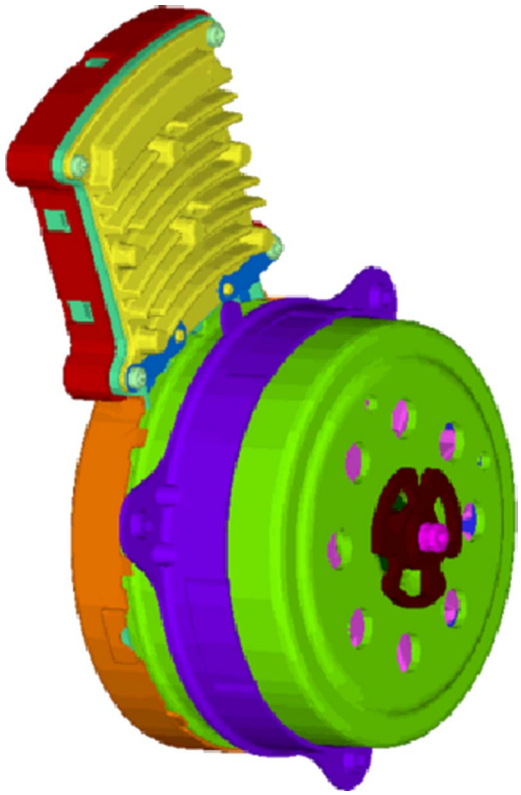

Fig. 1 Automotive engine cooling electrical motor

temperature and airflow inside the EEC motor. Theoretically, the thermal analysis of these electric motors includes:

- heat source analysis
- airflow and conjugate heat transfer (CHT) analysis

Both numerical analysis and experimental validation were carried out in [2] to establish a robust and practical methodology for thermal analysis of EEC motors. The turnaround of the three-dimensional simulations involved in the second step (the CHT analysis) limited the possibility of varying the geometrical parameters of these EEC motors and did not allow mapping its complete flow performances quickly. To achieve such simulations several hurdles had to be overcome. First, to simulate the inside of an electrical motor, one has to deal with an extreme geometrical complexity similar to the underhood environment of a vehicle. An electrical motor consists of about a hundred parts with thirty moving components and a wide range of clearances between these parts. The generation of the grid (Fig. 6 in Ref. [2]) required further simplification of the original CAD models. For instance, the crimping teeth, the screws and nuts were removed. In addition, the conjugate heat transfer analysis requires the meshing of both the fluid and solid regions. Overall, the complete CAD preparation and mesh generation required several months. The resulting numerical model had several millions nodes, which required several CPU days on a SGI Octane workstation. This makes a quick design or a quick adaptation to a particular thermal issue currently impossible.

3 Immersed Boundary Method

The present computational approach, namely IBRANS, is based on a simple, widely available description for geometrical components, the stereo-lithography (STL) format. In this context any three-dimensional surface is represented by a collection of triangles. These models are the same as those used for rapid prototyping and no constraints are imposed on the surface triangulation (other than being a sufficiently accurate representation of the geometry). In particular, highly irregular and skewed triangles can be successfully handled. The relation between the underlying Cartesian grid and the STL surface is constructed using a ray-tracing algorithm; this allows to tag the computational cells that are *cut* by the immersed surface *interface* and identify the *fluid* and *solid* cells as volumes that are completely outside and inside the STL surface, respectively. Our immersed boundary (IB) method uses interpolants to *reconstruct* the behavior of the solution in the neighborhood of the embedded surfaces so that the boundary conditions are enforced at the physical location, as opposed to the closest Cartesian location as in the stairstep approach used, for instance, in the commercial Cartesian RANS solver UH3D [3,4]. Note that the current approach is also different from some of the earlier versions of the IB methods where the governing equations are modified by adding forcing terms designed to enforce the boundary conditions. A detailed discussion of the differences between various IB approaches can be found in Refs. [5–7]; here we only describe the most important aspects focusing on the application of the technique for heat transfer calculation (see next section).

The approach is based on the solution of the RANS equations for an incompressible fluid using a SIMPLE approach [8,9]. The fluid cells are treated without any modifications while in the solid and the interface cells a special treatment is introduced. In the solid cells the velocity is set to zero, whereas in the interface cells a reconstruction is used to bridge the solution in the fluid cells and the desired no-slip boundary condition on the STL surface. The interpolant used is in the form

$$\phi = a_1 n^2 + a_2 n + a_3 t_1 + a_4 n t_1 + a_5 n t_2 + a_6 t_1 + a_7 t_2 + a_8 \quad (1)$$

where ϕ represents any independent variable (i.e., the velocity components), n, t_1 and t_2 are the normal and tangential directions to the surface and the a_i are the unknown interpolation coefficients. These coefficients are determined by imposing the boundary condition and the values of ϕ in the fluid cells surrounding the interface. Equation (1) can be rewritten in a form that explicitly shows the fluid cells contributions

$$\phi_p = \sum_{nb} b_{nb}\phi_{nb} + b_{bc}\phi_{bc} \quad (2)$$

The reconstruction Eq. (2) allows for an implicit treatment of the interface value ϕ_p thus it does not introduce any stability constraint.

It is worth mentioning that Eq. (1) requires the determination of eight coefficients, therefore seven fluid values and one boundary condition. In general, only nearest neighbors of the interface cell—cells that share at least one node—are used. If the specific conformation of the STL surface does not allow the use of enough neighbors, the interpolant is simplified by eliminating the quadratic terms.

The current approach uses the Boussinesq approximation to *close* the RANS equations. The eddy viscosity is computed using simple one- or two-equation turbulence models; the models are described in detail in [10]. The one-equation model is the Spalart-Allmaras model [11], whereas the two-equation model is a transformation of the k-ω model developed by Wilcox [12]; in the present appraoch, the variable g defined as $g=1/\sqrt{\beta\omega}$ is used instead of ω. The complete set of model damping functions, closure coefficients and auxiliary relationships for both turbulence models can be found in Ref. [10]. Both models are characterized by simple homogeneous wall boundary conditions for all the turbulent scalars and therefore the same reconstruction operators used for the velocity components are used.

A note of caution is related to the treatment of the pressure. In the current approach, the pressure equation is solved everywhere in the domain, including inside solid regions. This is done to simplify the solution of the elliptic equations without requiring a reconstruction of the pressure field. The pressure field is clearly

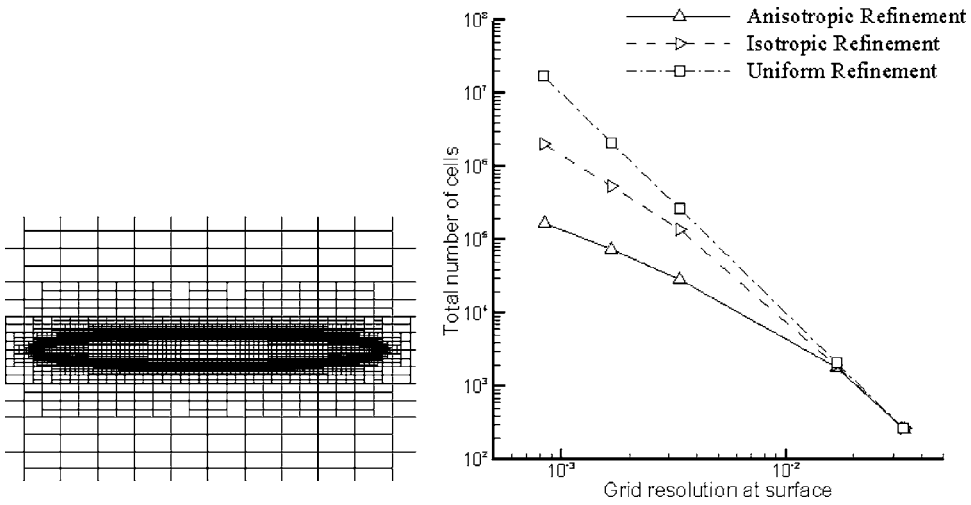

Fig. 2 Anisotropic grid refinement

used only in the fluid cells. Note that for no-slip boundary conditions this treatment is completely equivalent to imposing a Neumann condition on the pressure.

To increase the grid resolution and, therefore, the accuracy, the Cartesian cells are successively refined locally thus introducing hanging nodes. The procedure is anisotropic such that each cell can be subdivided in two, four or eight subcells; the grid refinement approach is described in detail in [13]. In summary, once the interface cells are identified, their size is compared to the desired normal and tangential resolution at the STL surface. If necessary, the cells are split in one or more directions and the tagging procedure applied again. An additional refinement procedure is applied to avoid jumps in cell size larger than one-to-eight; this smoothing also limits the number of neighbors for each cell at 24 (four per cell side). The advantages of the anisotropic grid refinements can be clearly seen in Fig. 2 where the necessary number of cells to achieve a given resolution around an elliptic profile is plotted. It is clear that the more alignment between the STL surfaces and the Cartesian direction, the more the anisotropic grid refinement is effective. The latter capability has first been validated on an actual turbine blade with its internal cooling passage [14]. The application of the present procedure to the complex geometry of an electric motor is presented in Fig. 3 with two cutting planes through the mesh. The left plot cuts through the motor stack at midspan of the motor case; the right plot goes through the motor front plate behind the drive plate.

4 Conjugate Heat Transfer

In a previous work [15], Iaccarino et al. showed that the heat transfer in heated ribbed passages is significantly modified when the heat conduction through the passage walls is accounted for. This motivates the need for solid/fluid CHT analysis.

As mentioned before, in the present IBRANS solver, a Cartesian grid nonconforming to the boundaries is used. The availability of a grid throughout the computational domain, including the inside of the solid embedded region, allows for a CHT calculation to be carried out naturally. The energy equation is solved in the entire domain consisting of the fluid plus the solid, in the form

$$\frac{\partial T}{\partial t} + u_i \frac{\partial T}{\partial x_i} = \frac{\partial}{\partial x_j}\left[(k + k_t) \frac{\partial T}{\partial x_j} \right] + S_T \tag{3}$$

where k is the thermal conductivity, k_t the turbulent diffusivity modeled here using a simple gradient diffusion hypothesis, k_t

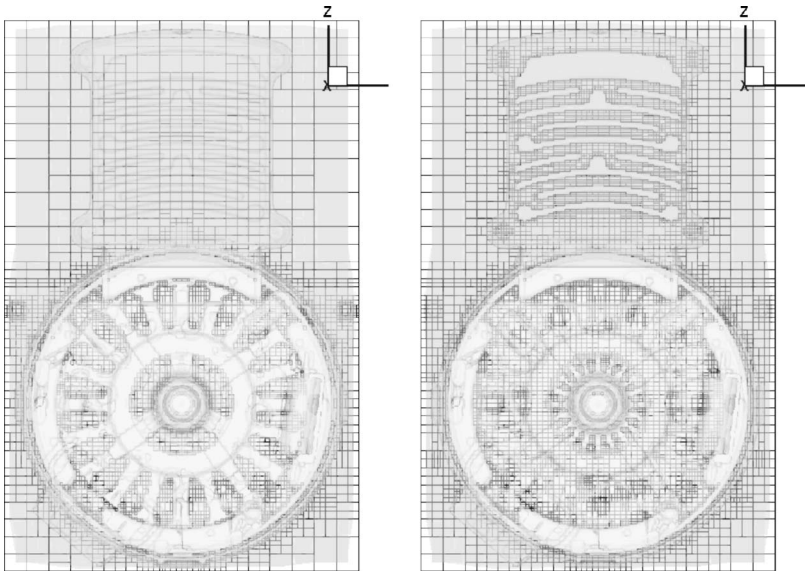

Fig. 3 Cartesian grid planes through the electrical motor

$= \nu_t Sc_t$, with the eddy viscosity based on either the one- or the two-equation model and Sc_t, the turbulent Prandtl number equal to 0.9. The source term S_T represents any user-specified volumetric source term present in the solid (representing heating due, for example, to electric currents). When natural convection is negligible with respect to forced convection, the energy Eq. (3) is *decoupled* from the momentum equation and can be solved separately. On the other hand, in buoyancy driven flows, the equations are linked and, in general, it is not possible to use the incompressible formulation due to the changes in density. In the present approach, the simple Boussinesq hypothesis is used to model the buoyancy force in the momentum equations. The additional source term in the momentum equation is in the form

$$S_{u_i} = \alpha(\rho - \rho_{\text{ref}})g_i \tag{4}$$

where g_i represents the gravity vector, ρ and ρ_{ref} the local density and a reference density, and, α is the expansion ratio of the fluid considered.

Appropriate material properties are considered for each solid and the fluid in the system, and (eventually) source terms are added locally in the solid regions. The energy equation is solved, similarly to the turbulence equations, segregated from the mean flow. The only other aspect to consider is the treatment of the interface cells, which correspond to the solid/fluid interfaces. From an IB point of view the reconstruction procedure (Eq. (1)) must be applied on both sides of the interfaces. In physical terms, the interface temperature is not known but the continuity of both temperature, T_w, and heat flux, Φ_w, must be enforced

$$\begin{cases} T_{w,s} = T_{w,f} \\ \Phi_{w,s} = \kappa_s \left(\dfrac{\partial T}{\partial n} \right)_{w,s} = \kappa_f \left(\dfrac{\partial T}{\partial n} \right)_{w,f} = \Phi_{w,f} \end{cases} \tag{5}$$

where the subscripts s and f refer to the solid and fluid side of the interface. In the present approach, a linear interpolation procedure is used on both sides of the interface; this together with the conditions (5) allows to obtain the temperature in the interface cells.

$$\begin{cases} T_f = a_1 n + a_2 t_1 + a_3 t_2 + a_4 \\ T_s = b_1 n + b_2 t_1 + b_3 t_2 + b_4 \\ \dfrac{\partial T}{\partial n_f} = a_1 \\ \dfrac{\partial T}{\partial n_s} = b_1 \end{cases} \tag{6}$$

The present reconstruction requires three cells on each side of the interface.

5 Verification of the IBRANS Solver

The RANS solver IBRANS has already been applied to several test cases to evaluate its accuracy. The flow in a wavy-wall channel at a Reynolds number $\text{Re}_H = 11{,}000$ was reported in [5], together with the challenging piston/cylinder assembly. The flow around road vehicles has then been recently tackled to study the unsteady dynamics of the wake and the modification induced by drag reduction devices [5,6]. The verification of the conjugate heat transfer capability in the immersed boundary code on adapted Cartesian grids is presently achieved by comparing with reference body-fitted simulations obtained with FLUENT 6.1 on several simple natural and forced convection problems described below.

5.1 Natural Convection Within Enclosures. The first verification of the natural convection conjugate heat transfer capability in IBRANS has been performed by studying the flow around a heated sphere in a simple cubic enclosure (Fig. 4). The cavity has a 2 m side and the sphere has a 1 m diameter and is centered within the cavity. No slip at a fixed temperature of 300 K is assumed on the cavity walls. No slip with coupled thermal conditions are imposed on the sphere with equal temperature and heat flux in the fluid and solid. The heat load is specified uniformly in the sphere to 100 W/m^3. The flow is assumed laminar and a steady state simulation is searched. Second order discretization is applied to both momentum and energy equations. The grid resolution is set to 0.05 m in the cavity and to 0.025 m on the sphere surface. Figure 5 compares the body-fitted unstructured grid with the corresponding Cartesian mesh in a plane cutting through the center of the sphere. The adapted Cartesian grid has about two times less cells. The convergence is also faster on this grid. The resulting temperature fields for both methods are compared in Fig. 6 in the same plane as the grid. Very similar diffusion of temperature to the top of the cavity is found with both codes.

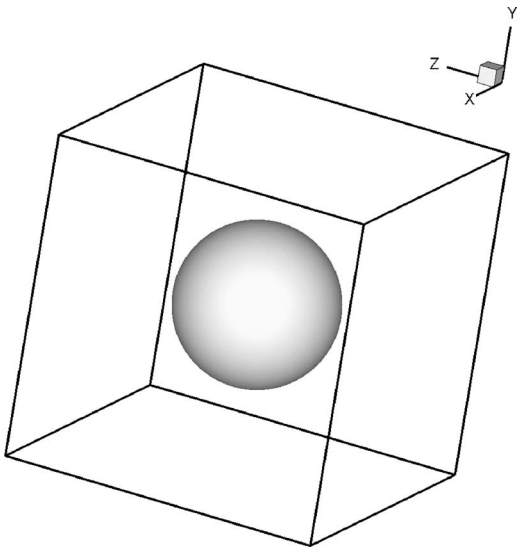

Fig. 4 Heated sphere in enclosure. Topology.

The second verification of the natural convection conjugate heat transfer capability in IBRANS is close to a typical electronic process. Two hot components within a mold are placed in an isothermal cavity. This last test case can also be seen as representative of the heat transfer within the sealed volume containing the power electronics of the electronized motor shown in Fig. 1. The resulting CHT analysis would then help properly designing its heat sink with fins. The cavity has a $0.25\ \text{m} \times 0.2\ \text{m} \times 0.25\ \text{m}$ dimension. The mold has a $0.1\ \text{m} \times 0.05\ \text{m} \times 0.025\ \text{m}$ dimension and is placed in the bottom corner of the cavity as shown in Fig. 7. The two hot spots have much smaller thicknesses. No slip at a fixed temperature of 300 K is assumed on the cavity walls. No slip with coupled thermal conditions are imposed on the mold with equal temperature and heat flux in the fluid and solid. The two components do not see any airflow and therefore only conduction and heat transfer are computed locally. The heat load is specified uniformly in the two hot spots: $6.81 \times 10^7\ \text{W/m}^3$ for the larger one

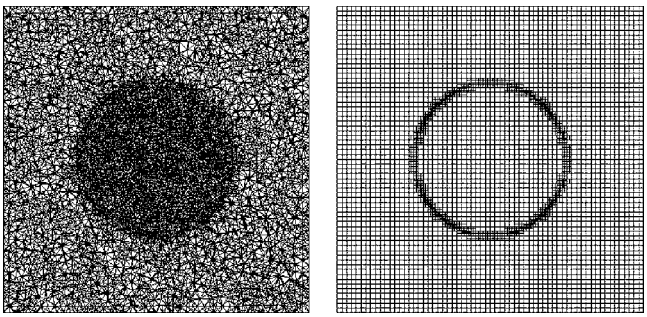

Fig. 5 Heated sphere in enclosure. Grid. Left: body fitted (FLUENT). Right: IB Cartesian with local grid refinement.

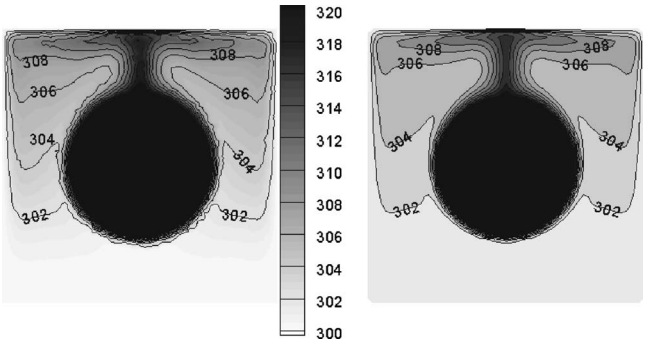

Fig. 6 Heated sphere in enclosure. Temperature contours. Left: body fitted (FLUENT). Right: IB Cartesian.

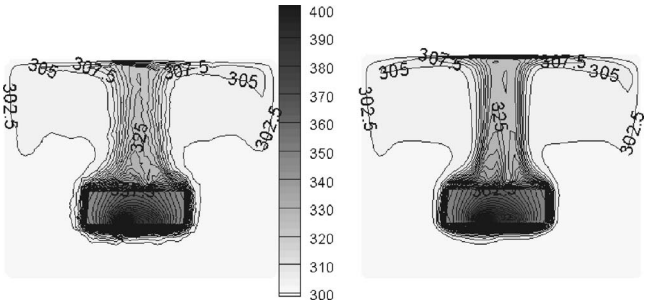

Fig. 9 Electronic mold in enclosure. Temperature contours in plane cutting through the cavity. Left: body fitted (FLUENT). Right: IB Cartesian.

and 5.12×10^7 W/m^3 for the smaller one. The flow is assumed laminar and a steady state simulation is searched. Second order discretization is applied to both momentum and energy equations. The grid resolution is set to 0.06 m in the cavity and to 10^{-4} m on the much smaller components. Figure 8 compares the body-fitted unstructured grid with the corresponding Cartesian mesh in a plane cutting through the center of the mold. The adapted Cartesian grid has about 20% less cells. The convergence is again faster on this grid. The resulting temperature fields for both methods are compared in Fig. 9 in the same plane as the grid. Figure 10 shows the temperature contours on the mold surface looking at the bottom of the mold where the hot chips are. In both cases, the IB temperature field matches the FLUENT one closely.

5.2 Heated Cylinders in Cross Flow. The verification of the forced convection conjugate heat transfer capability in IBRANS has been performed by studying the flow around a heated cylinder at various Reynolds numbers based on the cylinder diameter, Re_D. The cases selected correspond to three main flow regimes [16–18]: at $\mathrm{Re}_D=23$, the flow is two dimensional, laminar and steady; at $\mathrm{Re}_D=120$, the flow is two-dimensional, laminar and unsteady (counterrotating two-dimensional vortices are shed behind the cylinder); at $\mathrm{Re}_D=3900$, the flow is three dimensional, turbulent and unsteady.

Figures 11–14 present the results of the heated cylinder at $\mathrm{Re}_D=23$. Figure 11 compares the body-fitted unstructured grid with the corresponding Cartesian mesh. Figure 12 then compares temperature fields of the FLUENT simulation with that of the corresponding IBRANS simulation. A constant point heat source is applied in the cylinder near its center, for all simulations. However, two different thermal conductivities of the cylinder are considered to represent extreme conditions of solid conductivity. In the first case (Figs. 11(*a*) and 11(*b*)), the cylinder conductivity k_s nearly matches the fluid conductivity k_s: $k_s \simeq k_f$. The diffusion of temperature within the solid material is clearly evidenced. Figure

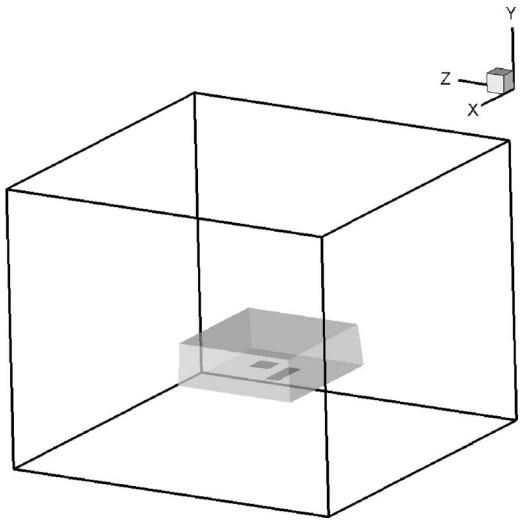

Fig. 7 Electronic mold in enclosure. Topology.

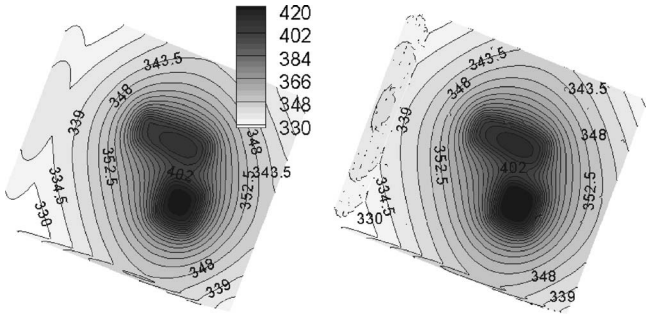

Fig. 10 Electronic mold in enclosure. Temperature contours on mold surface. Left: body fitted (FLUENT). Right: IB Cartesian.

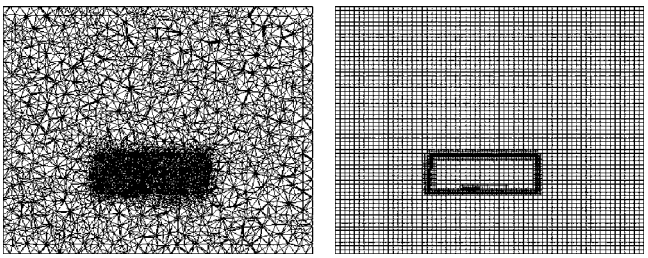

Fig. 8 Electronic mold in enclosure. Grid. Left: body fitted (FLUENT). Right: IB Cartesian with local grid refinement.

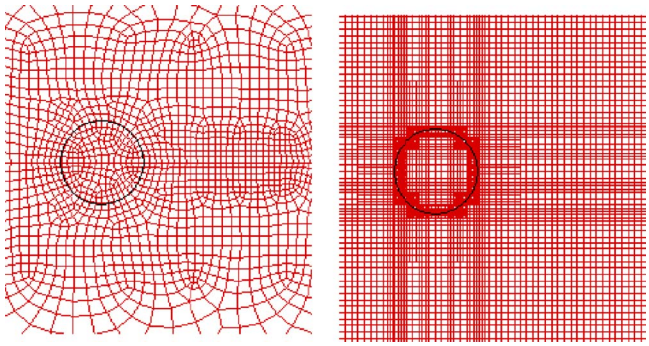

Fig. 11 Heated cylinder. Grid. Left: body fitted (FLUENT). Right: IB Cartesian with local grid refinement.

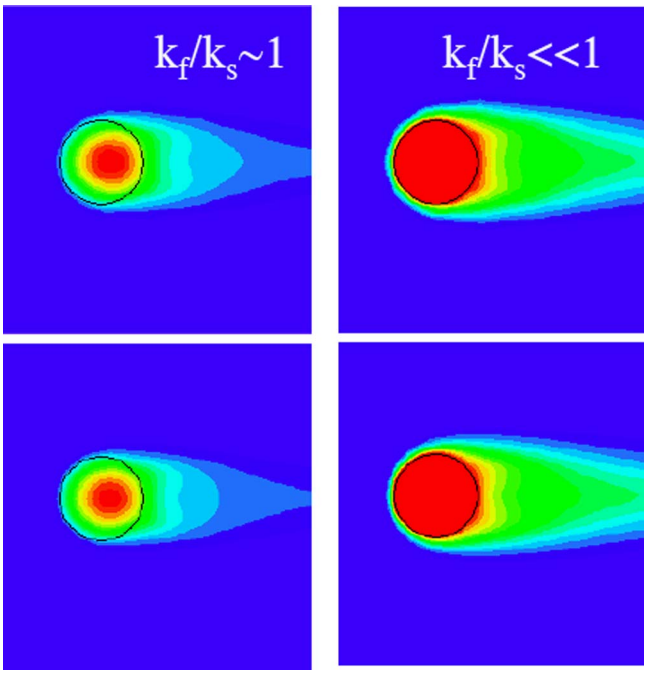

Fig. 12 Heated cylinder Re=23. Temperature contours. Top: body fitted (FLUENT). Bottom: IB Cartesian.

13 shows the velocity and temperature profiles along the centerline of the computational domain. Within the cylinder the temperature gradient is clearly seen and a maximum temperature of about 700 K is reached. In the second case (Figs. 11(*c*) and 11(*d*)), the solid conductivity is much higher than the fluid one: $k_s \gg k_f$. The hot spot produced by the point heat source has now been fully conducted to the cylinder surface (complete temperature diffusion within the solid material). Figure 14 again shows the velocity and temperature profiles along the centerline of the computational domain. Compared to the above case, the velocity profiles are similar, as the effect of temperature on the fluid properties is not accounted for here. On the contrary, the temperature is now constant within the cylinder, equal to a larger maximum temperature of about 1000 K. In both cases similar heat convection is observed in the cylinder wake as the Reynolds number is not changed and the fluid properties are not affected by the local temperature. The comparison between the two cases clearly shows the different role of conduction within the cylinder. Overall, the IB temperature contours compare very well with the corresponding body-fitted ones. Similarly, the velocity and temperature profiles obtained with IBRANS do not show any significant difference with the FLUENT body-fitted results.

Similar results are obtained at the other Reynolds numbers. For both $Re_D=120$ and $Re_D=3900$, the temperature contours follow the vortex shedding pattern leaving the cylinder in a very similar way between IBRANS and FLUENT. Figure 15 stresses that for the turbulent case ($Re_D=3900$), the periodic variation of the lift coefficient is almost identical between the body-fitted simulation with FLUENT and the Cartesian grid one with IBRANS, yielding similar Strouhal number and mean lift coefficient. Similar results are found on the drag coefficient. They also compare favorably with the existing experimental data for this well documented turbulent case [16–18].

6 Present Realistic 3D Model

The next step has been to tackle the complete electronized EEC motor shown in Fig. 1. The CAD transfer of the latest version of this motor, termed V6+, was successful without any modification and simplification of the industrial model meant for prototypes. To simulate the flow through the motor V6+, a box has been drawn around the motor and a wall has been put around the motor to force the flow through the motor. Figure 16 shows the resulting computational domain and topology. A uniform air stream is imposed on the left of the box to create airflow through the back plate of the motor. Three different velocities have been considered 1, 2 and 4 m/s, which cover the motor operating range on the fan system. This range can be found by separate CFD simulations, which couple the main flow through the fan and the internal flow under the fan hub through the motor modeled as a porous medium [19]. To remove the numerical difficulty associated with the wiring rotating closely to the magnets with a very narrow rotor-stator interface, only the 0 rpm case is presently considered (cold run).

A first qualitative verification of the flow field has been achieved by comparing the air paths at the design condition (2 m/s), with the previous body-fitted STAR-CD simulations in a similar EEC motor described in [2]. Figure 17 shows the results of this cold run through the motor in two different planes: in the middle of the wiring and collector on the left and close to the brush card on the right. As expected, the larger flow rate is achieved in the motor stack or around the collector where the larger air gaps are present to cool the copper wiring. Similarly the large gaps between the magnets allow a greater flow rate than the tiny gap between these magnetic poles and the rotor, which is kept

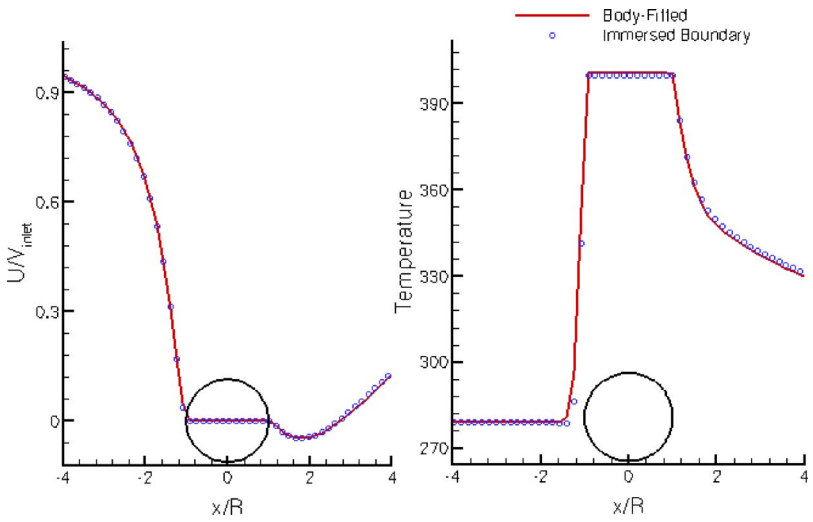

Fig. 13 Heated cylinder ($k_f=k_s$) Re=23. Mid-line velocity and temperature.

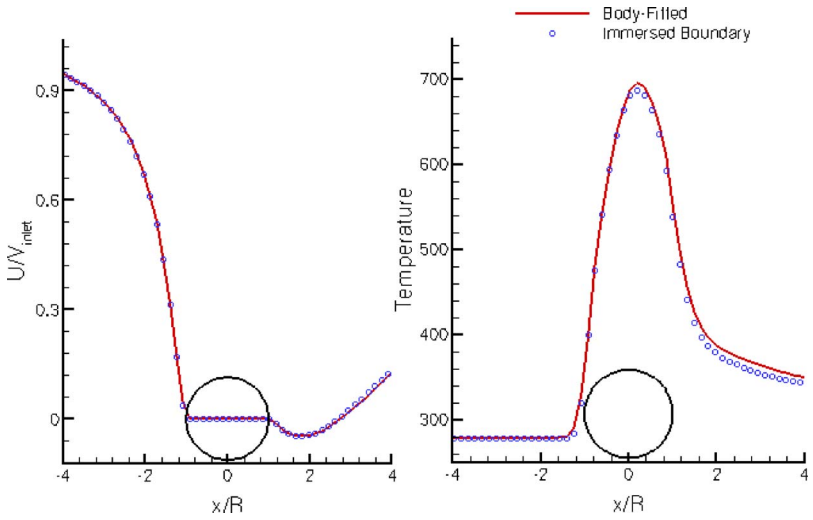

Fig. 14 Heated cylinder ($k_f \ll k_s$) Re=23. Mid-line velocity and temperature.

as small as possible to create the maximum electromagnetic flux and optimize the motor efficiency. The holes made in the brush card also bring maximum airflow around the hottest components, the brushes and the selfs.

To quantitatively verify the IBRANS predictions the motor flow characteristics have been compared to available measured data. The experimental apparatus is shown in Fig. 18. The setup consists of a flowmeter which forces a known flow rate through the motor. Two pressure taps close to venting holes in the front and back plates of the motor provide the pressure drop through the motor. The influence of the selected venting holes in the back and front plates has been shown to be negligible. More details can be found in Ref. [19]. Figure 19 shows the pressure drop through the electrical motor as a function of the flow rate. Two sets of data, termed V5 and V6+ in Fig. 19, correspond to two different prototypes of the same motor with slight differences on the brush card (minor design modifications) and heat sink. None of them should affect the flow paths significantly. Yet some scatter in the tolerance of assembly is expected at this prototype stage. Therefore, these two curves provide a good estimate of the combined experimental uncertainty and process scattering on the motor flow characteristics. The IBRANS results (solid square symbols) lay in between these two curves and therefore provide sufficient practical accuracy over the whole operating range.

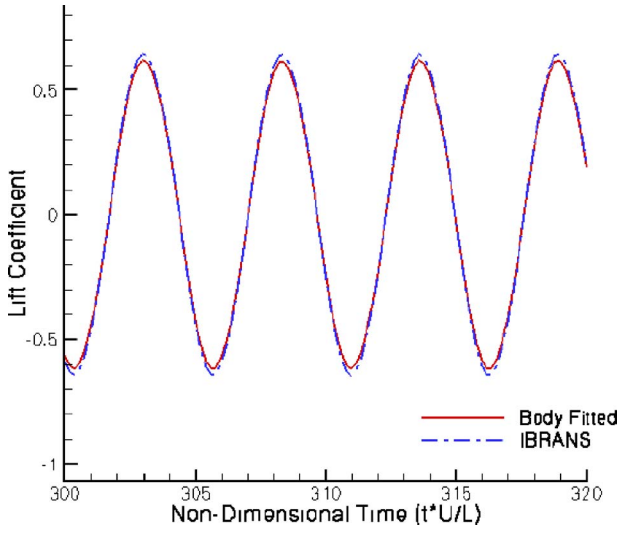

Fig. 15 Heated cylinder Re=3900. Lift coefficient.

7 Conclusions

The use of a Cartesian RANS solver for fluid and heat transfer problem in realistic, industrial configuration is presented. The approach is based on the use of the immersed boundary technique to represent the geometry on a non-body conformal grid. The major advantage is the ability to handle complex geometries defined in a CAD environment without the need for surface mesh generation.

A solid/fluid heat transfer module has been implemented and verified by several simple test cases for both natural and forced convection. The former deals with flows in enclosures around a sphere and electronic components. The latter copes with "classi-

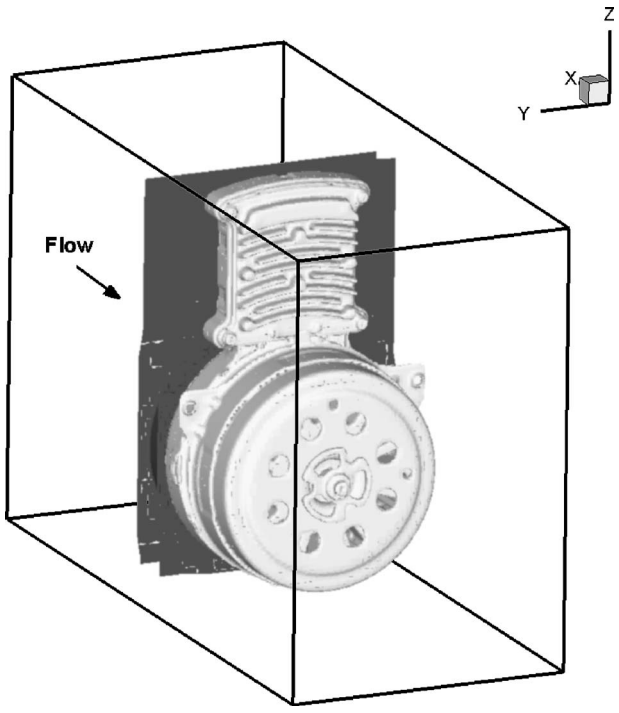

Fig. 16 IBRANS simulation domain for the electrical motor (blue: wall; grey: EEC motor)

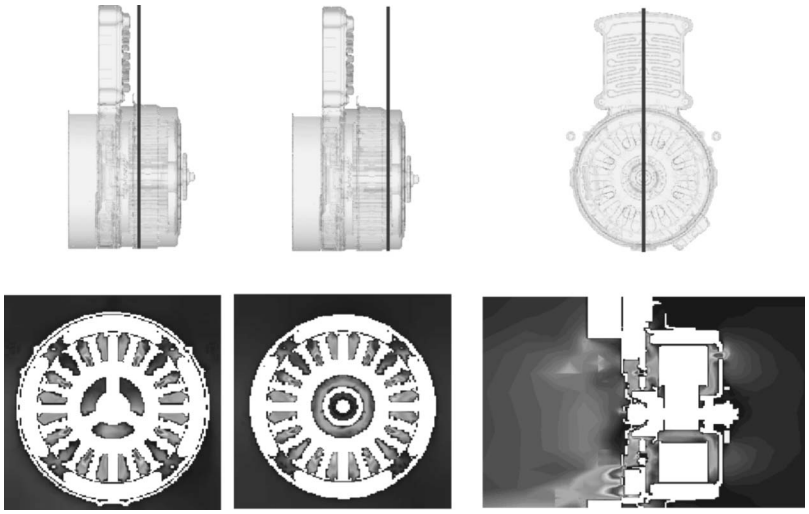

Fig. 17 Velocity contours within the electrical motor

cal" flows around heated cylinders. Both heat transfer problems are relevant to the industrial issues encountered in electrical motors. In fact, the natural convection heat transfer is found in the electronic box that might drive the speed of these machines and in sealed motors. The forced convection is also always present around the motor by the airflow created by the driven fan and inside the motor when it is open. All results are compared to body-fitted calculations over a range of Reynolds numbers and for different solid/fluid thermal conductivity. The consistency between the two methods is remarkable showing the feasibility of solving conjugate heat transfer problem with a non-body-fitted mesh.

Preliminary simulations of a complete electric motor consisting of about a 100 different CAD parts have also been carried out. An adaptively refined mesh was automatically generated and flow calculations performed over a range of flow rates. Comparison to experimental integral measurements (pressure drop versus flow rate) also demonstrated the sufficient accuracy of the present approach and the capability of handling extremely complicated geometry in a fully automatic fashion. The whole simulation process with the IB method took less than one day compared to the six months needed for the corresponding body-fitted simulation.

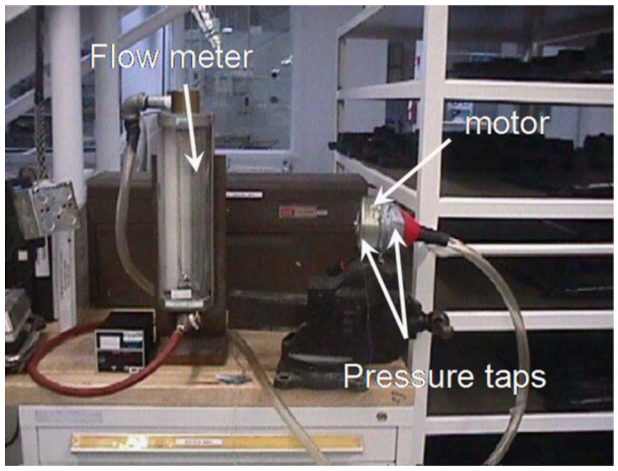

Fig. 18 Test rig for electrical motor's flow characteristics

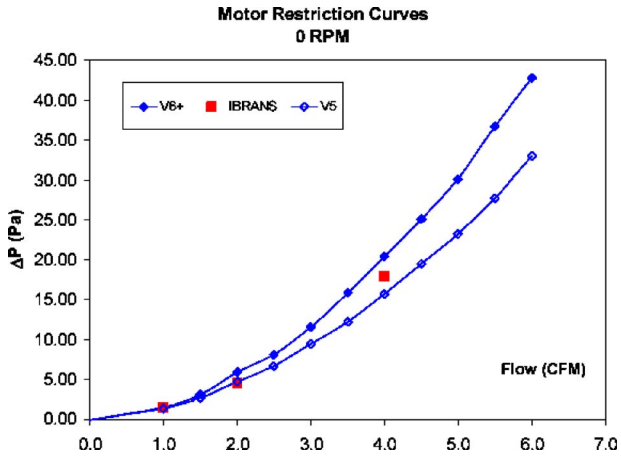

Fig. 19 Motor flow characteristics at rest (0 rpm)

Acknowledgment

The authors wish to thank G. Kalitzin for providing significant support in the development of the IBRANS code and the implementation of the conjugate heat transfer model.

References

[1] Péniguel, C., 1998, "Heat Transfer Simulation for Industrial Applications: Needs, Limitations, Expectations," Int. J. Heat Fluid Flow, **19**, pp. 102–114.
[2] Hong, T., Rakotovao, M., Moreau, S., and Savage, J., 2001, "Thermal Analysis of Electric Motors in Engine Cooling Fan Systems," SAE Paper No. 2001-01-1017.
[3] Williams, J., and Vemaganti, G., 1998, "CFD Quality—A Calibration Study for Front-End Cooling Airflow," SAE-980039 paper. Reprinted in "Developments in Vehicle Aerodynamics," SAE publication No. SP-1318.
[4] Markowitz, M., 1999, "Improving Vehicle A/C Performance by Underhood CFD Analysis With Regards to A/C Condenser Air Flow," C543/090/99 paper.
[5] Iaccarino, G., and Verzicco, R., 2003, "Immersed Boundary Technique for Turbulent Flow Simulations," Appl. Mech. Rev., **56**(3), pp. 331–347.
[6] Iaccarino, G., Kalitzin, G., and Khalighi, B., 2003,"Towards an Immersed Boundary RANS Flow Solver," AIAA Paper No. 2003-0770.
[7] Iaccarino, G., and Mittal, R., 2005, "Immersed Boundary Methods," Annu. Rev. Fluid Mech., **37**, pp. 239–261.
[8] Ferziger, J. H., and Peric, M., 2002, *Computational Methods for Fluid Dynamics*, Springer, Verlag.
[9] Vandoormaal, J. P., and Raithby, G. D., 1984, "Enhancements of the SIMPLE Method for Predicting Incompressible Fluid Flows," Numer. Heat Transfer, **7**, pp. 147–163.
[10] Iaccarino, G., and Kalitzin, G., 2002, "Turbulence Modeling in an Immersed Boundary RANS Method," Center for Turbulence Research Annual Research

Briefs, Stanford University.
[11] Spalart, P. R., and Allmaras, S. R., 1992, "A One-Equation Turbulence Model for Aerodynamic Flows," AIAA Paper No. 92-439.
[12] Wilcox, D. C., 1993, *Turbulence Modeling for CFD*, DCW Industries.
[13] Durbin, P. A., and Iaccarino, G., 2002, "An Approach to Local Refinement of Structured Grids," J. Comput. Phys., **181**, pp. 639–653.
[14] Kalitzin, G., and Iaccarino, G., 2003, "Toward Immersed Boundary Simulation of High Reynolds Number Flows," Center for Turbulence Research Annual Research Briefs, Stanford University.
[15] Iaccarino, G., Ooi, A., Durbin, P. A., and Behnia, M., 2002, "Conjugate Heat Transfer Predictions in Two-Dimensional Ribbed Passages," Int. J. Heat Fluid Flow, **23**, pp. 340–345.
[16] Beaudan, P., and Moin, P., 1994, "Numerical Experiments on the Flow Past a Circular Cylinder at Subcritical Reynolds Number," Report No. TF-62, Stanford University.
[17] Kravchenko, A. G., and Moin, P., 1998, "B-Spline Methods and Zonal Grids for Numerical Simulations of Turbulent Flows," Report No. TF-73, Stanford University.
[18] Kravchenko, A. G., and Moin, P., 2000, "Numerical Studies of Flow Over a Circular Cylinder at Re_D=3900," Phys. Fluids, **12**, pp. 403–417.
[19] Henner, M., Levasseur, A., and Moreau, S., 2003, "Detailed CFD Modeling of Engine Cooling Fan Systems Airflow," SAE Paper No. 2003-01-0615.

J.-C. Jouhaud[1]
Senior Researcher
Centre Européen de Recherche et de Formation
Avancée en Calcul Scientifique (CERFACS),
42, Avenue Gaspard Coriolis,
31057 Toulouse Cedex, France
e-mail: jjouhaud@cerfacs.fr

P. Sagaut
Professor
Laboratoire de Modélisation en Mécanique,
University of Paris VI,
4, place Jussieu,
75252 Paris Cedex 05, France
e-mail: sagaut@lmm.jussieu.fr

B. Labeyrie
Ph.D. Student
Centre Européen de Recherche et de Formation
Avancée en Calcul Scientifique (CERFACS),
42, Avenue Gaspard Coriolis,
31057 Toulouse Cedex, France

A Kriging Approach for CFD/Wind-Tunnel Data Comparison

A Kriging-based method for the parametrization of the response surface spanned by uncertain parameters in computational fluid dynamics is proposed. A multiresolution approach in the sampling space is used to improve the accuracy of the method. It is illustrated considering the problem of the computation of the corrections needed to recover equivalent free-flight conditions from wind-tunnel experiments. Using the surface response approach, optimal corrected values of the freestream Mach number and the angle of attack for the compressible turbulent flow around the RAE 2822 wing are computed. The use of the response surface to gain an insight into the sensitivity of the results with respect to other parameter is also assessed. [DOI: 10.1115/1.2201642]

Keywords: kriging, spatial interpolators, optimization, ELSA code, error estimation and control, validation of CFD simulations

1 Introduction

Validation and assessment of data obtained using numerical simulation are recognized as crucial steps in the development of reliable computational fluid dynamics (CFD) tools for engineering and academic research purposes. The importance of certification and validation strategies is now so large that some international agreements on the validation process for numerical data have been proposed [1–8]. Some best practice rules and guidelines for numerical models verification/validation/certification have been identified, which are now considered as mandatory steps before a physical model or a numerical scheme can be considered as fully assessed.

Despite a growing effort being devoted to the development of safe validation methodologies, both practical and theoretical problems arise when designing the validation process in terms of comparison between numerical results and wind-tunnel data. The first problem is the availability of sufficiently detailed reference databases, usually obtained through wind-tunnel experiments. The second problem, which is the one mainly addressed in the present paper, deals with the uncertainty in the definition of the validation cases.

The case of the turbulent statistically two-dimensional flow around a clean wing profile is retained as an illustration of this problem in the present paper. In such a configuration, it is well known that most wind-tunnel experiments suffer some secondary effects because of the limited spatial extent of the wind tunnel. The flow around the model is not fully identical to the flow around the same profile in an unbounded space, and wind-tunnel data must be corrected to mimic the corresponding free-flight flow. In the present work, the compressible turbulent flow around the RAE 2822 wing profile is selected. This flow is well known since it was selected as a validation case by the 16 partners of the EUROVAL European project [1] and by AGARD [2]. Significant outputs of the EUROVAL project dealing with this test case are corrected values of the Mach number and the angle of attack to achieve equivalent free-flight conditions: it is recommended that numerical simulations must be carried out using these corrected values [9], which are not equal to those of the experimental configuration.

Therefore, the important question of the evaluation of these corrected values arise, since these new values are the key to the validation process. Since they are not fully determined by theory, the corrections can be interpreted as uncertain values in the numerical simulations. The optimal corrections can be defined as those that lead to the best overall agreement between a given set of numerical simulations and the wind-tunnel data. A direct consequence is that optimal corrected values are not strictly independent of the set of computations that will be assessed using them. A crucial problem is therefore to develop a general strategy to compute these optimal corrections.

The present paper aims at presenting a strategy for generating the response surface of numerical tools, i.e., for describing the space of the solutions spanned by the numerical method, the turbulence model, and some configurational parameters (Mach number, angle of attack) based on the Kriging approach [10]. The Kriging method is first used to estimate unknown solutions that have not been computed by interpolation in the uncertain parameter space, and, in a second step, optimal corrections for wind-tunnel data are derived in an automatic way. The optimality is guaranteed, since the global extrema can be found. This systematic approach is to be compared to the usual approach, in which corrections are found in a heuristic way.

The paper is structured as follows. Section 2 displays the governing equations, including the turbulence models and the main features of the numerical method. The kriging method and the present implementation with local refinement in the uncertain parameter space are presented in Sec. 3. The application to the selected case is presented in Sec. 4. Conclusions are given in Sec. 5.

2 Governing Equations and Flow Solver

2.1 Physical Model. The governing equations are the 3D Navier-Stokes equations, which describe the conservation of mass, momentum, and energy of a viscous Newtonian fluid flow. Using Cartesian coordinates, these equations can be expressed in a conservative form as follows:

[1]Corresponding author.

Contributed by the Fluids Engineering Division of ASME for publication in the JOURNAL OF FLUIDS ENGINEERING. Manuscript received January 7, 2005; final manuscript received November 16, 2005. Assoc. Editor: Subrata Roy.

$$\frac{\partial \mathbf{W}}{\partial t} + \nabla . F = 0 \tag{1}$$

The state vector $\mathbf{W}$ and the flux $F = F_e - F_v$ decomposed in an inviscid and a viscous part, which are expressed as follows:

$$\mathbf{W} = [\rho, \rho\mathbf{U}, \rho E]^T$$

$$F_e = [\rho\mathbf{U}, \rho\mathbf{U} \otimes \mathbf{U} + p\bar{\bar{I}}, \mathbf{U}(\rho E + p)]^T$$

$$F_v = [0, \bar{\bar{\tau}}, \bar{\bar{\tau}} . \mathbf{U} - \mathbf{q}]^T \tag{2}$$

where ρ is the density, $\mathbf{U}$ the velocity, p the pressure, and E the total energy. For a Newtonian fluid, the shear stress tensor $\bar{\bar{\tau}}$ is given by

$$\bar{\bar{\tau}} = \mu(\nabla\mathbf{U} + (\nabla\mathbf{U})^T) + \lambda \nabla . \mathbf{U}\bar{\bar{I}} \tag{3}$$

with μ the dynamic viscosity and λ the second coefficient of viscosity. The Stokes assumption reduces the Lamé's relation to $2\mu + 3\lambda = 0$. The heat flux q is given by Fourier's law

$$\mathbf{q} = -K_T \nabla T \tag{4}$$

with T the temperature and K_T the thermal conductivity coefficient. The dynamic viscosity μ is given by the Sutherland's formulas

$$\mu = \mu_0 \left(\frac{T}{T_0}\right)^{3/2} \frac{T_0 + C_s}{T + C_s} \tag{5}$$

where μ_0 is the dynamic viscosity at the reference temperature T_0 and the constant C_s equals to 110.3 K. With a constant Prandtl number, the heat conductivity can be written as $K_T = \mu C_p / \mathrm{Pr}$ with C_p the specific heat at constant pressure and $\mathrm{Pr} = 0.72$ for air. For a caloric perfect gas, the state equation is given by $p = \rho RT$, where the gas constant R is equal to 287 J/kgK for air.

2.2 Numerical Method. The present study is carried out using the ELSA code developed at ONERA and CERFACS [11]. The ELSA code solves the three-dimensional (3D) compressible Navier-Stokes equations using a cell-centered finite-volume method. Integrating Eq. (1) over a domain Ω and applying Green's divergence theorem yield the following integral form:

$$\int_\Omega \frac{\partial U}{\partial t} dv + \oint_{\partial\Omega} F . \mathbf{n} dS = 0 \tag{6}$$

with $\mathbf{n}$ the outward normal of the boundary $\partial\Omega$ of the control volume Ω. The separated time/space discretization process leads to the following delta form:

$$A\Delta U^{n+1} = -\frac{\Delta t}{|\Omega|} R(U^n) \tag{7}$$

where the residual R comes from the space discretization and depends on the conservative variable field U^n. The Jacobian matrix A comes from the implicit time discretization and $\Delta U^{n+1} = U^{n+1} - U^n$ corresponds to the field correction also called the time increment.

In this paper, a standard multigrid [12] method combined with a local time stepping is used in order to accelerate the convergence to steady solutions. The classical second-order central scheme of Jameson [13] is used for spatial discretization and a LU-SSOR implicit method [14] for solving the time integration system (7).

2.3 Turbulence Modeling. Several turbulence models have been used for the present study, which are described below.

2.3.1 A One-Equation Turbulence Model: Spalart-Allmaras Model. Using the Spalart-Allmaras model [15], one has to solve the Reynolds-averaged Navier-Stokes equations and a transport equation for the eddy viscosity. Here, the eddy viscosity and the molecular viscosity are respectively noted ν_t and ν. The Reynolds stresses are given by $\overline{-u_i u_j} = 2\nu_t S_{ij}$ where $S_{ij} = 1/2[(\partial U_i/\partial x_j) + (\partial U_j/\partial x_i)]$ and $\tilde{\nu}$ is the working variable, which obeys to the transport equation:

$$\frac{\partial \rho\tilde{\nu}}{\partial t} + \nabla . [\mathbf{U}\rho\tilde{\nu}] = C_{b1}(1 - f_{t2})\tilde{S}\rho\tilde{\nu} + \frac{C_{b2}}{\sigma} \nabla \rho\tilde{\nu} . \nabla\tilde{\nu} + \nabla . \left[\frac{1}{\sigma}(\mu + \rho\tilde{\nu}) \nabla \tilde{\nu}\right] - \left(C_{\omega 1} f_\omega - \frac{C_{b1}}{\kappa^2} f_{t2}\right) \rho \frac{\tilde{\nu}^2}{d^2} \tag{8}$$

where the dynamic eddy viscosity μ_t is obtained by the formulas

$$\mu_t = \rho\tilde{\nu} f_{v1}; \quad f_{v1} = \frac{\chi^3}{\chi^3 + C_{v1}^3}; \quad \chi = \frac{\rho\tilde{\nu}}{\mu} \tag{9}$$

Here, S is the magnitude of the vorticity,

$$\tilde{S} = S + \frac{\tilde{\nu}}{\kappa^2 d^2} f_{v2}; \quad f_{v2} = 1 - \frac{\chi}{1 + \chi f_{v1}} \tag{10}$$

and d is the distance to the closest wall.

The function f_ω is

$$f_\omega = g\left(\frac{1 + C_{\omega_3}^6}{g^6 + C_{\omega_3}^6}\right)^{1/6}; \quad g = r + C_{\omega 2}(r^6 - r); \quad r = \frac{\tilde{\nu}}{\tilde{S}\kappa^2 d^2} \tag{11}$$

For large r, f_ω reaches a constant; thus, large values of r can be truncated to ten or so. The function f_{t2} is

$$f_{t2} = C_{t_3} \exp(-C_{t_4}\chi^2) \tag{12}$$

The constants are

$$C_{b1} = 0.1355; \quad C_{b2} = 0.622; \quad \sigma = \frac{2}{3}; \quad \kappa = 0.41$$

$$C_{\omega 1} = \frac{C_{b1}}{\kappa^2} + \frac{1 + C_{b2}}{\sigma}; \quad C_{\omega 2} = 0.3; \quad C_{\omega 3} = 2; \quad C_{v1} = 7.1$$

$$C_{t_3} = 1.1; \quad C_{t_4} = 2$$

Turbulent heat transfer obeys a turbulent Prandtl number equal to 0.09.

2.3.2 Two-Equations Turbulence Models: $k-\tilde{\epsilon}$, $k-\omega$, $k-l$. Other turbulence models considered in the present study belong to the two-equations model family. Following Deniau [16], all the classical two-equations models can be cast into the following formulation:

$$\frac{\partial \rho k}{\partial t} + \nabla . \left[\mathbf{U}\rho k - \left(\mu + \frac{\mu_t}{\sigma_k}\right) \nabla k\right] = P - \rho C_0 g(\phi, k) - D$$

$$\frac{\partial \rho\phi}{\partial t} + \nabla . \left[\mathbf{U}\rho\phi - \left(\mu + \frac{\mu_t}{\sigma_\phi}\right) \nabla \phi\right] = \frac{C_1}{T} P - \rho C_2 f_2 \frac{\phi}{T} + E \tag{13}$$

In Eq. (13), the variable ϕ corresponds to quantities $\tilde{\epsilon}$, ω, or l, respectively, the isotropic modeled dissipation rate, the specific dissipation rate, and the characteristic length; k is the turbulence kinetic energy; and $g(\phi, k)$ is a function depending only on ϕ and k. These quantities permit to evaluate a turbulence characteristic time scale T

- Jones-Launder [17] $k-\tilde{\epsilon}$ model: $T = k/\tilde{\epsilon}$
- Wilcox [18] $k-\omega$ model: $T = 1/\omega$
- Smith [19] $k-l$ model: $T = l/\sqrt{k}$

All these models are based on the Boussinesq assumption. P represents the term of k production and do not need additional clo-

sure hypothesis. D is a complementary term of dissipation that appears in some models ($k-\tilde{\epsilon}$ and $k-l$, for example), and E is a term that plays a major role in the buffer region of boundary layers. One obtains the following expressions:

$$P = \bar{\bar{\sigma}}:\nabla \mathbf{U}$$

$$\bar{\bar{\sigma}} = \mu_t\left(\nabla \mathbf{U} + \nabla \mathbf{U}^T - \frac{2}{3}\nabla \,.\, \mathbf{U}\right) - \frac{2}{3}\rho k \bar{\bar{I}}$$

$$\mu_t = \rho C_\mu f_\mu k T$$

In Eqs. (14) and (13), the coefficients C_μ, C_0, C_1, C_2, σ_k, and σ_ϕ are constants. f_2 and f_μ are damping functions, which depend on the turbulence models.

The Jones-Launder $k-\tilde{\epsilon}$ model equations are given by the following system:

$$\frac{\partial \rho k}{\partial t} + \nabla \,.\, \left[\mathbf{U}\rho k - \left(\mu + \frac{\mu_t}{\sigma_k}\right)\nabla k\right] = P - \rho\tilde{\epsilon} - D$$

$$\frac{\partial \rho \tilde{\epsilon}}{\partial t} + \nabla \,.\, \left[\mathbf{U}\rho\tilde{\epsilon} - \left(\mu + \frac{\mu_t}{\sigma_\epsilon}\right)\nabla \tilde{\epsilon}\right] = C_{\epsilon_1} f_\mu \frac{\tilde{\epsilon}}{k} P - C_{\epsilon_2} f_2 \rho \frac{\tilde{\epsilon}^2}{k} + E \tag{14}$$

with the following formulations:

$$\mu_t = \rho C_\mu f_\mu \frac{k^2}{\tilde{\epsilon}}; \quad f_\mu = \exp\left[\frac{-2.5}{(1+R_t/50)}\right]; \quad R_t = \frac{k^2}{\nu\tilde{\epsilon}}$$

$$D = 2\nu(\nabla\sqrt{k}) \,.\, (\nabla\sqrt{k})$$

$$E = 2\frac{\mu\mu_t}{\rho}[\nabla(\nabla \mathbf{U})]:[\nabla(\nabla \mathbf{U})]$$

$$f_2 = 1 - 0.3\exp(-R_t^2)$$

Concerning the coefficients, $C_\mu = 0.09$, $C_{\epsilon_1} = 1.55$, $C_{\epsilon_2} = 2$, $\sigma_k = 1.0$, and $\sigma_\epsilon = 1.3$.

The Wilcox $k-\omega$ model equations are given by

$$\frac{\partial \rho k}{\partial t} + \nabla \,.\, (\rho k \mathbf{U}) - \nabla \,.\, \left[\left(\mu + \frac{\mu_t}{\sigma_k}\right)\nabla k\right] = P - \beta_k \rho \omega k$$

$$\frac{\partial \rho \omega}{\partial t} + \nabla \,.\, (\rho \omega \mathbf{U}) - \nabla \,.\, \left[\left(\mu + \frac{\mu_t}{\sigma_\omega}\right)\nabla \omega\right] = \frac{\alpha_\omega \omega}{k} P - \beta_\omega \rho \omega^2 \tag{15}$$

with the eddy viscosity $\mu_t = \rho k/\omega$ and the closure coefficients $\sigma_k = 2.0$, $\sigma_\omega = 2.0$, $\beta_k = 0.09$, $\beta_\omega = 0.075$, and $\alpha_\omega = 0.5$.

In the case of the $k-l$ turbulence model proposed by Smith [19], the following transport equations are considered:

$$\frac{\partial \rho k}{\partial t} + \nabla \,.\, (\rho k \mathbf{U}) - \nabla \,.\, \left[\left(\mu + \frac{\mu_t}{\sigma_k}\right)\nabla k\right] = P - \frac{\rho(2k)^{3/2}}{B_1 l} - D$$

$$\frac{\partial \rho l}{\partial t} + \nabla \,.\, (\rho l \mathbf{U}) - \nabla \,.\, \left[\left(\mu + \frac{\mu_t}{\sigma_l}\right)\nabla l\right] = (2 - E_2)\frac{\rho\sqrt{2k}}{B_1}\left[1 - \left(\frac{l}{\kappa d}\right)^2\right] + \rho l \nabla \,.\, \mathbf{U} - \frac{\mu_t}{\sigma_l}(\nabla l \,.\, \nabla l)\left(\frac{l}{\kappa d}\right)^2 + 2\frac{\mu_t}{\sigma_l k}(\nabla l \,.\, \nabla k) \tag{16}$$

where P and D have been defined above and d is the distance to the wall. To complete system (16), we add the following formulations:

$$\mu_t = \mu\psi f_\mu; \quad \psi = \frac{\rho\sqrt{2k}l}{\mu B_1^{1/3}}$$

$$f_\mu = \left(\frac{C_1^4 f_* + C_2^2\psi^2 + \psi^4}{C_1^4 + C_2^2\psi^2 + \psi^4}\right)^{1/4}; \quad f_* = \exp\left[-50\left(\frac{l}{\kappa d}\right)^2\right]$$

$$C_1 = 25.5; \quad C_2 = 2.$$

The constants are $\kappa = 0.41$, $\sigma_k = \sigma_l = 1.43$, $B_1 = 18$, and $E_2 = 1.2$.

3 Response Surface Building Using the Kriging Method

3.1 What is Kriging? Spline interpolation [20] was originally developped for image processing. In GIS (geographic information system), it is mainly used in visualization of spatial data, where the appearance of interpolated surface is important. In geology and geomorphology, on the other hand, a different interpolation method referred to as kriging is widely used. This method was developed by a South African geologist G. Krige [10] in 1951. Since then, it has been extended to many fields of application, including agriculture, human geography [21], epidemiology [22], biostatistics, or archeology.

Kriging predictors are called optimal since they are statistically unbiased (e.g., on the average, the predicted value and the true value coincide) and they minimize prediction mean-squared error (see Eq. (23), a measure of uncertainly, or variability in the predicted values.

3.2 Principle of the Method. Kriging uses the covariogram [23], a function of the distance and direction separating two locations in the uncertain parameter space, to quantify the spatial autocorrelation in the data. The covariogram is then used to define the weights that determine the contribution of each data point to the prediction of new values at the unsampled locations in the space spanned by uncertain parameters.

The main statistical assumption underlying Kriging, called here assumption A1, is that statistical properties (such as mean, variance, covariance, etc.) do not depend on the exact spatial locations; thus, the mean and variance of a variable at one location is equal to the mean and variance at another location. Also, the correlation between any two locations depends only on the vector that separates them and not on their exact locations. When data cannot be assumed to satisfy this assumption, detrending techniques are used. Assumption A1 is very important since it provides a way to obtain replication from a single set of correlated data and allows us to estimate important parameters and make valid statistical inference.

3.3 Different Types of Kriging. Simple, ordinary, and universal Kriging predicators are all linear predicators, meaning that prediction at any location is obtained as a weighted average of neighboring data. The difference between these three models is in the assumption about the mean value of the variable under study: simple Kriging requires a known mean value as input to the model, while ordinary Kriging assumes a constant, but unknown mean, and estimates the mean value as a constant in the searching neighborhood (assumption A2). Thus, these two approaches model a spatial surface as deviations from a constant mean (assuming that the expectation of surface function is constant), where the deviations are spatially correlated (application to steady problems). Universal Kriging models local means as a sum of low-order polynomial functions of the spatial coordinates and then estimate the coefficients in this model. This type of model is appropriate when there are heterogeneity in the expectation of surface function (application to unsteady problems).

In the following, only ordinary Kriging will be considered. In fact, simple Kriging implies that functions to be estimated have a *known mean*, which is not true in the present application. And, universal kriging is not justified in the context of our applications,

since we are only here interested in steady flow simulations.

3.4 Mathematical Formulation. As seen above, the principle of Kriging method is to estimate, on a study region noted S, the attribute value of a surface function F at a location $x_p=(x,y)$, where we do not know the true value

$$\tilde{F}(x_p) = \sum_{i=1}^{n} W_i(x_p) F(x_i) \tag{17}$$

where $\tilde{F}(x_p)$ is the estimator function and (x,y) are the coordinates in the two-dimensional parameter space. Region S contains n data values $F(x_i)$, $i=1,\ldots,n$, and the Kriging approach consists of interpolating the value at a certain location by a weighted summation (W_i(x) weight functions) of the values surrounding sample points. The problem is how to determine the weight function, which is the main issue in Kriging approach.

Assumption A1 implies that the covariance C of the surface function F of two locations (x_i,x_j) is given by a function of only the distance between these locations

$$C[F(x_i),F(x_j)] = C(|x_i - x_j|) \tag{18}$$

where C is defined by the following formulation (assumption A2):

$$C(x_1,x_2) = E\{[F(x_1)-\mu][F(x_2)-\mu]\} \tag{19}$$

Covariances are usually represented as a matrix called the covariance matrix

$$\mathbf{C} = \begin{pmatrix} \sigma^2 & C(|x_1-x_2|) & \cdots & C(|x_1-x_n|) \\ C(|x_2-x_1|) & \sigma^2 & \cdots & C(|x_2-x_n|) \\ \vdots & \vdots & \ddots & \vdots \\ C(|x_n-x_1|) & C(|x_n-x_2|) & \cdots & \sigma^2 = C(0) \end{pmatrix} \tag{20}$$

Similarly, for plain explanation, covariance vector $\mathbf{c}$ is introduced

$$\mathbf{c}(x_p) = \begin{pmatrix} C(|x_p-x_1|) \\ C(|x_p-x_2|) \\ \vdots \\ C(|x_p-x_n|) \end{pmatrix} \tag{21}$$

In order to optimize the estimator function, one has to choose the weight functions W_i(x) $(i=1,\ldots,n)$, which minimize the variance of estimator functions represented here by the mean-square error (MSE)

$$\frac{\partial}{\partial W(x_p)} \mathrm{MSE}\hat{F}(x_p) = 0 \tag{22}$$

where MSE is defined by the following formula:

$$\begin{aligned} \mathrm{MSE}[\hat{F}(x_p)] &= E[\hat{F}(x_p) - F(x)_p]^2 \\ &= E[\hat{F}(x_p)]^2 + E[F(x_p)]^2 - 2E[F(x_p)\hat{F}(x_p)] \\ &= \sum_{i=1}^{n}\sum_{j=1}^{n} w_j(x_p) w_i(x_p) C(|x_i - x_j|) + \sigma^2 \\ &\quad - 2\sum_{i=1}^{n} w_i(x_p) C(|x_p - x_i|) \\ &= W^T(x_p) C W(x_p) + \sigma^2 - 2W^T(x_p)\mathbf{c}(x_p) \end{aligned} \tag{23}$$

The result is

$$W(x_p) = \mathbf{C}^{-1}\mathbf{c}(x_p) \tag{24}$$

In ordinary Kriging, the sum of weight functions $W_i(x_p)$ is equal to 1 at any location in S

$$\sum_{i=1}^{n} W_i(x_p) = 1 \tag{25}$$

To enforce this constraint, a Lagrange multiplier $\lambda(x_p)$ is introduced. The original problem (22) with constrain, (25) is then rewritten as

$$\frac{\partial}{\partial W(x_p)} \mathrm{MSE}\hat{F}(x_p) + W^T(x_p) I \lambda(x_p) = 0 \tag{26}$$

where I is the identity operator, leading to

$$W_+(x_p) = \mathbf{C}_+^{-1}\mathbf{c}_+(x_p) \tag{27}$$

where

$$W_+(x_p) = \begin{pmatrix} w_1(x_p) \\ w_2(x_p) \\ \vdots \\ w_n(x_p) \\ \lambda(x_p) \end{pmatrix} \tag{28}$$

$$\mathbf{C}_+ = \begin{pmatrix} \sigma^2 & C(|x_1-x_2|) & \cdots & C(|x_1-x_n|) & 1 \\ C(|x_2-x_1|) & \sigma^2 & \cdots & C(|x_2-x_n|) & 1 \\ \vdots & \vdots & \ddots & \vdots & 1 \\ C(|x_n-x_1|) & C(|x_n-x_2|) & \cdots & \sigma^2 = C(0) & 1 \\ 1 & 1 & \cdots & 1 & 0 \end{pmatrix} \tag{29}$$

and

$$\mathbf{c}_+(x) = \begin{pmatrix} C(|x-x_1|) \\ C(|x-x_2|) \\ \vdots \\ C(|x-x_n|) \\ 1 \end{pmatrix} \tag{30}$$

In ordinary Kriging, a covariogram function is arbitrarily chosen from typical theoretical functions or estimated from the observed data. Here, to estimate the surface function, the following model covariogram is used:

$$C(h) = 20\exp\left(-\frac{3h}{100}\right) \tag{31}$$

This surrogate expression for the covariogram is commonly used in cases in which the exact correlations are not known [24], since it yields the definition of a nonoscillatory interpolation procedure. The linear system (27) (inversion of matrix $\mathbf{C}$ for each x_p) is solved using the mathematical library of LAPACK (Linear Algebra Package).

3.5 Kriging Computational Suite. In this work, the Kriging method has been implemented in a *Kriging Computational Suite*, which is coupled with the ELSA solver. This suite (see Fig. 1) is divided into four stages:

1. definition of the following data
   (a) range of variation of the uncertain parameters
   (b) sampling in the selected subspace for uncertain parameters
2. CFD computations with ELSA
   (a) realization of the simulations for each sampling point in the uncertain parameter space.
3. data processing

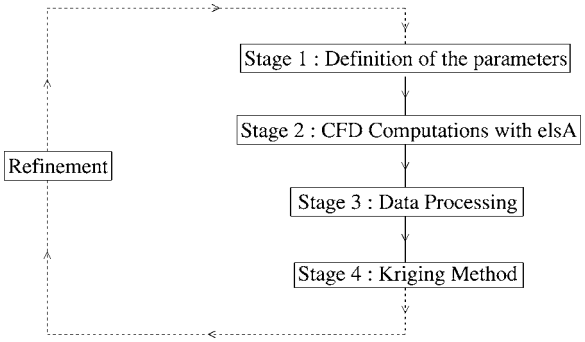

Fig. 1 Kriging computational suite

(a) computations of the values taken at sampling points by the function to be interpolated
(b) creation of data files for Kriging method

4. Kriging method

(a) reconstruction of the surface function
(b) computation of the mean-square error of Kriging method
(c) visualization of the surface function
(d) determination of the zone to be refined in the uncertain parameter space and return to the first stage

Within this multiresolution framework in the uncertain parameter space, the Kriging surface response is built using all data contained at all levels. It is worth noting that the present implementation is nonintrusive, since it does not require any modification of the basic CFD tool: the coupling between the Kriging tool and the CFD solver is performed via data file transfers. Another important feature is the capability of using a multiresolution approach in the uncertain parameter space to minimize the error in the response surface interpolation. In the present work, a local grid refinement in the uncertain parameter space is used.

4 Application to CFD/Wind-Tunnel Comparison for RAE2822 Profile

4.1 Definition of Test Case. The proposed methodology for identification of optimal wind-tunnel data corrections is illustrated here considering the two-dimensionnal, steady, turbulent, compressible flow around the RAE2822 wing profile. This case has been extensively used for validation of Navier-Stokes codes applied to transonic airfoil flow since it was retained as an international test case by AGARD [2] and within the EUROVAL project [1]. A large number of simulations with different flow parameters and turbulence models have been carried out. These simulations are related to numerous experimental work available in the literature.

In the work, the case investigated experimentaly by Cook et al. [2] is retained. These case is referred as Case 9 in the EUROVAL project and corresponds to the following experimental parameters:

$$M_\infty = 0.730, \quad \alpha = 3.19, \quad \mathrm{Re} = 6.5 \times 10^6 \tag{32}$$

where M_∞, α, and Re are the freestream Mach number, the angle of attack, and the chord-based Reynolds number, respectively. The transition of turbulence flow takes place at $xt = x/c = 0.03$ on both the upper and lower sides of the airfoil. In fact, transition trips were used in the experiments, and the transition location is prescribed in the simulations.

In the EUROVAL [1] validation project, empirically derived wind-tunnel corrections are applied to the above-mentioned flow parameters (32) and the values referred to as mandatory flow parameters for Case 9 are the following:

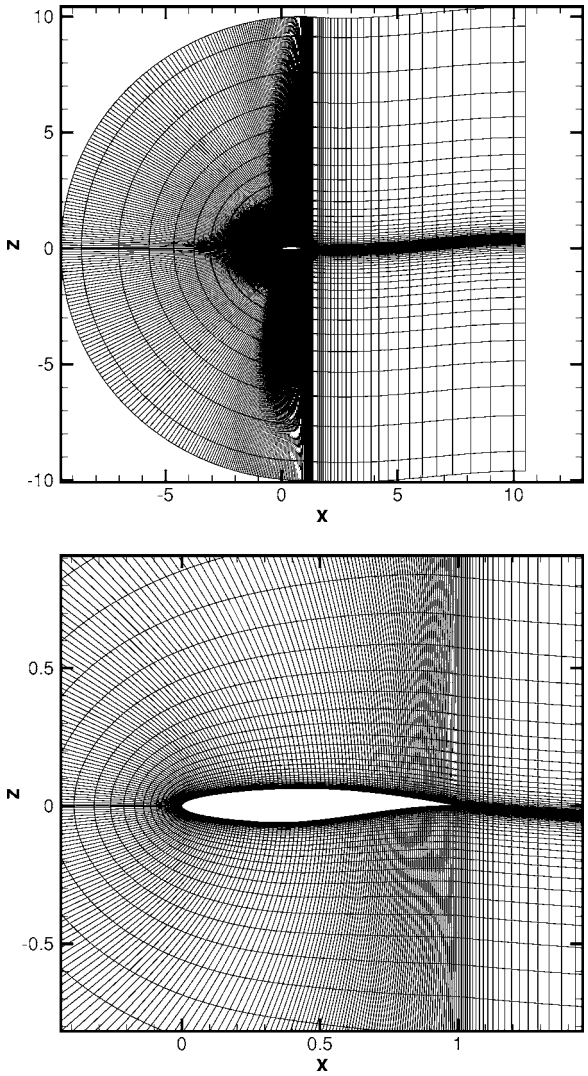

Fig. 2 View of the computational grid

$$M_\infty = 0.734, \quad \alpha = 2.79, \quad \mathrm{Re} = 6.5 \times 10^6 \tag{33}$$

These corrected values were obtained searching for the values that yield the best overall agreement between experimental values of the drag and the lift and those computed by ten research groups using different numerical methods, turbulence models, and computational grids. The targeted values of the aerodynamic forces are

$$C_d = 0.0168, \quad C_l = 0.803 \tag{34}$$

Following the work of EUROVAL, we propose here to use the Kriging method in order to find the optimal *optimized corrected* values of Mach_∞ and α for which four classical turbulence models (Spalart-Allmaras [15], Jones-Launder [18], Wilcox [19], and Smith [20]) will be in the best agreement with the experimental results (34). The sensitivity with respect to the location where transition to turbulence is prescribed (xt values) will also be investigated.

4.2 Reference Simulations. Before searching for the optimal corrected values, some reference simulations have been carried out using the four selected turbulence models described above for uncorrected values of the freestream Mach number and the angle of attack. All the reference simulations have been carried out on the same computational grid. The mesh is a C-mesh made of two blocks defined 177×65 points (see Fig. 2), which corresponds to

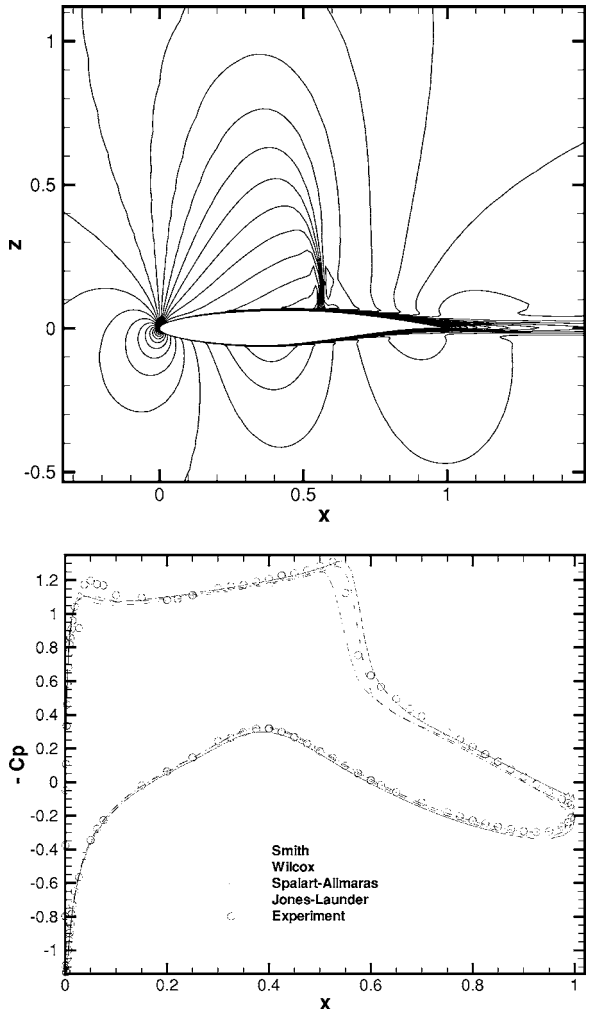

Fig. 3 Flow around the RAE2822 wing, Mach number contours for Spalart-Allmaras and -Cp stations.

a fine space discretization. It extends ten chord lengths in front, on the upper and lower side, as well as downstream of the trailing edge. There are 258 cells located on the airfoil's surface.

Figure 3 displays the Mach number contours computed using the Spalart-Allmaras model [15]: this flow is characterized by a supersonic zone with a shock on the upper surface. Pressure coefficient distributions on the airfoil are also plotted for all turbulence models in Fig. 3. It can be noted that computations are in good agreement with experimental data with only a few discrepancies, in particular, concerning the shock location. The corresponding values of drag and lift coefficients and relative errors are given in Table 1.

Table 1 Drag and lift coefficients and relative errors in reference simulations (without corrected values of the Mach number and the angle of attack)

Results	C_d	C_l	ΔC_d (%)	ΔC_l (%)
Spalart-Allmaras' model [15]	0.01629	0.7510	3.03	6.26
Wilcox's model [19]	0.01720	0.7833	2.38	2.45
Smith's model [20]	0.01537	0.8371	8.51	4.25
Jones-Launder's model [18]	0.01828	0.7582	8.81	5.58
Experimental data	0.0168	0.803		

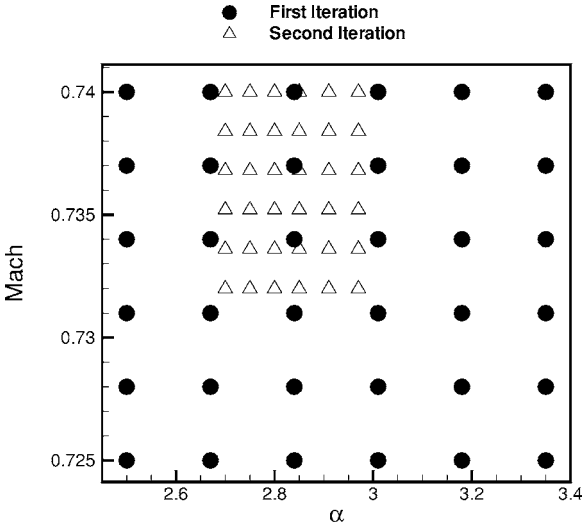

Fig. 4 Location of sampling points in the $(M\infty, \alpha)$ plane for building of the response surface via Kriging interpolation. Black circles: first grid level; white triangle: second grid level.

4.3 Kriging Interpolation, Cost Function Definition, and Optimal Corrections. In order to compute optimal corrected values of control parameters, it is necessary to define a cost function to be minimized. It is chosen here to use a multiobjective cost function, which combines the relative errors computed on both lift and drag coefficients using the four selected turbulence models. The computed corrections will be expected to be robust, meaning that they should lead to an improvement of computational data and/or wind-tunnel data for a wide class of numerical models.

The mathematical expression of the cost function used in this study is

$$F_{\text{cost}} = \left| \frac{C_{dm} - C_{d\,\text{exp}}}{C_{d\,\text{exp}}} \right| + \left| \frac{C_{lm} - C_{l\,\text{exp}}}{C_{l\,\text{exp}}} \right| \tag{35}$$

where $C_{d\,\text{exp}}$ and $C_{l\,\text{exp}}$ are experimental values of the drag and lift coefficients, respectively, and

$$C_{dm} = \frac{1}{4}[C_d(k-\tilde{\epsilon}) + C_d(k-\omega) + C_d(k-l) + C_d(SA)] \tag{36}$$

$$C_{lm} = \frac{1}{4}[C_l(k-\tilde{\epsilon}) + C_l(k-\omega) + C_l(k-l) + C_l(SA)] \tag{37}$$

where C_{dm} (model) (resp. C_{lm} (model)) refers to he value of the drag coefficient (resp. the lift coefficient) computed using the turbulence model named *model*.

The construction of the surface response of the cost function defined above in the two-dimensional space spanned by the freestream Mach number and the angle of attack is first addressed. These two parameters are considered as uncertain parameters. All other parameters, both numerical and physical ones, such as the prescribed location of transition to turbulence, numerical viscosity, parameters, etc., are kept unchanged with respect to the reference simulations.

For the sake of physical consistency, it is assumed that corrections to be imposed to wind-tunnel parameters must correspond to small relative variations in order to prevent any bifurcation of the solution (e.g., relaminarization, shock disappearance, etc.). The allowed ranges of variation of these two parameters are

$$2.5 \text{ deg} < \alpha < 3.35 \text{ deg}, \quad 0.725 < M_\infty < 0.74 \tag{38}$$

The grid in the uncertain parameter space spanned by these values is shown in Fig. 4. The basic uniform grid corresponds to the black circles, while the local refined grid used to improve the

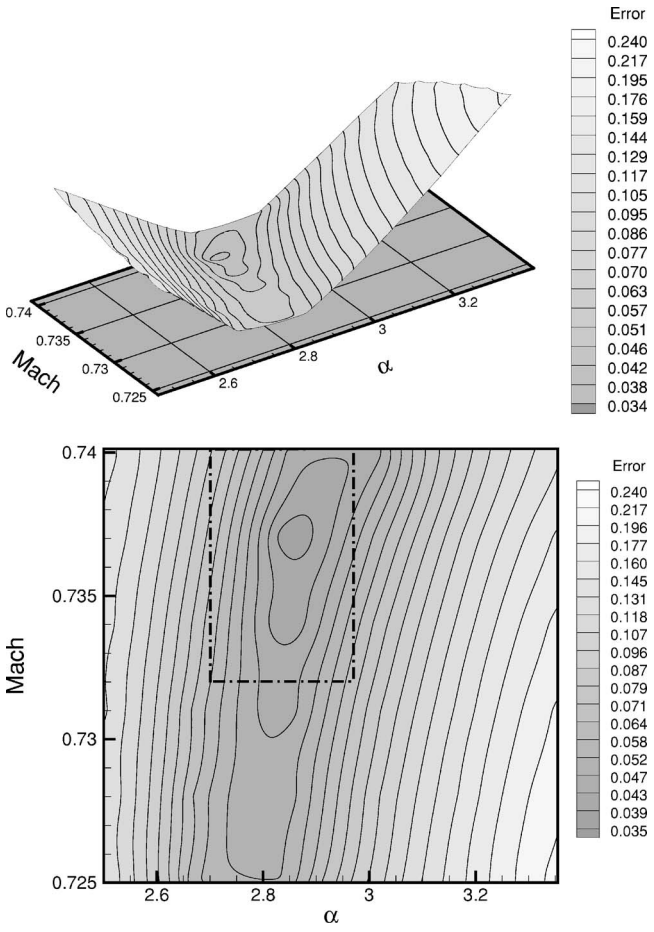

Fig. 5 Surface function of the cost function in the $(M\infty, \alpha)$ plane: coarse resolution sampling

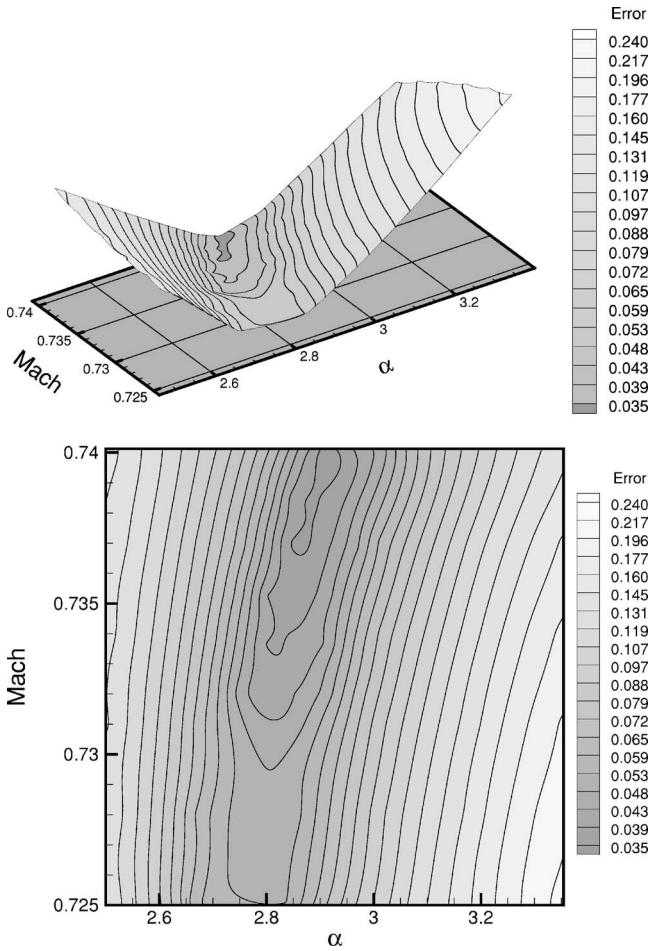

Fig. 6 Surface function of the cost function in the $(M\infty, \alpha)$ plane: locally refined resolution

accuracy of the response surface corresponds to the white triangle. The local refinement region was defined to improve the accuracy around the global minimum of the surface response computed on the first grid level.

The surface response of the cost function computed using the coarse grid resolution in the (M_∞, α) plane is shown in Fig. 5, and the one computed using the locally refined grid is presented in Fig. 6. The global minimum of the cost function is found at $M_\infty = 0.737$ and $\alpha = 2.84$ using the coarse resolution-based response surface, while it is found at $M_\infty = 0.737$ and $\alpha = 2.91$ using the locally refined grid. These values are not identical to the ones proposed in the EUROVAL project, but are close to them.

The response surface build using the Kriging estimator can also be used to gain insight into the sensitivity of the solution with respect to some computational parameter. To illustrate this point, the sensitivity of the results and the dependency of the optimal corrections for the freestream Mach number with respect to another partially arbitrary parameter, namely, the location where the transition to turbulence is imposed in the computation, xt, is investigated. The uncertainty domain considered here is defined as

$$0.725 < M_\infty < 0.74, \quad 2.40 < xt < 4.17 \tag{39}$$

As in the previous case, a two-level grid resolution is used to build the response surface. The response surfaces built using the coarse grid resolution and the locally refined fine grid are shown in Figs. 7 and 8, respectively. The optimal values found on the two surfaces are the same: $M_\infty = 0.737$ and $xt = 2.7 \times 10^{-2}$, revealing that the previous optimal value of the freestream Mach number can be kept unchanged.

New simulations using the corrected values computed using the Kriging-based response surface, $M_\infty = 0.737$ and $\alpha = 2.91$, have been carried out to check that these new parameters yield an effective improvement in the prediction of drag and lift. All other parameters are kept unchanged with respect to the reference simulations. The computed values and the associated relative errors are displayed in Table 2. By comparison to Table 1, it is observed that all values but one (lift coefficient predicted using the Smith's model) are improved using the corrected parameters, showing the efficiency of the method.

5 Conclusion

A Kriging-based method for the parametrization of the surface response spanned by uncertain parameters in CFD calculations is proposed. It was shown using the case of the flow around a two-dimensional wing that this method is efficient. The most interesting features of the proposed method is that it is nonintrusive (i.e., it does not involve any modification of the basic CFD tool) and that it was coupled with a multiresolution approach in the uncertain parameter space to increase the accuracy.

It was shown that such a tool makes it possible to compute optimal corrections for wind-tunnel parameters to recover free-flight conditions. Here, the optimality is associated to the fact that the proposed corrections lead to best overall agreement for a aggregated cost function, which includes both drag and lift but also a relevant set of turbulence models. The new corrected values are observed to yield a significant improvement in the prediction of both drag and lift in almost all cases.

The use of the Kriging-based response surface to evaluate the sensitivity of the solution was also illustrated, considering the

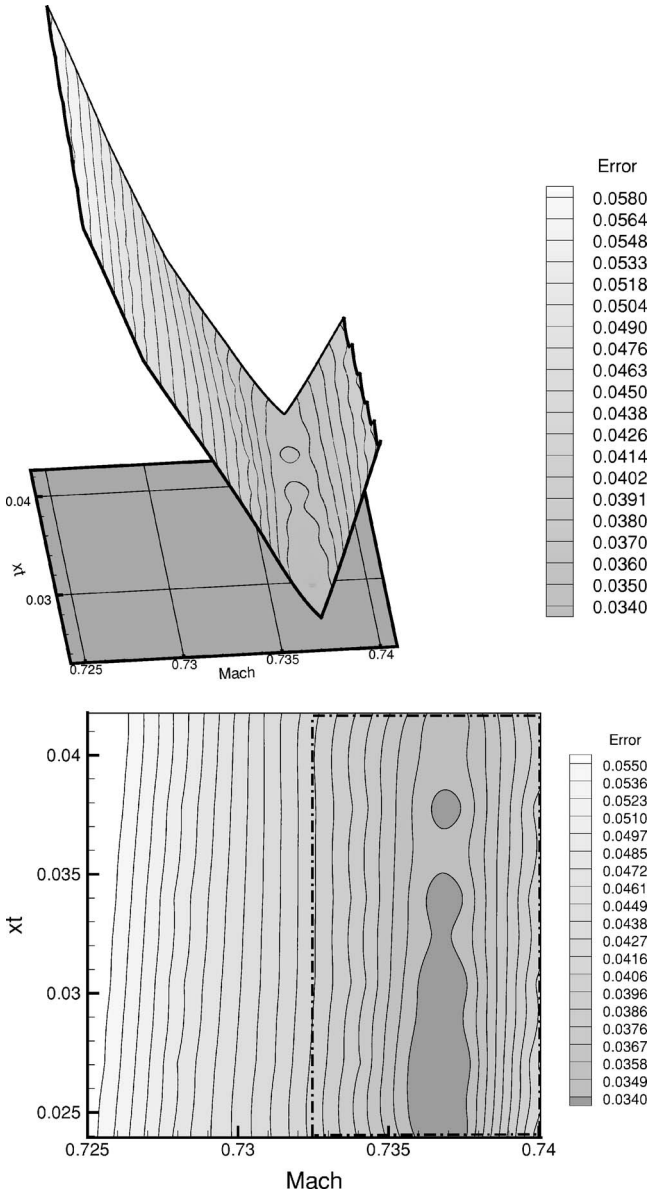

Fig. 7 Surface function of the cost function in the (M∞, *xt*) plane: coarse resolution sampling

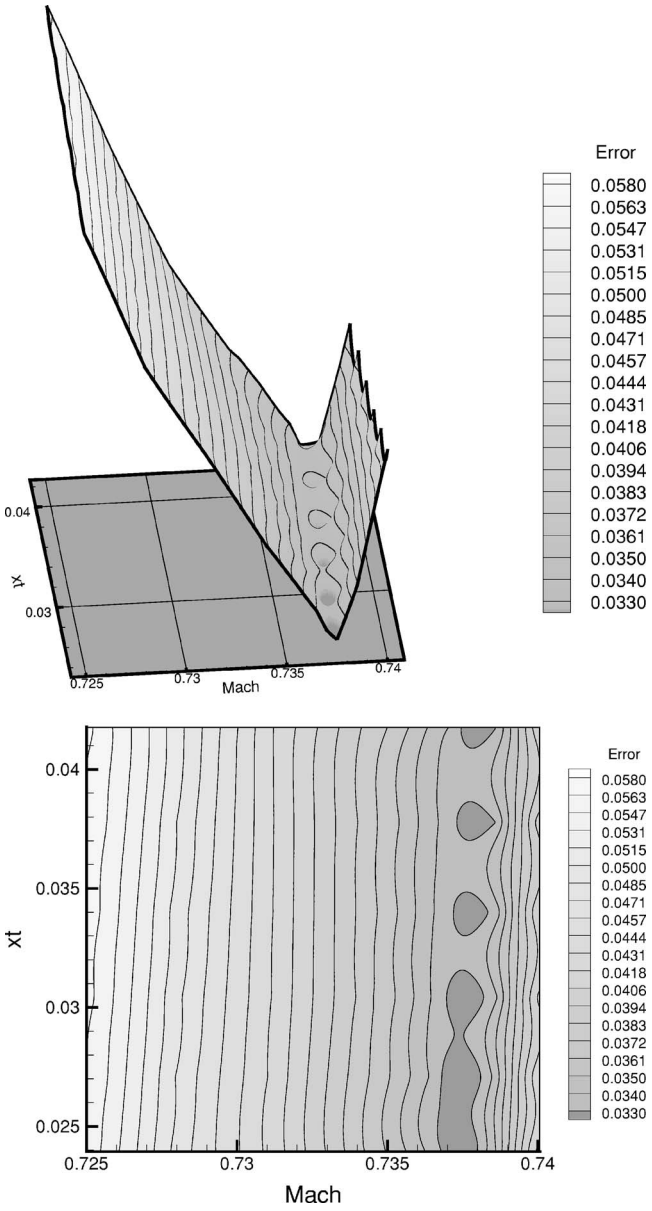

Fig. 8 Surface function of the cost function in the (M∞, *xt*) plane: locally refined resolution

location where the transition to turbulence is prescribed as an uncertain parameter. The present surrogate modeling approach is fully general, in the sense that it does not rely on any assumptions about the nature of the uncertain parameters and the features of the computational model.

A last comment is that the Kriging approach can easily be applied to discontinuous function or function with strong gradients in the uncertain parameter space using the local approach implementation, i.e., by limiting the interpolation to closest sampling points. Since it does not rely on any explicit decomposition on a polynomial basis, the implementation of multiresolution-based Kriging computational suites is easy.

Table 2 Drag and lift coefficients and relative errors in reference simulations with corrected values of the Mach number and the angle of attack

Results	C_d	C_l	ΔC_d (%)	ΔC_l (%)
Spalart-Allmaras's model [15]	0.01642	0.7568	2.26	5.75
Wilcox's model [19]	0.01717	0.8019	2.20	1.36
Smith's model [20]	0.01601	0.8461	4.70	5.37
Jones-Launder's model [18]	0.01749	0.7815	4.11	2.68

References

[1] Haase, W., Brandsma, F., Elsholz, F., Leschziner, M., and Schwamborn, D., eds., 1993, *An European Initiative on Validation of CFD-Codes*, Notes on Numerical Fluid Mechanics, Vieweg-Verlag, Braunschweig.

[2] Cook, P. H., McDonald, M. A., and Firmin, M. C. P., "Aerofoil RAE 2822-Pressure Distributions and Boundary Layer and Wake Measurements," AGARD AR 138, pp. A6-1–A6-77.

[3] Barber, T. J., 1998, "Role of Code Validation and Certification in the Design Environment," AIAA J., **36**(5), pp. 753–758.

[4] Benek, J. A., Lauer, R. F., and Kraft, E. M., 1998, "Validation Issues for Engine-Airframe Integration," AIAA J., **36**(5), pp. 759–764.

[5] Rumsey, C. L., Gatski, T. B., and Bertelrud, A., 1998, "Prediction of High-Lift Flows Using Turbulent Closure Models," AIAA J., **36**(5), pp. 765–774.

[6] Roache, P. J., 1998, "Verification of Codes and Calculations," AIAA J., **36**(5), pp. 697–702.

[7] Rizzi, A., and Vos, J., 1998, "Toward Establishing Credibility in Computational Fluid Dynamics Simulations," AIAA J., **36**(5), pp. 668–675.

[8] Mehta, U. B., 1998, "Credible Computational Fluid Dynamics Simulations," AIAA J., **36**(5), pp. 665–667.
[9] Hellstrom, T., and Davidson, L., 1994, "Reynolds Stress Transport Modelling of Transonic Flow Around the RAE2822 Airfoil," AIAA Paper No. 94-0309.
[10] Krige, D. G., 1951, "A Statistical Approach to Some Basic Mine Valuations Problems on the Witwatersrand," J. Chem. Metal. Mining Soc. S. Africa, **52**, pp. 119–139.
[11] Cambier, L., and Gazaix, M., 2002, "ELSA: An Efficient Object-Oriented Solution to CFD Complexity," 40th AIAA Aerospace Science Meeting & Exhibit, Reno, AIAA Paper No. 2002-0108.
[12] Jameson, A., 1982, *Steady State Solutions of the Euler Equations for Transonic Flow by a Multigrid Method*, Advances in Scientific Comput., Academic Press, New York, pp. 37–70.
[13] Jameson, A., Schmidt, W., and Turkel, E., 1981, "Numerical Solutions of the Euler Equations by Finite Volume Methods Using Runge-Kutta Time-Stepping Schemes," AIAA Paper No. 81-1259.
[14] Yoon, S., and Jameson, A., 1987, "An LU-SSOR Scheme for the Euler and Navier-Stokes Equations," AIAA Paper No. 87-0600.
[15] Spalart, P. R., and Allmaras, S. R., 1994, "A One-Equation Turbulence Model for Aerodynamic Flows," Rech. Aerosp., **1**, pp. 5–21.
[16] Deniau, H., 1996, "Calcul d'Écoulements Supersoniques Pour la Résolution des Équations de Navier-Stokes Parabolisées: Modélisation de la Turbulence, Traitement des Poches Supersoniques," Ph.D. thesis, Ecole Nationale Supérieure de l'Aéronautique et de l'Espace.
[17] Jones, W. P., and Launder, B. I., 1972, "The Prediction of Laminarization With a 2-Equations Model of Turbulence," Int. J. Heat Mass Transfer, **15**, pp. 301–314.
[18] Wilcox, D. C., 1994, "Simulation of Transition with a Two-Equation Turbulence Model," AIAA J., **32**(2), pp. 247–255.
[19] Smith, B. R., 1990, "The k-kl Turbulence Model and Wall Layer Model for Compressible Flows," AIAA Paper No. 90-1483.
[20] Dubrule, O., 1984, "Comparing Splines and Kriging," Comput. Geosci., **10**(2–3), pp. 327–333.
[21] Oliver, M. A., and Webster, R., 1990, "Kriging: A Method of Interpolation for Geographical Information System," Int. J. Geogr. Inf. Syst., **4**(3), pp. 313–332.
[22] Christakos, G., and Hristopulos, D. T., 1988, "Spatiotemporal Environmental Health Modelling," Kluwer, Dordrecht.
[23] Journel, A. G., and Huijbregts, C. J., 1978, *Mining Geostatistics*, Academic Press, New York, pp. 600.
[24] Sacks, J., Schiller, S., and Welch, W., 1989, "Designs for Computer Experiments," Technometrics, **31**, pp. 41–47.

Galerkin Least-Squares Finite Element Approximations for Isochoric Flows of Viscoplastic Liquids

Flávia Zinani
Graduate Student

Sérgio Frey[1]
e-mail: frey@mecanica.ufrgs.br

Laboratory of Applied and Computational Fluid Mechanics (LAMAC),
Mechanical Engineering Department,
Federal University of Rio Grande do Sul,
Rua Sarmento Leite, 425,
Porto Alegre, RS, CEP: 90050-170, Brazil

The flow of viscoplastic liquids is studied via a finite element stabilized method. Fluids, such as some food products, blood, mud, and polymer solutions, exhibit viscoplastic behavior. In order to approximate this class of liquids, a mechanical model, based on the principles of power expended and mass conservation, is exploited with the Papanastasiou approximation for Casson equation employed to model viscoplasticity. The approximation for the nonlinear set of partial differential equations is performed, using a stabilized finite element methodology. A Galerkin least-squares strategy is employed to avoid the well-known difficulties of the classical Galerkin method in isochoric flows. It circumvents the Babuška-Brezzi condition and handles the asymmetry of the advective operator in high advective flows. Some two-dimensional (2D) viscoplastic flows through a 4:1 planar expansion, for a range of Casson $(0 \leqslant \mathrm{Ca} \leqslant 10)$ *and Reynolds* $(0 \leqslant \mathrm{Re} \leqslant 50)$ *numbers, have been investigated, paying special attention to the characterization of vortex length and unyielded regions. The numerical results show the arising of regions of unyielded material throughout the flow, strongly affecting the vortex structure, which is reduced with the increase of the Casson number even in flows with considerable inertia.* [DOI: 10.1115/1.2201633]

Keywords: principle of power expended, viscoplasticity, Casson model, finite elements in fluids, Galerkin least-squares

1 Introduction

The analysis of non-Newtonian flows has always been a challenge in fluid mechanics research. In the last three decades, with the improvement of numerical techniques and digital computers, numerical simulation of non-Newtonian fluid flow has risen as a vast and powerful research field, with a large range of engineering applications ([1,2], and references therein). Prediction of fluid behavior and detailed flow visualization in complex geometry, mostly not accomplishable in experimental analysis, has increased the interest in this area.

The numerical simulation of non-Newtonian fluid flows involves the approximation of the motion equations coupled to specific rheological models. The generalized Newtonian rheological model [3,4] was introduced as a modification of the classical Newtonian constitutive equation in order to accommodate experimental deviations that are observed in the linear Newtonian behavior. This class of constitutive equation is based on the concept of an apparent shear rate-dependent viscosity, adjusting the commonly observed phenomena of shear-thinning (pseudoplasticity) or shear-thickening [4]. Although these models do not describe normal stress differences or time-dependent elastic effects, they have been used to predict the behavior of a large scope of industrial materials. Some of them—called viscoplastic models—may also predict a yield stress for the material, i.e., the fluid only deforms/flows when the applied stress lies beyond this yield stress. They usually present shear-thinning behavior as well [5,6]. (In fact, the yield stress is a model for the behavior of some structured liquids that present deep changes in their mechanical properties inside a small range of stress, as pointed out in [6], and references therein.) Casson has proposed a classical model of viscoplastic behavior in [7].

From the theoretical point of view, generalized Newtonian models represent the mechanical behavior of materials subjected to steady-state pure shear flows. In practice, however, they have successfully been used in many engineering applications to model non steady-state or non pure shear flows [4]. This may be explained by the fact that, in many industrial applications, shear-thinning and viscoplasticity represent the most relevant non-Newtonian features when predicting the kinematics and dynamics of the fluid flow. Examples of materials exhibiting these features are molten chocolate [8], xanthan gum solutions [9], ketchup [10], and blood [11].

Several authors have studied flows of viscoplastic materials inside axisymmetric and planar channels. Pak et al. [12] observed experimentally that the reattachment length, for purely viscous fluids, was almost the same as in Newtonian fluids. Abdali et al. [13] approximated, via finite element method, the contraction and exit flows of Bingham fluids through axisymmetric and planar channels, capturing yielded and unyielded material regions. Pham and Mitsoulis [14] studied entry and exit flows of Casson fluids employing Papanastasiou modified equation [5] and a finite element methodology. Vradis and Ötüngen [15] used a finite-difference scheme to simulate the Bingham flow through a 1:2 sudden expansion, concluding that the flow was strongly dependent on the yield stress, but weakly dependent on the power-law index. Jay et al. [16] investigated viscoplastic flows in an axisymmetric 4:1 expansion, employing the model of Herschel-Bulkley and performing numerical and experimental comparisons. Reis and Naccache [17] simulated viscoplastic flows through contractions via a finite volume method, with the plasticity behavior

[1]Corresponding author.

Contributed by the Fluids Engineering Division of ASME for publication in the JOURNAL OF FLUIDS ENGINEERING. Manuscript received April 1, 2005; final manuscript received December 6, 2005. Assoc. Editor: Dennis Siginer.

modeled by the Carreau equation subjected to a very high low-shear-rate viscosity. Neofytou and Drikakis [18] investigated the flows of three different fluid models (Casson, Quemada, and power law) in a sudden expansion channel. More recently, Mitsoulis and Huilgol [19] simulated entry flows of Bingham plastics in expansions by a finite element method, computing the vortex size and intensity, as well as the entrance correction, as functions of the material yield stress.

The classical Galerkin method for incompressible fluids suffers from two major difficulties. First, the need to satisfy the Babuška-Brezzi condition [20] in order to employ a compatible combination of velocity and pressure subspaces. Second, the inherent instability of central difference schemes in the approximation of advective dominated flows [21]. The Galerkin least-squares (GLS) method, introduced for Stokes equations in [22], has been developed to enhance the stability of the original Galerkin method, by adding mesh-dependent terms to the Galerkin formulation, which are functions of the residuals of Euler-Lagrange equations evaluated elementwise. Since the residuals of the Euler-Lagrange equations are satisfied by the exact solutions, consistency is preserved in these methods. This methodology was also extended to incompressible Navier-Stokes equations in [23], preserving the capability to circumvent Babuška-Brezzi condition and to generate stable approximations even for highly advective flows.

In the context of generalized Newtonian flows, some stabilized methods have already been proposed. Karam Filho et al. [24] present a stabilized formulation for a modified power-law equation that may accommodate mild advective flows. Perić and Slijepčević [25] employed a GLS scheme in the approximation of flows of Bingham materials, based on a Newton-backward Euler algorithm. Maniatty et al. [26] presented a stabilized mixed method for the calculation of viscoplastic flows employing a Petrov-Galerkin formulation, investigating the three-dimensional flow through a metal extruder.

This paper performs the stabilized finite element approximation of isochoric viscoplastic flows through a 4:1 planar expansion, also taking into account inertial effects. The employed mechanical model is based on the principle of power expended [27], and the principle of mass conservation, in a variational sense. In order to model the extra-stress tensor of a viscoplastic material, the Casson equation [7] has been employed, with the von Mises criteria [28] smoothed by Papanastasiou approximation [5]. A Newton-like algorithm for the solution of the resulting nonlinear algebraic system is also presented. Numerical results show the good stabilization features of the employed method even for flows subjected to high inertial effects and material nonlinearity.

2 Some Notation

The problems considered herein are defined on a bounded domain $\Omega \subset \mathbb{R}^{nsd=2,3}$ with a polygonal or polyhedral boundary Γ, formed by the union of Γ_g (the portion of Γ where Dirichlet conditions are imposed) and Γ_h (the portion subjected to Neumann boundary conditions). A partition C_h of $\bar{\Omega}$ into elements is performed in the usual way: no overlapping is allowed between any two elements, the union of all element domains Ω_K reproduces $\bar{\Omega}$ and a combination of triangles and quadrilaterals for the two-dimensional case can be accommodated. Quasi-uniformity is not assumed. Also, R_k and R_l denote the polynomial spaces of degree k and l, respectively [20].

As usual, $L^2(\Omega)$, $L^2_0(\Omega)$, $H^1(\Omega)$, and $H^1_0(\Omega)$ stand for Hilbert and Sobolev functional spaces, respectively, as follows:

$$L^2(\Omega) = \left\{ q \middle| \int_\Omega q^2 d\Omega < \infty \right\}$$

$$L^2_0(\Omega) = \left\{ q \in L^2(\Omega) \middle| \int_\Omega q d\Omega = 0 \right\}$$

$$H^1(\Omega) = \{ v \in L^2(\Omega) | \partial v/\partial x_i \in L^2(\Omega), \quad i = 1, nsd \} \tag{1}$$

$$H^1_0(\Omega) = \{ v \in L^2(\Omega) | \partial v/\partial x_i \in L^2(\Omega) | v = 0 \text{ on } \Gamma_g, \quad i = 1, nsd \}$$

with $C^0(\Omega)$ representing the space of continuous functions in Ω.

3 Mechanical Model

The mechanical modeling presented herein concerns a material body B for which its flow is defined by the triple velocity, mass density, and stress tensor fields, $(\mathbf{v}, \rho, \mathbf{T})$, and the associated system of contact and body forces, $(\mathbf{t}(\mathbf{n}), \mathbf{f})$.

3.1 Principle of Mass Conservation. The mass of a mechanical body B does not change with time. Making use of the Reynolds transport theorem [29] and assuming an incompressible fluid model, a variational mass principle for an isochoric motion may be stated as

$$\int_\Omega q \, \text{div} \, \mathbf{v} d\Omega = 0 \quad \forall \, q \in L^2(\Omega) \tag{2}$$

where Ω denotes a region of B with boundary Γ, $\mathbf{v}$ a virtual velocity field of the flow, and $L^2(\Omega)$, defined by Eq. (1), accounts for the functional space of the pressure field.

3.2 Principle of Power Expended (PPE) [27]. This dynamic principle is equivalent to the laws of conservation of momentum, formulated in a variational sense. Note that the PPE has the advantage of establishing a variational formulation for mechanical problems, which allows a natural and intuitive introduction of variational methods in fluid mechanics. The PPE asserts that, for any material volume Ω of a configuration B_t of body B at the time t, with $H^1(\Omega)^{nsd}$ denoting the space of virtual velocities associated to Ω:

(i) The power expended on Ω by body forces $\mathbf{f}$ and surface forces $\mathbf{t}(\mathbf{n})$ is equal to the stress power plus the rate of change of kinetic energy

$$\int_\Omega \rho \mathbf{f} \cdot \mathbf{v} d\Omega + \int_\Gamma \mathbf{t}(\mathbf{n}) \cdot \mathbf{v} d\Gamma = \int_\Omega \mathbf{T} \cdot \mathbf{D} d\Omega + \int_\Omega \rho \dot{\mathbf{v}} \cdot \mathbf{v} d\Omega$$
$$\forall \mathbf{v} \in H^1(\Omega)^{nsd} \tag{3}$$

where $\mathbf{T}$ stands for a second-order symmetric tensor.

(ii) For every rigid displacement of body B, at each time t, $\mathbf{v}(\cdot, t)$ has the form of an infinitesimal rigid displacement of B and admits the representation

$$\mathbf{v}(\mathbf{x}, t) = \mathbf{W}(t)(\mathbf{x} - \mathbf{x}_0) + \mathbf{v}(\mathbf{x}_0, t) \tag{4}$$

with $\mathbf{x}$ and $\mathbf{x}_0$ representing usual position vectors in relation to an inertial frame of reference and $\mathbf{W}$ the vorticity skew-symmetric tensor [27], it follows that

$$\int_\Omega \mathbf{T} \cdot \mathbf{D} d\Omega = 0 \quad \forall \, \mathbf{v} \in H^1(\Omega)^{nsd} \tag{5}$$

4 Finite Element Approximation

In this section, a Galerkin least-squares (GLS) formulation (see, for instance, [22,23]) for isochoric flows of generalized Newtonian fluids is presented. Enunciating the principle of power expended, Eqs. (3)–(5), to this class of liquids and imposing the principle of mass conservation, Eq. (2), a dimensionless variational formulation for the model defined by Eqs. (2)–(5) runs as

$$\int_\Omega [\text{grad}\,\mathbf{u}]\mathbf{u}\cdot\mathbf{v}d\Omega - \int_\Omega p\,\text{div}\,\mathbf{v}d\Omega + \int_\Omega 2\,\text{Re}^{-1}\,\eta^*(\dot\gamma^*)\mathbf{D}(\mathbf{u})\cdot\mathbf{D}(\mathbf{v})d\Omega - \int_\Omega q\,\text{div}\,\mathbf{u}d\Omega = \int_\Omega \text{Fr}^{-2}\mathbf{f}\cdot\mathbf{v}d\Omega + \int_{\Gamma_h}\mathbf{t}_h\cdot\mathbf{v}d\Gamma_h \quad \forall\,(\mathbf{v},q)\in H^1(\Omega)^{nsd}\times L^2(\Omega) \tag{6}$$

where $\mathbf{v}$ and $\mathbf{u}$ are, respectively, the virtual and admissible velocity fields, p the pressure one, Re the Reynolds number, Fr the Froude number, $\mathbf{D}$ the rate of strain tensor, $\eta(\dot\gamma)$ the fluid apparent viscosity [4], q the pressure weighting function, $\mathbf{f}$ the body force, and $\mathbf{t}_h$ the surface one. Furthermore, the flow characteristic velocity u_0, length L, viscosity η_0, and force f have been employed to normalize Eq. (6) in the following way:

$$\mathbf{x}=\frac{\mathbf{x}}{L};\quad \mathbf{u}=\frac{\mathbf{u}}{u_0};\quad p=\frac{pL}{\rho u_0^2};\quad \text{Fr}=\frac{u_0}{\sqrt{Lf}};\quad \mathbf{f}=\frac{\mathbf{f}}{f};\quad \eta^*(\dot\gamma^*)=\frac{\eta(\dot\gamma)}{\eta_0} \tag{7}$$

The usual functional spaces for fluid dynamics were employed to define the finite element subspaces for velocity ($\mathbf{V}^h$ and $\mathbf{V}_g^h$) and pressure (P^h) fields, over a partition C_h of the closed problem domain $\bar\Omega$ parametrized by a characteristic mesh size h [20]

$$P^h=\{p\in C^0(\Omega)\cap L_0^2(\Omega)|p_{|K}\in R_l(\Omega_K),\quad \Omega_K\in C_h\}$$

$$\mathbf{V}^h=\{\mathbf{v}\in H_0^1(\Omega)^{nsd}|\mathbf{v}_{|K}\in R_k(\Omega_K)^{nsd},\quad \Omega_K\in C_h\} \tag{8}$$

$$\mathbf{V}_g^h=\{\mathbf{v}\in H^1(\Omega)^{nsd}|\mathbf{v}_{|K}\in R_k(\Omega_K)^{nsd},\quad \Omega_K\in C_h,\quad \mathbf{v}=\mathbf{u}_g\ \text{on}\ \Gamma_g\}$$

Based on Eqs. (8), a Galerkin least-squares formulation for the nonlinear variational principle defined by Eq. (6) may be stated as: *Find the pair* $(\mathbf{u}^h,p^h)\times\mathbf{V}_g^h\cdot P^h$, *such as*

$$B(\mathbf{u}^h{:}\mathbf{u}^h,p^h;\mathbf{v}{:}\mathbf{u}^h,q)=F(\mathbf{v}{:}\mathbf{u}^h,q),\quad \forall\,(\mathbf{v},q)\in\mathbf{V}^h\times P^h \tag{9}$$

where

$$B(\mathbf{u}{:}\mathbf{u},p;\mathbf{v}{:}\mathbf{u},q)=\int_\Omega [\text{grad}\,\mathbf{u}]\mathbf{u}\cdot\mathbf{v}d\Omega + \int_\Omega 2\,\text{Re}^{-1}\,\eta^*(\dot\gamma^*)\mathbf{D}(\mathbf{u})\cdot\mathbf{D}(\mathbf{v})d\Omega - \int_\Omega p\,\text{div}\,\mathbf{v}d\Omega - \int_\Omega q\,\text{div}\,\mathbf{u}d\Omega + \sum_{\Omega_K\in C_h}\int_{\Omega_K}\{[\text{grad}\,\mathbf{u}]\mathbf{u}+\text{grad}\,p - 2\,\text{Re}^{-1}\,\text{div}[\eta^*(\dot\gamma^*)\mathbf{D}(\mathbf{u})]\}\cdot\{\tau(\text{Re}_K)([\text{grad}\,\mathbf{v}]\mathbf{u} - 2\,\text{Re}^{-1}\,\text{div}[\eta^*(\dot\gamma^*)\mathbf{D}(\mathbf{v})]-\text{grad}\,q)\}d\Omega_K \tag{10}$$

and

$$F(\mathbf{v}{:}\mathbf{u},q)=\int_\Omega \text{Fr}^{-2}\mathbf{f}\cdot\mathbf{v}d\Omega+\int_\Gamma\mathbf{t}\cdot\mathbf{v}d\Gamma + \sum_{\Omega_K\in C_h}\int_{\Omega_K}\text{Fr}^{-2}\mathbf{f}\cdot(\tau(\text{Re}_K)\{(\text{grad}\,\mathbf{v})\mathbf{u} - 2\,\text{Re}^{-1}\,\text{div}[\eta^*(\dot\gamma^*)\mathbf{D}(\mathbf{v})]-\text{grad}\,q\})d\Omega_K \tag{11}$$

with the terms within the sums of Eqs. (10) and (11) evaluated elementwise and its stability parameter τ being the same as in Franca and Frey [23], for the linear Newtonian fluid

$$\tau(\text{Re}_K)=\frac{h_K}{2|\mathbf{u}|_p}\xi(\text{Re}_K)\quad\text{with}\quad \xi(\text{Re}_K)=\begin{cases}\text{Re}_K, & 0\leqslant\text{Re}_K<1\\ 1, & \text{Re}_K\geqslant 1\end{cases} \tag{12}$$

where h_K stands for the K-element size, Re_K the grid Reynolds number and the $|.|_p$ the p-norm on $\mathbb{R}^{nsd}$.

4.1 Nonlinear Strategy. When the shape functions for $\mathbf{u}^h$ and p^h are introduced in the GLS formulation, Eqs. (9)–(12), an algebraic residual set of equation is yielded in the form:

$$\mathbf{R}(\mathbf{U})=\mathbf{0} \tag{13}$$

where $\mathbf{U}$ is the vector of degrees of freedom of $\mathbf{u}^h$ and p^h, and $\mathbf{R}(\mathbf{U})$ is given by the set of matrices

$$\mathbf{R}(\mathbf{U})=\mathbf{N}(\mathbf{u})\mathbf{u}+\mathbf{N}_\tau(\eta^*(\dot\gamma^*),\mathbf{u})\mathbf{u}+[\mathbf{K}(\eta^*(\dot\gamma^*))+\mathbf{K}_\tau(\eta^*(\dot\gamma^*),\mathbf{u})]\mathbf{u} + [\mathbf{G}+\mathbf{G}_\tau(\eta^*(\dot\gamma^*),\mathbf{u})]\mathbf{p}+\mathbf{G}^T\mathbf{u}-\mathbf{F}-\mathbf{F}_\tau(\eta^*(\dot\gamma^*),\mathbf{u}) \tag{14}$$

In Eq. (14), matrices $[\mathbf{K}]$ and $[\mathbf{G}]$ are, respectively, originated by the diffusive and pressure terms of Eqs. (10) and (11), and $\mathbf{N}(\mathbf{u})$, $\mathbf{G}^T$, $\mathbf{F}$ by the advective, incompressibility and body force ones. (The $\mathbf{N}(\mathbf{u})_\tau$, $[\mathbf{K}]_\tau$, $[\mathbf{G}]_\tau$, $\mathbf{N}(\mathbf{u})_\tau$, and $\mathbf{F}_\tau$ in Eq. (14) are generated by the least-squares terms of Eqs. (10) and (11).) To solve system (13) and (14), we have implemented a quasi-Newton method (see for instance, Dalquist and Bjorck [30]), where the Jacobian matrix was updated only at each two or three iterations.

Algorithm.

I. Estimate vector $\mathbf{U}^0$ and set the number of iterations (n) to update Jacobian matrix $\mathbf{J}(\mathbf{U})$.

II. Set $i=0, j=0, \varepsilon=10^{-7}$.

III. If $i-\text{int}(i/n)*i=0$, then $j=i$.

IV. Solve for incremental vector $\mathbf{a}^{i+1}$:

$$\mathbf{J}(\mathbf{U}^j)\mathbf{a}^{i+1}=-\mathbf{R}(\mathbf{U}^i) \tag{15}$$

where $\mathbf{R}(\mathbf{U})$ is given by Eq. (14) and $\mathbf{J}(\mathbf{U})$ defined by

$$\mathbf{J}(\mathbf{U})=\mathbf{N}(\mathbf{u})+\frac{\partial\mathbf{N}(\mathbf{u})}{\partial\mathbf{u}}\mathbf{u}+\mathbf{N}_\tau[\eta^*(\dot\gamma^*),\mathbf{u}]+\frac{\partial\mathbf{N}_\tau[\eta^*(\dot\gamma^*),\mathbf{u}]}{\partial\mathbf{u}}\mathbf{u} + \mathbf{K}[\eta^*(\dot\gamma^*)]+\mathbf{K}_\tau[\eta^*(\dot\gamma^*),\mathbf{u}]+\frac{\partial\mathbf{K}_\tau(\eta^*(\dot\gamma^*),\mathbf{u})}{\partial\mathbf{u}}\mathbf{u}+\mathbf{G} + \frac{\partial\mathbf{G}_\tau(\eta^*(\dot\gamma^*),\mathbf{u})}{\partial\mathbf{u}}\mathbf{p}+\mathbf{G}_\tau[\eta^*(\dot\gamma^*),\mathbf{u}]+\mathbf{G}^T-\frac{\partial\mathbf{F}_\tau(\eta^*(\dot\gamma^*),\mathbf{u})}{\partial\mathbf{u}} \tag{16}$$

IV. Compute vector $\mathbf{U}^{i+1}$:

$$\mathbf{U}^{i+1}=\mathbf{U}^i+\mathbf{a}^{i+1} \tag{17}$$

V. Compute $|\mathbf{R}(\mathbf{U}^i)|_\infty$. If $|\mathbf{R}(\mathbf{U}^i)|_\infty>\varepsilon$, then do $i=i+1$ and go to step III; otherwise, store solution $\mathbf{U}^{i+1}$ and exit from the algorithm.

Remark. As initial solution estimates, null velocity and pressure fields were employed in the algorithm. In order to improve algorithm convergence, we implemented a continuation method [30] on advective terms of Eqs. (13) and (14).

5 Numerical Results

In this section, the Galerkin least-squares approximation (Eqs. (9)–(12)) for two-dimensional steady-state flows of viscoplastic fluids was performed. In all numerical simulations, a pair of bilinear Lagrangean interpolations was employed to approximate velocity and pressure fields. All computations were carried out by a finite element code for nonlinear fluids under development in the Laboratory of Computational and Applied Fluid Mechanics (LAMAC) of the Federal University of Rio Grande do Sul.

5.1 Code Validation. As a check for the computational implementation of the GLS formulation defined by Eqs. (9)–(12), two distinct classes of nonlinear flows have been approximated. First, we performed the simulation of Newtonian flows subjected to high advective transport of momentum. The lid-driven cavity problem was built in the usual manner (see, for instance, Franca and Frey [23] for details of the problem statement). The velocity boundary conditions were impermeability and nonslip at cavity walls except the upper one, on which a horizontal velocity u_0 was prescribed. In the Reynolds definition, the zero-shear-rate viscosity η_0 was taken as the flow characteristic viscosity and the characteristic length was set as one. The Reynolds number was investigated for values from 400 to 5000, although the latter one is no more within the flow laminar regime.

The velocity and pressure computations were compared to the results presented in Hannani et al. [31] and their references. These authors compiled the performance of various finite element methods for the lid-driven cavity benchmark, employing regular meshes of 30×30, 32×32, 45×45, and 80×80 Q_1/Q_1 elements. In the present work, the results obtained employing an 80×80 mesh were very close to those presented in [31], as depicted in Figs. 1(*a*) and 1(*b*), for velocity and pressure transversal profiles, respectively, in the middle of the cavity and Re=400. As indicated in these figures, the results for the coarser mesh of 20×20 Q_1/Q_1 elements shown to be a little overdiffusive.

The code capability to deal with material nonlinearity was also checked via the approximation of viscoplastic flows in a lid-driven cavity, as proposed by Mitsoulis and Zisis [32]. The material model employed was the modified Bingham equation [5]

$$\eta = \eta_0 + \frac{\tau_0}{\dot{\gamma}}[1-\exp(-m\dot{\gamma})] \tag{18}$$

for which τ_0 stands for the extra stress tensor and the Bingham number is defined as

$$\mathrm{Bi} = \frac{\tau_0 L}{\eta_0 u_0} \tag{19}$$

The Reynolds number was assumed negligible, and results were obtained for the Bingham number varying from zero (Newtonian fluid) to 200, employing a 80×80 Q_1/Q_1 finite element mesh. The parameter m in Eq. (18) was taken equal to 200 as suggested in Mitsoulis and Zisis [32] in order to reproduce the Bingham model. Streamlines, yielded zones, vortex size, as well as its eye position, were successfully compared to [32]. Figure 2(*a*) shows the position of the eye of the vortex versus Bingham number and, in Fig. 2(*b*), the material unyielded zones are depicted for Bi =50. As it may be noticed, in the regions subjected to low shear stress (the two black zones of Fig. 2(*b*)), the material remains unyielded, with its yield stress not being reached in both regions. In the upper black region, the material underwent a rigid body motion while, in the lower one, the material remained stagnated, as it may be observed in the streamlines of Fig. 2(*c*). In this figure, the clockwise motion imposed by velocity boundary conditions is illustrated by the streamline labels.

Remark. The nonsmoothness of yield contours in Fig. 2(*b*) is due to the stress post-processing. As the velocity gradient components are smooth (piecewise constant functions) on each element interior but discontinuous across each element boundary, the bilinear shape functions, employed in the stress post-processing, were only able to generate the steplike pattern illustrated in Fig. 2(*b*). (It is worth noting that a similar pattern was also presented by Mitsoulis and Zisis [32].)

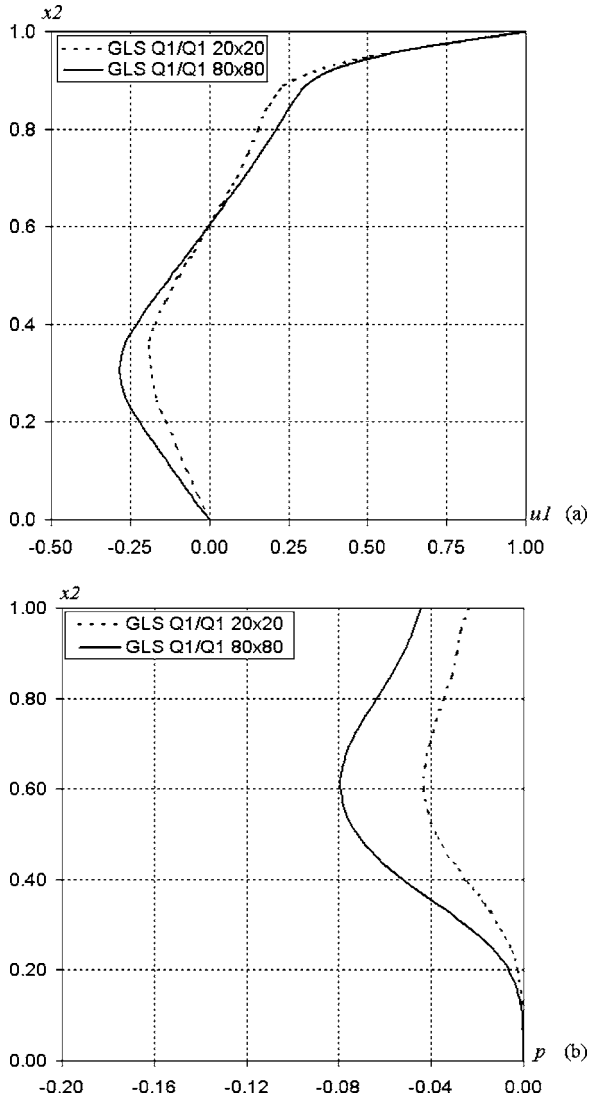

Fig. 1 Lid-driven cavity flow, for Re=400: (*a*) velocity and (*b*) pressure profiles

5.2 Planar Expansion of Viscoplastic Flows. In this section, Galerkin least-squares approximations (Eqs. (9)–(12)) have been performed for flows of viscoplastic fluids through a 4:1 planar expansion (see Fig. 3 for the problem statement). As velocity boundary conditions, we have imposed impermeability and no-slip at expansion walls, a flat horizontal profile at channel inlet and free traction at its exit. (Because of computational tasks, only half domain has been considered. At symmetry line, the vertical velocity and the transversal gradient of the horizontal velocity were set as zero.)

In order to model the fluid viscoplastic behavior, a widely employed constitutive equation, the Casson equation [7], was used

$$\eta^{1/2} = \eta_0^{1/2} + \left(\frac{\tau_0}{\dot{\gamma}}\right)^{1/2} \quad \text{for } |\boldsymbol{\tau}|_2 > \tau_0$$
$$\dot{\gamma} = 0 \quad \text{for } |\boldsymbol{\tau}|_2 \leq \tau_0 \tag{20}$$

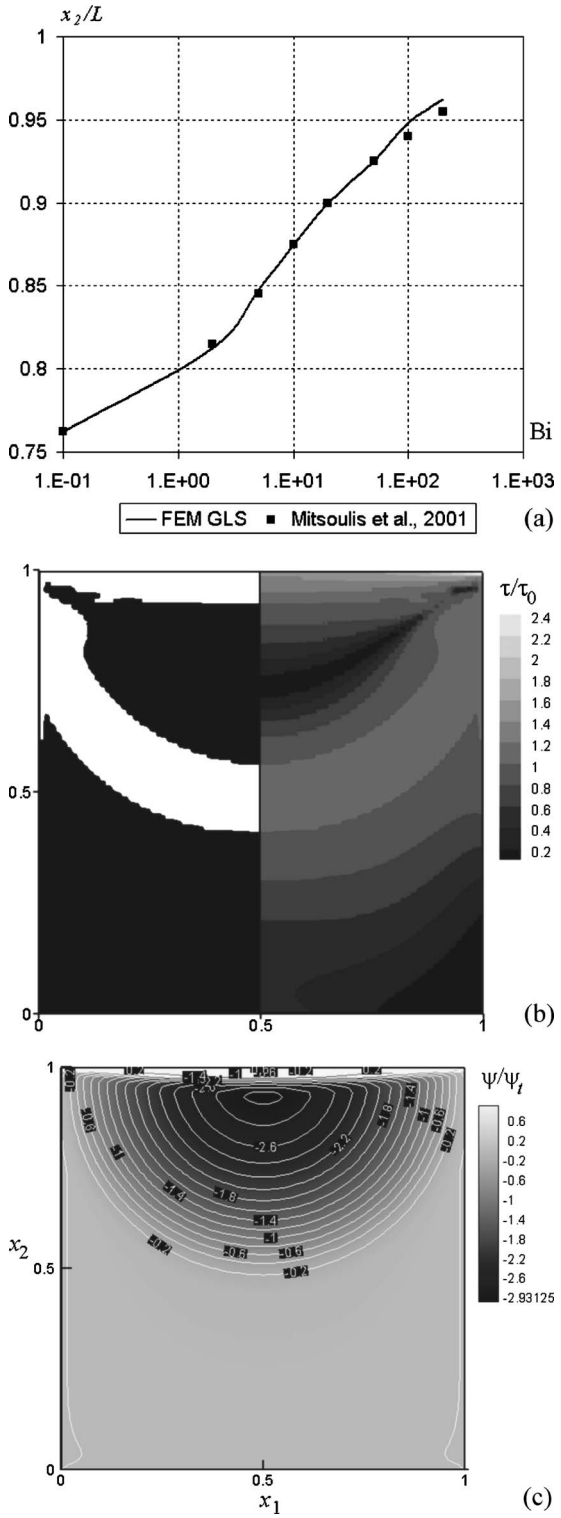

Fig. 2 The lid-driven cavity flow of a Bingham liquid, for Bi =50: (*a*) eye of the vortex position, (*b*) unyielded zones and extra-stress contours, and (*c*) flow streamlines

with τ denoting the extra stress tensor, $\boldsymbol{\tau}=\mathbf{T}-p\mathbf{I}$.

Furthermore, aiming to circumvent the discontinuity of the shear stress magnitude inherent from the von Mises criterion, Papanastasiou [5] proposed a modification for viscoplastic models that, when applied to the Casson equation (7), results into the following modified Casson dimensionless viscosity,

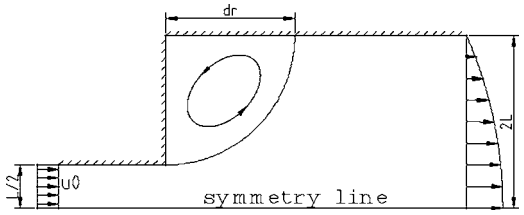

Fig. 3 Planar 4:1 expansion: problem statement

$$(\eta^*)^{1/2} = 1 + \left(\frac{\mathrm{Ca}}{\dot{\gamma}^*}\right)^{1/2} \{1 - \exp[-(m\dot{\gamma}^*)^{1/2}]\} \tag{21}$$

where

$$\eta^*(\dot{\gamma}^*) = \frac{\eta(\dot{\gamma})}{\eta_0}; \quad \dot{\gamma}^* = \frac{\dot{\gamma}}{u_0/L}; \quad \mathrm{Ca} = \frac{\tau_0 L}{\eta_0 u_0} \tag{22}$$

and Ca is denoted as Casson number. Equation (21) is valid to both yielded and unyielded regions of the flow, and the exponent m controls the smoothness of its function. For $m \geqslant 100$, this equation mimics the original Casson model [14]. (In our computation, we have set $m=200$ in Eq. (21).) The results shown herein were obtained using a finite element mesh of 6200 Q_1/Q_1 elements. In order to guarantee fully developed flow upstream and downstream the expansion, an appropriate channel length has been selected. The values of Reynolds number were equal to 1, 10, and 50, and the Casson number (Eq. (22)) varied between 0 (Newtonian fluid) and 10.

Flows of viscoplastic materials inside ducts are known to form a plug flow region due to the low shear stresses far from the walls [28]. In the particular case of flows through expansions, the low shear stresses in their corners may form plastic (unyielded) regions, a phenomenon which is more severe for higher values of Casson number ([14–16]). In order to illustrate that behavior, the arising and position of unyielded zones were verified applying the von Mises criterion [28] to the stress post-processing. Figures 4(*a*)–4(*d*) show a detail of the growth of the unyielded zones with the increasing of Casson number (Ca=0.1, 1, 3, and 10). Similar behavior was observed for the other investigated Reynolds numbers and, for this reason, these results were omitted.

The unyielded zone in the corner of the expansion may become an obstacle to the vortex development. Based on the performed computations, it was possible to note that the vortex arising is subjected to sufficient high values of Reynolds number combined with low Casson ones. For low Reynolds flows, namely, Re=1 and Re=10, with the results for the latter depicted in Figs. 4, the vortex was mild even for the Newtonian fluid (Ca=0) and, for viscoplastic ones, a stagnant region was generated in the corner of the expansion for Casson numbers equal to 1, 3, and 10, respec-

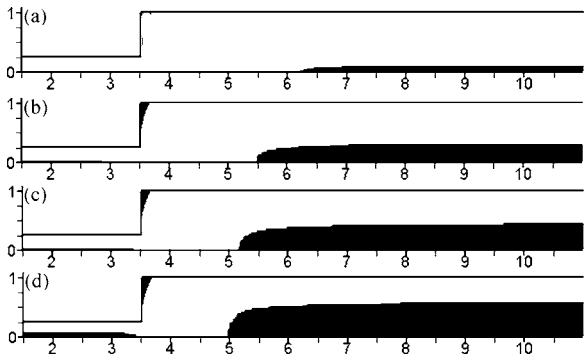

Fig. 4 Details of unyielded zones (in black), Re=10: (*a*) Ca =0.1, (*b*) Ca=1, (*c*) Ca=3, and (*d*) Ca=10

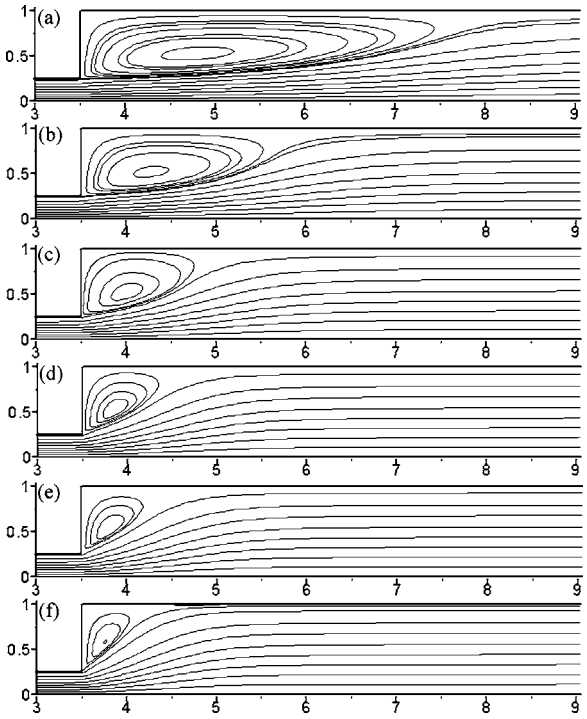

Fig. 5 Detail of viscoplastic flow streamlines, Re=50: (*a*) Ca =0, (*b*) Ca=0.1, (*c*) Ca=0.4, (*d*) Ca=0.8, (*e*) Ca=1 and (*f*) Ca =1.5

tively, Figures 4(*b*)–4(*d*). For Re=50, if the Casson number is sufficiently small, as in Figs. 5(*b*) and 5(*c*), a Newtonian-like vortex still appears. However, for higher values of Casson number, as in Figs. 5(*d*)–5(*f*), the vortex enhancement with the increase of the Reynolds number was counterbalance by the rigid zone enhancement, which opposes the vortex growth. The topology of this rigid zone may be a good explanation for the distinct vortex shapes in viscoplastic and Newtonian flows.

In Fig. 6, one may note the growth of the unyielded zone. First, for small values of Casson number (Figs. 6(*a*)–6(*c*)), there is the formation of two distinct unyielded portions, one at the expansion corner and another, at the upper wall, in the stagnation point between the vortex and the main flow. Following, with the increase of the Casson number (as illustrated in Figs. 6(*d*) and 6(*e*)), these two regions grow until an unique unyielded rigid zone is formed. (Find, in Fig. 7, the stress and streamline contours for this latter case, namely, Ca=1.5 and Re=50.) This phenomenon was first observed by Jay et al. [16] in their numerical investigation using a Herschel-Bulkley model in axisymmetric flows—a phenomenon also experimentally confirmed by the authors employing a viscoplastic material.

In Fig. 8, the dimensionless reattachment length, $d=d_r/L$, is plotted versus the Casson number for two different meshes, in order to test the mesh independence of the results presented in Figs. 4–7. As it may be observed, for Casson numbers greater than 2.5, the vortex structure has become so small that a reattachment length could hardly be perceptive. This feature is due to the already discussed vortex spacing from the expansion corner with the increase of the unyielded zone.

6 Concluding Remarks

This paper exploited a continuum mechanical model for generalized Newtonian flows that suits even advective-dominated and geometrically complex flows. A Galerkin least-squares formulation for that model was able to achieve stable and physical realistic results for flows of a viscoplastic fluid, modeled by the Casson constitutive equation, through a 4:1 planar expansion. The

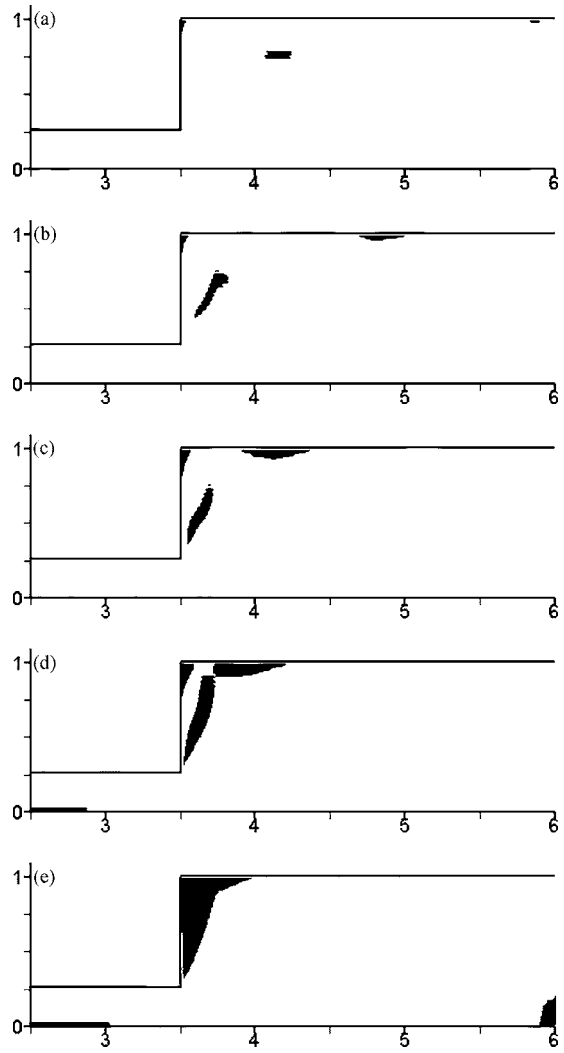

Fig. 6 Structure of the unyielded zone (detail), Re=50: (*a*) Ca =0.1, (*b*) Ca=0.4, (*c*) Ca=0.8, (*d*) Ca=1, and (*e*) Ca=1.5

arising of unyielded regions in the material seems to strongly affect its flow pattern, specially concerning its vortex structure. This one is plainly reduced with the increase of the Casson number even for flows in which the inertia effects may not be neglected.

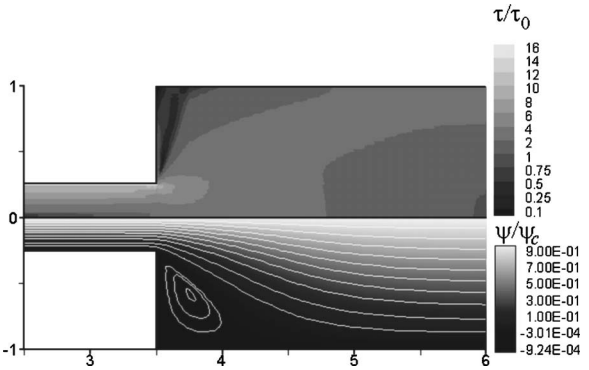

Fig. 7 Extra stress and streamlines contours (detail), for Re =50 and Ca=1.5

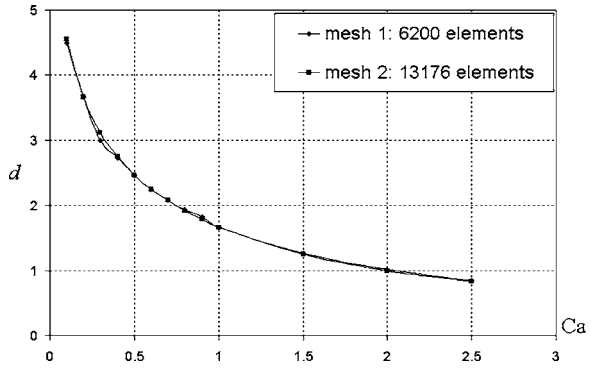

Fig. 8 Reattachment length versus Ca for Re=50

Acknowledgment

Author F. Zinani thanks the doctoral grant provided by CAPES and author S. Frey thanks the agency CNPq for the researcher Grant No. 50747/1993-8. The authors also acknowledge the agency MCT/CNPq for the financial support provided by Project No. 475432/2003-7.

Nomenclature

$\mathbf{a}$ = incremental vector
B = mechanical body
B = GLS functional
Bi = Bingham number
C^0 = space of continuous functions
Ca = Casson number
C_h = finite element partition
$\mathbf{D}$ = strain rate tensor
d = reattachment length
div = divergence operator
d_r = reattachment length
F = GLS functional
$\mathbf{F}$ = momentum load vector
Fr = Froude number
$\mathbf{f}$ = body force
f = characteristic body force
$\mathbf{G}$ = incompressibility matrix
grad = gradient operator
H^1 = Sobolev functional space
h_K = element size
$\mathbf{I}$ = identity tensor
int(i) = value of i truncated to an integer
$\mathbf{J}$ = Jacobian matrix
$\mathbf{K}$ = momentum diffusive matrix
L = characteristic length
L^2 = Hilbert functional space
m = Papanastasiou's approximation parameter
$\mathbf{N}$ = momentum advective matrix
$\mathbf{n}$ = unit vector
P = pressure functional space
p = pressure field
q = pressure variation function
$\mathbf{R}$ = residual vector
$\mathbb{R}$ = set of real numbers
Re = Reynolds number
R_k = polynomial functional space of degree k
$\mathbf{T}$ = stress tensor
$\mathbf{t}$ = stress vector
t = time instant
$\mathbf{U}$ = vector of degrees of freedom
$\mathbf{u}$ = admissible velocity field
u_0 = characteristic velocity
$\mathbf{V}$ = velocity functional space
$\mathbf{v}$ = virtual velocity field
$\mathbf{W}$ = vorticity tensor
$\mathbf{x}$ = position vector
$|.|_p$ = p-norm on $\mathbb{R}^{nsd}$

Greek Symbols

ε = maximum error
$\dot{\gamma}$ = magnitude of tensor $\mathbf{D}$
Γ = domain boundary
η = fluid viscosity
η_0 = characteristic viscosity
ρ = mass density
τ = GLS stability parameter
τ_0 = yield stress
Ω = problem domain
Ω_K = element domain
ξ = upwind function

Subscripts

g = Dirichlet boundary condition
h = Neumann boundary condition
K = finite element
τ = GLS stabilized matix

Superscripts

h = finite element approximation
nsd = number of space dimension
* = dimensionless

References

[1] Crochet, M. J., Davies, A. R., and Walters, K., 1984, *Numerical Simulation of Non-Newtonian Flow*, Vol. 1, Rheology Series, Elsevier, Amsterdam.
[2] Owens, R. G., and Phillips, T. N., 2002, *Computational Rheology*, Imperial College Press, London.
[3] Reiner, M., 1960, *Deformation, Strain and Flow*, Interscience, New York.
[4] Bird, R. B., Armstrong, R. C., and Hassager, O., 1987, *Dynamics of Polymeric Liquids, Vol. 1, Fluid Dynamics*, John Wiley, New York.
[5] Papanastasiou, T. C., 1987, "Flows of Materials With Yield," J. Rheol., **31**, pp. 385–404.
[6] Barnes, H. A., 1999, "The Yield Stress—A Review or '$\pi\alpha\nu\tau\alpha$ $\rho\varepsilon\iota$'—Everything Flows?," J. Non-Newtonian Fluid Mech., **81**, pp. 133–178.
[7] Casson, N. A., 1959, "Rheology of Disperse Systems," *Proceedings of a Conference Organized by the British Society of Rheology*, C. C. Mills, Ed., Pergamon Press, New York.
[8] Chevalley, J., 1974, "Rheology of Chocolate," J. Texture Stud., **6**, pp. 177–196.
[9] Casas, J. A., Santos, V. E., and Garcya-Ochoa, F., 2000, "Xanthan Gum Production Under Several Operational Conditions: Molecular Structure and Rheological Properties," Enzyme Microb. Technol., **26**(2–4), pp. 282–291.
[10] Macosko, C. W., 1994, *Rheology, Principles, Measurements and Applications*, Wiley-VCH, New York.
[11] Cokelet, G. R., 1999, "Viscometric, in Vitro and in Vivo Blood Viscosity Relationships: How Are They Related?," Biorheology, **36**(5–6), pp. 343–358.
[12] Pak, B., Cho, Y. I., and Choi, S. U. S., 1990, "Separation and Reattachment of Non-Newtonian Fluid Flows in a Sudden Expansion Pipe," J. Non-Newtonian Fluid Mech., **37**, pp. 175–199.
[13] Abdali, S. S., Mitsoulis, E., and Markatos, N. C., 1992, "Entry and Exit Flows of Bingham Fluids," J. Rheol., **36**, pp. 389–407.
[14] Pham, T. V., and Mitsoulis, E., 1994, "Entry and Exit Flows of Casson Fluids," Can. J. Chem. Eng., **72**, pp. 1080–1084.
[15] Vradis, G. C., and Ötüngen, M. V., 1997, "The Axisymmetric Sudden Expansion of a Non-Newtonian Viscoplastic Fluid," ASME J. Fluids Eng., **119**, pp. 193–200.
[16] Jay, P., Magnin, A., and Piau, J. M., 2001, "Viscoplastic Fluid Flow Through a Sudden Axisymmetric Expansion," AIChE J., **47**, pp. 2155–2166.
[17] Reis, L. A., Jr., and Naccache, M. F., 2003, "Analysis of Non-Newtonian Flows Through Contractions and Expansions," *Proceedings of XVII COBEM*, São Paulo, ABCM, São Paulo.
[18] Neofytou, P., and Drikakis, D., 2003, "Non-Newtonian Flow Instability in a Channel With a Sudden Expansion," J. Non-Newtonian Fluid Mech., **111**, pp. 127–150.
[19] Mitsoulis, E., and Huilgol, R. R., 2004, "Entry Flows of Bingham Plastics in Expansions," J. Non-Newtonian Fluid Mech., **122**, pp. 45–54.
[20] Ciarlet, P. G., 1978, *The Finite Element Method for Elliptic Problems*, North-Holland, Amsterdam.
[21] Brooks, A. N., and Hughes, T. J. R., 1982, "Streamline Upwind/Petrov-Galerkin Formulations for Convective Dominated Flows With Particular Emphasis on the Incompressible Navier-Stokes Equations," Comput. Methods

Appl. Mech. Eng., **32**, p. 199–259.
[22] Hughes, T. J. R., Franca, L. P., and Balestra, M., 1986, "A New Finite Element Formulation for Computational Fluid Dynamics: V. Circumventing the Babuška-Brezzi Condition: A Stable Petrov-Galerkin Formulation of the Stokes Problem Accommodating Equal-Order Interpolations," Comput. Methods Appl. Mech. Eng., **59**, pp. 85–99.
[23] Franca, L. P., and Frey, S., 1992, "Stabilized Finite Element Methods: II. The Incompressible Navier-Stokes Equations," Comput. Methods Appl. Mech. Eng., **99**, pp. 209–233.
[24] Karam Filho, J., Guerreiro, J. N., and Almeida, R. C., 2003, "Stabilized FEM Methods for Generalized Newtonian Flows," *Proceedings of the XVII COBEM*, São Paulo, ABCM, São Paulo.
[25] Perić, D., and Slijepčević, S., 2001, "Computational Modelling of Viscoplastic Fluids Based on a Stabilized Finite Element Method," Eng. Comput., **18**, pp. 577–591.
[26] Maniatty, A. M., Liu, Y., Klaas, O., and Shephard, M S., 2001, "Stabilized Finite Element Method for Viscoplastic Flow: Formulation and a Simple Progressive Solution Strategy," Comput. Methods Appl. Mech. Eng., **190**, pp. 4609–4625.
[27] Gurtin, M. E., 1981, *An Introduction to Continuum Mechanics*, Academic Press, New York.
[28] Bird, R. B., Dai, G. C., and Yarusso, B. J., 1982, "The Rheology and Flow of Viscoplastic Materials," Rev. Chem. Eng., **1**, pp. 1–70.
[29] Truesdell, C., and Toupin, R. A., 1960, "The Classical Field Theories," *Encyclopedia of Physics*, S. Flugge (ed.), Springer-Verlag, Berlin, Vol. III/1.
[30] Dahlquist, G., and Bjorck, A., 1969, *Numerical Methods*, Prentice-Hall, Englewood Cliffs, N.J..
[31] Hannani, S. K., Stanislas, M., and Dupont, P., 1995, "Incompressible Navier-Stokes Computations With SUPG and GLS Formulations—A Comparison Study," Comput. Methods Appl. Mech. Eng., **124**, pp. 153–170.
[32] Mitsoulis, E., and Zisis, T., 2001, "Flow of Bingham Plastics in a Lid-Driven Square Cavity," J. Non-Newtonian Fluid Mech., **101**, pp. 173–180.

Roberto C. Aguirre
Graduate Student
Mem.ASME

Haris J. Catrakis[1]
Associate Professor
Mem.ASME
e-mail: catrakis@uci.edu

Jennifer C. Nathman
Graduate student
Mem.ASME

Philip J. Garcia
Graduate student
Mem.ASME

Iracletos Flow Dynamics and Turbulence Laboratories,
Mechanical and Aerospace Engineering,
University of California,
Irvine, CA 92697

Robust Volume-Based Approach for the Turbulent Mixing Efficiency

This paper considers the mixture fraction which is often used to quantify the turbulent mixing efficiency in fluid engineering devices. We contrast a volume-based approach, where the mixture fraction is quantified directly using the volume bounded by the interface between mixed versus pure fluid, to a surface-based approach that requires area integrals of all mixed-fluid interfaces. Experimentally, we investigate the resolution-scale robustness of the volume-based approach compared to the small-scale sensitivity of the surface-based approach. The difference in robustness between these approaches has implications for examining, modeling, and optimizing the turbulent mixing efficiency.
[DOI: 10.1115/1.2201628]

1 Introduction

In a variety of engineering devices involving turbulent mixing, improved design and performance often require knowledge of the turbulent mixture fraction which is sometimes also known as the mixing efficiency [1–15]. Examples of engineering applications include fluid-injection systems for mass transfer and/or heat transfer, combustors for vehicle propulsion, signature-reduction methods for transport vehicles, directed fluid-projection systems, internal film cooling for turbomachinery, external film cooling for high-speed flight, and aero-optical systems for directed-energy propagation [16–21]. Optimization of the mixing efficiency, as well as knowledge of its dependence on flow geometry and on flow/fluid parameters such as Reynolds number, Mach number, and Schmidt number, are needed in such applications [1]. Mixing reduction, for example, is typically needed for film-cooling applications while mixing enhancement is generally needed for signature-reduction or combustion applications. In addition, with the increasing use of computational simulations of turbulent mixing, accurate physical modeling of the mixing efficiency is desired from large-eddy simulations of large-Reynolds-number mixing for various applications [2]. Quantified as the volume fraction of mixed fluid, the mixing efficiency is directly related to the geometrical properties of the mixed-fluid interfaces [4,9]. In particular, much emphasis has been placed in previous works on the interfacial area-volume ratio [4,6] as a means to model the mixing efficiency.

Practical and basic questions remain unresolved regarding the turbulent mixing efficiency. How does the mixing efficiency vary with increasing Reynolds number? What is its limiting behavior, i.e., at large Reynolds numbers? What are the compressibility effects on the mixing efficiency? How does the mixing efficiency depend on the flow geometry? While previous work has provided some answers to such questions [4,13], challenges remain with regard to the examination, modeling, and optimization of the mixing efficiency which need to be resolved in order to improve the prediction and performance of devices which rely on, or involve, mixing [4]. In particular, to extrapolate results from laboratory-scale Reynolds numbers to the larger Reynolds numbers typical in various mixing applications, it will help to be able to identify the dominant contributions to the mixing efficiency. This provides a helpful prospect for optimizing mixing-enhancement or mixing-reduction techniques. Enhancement/reduction techniques typically rely on increasing or decreasing the growth rate, respectively. Beyond this, further enhancement or reduction require other means to modify the mixing efficiency.

Previous efforts to examine the mixing efficiency have primarily focused on evaluating the surface area of the mixed-fluid interfaces [3,4,6–13], even though the definition of the mixing efficiency is directly as a volume fraction. Because these interfaces can be highly convoluted and exhibit complex geometrical structure over a wide range of scales, it is challenging to accurately capture their surface area [4,22–24] especially at large Reynolds numbers. Also, it is known that flow conditions above the mixing transition are needed in order to observe mixing behavior that is representative of fully developed turbulent mixing and therefore that can be extrapolated to larger Reynolds numbers [3,4,25]. The mixing transition is equivalent to the transition to fully developed turbulence. It requires a Reynolds number of at least Re $\sim$10,000 to occur. This corresponds to a separation between the larger scales, whose dynamics are directly determined by the energy-containing vortices, and the smaller scales which are directly affected by viscosity [25]. As a result of the presence of additional smaller scales above the mixing transition, methods based on direct examination of the interfacial surface area have practical limitations. There exist alternative experimental approaches, e.g., based on chemical reactions, that overcome some of these limitations [13,26,27], but without relating the mixing efficiency to the interfacial behavior of the flow.

In the present work, we contrast a volume-based approach to the traditional surface-based approach to the mixing efficiency. Recently, a volume-based methodology [15,28] utilizing directly the definition of the mixing efficiency as a volume fraction has been considered based on the properties of the outer interface between pure fluid and mixed fluid. In the volume-based approach, in contrast to the surface-based approach, one examines directly the volume of the region of fluid bounded by the outer interface. In the recent work [28], the robustness to resolution

[1]Corresponding author.

Contributed by the Fluids Engineering Division of ASME for publication in the JOURNAL OF FLUIDS ENGINEERING. Manuscript received September 15, 2004; final manuscript received November 12, 2005. Assoc. Editor: Malcolm J. Andrews. Paper presented at the 2004 ASME International Mechanical Engineering Congress (IMECE2004), November 13–19, 2004, Anaheim, California, USA.

scale was reported for spatial two-dimensional data only and without a comparison to the surface-based approach. In the present work, we report results for three-dimensional space-time data combined with Taylor's hypothesis in order to compare the resolution-scale robustness of the volume-based approach to the small-scale sensitivity of the surface-based approach. In Sec. 2, the theoretical ideas are described with a focus on geometrical relations between volume-based and surface-based interfacial quantities. Depending on the application, knowledge of either or both of these types of quantities may be necessary. For the particular case of the mixing efficiency, we consider theoretical aspects of the differences in interfacial properties for the volume-based versus surface-based approaches. In Sec. 3, the experimental flow facility and imaging technique are described that were utilized to conduct direct imaging of turbulent fluid interfaces at fully developed flow conditions, with resolution over a wide range of scales. A specially constructed large-scale flow facility was operated, combined with laser-induced fluorescence digital-imaging techniques, in order to provide sufficient flow size and attain whole-field high resolution. Examples of visualizations of resolution-scale effects on the outer interfaces are presented. In Sec. 4, quantitative results contrasting the volume-based versus surface-based approaches are presented. A comparison of scalar-threshold effects is made between the interfacial surface area, the probability density of mixed fluid, and the strain-limited diffusion thickness of the interfaces. Resolution-scale effects are examined on the probability of finding pure fluid, the volume of mixed fluid bounded by the outer interface, and the dynamic behavior of the mixing efficiency. While the main focus of this paper is on the effects of modifying the resolution with regard to robustness and sensitivity, the effects of modifying the flow geometry are examined in the companion technical brief [29]. In Sec. 5, implications are discussed in the context of examining, modeling, and optimizing the mixing efficiency.

2 Theoretical Considerations

As in a large body of preceding work on turbulent mixing [1–15], we consider the mixture fraction or volume fraction of mixed fluid as a measure of the mixing efficiency which we denote as α_m. The turbulent mixing efficiency can be expected in general to be a function of Reynolds number Re, Mach number M, Schmidt number Sc, flow geometry, and other parameters

$$\alpha_m \equiv \alpha_m(\mathrm{Re},\mathrm{M},\mathrm{Sc},\ \text{flow geometry},\ \ldots) \tag{1}$$

with

$$\alpha_m = \int_{\text{mixed}} p(c)dc = 1 - \int_{\text{pure}} p(c)dc \tag{2}$$

where $p(c)$ denotes the probability density of concentration c, and the mixing efficiency is in the range

$$0 \leqslant \alpha_m \leqslant 1 \tag{3}$$

The integrals in Eq. (2) are continuous integrals since the concentration is a continuous variable as well. The first integral in Eq. (2) is over the region of mixed fluid and the second integral is over the region of pure fluid. In practice, this requires particular care to ensure that one has properly identified the mixed fluid as opposed to pure fluid [8]. Adopting a normalized range of concentration values $0 \leqslant c \leqslant 1$, with pure fluids corresponding to $c=0$ and $c=1$, the mixed fluid has values in the range $0<c<1$. As long as the fluids are miscible, diffusion even in competition with straining ensures the existence of a range of mixed-fluid concentration values. For miscible fluids, the Schmidt number $\mathrm{Sc}=\nu/\mathcal{D}$ is finite and $0<\alpha_m \leqslant 1$. Here ν is the kinematic viscosity and $\mathcal{D}$ is the molecular diffusivity. The upper limiting value of the mixing efficiency, $\alpha_m=1$ can be expected to be, most likely, unattainable in practice even at large Re where $\mathrm{Re}=UL/\nu$ is the Reynolds number, even with flow control [1]. This is because the outer interface, that separates pure fluid from mixed fluid, is highly convoluted at large Reynolds numbers [23]. Since the mixing efficiency is essentially the amount of mixed fluid normalized by the maximum extent of the turbulent flow region under consideration, the irregular structure of the convoluted outer interfaces prevents the limiting value $\alpha_m=1$ from being attained. One can appreciate that the mixing efficiency α_m can be examined as a dynamic quantity, i.e., as a function of time, or as an ensemble-averaged quantity for given flow conditions. It can be noted that there are other measures of the mixing efficiency also in use in the literature [30–32]. Previously employed equivalent terminologies for the mixing efficiency, quantified as the volume fraction of mixed fluid, are mixture fraction [2], mixed-fluid fraction [6], and mixedness [3].

In the interest of developing ideas useful for engineering devices operating in large-Reynolds-number flow regimes, a useful starting point is to appreciate that a minimum Reynolds number of $\mathrm{Re}\sim 10{,}000$ is necessary for the mixing behavior to be fully developed [25]. Turbulent mixing and mixed-fluid interfaces exhibit strong qualitative differences across the mixing transition [25] which corresponds physically to the transition to fully developed turbulence. In particular, mixing of pure fluid is initiated near the unsteady large-scale flow boundaries above the mixing transition [15] in contrast to mixing behavior below the transition where unmixed fluid can often be found in the interior. It is useful to consider the entire range of scales as consisting of the upper or energy-containing range of scales and the remaining lower range of scales, i.e.,

$$\lambda_{\mathrm{LT}} \lesssim \lambda \lesssim L \quad \text{versus} \quad \lambda_{\min} \lesssim \lambda \lesssim \lambda_{\mathrm{LT}} \tag{4}$$

respectively. The intermediate scale λ_{LT} is the Liepmann-Taylor scale [25]

$$\lambda_{\mathrm{LT}} = (\nu L/U)^{1/2} \sim (\nu/\bar{\epsilon})^{1/2} u' \sim L\,\mathrm{Re}^{-1/2} \tag{5}$$

which separates those scales at $\lambda \gtrsim \lambda_{\mathrm{LT}}$ that are directly affected by the large scales and the smaller scales at $\lambda \lesssim \lambda_{\mathrm{LT}}$ which are either inertial scales or viscous scales. In the present notation, U is a characteristic large-scale flow speed or shear, L is a characteristic spatial large scale, ν is the kinematic viscosity, $\bar{\epsilon}$ is the energy dissipation rate per unit mass, and u' is the root-mean-square (rms.) streamwise velocity-component fluctuation. In Eq. (4), the minimum scale $\lambda_{\min}$ depends on the Schmidt number $\mathrm{Sc}\equiv\nu/\mathcal{D}$ as well as Reynolds number $\mathrm{Re}\equiv UL/\nu$, where $\mathcal{D}$ is the species diffusivity. For example, for $\mathrm{Sc}\sim 1$ which is applicable to gas-phase mixing, the smallest scale is the Kolmogorov scale $\lambda_{\mathrm{K}}\sim L\mathrm{Re}^{-3/4}$, i.e., $\lambda_{\min}=\lambda_{\mathrm{K}}$. For $Sc \gg 1$, which is applicable to liquid-phase mixing, the Batchelor scale $\lambda_{\mathrm{B}}\sim L\mathrm{Re}^{-3/4}\mathrm{Sc}^{-1/2}$ determines the smallest scale. Considering the large scale L as fixed in size, as well as a given Schmidt number Sc, we see that increasing the Reynolds number will widen the upper range faster than the lower range. This is because the Liepmann-Taylor scale $\lambda_{\mathrm{LT}}\sim L\mathrm{Re}^{-1/2}$ decreases more slowly than the Kolmogorov scale $\lambda_{\mathrm{K}}\sim L\mathrm{Re}^{-3/4}$ or the Batchelor scale $\lambda_{\mathrm{B}}\sim L\mathrm{Re}^{-3/4}\mathrm{Sc}^{-1/2}$, with increasing Reynolds number.

Examples of quantitative visualizations above the mixing transition are shown in Figs. 1 and 2 in gas-phase and liquid-phase flows, respectively. The visualization in Fig. 1 is in a large-Reynolds-number gas-phase separated turbulent shear layer. The visualization in Fig. 2 is in a moderate-Reynolds-number liquid-phase turbulent jet. In the context of the mixing efficiency, a key interface is the outer interface which separates mixed fluid from pure fluid. Previous works on turbulent mixing in various flow geometries have examined various aspects of the outer interface both experimentally and computationally [15,33,34]. As is evident in the images in Figs. 1 and 2, and as also suggested by several previous investigations [15,34], the outer interface is a relatively thin interface as a result of the fluid-dynamic small-scale strain rate limiting the local extent of molecular diffusion. A good discussion of the physical mechanisms responsible for the sharpness

Fig. 1 This experimental visualization shows an example of the sharpness of outer interface between mixed fluid and pure fluid in a gas-phase turbulent separated shear layer at a Reynolds number of Re$\sim 10^6$, freestream Mach number of $M\sim 0.9$, and Schmidt number of Sc$\sim$1, recorded at a test-section pressure of $\sim$3 atm. The image was recorded in the UC Irvine variable-pressure aero-optics facility using visible laser-induced fluorescence of acetone vapor seeded in air, excited by ultraviolet Nd:yttrium–aluminum–garnet laser illumination. The freestream is on the upper side of the image and is flowing from left to right. Ambient gas initially at rest is present below the shear layer. The sharpness of the outer interface is due, in part, to the local strain from eddies near the interface.

of the outer interface can be found in earlier works [34,35]. The outer interface is unsteady and its location traces the extent of the mixed-fluid region.

As indicated in the schematic in Fig. 3, mixed-fluid interfaces generated by turbulent mixing can be considered as the regions of fluid corresponding to each differential range of concentration, i.e.,

$$\{c, c+dc\} \tag{6}$$

Closely related to the fluid interfaces are the isosurfaces of the concentration field, i.e.,

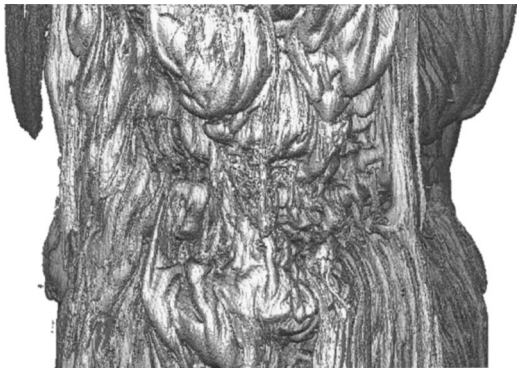

Fig. 2 High-resolution quantitative visualization of a turbulent outer interface derived from space-time $\sim 1000^3$ measurements of the concentration field in a fully developed liquid-phase jet. The Reynolds number is Re$\sim$20,000 and the Schmidt number is Sc$\sim$2000 so that the flow conditions are above the mixing transition. The measurements were recorded in the UC Irvine large-scale water tank facility using visible laser-induced fluorescence of dilute disodium fluorescein seeded in water, excited by argon-ion laser illumination. This space-time visualization captures the dynamics of the outer interface with the time axis in the vertical direction. The full transverse spatial extent of the interfaces is captured including the small scales. The interface shown corresponds to a concentration threshold of $c/c_1=1$, cf. Figs. 11 and 12.

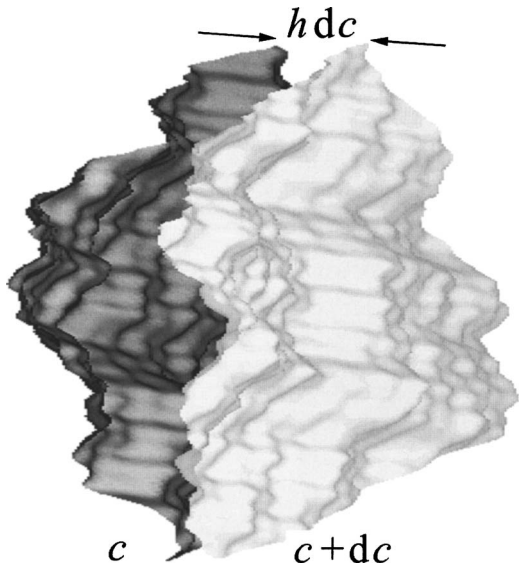

Fig. 3 Schematic illustrating the local physical thickness *hdc* of a mixed-fluid interface associated with the differential range of concentration values $\{c, c+dc\}$, with the two surfaces shown corresponding to the c and $c+dc$ isosurfaces. The region in between the two isosurfaces corresponds to the interfacial fluid.

$$c(\mathbf{x},t) = \text{const.} \tag{7}$$

Although the isosurfaces have zero thickness mathematically, the interfaces have a finite physical thickness for miscible fluids. This is the strain-limited diffusion thickness which results from a balance between molecular diffusion and the local fluid-dynamic strain rate. For an interface corresponding to a differential concentration dc, this thickness is hdc and is determined by the inverse magnitude of the local concentration gradient, i.e.,

$$h(\mathbf{x},t) = \frac{1}{|\nabla c|} = \left|\frac{\partial c}{\partial n}\right|^{-1} \tag{8}$$

Thus h is the local interfacial thickness per unit c. The concentration gradient ∇c is normal to the c interface everywhere along it, with n denoting distance along the local normal to the interface. The interfacial thickness is illustrated schematically in Fig. 3.

The volume $V_c(c)$ physically occupied by the c-threshold fluid interface, i.e., the volume of interfacial fluid, can be expressed as

$$\frac{V_c(c)}{V_{\text{ref}}} = \frac{A(c)}{V_{\text{ref}}}\bar{h}(c)|dc| \tag{9}$$

where V_{ref} is a reference volume defined by the ensemble-averaged maximum boundaries of the turbulent region of interest. The transverse extent of the reference region, for example, corresponds to the visual thickness as used in previous works [36]. The two key quantities that enter are the interfacial area-volume ratio $A(c)/V_{\text{ref}}$ and the physical thickness $\bar{h}(c)$ averaged along the surface S_c of each interface, i.e.

$$\frac{A(c)}{V_{\text{ref}}}, \quad \text{and,} \quad \bar{h}(c) = \left\langle \left|\frac{\partial c}{\partial n}\right|^{-1} \right\rangle_c = \frac{1}{A(c)} \int\int_{S_c} \left|\frac{\partial c}{\partial n}\right|^{-1} dS_c \tag{10}$$

We can distinguish between the volume $V_c(c)$ of interfacial fluid and the volume $V(c)$ of fluid residing in the interior of the interfaces, which are related as

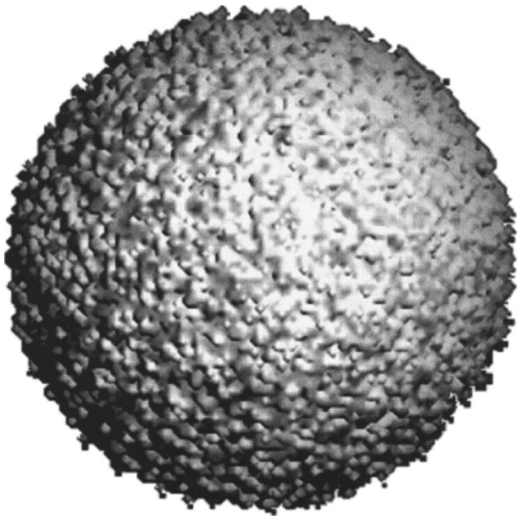

Fig. 4 In this schematic, a highly wrinkled surface is shown to illustrate that small-scale features of turbulent mixed-fluid interfaces can be expected to introduce pronounced sensitivity of the surface area to those features. In contrast, the volume enclosed by such interfaces can be expected to be weakly sensitive to the small-scale features. This robustness of the volume to small-scale features, as opposed to the sensitivity of the surface area to those features, provides a useful ingredient to facilitate practical studies of the mixture fraction.

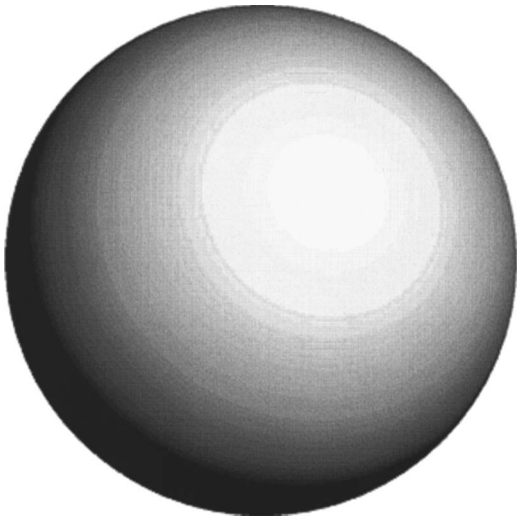

Fig. 5 The smooth surface shown in this schematic has been chosen to have a similar large-scale shape to the highly wrinkled surface in Fig. 4. Whereas the area of the smooth surface can be expected to be substantially lower than the area of the highly wrinkled surface, the volumes enclosed can be expected to be nearly the same since they are dominated by the large-scale features. In the context of mixing and mixed-fluid interfaces, this distinction can be utilized and applied to the average as well as dynamic behavior of the mixture fraction.

$$V_c(c) = |dV(c)| \tag{11}$$

The absolute values in Eq. (11) are needed since the geometrical quantities cannot be negative, while the differentials dc or $dV(c)$ can be positive or negative depending on the definition of the c values corresponding to the pure fluids. Combining Eqs. (9) and (11), we have

$$A(c) = \frac{V_c(c)}{\bar{h}(c)|dc|} = \frac{1}{\bar{h}(c)}\left|\frac{dV(c)}{dc}\right| \tag{12}$$

where it is assumed that $V(c)$ is differentiable. Inversely

$$V(c) = \int^{c} A(c')\bar{h}(c')|dc'| \tag{13}$$

where the lower integration limit can be the maximum or minimum concentration value which again depends on the choice of c values associated with the pure fluids.

Closely related to the interfacial area-volume ratio is the concentration-field probability density function $p(c)$ which is fundamentally and practically crucial because it reflects scalar-threshold effects on mixing and especially on the geometrical structure of the mixed-fluid interfaces. How is the probability density $p(c)$ related to the geometrical properties of the interfaces? The most direct relation is in terms of the volume $V_c(c)$ of interfacial fluid, i.e., as the volume fraction of fluid occupied by the c interface

$$p(c)|dc| = \frac{V_c(c)}{V_{\text{ref}}} \tag{14}$$

cf. Eq. (9). In addition, the probability density $p(c)$ of finding c-concentration fluid is intimately related to both the interfacial surface area $A(c)$ and the volume $V(c)$ enclosed by the interfaces. To relate $p(c)$ to the surface area $A(c)$, the average interfacial thickness $\bar{h}(c)$ is needed, i.e.,

$$p(c) = \frac{A(c)}{V_{\text{ref}}}\bar{h}(c) \tag{15}$$

In other words, the interfacial interpretation of $p(c)$ in terms of the surface area requires knowledge of the interfacial-thickness properties. In contrast, the relation of $p(c)$ to the volume $V(c)$ enclosed by the interfaces does not require knowledge of the interfacial thickness. Interpreted as the volume fraction of fluid residing in the interior of the interfaces, $p(c)$ can be written as

$$p(c) \equiv \frac{1}{V_{\text{ref}}}\left|\frac{dV(c)}{dc}\right| \tag{16}$$

Comparing Eqs. (12) and (13), which are inverses of each other, we can appreciate that the volume $V(c)$ enclosed by any given internal interface can be expected to be weakly sensitive to the small scales, as opposed to the surface area $A(c)$ which is known to be sensitive to the small scales. This is intuitively clear as can be appreciated using the schematics in Figs. 4 and 5, which show a highly wrinkled surface and a smooth surface, respectively, that enclose nearly the same volume but with greatly different surface areas. The general observation of robustness of the volume in contrast to sensitivity of the surface area is analogous to the comparison between the derivative of a noisy signal and its integral: while the derivative of the signal is highly sensitive to the small scales, the integral is weakly sensitive to the small scales. We can make two key general observations therefore:

i. *Surface area $A(c)$ of interfaces*: The surface area, as a derivative of the volume $V(c)$, is highly sensitive to small-scale features and also to noise if present.
ii. *Volume $V(c)$ enclosed by interfaces*: The volume, as an integral of the area $A(c)$, is weakly sensitive to small-scale features or to noise if present.

Returning to the mixing efficiency α_m, it can be appreciated that it can be expressed in several ways that are equivalent theoretically

$$\alpha_m = \int_{\text{mixed}} p(c)dc = \int_{\text{mixed}} \frac{A(c)}{V_{\text{ref}}}\bar{h}(c)dc = \int_{\text{mixed}} \frac{|dV(c)|}{V_{\text{ref}}} = \frac{V_{\text{mixed}}}{V_{\text{ref}}} \tag{17}$$

where the integrals are over the region of mixed fluid. Considering Eqs. (9) and (17), it is apparent that two alternative approaches are possible in principle in order to examine the mixing efficiency in terms of interfacial properties.

One approach, which is the traditional surface-based approach, is to require knowledge of the area $A(c)$ of all mixed-fluid interfaces, i.e., the internal interfaces and the outer interface, as well as of the mean thickness $\bar{h}(c)$ of all mixed-fluid interfaces. A difficulty with the surface-based approach, however, is that the surface area $A(c)$ is highly sensitive to the small scales as discussed above in the context of Eq. (12). Experimental and numerical studies, in addition, have suggested that the surface area of turbulent interfaces is actually dominated by the small scales [34,37,38]. The mean interfacial thickness is also sensitive to the small scales since it is a gradient-based quantity and also because of the intermittency of turbulent mixing [5]. Thus, modeling and descriptions of the mixing efficiency using the surface-based approach [4] are possible in principle but can be expected to be highly sensitive to resolution limitations.

The second approach, which has been termed the volume-based approach, [28] is directly based on the volume V_{mixed} of the mixed-fluid region bounded by the outer interfaces. This volume can be expected to be dominated by the large scales, i.e., to be weakly sensitive to the small scales, especially above the mixing transition. This is because of the strong large-scale vorticity/concentration correlations that occur above the transition, as opposed to below the transition, as indicated by recent work [15,28]. Furthermore, the volume-based approach does not require knowledge of the concentration-threshold dependence, since it only requires outer-interface information. Thus, in contrast to the surface-based approach, one can anticipate robustness to resolution-scale effects by using the volume-based approach.

Recalling the upper and lower ranges of interfacial scales, as in the discussion above for Eq. (4), one can anticipate therefore that the volume will be dominated by the upper scales, whereas the surface area will be dominated by the lower scales. Especially when resolution effects are present, the anticipated robustness of the volume-based approach is helpful. We examine these ideas below on the basis of high-resolution measurements above the mixing transition recorded in a large-scale flow facility.

3 Experimental Facility and Flow Imaging

In the present work, we utilize high-resolution measurements of the concentration field in fully developed liquid-phase turbulent jets recorded in the large-scale octagonal-tank flow facility at UC Irvine. A schematic of the flow-imaging geometry is shown in Fig. 6 and a photograph of the facility is shown in Fig. 7. The facility has an internal diameter of 1.83 m (6 ft) and an internal height of 2.74 m (9 ft). It has extensive optical access with eight vertical rectangular windows of size 0.61 m by 2.13 m (2 ft by 7 ft) each as well as a horizontal circular window of diameter 0.61 m (2 ft) on the bottom face of the tank. The facility consists of structural steel and glass that can support up to 8 tons or 2000 gallons of water when the tank is fully filled. The reasons for the choice of a large-scale facility are threefold. First, a large facility enables higher Reynolds numbers to be achieved. Second, the small scales are more amenable to resolution using laser scattering techniques because the latter typically require a minimum laser-sheet thickness for two-dimensional or higher-dimensional imaging. Third, the temporal framing rates needed for imaging of the dynamics of the interfaces are relatively lower because of the large size of the facility.

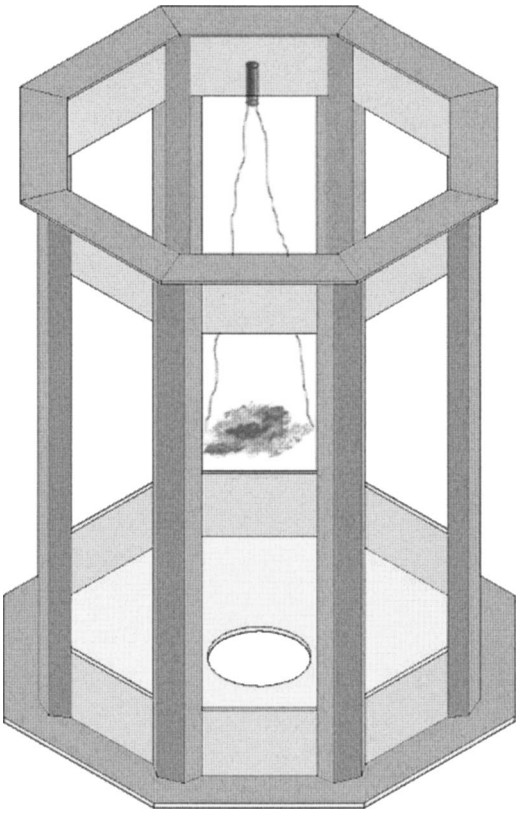

Fig. 6 Schematic of the large-scale water tank facility at UC Irvine, in which various flow configurations can be examined. The flow geometry examined in the present work is the round turbulent jet, as indicated in the schematic. A liquid-phase jet is issued vertically from the top and grows downwards. Imaging of the concentration field of the jet is conducted in the similarity plane normal to the jet axis, at a downstream location of ~500 nozzle diameters. This is in the far field of the jet and corresponds to a physical location approximately halfway down the tank in order to avoid end-wall and sidewall effects.

The flow geometry chosen to create the high-resolution experimental database is the round jet as indicated in Fig. 6. Although this flow geometry has been studied much in the past, various questions remain open such as the degree to which the mixed-fluid interfaces are convoluted and the behavior of the mixing efficiency [1,5,13,23,39]. The facility is operated in a blow-down manner to produce a momentum-dominated jet growing vertically downwards as indicated in the schematic. End-wall and sidewall effects are minimized by conducting the flow imaging at approximately half way down the total height of the facility. The flow parameters are chosen in order to ensure flow conditions above the mixing transition yet maintain high resolution. The Reynolds number is $\text{Re} \sim 20{,}000$ and the Schmidt number of $\text{Sc} \sim 2000$. The imaging location corresponds to the far field of the jet, at a downstream location of ~500 nozzle diameters. Because the measurements are in the far field, there is no unmixed jet fluid present at the imaging station used and thus the only interface between pure fluid and mixed fluid is the interface between pure ambient fluid and jet fluid.

The experimental procedure and flow-imaging technique have been described before [15] and only a brief mention will be made here. The octagonal tank is filled with filtered water prior to each experiment. The plenum fluid needed for the jet is prepared as a solution of disodium fluorescein dye premixed at a molecular level with water of the same temperature as of the water in the tank. Low concentration of the dye is utilized in order to ensure negligible laser power attenuation through the fluid during the

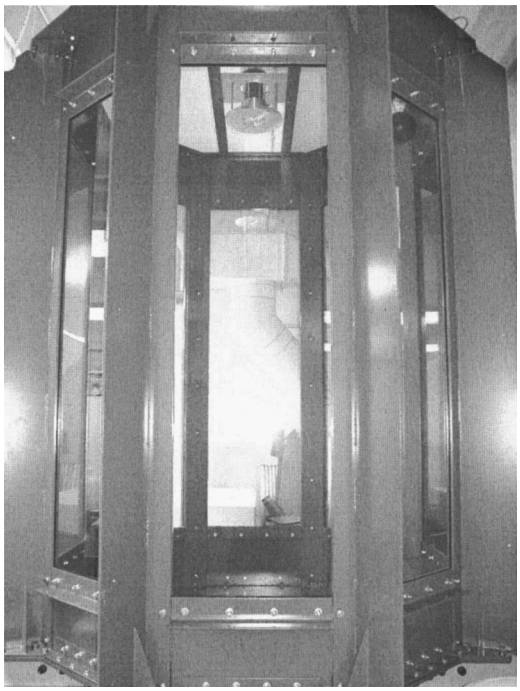

Fig. 7 Photograph of the water tank facility at UC Irvine. The tank is octagonally shaped with an internal height of 2.74 m (6 ft) and a diameter of 1.83 m (9 ft). The capacity of the tank is 8 tons or 2000 gallons of water. The tank has extensive optical access by way of eight vertical 0.61 m by 2.13 m (2 ft by 7 ft) windows and one horizontal 0.61 m (2 ft) diameter window at the base. The large size of the tank facilitates large-scale high-resolution imaging of the concentration field while at the same time enabling flow conditions above the mixing transition.

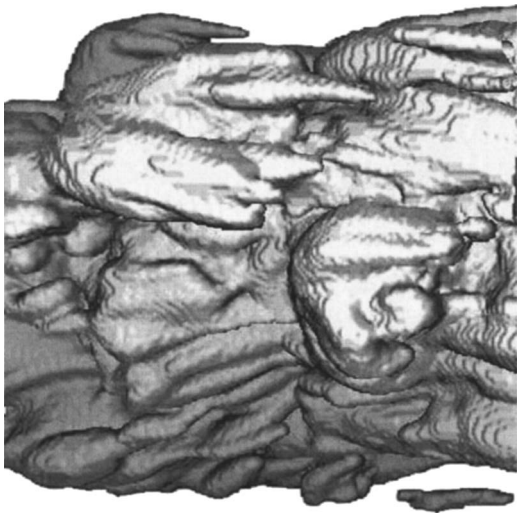

Fig. 8 Coarse-grained quantitative visualization of an outer interface derived from three-dimensional space-time measurements of the concentration field in a liquid-phase fully developed turbulent jet. This image corresponds to coarse graining of the full-resolution $\sim 1000^3$ data to a reduced resolution of $\sim 32^3$. Time varies horizontally and increases from left to right. The flow conditions are above the mixing transition with a Reynolds number of Re$\sim$20,000 and a Schmidt number of Sc $\sim$2000.

flow imaging. The jet is operated such that a steady jet-exit velocity is attained for the duration of the flow imaging. The linear full-angle growth rate of the resulting jet is $\sim$24 deg in agreement with previous studies. A plane slicing the jet normal to the flow centerline is illuminated with an argon-ion laser sheet. The laser-induced fluorescence from the concentration field in that plane is recorded with a charge-coupled-device camera of resolution $\sim 1000 \times 1000$. In each experiment, a set of $\sim$1000 such two-dimensional images is continuously recorded at a framing rate which matches the passage frequency of the outer interface as described in earlier studies [15]. The data are normalized and calibrated pixel by pixel using uniform-concentration images recorded after each experiment by mixing completely a known amount of dye into the entire water tank. This produces three-dimensional $\sim 1000 \times 1000 \times 1000$ space-time concentration-field data.

Because turbulent mixing and mixed-fluid interfaces are known to exhibit strong qualitative differences across the mixing transition, [3,25] it is helpful to examine the behavior above the mixing transition as discussed above in Sec. 2, if one is interested in developing descriptions and physical-modeling methodologies that are useful at large Reynolds numbers. Since the minimum Reynolds number at which this can occur, based on the large-scale extent of the flow, is Re$\sim$10,000 as stated above in Sec. 2, the Reynolds number chosen for the experiments in this study is Re $\sim$20,000 so that the observed behavior is relevant also for larger-Reynolds-number conditions. The choice of Re$\sim$20,000 in the present study ensures flow conditions corresponding to fully developed turbulent mixing.

The mixed-fluid interfaces, extracted from the concentration-field database, exhibit dynamics consistent with the behavior of interfaces in other flows above the mixing transition [5,25]. Visualizations of mixed-fluid interfaces, or scalar isosurfaces, in various turbulent flows indicate that there are strong qualitative differences across the mixing transition. Previous work has indicated that the internal structure of turbulent mixing, e.g., the behavior of scalar isosurfaces at thresholds corresponding to the interior of the flow, changes qualitatively across the mixing transition [8,10,40]. One of the most striking and well-known differences, at least for incompressible-flow conditions or low-compressibility conditions, is that there are large-scale well-mixed regions above the transition. In contrast, below the transition, the interior of the large-scale regions is not well mixed [40]. A consequence of this is that pure fluid is rarely found in the interior of the large-scale regions above the transition. The large-scale facility enables the trading of flow velocity for size while maintaining flow conditions above the mixing transition. This permits the effective use of high-spatial-resolution imaging to capture the full range of outer-interface features at fully developed conditions.

Examples of resolution-scale effects on the outer interfaces are shown in Figs. 8–10. The full-resolution concentration field was utilized to derive the $\sim 1000^3$ outer interface in Fig. 10. The reduced-resolution interfaces, in Figs. 8 and 9, were generated by successively coarse graining the full-resolution concentration field. The interface shown in Fig. 9 is at a reduced resolution of $\sim 256^3$ and the interface in Fig. 8 is at a reduced resolution of $\sim 32^3$. As expected, the large-scale interfacial features persist during the coarse graining but the small-scale interfacial behavior changes substantially.

In the visualizations in Figs. 8–10, a concentration interface is extracted each time from the three-dimensional space-time measurements recorded in the similarity plane of the flow. As with all cases of identifying or extracting interfaces from measured or computed data, a practical question concerns the choice of threshold [34]. In the data presently employed, the signal-to-noise ratio is sufficiently high to permit identification of interfaces at the lowest threshold above the noise floor such that their maximum spatial extent is consistent with the accepted growth rate of turbulent jets [15]. This scalar threshold is denoted as c_1 and is utilized to normalize the concentration values. We have verified independently that concentration values below c_1 are infected by noise

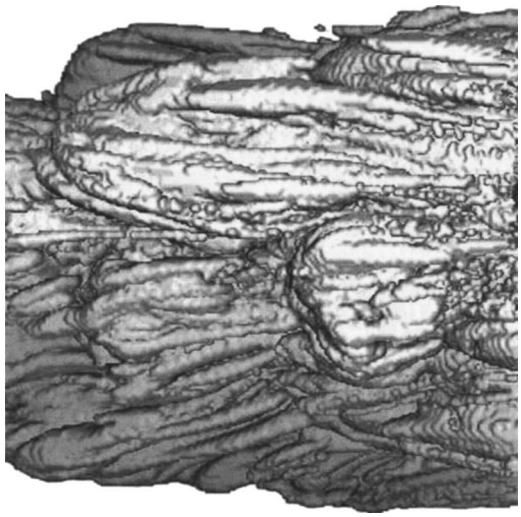

Fig. 9 Coarse-grained visualization of a turbulent outer interface at a resolution of $\sim 256^3$, derived from the same full-resolution $\sim 1000^3$ data as for Fig. 8. Additional smaller-scale features are evident, as expected, compared to the $\sim 32^3$ coarse-grained visualization in Fig. 8.

which, artificially, would correspond to transverse spatial scales beyond the maximum extent of the flow. A discussion on guidelines for selecting accurate scalar thresholds to identify outer interfaces is available in previous work [41]. The wide range of scales captured at the present flow conditions, together with application of Taylor's hypothesis [15] to obtain the volume of the mixed-fluid region, enable an examination of resolution-scale effects on the mixing efficiency.

4 Results on the Mixing Efficiency

To illustrate the challenges involved in the surface-based approach, a comparison between the probability density function of the concentration field and the surface area of the mixed-fluid interfaces is shown in Fig. 11. The reference volume V_{ref}, in which the probability density of concentration is normalized to unity, was identified in terms of the maximum transverse extent of the

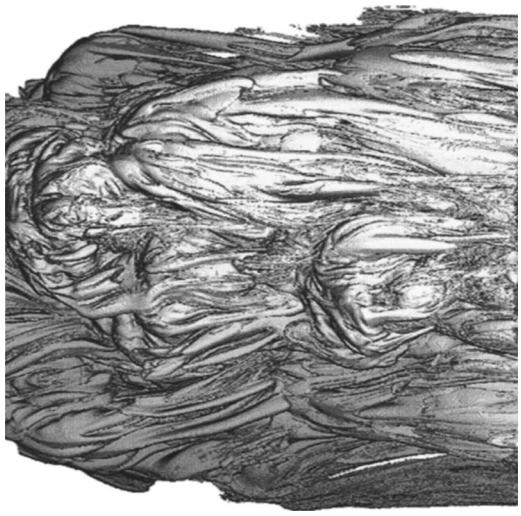

Fig. 10 Full-resolution $\sim 1000^3$ quantitative visualization of a turbulent outer interface corresponding to the coarse-grained $\sim 256^3$ and $\sim 32^3$ visualizations in Figs. 8 and 9. The full transverse spatial extent of the interface is captured including the small scales.

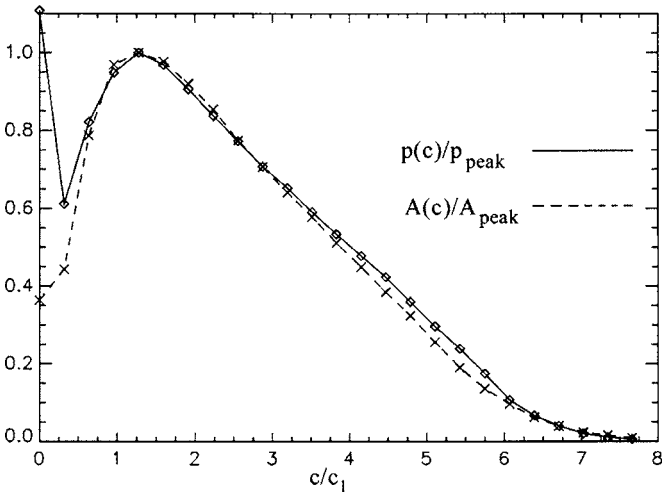

Fig. 11 Comparison between the probability density function of the concentration field (solid curve with diamonds) and the surface area of the mixed-fluid interfaces (dashed curve with crosses). Both curves correspond to the high-resolution scalar measurements of the turbulent jet. Both quantities plotted are normalized by their respective peak values, excluding the peak value of the probability density of pure ambient fluid. The deviation between the two curves, at large scalar thresholds, is attributable to insufficient resolution of the internal interfaces corresponding to those thresholds.

jet in agreement with the accepted growth rate of unforced jets. Both the probability density of concentration and the interfacial surface area, shown in Fig. 11, correspond to the high-resolution scalar measurements of the turbulent jet. Nevertheless, it is evident that there is a notable deviation between the two curves, at large scalar thresholds. This is likely attributable to insufficient resolution of the internal interfaces corresponding to those thresholds. In fact, the difference in the two curves in Fig. 11 is directly due to the behavior of the interfacial thickness which is discussed below and shown in Fig. 12. The results in Fig. 11 are for ensemble-averaged statistics and, because they evaluated over a

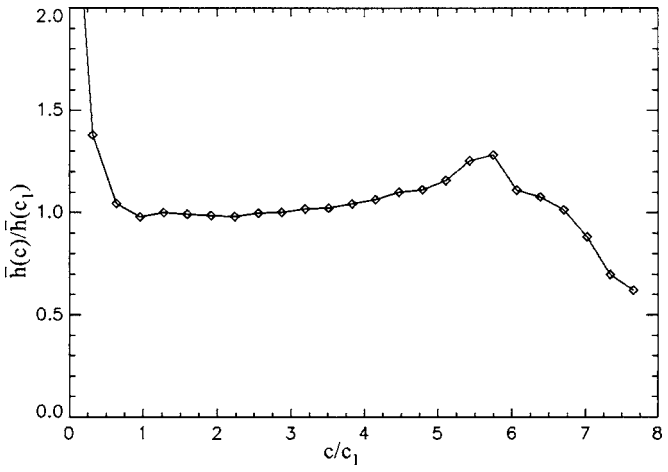

Fig. 12 Dependence of the interfacial thickness as a function of concentration threshold for the high-resolution measurements of the turbulent jet. The high resolution ($\sim 1000^3$) is adequate to capture the uniformity of the interfacial thickness for the lower scalar thresholds or internal interfaces near the outer regions of the jet. However, the $\sim 1000^3$ resolution is inadequate at the higher scalar thresholds with deviations as large as 30%, illustrating the sensitivity of the interfacial thickness to the resolution.

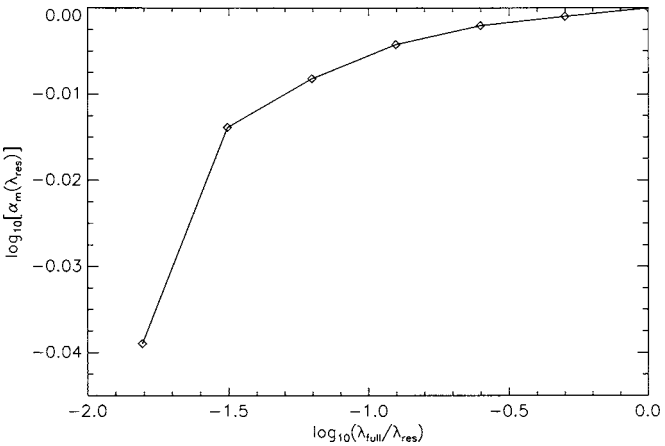

Fig. 13 Resolution-scale effects on the mixing efficiency evaluated directly in terms of the volume fraction of mixed fluid. Robustness is evident for several reductions in resolution scale. For example, for a resolution reduction of $1:10^{-1.5}\sim 30:1$ per dimension the mixing efficiency is captured by $\sim 10^{-0.014}\sim 97\%$. In other words, there is only a ~3% difference in the mixing efficiency even though there is a substantial $\sim 30^3:1=27{,}000:1$ reduction in three-dimensional concentration field information.

large number of realizations, the uncertainty is within the size of the symbols shown in Fig. 11. For thresholds corresponding to the outer interface or internal interfaces near the outer boundaries, the resolution of the imaging technique and the size of the facility are sufficient to ensure fully resolved behavior. However, for larger thresholds corresponding to interfaces far in the interior of the flow, the present experiments are under-resolved due to the higher flow velocities near the jet centerline. While this is not a problem for identifying the outer interface, which resides near the low-speed large-scale boundaries of the flow, the consequence is that there are significant resolution-scale effects on both the surface area and the interfacial thickness. This is evident in Fig. 12 which shows the measured dependence of the interfacial thickness as a function of concentration threshold. The high resolution of $\sim 1000^3$ is able to capture the uniformity of the interfacial thickness for the lower scalar thresholds or internal interfaces near the outer regions of the jet. For mixing in fully developed turbulent jets, it is known that the interfacial thickness is uniform and is not a function of the scalar threshold [42]. In the behavior in Fig. 12, the $\sim 1000^3$ resolution is inadequate at the higher scalar thresholds of $c/c_1 \gtrsim 4$, which correspond to under-resolved regions near the center of the jet [15]. Deviations as large as 30% illustrate the high sensitivity of the interfacial thickness to the resolution. Furthermore, prior experimental evidence [24] at the same flow conditions has shown that the interfacial surface area is highly sensitive to resolution-scale effects. For example, the surface area of the outer interfaces is under-estimated by ~40% for a reduction in resolution by a factor of 10 per dimension, i.e., from $\sim 1{,}000^3$ to $\sim 100^3$. Both for the surface area and for the interfacial thickness, therefore, there is significant sensitivity to resolution-scale effects. Appreciating that in the surface-based approach the mixing efficiency requires evaluating the surface area and interfacial thickness over the entire range of mixed-fluid concentration thresholds, cf. Eq. (17), it is apparent that this does not offer a robust methodology regarding resolution-scale effects.

To assess the resolution-scale effects on the volume-based approach, Fig. 13 is shown which depicts the dependence of the volume fraction of mixed fluid on the resolution-scale cutoff. A normalized resolution-scale cutoff is employed as $\lambda_{full}/\lambda_{res}$ where λ_{res} denotes the coarse-graining solution scale and λ_{full} denotes the full-resolution scale of the experiments. Significant robustness is evident in Fig. 13 for several reductions in resolution scale. For example, for a resolution reduction of $1:10^{-1.5}\sim 30:1$ per dimension, the mixing efficiency is captured by $\sim 10^{-0.014}\sim 96.8\%$, i.e.,

$$\frac{[\alpha_m]_{30\times 30\times 30}}{[\alpha_m]_{1000\times 1000\times 1000}} \simeq 96.8\% \tag{18}$$

In other words, there is only a ~3.2% difference in the mixing efficiency even though there is a substantial $\sim 30^3:1=27{,}000:1$ reduction in three-dimensional concentration field information. Thus, there is persistent robustness to resolution-scale effects in utilizing the volume fraction of mixed fluid. We note that, for the present flow conditions, the ensemble-averaged value of the mixing efficiency evaluated at full resolution from the three-dimensional space-time outer interfaces is

$$\alpha_m \simeq 60.7\% \tag{19}$$

with an uncertainty estimated at less than ±0.05%. This uncertainty estimate is based, indirectly, by the effect on α_m of halving the resolution using the resolution-dependence results in Fig. 13. In other words, Fig. 13 indicates a rapid convergence as the experimental resolution is approached. Accepting, as an upper-bound uncertainty estimate, that doubling the resolution would have at most an effect of the same magnitude as halving the resolution, we obtain an estimate of 0.1% in magnitude or ±0.05%. The present result of $\alpha_m \simeq 60.7\%$ for the mixing efficiency is consistent with the earlier reports derived from the evaluation of spatial two-dimensional data [28]

The robustness to resolution-scale effects is due to the dominance of the volume of fluid in the interior of the outer interface by the large-scale features, as expected theoretically in the discussions above in Sec. 2. Additional insight into this robustness can be seen by examining the resolution-scale effect on the probability of finding pure fluid as a function of distance from the flow centerline. In the present volume-based approach, the mixing efficiency can be evaluated directly in terms of information on the pure fluid rather than on the mixed fluid. This is advantageous in practice because pure fluid, at a given resolution scale, can be identified without the ambiguities associated with discerning mixed fluid [13,27]. The mixing efficiency α_m can be expressed directly [15] in terms of the probability $P_{\text{pure}}(r)$ of finding pure fluid at a distance r from the flow centerline

$$\alpha_m = 1 - \int_0^1 P_{\text{pure}}(r')d\left(\frac{2r'}{L}\right) \tag{20}$$

Figure 14 shows the resolution-scale effect on the probability $P_{\text{pure}}(r)$ for the present flow conditions. The robustness of the probability of finding pure fluid to resolution is evident by the very weak effect of the coarse graining. As the area above each curve, in Fig. 14, corresponds to α_m, the observed robustness directly applies to the mixing efficiency. Therefore, the mixing efficiency can be obtained in the present volume-based approach by identifying the pure fluid as an alternative to identifying the mixed fluid. In practice, for under-resolved data at large Reynolds numbers, this is especially helpful because it is known from previous studies that mixed fluid cannot be unambiguously identified from under-resolved data [27]. In contrast, for sufficiently high signal-to-noise ratio data, identification of pure fluid at scales at or above the resolution scale does not have this limitation [28].

An example of the dynamical behavior of the mixing efficiency is shown in Fig. 15, for a time duration equivalent to the passage time of a large-scale structure, by utilizing a temporal sequence of consecutive two-dimensional spatial concentration-field images normal to the jet centerline at the same flow conditions. The profile corresponding to the full-resolution data is shown as a solid curve. The dashed curve corresponds to the coarse-grained mixing efficiency evaluated by reducing the data resolution by a factor of 10 per dimension. It is evident, in Fig. 15, that the coarse-grained profile is able to capture and reproduce at a high accuracy the dynamics of the full-resolution mixing efficiency. Both large-scale

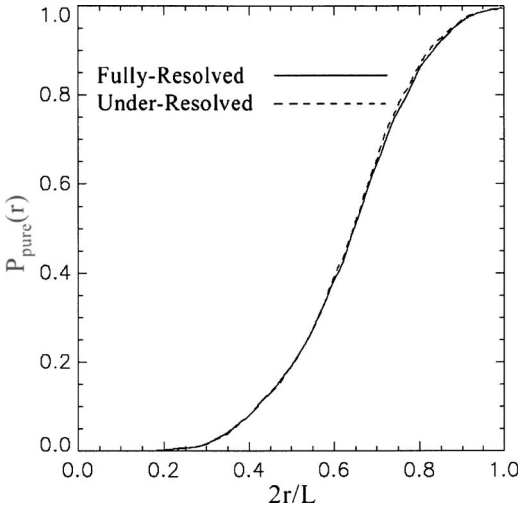

Fig. 14 Evaluation of resolution-scale effects on the probability of finding pure fluid as a function of distance from the jet centerline. The solid curve corresponds to the $\sim 1000^3$ resolution. The dashed curve corresponds to a resolution reduced by a factor of 10 per dimension, i.e., at a coarse-grained resolution of $\sim 100^3$. The robustness of the probability of finding pure fluid to resolution is evident by the very weak effect of the coarse graining. As the area above each curve corresponds to the mixing efficiency, this robustness directly applies to the mixing efficiency as well and is evaluated further in Fig. 13.

and small-scale dynamics are captured with less than $\sim 2\%$ difference. This demonstrates the robustness of the volume-based technique to resolution effects for evaluating the dynamical behavior of the mixing efficiency. As discussed in the introduction (Sec. 1), much emphasis in previous works [4,6] has been placed on the

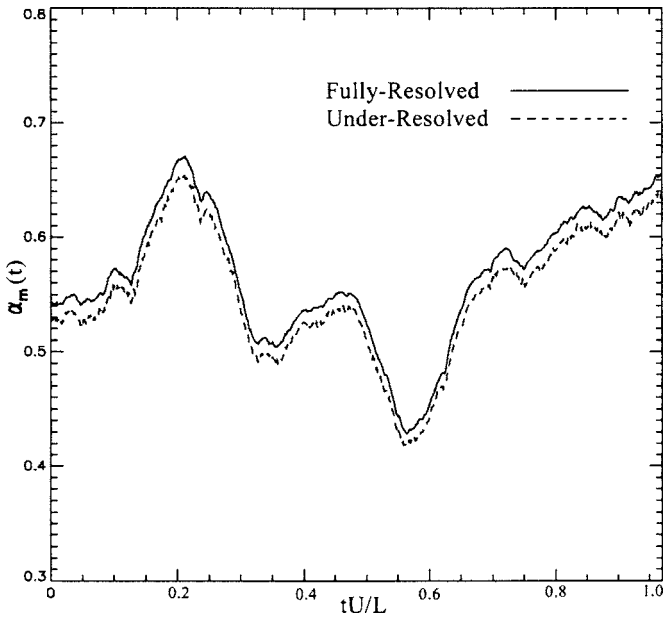

Fig. 15 Dynamical behavior of the mixing efficiency and demonstration of the robustness to resolution-scale effects. Solid curve: mixing efficiency for full-resolution ($\sim 1000^3$) data. Dashed curve: mixing efficiency for data coarse grained at ten times lower resolution per dimension, i.e., at a reduced resolution of $\sim 100^3$. The robustness to coarse graining is evident dynamically. Even though large excursions of the instantaneous value of the mixing efficiency are observed, the robustness to resolution-scale effects persists dynamically.

area-volume ratio of interfaces which is highly sensitive to the small scales, as opposed to the present volume-based measures. The present observations of robustness are due, in part, to the fact that the outer interface is primarily confined near the unsteady large-scale boundaries of the jet. This is due to strong large-scale vorticity/concentration correlations above the mixing transition [15]. Thus, it is the large scales of the outer interface, in the upper range of scales or energy-containing range of scales, that provide the dominant contribution to the mixing efficiency above the mixing transition. Together with the present observations of robustness, this has several practical implications.

Experimentally, the implication is that direct imaging of the outer interface even at moderate resolution can be utilized at large Reynolds numbers to capture the dominant behavior of the mixing efficiency, because of the robustness to the small scales and thus to noise. In addition, by identifying pure fluid rather than mixed fluid, the limitations [27] with quantifying the local extent of mixing in under-resolved measurements are reduced. Computationally, the implication is that large-eddy simulations can be expected to be able to capture the dominant behavior of the mixing efficiency. For physical modeling, the implication is that knowledge of the large scales of the outer interface is useful to quantify the dominant behavior of the mixing efficiency including its limiting behavior at the large Reynolds numbers of aeronautical applications. There are also implications regarding flow control. For a given growth rate, one can investigate suppressing or increasing the large-scale outer-interface fluctuations to enhance or reduce, respectively, the mixing efficiency. In closed-loop active flow control studies, including for example systems for aero-optical beam control [20,21,43], the reduction in flow information needed can reduce the bandwidth requirements.

In the context of large-eddy simulations, the robustness to small scales has two implications regarding subgrid scale modeling for the mixture fraction. For a given large-eddy simulation grid resolution, only a weak dependence of the mixture fraction on the particular subgrid scale model is expected, as long as the large-scale dynamics are accurately computed [2]. Also, for a given large-eddy simulation methodology, simulations with relatively coarse grids can be expected to be able to capture the mixing efficiency and its dynamics at relatively high accuracy. Regarding the limiting behavior of the mixing efficiency at large Reynolds numbers, which is needed in applications, the present findings indicate that it can be physically modeled in terms of the large-scale features of the outer interfaces and thus will be strongly dependent on the flow geometry. For flow optimization [1], this indicates that modification of the large-scale features of the outer interfaces can be effective in enhancing, or reducing, the mixing efficiency.

5 Conclusions and Implications

We have investigated the resolution-scale robustness of the volume-based approach for the turbulent mixing efficiency, with comparisons to the small-scale sensitivity of the surface-based approach. High-resolution three-dimensional space-time data of concentration interfaces obtained experimentally using a flow facility especially designed for direct imaging of interfaces in fully-developed turbulent flows have been utilized for this purpose. The mixing efficiency is found to be very weakly sensitive to changes in resolution. This means that the dominant interfacial contributions to the mixing efficiency are from the large-scale dynamic features of the outer interface, i.e., the interface separating pure fluid from mixed fluid. This finding is particularly useful for the design of fluid-mixing devices and provides several benefits. First, because the method relies on the volume enclosed by interfaces which is dominated by the large scales, the method is weakly sensitive to the small scales. Second, for the same reason, the method can be expected to be weakly sensitive to noise in contrast to surface-based methods. Third, the method relies on the identification of pure fluid rather than of the mixed fluid. While mixed

fluid cannot be unambiguously deduced from under-resolved images, pure fluid can be identified at or above the pixel scale even for under-resolved images. These three reasons provide helpful advantages for evaluating the mixing efficiency in fluid-engineering devices.

Acknowledgment

This work is part of a research program on turbulent flows and fluid interfaces, with support by the National Science Foundation and by the Air Force Office of Scientific Research. The authors are grateful to the referees for their insightful comments.

Nomenclature

A = interfacial surface area
c = fluid concentration
h = local interfacial thickness
$\bar{h}$ = average thickness along interface
L = large scale
n = distance along interfacial normal
p = probability density of concentration
P_{pure} = probability of pure fluid
r = transverse distance from flow centerline
Re = Reynolds number
Sc = Schmidt number
S_c = surface associated with a concentration interface
u' = streamwise root-mean-square velocity fluctuation
V = volume of fluid bounded by concentration interfaces
V_c = volume of interfacial fluid
V_{mixed} = volume of mixed-fluid region
V_{pure} = volume of pure-fluid region
V_{ref} = normalizing volume
α_m = mixing efficiency
$\bar{\epsilon}$ = energy dissipation rate
λ = interfacial scale
λ_K = kolmogorov scale
λ_B = batchelor scale
λ_{LT} = liepmann-Taylor scale
ν = kinematic viscosity

References

[1] Mi, J., Nathan, G. J., and Nobes, D. S., 2001, "Mixing Characteristics of Axisymmetric Free Jets From a Contoured Nozzle, an Orifice Plate and a Pipe," ASME J. Fluids Eng., **123**, pp. 878–883.
[2] deBruynKops, S. M., and Riley, J. J., 2001, "Mixing Models for Large-Eddy Simulation of Nonpremixed Turbulent Combustion," ASME J. Fluids Eng., **123**, pp. 341–346.
[3] Roshko, A., 1991, "The Mixing Transition in Free Shear Flows," In *The Global Geometry of Turbulence*, J. Jiménez, ed., Plenum, New York, pp. 3–11.
[4] Dimotakis, P. E., 1991, "Turbulent Free Shear Layer Mixing and Combustion," In *High Speed Flight Propulsion Systems*, S. Murthy and E. Curran eds., 137, *Progress in Astronautics and Aeronautics*, AIAA, Washington, DC.
[5] Catrakis, H. J., 2004, "Turbulence and the Dynamics of Fluid Interfaces With Applications to Mixing and Aero-Optics," In *Recent Research Developments in Fluid Dynamics*, N. Ashgriz and R. Anthony, eds., 5. Transworld Research Network Publishers, Kerala, India, pp. 115–158.
[6] Dimotakis, P. E., 2005, "Turbulent Mixing," Annu. Rev. Fluid Mech., **37**, pp. 329–356.
[7] Broadwell, J. E., and Briedenthal, R. E., 1982, "A Simple Model of Mixing and Chemical Reaction in a Turbulent Shear Layer," J. Fluid Mech., **125**, pp. 397–410.
[8] Koochesfahani, M. M., and Dimotakis, P. E., 1986, "Mixing and Chemical Reactions in a Turbulent Liquid Mixing Layer," J. Fluid Mech., **170**, pp. 83–112.
[9] Sreenivasan, K. R., Ramshankar, R., and Meneveau, C., 1989, "Mixing, Entrainment and Fractal Dimensions of Surfaces in Turbulent Flows," Proc. R. Soc. London, Ser. A, **421**, pp. 79–108.
[10] Dahm, W. J. A., and Dimotakis, P. E., 1990, "Mixing at Large Schmidt Number in the Self-Similar Far Field of Turbulent Jets," J. Fluid Mech., **217**, pp. 299–330.
[11] Dowling, D. R., and Dimotakis, P. E., 1990, "Similarity of the Concentration Field of Gas-Phase Turbulent Jets," J. Fluid Mech., **218**, pp. 109–141.
[12] Broadwell, J. E., and Mungal, M. G., 1991, "Large-Scale Structures and Molecular Mixing," Phys. Fluids A, **3**(5), pp. 1193–1206.
[13] King, G. F., Dutton, J. C., and Lucht, R. P., 1999, "Instantaneous, Quantitative Measurements of Molecular Mixing in the Axisymmetric Jet Near Field," Phys. Fluids, **11**, pp. 403–416.
[14] Villermaux, E., and Innocenti, C., 1999, "On the Geometry of Turbulent Mixing," J. Fluid Mech., **393**, pp. 123–147.
[15] Catrakis, H. J., Aguirre, R. C., Ruiz-Plancarte, J., Thayne, R. D., McDonald, B. A., and Hearn, J. W., 2002, "Large-Scale Dynamics in Turbulent Mixing and the Three-Dimensional Space-Time Behaviour of Outer Fluid Interfaces," J. Fluid Mech., **471**, pp. 381–408.
[16] Fiedler, H. E., 1998, "Control of Free Turbulent Shear Flows," In *Flow Control: Fundamentals and Practices*, M. Gad-el Hak, A. Pollard, and J.-P. Bonnet, eds., Springer, Berlin, pp. 335–429.
[17] Hale, C. A., Plesniak, M. W., and Ramadhyani, S., 2000, "Film Cooling Effectiveness for Short Film Cooling Holes Fed by a Narrow Plenum," ASME J. Turbomach., **122**, pp. 553–557.
[18] Dimotakis, P. E., Catrakis, H. J., and Fourguette, D. C. L., 2001, "Flow Structure and Optical Beam Propagation in High-Reynolds-Number Gas-Phase Shear Layers and Jets," J. Fluid Mech., **433**, pp. 105–134.
[19] Gad-el Hak, M., 2000, *Flow Control: Passive, Active, and Reactive Flow Management*, Cambridge University Press, Cambridge.
[20] Jumper, E. J., and Fitzgerald, E. J., 2001, "Recent Advances in Aero-Optics," Prog. Aerosp. Sci., **37**, pp. 299–339.
[21] Catrakis, H. J., and Aguirre, R. C., 2004, "New Interfacial Fluid Thickness Approach in Aero-Optics With Applications to Compressible Turbulence," AIAA J., **42**(10), pp. 1973–1981.
[22] Dimotakis, P. E., Miake-Lye, R. C., and Papantoniou, D. A., 1983, "Structure and Dynamics of Round Turbulent Jets," Phys. Fluids, **26**, pp. 3185–3192.
[23] Sreenivasan, K. R., 1991, "Fractals and Multifractals in Fluid Turbulence," Annu. Rev. Fluid Mech., **23**, pp. 539–600.
[24] Catrakis, H. J., Aguirre, R. C., and Ruiz-Plancarte, J., 2002, "Area-Volume Properties of Fluid Interfaces in Turbulence: Scale-Local Self-Similarity and Cumulative Scale Dependence," J. Fluid Mech., **462**, pp. 245–254.
[25] Dimotakis, P. E., 2000, "The Mixing Transition in Turbulent Flows," J. Fluid Mech., **409**, pp. 69–98.
[26] Koochesfahani, M. M., Dimotakis, P. E., and Broadwell, J. E., 1985, "A 'Flip' Experiment in a Chemically Reacting Turbulent Mixing Layer," AIAA J., **23**, pp. 1191–1194.
[27] Koochesfahani, M. M., and Dimotakis, P. E., 1985, "Laser-Induced Fluorescence Measurements of Mixed Fluid Concentration in a Liquid Plane Shear Layer," AIAA J., **23**, pp. 1700–1707.
[28] Catrakis, H. J., and Aguirre, R. C., 2004, "Interfacial-Fluid Dynamics and the Mixing Efficiency of Turbulent Flows," Phys. Fluids, **16**(12), pp. 4746–4749.
[29] Aguirre, R. C., Nathman, J. C., and Catrakis, H. J., 2006, "Flow Geometry Effects on the Turbulent Mixing Efficiency," ASME J. Fluids Eng., **129**, pp. 874–879.
[30] Caulfield, C. P., and Kerswell, R. R., 2001, "Maximal Mixing Rate in Turbulent Stably Stratified Couette Flow," Phys. Fluids, **13**(4), pp. 894–900.
[31] Everson, R., Manin, D., Sirovich, L., and Winter, M., 1998, "Quantification of Mixing and Mixing Rate From Experimental Observations," AIAA J., **36**(2), pp. 121–127.
[32] Geurts, B. J., 2001, "Mixing Efficiency in Turbulent Shear Layers," J. Turbul., **2**(17), pp. 1–23.
[33] LaRue, J. C., and Libby, P. A., 1975, "Temperature and Intermittency in the Turbulent Wake of a Heated Cylinder," Phys. Fluids, **17**, pp. 873–878.
[34] Bisset, D. K., Hunt, J. C., and Rogers, M. M., 2002, "The Turbulent/Non-Turbulent Interface Bounding a Far Wake," J. Fluid Mech., **451**, pp. 381–410.
[35] Joseph, D. D., and Preziosi, L., 1989, "Heat Waves," Rev. Mod. Phys., **61**, pp. 41–73.
[36] Brown, G. L., and Roshko, A., 1974, "On Density Effects and Large Scale Structure in Turbulent Mixing Layers," J. Fluid Mech., **64**, pp. 775–816.
[37] Paizis, S. T., and Schwarz, W. H., 1974, "An Investigation of the Topography and Motion of the Turbulent Interface," J. Fluid Mech., **63**(2), pp. 315–343.
[38] Catrakis, H. J., Aguirre, R. C., Ruiz-Plancarte, J., and Thayne, R. D., 2002, "Shape Complexity of Whole-Field Three-Dimensional Space-Time Fluid Interfaces in Turbulence," Phys. Fluids, **14**, pp. 3891–3898.
[39] Frederiksen, R. D., Dahm, W. J. A., and Dowling, D. R., 1996, "Experimental Assessment of Fractal Scale Similarity in Turbulent Flows. Part 1: One-Dimensional Intersections," J. Fluid Mech., **327**, pp. 35–72.
[40] Catrakis, H. J., and Dimotakis, P. E., 1996, "Mixing in Turbulent Jets: Scalar Measures and Isosurface Geometry," J. Fluid Mech., **317**, pp. 369–406.
[41] Prasad, R. R., and Sreenivasan, K. R., 1989, "Scalar Interfaces in Digital Images of Turbulent Flows," Exp. Fluids, **7**, pp. 259–264.
[42] Aguirre, R. C., and Catrakis, H. J., 2005, "Scalar-Threshold Dependence and Internal Dynamics in Turbulent Jets," Phys. Fluids, **17**, p. 038103.
[43] Aguirre, R. C., and Catrakis, H. J., 2004, "Aero-Optical Wavefronts and Scale-Local Characterization In Large-Reynolds-Number Compressible Turbulence," AIAA J., **42**(10), pp. 1982–1990.

Journal of Fluids Engineering

Technical Briefs

Flow Geometry Effects on the Turbulent Mixing Efficiency

Roberto C. Aguirre
Graduate Student
Mem. ASME
e-mail: raguirre@uci.edu

Jennifer C. Nathman
Graduate Student
Mem. ASME
e-mail: jnathman@uci.edu

Haris C. Catrakis[1]
Associate Professor
Mem. ASME
e-mail: catrakis@uci.edu

Iracletos Flow Dynamics and Turbulence Laboratories,
Mechanical and Aerospace Engineering,
University of California,
Irvine, CA 92697

Flow geometry effects are examined on the turbulent mixing efficiency quantified as the mixture fraction. Two different flow geometries are compared at similar Reynolds numbers, Schmidt numbers, and growth rates, with fully developed turbulence conditions. The two geometries are the round jet and the single-stream planar shear layer. At the flow conditions examined, the jet exhibits an ensemble-averaged mixing efficiency which is approximately double the value for the shear layer. This substantial difference is explained fluid mechanically in terms of the distinct large-scale entrainment and mixing-initiation environments and is therefore directly due to flow geometry effects.
[DOI: 10.1115/1.2201696]

Introduction

A practical measure of the capability of a given flow configuration, or flow geometry, to mix fluids is the mixing efficiency as examined in the companion regular paper [1]. Knowledge of the dependence of the mixing behavior on the flow geometry is very useful for optimizing the performance in various fluid systems, by mixing-efficiency enhancement or reduction, in applications ranging from film cooling for turbomachinery to laser beam propagation through high-speed flows [2–6]. There are several different definitions in use in the literature to quantify the mixing efficiency [7–10]. In this work, we utilize the mixture fraction or volume fraction of mixed fluid as a measure of the mixing efficiency with the same definition as in various previous studies [5,7,8,11]. It is helpful to recall that, with this definition, the mixing efficiency is essentially the amount of mixed fluid normalized by the large scale of the flow, with the large scale determined directly by the growth rate [11].

Previous studies have examined various aspects of mixing and of the mixing efficiency, including effects of Reynolds number, Schmidt number, and Mach number, as well as changes in boundary/inflow conditions [3,5,12–17]. Because the mixing efficiency, as a mixture fraction, is sensitive to the behavior of the mixed-fluid interfaces which are highly irregular in turbulent flows, several open questions remain. For example, it is not clear what the limiting behavior of the mixing efficiency is at large Reynolds numbers [5,15,17–19]. It is also not clear to what extent the limiting behavior may depend on the flow geometry. For fluid-engineering devices operating in flow regimes corresponding to fully developed or large-Reynolds-number turbulence, it would be useful to be able to physically model effects such as those of the flow geometry.

In the present work, we consider two different flow geometries and we examine the mixing efficiency on the basis of experimental data. The two flow geometries chosen are the single-stream shear layer and the jet. While the shear layer has essentially two-dimensional large-scale entraining vortices, the jet has three-dimensional large-scale entraining vortices. At the flow conditions examined in this work and the flow measurement location, these two cases have similar Reynolds numbers, Schmidt numbers, and growth rates in the far field of each flow in order to facilitate a direct comparison of the mixing efficiency. A large difference in the mixing efficiency is found between the two flow geometries, with the jet having a mixing efficiency approximately twice that of the single-stream shear layer at the flow conditions examined. We attribute this large difference directly to flow-geometry effects and we suggest a reason traceable to the different large-scale dynamics between the two flows examined. Implications for mixing-efficiency modeling and optimization are discussed briefly in the conclusions.

Theoretical Basis

As discussed in the companion paper [1], the mixing efficiency can be expressed in several theoretically equivalent ways, yet with varying practical implementation advantages and disadvantages, in terms of properties of the concentration field $c(\mathbf{x},t)$ and of the mixed-fluid interfaces which are associated with the isosurfaces of concentration, i.e., $c=$const. Denoting the mixing efficiency by α_m, we have [5,7,8,11,20–22]

[1]Corresponding author.

Contributed by the Fluids Engineering Division of ASME for publication in the JOURNAL OF FLUIDS ENGINEERING. Manuscript received September 16, 2004; final manuscript received February 9, 2006. Assoc. Editor: Malcolm J. Andrews. Paper presented at the 2004 ASME International Mechanical Engineering Congress (IMECE2004), November, 13–19, 2004, Anaheim, CA.

$$\alpha_m = \int_{\text{mixed}} p(c)dc = \int_{\text{mixed}} \frac{A(c)}{V_{\text{ref}}} \bar{h}(c)dc \tag{1}$$

where $p(c)$ is the probability density function of the concentration field, $A(c)$ is the surface area of the mixed-fluid interfaces, $\bar{h}(c)$ is the mean interfacial thickness, $V(c)$ is the volume of mixed fluid bounded by the interfaces, and V_{ref} is the total reference volume. From a practical implementation point of view, it is advantageous to express the mixing efficiency in terms of the volume of fluid bounded by the outer interfaces [1,20,21]

$$\alpha_m = \int_{\text{mixed}} \frac{|dV(c)|}{V_{\text{ref}}} = \frac{V_{\text{mixed}}}{V_{\text{ref}}} = 1 - \frac{V_{\text{pure}}}{V_{\text{ref}}} \tag{2}$$

where $V(c)$ is the volume of mixed fluid bounded by the interfaces as a function of concentration threshold c, V_{mixed} is the total volume of mixed fluid, and V_{pure} is the total volume of pure fluid. By pure fluid, we denote ambient pure fluid as well as any unmixed fluid present in the reference region. Thus the pure fluid volume includes the volume of each region of pure fluid that may be present within the reference region. In the shear layer, there is pure fluid always outside the layer on either side of the layer. In the jet, there is pure fluid always outside the jet. It is also important to consider any pure fluid present within the layer or within the jet. This is where it is essential to appreciate that there is a major qualitative difference below the mixing transition compared to above the mixing transition [20]. Below the transition, pure fluid is prevalent in several regions within the core of the turbulent region [23,24]. Above the transition, however, pure fluid is rarely found within the core of the turbulent region as has been shown directly in high-resolution imaging experiments [20]. This is, actually, the key reason for the observed increase in the mixing efficiency across the transition, hence, the use of the term mixing transition when this occurs. Thus, as long as the flow conditions are above the mixing transition, pure fluid will be primarily found outside the turbulent region. The flow conditions examined in the present work are above the mixing transition. Regarding the choice of the reference region, corresponding to the volume V_{ref}, the approach followed in this work is to define it in terms of the ensemble-averaged outer boundaries of the turbulent mixing regions. Thus the transverse extent of the reference region corresponds to what is commonly termed as the visual thickness defined as the average transverse extent of the turbulent mixing region [25].

The above relations, including the integral of the surface area and interfacial thickness, are included here for completeness from a theoretical point of view. Practically, the pure-fluid volume fraction is the quantity that is most robust and most easily accessible experimentally. Since the volume V_{pure} of the pure-fluid region is

$$V_{\text{pure}} = V_{\text{ref}} - V_{\text{mixed}} \tag{3}$$

the mixing efficiency must always be in the range

$$0 \leqslant \alpha_m \leqslant 1 \tag{4}$$

where, for miscible fluids, one must have $0 < \alpha_m \leqslant 1$. The extents to which a (forced) turbulent flow can approach the limiting values $\alpha_m \to 1$ or $\alpha_m \to 0$ are interesting open questions in flow optimization [26]. By flow optimization, we are referring to flow control for the use of enhancement, reduction, or regularization of the mixing efficiency. The integrations, in Eq. (2), are carried out over the region of mixed fluid. Care must be taken to identify, therefore, the mixed fluid versus the pure fluid and, for this reason, procedures for identifying the outer interface separating mixed fluid from pure fluid have been described before in several experimental and computational studies [12,20,21,27,28]. The ensemble-averaged mixing efficiency α_m can be expected in general to exhibit dependence on various flow/fluid parameters including the flow geometry, i.e.,

$$\alpha_m \equiv \alpha_m(\text{Re}, \text{Sc}, \text{M}, \text{BC/IC flow geometry, forcing}) \tag{5}$$

where Re, Sc, and M denote the Reynolds number, Schmidt number, and Mach number. The boundary/inflow conditions are denoted as BCs/ICs and the possibility of additional forcing such as electromagnetic flow forcing is also indicated [26].

Experiments and Flow Imaging

The experiments were conducted in the large-scale octagonal-tank flow facility at UC Irvine. The facility and imaging technique have been described before [20] and only a brief description will be included here. The octagonal tank has a height of 2.74 m (9 ft) and a diameter of 1.83 m (6 ft). There is optical access on all eight vertical sides by means of rectangular windows of size 0.61 m by 2.13 m (2 ft by 7 ft). There is also circular window of diameter 0.61 m (2 ft) on the bottom side of the tank. The facility can be filled with up to 8 tons or 2000 gallons of water. The large size of the facility, in combination with laser-induced fluorescence and digital-imaging techniques, is useful for studies of mixed-fluid interfaces above the mixing transition [21], i.e., at Reynolds numbers of $\text{Re} \gtrsim 10^4$, corresponding to fully developed turbulent mixing. The imaging technique employed relies on premixing at a molecular level pure water with dilute disodium fluorescein dye, exciting the dyed water with a continuous-wave laser sheet, and imaging the resulting fluorescence with a high-resolution charge-coupled-device camera system [21].

The two flow geometries compared in the present work are the single-stream planar shear layer and the round jet. Schematics of these flow geometries are shown in Fig. 1, where the single-stream shear layer is indicated on the top part of the figure and the round jet is indicated on the bottom part of the figure. To facilitate the examination and comparison of the mixing efficiency for these flow geometries, the flow imaging was conducted at the same Reynolds number of $\text{Re} \sim 20{,}000$ and the same Schmidt number of $\text{Sc} \sim 2000$ corresponding to liquid-phase fully developed turbulent mixing. Flow imaging was conducted in both cases in the far field, similarly to previous studies [15,21], to ensure a linear growth rate and self-similarity of the flow profile. In the round jet, the Reynolds number does not vary with downstream distance in the far field, whereas in the planar shear layer the Reynolds number increases linearly with downstream distance in the far field. The Reynolds number for the jet is based on the nozzle exit flow velocity of $U_0 \sim 8$ m/s and the nozzle exit diameter of $d_0 \sim 2.5$ nm. The Reynolds number for the shear layer, at the imaging location, is based on the large-scale characteristic velocity difference of $\Delta U \sim 10$ cm/s and the large spatial transverse extent or visual thickness of $L \sim 20$ cm. A spatial resolution of $\sim 1000 \times 1000$ was employed in the digital imaging to capture the upper three decades of scales, i.e., those scales which span three decades up to the largest transverse scales of the flow, which are useful to capture the dominant behavior of the volume of the pure-fluid region and therefore of the mixing efficiency [20,21]. Examples of flow visualizations of the concentration field for both flow geometries are shown in Fig. 2, where the top figure shows a streamwise slice of the single-stream shear layer and the bottom figure shows a space-time visualization of a slice of the jet. The same Schmidt number was achieved by utilizing the same disodium fluorescein dye, at the same dilute concentration to avoid laser-power attenuation, in pure water in each case. The images employed to examine flow geometry effects are in the far fields of both flows which, for the present flow conditions, correspond to behavior above the mixing transition. Thus pure fluid is rarely present in the interior of the turbulent regions, as has been directly shown in previous studies [20]. The robust outer fluid interface method, discussed in the companion paper [1], was applied to determine the mixing efficiency for each flow geometry.

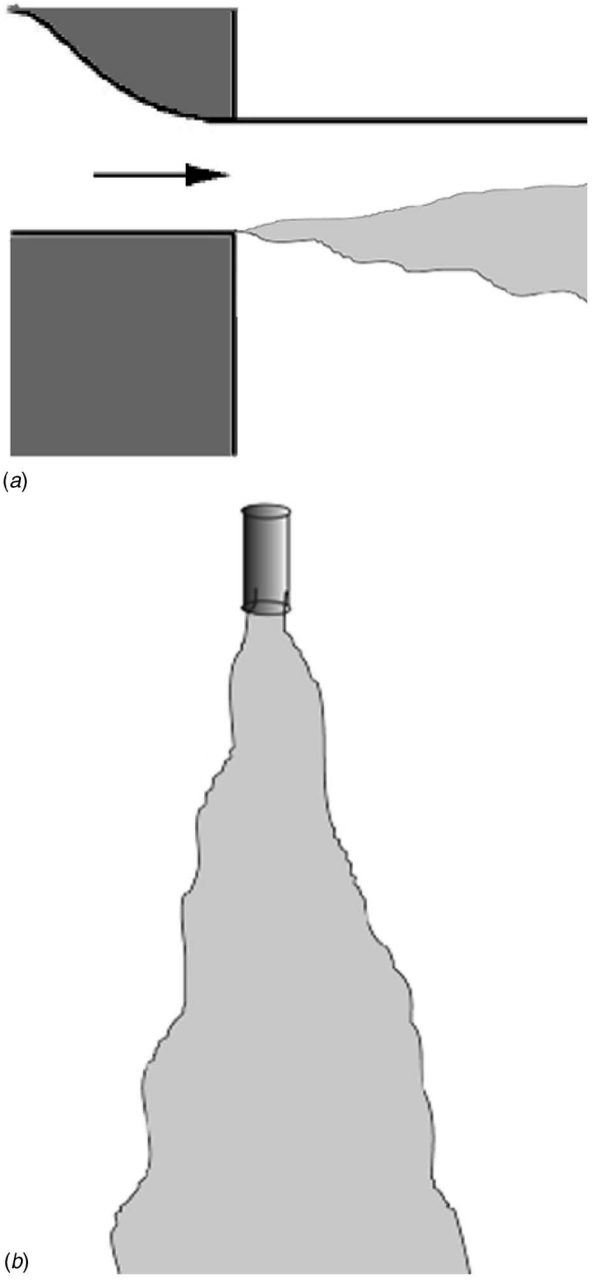

Fig. 1 Schematics of the two flow geometries examined and compared presently: the single-stream planar shear layer (top) and the round jet (bottom)

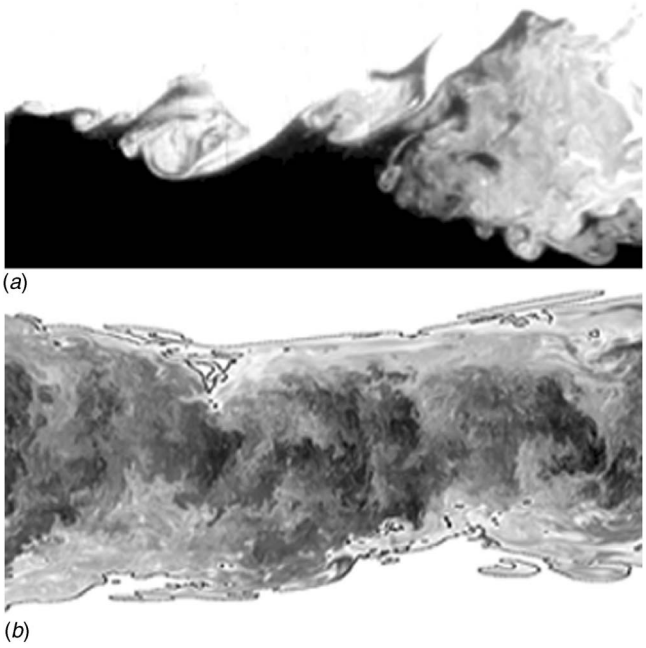

Fig. 2 Top: Example of an experimental high-resolution quantitative visualization of the spatial concentration field generated by a single-stream planar shear layer, showing a streamwise slice. While both the near field and far field are shown in this visualization, the image data utilized to evaluate the mixing efficiency are from the far field. Bottom: Example of an experimental high-resolution quantitative visualization of the space-time concentration far field of a round jet, with time increasing from left to right and the vertical dimension corresponding to transverse distance through the jet and containing the flow centerline.

Flow Geometry Effects

The present experiments and choice of flow conditions enable a direct comparison of the mixing efficiency. In other words, with regard to the general dependence of the mixing efficiency in Eq. (5), the present flow conditions are at a given Reynolds number and Schmidt number with no flow forcing but with different boundary/inflow conditions, i.e., the shear layer versus jet configurations. Figure 3 shows examples of visualizations of the mixed-fluid interfaces and high-gradient regions for the shear layer (top) and for the jet (bottom). The grey levels correspond to the magnitude of the in-plane components of the concentration-field gradient for each flow geometry, with darker regions denoting higher-gradient locally thinner interfaces. In the single-stream planar shear layer, the high-gradient regions are primarily located near the unsteady outer interfaces separating mixed fluid from pure fluid as is evident in Fig. 3 (top). In contrast, in the round jet, there are high-gradient regions interspersed throughout the interior of the jet as well as near the unsteady outer interfaces as is evident in Fig. 3 (bottom). These visualizations are consistent with previous studies of the scalar dissipation rate [29]. The higher-gradient regions are particularly significant because they are associated with higher rates of mixing. For example, in the planar shear-layer image in Fig. 3 (top), the high-gradient regions near the unsteady outer interfaces are primarily responsible for the initiation of the mixing of pure ambient fluid with already-mixed fluid.

Figure 4 shows examples of the regions of mixed fluid, marked with black, for a streamwise slice of the single-stream shear layer in the top part of the figure and for a transverse slice of the jet in the bottom part of the figure. The boundaries of the mixed-fluid regions correspond to the outer interfaces separating mixed fluid, shown as black, from pure fluid shown as white in Fig. 4. The scalar threshold(s) employed to identify the boundaries between pure fluid and mixed fluid were chosen as the values at 0.03% of the pure fluid concentration(s) as was done in earlier work [20]. This corresponds to the dynamic range of the imaged data which is 300:1. It must be noted that, physically as well as theoretically, it is well appreciated that the outer interfaces between pure fluid and mixed fluid are relatively sharp as a result of the strain-rate limited diffusion in the outer regions [28]. Thus, the outer boundaries between pure fluid and mixed fluid can be identified to within the limitations of the dynamic range of the data. The mixing efficiency was evaluated for the two flow geometries using the volume-based approach developed in previous work [21]. For the present study, two-dimensional image data at the $\sim 1000 \times 1000$

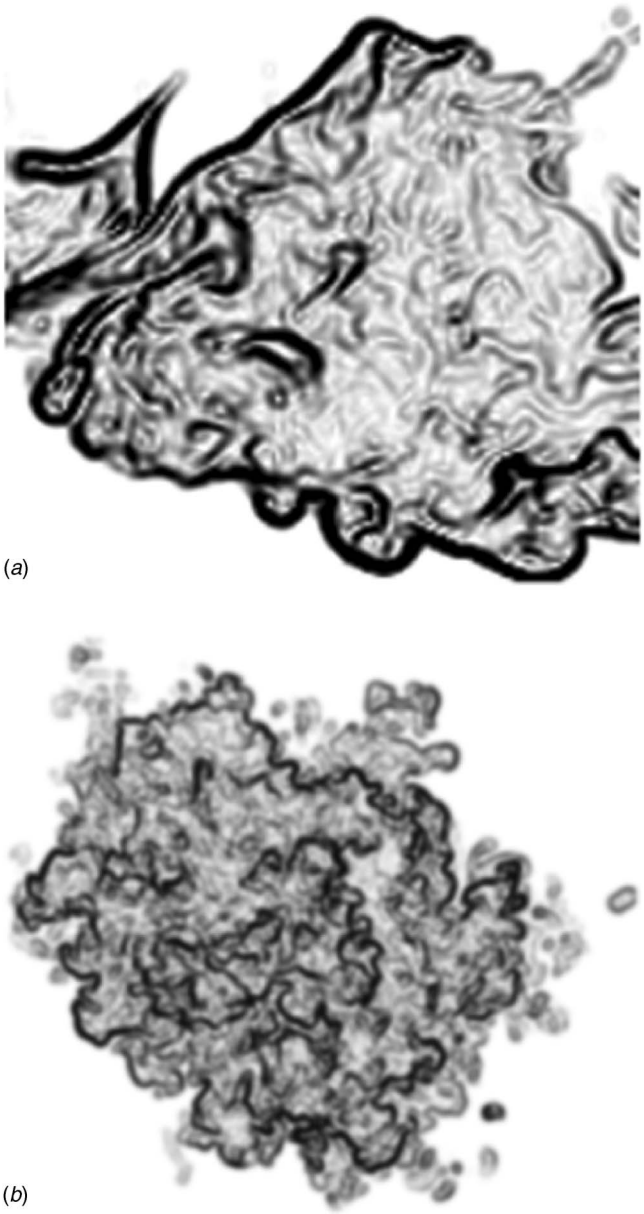

Fig. 3 Visualizations of the mixed-fluid interfaces and high-gradient regions for the shear layer (top) in a streamwise slice, and for the jet (bottom) in a transverse slice. The grey levels correspond to the magnitude of the in-plane components of the concentration-field gradient for each flow geometry, with darker regions denoting higher-gradient locally thinner interfaces.

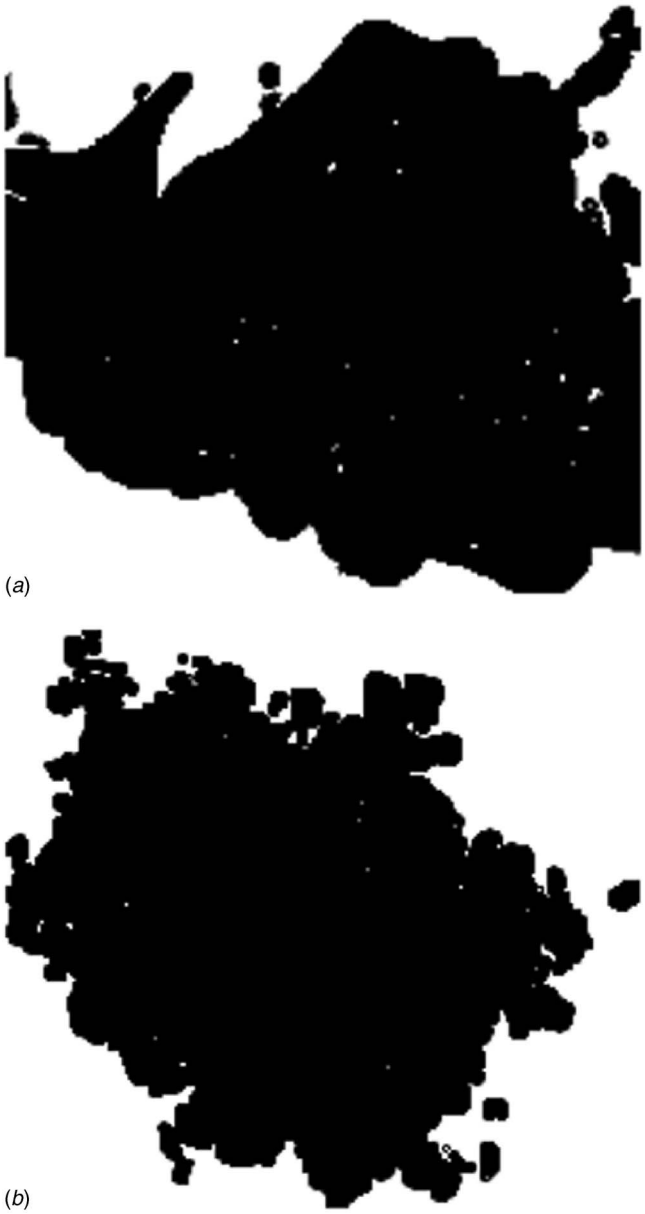

Fig. 4 Examples of the regions of mixed fluid (black) in the single-stream shear layer (top) and in the jet (bottom). The boundaries of the mixed-fluid regions correspond to the outer interfaces separating mixed fluid shown in black from the pure fluid(s) shown in white.

resolution were utilized for both flow geometries. Therefore, instead of the volume fraction, the area fraction was computed so that

$$\alpha_m = 1 - A_{pure}/A_{ref}, \tag{6}$$

cf. Eq. (2). The mixing efficiency was then ensemble-averaged over several realizations. The reference area A_{ref} and outer-interface scalar threshold were identified as described in recent work [21] and in the companion paper [1]. This procedure was repeated for both the single-stream shear layer and the jet, with ensemble averages computed over several realizations at similar values of the Reynolds number and Schmidt number as indicated above.

For the round jet, the ensemble-averaged mixing efficiency is found to be

$$\alpha_{m,jet} \sim 0.6 \tag{7}$$

for the present conditions. In contrast, even though the Reynolds numbers and Schmidt numbers are similar for the two distinct flow geometries, the ensemble-averaged mixing efficiency for the single-stream planar shear layer is found to be

$$\alpha_{m,sl} \sim 0.3 \tag{8}$$

These two mixing efficiency values differ greatly. The difference in the mixing efficiency is $\sim 100\%$, i.e., approximately a factor of 2, for the jet relative to the single-stream shear layer. The uncertainty in evaluating the mixing efficiency, based on the robust outer fluid interface method as discussed in the companion paper [1], is estimated to be of the order of $\sim 0.1\%$ which is much

smaller than the difference between the two mixing efficiency values for the two flow geometries. It must be appreciated that, while the mixing efficiency value for the shear layer corresponds to streamwise images, the mixing efficiency value for the jet corresponds to transverse images. However, the mixing values are each normalized by the appropriate reference region of fluid as discussed above. Furthermore, both of the present values are consistent with several previous experimental studies of the mixing efficiency in shear layers [5,15,18] and in jets [7,14,20].

The present findings suggest that the mixing efficiency for the two flow geometries differs significantly, by $\sim 100\%$, even though the Reynolds number and Schmidt number have similar values between the two flows. Also, as pointed out above, the growth rates are similar for these two flows. The growth rate is normalized out, in any case, for the mixing efficiency since it is the fraction of mixed fluid. The large difference in the mixing efficiency, which in this case also implies a large difference in the amount of mixed fluid since the growth rates are similar, must be attributable to the difference in the mixing environment of the large-scale vortical structures in the two flows. By mixing environment, we are referring to the flow geometry of the regions surrounding the large-scale entraining vortices and to the mixed or unmixed state of the fluid in those regions. In the round jet, the large-scale vortices continuously remix jet fluid that has already been mixed upstream, in addition to entraining pure ambient fluid. This is in stark contrast from the mixing environment of the shear-layer geometry where the large-scale shear-layer vortices continuously mix primarily pure fluids. Furthermore, previous studies of the small-scale interfacial geometry have shown that such flows exhibit similar properties for the area-volume ratio and the interfacial fractal-dimension behavior [5,27,30]. Therefore, the substantial difference in mixing efficiency reflects the large-scale effects, i.e., the three-dimensionality versus two-dimensionality of the large-scale vortical structures in the jet versus the shear layer in the context of their mixing environment. The present findings are for incompressible flow conditions and provide a useful reference point for also examining effects of compressibility.

Conclusions and Implications

Flow-geometry effects have been examined on the mixing efficiency quantified as the mixture fraction. The two flow geometries considered are the single-stream planar shear layer and the round jet, with measurements of the concentration field in the far field of both flows. The flow conditions examined, in both geometries, are at similar values of the Reynolds number and Schmidt number, as well as for similar growth rates. For the round jet, the mixing efficiency is found to be $\alpha_{m,jet} \sim 0.6$. In contrast, for the single-stream shear layer, the mixing efficiency is found to be $\alpha_{m,sl} \sim 0.3$. The large difference between these mixing efficiency values, which are each consistent with previous studies, are attributable directly to the flow-geometry effects. Specifically, while the large-scale jet vortices continuously remix jet fluid that has already been mixed upstream in addition to entraining and mixing pure ambient fluid, the large-scale shear-layer vortices continuously initiate mixing of pure fluids primarily. The implications of these findings are that the design of the flow geometry can be tailored to have direct effect for optimization of the mixing efficiency, e.g., for enhancement or reduction, as it is the flow geometry that can significantly affect the mixing-initiation environment of the large-scale vortices and thereby the mixing efficiency.

Acknowledgment

This work is part of a research program on turbulence and flow dynamics, supported by the National Science Foundation and by the Air Force Office of Scientific Research. The authors are grateful to J. Ruiz-Plancarte for assistance with the experiments and to the referees for their insightful comments.

Nomenclature

A = interfacial surface area
c = fluid concentration
d_0 = jet nozzle exit diameter
$\bar{h}$ = average thickness along interface
L = large scale
M = Mach number
P = probability density of concentration
Re = Reynolds number
Sc = Schmidt number
U_0 = jet nozzle exit velocity
ΔU = large-scale velocity difference
V = volume of fluid bounded by concentration interfaces
V_{mixed} = volume of mixed-fluid region
V_{pure} = volume of pure-fluid region
V_{ref} = normalizing volume
α_m = turbulent mixing efficiency
$\alpha_{m,jet}$ = jet turbulent mixing efficiency
$\alpha_{m,sl}$ = shear layer mixing efficiency

References

[1] Aguirre, R. C., Catrakis, H. J., Nathman, J. C., and Garcia, P. J., 2006, "Robust Volume-Based Approach for the Turbulent Mixing Efficiency," ASME J. Fluids Eng., **128**, pp. 864–873.
[2] Hale, C. A., Plesniak, M. W., and Ramadhyani, S., 2000, "Film Cooling Effectiveness for Short Film Cooling Holes Fed by a Narrow Plenum," ASME J. Turbomach., **122**, pp. 553–557.
[3] Mi, J., Nathan, G. J., and Nobes, D. S., 2001, "Mixing Characteristics of Axisymmetric Free Jets From a Contoured Nozzle, an Orifice Plate and a Pipe," ASME J. Fluids Eng., **123**, pp. 878–883.
[4] Jumper, E. J., and Fitzgerald, E. J., 2001, "Recent Advances in Aero-Optics," Prog. Aerosp. Sci., **37**, pp. 299–339.
[5] Dimotakis, P. E., 1991, "Turbulent Free Shear Layer Mixing and Combustion," *High Speed Flight Propulsion Systems* (Progress in Astronautics and Aeronautics Vol. 37), S. Murthy and E. Curran, eds., AIAA, Washington, DC.
[6] Catrakis, H. J., 2004, "Turbulence and the Dynamics of Fluid Interfaces With Applications to Mixing and Aero-Optics," *Recent Research Developments in Fluid Dynamics*, N. Ashgriz and R. Anthony, eds., Transworld Research Network Publishers, Kerala, India, Vol. 5, pp. 115–158.
[7] King, G. F., Dutton, J. C., and Lucht, R. P., 1999, "Instantaneous, Quantitative Measurements of Molecular Mixing in the Axisymmetric Jet Near Field," Phys. Fluids, **11**, pp. 403–416.
[8] deBruynKops, S. M., and Riley, J. J., 2001, "Mixing Models for Large-Eddy Simulation of Nonpremixed Turbulent Combustion," ASME J. Fluids Eng., **123**, pp. 341–346.
[9] Geurts, B. J., 2001, "Mixing Efficiency in Turbulent Shear Layers," IEEE Trans. Power Syst., **2**(17), pp. 1–23.
[10] Caulfield, C. P., and Kerswell, R. R., 2001, "Maximal Mixing Rate in Turbulent Stably Stratified Couette Flow," Phys. Fluids, **13**(4), pp. 894–900.
[11] Roshko, A., 1991, "The Mixing Transition in Free Shear Flows," *The Global Geometry of Turbulence*, J. Jiménez, ed., Plenum, New York, pp. 3–11.
[12] Koochesfahani, M. M., and Dimotakis, P. E., 1986, "Mixing and Chemical Reactions in a Turbulent Liquid Mixing Layer," J. Fluid Mech., **170**, pp. 83–112.
[13] Mungal, M. G., and Dimotakis, P. E., 1984, "Mixing and Combustion With Low Heat Release in a Turbulent Shear Layer," J. Fluid Mech., **148**, pp. 349–382.
[14] Dahm, W. J. A., and Dimotakis, P. E., 1990, "Mixing at Large Schmidt Number in the Self-Similar Far Field of Turbulent Jets," J. Fluid Mech., **217**, pp. 299–330.
[15] Karasso, P. S., and Mungal, M. G., 1996, "Scalar Mixing and Reaction in Plane Liquid Shear Layers," J. Fluid Mech., **323**, pp. 23–63.
[16] MacKinnon, C. G., and Koochesfahani, M. M., 1997, "Flow Structure and Mixing in a Low Reynolds Number Forced Wake Inside a Confined Channel," Phys. Fluids, **9**, pp. 3099–3101.
[17] Freund, J. B., Moin, P., and Lele, S. K., 2000, "Compressibility Effects in a Turbulent Annular Mixing Layer. Part 2. Mixing of a Passive Scalar," J. Fluid Mech., **421**, pp. 269–292.
[18] Clemens, N. T., and Mungal, M. G., 1995, "Large-Scale Structure and Entrainment in the Supersonic Mixing Layer," J. Fluid Mech., **284**, pp. 171–216.
[19] Fernando, H. J. S., and Hunt, J. C. R., 1996, "Some Aspects of Turbulence and Mixing in Stably Stratified Fluids," Dyn. Atmos. Oceans, **23**, pp. 35–62.
[20] Catrakis, H. J., Aguirre, R. C., Ruiz-Plancarte, J., Thayne, R. D., McDonald, B. A., and Hearn, J. W., 2002, "Large-Scale Dynamics in Turbulent Mixing and the Three-Dimensional Space-Time Behaviour of Outer Fluid Interfaces," J. Fluid Mech., **471**, pp. 381–408.
[21] Catrakis, H. J., and Aguirre, R. C., 2004, "Interfacial-Fluid Dynamics and the

Mixing Efficiency of Turbulent Flows," Phys. Fluids, **16**(12), pp. 4746–4749.
[22] Aguirre, R. C., and Catrakis, H. J., 2005, "On Intermittency and the Physical Thickness of Turbulent Fluid Interfaces," J. Fluid Mech., **540**, pp. 39–48.
[23] Dimotakis, P. E., 2000, "The Mixing Transition in Turbulent Flows," J. Fluid Mech., **409**, pp. 69–98.
[24] Dimotakis, P. E., 2005, "Turbulent Mixing," Annu. Rev. Fluid Mech., **37**, pp. 329–356.
[25] Brown, G. L., and Roshko, A., 1974, "On Density Effects and Large Scale Structure in Turbulent Mixing Layers," J. Fluid Mech., **64**, pp. 775–816.
[26] Gad-el Hak, M., 2000, *Flow Control: Passive, Active, and Reactive Flow Management*, Cambridge University Press, Cambridge.
[27] Sreenivasan, K. R., 1991, "Fractals and Multifractals in Fluid Turbulence," Annu. Rev. Fluid Mech., **23**, pp. 539–600.
[28] Bisset, D. K., Hunt, J. C., and Rogers, M. M., 2002, "The Turbulent/Non-Turbulent Interface Bounding a Far Wake," J. Fluid Mech., **451**, pp. 381–410.
[29] Su, L. K., and Clemens, N. T., 1999, "Planar Measurements of the Full Three-Dimensional Scalar Dissipation Rate in Gas-Phase Turbulent Flows," Exp. Fluids, **27**, pp. 507–521.
[30] Jiménez, J., and Martel, C., 1991, "Fractal Interfaces and Product Generation in the Two-Dimensional Mixing Layer," Phys. Fluids A, **3**(5), pp. 1261–1268.

Oscillation in Height of a Negatively Buoyant Jet

P. D. Friedman
Department of Mechanical Engineering,
University of Massachusetts Dartmouth,
Dartmouth, MA 02747
e-mail: pfriedman@umassd.edu

Introduction

Jets and fountains with reversing buoyancy occur in numerous natural and man-made situations [1] including, for example, oxygen jets directed into molten metal furnaces [2], the overshoot stage of a smokestack discharging into a stratified atmosphere [3], and underwater volcanic eruptions [4]. For simplicity, we assume an upward directed jet or fountain with downward buoyancy as shown in Fig. 1, although the results apply equally to downward directed jets and fountains with upward buoyancy. The flow structure consists of a rising central core, surrounded by an annular downward flow [5,6], and under appropriate conditions includes mixing [7,8] and phase mingling [9,10]. The primary parameter governing this flow structure is the Richardson number [11], which is the ratio of negative buoyancy to inertial forces

$$\mathrm{Ri} = \frac{Dg\Delta\rho}{\rho_j U^2}$$

where D is the vent diameter, ρ_j is the jet fluid density, and $\Delta\rho$ is the difference in density between the jet and surrounding fluids. For turbulent flows, the characteristic jet velocity is the volumetric flow rate divided by the cross-sectional area ($U=U_{Ave}$). For laminar flows, which have a higher total momentum for a similar average velocity, the characteristic velocity is the root-mean-square velocity ($U=\sqrt{2}U_{Ave}$) [6]. Apart from predicting the onset of turbulence, the Reynolds number has no effect. Regardless of the fluid pair selected, the maximum height (h—see Fig. 1) collapses to a single curve [$h/D=f(\mathrm{Ri})$] [6], and the flow transitions through distinct regimes, which are a function of Ri [11]. At $\mathrm{Ri}>1$, negative buoyancy dominates and the jet forms a shallow and stable penetration into the fluid above [Fig. 2(*a*)], characterized by a nearly constant height with only slight fluctuations that result from waves on the interface. At $\mathrm{Ri}<1$, the flow oscillates in height in a cycle that consists of the formation of a tall, steep, walled fountain [Fig. 2(*b*)] followed by an asymmetric collapse [Figs. 2(*c*) and 2(*d*)]. Through dimensional analysis, the frequency of this oscillation is predicted to follow a functional relationship for Strouhal number

$$\frac{fD}{U} = f\left(\frac{Dg\Delta\rho}{\rho U^2}, \frac{\rho UD}{\mu}\right) \quad \text{or} \quad \mathrm{St} = f(\mathrm{Ri},\mathrm{Re})$$

As shown below, the effect of the Reynolds number is again limited to establishing the onset of turbulence and determining the appropriate characteristic velocity.

The purpose of this paper is to characterize the frequency and amplitude of the oscillations in height, which produce a number of important effects. For example, in the case of a subaqueous volcanic eruption, phase mingling between the rising magma and water above can potentially cause cyclical phreatomagmatic explosions [12] that are significantly more violent than dry eruptions [13,14] and account for a disproportionate number of fatalities [15].

Experiment

The data analyzed in this paper results from experiments performed at The Johns Hopkins University during the period 1999–2000. The experiments, described more fully in [11], consisted of directing a water fountain upward into diesel fuel (LSRD-4, Specified Fuels and Chemicals of Channelview, Texas) and recording the results on SVHS video. The Richardson number was varied over four orders of magnitude using six different pipe diameters ranging from 1.38 to 5.25 cm. A total of 125 different flow rate and pipe diameter combinations were tested and recorded for 1-minute experiments. Silhouette photography was performed by back illuminating through a diffuser screen. Rise heights were measured in a frame-by-frame analysis [6,11]. The maximum error based on pixel resolution was 2% of the measured height.

Data and Results

Figures 3 and 4 summarize the magnitude and frequency of oscillations in the rise height of the jet. Figure 3 shows the relationship between the Richardson number and amplitude of oscillation $[(h_{Upper}-h_{Lower})/h_{Lower}\times 100\%]$, where $h_{Upper}=\bar{h}_{\mathrm{Max}}+\sigma_{h_{\mathrm{Max}}}$ (the average height at the top of the oscillations plus one standard deviation). The lower height is similarly defined, $h_{Lower}=\bar{h}_{\mathrm{Min}}-\sigma_{h_{\mathrm{Min}}}$. At the high Richardson numbers associated with a stable flow pattern ($\mathrm{Ri}>1.0$), the resulting fluctuation is small. The percentage change in height is generally less than about 20% and examination of the video recording indicates that the fluctuations that are present result from waves that form on the interface. As the Richardson number is decreased to the onset of an unstable regime ($\mathrm{Ri}<1.0$) the magnitude of the height fluctuation increases reaching a maximum at about $\mathrm{Ri}=0.5$. As the Richardson number is further decreased, the jet continuously reforms as it collapses and the resulting height fluctuations decrease in magnitude.

Figure 4 is a plot of $\mathrm{St}=f(\mathrm{Ri})$. At $\mathrm{Ri}>1.0$, the jet produces a stable flow pattern that forms a smooth and nonoscillatory deformation in the upper fluid. As Ri is decreased to $\mathrm{Ri}\cong 1$, there is a transitional range that is intermittently stable or unstable. In this range, the jet would form a stable pattern for periods of several seconds up to about a minute, and then begin to oscillate. After a period of unsteady oscillation, it would return to the stable flow pattern. In this transitional range of Ri, it is not possible to quantify St. At moderate Richardson numbers ($0.1<\mathrm{Ri}<1.0$), the flow structure collapses and reforms in a cyclical pattern. Here the Strouhal number is constant ($\mathrm{St}\cong 0.16$). As the Richardson number is further decreased ($\mathrm{Ri}<0.1$), the flow remains unstable, but changes to a pattern with a deep and continuously collapsing fountain where instead of completely collapsing, it sheds finger-like projections. The depth of penetration becomes more uniform, although the entire flow pattern occasionally collapses without any consistent frequency. For this reason it becomes more difficult to quantify the Strouhal number at $\mathrm{Ri}<0.1$.

Conclusions

A negatively buoyant jet will oscillate in height for $\mathrm{Ri}<1$ with a maximum fluctuation in height of 60%–90% based on the minimum height, occurring at about $\mathrm{Ri}=0.5$. The Strouhal number for the oscillation is approximately $\mathrm{St}\cong 0.16$ for $0.1<\mathrm{Ri}<1.0$.

Contributed by the Fluids Engineering Division of ASME for publication in the JOURNAL OF FLUIDS ENGINEERING. Manuscript received March 14, 2005; final manuscript received December 1, 2005. Assoc. Editor: James A. Liburdy.

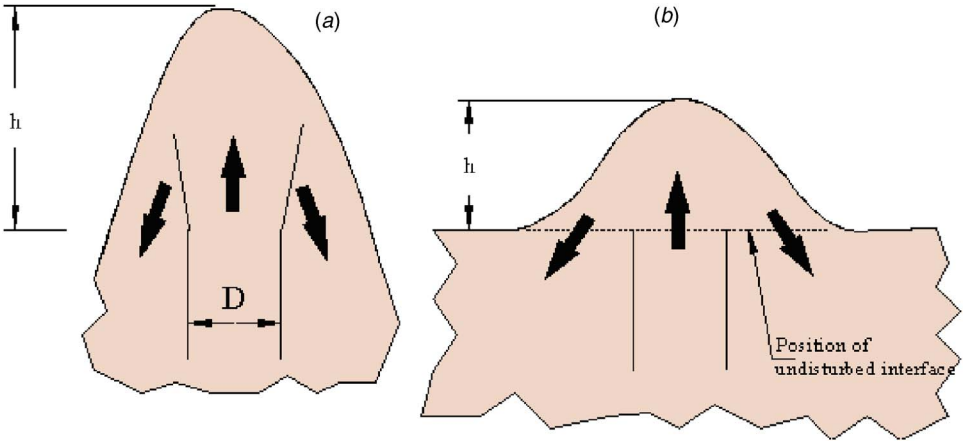

Fig. 1 (*a*) **Negatively buoyant fountain discharging into a lighter fluid above;** (*b*) **Negatively buoyant jet impinges on an interface with a lighter fluid**

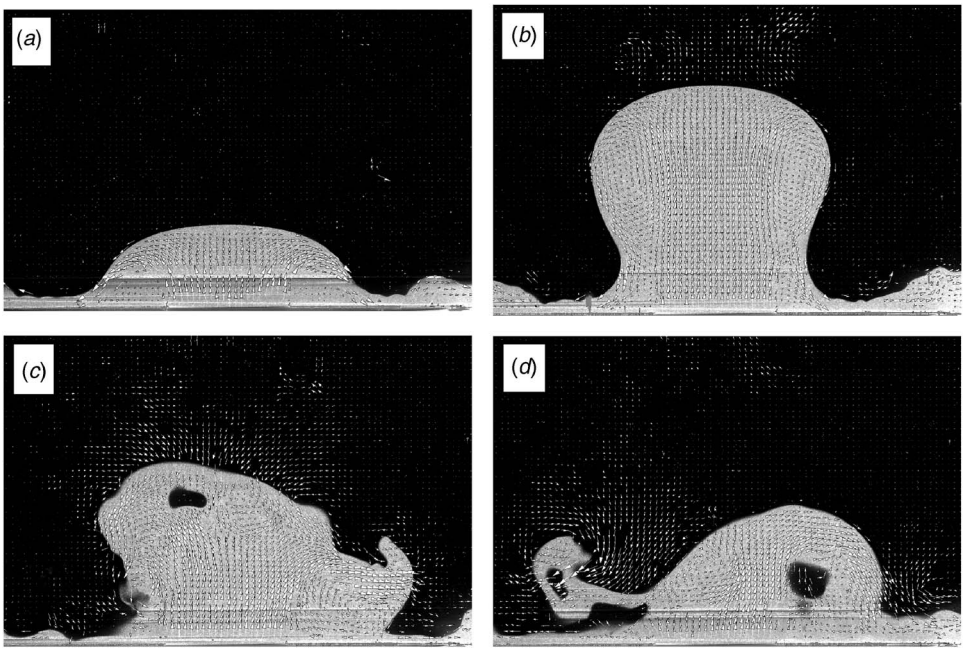

Fig. 2 (*a*) **Stable, nonoscillatory flow pattern above the transitional Richardson number (Ri >1). For (Ri<1) a cycle develops that starts with** (*b*)**, the formation of a tall unstable fountain, which loses symmetry** (*c*) **and collapses** (*d*)

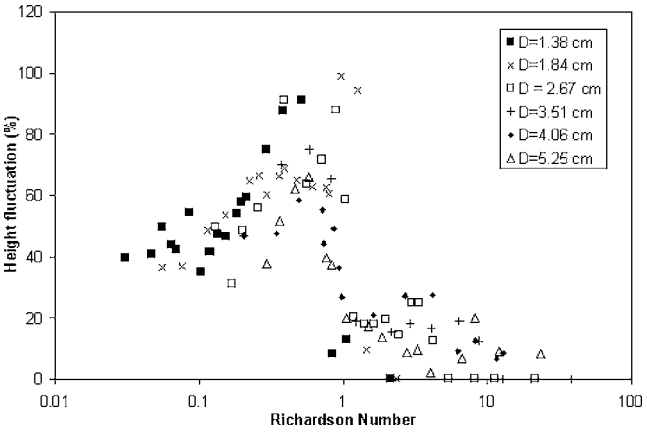

Fig. 3 Amplitude of oscillation in height of a negatively buoyant jet $[(h_{Upper}-h_{Lower})/h_{Lower}\times 100\%]$, **where** $h_{Upper}=\bar{h}_{Max}+\sigma_{h_{Max}}$ **(the average height at the top of the oscillations plus the standard deviation in the upper height). The lower height is defined similarly** $h_{Lower}=\bar{h}_{Min}-\sigma_{h_{Min}}$

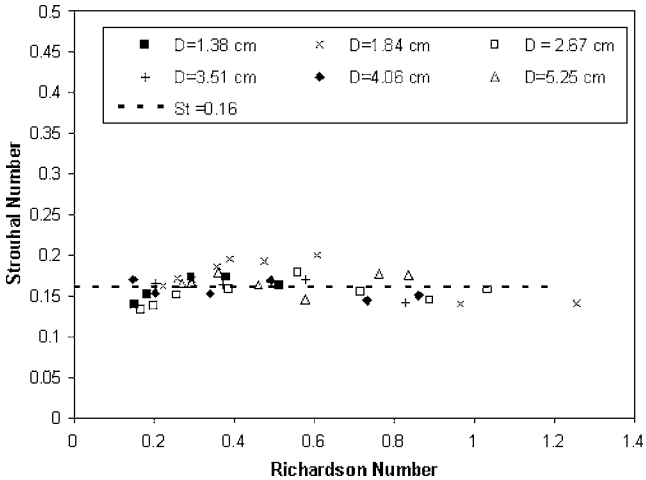

Fig. 4 Oscillation frequency of a negatively buoyant jet in terms of a dimensionless Strouhal number (fD/U).

Acknowledgment

This material is based on work supported by the National Science Foundation under Grant No. 0408946, Program Manager Sonia Esperanca.

References

[1] List E. J., 1982, "Turbulent Jets and Plumes," Annu. Rev. Fluid Mech., **14**, pp. 189–212.
[2] Qian, F., Mutharasan, R., and Farouk, B., 1996, "Studies of Interface Deformations in Single- and Multi-Layered Liquid Baths Due to an Impinging Gas Jet," Metall. Mater. Trans. B, **27**, pp. 911–920.
[3] Baines, W. D., 1975, "Entrainment by a Plume or Jet at a Density Interface," J. Fluid Mech., **68**, pp. 309–320.
[4] Kokelaar, B. P., 1986, "Magma-Water Interactions in Subaqueous and Emergent Balasatic Volcanism," Bull. Volcanol. (Heidelberg), **48**, pp. 275–289.
[5] Turner, J. S., 1966, "Jets and Plumes With Negative or Reversing Buoyancy," J. Fluid Mech., **26**, pp. 779–792.
[6] Friedman, P. D. and Katz, J., 2000, "Rise Height for Negatively Buoyant Fountains and Depth of Penetration for Negatively Buoyant Jets Impacting an Interface," ASME J. Fluids Eng., **122**, pp. 779–782.
[7] Corriveau, A. F. and Baines, W. D., 1994, "A pH Indicator Technique for Measurement of Concentration During Mixing in a Container by a Negative Buoyant Jet," J. Hydraul. Res., **32**, pp. 291–302.
[8] Shy, S. S., 1995, "Mixing Dynamics of Jet Interaction With a Sharp Density Interface," Exp. Therm. Fluid Sci., **10**, pp. 355–369.
[9] Banks, R. B. and Chandrasekhara, D. V., 1962, "Experimental Investigation of the Penetration of a High Velocity Gas Jet Through a Liquid Surface," J. Fluid Mech., **15**, pp. 13–34.
[10] Friedman, P. D., Winthrop, A. L., and Katz, J., 2001, "Droplet Formation and Size Distributions from an Immiscible Interface Impinged with a Vertical Negatively Buoyant Jet," Atomization Sprays, **11**, pp. 269–290.
[11] Friedman, P. D. and Katz, J., 1999, "The Flow and Mixing Mechanisms Caused by the Impingement of an Immiscible Interface With a Vertical Jet," Phys. Fluids, **11**, pp. 2598–2606.
[12] Thorarinsson, S., 1967, *Surtsey—The New Island in the North Atlantic*, Viking, New York, pp. 47.
[13] Wohletz, K. H., 1986, "Explosive Magma-Water Interactions: Thermodynamics, Explosion Mechanisms, and Field Studies," Bull. Volcanol. (Heidelberg), **48**, pp. 31–64.
[14] Zimanowski, B., 1998, "Phreatomagmatic Explosions," in *From Magma to Tephra*, A. Freundt, and M. Rosi eds. Elsevier, Netherlands, pp. 25–50.
[15] Mastin, L. G. and Witter, J. B., 2000, "The Hazards of Eruptions Through Lakes and Seawater," J. Volcanol. Geotherm. Res., **97**, pp. 195–214.

The Depth of Correlation in Micro-PIV for High Numerical Aperture and Immersion Objectives

Christopher J. Bourdon
Experimental Thermal Fluids and Aero Sciences,
Engineering Sciences Center,
Sandia National Laboratories,
PO Box 5800, MS 0834,
Albuquerque, NM 87185

Michael G. Olsen
Department of Mechanical Engineering,
Iowa State University,
3025 H. M. Black Engineering Building,
Ames, IA 50011

Allen D. Gorby
Experimental Thermal Fluids and Aero Sciences,
Engineering Sciences Center,
Sandia National Laboratories,
PO Box 5800, MS 0834,
Albuquerque, NM 87185

*The analytical model for the depth of correlation (measurement depth) of a microscopic particle image velocimetry (micro-PIV) experiment derived by Olsen and Adrian (Exp. Fluids, **29**, pp. S166–S174, 2000) has been modified to be applicable to experiments using high numerical aperture optics. A series of measurements are presented that experimentally quantify the depth of correlation of micro-PIV velocity measurements which employ high numerical aperture and magnification optics. These measurements demonstrate that the modified analytical model is quite accurate in estimating the depth of correlation in micro-PIV measurements using this class of optics. Additionally, it was found that the Gaussian particle approximation made in this model does not significantly affect the model's performance. It is also demonstrated that this modified analytical model easily predicts the depth of correlation when viewing into a medium of a different index of refraction than the immersion medium.*
[DOI: 10.1115/1.2201649]

Keywords: micro-PIV, depth of correlation, microfluidics, PIV

Introduction

Microscopic particle image velocimetry (micro-PIV) has emerged as an important tool for measuring fluid velocity within microfluidic devices. Micro-PIV utilizes volume illumination of the entire depth of a microfluidic device and relies on microscope optics to provide particle images from which velocity information is extracted. Thus, the measurement depth, or *depth of correlation*, of velocity measurements generated by a micro-PIV system is dependent on the optics of the imaging system [1] and can be influenced by the particle size, magnitude of Brownian motion [2], and the out-of-plane velocity component [3]. The characterization of the depth of correlation and its dependence on the imaging system, particle size, and flowfield thermodynamics and fluid dynamics is therefore critical for both design of experiments and for the interpretation of experimental results.

Olsen and Adrian [1] developed a simple model of the depth of correlation which stated that the depth of correlation is based on the optics of the imaging system and the physical characteristics of the imaged particles. Experiments have already been performed to verify this model for low-numerical aperture (NA) and low-magnification applications [4]. The comparison of experimental measurements to this analytical expression of the depth of correlation was highly accurate for numerical aperture values of 0.4 or less, the upper range of that work (note that $\mathrm{NA}=1/2f_{\#}$ if the paraxial approximation is used, where $f_{\#}$ is the focal number of the imaging system).

Often, micro-PIV experiments are performed using oil or water immersion optics in order to increase the amount of light gathered from the seed particles and increase the image resolution and signal-to-noise ratio. It is at these conditions that some of the assumptions made in the analytical model of the depth of correlation come most into question. Namely, the model describes the particle image as a Gaussian envelope whose diameter is determined by the convolution of the geometric particle with a diffractive term, and the optical system is approximated as a thin lens system. Additionally, this model does not explicitly allow for the use of immersion optics.

It is the intention of this report to investigate several important concerns in order to confidently apply the estimate of the depth of correlation to experiments incorporating high-NA and immersion optics. First, the appropriateness of Gaussian particle and thin lens approximations used in this model must be investigated at higher NA and magnification than the earlier study. As the light-gathering power and magnification of the optical system increases, the non-Gaussian nature of the experimental particle images becomes more apparent and could potentially lead to significant discrepancies in the depth of correlation obtained by this model and an actual experiment. Second, it must be determined how this model may be used when an immersion objective lens is used for imaging. Third, it has also been suggested that the effective NA of the imaging system will be affected by imaging into a fluid of a different index of refraction than the immersion medium (i.e., looking into a water-filled microchannel with an oil immersion lens) [5].

Analytical Solution of the Depth of Correlation

Olsen and Adrian [1] developed an analytical model to describe the relative contribution of tracer particles to the resulting velocity measurement in a micro-PIV experiment employing a cross-correlation algorithm. This model describes an individual particle's image as a Gaussian envelope, whose apparent diameter is a convolution of the geometric particle image and the point response function of a diffraction-limited lens measured at the first dark ring of the Airy disk intensity distribution. The average relative contribution of a particle image pair to measured velocity as determined from the displacement portion of the correlation function is captured in a quantity termed the weighting function.

The model, when all reasonable assumptions are applied, defines the contribution of particles at a distance Δz from the object (focal) plane to the overall correlation function in the absence of diffusion and out-of-plane motion as

$$W(\Delta z) = \left[M^2 d_p^2 + 5.95(M+1)^2 \lambda^2 (1/2\mathrm{NA})^2 + \frac{M^2 \Delta z^2}{(1/2\mathrm{NA})^2} \right]^2 \tag{1}$$

where d_p is the particle diameter, NA is the numerical aperture of the objective, M is the objective magnification, and λ is the wavelength of light collected. The assumptions necessary to obtain Eq. (1) from Ref. [1], Eq. (42) include uniform illumination through-

Contributed by the Fluids Engineering Division of ASME for publication in the JOURNAL OF FLUIDS ENGINEERING. Manuscript received February 15, 2005; final manuscript received November 17, 2005. Review conducted by Joseph Katz. Paper presented at the 2004 ASME International Mechanical Engineering Congress (IMECE2004), Anaheim, CA, November 13–19, 2004.

out the interrogation volume, uniform weighting of the entire correlation window in calculating the crosscorrelation, and that the particle separation from the image plane is much smaller than the working distance of the objective. The authors would also point out that we have used the NA above in Eq. (1) rather than the f number ($f_\#$), as was used in the original publication [1]. This is because the intensity distribution of the three-dimensional diffraction pattern of a point source imaged through a circular aperture is determined from the converging spherical light wavefront passing through the aperture, rather than the plane of the aperture itself [6]. Therefore, the numerical aperture (sine of the light collection half-angle in air) is the appropriate quantity rather than the f number (tangent of the light collection half-angle). Olsen and Adrian's work dealt with standard macroscale PIV as well as the microscale case, where $f_\#$ is commonly used. For low-NA applications ($NA < 0.4$), $\tan\theta \cong \sin\theta$, and does lead to significant error.

The depth of correlation is then defined as

$$z_{\text{corr}} = 2\left\{\frac{(1-\sqrt{\epsilon})}{\sqrt{\epsilon}}\left[\frac{d_p^2}{4\text{NA}^2} + \frac{5.95(M+1)^2\lambda^2}{16M^2\text{NA}^4}\right]\right\}^{1/2} \tag{2}$$

where ϵ is the threshold weighting function value where particles are no longer considered to contribute to the calculated velocity (normally taken as 0.01). The particle images are approximated as Gaussian functions in order to attain this closed-form solution. This analysis did not account for the presence of any immersion medium between the objective and particles. Experiments have already been performed to verify this model for low-NA and low-magnification applications [4]. The comparison of experimental measurements to this analytical expression of the depth of correlation demonstrated that Eq. (1) was highly accurate for numerical aperture values of 0.4 or less, the upper range of that work.

Because the depth of correlation equation (Eq. (2)) has been developed without accounting for the presence of an immersion medium (other than air) between the lens and the particles, this model must be slightly modified to be extended to this case. Meinhart and Wereley [5] suggest that it is the angle of the light collection cone that determines the nature of the particle image, and not the numerical aperture directly. Since the numerical aperture of a lens is defined as

$$\text{NA} = n_0 \sin\theta \tag{3}$$

where θ is the half-angle of the cone of light subtended by the objective lens, and n_0 is the index of refraction of the immersion medium, this suggestion would be irrelevant for an air immersion lens ($n_0 = 1.0$). If we replace the $f_\#$ in Eqs. (1) and (2) with the half-angle of the light collection cone and express it in terms of the numerical aperture and index of refraction of the immersion medium (Eq. (3)), the weighting function becomes

$$W(\Delta z) = \left[M^2 d_p^2 + 5.95(M+1)^2\lambda^2(n_0/2\text{NA})^2 + \frac{M^2\Delta z^2}{(n_0/2\text{NA})^2}\right]^{-2} \tag{4}$$

and the depth of correlation is defined as

$$z_{\text{corr}} = 2\left\{\frac{(1-\sqrt{\epsilon})}{\sqrt{\epsilon}}\left[\frac{n_0^2 d_p^2}{4\text{NA}^2} + \frac{5.95(M+1)^2\lambda^2 n_0^4}{16M^2\text{NA}^4}\right]\right\}^{\frac{1}{2}} \tag{5}$$

It has also been suggested that the effective NA of the imaging system will be affected by imaging into a fluid of a different index of refraction than the immersion medium (i.e., looking into a water-filled microchannel with an oil immersion lens) [5].

Measurement of the Depth of Correlation

It has been demonstrated [4] that the weighting function of a particle located at a fixed displacement from the focal plane is directly proportional to the curvature of the correlation function at the location that corresponds to the particle displacement between the first and second images (the correlation peak). This conclusion was formed by recognizing that the contribution of a particle to the weighting function is determined by its ability to move the correlation peak, and not just its overall contribution to the correlation function. In other words, an in-focus particle, which will have a sharp, well defined correlation function, is more likely to influence the estimate of the average displacement of a group of particles in an interrogation volume than an out-of-focus particle, which will have a broad, rounded correlation function. In order to validate the analytical model [1], the curvature about the peak of the correlation function generated from particles at a known displacement from the focal plane of the imaging system must be measured experimentally.

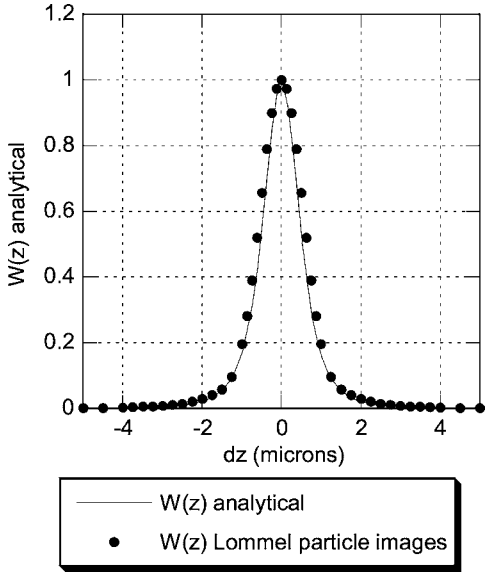

Fig. 1 Comparison of the weighting function calculated using three-dimensional diffraction pattern of a 1 μm particle image and Eq. (4) for a $M=40$, NA=1.25 oil immersion lens

This measurement cannot be performed in a typical micro-PIV experiment, since the particles are positioned at random (and not directly measurable) depths within the flow device. Therefore, all measurements performed in this work were performed on images of particles affixed to a microscope slide in a thin layer. The separation from focus can thus be controlled directly by adjusting the position of the slide in relation to the objective. In order to extract the shape of the weighting function, a series of particle image pairs are acquired at successive separations from the focal plane, from positive (focus before the particles) to negative (focus after the particles) separations. The weighting function is then determined from measuring the curvature of the correlation function about its peak for each image pair at each separation.

Results and Discussion

Three separate experiments were performed to address the performance of the analytical model of the depth of correlation [1]. These experiments were performed using 1.0 μm fluorescent particles with a capacitance-voltage of 0.01, whose peak emission occurred at 610 nm. First, the weighting function was determined from "synthetic" particle images generated by convolving the three-dimensional diffraction pattern of a point source with the geometric image of a particle in the image plane. The weighting function was calculated from these computer-generated particle images using the technique described in the previous section. Figure 1 displays the weighting function determined from these synthetic images along with the analytical solution for the weighting function for an optical system with a magnification $M=40$, and numerical aperture NA=1.25. This demonstrates quite excellent agreement between the two methods. Therefore, even though the

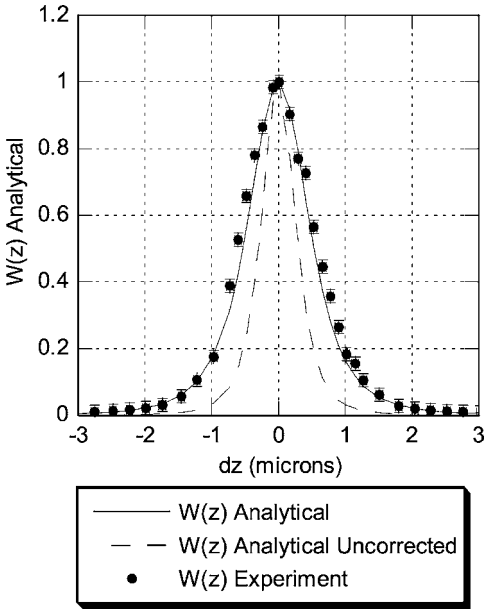

Fig. 2 Comparison of the weighting function from Eqs. (1) and (4) to experimental data for $M=40$, NA=1.25 oil immersion objective

three-dimensional diffraction pattern of a point source deviates from a Gaussian shape, this difference does not appear to affect the results. This occurs because the Gaussian and Lommel-generated particle images do not significantly deviate in appearance until the separation from focus is large enough that the particles are no longer significantly contributing to the weighting function.

In order to verify the performance of the depth of correlation model for high numerical aperture and magnification oil immersion optics, experiments to measure the weighting function were performed using 40×, NA 1.25 and 63×, NA 1.4 imaging optics. The results of these experiments are displayed in Figs. 2 and 3,

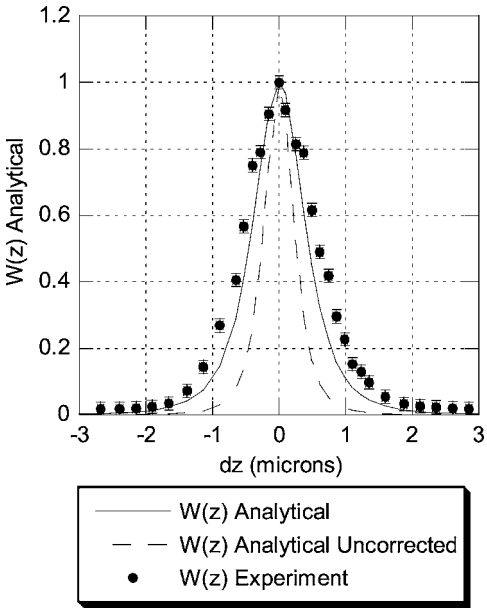

Fig. 3 Comparison of the weighting function from Eqs. (1) and (4) to experimental data for $M=63$, NA=1.4 oil immersion objective

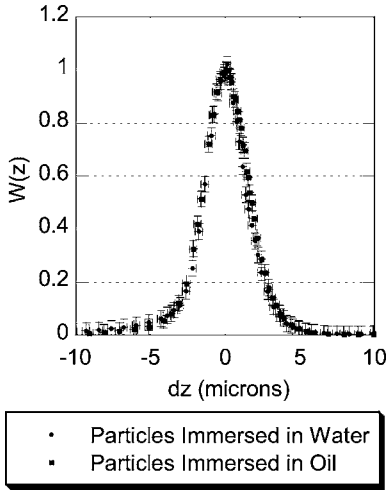

Fig. 4 Comparison of the weighting function from experimental data for $M=20$, NA=0.7 oil immersion objective viewing particles immersed in either water or oil

along with the weighting function both with the proposed correction for oil immersion objectives (Eq. (4)) and without the correction (Eq. (1)). The particles in these cases are adsorbed onto a glass substrate and imaged directly through the oil immersion medium. These results demonstrate quite clearly that the light collection half-angle, and not the numerical aperture, is the appropriate variable for use in determining the depth of correlation. If the corrections in Eqs. (4) and (5) were not applied, the analytical estimate of the depth of correlation would be significantly shallower.

Figure 4 presents the weighting function derived from viewing particles adsorbed onto a microscope slide through a thin layer (50 μm thick) of water trapped between a coverslip and glass slide, and viewed with a $M=20$, NA=0.7 oil immersion lens in comparison to data taken through oil only. There appears to be virtually no difference between the two datasets. It must be noted, however, that the images appeared to be significantly dimmer when viewing through the thin layer of water. These results agree with previously reported results [4] that showed no measurable difference in the weighting function between data taken with a 20×, NA=0.37 objective imaging particles through air and through immersion oil. These results show that, while the image quality and the measurement location are affected by the measurement medium, the depth of correlation is not influenced and Eq. (4) is applicable.

Conclusions

These results lead to three major conclusions.

(1) The Gaussian particle image assumption leads to minimal error in the ability of the analytical model of the depth of correlation to correctly capture the shape of the weighting function. This occurs because the cross correlation of the three-dimensional diffraction pattern generated by a particle only differs from that generated by an approximate Gaussian particle image once the particles are no longer significantly contributing to the weighting function.

(2) If the collection angle is used rather than the numerical aperture in the analytical model, the model correctly estimates the weighting function and depth of correlation for micro-PIV using oil immersion lenses.

(3) The shape of the weighting function and depth of correlation for micro-PIV measurements do not seem to be changed when observing into a differing index of refraction medium than

the immersion medium of the objective. This was seen for both the oil-water case (shown here) and for air-oil cases (shown previously).

Acknowledgment

This work was funded by Sandia Engineering Sciences Research Foundation. Sandia is a multiprogram laboratory operated by Sandia Corporation, a Lockheed-Martin Company, for the United States Department of Energy under Contract No. DE-AC04094AL85000. Additionally, a portion of this work was supported by the National Science Foundation under Grant No. CTS-0134469.

References

[1] Olsen, M. G., and Adrian, R. J., 2000, "Out-of-Focus Effects on Particle Image Visibility and Correlation in Microscopic Particle Image Velocimetry," Exp. Fluids, **29**, pp. S166–S174.
[2] Olsen, M. G., and Adrian, R. J., 2000, "Brownian Motion and Correlation in Particle Image Velocimetry," Opt. Laser Technol., **32**, pp. 621–627.
[3] Olsen, M. G., and Bourdon, C. J., 2003, "Out-of-Plane Motion Effects in Microscopic Particle Image Velocimetry," ASME J. Fluids Eng., **125**, pp. 895–901.
[4] Bourdon, C. J., Olsen, M. G., and Gorby, A. D., 2004, "Validation of Analytical Solution for Depth of Correlation in Microscopic Particle Image Velocimetry," Meas. Sci. Technol., **15**(2), pp. 318–327.
[5] Meinhart, C. D., and Wereley, S. T., 2003, "The Theory of Diffraction-Limited Resolution in Microparticle Image Velocimetry," Meas. Sci. Technol., **14**, pp. 1047–1053.
[6] Born, M., and Wolf, E., 1997, *Principles of Optics*, Pergamon, Oxford.

Stokes Drag on a Thin Circular Disk Moving Edgewise Midway Between Parallel Plane Boundaries

Jeffrey F. Trahan
Department of Physics,
Centenary College of Louisiana,
Shreveport, Louisiana 71134
e-mail: jtrahan@centenary.edu

Introduction

This technical brief presents experimental results for the drag on a circular disk moving at terminal velocity through a viscous fluid midway between parallel plane walls. The axis of the disk is oriented perpendicularly to these walls. The notation is shown in Fig. 1. A circular disk of diameter d and thickness t moves edgewise with a velocity U through a viscous fluid of density ρ and viscosity μ midway between two plane walls that are parallel to the plane of the disk. The distance between the parallel walls is D. Define the aspect ratio of the disk as $A=t/d$ and the Reynolds number as $\mathrm{Re}=d\rho U/\mu$. I will assume that the flow is a Stokes flow ($\mathrm{Re}\ll 1$) and that the disks are thin ($A\ll 1$).

In an infinite fluid, the drag on a disk of zero thickness moving edgewise is the Stokes drag F_S given by Overbeck [1]

$$F_S = 16\mu U d/3 \tag{1}$$

For a finite fluid, the drag F is greater than F_S due to the influence of the boundaries. It is customary to use the symbol K for the ratio F/F_S, so $K\geqslant 1$. The first-order boundary effect has been obtained by Brenner [2]

$$K_B^{-1} = 1 - k\frac{16}{9\pi}\frac{d}{D} \tag{2}$$

where, for this geometry, $k=1.004$.

In the real experimental situation, the liquid is contained in a rectangular glass tank as shown in Fig. 2. The disk is released from rest just below the free surface of the liquid and falls in the vertical plane toward the bottom of the tank. Measurements of the velocity of the disk are made midway between the free surface and the bottom of the tank. Because the flow is steady, $F_S/F = U/U_S = K^{-1}$, where U is the velocity of the disk, and where

$$U_S = \frac{3g}{16\mu d}\left(m - \frac{\rho t\pi d^2}{4}\right) \tag{3}$$

In this expression m is the mass of the disk and g is the acceleration due to gravity. This expression was obtained by equating the Stokes drag F_S given by Eq. (1) to the apparent weight of the disk falling in the fluid. Thus, U_S is the velocity of a disk of zero thickness in an unbounded fluid subject to the same drag $mg - (\rho d^2 t\pi/4)g$ as the experimental disk.

This work has been done to test the theoretical calculations of Davis [3] who calculated the drag on thin rigid disks moving steadily in a viscous fluid bounded by plane walls parallel to the motion of the disk. Through private communication, Davis also provided values of the dimensionless drag for values of d/D down to 0.0333. The results of the present experiment will be compared with the results of Davis' theoretical calculations.

I report here observations of thin circular disks falling edgewise midway between parallel plane walls in a rectangular tank filled with silicone oil. The observations cover the range of parameters: $0.0025<A<0.0759$, $0.1623<d/D<3.890$, and $0.0048<\mathrm{Re}<0.11$.

Contributed by the Fluids Engineering Division of ASME for publication in the JOURNAL OF FLUIDS ENGINEERING. Manuscript received August 1, 2005; final manuscript received December 8, 2005. Review conducted by Joseph Katz.

Experiment

Disks were released from rest in a silicone liquid contained in a glass-walled tank of rectangular cross section. The tank was constructed with a rectangular base 61.7×31.45 cm^2 (inside dimensions) and was filled to a depth of 41 cm. The axis of the disk was always oriented perpendicularly to the plane of the long sidewalls of the tank. The distance between the long sidewalls D was adjustable. The dropping mechanism used to release the disks was a tweezers mounted on a firm support above the tank. The disk was held vertically in the fluid by the tweezers and was released by opening the tweezers slowly with a screw mechanism. The disks were centered between the sidewalls before release by visually lining them up between vertical lines accurately drawn on the end walls of the tank midway between the sidewalls. Disks released in this way were observed to fall stably and vertically to the bottom of the tank. All but very thin disks stood on edge midway between the sidewalls when reaching the bottom. Disks purposely released off center were unstable and wobbled back and forth between the sidewalls while falling to the bottom. The velocity of the disks was measured by the time of flight between two horizontal, focused laser beams separated by 5.00 cm, situated midway between the top and bottom surfaces of the fluid.

The temperature dependences of both the kinematic viscosity and the fluid density were measured and used to correct the velocities under the assumption that the product μU was constant. All of the velocities were adjusted to a temperature of 22.00 °C, at which the kinematic viscosity was 41.40 cm^2/s and the density was 0.971 g/cm^3. All measurements were made with the oil temperature 22.00 ± 1.08 °C.

Fifty-six disks were made from aluminum, brass, and steel. The disk thickness t ranged from 0.007 87 to 0.1567 cm, the diameter d ranged from 1.265 to 4.991 cm, and the mass m ranged from 0.0766 to 6.295 g. The distance D between the parallel sidewalls ranged from 1.28 to 7.81 cm.

The total experimental error in the measured values of the dimensionless drag K was calculated by assuming reasonable experimental errors in each of the measured quantities that contributed to the final error in K. The results of these calculations show that the experimental error in K is less than 1.5% of K for all measurements. The experimental results are presented in Fig. 3, which shows a graph of the dimensionless drag K on the disks versus the aspect ratio t/d. The error in each measurement is smaller than the symbol size used to display the results. In addition, most of the data points are the result of several measurements, the results of which were averaged. The technique used in this experiment for measuring the drag on falling disks at a very low Reynolds number has been thoroughly tested by measuring the drag on falling spheres. For Reynolds numbers less than 0.15, the dimensionless drag on spheres was measured to be within 0.50% of the value predicted by the analytical expression $K=1+(3/16)\mathrm{Re}$ of Oseen [4] for the drag, where K is the ratio of the drag on the sphere to the Stokes drag.

Results

Roger used the beads-on-a-shell model (BOS) [5] to calculate the dimensionless drag on cylinders with aspect ratios ranging from 0.005 13 to 10.0 moving perpendicularly to their axes in an infinite viscous fluid. These results were reported in Ref. [6] in which the authors presented two empirical relationships that fit the calculated points well. Because the BOS calculations for which $d/D=0$ fit an equation of the form $K=B(t/d)^C$, where B and C are constants, it seemed reasonable that the experimental results of this experiment, for which d/D is small, would fit a similar func-

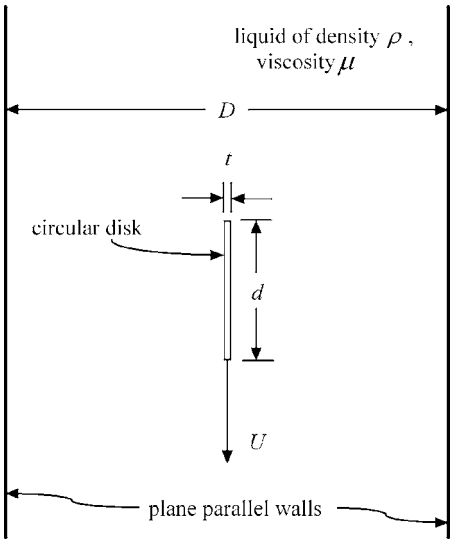

Fig. 1 Notation

tion but where the constants B and C would depend on d/D. The resulting empirical expression that fits the data is

$$K = A + B\left(\frac{t}{d}\right)^C \tag{4}$$

The functions A, B, and C in Eq. (4) depend on d/D as follows

$$A = 1 + a\left(\frac{d}{D}\right)^b, \quad B = \left(f + g\frac{d}{D}\right)^2, \quad C = 1 - ke^{-p(d/D)} \tag{5}$$

The constants in Eq. (5) have values $a=0.8160$, $b=1.0754$, $f=1.0418$, $g=1.3312$, $k=0.2269$, and $p=1.51$. This fit to the data is shown in Fig. 3 as solid curves passing through the data points.

The data can now be extrapolated to find the dimensionless drag on disks moving edgewise in an infinite fluid by setting $d/D=0$ in Eqs. (4) and (5). The results are shown in Fig. 3, where the solid line for $d/D=0$ clearly passes through the three data points calculated by Roger using the beads-on-a-shell calculation.

The dimensionless drag on infinitely thin disks moving midway between parallel plane walls K_0 can be found by letting $t/d \to 0$ in Eqs. (4) and (5). The result is

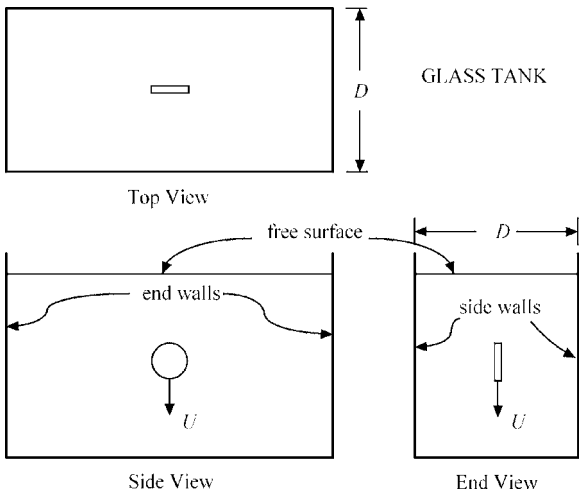

Fig. 2 Geometry of the real problem: a circular disk of thickness *t* and diameter *d* falls vertically in a tank filled with viscous liquid between sidewalls spaced a distance *D* apart

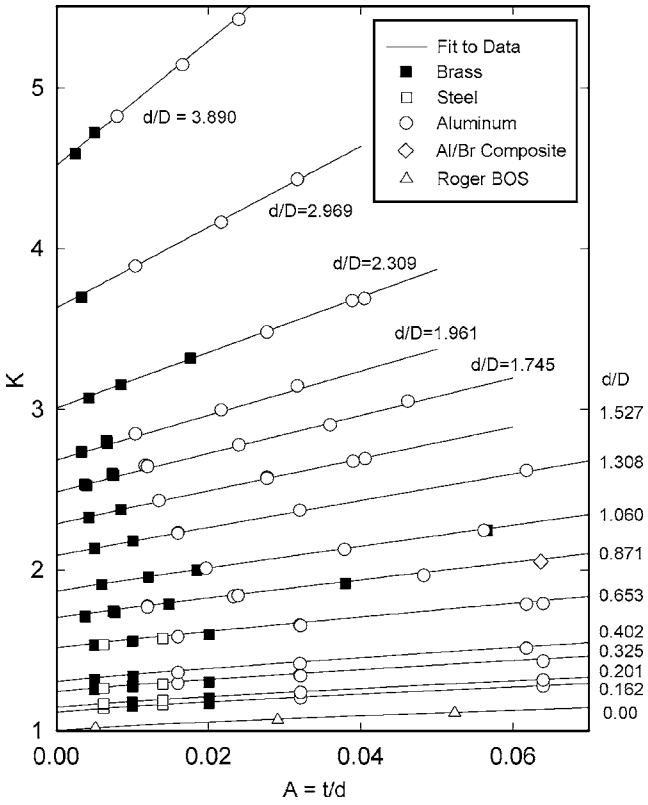

Fig. 3 Dimensionless drag vs the aspect ratio of the disks. The symbols that are circles or squares represent the different types of disk materials, the triangular symbols are the results of the theoretical beads-on-a-shell calculations for disks in an infinite fluid, and the solid lines follow the empirical fit to the data.

$$K_0 = 1 + a\left(\frac{d}{D}\right)^b \tag{6}$$

where the constants a and b are given above. Figure 4 shows this result and theoretical calculations of Davis [4] and Brenner [2]. The experimental results, designated by open circles in Fig. 4, agree very well with the calculations of Davis over the entire range of experimental measurements. The first-order boundary effect of Brenner agrees with the experimental observations within 1% provided $d/D<0.5$. This is expected since this expression is a first-order approximation and will only be valid if the distance to the walls is large compared to the dimensions of the object. In a private communication, Davis calculated an additional term to Brenner's expression. The result is

$$K_{DB}^{-1} = 1 - 0.5682\left(\frac{d}{D}\right) + 0.2327\left(\frac{d}{D}\right)^3 \tag{7}$$

and is shown as the dashed curve in Fig. 4. The Davis-Brenner result as expressed in Eq. (7) agrees with the experimental observations within 1% if $d/D<0.65$.

I have assumed that the end walls, the free surface, and the bottom wall are far enough away so that they do not influence the dimensionless drag on the disk at the position where the drag is measured midway between the free surface and the bottom wall. This assumption was tested and shown to be valid for the experimental parameters used by measuring the velocities of disks as a function of position as they fell between the two sidewalls with a photographic strobe technique described in previous papers by Trahan and Hussey [7] and Trahan, Wehbeh, and Hussey [8]. Also, the use of disks with twice the value of D but the same

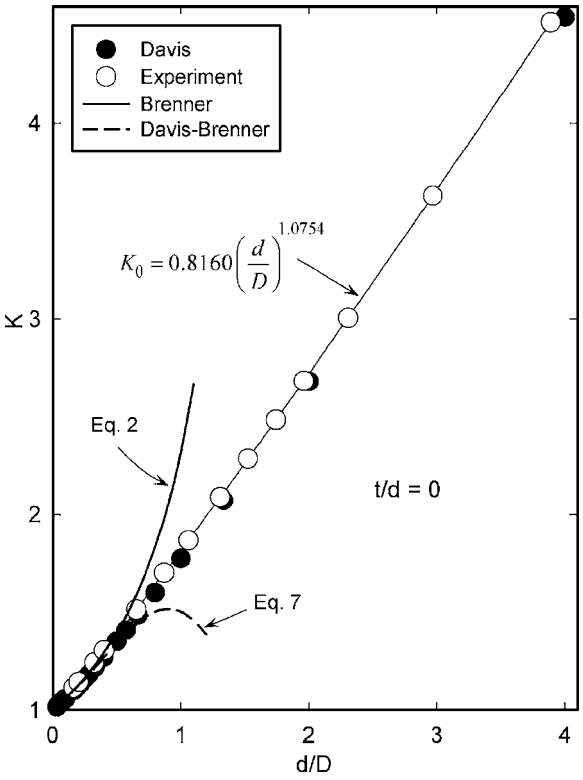

Fig. 4 Comparison of the theoretical and experimental dimensionless drag K for infinitely thin disks of diameter d falling edgewise midway between parallel walls spaced a distance D apart. The equation for K_0 is Eq. (6). It is an empirical equation obtained from the experimental data.

value of d/D gave the same values of K as a function of t/d, showing that the effects of end walls and the distance to the bottom and the top are negligible.

Conclusions

The results of measurements have been presented for the drag on thin circular disks as they move edgewise midway between two parallel plane boundaries at very low Reynolds number. An empirical expression presented in Eqs. (4) and (5) has been devised to accurately represent the results of this experiment. First, the dimensionless drag was compared with the idealized case of a disk of zero thickness. After empirical extrapolation to zero thickness, the experimental results are in good agreement with the theoretical prediction of Brenner [2] provided d/D is sufficiently small, and in very good agreement with the calculations of Davis [3]. When the experimental values are extrapolated to an infinite fluid, the results are in good agreement with the beads-on-a-shell calculations of Roger (Trahan, Hussey, and Roger [6] and Ui, Hussey, and Roger [9]). Thus, this work confirms experimentally the theoretical work of Davis [3] on infinitely thin disks falling midway between parallel walls and agrees with the work of Roger's beads-on-a-shell calculations of the drag on disks of finite thickness falling edgewise in infinite fluid. In addition, this work extends the knowledge of the drag on disks to disks of finite thickness moving midway between parallel plane walls.

Acknowledgment

The author expresses thanks to Prof. Greg Hussey, Prof. Anthony Davis, and Prof. Raymond Folse for helpful discussions of this work.

References

[1] Oberbeck, H. A., 1876, "Ueber Stationäre Flussigkeitsbewegung mit Berucksichtigung der Inneren Reibung," J. Reine Angew. Math., **81**, pp. 62–80.
[2] Brenner, H., 1962, "Effect of Finite Boundaries on the Stokes Resistance of an Arbitrary Particle," J. Fluid Mech., **12**, pp. 35–48.
[3] Davis, A. M. J., 1991, "Slow Viscous Flow due to Motion of an Annular Disk; Pressure-Driven Extrusion Through an Annular Hole in a Wall," J. Fluid Mech., **231**, pp. 51–71.
[4] Oseen, C. W., 1913, "Über den Gültigkeitsbereich der Stokesschen Widerstandsformel. Arkiv Matem," Ark. Mat., Astron. Fys., **9**, Article No. 16, pp. 1–15.
[5] Roger, R. P., and Hussey, R. G., 1982, "Stokes Drag on a Flat Annular Ring," Phys. Fluids, **25**, pp. 915–922.
[6] Trahan, J. F., Hussey, R. G., and Roger, R. P., 1999, "The Velocity of a Circular Disk Moving Edgewise in Quasi-Steady Stokes Flow Toward a Plane Boundary," Phys. Fluids, **11**, pp. 2463–2469.
[7] Trahan, J. F., and Hussey, R. G., 1985, "The Stokes Drag on a Horizontal Cylinder Falling Toward a Horizontal Plane," Phys. Fluids, **28**, pp. 2961–2967.
[8] Trahan, J. F., Wehbeh, E. G., and Hussey, R. G., 1987, "The Limits of Lubrication Theory for a Disk Approaching a Parallel Plane Wall," Phys. Fluids, **30**, pp. 939–943.
[9] Ui, T. J., Hussey, R. G., and Roger, R. P., 1984, "Stokes Drag on a Cylinder in Axial Motion," Phys. Fluids, **27**, pp. 787–795.